

Influence of geometrical imperfections and flaws at welds of steel liners on fatigue behavior of pressure tunnels and shafts in anisotropic rock

THÈSE N° 7305 (2017)

PRÉSENTÉE LE 3 MARS 2017

À LA FACULTÉ DE L'ENVIRONNEMENT NATUREL, ARCHITECTURAL ET CONSTRUIT
LABORATOIRE DE CONSTRUCTIONS HYDRAULIQUES
PROGRAMME DOCTORAL EN GÉNIE CIVIL ET ENVIRONNEMENT

ÉCOLE POLYTECHNIQUE FÉDÉRALE DE LAUSANNE

POUR L'OBTENTION DU GRADE DE DOCTEUR ÈS SCIENCES

PAR

Alexandre Jean PACHOUD

acceptée sur proposition du jury:

Prof. K. Beyer, présidente du jury
Prof. A. Schleiss, Dr P. F. De Almeida Manso, directeurs de thèse
Dr O. Chène, rapporteur
Prof. G. Anagnostou, rapporteur
Prof. A. Nussbaumer, rapporteur



ÉCOLE POLYTECHNIQUE
FÉDÉRALE DE LAUSANNE

Suisse
2017

[...] if we do discover a complete theory, it should in time be understandable in broad principle by everyone, not just a few scientists. Then we shall all, philosophers, scientists, and just ordinary people, be able to take part in the discussion of the question of why it is that we and the universe exist. If we find the answer to that, it would be the ultimate triumph of human reason – for then we would know the mind of God.

— Stephen Hawking, in *A Brief History of Time*, 1988.



Abstract

The recent development of high-strength (HSS) weldable steels has enlarged the range of design alternatives for the optimization of high-head steel-lined pressure tunnels and shafts (SLPT&S) in the hydropower industry. With the liberalization of the European energy market and increasing contribution of new renewable volatile energies in the electricity grid due to high subsidies, storage hydropower and pumped-storage plants are subject to more and more severe operation conditions resulting in more frequent transients. The use of HSS allows the design of thinner and thus more economic steel liners. However, welded HSS do not provide higher fatigue resistance than lower steel grades, and may be particularly subject to the risk of cold cracking in the weld material as dramatically illustrated by the failure of the Cleuson–Dixence pressure shaft in 2000. Fatigue behavior may become the leading limit state criterion.

This research project aims at improving the comprehension of the mechanical behavior of SLPT&S and at developing a framework for probabilistic fatigue crack growth and fracture assessment of crack-like flaws in the weld material of longitudinal butt welded joints, considering all possible steel grades for high-head hydropower schemes.

The influence of anisotropic rock behavior and geometrical imperfections at the longitudinal joints on the structural stresses have been studied by means of the finite element method accounting for the interaction with the backfill concrete–rock multilayer system. Parametric correction factors have been derived to estimate stress concentrations and structural stresses in steel liners with ease in practice, allowing the use of S – N based engineering fatigue assessment approaches. Stress intensity factors (SIF) for axial cracks in the weld material of the longitudinal joints have also been obtained by means of computational linear elastic fracture mechanics (LEFM). The use of the previously developed parametric equations in the classical formulas for SIF in cracked plated structures has been validated, and new parametric equations for the weld shape correction have been proposed.

A probabilistic model for fatigue crack growth assessment has been developed in the framework of LEFM in combination with the Paris–Erdogan law. The probability of failure is estimated by means of the Monte Carlo simulation procedure, in which the crack growth rate parameters

Abstract

and the crack shape ratio are defined as stochastic variables. A week-long normalized loading spectrum derived from prototype measurements on an alpine pumped-storage hydropower plant in Switzerland is used. This approach provides relative and quantitative results through parametric studies, giving new insights on the fatigue behavior of steel liners containing cracks in the weld material of the longitudinal joints.

Finally, a fatigue assessment case study is presented, detailing the entire calculation procedures developed in this research. It aims at ensuring the transfer of knowledge toward practitioners.

KEYWORDS: *steel liners, pressure tunnels and shafts, finite element method, anisotropy, welded joints, stress concentration factors, stress intensity factors, linear elastic fracture mechanics, variable amplitude loading, probabilistic fatigue crack growth.*

Résumé

Le développement des aciers à haute-résistance (HSS, high-strength steel) ainsi que des turbines Pelton à haute-chute ont permis le dimensionnement de puits et tunnels blindés (SLPT&S, steel-lined pressure tunnels and shafts) sous haute pression. La conjonction de la libéralisation du marché européen de l'énergie et de l'augmentation de la contribution des énergies renouvelables volatiles dans le réseau électrique soumet les aménagements hydroélectriques, particulièrement de pompage-turbinage, à des événements transitoires de plus en plus sévères (coups de bélier). L'utilisation des HSS permet de dimensionner des blindages plus fins et donc plus économiques. Cependant, les HSS soudés ne présentent pas une meilleure résistance à la fatigue que les nuances plus basses, et sont par ailleurs soumis à un risque plus élevé de fissuration à froid. Cela fut dramatiquement illustré par l'accident de Cleuson–Dixence en 2000. Dans ce contexte, le comportement à la fatigue peut devenir l'état limite ultime prépondérant pour le dimensionnement.

Ce projet de recherche a pour but d'améliorer la compréhension du comportement mécanique des SLPT&S ainsi que de développer un cadre d'application pour une approche probabiliste de la propagation de fissures situées dans le cordon de soudure des joints longitudinaux des blindages, jusqu'à la rupture.

L'influence du comportement anisotrope du rocher ainsi que des imperfections géométriques dans le blindage, et plus particulièrement aux soudures longitudinales, a été étudiée par la méthode des éléments finis, en tenant compte de l'interaction entre le blindage et le système béton–rocher. Des facteurs de correction ont été dérivés afin d'estimer avec facilité dans la pratique les concentrations de contrainte ainsi que les contraintes structurelles dans le blindage. Ces résultats peuvent être utilisés pour appliquer les approches locales de vérification à la fatigue basées sur les courbes $S-N$. Les facteurs d'intensité de contrainte (SIF, stress intensity factor) pour des fissures axiales dans les cordons de soudures longitudinales ont également été étudiés par la méthode des éléments finis appliquée à la mécanique de la rupture linéaire élastique (LEFM, linear elastic fracture mechanics). L'utilisation des expressions analytiques précédemment développées dans les solutions classiques pour les SIF dans les plaques soudées contenant des fissures a été vérifiée. Enfin, des facteurs de correction afin de considérer l'influence du profil de soudure ont été proposés.

Résumé

Un modèle probabiliste pour la propagation de fissures a été développé dans le cadre de la LEFM en combinaison avec la loi de Paris–Erdogan. La probabilité de rupture a été estimée par la méthode de simulation de Monte Carlo, dans laquelle les paramètres de l’acier liés au taux de propagation ainsi que la géométrie des fissures ont été définis de façon stochastique. Un spectre de chargement adimensionnel lors d’une semaine type d’opération a été déterminé grâce à des mesures effectuées dans un aménagement de pompage-turbinage dans les Alpes suisses. Cette approche a permis d’obtenir des résultats relatifs et quantitatifs à travers des études paramétriques, donnant de nouvelles indications sur le comportement à la fatigue des blindages contenant des fissures dans les cordons de soudures longitudinaux.

Enfin, un cas d’étude d’évaluation à la fatigue a été présenté. L’entière procédure de calcul développée dans cette recherche y est présentée, avec pour but d’assurer le transfert de connaissance vers la pratique.

MOTS CLÉS : *revêtements en acier, tunnels et puits en charge, méthode des éléments finis, anisotropie, joints soudés, facteurs de concentration de contrainte, facteurs d’intensité de contrainte, mécanique de la rupture linéaire élastique, chargement à amplitude variable, propagation probabiliste de fissures de fatigue.*



Zusammenfassung

Wasserkraftwerke mit grossen Fallhöhen und Pelton-turbinen haben meist mit hochbelastbarem Stahl ausgekleidete Druckstollen und Schächte (SLPT&S, steel-lined pressure tunnels and shafts). Für diese Stahlpanzerung kommt vermehrt hochfester (HSS, high-strength steel) schweisssbarer Stahl zum Einsatz. Mit der Liberalisierung des europäischen Strommarktes und dem steigenden Anteil an stark volatilen neuen erneuerbaren Energien im Elektrizitätsnetz, gefördert durch hohe Subventionen, änderten sich die Betriebsbedingungen für Speicherkraftwerke und Pumpspeicherwerke. Mittlerweile stellen diese vermehrt die Netzstabilität sicher. Die Verwendung von HSS ermöglicht dünnere und somit günstigere Stahlpanzerungen. Jedoch verbessert HSS die Materialermüdung nicht, wenn verglichen mit Stahl von geringerer Qualität. Deshalb kann ein erhöhtes Risiko der Kaltrissanfälligkeit auftreten. Der dramatische Panzerungsbruch im Kraftwerk Cleuson-Dixence im Jahre 2000 veranschaulicht dies. Materialermüdung kann ein limitierendes Kriterium bei HSS sein kann.

Dieses Forschungsprojekt hat zum Ziel, das mechanische Verhalten von SLPT&S besser zu verstehen. Des weiteren soll ein Probabilistisches Modell der Ausbreitung von Materialermüdungsrissen und eine Bruchbeurteilung von rissartigen Imperfektionen im Schweissmaterial von stumpfgeschweissten Längsnähten entwickelt werden.

Der Einfluss von anisotropem Felsverhalten sowie geometrischen Mangelhaftigkeit von Längsnähten wurde mit der finite-Elemente Methode untersucht, welche die Interaktionen des Füllbetons mit den verschiedenen Felsschichten berücksichtigt. Für die Praxis hilfreich sind parametrische Korrekturfaktoren welche die Spannungskonzentrationen und strukturelle Belastungen in der Stahlpanzerung abschätzen. Das erlaubt die Verwendung von $S-N$ basierten, Ermüdungsansätzen. Spannungsintensitätsfaktoren (SIF, stress intensity factor) für axiale Risse im Schweissmaterial der Längsnähte wurden ebenfalls mittels rechnergestützter linear-elastischer Bruchmechanik (LEFM, linear elastic fracture mechanics) untersucht. Die vorgängig entwickelten parametrischen Gleichungen in den klassischen Formeln der SIF in gerissenen beschichteten Strukturen wurden validiert und neue parametrische Gleichungen für die Korrektur der Schweissnaht vorgeschlagen.

Ein Probabilistisches Modell der Ausbreitung von Rissen aufgrund Materialermüdung wurde mit LEFM in Kombination mit dem Paris-Erdogan Gesetz entwickelt. Die Versagenswahrschein-

Zusammenfassung

lichkeit wurde mit Hilfe des Monte Carlo Simulationsverfahrens, bei dem die Parameter der Rissausbreitungsrate und das Rissformverhältnis als stochastische Variablen definiert sind untersucht. Ein normalisiertes wöchentliches Belastungsspektrum wurde von Prototypmessungen eines Schweizer Pumpspeicherkraftwerks abgeleitet. Dieser Ansatz gab mittels Parameterstudien relative und quantitative Resultate, was einen vertieften Einblick in das Ermüdungsverhalten von Stahlpanzerungen mit Rissen im Schweissmaterial der Längsnähte gab.

Abschliessend wird eine Fallstudie zur Ermittlung der Materialermüdungsbewertung vorgestellt, welche die gesamte Berechnungsmethode, die im Rahmen dieser wissenschaftlichen Arbeit entwickelt wurde anwendet, und dies mit dem Ziel den Wissenstransfer in die Praxis zu gewährleisten.

STICHWÖRTER: *Stahlpanzerung, Druckstollen und Schächte, Finite Elemente Methode, Anisotropie, Schweissnähte, Spannungskonzentrationsfaktoren, Spannungsintensitätsfaktoren, linear-elastische Bruchmechanik, variable Belastungsamplituden, probabilistische Materialermüdungsrissausbreitung.*



Sommario

Lo sviluppo di materiali in acciaio saldabili ad alta resistenza (HSS, high-strength steel) e di turbine Pelton ad alta prevalenza ha portato alla progettazione di condotte forzate in pressione rinforzate con acciaio ad alta resistenza (SLPT&S, steel-lined pressure tunnels and shafts). Con la liberalizzazione del mercato energetico europeo e l'aumento di produzione elettrica ad opera di altre fonti rinnovabili non accumulabili, dovuta ai recenti finanziamenti, gli impianti di produzione idroelettrica sono soggetti a sempre più numerose e difficili condizioni di produzione caratterizzate da sempre più importanti e frequenti transitori idraulici. L'uso di materiali in acciaio ad alta resistenza consente la realizzazione di condotte di minor spessore e di conseguenza più economiche. Tuttavia, rispetto ad acciai di minor qualità, gli acciai saldabili ad alta resistenza non offrono maggiore resistenza alla fatica e, in corrispondenza alla saldatura, potrebbero essere particolarmente soggetti al rischio di fratturazione a freddo come testimonia il drammatico incidente avvenuto nel 2000 nell'impianto Cleuson–Dixence. In questo contesto, il comportamento a fatica potrebbe rappresentare un limite nell'applicazione degli acciai saldabili ad alta resistenza.

Questo progetto di ricerca mira a migliorare la comprensione del comportamento meccanico di condotte forzate rinforzate con acciaio ad alta resistenza (SLPT&S) e a sviluppare un quadro di riferimento per la verifica probabilistica della propagazione a fatica delle fratture in corrispondenza dei giunti longitudinali.

L'influenza del comportamento anisotropico della roccia e delle imperfezioni geometriche in corrispondenza dei giunti longitudinali è stata studiata grazie a metodi agli elementi finiti considerando l'interazione con il riempimento multistrato in cemento e roccia. Sono stati derivati fattori di correzione parametrici utili per ottenere una semplice e pratica stima della concentrazione e dell'entità degli sforzi strutturali, utilizzando per la verifica a fatica, metodi ingegneristici basati su curve $S-N$. Secondo le leggi di meccanica lineare elastica della frattura, sono stati studiati i fattori di intensità dello sforzo (SIF, stress intensity factor) in fratture assiali in corrispondenza dei giunti longitudinali. È stato validato l'uso delle equazioni parametriche precedentemente utilizzate nel calcolo dei fattori di entità dello sforzo (SIF) in strutture piane fratturate. Sono state proposte nuove equazioni parametriche relative alla geometria delle saldature.

È stato sviluppato un modello probabilistico per la verifica della propagazione della frattura

Sommario

a fatica secondo la legge di Paris–Erdogan nell’ambito della meccanica lineare elastica. La probabilità di rottura è stata stimata grazie alla procedura statistica di Monte Carlo in cui la rapidità di propagazione della frattura e il coefficiente di forma della frattura sono definite come variabili stocastiche. Uno spettro normalizzato di carico è stato derivato in seguito a una settimana di misure in un prototipo di impianto idroelettrico nelle alpi Svizzere. Tale approccio, grazie a studi parametrici, ha fornito risultati relativi e quantitativi fornendo nuove nozioni sul comportamento a fatica di condotte forzate caratterizzate da fessure in corrispondenza delle saldature dei giunti longitudinali.

Infine è stata effettuata la verifica di un caso studio che presenta nel dettaglio le procedure di calcolo sviluppate in questa tesi. Essa assicura l’applicazione delle nozioni teoriche acquisite in ambito pratico.

PAROLE CHIAVE: *condotte forzate, tunnele pozzi in pressione, metodo agli elementi finiti, anisotropia, giunti saldati, fattori di concentrazione degli sforzi, fattori di intensità degli sforzi, meccanica lineare elastica della frattura, carico di ampiezza variabile, propagazione probabilistica della frattura a fatica.*

Contents

Abstract (English/Français/Deutsch/Italiano)	i
Contents	ix
List of figures	xvii
List of tables	xxv
Nomenclature	xxvii
1 Introduction	1
1.1 Context of hydropower and recent developments of high-head hydroelectric power plants	1
1.2 Problem statement	3
1.2.1 Sensitivity of high-strength steels	3
1.2.2 Interaction with the concrete–rock system	3
1.2.3 Requirements for fatigue assessment by means of local stresses approaches	3
1.2.4 Requirements for fatigue assessment by means of the fracture mechanics approach	4
1.2.5 Justification for a probabilistic approach for fatigue crack growth	4
1.3 Objectives and practical relevance of the research project	5
1.4 Finite element method (FEM)	6
1.5 Structure and methodology of the study	6
1.6 Project framework	8
I Literature review	11
2 Steel-lined pressure tunnels and shafts	15
2.1 Axisymmetrical multilayer model in isotropic rock	15
2.1.1 The steel liner	16
2.1.2 The initial gap	16
2.1.3 The backfill concrete	16
2.1.4 The near-field rock	16

Contents

2.1.5	The far-field rock	17
2.2	Closed-form solution in isotropic rock	17
2.2.1	Compatibility conditions	17
2.2.2	Displacements	19
2.2.3	Stresses	19
2.3	Basic design criteria	20
2.4	Pressure tunnels and shafts in anisotropic rock	22
2.5	High-strength steels for steel-lined pressure tunnels and shafts	22
2.5.1	High-strength steels (HSS)	22
2.5.2	Constructional aspects	25
2.6	Transient pressure phenomena	27
2.7	Changed operational conditions	32
2.8	New and innovative non-intrusive monitoring methods	33
2.8.1	Historical development	34
2.8.2	Water hammer signals	34
2.8.3	Actively generated cavitation bubble signals	35
2.8.4	Ranges of application	36
2.9	Conclusions	38
3	Fatigue and fracture assessment of welded joints	41
3.1	Introduction to fatigue	41
3.2	Fatigue assessment methods for welded steel structures	42
3.2.1	Nominal stress approach	42
3.2.2	Structural hot-spot stress approach	43
3.2.3	Effective notch stress approach	44
3.2.4	Fracture mechanics (crack propagation) approach	45
3.3	Damage and fatigue life calculation for variable amplitude loading	47
3.4	Theoretical background on fracture mechanics	49
3.4.1	Linear elastic fracture mechanics (LEFM)	49
3.4.2	Plasticity of the crack-tip	51
3.4.3	Elastic–plastic fracture mechanics (EPFM)	53
3.4.4	Fracture strength	55
3.5	Failure and fatigue assessment procedures	57
3.6	Reliability assessment	57
3.6.1	Probabilistic approaches in engineering	57
3.6.2	Probabilistic fracture mechanics	60
3.6.3	Monte Carlo simulation technique	61
3.7	Review of formulas for stress concentration factors at butt welded plates with linear misalignment	62
3.7.1	Decomposition of stress components	62
3.7.2	Definition of the stress concentration factors (SCF)	63
3.7.3	Structural SCF due to linear misalignment	64

3.7.4	Notch SCF due to weld shape	64
3.7.5	Comparison of published notch SCF equations	66
3.8	Review of formulas for structural stress concentration factors in steel cylindrical structures	67
3.9	Review of formulas for stress intensity factors for cracks in plates and shells . .	68
3.9.1	General formulation	68
3.9.2	Axial semi-elliptical surface cracks in plates	70
3.9.3	Axial embedded elliptical cracks in plates	71
3.9.4	Influence of the weld shape	71
3.10	Conclusions	72
II	Anisotropic rock behavior	73
4	Parametric study	77
4.1	Constitutive modeling of anisotropic rock	77
4.1.1	Definition of stress and strain vectors in the Cartesian coordinate system	78
4.1.2	Stress–strain relations in an orthotropic medium	78
4.1.3	Stress–strain relations in a transversely isotropic medium	79
4.1.4	Admissible values for the elastic constants	80
4.1.5	Ranges of properties of transversely isotropic rocks	80
4.2	Constitutive modeling of the cracked layers	81
4.3	Finite element model	82
4.3.1	Model	82
4.3.2	Nomenclature	83
4.3.3	Validation in isotropic rock	83
4.4	Parametric study	85
4.4.1	Preliminary discussion on the parameters	85
4.4.2	Set of calculation cases	86
4.4.3	Normalized results	86
4.4.4	Stresses and displacements in the steel liner	87
4.4.5	Stresses in the far-field rock	94
4.5	Discussion	102
4.6	Conclusions	103
5	Estimation of the maximum stresses	105
5.1	Derivation of correction factors to be included in the isotropic closed-form solution	105
5.1.1	Database	105
5.1.2	Derivation of the correction factors	105
5.1.3	Synthesis	108
5.2	Examples of application	110
5.2.1	Example 1	110
5.2.2	Example 2	110

Contents

5.3	Discussion	112
5.4	Conclusions	112
III Geometrical imperfections and weld profile at longitudinal butt welded joints of steel liners		115
6	Stress concentration at butt welded joints of straight plates	119
6.1	Finite element analysis	119
6.1.1	FE model description and hypotheses	119
6.1.2	Validation of the FE model	121
6.2	Parametric study	128
6.3	Parametric equations	129
6.4	Conclusions	133
7	Stress concentration at longitudinal butt welded joints of steel liners	137
7.1	Conceptual model	137
7.1.1	Types of geometrical imperfections	137
7.1.2	Global geometry	139
7.1.3	Local geometry of the longitudinal butt welded joints	140
7.2	Finite element model	141
7.2.1	Assumptions	141
7.2.2	Mesh	142
7.2.3	Validation for open-air steel liners (penstocks)	142
7.3	Parametric study	147
7.3.1	Parameters	147
7.3.2	Structural SCF in the steel liner	148
7.3.3	Pressure transmitted to the far-field surrounding rock mass	154
7.3.4	Remarks on the initial gap	154
7.4	Derivation of parametric equations	155
7.4.1	Structural SCF at the longitudinal butt welded joints for major principal stresses	156
7.4.2	Notch SCF at longitudinal butt welded joints for major principal stresses	158
7.4.3	Extrapolation to equivalent stresses	158
7.4.4	Application examples	160
7.5	Application limits	162
7.6	Conclusions	162
IV Crack-like flaws at longitudinal butt welded joints of steel liners		163
8	Stress intensity factors (SIF) for axial cracks in the weld material	167
8.1	Types of studied cracks	167

8.2	Definition of weld shape correction factor M_w for axial cracks at longitudinal butt welded joints of SLPT&S	170
8.2.1	Membrane and bending stresses in steel liners of pressure tunnels and shafts	170
8.2.2	Definition of weld shape correction factor M_w	171
8.3	Finite element model	172
8.3.1	Conceptual model	172
8.3.2	Assumptions of the FE model	173
8.3.3	Mesh	174
8.3.4	Evaluation of stress intensity factors	181
8.3.5	Normalization	181
8.3.6	Validation	182
8.3.7	Applicability of the analytical solutions	186
8.4	Parametric study	186
8.4.1	Semi-elliptical surface cracks	186
8.4.2	Embedded elliptical cracks	188
8.4.3	Commentaries on the results	188
8.5	Parametric equation to estimate the weld shape correction factor M_w for semi-elliptical surface cracks	196
8.6	Application limits	198
8.7	Conclusions	200
V	Fatigue assessment of steel liners under variable amplitude loading	203
9	Loading spectra	207
9.1	Introduction	207
9.2	Prototype measurements under normal operation conditions	208
9.3	Cycle-counting	208
9.4	Conclusions	211
10	Fatigue assessment with the effective notch stress approach	213
10.1	Effective notch stress approach	213
10.1.1	$S-N$ curves	213
10.1.2	Stress ranges	213
10.1.3	Linear damage calculation by means of the Palmgren–Miner rule	215
10.2	Parametric study	216
10.3	Results	218
10.4	Commentaries on the results	222
10.5	Conclusions	226

11 Probabilistic model for fatigue crack growth and fracture	227
11.1 LEFM approach for fatigue crack growth and fracture	227
11.1.1 Fatigue crack growth	227
11.1.2 Types of studied cracks	227
11.1.3 Failure criteria	230
11.1.4 Fracture toughness	230
11.2 Monte Carlo procedure	231
11.2.1 Stochastic variables	231
11.2.2 Deterministic model to compute ΔK	234
11.2.3 Flowchart of the procedure	237
11.2.4 Probability of failure and accuracy	239
11.3 Parametric study	240
11.4 Results	241
11.5 Discussion	243
11.6 Conclusions	249
12 Case study	251
12.1 Case description	251
12.2 Standard design with the working stress criterion	254
12.3 Fatigue assessment	255
12.4 Detailed example of the calculation of the crack growth for the k^{th} cycle	255
12.4.1 Compute $K_{\text{rm,aniso}}^*$ (Chapter 5)	256
12.4.2 Compute maximum and minimum membrane and bending stresses (Chapter 7)	257
12.4.3 Compute maximum and minimum stress intensity factors (Chapter 8) .	258
12.4.4 Compute the new crack size	263
12.5 Detailed example of the calculation of the k^{th} term of the cumulative damage sum	264
12.6 Results from the LEFM approach for fatigue propagation of cracks in the weld material	266
12.7 Conclusions	267
VI Conclusions	269
13 Conclusions	271
13.1 Summary and conclusions	271
13.2 Recommendations	274
13.3 Future research	274
A Mathematical model for geometrical imperfections of steel liners	279
A.1 Parameters and nomenclature	279
A.2 Rolled plates	281
A.3 Straight edges	283

A.4	Notches	284
A.4.1	Weld reinforcement $\delta > 0$	284
A.4.2	Weld reinforcement $\delta = 0$	285
A.4.3	Weld reinforcement $\delta < 0$	288
A.5	Control points for the weld profile	289
A.5.1	Internal weld surface	290
A.5.2	External weld surface	291
A.6	Splines for weld's profile in ANSYS® Mechanical™	293
A.7	Splines for weld's in MATLAB® for presentation purposes, using the NURBS Libraries (based on Dedè 2015 and Cottrell <i>et al.</i> 2009)	293
B	Stress intensity factors solutions	295
B.1	Axial semi-elliptical surface crack in plates subject to membrane and bending stresses ($a/c \leq 1$)	295
B.1.1	Membrane correction factor	295
B.1.2	Bending correction factor	296
B.2	Axial embedded elliptical crack in plates subject to membrane and bending stresses ($a/c \leq 1$)	297
B.2.1	Membrane correction factor	297
B.2.2	Bending correction factor	298
C	Lognormal distribution	299
D	Results from the Monte Carlo simulations conducted in Chapter 11	301
E	Results from the Monte Carlo simulations conducted in Chapter 12	315
	Bibliography	319
	Acknowledgments	347
	Curriculum Vitae	349

List of Figures

1.1	Longitudinal schematic view of a typical high-head power plant (head > 200 m) and sectional view of the standard multilayer system for steel-lined pressure tunnels and shafts. The relative dimensions are distorted for the sake of presentation.	2
1.2	Structure of the report.	7
1.3	Project objectives, main tasks and partners.	9
2.1	Definition sketch of the standard multilayer system for pressure tunnels and shafts embedded in elastic, isotropic rock mass (axisymmetrical case).	15
2.2	Flowchart of the conventional design procedure (after Schleiss 1988).	21
2.3	Qualitative examples of engineering stress–strain curves for different steel grades, with typical ultimate to yield strengths f_u/f_y ratios.	23
2.4	Cross section of longitudinal hydrogen induced cold crack in the weld deposit of steel grade S890 Q+T (modified after Cerjak <i>et al.</i> 2013a).	24
2.5	Examples of hydrogen induced cold cracks in the original material of the Cleuson–Dixence shaft (modified after Enzinger & Cerjak 2006, 2009).	25
2.6	Cleuson–Dixence: the accident of the 12th of December 2000 (from Hagin 2005).	26
2.7	Photographs taken at the Nant de Drance project in Switzerland (©A. J. Pachoud, 2016). The author acknowledges the authorization provided by ANDRITZ and Nant de Drance to use these photographs herein.	30
2.8	Computation model used for the frequency-dependent wave speed: (a) transverse profile and (c) longitudinal profile (figures from Hachem & Schleiss 2011c).	31
2.9	Number of cumulated annual starts of a typical high-head storage hydropower plant in Switzerland equipped with Francis turbines and multistage pumps (after Manso <i>et al.</i> 2016a).	33
2.10	Wave speeds in real SLPT&S (modified after Mazzocchi <i>et al.</i> 2016).	37
2.11	Theoretical ratios of wave transmission and reflection as a function of the ratio of the wave speed inside the weak reach $a_{\text{weak reach}}$ and the other stretches of the test pipe a_{steel} . The range of estimated possible values for SLPT&S are highlighted in gray (modified after Mazzocchi <i>et al.</i> 2016).	38
3.1	S–N curves for steel at constant amplitude loading (reproduced after Hobbacher 2016).	43

List of Figures

3.2	Modified S – N curves for steel at variable amplitude loading for Palmgren–Miner summation.	44
3.3	Typical behavior of fatigue crack growth in steels: log-log plot of crack growth rate da/dN versus stress intensity range ΔK	46
3.4	Some nomenclature in a cracked body (figure from Gross & Seelig 2011). . . .	50
3.5	Fracture modes (adapted from Gross & Seelig 2011).	50
3.6	Local coordinate system at crack-tip and example of an arbitrary counterclockwise path Γ around the crack-tip.	51
3.7	Crack-tip with first- and second-order estimates of plastic zone sizes r_y and r_p , respectively.	52
3.8	Qualitative representation of the effect of thickness on fracture toughness. . . .	56
3.9	Decomposition of the nonlinear stress profile in a butt welded joint with linear misalignment.	62
3.10	Notch SCF as a function of the flank angle β , estimated with the equations of Group 1. Legend: $(-\circ-)$ FEA; $(- \circ -)$ Eq. 3.41; $(-\triangle-)$ Eq. 3.42; and $(-\square-)$ Eq. 3.43.	67
3.11	Notch SCF as a function of the flank angle β , estimated with the equations of Group 2. Legend: $(-\circ-)$ FEA; $(- \times -)$ Eqs. 3.44–3.46; $(-\nabla-)$ Eq. 3.47; $(-\diamond-)$ Eq. 3.48; and $(-+-)$ Eq. 3.49.	68
4.1	Definition sketch of the standard multilayer system for pressure tunnels and shafts embedded in: (a) elastic, isotropic rock mass (axisymmetrical case); (b) transversely isotropic, elastic rock mass; and (c) transversely isotropic, elastic rock mass with two sets of discontinuities.	77
4.2	Example of a mesh of the FE model around the opening for $r_i = 2.0$ m, $t_s = 0.055$ m, $t_c = 0.50$ m and $t_{\text{crm}} = 0.70$ m.	84
4.3	Nomenclature used for the discussion of the results.	85
4.4	Maximum normalized major principal stresses in the steel liner $\hat{\sigma}_{1,\text{max}}^s$ as a function of the degree of anisotropy E/E' for different: (a) near-field rock thickness to steel liner's internal radius ratios t_{crm}/r_i ; (b) rock mass elastic modulus to steel elastic modulus ratios E/E_s ; and (c) cross-shear modulus to Saint-Venant empirical relation ratios $G'/G'_{\text{S-V}}$, and by varying the steel liner's thickness to the internal radius ratio t_s/r_i	88
4.5	Normalized major principal stresses in the steel liner $\hat{\sigma}_1^s$ at the internal and external fibers as a function of the angle θ with respect to the plane of isotropy for different: (a) near-field rock thickness to steel liner's internal radius ratios t_{crm}/r_i ; (b) rock mass elastic modulus to steel elastic modulus ratios E/E_s ; and (c) cross-shear modulus to Saint-Venant empirical relation ratios $G'/G'_{\text{S-V}}$, and by varying the steel liner's thickness to the internal radius ratio t_s/r_i and the degree of anisotropy E/E'	91

4.5	Normalized radial displacements at the internal fiber of the steel liner \hat{u}_r^s as a function of the angle θ with respect to the plane of isotropy for different: (a) near-field rock thickness to steel liner's internal radius ratios t_{crm}/r_i ; (b) rock mass elastic modulus to steel elastic modulus ratios E/E_s ; and (c) cross-shear modulus to Saint-Venant empirical relation ratios $G'/G'_{\text{S-V}}$, and by varying the steel liner's thickness to the internal radius ratio t_s/r_i and the degree of anisotropy E/E'	93
4.6	Maximum normalized major principal stresses in the far-field rock $\hat{\sigma}_{1,\text{max}}^{\text{rm}}$ as a function of the degree of anisotropy E/E' for different: (a) near-field rock thickness to steel liner's internal radius ratios t_{crm}/r_i ; (b) rock mass elastic modulus to steel elastic modulus ratios E/E_s ; and (c) cross-shear modulus to Saint-Venant empirical relation ratios $G'/G'_{\text{S-V}}$, and by varying the steel liner's thickness to the internal radius ratio t_s/r_i	95
4.6	Normalized major principal stresses in the far-field rock $\hat{\sigma}_1^{\text{rm}}$ at radius r_{rm} as a function of the angle θ with respect to the plane of isotropy for different: (a) near-field rock thickness to steel liner's internal radius ratios t_{crm}/r_i ; (b) rock mass elastic modulus to steel elastic modulus ratios E/E_s ; and (c) cross-shear modulus to Saint-Venant empirical relation ratios $G'/G'_{\text{S-V}}$, and by varying the steel liner's thickness to the internal radius ratio t_s/r_i and the degree of anisotropy E/E'	98
4.6	Normalized minor principal stresses in the far-field rock $\hat{\sigma}_3^{\text{rm}}$ at radius r_{rm} as a function of the angle θ with respect to the plane of isotropy for different: (a) near-field rock thickness to steel liner's internal radius ratios t_{crm}/r_i ; (b) rock mass elastic modulus to steel elastic modulus ratios E/E_s ; and (c) cross-shear modulus to Saint-Venant empirical relation ratios $G'/G'_{\text{S-V}}$, and by varying the steel liner's thickness to the internal radius ratio t_s/r_i and the degree of anisotropy E/E'	100
4.7	Normalized major principal stresses in the far-field rock shown up to $2r_{\text{rm}}$: (a) $\hat{\sigma}_1$ in the isotropic case; $\hat{\sigma}_1$ in the anisotropic case for cross-shear moduli ratios of (b) $G'/G'_{\text{S-V}} = 0.7$; (c) $G'/G'_{\text{S-V}} = 1.0$; and (d) $G'/G'_{\text{S-V}} = 1.3$	101
5.1	Regression plots of the normalized corrected maximum stresses $\hat{\sigma}_{\text{corr}}$ vs. the normalized numerical maximum stresses $\hat{\sigma}_{\text{num}}$ with $\alpha = \{-0.65, +0.50, -0.56\}$. The maximum (a) major principal stresses $\hat{\sigma}_{1,\text{corr}}^s$ and (b) equivalent stresses $\hat{\sigma}_{\text{eq,corr}}^s$ in the steel liner are represented for a test group of 10% of the 2000 cases. The maximum major principal stresses $\hat{\sigma}_{1,\text{corr}}^{\text{rm}}$ in the far-field rock are represented in (c) for all the 155 generated cases in which $G'/G'_{\text{S-V}} = 1$ and in (d) for all the 2000 cases.	107
6.1	Static scheme of the model.	119
6.2	Definition sketch of butt welded joints (a) without linear misalignment and (b) with linear misalignment e	120

List of Figures

6.3	Three examples of butt welded joints without linear misalignment with (a)–(b): a relatively low reinforcement height and a low flank angle; (c)–(d): a relatively large reinforcement height and a low flank angle; and (e)–(f): a relatively large reinforcement height and a large flank angle.	123
6.4	Three examples of butt welded joints with linear misalignment with (a)–(b): a relatively low reinforcement height and a low flank angle; (c)–(d): a relatively large reinforcement height and a low flank angle; and (e)–(f): a relatively large reinforcement height and a large flank angle.	125
6.5	Evaluation of the structural SCF K_m for different relative eccentricities e/t_s according to Eq. 6.2 (---), Eq. 6.3 (--) and Eqs. 6.4–6.5 (–); and for three different thicknesses $t_s = 20$ mm (○), $t_s = 35$ mm (+) and $t_s = 50$ mm (□). The theoretical values of K_m are evaluated according to Eq. 3.39 (– × –). . . .	126
6.6	Major principal stress profiles at different distances from the right weld toe (accordingly to Fig. 6.2), for a butt welded joint (a) without misalignment and (b) with misalignment. Parameters: $t_s = 20$ mm, $\rho = r_{\text{ref}} = 1$ mm, $\delta/t_s = 0.060$, $\beta = 30^\circ$, and $l_w = 13$ mm.	127
6.7	Notch SCF K_t as a function of flank angle β for three thicknesses t_s . Constant parameters: $\rho = r_{\text{ref}} = 1$ mm, $\delta/t_s = 0.060$, $e/t_s = 0.00$, and $\alpha = 90^\circ$. . .	129
6.8	Notch SCF K_t as a function of the weld toe radius ρ for three thicknesses t_s . Constant parameters: $\beta = 20^\circ$, $\delta/t_s = 0.040$, $e/t_s = 0.00$, and $\alpha = 60^\circ$. . .	129
6.9	Notch SCF K_t as a function of the relative weld reinforcement height δ/t_s for three thicknesses t_s . Constant parameters: $\beta = 20^\circ$, $\rho = r_{\text{ref}} = 1$ mm, $e/t_s = 0.00$ and $\alpha = 70^\circ$	129
6.10	Notch SCF K_t as a function of the edge preparation angle α for three thicknesses t_s . Constant parameters: $\beta = 25^\circ$, $\rho = r_{\text{ref}} = 1$ mm, $\delta/t_s = 0.055$ and $e/t_s = 0.00$	130
6.11	Notch SCF K_t as a function of the relative eccentricity e/t_s for three thicknesses t_s . Constant parameters: $\beta = 30^\circ$, $\rho = r_{\text{ref}} = 1$ mm, $\delta/t_s = 0.50$ and $\alpha = 60^\circ$. The corresponding structural SCF K_m are shown in Fig. 6.5.	130
6.12	Regression plots of the numerical SCF $K_{t,m}$ and K_t obtained by FEA vs. the empirical SCF fitted by GA.	133
6.13	Regression plots of the numerical SCF $K_{t,m}^{\rho=r_{\text{ref}}}$ and $K_t^{\rho=r_{\text{ref}}}$ obtained by FEA vs. the empirical SCF fitted by GA.	134
7.1	Definition sketch of the geometrical imperfections and the local butt welded joints' geometry at steel liners of pressure tunnels and shafts. The geometrical imperfections and the thickness of the liner are magnified for presentation purposes.	138
7.2	Sketches illustrating the boundary conditions of the model.	143
7.3	Example of a mesh in the vicinity of the longitudinal butt welded joint ($r_i = 2$ m, $t_s = 35$ mm, $\rho = 1$ mm, $\psi_\eta = 1.25$, $\psi_u = 2.00$, $\delta/t_s = 0.030$, $e/t_s = 0.061$, $\beta = 5^\circ$, $\alpha = 50^\circ$ and $\Delta r_0 = 0.025\% \cdot r_i$).	144

7.4	Structural SCF $K_{m,i}$ for open-air penstocks as a function of the nominal stress σ_{nom} for different: (a) out-of-roundness factors ψ_η ; (b) peaking factors ψ_u ; and (c) relative eccentricities e/t_s	146
7.5	Correction coefficient $K_{\text{rm},\text{aniso}}^*$ for embedded steel liners as a function of the degree of anisotropy E/E' for different lowest rock moduli E' , and for $\sigma_{\text{nom}} = 300$ MPa. 147	
7.6	Structural SCF from FEA as a function of the magnitude of the corresponding geometrical imperfections for different lowest rock moduli E' , and for $\sigma_{\text{nom}} = 300$ MPa.	149
7.7	Major principal stress profiles at weld toes in steel liners ($r_i = 1.5$ m and $t_s = 35$ mm) with out-of-roundness in open-air (a, b, c, d) and embedded in isotropic rock of elastic modulus $E = 5$ GPa (e, f, g, h). The gray solid lines (—) on the mean axis of the steel liners represent the length of the straight edges, and the gray dashed lines (- - -) are the circular internal and external fibers. The stress profiles are scaled so that $t_s/2$ represents the magnitude of the membrane stress σ_m in the xy plan.	151
7.8	Major principal stress profiles at weld toes in steel liners ($r_i = 1.5$ m and $t_s = 35$ mm) with peaking defects (a, b, c, d) and linear misalignment defects (e, f, g, h) considering the interaction with isotropic rock of elastic modulus $E = 5$ GPa. The gray solid lines (—) on the mean axis of the steel liners represent the length of the straight edges, and the gray dashed lines (- - -) are the circular internal and external fibers. The stress profiles are scaled so that $t_s/2$ represents the magnitude of the membrane stress σ_m in the xy plan.	153
7.9	Correction coefficient at far-field rock $K_{m,\eta}^{\text{rm}}$ as a function of the circumferential location θ for different out-of-roundness factors ψ_η	154
7.10	Regression plots of the numerical results vs. the empirical results fitted by GA.	157
7.11	Regression plots of the numerical results vs. the empirical results fitted by GA.	159
7.12	Numerical equivalent notch stresses $\sigma_{n,\text{eq}}^{\text{num}}$ obtained by FEA vs. the empirical $\sigma_{n,\text{eq}}^{\text{emp}}$ obtained via Eq. 7.22.	160
8.1	Definition sketch of the standard multilayer system for SLPT&S. The longitudinal butt welded joint is emphasized in the upper right corner, with an axial surface crack in the weld material.	167
8.2	Definition sketch of a steel liner with an axial semi-elliptical surface crack at the longitudinal butt welded joint, on the internal surface.	168
8.3	Definition sketch of a steel liner with an axial embedded elliptical crack at the longitudinal butt welded joint.	169
8.4	Definition sketch of the geometrical imperfections of pressure tunnels and shafts. The geometrical imperfections and the thickness of the liner are magnified for presentation purposes.	171
8.5	Boundary conditions of the model.	174
8.6	FE mesh and deformed mesh of a steel liner with a semi-elliptical surface crack in the weld material of the welded joint.	177

List of Figures

8.7	FE mesh and deformed mesh of a steel liner with an embedded elliptical crack in the weld material of the welded joint.	180
8.8	Error histograms of the prediction of the FE models compared to the corresponding analytical solutions.	183
8.9	Normalized SIF \hat{K}_I along the crack front of semi-elliptical surface cracks. . . .	184
8.10	Normalized SIF \hat{K}_I along the crack front of embedded elliptical cracks.	185
8.11	Normalized SIF \hat{K}_I at the deepest point of semi-elliptical surface cracks.	190
8.12	Influence of relative weld reinforcement on the normalized SIF \hat{K}_I along the crack front of semi-elliptical surface cracks.	191
8.13	Major principal stress profiles in the weld material ($r_i = 2$ m, $t_s = 25$ mm, $\rho = 1$ mm): (a,b,c,d) influence of the relative weld reinforcement δ/t_s ($\beta = 2$ deg, $\alpha = 50$ deg); (e,f,g,h) influence of the flank angle β ($\delta/t_s = 0.060$, $\alpha = 50$ deg); and (i,j,k,l) influence of the edge preparation angle α ($\delta/t_s = 0.060$, $\beta = 20$ deg). The stress profiles are scaled so that $t_s/2$ represents the magnitude of the membrane stress.	194
8.14	Maximum normalized SIF \hat{K}_I (at $\phi = -\pi/2$) of embedded elliptical cracks. . .	195
8.15	Regression plots of the empirical results against the numerical results fitted by GA. . .	198
8.16	Error histograms of the predictions of the parametric equation compared to the FE results.	199
8.17	Convergence of the 3D solution for normalized SIF \hat{K}_I along semi-elliptical surface crack for different aspect ratios a/c toward the 2D single-edge crack solution in a plate.	200
9.1	Pressure history for a normal week of operation.	209
9.2	Loading spectrum histogram obtained with RFC. The ordinates axis representing the number of occurrences N is in logarithmic scale for presentation purposes. .	210
10.1	Modified $S-N$ curves for steel at variable amplitude loading for Palmgren–Miner summation using the effective notch stress approach.	214
10.2	Variation of the nominal stress during one week under normal loading spectrum with $[\Delta p_i/p_{i,\text{mean}}]_{\text{th}} = 1\%$, representative of all cases presented in Figs. 10.3 and 10.4.	221
10.3	Variation of the notch stress during one week under normal loading spectrum with $[\Delta p_i/p_{i,\text{mean}}]_{\text{th}} = 1\%$. In all cases, $SF = 2.0$, $E' = 5$ MPa, and $E/E' = 1.0$	223
10.4	Variation of notch stress ranges during one week under normal loading spectrum with $[\Delta p_i/p_{i,\text{mean}}]_{\text{th}} = 1\%$. In all cases, $SF = 2.0$, $E' = 5$ MPa and $E/E' = 1.0$	224
10.5	Maximum number of cycles to failure N_{max} associated to the maximum notch stress range $\Delta\sigma_n^{\text{max}}$ for the case characterized by $p_{i,\text{mean}} = 15$ MPa, S960 QL, $SF = 2.0$, $E' = 5$ MPa, $E/E' = 1.0$ and $t_s = 32.8$ mm.	225
11.1	Definition sketch of a steel-lined pressure tunnel or shaft with an axial semi-elliptical surface crack at the longitudinal butt welded joint, on the internal surface. The slenderness of the steel liner is distorted for the sake of presentation.	228

11.2	Definition sketch of a steel-lined pressure tunnel or shaft with an axial embedded elliptical crack at the longitudinal butt welded joint. The slenderness of the steel liner is distorted for the sake of presentation.	229
11.3	Truncated lognormal distribution for the crack shape ratio a/c . The histogram was generated from a sampling of 10^4 values, and its number of bins was defined according to the Freedman & Diaconis (1981) rule for the sake of presentation.	233
11.4	Lognormal distribution for the threshold stress intensity factor ΔK_{th} of the Paris–Erdogan law. The histograms were generated from a sampling of 10^4 values, and their number of bins was defined according to the Freedman & Diaconis (1981) rule for the sake of presentation. The unit change is performed as $\Delta K_{th}(\text{MPa}, m) = 1/31.62 \cdot \Delta K_{th}(\text{N}, \text{mm})$	233
11.5	Lognormal distributions for the parameter C of the Paris–Erdogan law in inert and aggressive environments. The histograms were generated from a sampling of 10^4 values, and their number of bins was defined according to the Freedman & Diaconis (1981) rule for the sake of presentation. The unit change is performed as $C(\text{MPa}, m) = 31.62 \cdot C(\text{N}, \text{mm})$, valid only for $m = 3$	235
11.6	Flowchart of the proposed Monte Carlo simulation procedure.	238
11.7	Probability of failure along lifespan of steel liners with semi-elliptical surface cracks in aggressive environment for $p_{i,\text{mean}} = 15 \text{ MPa}$ and $a_i = 4 \text{ mm}$	244
11.8	Results from the probabilistic fatigue crack growth and fracture model (for random 1000 trials) of semi-elliptical surface cracks in aggressive environment for $p_{i,\text{mean}} = 15 \text{ MPa}$, $t_s = 27.3 \text{ mm}$, $a_i = 4 \text{ mm}$, $f_y = 960 \text{ MPa}$, $\text{SF} = 1.8$, $E' = 5.0 \text{ GPa}$ and $E/E' = 1$	245
11.9	Results from the probabilistic fatigue crack growth and fracture model (for random 1000 trials) of semi-elliptical surface cracks in aggressive environment for $p_{i,\text{mean}} = 15 \text{ MPa}$, $t_s = 32.8 \text{ mm}$, $a_i = 4 \text{ mm}$, $f_y = 960 \text{ MPa}$, $\text{SF} = 2.0$, $E' = 5.0 \text{ GPa}$ and $E/E' = 1$	246
11.10	Results from the probabilistic fatigue crack growth and fracture model (for random 1000 trials) of semi-elliptical surface cracks in aggressive environment for $p_{i,\text{mean}} = 15 \text{ MPa}$, $t_s = 38.3 \text{ mm}$, $a_i = 4 \text{ mm}$, $f_y = 960 \text{ MPa}$, $\text{SF} = 2.2$, $E' = 5.0 \text{ GPa}$ and $E/E' = 1$	247
11.11	Results from the probabilistic fatigue crack growth and fracture model (for random 1000 trials) of semi-elliptical surface cracks in aggressive environment for $p_{i,\text{mean}} = 15 \text{ MPa}$, $t_s = 22.7 \text{ mm}$, $a_i = 4 \text{ mm}$, $f_y = 960 \text{ MPa}$, $\text{SF} = 1.8$, $E' = 10.0 \text{ GPa}$ and $E/E' = 1$	248
12.1	Longitudinal schematic view of the studied alpine high-head power plant and sectional view of the steel-lined pressure shaft. The relative dimensions are adapted for the sake of presentation.	252

List of Figures

12.2	Determination of $N_k = \min \{N_{k,225}; N_{k,160 \times K_w}; N_{k,160}\}$ for a given $\Delta\sigma_n^k$ (and $\Delta\sigma_{hs}^k$) with modified S – N curves for steel at variable amplitude loading within the effective notch stress approach. In this example, $K_m^* = 1.3$, $K_w = 1.7$, and $\Delta\sigma_{nom}^k = 90$ MPa.	266
12.3	Probability of failure considering initial semi-elliptical surface cracks in aggressive environment.	268
13.1	Recommended design procedure, extended after Schleiss (1988) to the consideration of fatigue crack propagation and fracture.	277
13.2	Fatigue and fracture analysis within the framework of Damage Tolerant Design (modified after Zerbst <i>et al.</i> 2007). POD: probability of detection; NDT: nondestructive testing.	278
A.1	Definition sketch of the geometrical imperfections and the local butt welded joint's geometry at steel liners presenting the main points of the mathematical model for the geometry. The geometrical imperfections and the thickness of the liner are distorted for presentation purposes.	282

List of Tables

2.1	Minimum yield strengths for different steel grades used in hydropower construction.	23
3.1	Overview on some engineering procedures for failure assessment of structures containing flaws.	58
3.2	Overview on some engineering procedures for fatigue assessment of structures.	59
3.3	Variation of the relative weld reinforcement δ/t_s accordingly to the flank angle β for the FEA results shown in Figs. 3.10 and 3.11.	66
3.4	Selected structural SCF at longitudinal butt welded joints in cylindrical open-air penstocks or pipelines published in literature (see the nomenclature in Fig. 7.1).	69
4.1	Variable parameters of the FE model.	82
4.2	Constant parameters of the FE model.	82
4.3	Variation of the dimensionless parameters with respect to the reference set of cases.	86
4.4	Variation range of the variable dimensionless parameters for each set of cases.	86
5.1	Variation range of the parameters for the random user-defined sampling.	105
5.2	Synthesis of the conceptual formulas derived to obtain some maximum stresses in steel-lined pressure tunnels and shafts in anisotropic rock.	109
5.3	Maximum major principal stresses in the steel liner and in the far-field rock for the cases of examples 1 and 2.	111
6.1	Ranges of variation of the parameters in the series of simulations used to derive the parametric equations.	132
6.2	Coefficient and exponents α_i for the parametric equations for the notch SCF $K_{t,m}$ and K_t .	132
6.3	Coefficient and exponents α_i for the parametric equations for the notch SCF $K_{t,m}^{\rho=r_{\text{ref}}}$ and $K_t^{\rho=r_{\text{ref}}}$.	132
7.1	Variation ranges (minimum and maximum values) of the parameters for the 161 simulations used to derive structural and notch SCF at longitudinal butt welded joints of SLPT&S.	155
7.2	(a) Parameters and (b) results for the application examples.	161

List of Tables

8.1	Matrix of performed simulations for steel liners with axial semi-elliptical surface cracks at longitudinal butt welded joints (total of approximately 2100 simulations). The so-called base studies are highlighted in bold . The superscript * indicates that large-deflections effects were considered.	187
8.2	Matrix of performed simulations for steel liners with axial embedded elliptical cracks at longitudinal butt welded joints (total of approximately 330 simulations). The so-called base studies are highlighted in bold . The superscript * indicates that large-deflections effects were considered.	196
8.3	Coefficients and exponents χ_i for the parametric equation of M_w fitted by GA. .	198
10.1	Minimum yield strengths for different steel grades used in hydropower construction considered for the parametric analysis of fatigue assessment by means of the effective notch stress approach.	217
10.2	Constant parameters (or depending on constants) of the parametric analysis of fatigue assessment by means of the effective notch stress approach.	217
10.3	Results from the effective notch stress approach ($\gamma_{\text{freq}} = 1.0$, $\gamma_{\text{ampl}} = 1.0$). . .	218
10.4	Results from the effective notch stress approach with magnified loading spectra ($\gamma_{\text{freq}} = 1.2$, $\gamma_{\text{ampl}} = 1.2$).	219
11.1	Minimum yield strengths for different steel grades used in hydropower construction considered for the parametric analysis of fatigue assessment by means of linear elastic fracture mechanics approach.	240
11.2	Constant parameters (or depending on constants) of the parametric analysis performed with the probabilistic model for fatigue crack growth and fracture. .	242
12.1	Deterministic parameters of the case study.	253
12.2	Minimum yield strengths for the different studied steel grades.	254
D.1	Results from the Monte Carlo simulations of semi-elliptical internal surface cracks in inert environment	302
D.2	Results from the Monte Carlo simulations of semi-elliptical internal surface cracks in aggressive environment	306
D.3	Results from the Monte Carlo simulations of embedded elliptical cracks in inert environment	310
E.1	Results from the Monte Carlo simulations of semi-elliptical internal surface cracks in inert environment	316
E.2	Results from the Monte Carlo simulations of semi-elliptical internal surface cracks in aggressive environment	317
E.3	Results from the Monte Carlo simulations of embedded elliptical cracks in inert environment	318

Nomenclature

The main nomenclature adopted in this report is presented hereafter.

Abbreviations

APDL	ANSYS Parametric Design Language
DOB	Degree of bending
FE	Finite element
FEA	Finite element analysis
FEM	Finite element method
GA	Genetic algorithm
HAZ	Heat-affected zone
HICC	Hydrogen induced cold cracking
HPP	Hydroelectric power plants
HSS	High-strength steel
LEFM	Linear elastic fracture mechanics
MSE	Mean squared error
RMSE	Root mean squared error
PDS	Probabilistic Design System (ANSYS)
PFM	Probabilistic fracture mechanics
Q+T	Quenched and tempered
SCF	Stress concentration factor
SIF	Stress intensity factor
SLPT&S	Steel-lined pressure tunnels and shafts
SSY	Small-scale yielding

Latin characters

a	Crack minor semi-axis (crack depth for semi-elliptical surface cracks and half crack depth for embedded elliptical cracks)	(m)
c	Crack major semi-axis (half crack length)	(m)
C	Coefficient of the Paris–Erdogan law (units depend on the exponent m)	
d_1, d_2	Distance of embedded crack center from internal and external fibers of the steel liner, respectively	(m)

Nomenclature

D_{calc}	Calculated damage sum according to the Palmgren–Miner rule	(–)
e	Linear misalignment (eccentricity)	(m)
E, E'	Elastic moduli of a transversely isotropic rock	(GPa)
$E_c, E_{\text{crm}}, E_{\text{rm}}, E_s$	Elastic moduli of the backfill concrete, the near-field rock, the isotropic far-field rock and the steel liner, respectively	(GPa)
E_θ	Elastic modulus in the tangential direction in polar coordinates	(GPa)
f_u	Tensile or ultimate strength	(MPa)
f_y	Yield strength	(MPa)
G, G'	Shear moduli of a transversely isotropic rock	(GPa)
$G'_{\text{S-V}}$	Empirical cross-shear modulus of a transversely isotropic rock according to Saint-Venant	(GPa)
$G_{\theta r}, G_{\theta z}$	Shear moduli in polar coordinates	(GPa)
J	J -integral	(MPa · m)
K_{IC}	Plane strain fracture toughness	(MPa $\sqrt{\text{m}}$)
K_I	Stress intensity factor	(MPa $\sqrt{\text{m}}$)
\hat{K}_I	Normalized stress intensity factor	(–)
K_m	Stress concentration factor characterizing the structural stress concentration	(–)
$K_{m,e}$	Stress concentration factor characterizing the structural stress concentration due to linear misalignment	(–)
$K_{m,p}$	Stress concentration factor characterizing the structural stress concentration due to peaking	(–)
$K_{m,\eta}$	Stress concentration factor characterizing the structural stress concentration due to out-of-roundness	(–)
K_m^*	Stress concentration factor characterizing the structural stress concentration at the longitudinal butt welded joints considering the interaction with the concrete–rock system	(–)
$K_{m,e}^*$	Stress concentration factor characterizing the structural stress concentration due to linear misalignment at the longitudinal butt welded joints considering the interaction with the concrete–rock system	(–)
$K_{m,p}^*$	Stress concentration factor characterizing the structural stress concentration due to peaking at the longitudinal butt welded joints considering the interaction with the concrete–rock system	(–)
$K_{\text{rm},\text{aniso}}^*$	Stress concentration factor characterizing the influence of the anisotropic rock mass on the nominal stress in the steel liner	(–)
$K_t, K_{t,m}$	Stress concentration factors characterizing the notch stress concentration	(–)
K_w	Stress concentration factor characterizing the weld notch stress concentration	(–)
l_u	Straight edge length	(m)
l_w	Weld length	(m)

m	Exponent of the the Paris–Erdogan law	(–)
M_0	Shape factor without welded joint	(–)
M_b	Bending shape factor without welded joint	(–)
M_m	Membrane shape factor without welded joint	(–)
M_w	Weld shape correction factor	(–)
n_f	Number of failure	(–)
N	Number of stress cycles	(–)
N_{MC}	Number of trials in a Monte Carlo simulation	(–)
p_{cr}	Applied pressure on crack face	(MPa)
$p_c, p_{c,corr}, p_{crm}, p_{rm}$	Pressures transmitted at radii r_c (and its correction), r_{crm} and r_{rm} , respectively	(MPa)
p_f	Probability of failure	(–)
p_i	Quasi-static internal water pressure	(MPa)
$p_{i,mean}$	Mean internal water pressure	(MPa)
Q	Elliptical integral of the second kind	(–)
$r_c, r_{crm}, r_i, r_{rm}$	Internal radii of the backfill concrete, the near-field rock, the steel liner and the far-field rock, respectively	(m)
r_y, r_p	First- and second-order estimates of plastic zone sizes ahead of crack-tips	(m)
r_{ref}	Reference radius within the effective notch stress approach	(m)
SF	Global security factor for the design of steel-lined pressure tunnels and shafts	(–)
t_c, t_{crm}, t_s	Thicknesses of the backfill concrete, the near-field rock and the steel liner, respectively	(m)
$u_r^c, u_r^{crm}, u_r^{rm}, u_r^s$	Radial displacements of the backfill concrete, the near-field rock, the far-field rock and the steel liner, respectively	(m)
$\hat{u}_r^s, \hat{u}_{r,max}^s, \hat{u}_{r,min}^s$	Normalized radial displacements in the steel liner, and the maximum and minimum values, respectively	(–)
$u_{r,iso}^s, u_{r,aniso}^s$	Radial displacements in the steel liner considering isotropic and anisotropic rock, respectively	(m)
Y	Global shape factor	(–)

Greek symbols

α	Plate's edge preparation angle	(deg)
β	Flank angle	(deg)
γ	Angular misalignment angle	(deg)
γ_{ampl}	Amplitude magnification factor of loading spectra	(–)
γ_{freq}	Frequency magnification factor of loading spectra	(–)
$\gamma_{xy}, \gamma_{xz}, \gamma_{yz}$	Shear strains in Cartesian coordinates	(–)
δ	Weld reinforcement height	(m)
Δh	Radial deviation from the circular shape at the roof top of a steel liner with peaking	(m)

Nomenclature

ΔK_{th}	Threshold range of stress intensity factor in the Paris–Erdogan law	(MPa \sqrt{m})
Δp_i	Range of internal water pressure	(MPa)
Δp^+	Maximum overpressure considered for the design of steel liners	(MPa)
Δr_0	Initial gap between the steel liner and the backfill concrete	(m)
$\Delta \sigma_{hs}$	Range of structural hot-spot stress	(MPa)
$\Delta \sigma_n$	Range of notch stress	(MPa)
$\Delta \sigma_{nom}$	Range of nominal stress	(MPa)
ε	Strain	(–)
ε	Accuracy of the probability of failure obtained by means of a Monte Carlo simulation	(–)
$\varepsilon_x, \varepsilon_y, \varepsilon_z$	Strains in Cartesian coordinates	(–)
η	Radial deviation from the circular shape of a steel liner with out-of-roundness	(m)
θ	Angle in polar coordinates	(deg)
ν, ν'	Poisson's ratios of a transversely isotropic rock	(–)
$\nu_c, \nu_{crm}, \nu_{rm}, \nu_s$	Poisson's ratios of the backfill concrete, the near-field rock, the isotropic far-field rock and the steel liner, respectively	(–)
$\nu_{\theta r}, \nu_{\theta z}$	Poisson's ratio in polar coordinates	(–)
ρ	Weld toe radius	(m)
σ	Stress	(MPa)
$\sigma_1^s, \sigma_2^s, \sigma_3^s$	Principal stresses in the steel liner	(MPa)
$\sigma_{1,iso}^s, \sigma_{1,aniso}^s$	Major principal stresses in the steel liner considering isotropic and anisotropic rocks, respectively	(MPa)
$\sigma_{1,iso}^{rm}, \sigma_{1,aniso}^{rm}, \sigma_{3,iso}^{rm}, \sigma_{3,aniso}^{rm}, \hat{\sigma}_{1,iso}^{rm}, \hat{\sigma}_{1,aniso}^{rm}$	Major and minor principal stresses in the far-field rock considering isotropic and anisotropic rocks, respectively, and their normalized values for the major principal stresses	(MPa, –)
$\hat{\sigma}_{1,max}^s, \hat{\sigma}_1^s$	Normalized maximum and major principal stresses in the steel liner, respectively	(–)
$\hat{\sigma}_1^{rm}, \hat{\sigma}_{1,max}^{rm}, \hat{\sigma}_{1,min}^{rm}$	Normalized major principal stresses in the far-field rock, and their maximum and minimum values, respectively	(–)
$\hat{\sigma}_3^{rm}, \hat{\sigma}_{3,max}^{rm}$	Normalized minor principal stresses in the far-field rock and their maximum value, respectively	(–)
$\hat{\sigma}_{1,num}^s, \hat{\sigma}_{eq,num}^s$	Normalized numerical major principal and equivalent stresses in anisotropic rock	(–)
$\sigma_{1,corr}^s, \sigma_{eq,corr}^s, \hat{\sigma}_{1,corr}^s, \hat{\sigma}_{eq,corr}^s, \sigma_{1,corr}^{rm}, \hat{\sigma}_{1,corr}^{rm}$	Corrected maximum major principal and equivalent stresses in the steel liner and in the far-field rock, and their normalized values, respectively	(MPa, –)
$\sigma_{1,int}^s, \sigma_{1,ext}^s$	Major principal stresses at the internal and external fibers, respectively	(MPa)
$\sigma_{1,max}^s, \sigma_{eq,max}^s$	Maximum major principal and equivalent stresses in the steel liner	(MPa)
$\sigma_{2,corr}^s$	Corrected intermediate principal stress in the steel liner, corresponding to the corrected major principal stress	(MPa)

σ_b	Bending component of stress	(MPa)
σ_m	Membrane component of stress	(MPa)
$\sigma_{m,iso}$	Membrane component of stress in a steel liner embedded in isotropic rock	(MPa)
$\sigma_{m,aniso}$	Membrane component of stress in a steel liner embedded in anisotropic rock	(MPa)
σ_s	Structural stress	(MPa)
σ_{hs}	Structural hot-spot stress	(MPa)
σ_n	Notch stress	(MPa)
σ_{nom}	Nominal stress	(MPa)
σ_{eq}^s	Equivalent stress in the steel liner	(MPa)
$\sigma_i^s, \sigma_i^c, \sigma_i^{crm}, \sigma_i^{rm}$	Stresses in the steel liner, the backfill concrete, the near-field rock, the isotropic far-field rock and the steel liner, respectively, along the i -coordinate	(MPa)
$\sigma_x, \sigma_y, \sigma_z$	Stresses in Cartesian coordinates	(MPa)
$\tau_{xy}, \tau_{xz}, \tau_{yz}$	Shear stresses in Cartesian coordinates	(MPa)
ϕ	Angular position along crack front in polar coordinates	(deg)
χ_i	Fitted coefficients and exponents in the parametric equation for M_w	(–)
ψ_e	Parameter characterizing the linear misalignment with respect to the tolerance given by the C.E.C.T. (1980)	(–)
ψ_u	Parameter characterizing peaking	(–)
ψ_δ	Parameter characterizing the weld reinforcement height with respect to the tolerance given by the C.E.C.T. (1980)	(–)
ψ_η	Parameter characterizing the out-of-roundness with respect to the tolerance given by the C.E.C.T. (1980)	(–)

Sub- and superscripts

*	Superscript for interaction with the concrete–rock system
1, 2, 3	Subscripts for principal stress/strain directions
I, II, III	Subscripts for fracture modes
aniso	Subscripts for values considering anisotropic rock behavior
ANSYS	Superscript for results obtained by means of FE modeling in ANSYS
b	Subscript for bending
c	Sub- and superscript for concrete
corr	Subscript for corrected value
crm	Sub- and superscript for near-field rock (cracked rock mass)
e	Subscript for linear misalignment (eccentricity)
emp	Superscript for values obtained from empirical equations
eq	Subscript for equivalent
ext	Subscript for values at an external surface/fiber

Nomenclature

hs	Subscript for structural hot-spot stress
i	Subscript for internal or initial
int	Subscript for values at an internal surface/fiber
iso	Subscripts for values considering isotropic rock behavior
m	Subscripts for membrane or structural
min	Subscript for minimum value
max	Subscript for maximum value
n	Subscript for notch
nom	Subscript for nominal
num	Sub- and superscript for values obtained from numerical simulations
r, θ, z	Subscript for r , θ and z directions in polar coordinates, respectively
rm	Sub- and superscript for far-field rock (rock mass)
s	Sub- and superscript for steel liner or subscript for structural
u	Subscript for straight edges (unrolled edges)
x, y, z	Subscript for x , y and z directions in Cartesian coordinates, respectively
w	Subscript for weld
δ	Subscript for weld reinforcement height
η	Subscript for out-of-roundness

1 Introduction

1.1 Context of hydropower and recent developments of high-head hydroelectric power plants

Steel-lined pressure tunnels and shafts (SLPT&S) are the high pressure conduits of the waterway system connecting dam reservoirs to hydropower plants (HPP) (Schleiss 2012). Figure 1.1 presents the longitudinal schematic view of a typical high-head plant. Steel-lined pressure tunnels and shafts are multilayer structures made of a steel liner, a backfill concrete layer, and generally a cracked or loosened near-field rock zone and a sound far-field rock zone (see Fig. 1.1). Steel liners are manufactured from steel plates that are rolled and welded longitudinally, i.e., out-of-plane in Fig. 1.1, Section A-A. These longitudinal butt welded joints have to be considered with great care, as they are perpendicular to the major principal stresses direction (i.e., circumferential direction).

Pressure tunnels and shafts of high-head HPP usually have a major influence on the economic feasibility of the project (Vigl 2013; Schleiss 2013). Despite their importance, limited effort has been dedicated to study the design of liners of pressure tunnels in general, compared to other types of tunnels (Bobet & Nam 2007).

The contribution of new renewable highly volatile energies is growing fast in the European electricity grid due to high subsidies, while the demand for energy is still increasing. As a result storage hydropower as well as pumped-storage plants, which are used to balance the electricity grid on an intra-daily time scale, are subject to more and more severe operation conditions resulting in highly dynamic pressures in SLPT&S, called water hammer. The issue of fatigue thus becomes a new and significant concern for SLPT&S (see, e.g., Hachem & Schleiss 2009; Nicolet *et al.* 2010; Hachem & Giovanola 2013; Demal & Moser 2013; Duparchy *et al.* 2013; Greiner & Lechner 2013a,b; Greiner *et al.* 2013a,b,c), which was not traditionally considered relevant for the design in the past.

The recent development of high-strength (HSS) weldable steels has enlarged the range of design alternatives for the optimization of high-head SLPT&S. In new high-head hydroelectric projects

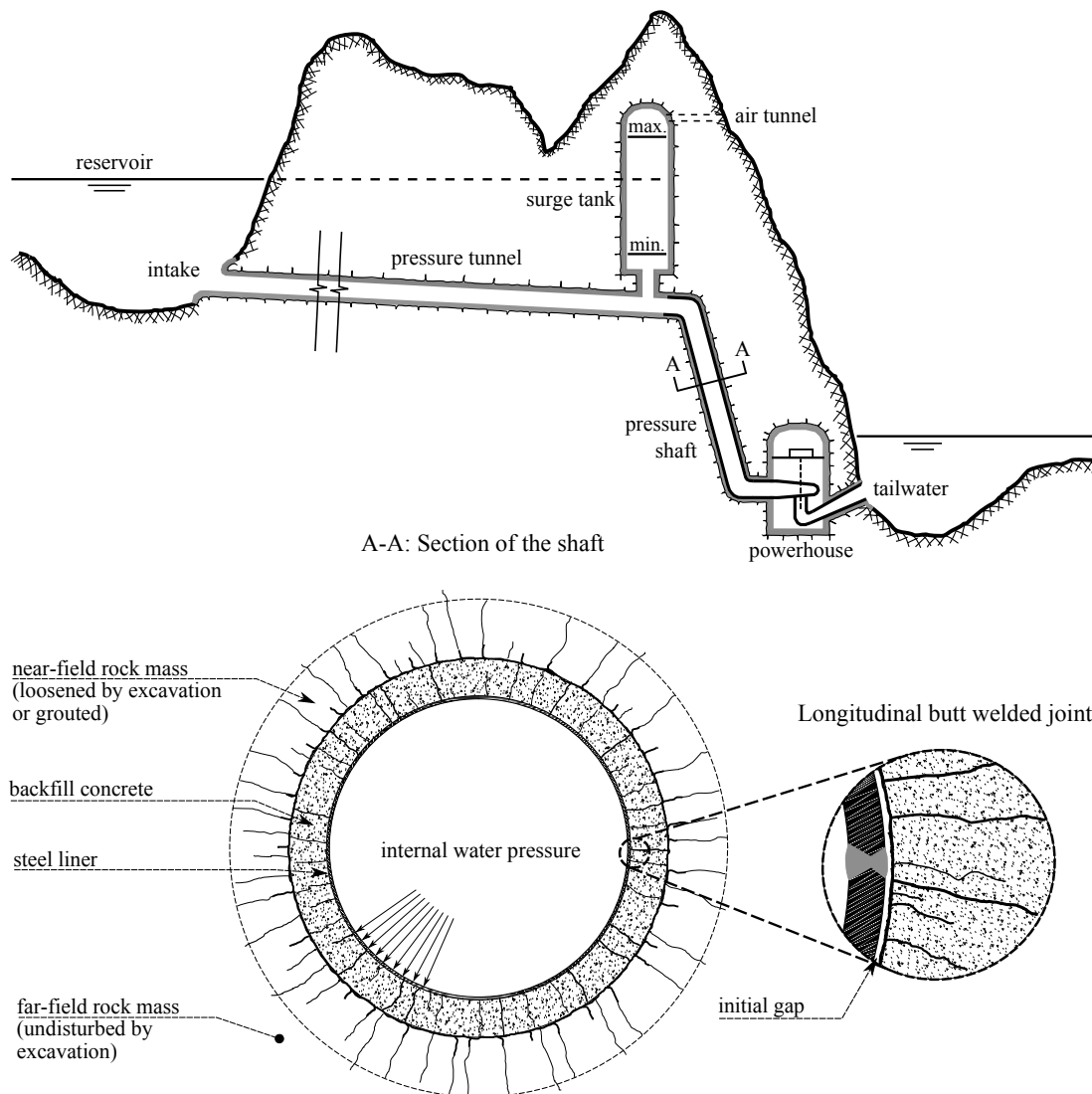


Figure 1.1: Longitudinal schematic view of a typical high-head power plant (head > 200 m) and sectional view of the standard multilayer system for steel-lined pressure tunnels and shafts. The relative dimensions are distorted for the sake of presentation.

as well as in existing plants the internal water pressure on SLPT&S can be higher than 150 bar (Benson 1989; Schleiss & Manso 2012), and dynamic pressures can cause additional loading in the system of about 15 to 25% of the static head (Brekke & Ripley 1987). In 1998, the Cleuson–Dixence shaft attained world record conditions with a discharge of $75 \text{ m}^3/\text{s}$ and a dynamic internal water pressure of more than 200 bar (Ribordy 1998).

1.2 Problem statement

1.2.1 Sensitivity of high-strength steels

High-strength steels have allowed thinner and thus more economic liners. However, although the high mechanical performance of HSS can address the working stress criterion in the design, it is often assumed that welded HSS do not provide a higher fatigue strength than lower (and in general more ductile) grades. They exhibit a higher notch sensitivity (Nykänen *et al.* 2013) and are as prone to contain initial defects (e.g., hydrogen induced cold cracking, undercuts, lack of fusion, stress corrosion cracks, porosity, incomplete penetration, slag inclusion) as lower welded steel grades, which makes the initiation period of the fatigue life negligible. This assertion is still under extensive investigation (see, e.g., Kaufmann *et al.* 2008; Pijpers *et al.* 2009; Sonsino 2009b; de Jesus *et al.* 2012; Nykänen *et al.* 2013).

A better comprehension of the behavior of the multilayer system and the possible presence of crack-like flaws in the weld material is required for an accurate fatigue assessment of the longitudinal butt welded joints (which are normally the critical parts) by means of engineering procedures.

1.2.2 Interaction with the concrete–rock system

When the rock conditions are adequate (depending on the rock overburden and the in situ stress field) the design can consider that a significant part of the internal water pressure can be transferred to the concrete–rock system. Thereby, the thickness of the steel liner can be decreased. This also facilitates welding when using HSS. However, the mechanical behavior of SLPT&S considering the interaction between the steel liner and the concrete–rock system is still not fully understood, particularly when the surrounding rock mass does not have an isotropic behavior.

1.2.3 Requirements for fatigue assessment by means of local stresses approaches

The recent development of local stresses concepts for fatigue life estimation such as the structural hot-spot stress and the effective notch stress methods (Niemi *et al.* 2006; Radaj *et al.* 2009; Fricke 2012; Radaj *et al.* 2013) provides designers with a higher accuracy than the traditional nominal stress concept, proposed by commonly used standards (EN 1993-1-9 2005; Koçak *et al.* 2008; EN 13445-3 2014). Numerous applications can be found in the literature, and the latest recommendations of the International Institute of Welding (IIW) cover the current local approaches (Hobbacher 2008, 2016). However, these methods are more time-consuming and often require finite element (FE) computations when analytical solutions for stress concentration factors (SCF) are not available.

Global geometrical imperfections (inherent to the manufacturing and erection processes) and the local geometry of the weld have a great influence on the SCF at welded shells. Some studies

on SCF at longitudinally welded cylindrical shells can be found in the literature. Parametric formulas, from various sources, are also proposed in standards (Hobbacher 2016; EN 13445-3 2014; API 2007). Nevertheless, the specific case of SLPT&S with contact between the steel liner and the concrete–rock system was never studied. The latter feature may greatly contribute to the overall structural behavior of SLPT&S.

In SLPT&S the geometrical imperfections and the concrete–rock confinement are often considered for buckling analysis (Valdeolivas & Mosquera 2013, 2015a,b). In Europe, the C.E.C.T. (1980) recommendations are used for the design of SLPT&S; they give tolerances on geometrical imperfections and weld geometries, but do not provide specific formulas for SCF estimation. Moreover, these recommendations have not been originally developed for HSS and the changing operating conditions of HPP.

1.2.4 Requirements for fatigue assessment by means of the fracture mechanics approach

The risk of hydrogen induced cold cracking (HICC) together with harsh loading spectra on SLPT&S emphasize the need for an optimized engineering fatigue and fracture assessment. The traditional nominal and local stresses approaches do not cover fatigue failure from such crack-like flaws due to actual cracking mechanisms such as HICC (Maddox 2011). These defects are considered as unacceptable and are repaired if detected by nondestructive testing. However, the absence of such flaws cannot be ensured with an absolute certainty as nondestructive techniques usually have a lower crack size limit of detectability, as well as a probability of detection (POD).

For fatigue crack growth and fracture analysis, linear elastic fracture mechanics (LEFM) is a widespread method (see, e.g., McFadyen *et al.* 1990; Maddox 2011; Zerbst *et al.* 2014), which is formulated in well recognized standards in association with the Paris–Erdogan law. In the latter, the crack growth rate is related to the stress intensity factor (SIF), denoted K_I in Mode I (opening mode). For an accurate estimation of the SIF during the crack propagation, the global behavior of the welded structure as well as the local geometry, including the welded joint, should be known.

1.2.5 Justification for a probabilistic approach for fatigue crack growth

Although reaching absolute results from probabilistic models in engineering are unrealistic for most practical applications, the relative and quantitative results from such approaches provide valuable information on the influence of each stochastic input, and allow identifying the weaknesses of a design. Moreover, it may, in certain cases, produce results showing satisfactory boundaries to the studied problem (Besuner 1987).

Probabilistic approaches for reliability assessment have been extensively developed in engineering fields such as the nuclear power generation industry and aeronautics. Structural engineering was also early involved in the scope of offshore and earthquake engineering. First steps toward

1.3. Objectives and practical relevance of the research project

a comprehensive probabilistic approach for fatigue crack growth analysis in welded joints of steel liners of pressure tunnels and shafts, in the aforementioned context, are of great interest for practice.

1.3 Objectives and practical relevance of the research project

This research project aims at providing a better comprehension of the mechanical behavior of SLPT&S, and developing a comprehensive model and a methodology for fatigue and reliability assessment of SLPT&S. The objectives can be enumerated as follows.

1. By means of the finite element method (FEM), the mechanical behavior of SLPT&S is investigated through the following steps:
 - (a) study the influence of anisotropic rock behavior on stresses and displacements in SLPT&S;
 - (b) study the structural and notch stress concentrations at longitudinal butt welded joints of SLPT&S, considering the global geometrical imperfections, the local weld shape, and the interaction with the backfill concrete–rock system;
 - (c) evaluate the applicability of the aforementioned contributions to the computation of stress intensity factors for crack-like flaws in the weld material at longitudinal butt welded joints of SLPT&S and study the influence of the weld shape.
2. Based on this step-by-step approach where complexity is added stepwise, new empirical analytical equations or correction factors will be derived allowing the estimation of:
 - (a) maximum nominal stresses in steel liners of SLPT&S;
 - (b) stress concentrations at longitudinal butt welded joints of SLPT&S; and
 - (c) stress intensity factors for three-dimensional crack-like flaws in the weld material at the longitudinal butt welded joints of SLPT&S.
3. Finally, a comprehensive methodology for fatigue and reliability assessment of SLPT&S will be proposed using this new analytical model, allowing to:
 - (a) assess the fatigue life by means of local stresses approaches; and
 - (b) develop a probabilistic fatigue crack growth model for crack-like flaws in the weld material at the longitudinal butt welded joints of SLPT&S.

This research project has a high practical relevance by addressing the need for a framework adapted to the specific use of engineering fatigue and reliability assessment procedures to SLPT&S. The methodologies developed herein may be practically useful for the design of steel liners in new hydropower plants, as well as for the rehabilitation of existing plants.

1.4 Finite element method (FEM)

In this research project, the FEM was used by means of the commercial code ANSYS® Mechanical™ software of the product *ANSYS® Academic Research, Release 14.0* (ANSYS Inc 2011, Chapters 4–5), and *ANSYS® Academic Research, Release 16.1* (ANSYS Inc 2015, Chapters 6–8). The FE models developed within this work will be described in the corresponding chapters. Although some specific details on the FEM procedures used herein will be briefly developed when necessary, the basics of the FEM will not be presented in this document. The reader not familiar with the FEM may find interest in fundamental books introducing the FE procedures such as Hughes (1987), Bathe (1996) and Zienkiewicz *et al.* (2005). Some literature is also available in French see, e.g., Gmür (2007), Gmür (2008) and Frey (2006). Finally, some specific applications with ANSYS® can be found, e.g., in Nakasone *et al.* (2006), Madenci & Guven (2006), Alawadhi (2010) and Dill (2012).

1.5 Structure and methodology of the study

The structure of the present report is presented in Fig. 1.2. The main objectives of each part and chapter can be summarized as follows.

- Part I presents a literature review of the scientific and technical fields that are related to this research project. Chapter 2 focuses on SLPT&S, and presents in particular the standard model for the design, the use of HSS for steel liners, transients phenomena and the last advances in non-intrusive monitoring methods. Chapter 3 provides technical background for fatigue assessment of welded joints and fracture mechanics, introduces probabilistic approaches in engineering and reviews stress concentration factors as well as stress intensity factors for cracks in butt welded joints.
- In Part II, the influence of anisotropic rock behavior on stresses in the steel liners of SLPT&S is studied by means of the FEM. Chapter 4 presents the constitutive models adopted for the materials, the FE model and an extensive systematic parametric study. In Chapter 5, parametric correction factors to be included in the analytical solution in isotropic rock are derived in order to estimate the maximum stresses in the steel liner accounting for the anisotropic rock behavior.
- Part III is dedicated to the study of the influence of the geometrical imperfections and the weld profile on the stress concentrations at the longitudinal butt welded joints of the steel liners, by means of the FEM. At first, notch stress concentration factors are studied at butt welded straight plates in Chapter 6. Then, in Chapter 7, structural stress concentration factors at the longitudinal butt welded joints of SLPT&S are studied, accounting for geometrical imperfections and the interaction with the backfill concrete–rock system. New correction factors to be included in formerly published expressions allowing to estimate notch and structural stress concentration factors at the longitudinal butt welded joints of

1.5. Structure and methodology of the study

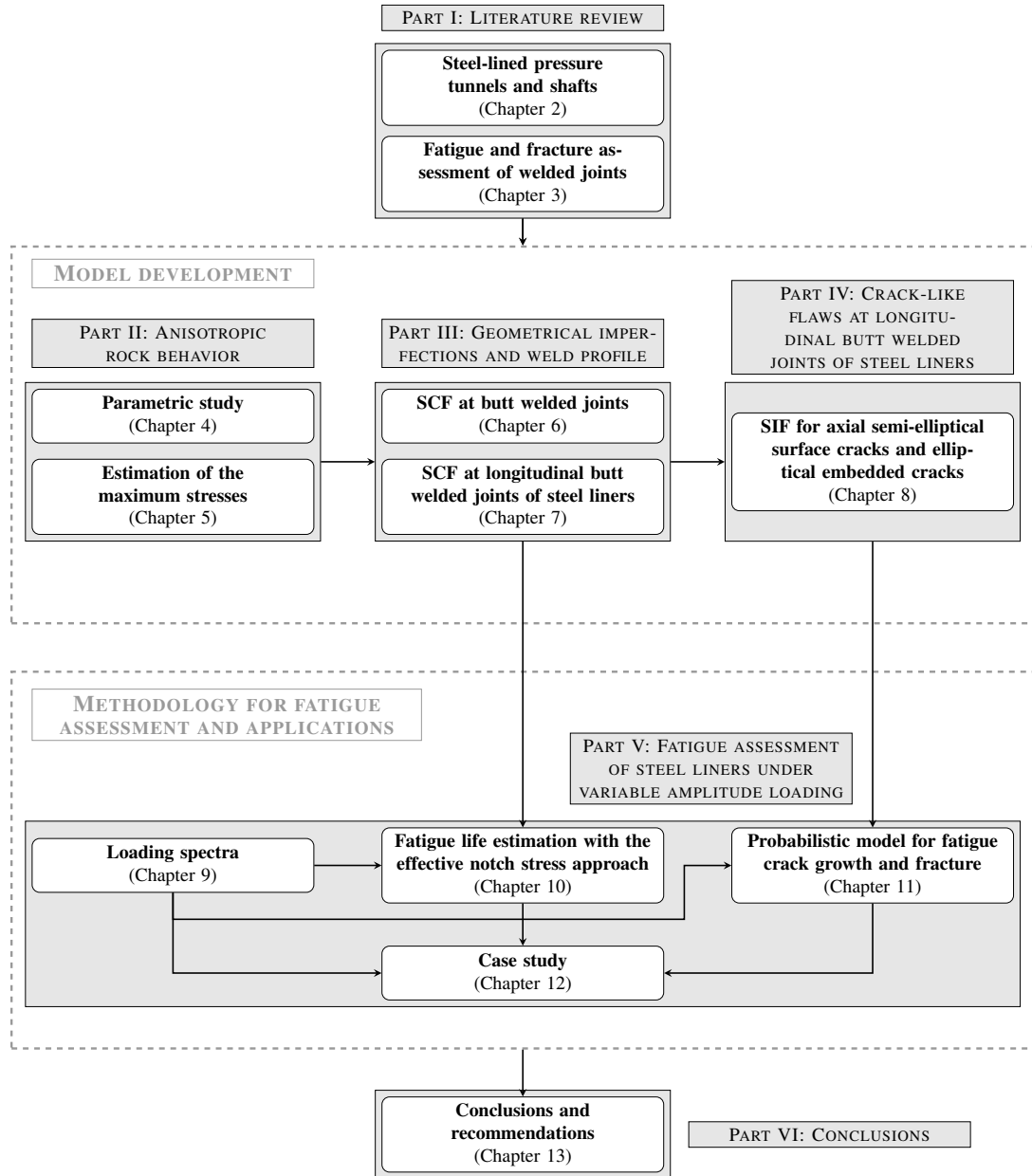


Figure 1.2: Structure of the report.

SLPT&S are proposed.

- Part IV, constituted of Chapter 8, presents the study of SIF for axial cracks in the weld material of the longitudinal butt welded joints of SLPT&S. By means of the FEM, it is first verified that the previously developed parametric equations to estimate membrane and bending stresses at the longitudinal butt welded joints can successfully predict SIF for 3D axial cracks by using published formulas. Finally, a new parametric equation is proposed to account for the influence of the weld shape.
- Part V aims at developing a framework for the fatigue assessment of the steel liners of SLPT&S. In Chapter 9, a week-long loading spectrum under normal operation conditions of a pumped-storage HPP is derived from prototype measurements performed by Hachem & Schleiss (2012c). This spectrum is normalized with respect to the mean internal water pressure and is considered as an input for the engineering fatigue assessment procedures used in this research project. A parametric study of fatigue assessment by means of the effective notch stress approach is performed in Chapter 10, using the parametric equations previously developed. In Chapter 11, a probabilistic model for fatigue crack growth and fracture is developed. The crack propagation is based on LEFM and the Paris–Erdogan law. The ranges of SIF are computed by means of the previously developed parametric equations or correction factors, and the probability of failure is assessed by means of the Monte Carlo simulation procedure. Similarly to Chapter 10, a parametric study is performed. Finally, a case study is presented in Chapter 12. While Chapters 10 and 11 focus on proposing a framework for the application of the aforementioned fatigue assessment engineering procedures and performing parametric studies, Chapter 12 synthesizes all the procedure proposed in this research project to compute stresses, SCF and SIF at the longitudinal butt welded joints of SLPT&S. Through the case study, additional comparative fatigue assessment results are provided.
- Finally, Chapter 13 of Part VI summarizes the conclusions of this research project, gives recommendations, and provide an outlook toward future research.

1.6 Project framework

This research project was conducted at the Laboratory of Hydraulic Constructions (LCH), at the Ecole Polytechnique Fédérale de Lausanne (EPFL), within the consortium named *HydroNet 2: Modern methodologies for design, manufacturing and operation of hydropower plants*. This research project was funded by the Swiss Competence Center Energy and Mobility (CCEM). The consortium partners are illustrated in Figure 1.3. This multidisciplinary consortium aims at addressing various aspects of hydropower generation to improve the design, manufacturing and operation of hydropower plants.

The project also took part in the Swiss Competence Center for Energy Research–Supply of Electricity (SCCER-SoE), which aims at carrying out innovative and sustainable research in the

areas of geo-energy and hydropower.

Finally, this study also received a contribution from the Swiss Committee On Dams (SwissCOD).

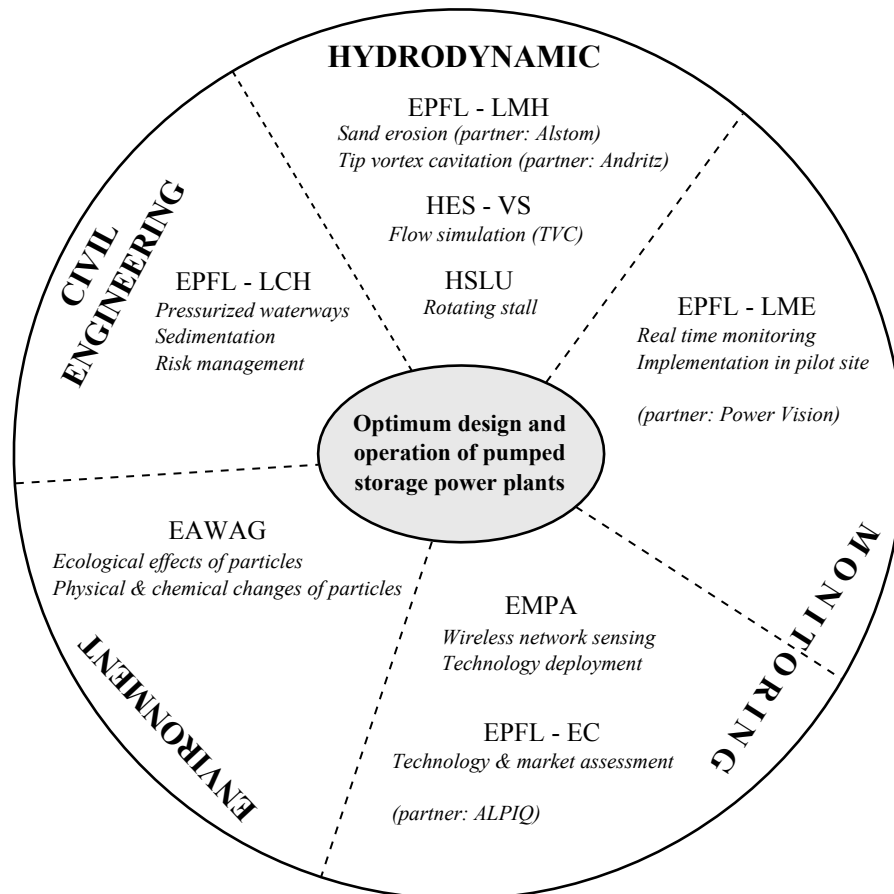


Figure 1.3: Project objectives, main tasks and partners.

Literature review **Part I**

The ancient structures that are still standing today obviously represent successful designs. There were undoubtedly many more unsuccessful designs with much shorter life spans. Because knowledge of mechanics was limited prior to the time of Isaac Newton, workable designs were probably achieved largely by trial and error. The Romans supposedly tested each new bridge by requiring the design engineer to stand underneath while chariots drove over it. Such a practice would not only provide an incentive for developing good designs, but would also result in the social equivalent of Darwinian natural selection, where the worst engineers were removed from the profession.

– Anderson (2005)

2 Steel-lined pressure tunnels and shafts

2.1 Axisymmetrical multilayer model in isotropic rock

The standard model as well as the nomenclature for the calculation of stresses and displacements in steel-lined pressure tunnels and shafts (SLPT&S) in isotropic rock are illustrated in Fig. 2.1. It represents an axisymmetrical multilayer system where five zones are commonly distinguished (see e.g., Brekke & Ripley 1987; Schleiss 1988; USACE 1997; ASCE 2012): (1) the steel liner; (2) an initial gap denoted Δr_0 between the steel liner and the backfill concrete; (3) the backfill concrete; (4) the near-field rock; and (5) the far-field rock, of *infinite* thickness.

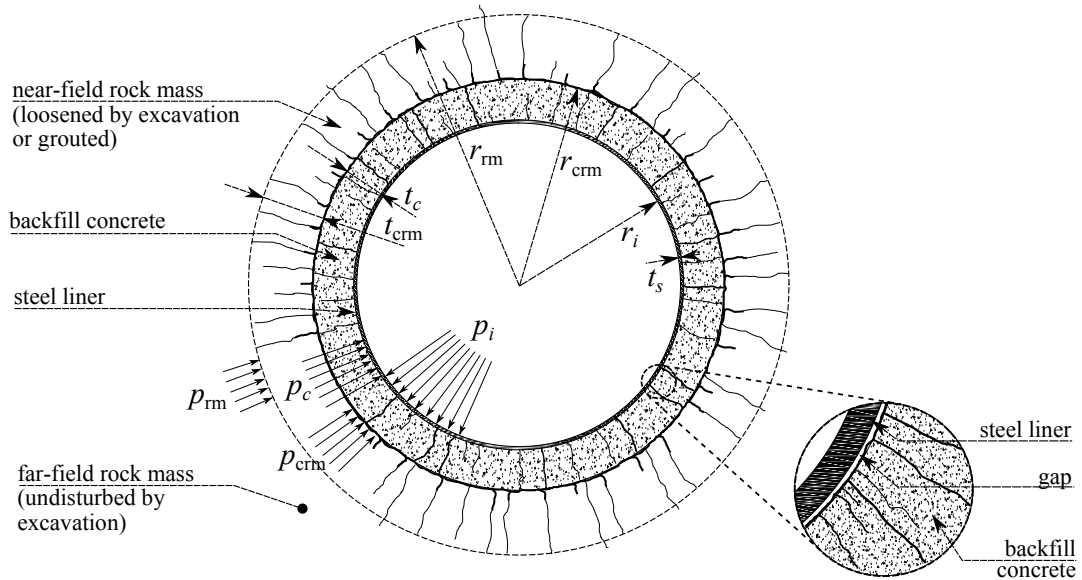


Figure 2.1: Definition sketch of the standard multilayer system for pressure tunnels and shafts embedded in elastic, isotropic rock mass (axisymmetrical case).

2.1.1 The steel liner

The steel liner is regarded as a linear and isotropic material, of elastic modulus E_s and Poisson's ratio ν_s . It is impervious, and its internal surface is in contact with the pressurized water with pressure p_i (Fig. 2.1).

2.1.2 The initial gap

The initial gap Δr_0 is an annular space at the interface between the steel liner and the backfill concrete (Fig. 2.1). It results from the thermal shrinking of the steel as a consequence of the contact with cold water and the non-recoverable deformations of the backfill concrete and the rock system (Brekke & Ripley 1987). Hachem & Schleiss (2009) summarize several assumptions made by designers to estimate Δr_0 .

2.1.3 The backfill concrete

Concrete is a quasi-brittle material with low tensile strength (1–2 MPa). Therefore, for the design of SLPT&S, the backfill concrete is regarded as a radially cracked material (as major principal stresses are tensile stresses in the tangential direction). The result is that the backfill concrete cannot transmit tangential stresses. It is regarded as a linear elastic material and its elastic modulus and Poisson's ratio are denoted E_c and ν_c , respectively.

2.1.4 The near-field rock

The near-field rock is a loosened (distressed, cracked) zone of the rock mass as a result of the excavation method (e.g., blasting effects), the rock properties, etc. Similarly to the backfill concrete, the near-field rock is regarded as radially cracked, and thus cannot transmit tensile stresses. The depth t_{crm} of this loosened zone (Fig. 2.1) is variable and is important to be determined because of its influence on the global deformability of the system. For instance, Benson (1989) states that excavation in hard rock with tunnel boring machines induces a low damage on the rock, resulting in a loosened layer generally restricted to 0.3–0.5 m depending on tunnel diameter. For excavation with the drill and blast method, the loosened layer is generally less than 1 m in good rock, although it can reach 2–3 m in brittle rock. Another important parameter to be determined is the elastic modulus E_{crm} of the loosened layer. It is in general lower than the sound rock modulus of elasticity, e.g., found to be reduced by 40% by measurements during the initial filling of a steel-lined pressure tunnel by Bowling (2010). The characteristics of the loosened rock zones for several projects can be found for example in Brekke & Ripley (1987). The Poisson's ratio for the near-field rock is denoted ν_{crm} . This near-field zone may be grouted to increase the stress transfer from the lining to the sound rock as well as to decrease irreversible deformations. Then, E_{crm} may reach or even exceed the modulus of the far-field rock.

2.1.5 The far-field rock

The far-field rock is a non-disturbed zone of the rock mass, assumed as a homogeneous, isotropic and elastic material. Its elastic modulus and Poisson's ratio are denoted E_{rm} and ν_{rm} , respectively. The far-field rock layer is normally considered as infinite for deep tunnels. The estimation of the mechanical parameters of the rock mass is very important as they have a significant influence on the global deformability of the system and its capability to withstand transmitted load. The deformability of the rock mass should be measured in the vicinity of the tunnel with in situ testings as for example large plate load tests. Furthermore, in situ stresses have to be known in order to verify the capability of the rock to absorb the transmitted internal water pressure (Seeber 1985). Deformations in SLPT&S can be monitored for a limited time during operation with instruments installed during the construction (Bowling 2010; Chène 2013).

2.2 Closed-form solution in isotropic rock

2.2.1 Compatibility conditions

The displacements in the axisymmetrical multilayer system (Fig. 2.1) are derived from the compatibility conditions on the displacements at the interfaces between the layers (Hachem & Schleiss 2011c). The radial displacement at r_c must be equal in the steel liner and the backfill concrete, as between the backfill concrete and the near-field rock and between the near- and far-field rocks. This is expressed as follows, taking into account a positive initial gap between the steel liner and the backfill concrete:

$$\begin{aligned} u_r^s(r = r_c) - \Delta r_0 &= u_r^c(r = r_c) \\ \text{with } \Delta r_0 &\geq 0; \\ u_r^c(r = r_{crm}) &= u_r^{crm}(r = r_{crm}); \\ u_r^{crm}(r = r_{rm}) &= u_r^{rm}(r = r_{rm}). \end{aligned} \tag{2.1}$$

The superscript s is related to the steel, c to the backfill concrete, crm to the near-field rock mass (cracked) and rm to the far-field rock mass. The subscript r indicates the radial direction.

The steel liner is modeled according to the thick-walled cylinder theory (Timoshenko & Goodier 1970). As already mentioned before, it is assumed that tensile stresses cannot be transmitted in the cracked layers (backfill concrete and near-field rock). The far-field rock is modeled as an infinite homogeneous, elastic and isotropic layer. In the case of pressure tunnels and shafts, the longitudinal dimension is very large (out-of-plane in Fig. 2.1) and the assumption of plane strain condition is made.

Some conventions are used herein: (i) pressures are always positive; (ii) tensile stresses are denoted with positive values and compressive stresses are denoted with negative values; and (iii) the sign convention for the displacements are according to the corresponding coordinate axes.

Chapter 2. Steel-lined pressure tunnels and shafts

Considering the aforementioned assumptions, the radial displacements at the layers' interfaces can be expressed analytically (Hachem & Schleiss 2011c):

1. in the steel liner:

$$u_r^s(r_c) = \frac{1 + \nu_s}{E_s} \frac{r_c}{r_c^2 - r_i^2} \cdot [(1 - 2\nu_s)(p_i r_i^2 - p_c r_c^2) + (p_i - p_c) r_i^2]; \quad (2.2)$$

2. in the backfill concrete:

$$u_r^c(r_{\text{crm}}) = u_r^c(r_c) + \frac{(1 - \nu_c^2) p_c r_c}{E_c} \ln \left(\frac{r_c}{r_{\text{crm}}} \right) \quad (2.3)$$

with

$$p_c r_c = p_{\text{crm}} r_{\text{crm}}; \quad (2.4)$$

3. in the near-field rock:

$$u_r^{\text{crm}}(r_{\text{rm}}) = u_r^{\text{crm}}(r_{\text{crm}}) + \frac{(1 - \nu_{\text{crm}}^2) p_{\text{crm}} r_{\text{crm}}}{E_{\text{crm}}} \ln \left(\frac{r_{\text{crm}}}{r_{\text{rm}}} \right) \quad (2.5)$$

with

$$p_{\text{crm}} r_{\text{crm}} = p_{\text{rm}} r_{\text{rm}}; \quad (2.6)$$

4. and in the infinite far-field rock:

$$u_r^{\text{rm}}(r_{\text{rm}}) = \frac{1 + \nu_{\text{rm}}}{E_{\text{rm}}} p_{\text{rm}} r_{\text{rm}}. \quad (2.7)$$

Combining Eqs. 2.3–2.7, and assuming a tied contact between the steel liner and the backfill concrete ($\Delta r_0 = 0$), the pressure p_c taken by the concrete–rock system can be obtained as:

$$p_c = \frac{\frac{1 + \nu_s}{E_s} \frac{r_c}{r_c^2 - r_i^2} [(1 - 2\nu_s) p_i r_i^2 + p_i r_i^2]}{\frac{1 + \nu_s}{E_s} \frac{r_c}{r_c^2 - r_i^2} [(1 - 2\nu_s) r_c^2 + r_i^2] + r_c \frac{1}{E_{\text{eq}}}} \quad (2.8)$$

where

$$\frac{1}{E_{\text{eq}}} = \frac{1 - \nu_c^2}{E_c} \ln \left(\frac{r_{\text{crm}}}{r_c} \right) + \frac{1 - \nu_{\text{crm}}^2}{E_{\text{crm}}} \ln \left(\frac{r_{\text{rm}}}{r_{\text{crm}}} \right) + \frac{1 + \nu_{\text{rm}}}{E_{\text{rm}}}. \quad (2.9)$$

2.2.2 Displacements

Given p_c , the radial displacements in the steel liner can be computed by

$$u_r^s(r) = \frac{1 + \nu_s}{E_s} \frac{r}{r_c^2 - r_i^2} \cdot \left[(1 - 2\nu_s)(p_i r_i^2 - p_c r_c^2) + (p_i - p_c) \frac{r_i^2 r_c^2}{r^2} \right]. \quad (2.10)$$

In the backfill concrete and the near-field rock, the radial displacements are, respectively

$$u_r^c(r) = u_r^s(r_c) + \frac{(1 - \nu_c^2) p_c r_c}{E_c} \ln \left(\frac{r_c}{r} \right) \quad (2.11)$$

and

$$u_r^{\text{crm}}(r) = u_r^c(r_{\text{crm}}) + \frac{(1 - \nu_{\text{crm}}^2) p_{\text{crm}} r_{\text{crm}}}{E_{\text{crm}}} \ln \left(\frac{r_{\text{crm}}}{r} \right). \quad (2.12)$$

Finally, the radial displacements in the far-field rock are expressed by:

$$u_r^{\text{rm}}(r) = \frac{1 + \nu_{\text{rm}}}{E_{\text{rm}}} \frac{r_{\text{rm}}^2}{r} p_{\text{rm}}. \quad (2.13)$$

2.2.3 Stresses

The tangential, radial and longitudinal stresses in the steel liner are given, respectively, by

$$\sigma_\theta^s(r) = \frac{1}{r_c^2 - r_i^2} \left[r_i^2 p_i - r_c^2 p_c - \frac{r_i^2 r_c^2}{r^2} (p_c - p_i) \right], \quad (2.14)$$

$$\sigma_r^s(r) = \frac{1}{r_c^2 - r_i^2} \left[r_i^2 p_i - r_c^2 p_c + \frac{r_i^2 r_c^2}{r^2} (p_c - p_i) \right], \quad (2.15)$$

and

$$\sigma_z^s(r) = \nu_s [\sigma_\theta^s(r) + \sigma_r^s(r)] = \frac{2\nu_s}{r_c^2 - r_i^2} (r_i^2 p_i - r_c^2 p_c). \quad (2.16)$$

For the backfill concrete, $\sigma_\theta^c = 0$ and

$$\sigma_r^c(r) = -\frac{r_c}{r} p_c. \quad (2.17)$$

Chapter 2. Steel-lined pressure tunnels and shafts

Similarly, for the near-field rock, $\sigma_{\theta}^{\text{crm}} = 0$ and

$$\sigma_r^{\text{crm}}(r) = -\frac{r_{\text{crm}}}{r} p_{\text{crm}}. \quad (2.18)$$

Finally, for the far-field rock

$$\sigma_{\theta}^{\text{rm}}(r) = \left(\frac{r_{\text{rm}}}{r}\right)^2 p_{\text{rm}} \quad (2.19)$$

and

$$\sigma_r^{\text{rm}}(r) = -\left(\frac{r_{\text{rm}}}{r}\right)^2 p_{\text{rm}}. \quad (2.20)$$

2.3 Basic design criteria

Pressure tunnels and shafts drilled in rock may be steel-lined where rock confinement is not sufficient or when leakage into the rock mass is not acceptable (Brekke & Ripley 1987). Steel linings address these issues by providing greater stiffness, strength, and impermeability. The basic design criteria for the steel liners are summarized by Schleiss (1988) as follows:

1. the working stress and deformation in the steel liner:
 - (a) stability of the steel liner under external water pressure (buckling);
 - (b) limiting working stresses in the steel liner under internal water pressure;
 - (c) limiting local deformation of the steel liner (crack bridging); and
2. the load-bearing capacity of the rock mass.

The second criterion refers to the verification of the load-sharing assumed for the limiting working stresses in the steel liner and to ensure the required security against the rock mass failure. The portion of the internal water pressure taken by the rock should not exceed the in situ stress or the tensile strength of the rock material (Schleiss 1988; Olsson *et al.* 1997).

In Europe, the C.E.C.T. (1980) recommendations for the design of SLPT&S have been developed for both the design and the construction. Load combinations and allowable equivalent stresses in steel liners according to the Hencky–Von Mises theory in triaxial state of stresses are discussed in these recommendations.

For the design it is common practice to consider an isotropic rock behavior, with the most unfavorable elastic modulus measured in situ. This is usually a conservative assumption in the quasi-static case.

2.4 Pressure tunnels and shafts in anisotropic rock

Several authors have studied pressure tunnels and shafts subject to internal water pressure considering the rock mass anisotropy. Experimental studies of linings in anisotropic media and an analytical method of the lining behavior in elastic orthotropic media by partitioning the lining into beam elements were published by Éristov (1967a,b). The latter analytical method is similar to the FEM approach presented in USACE (1997), as noted by Hachem & Schleiss (2009). Baslavskii (1973) derived an analytical solution for the stresses in the lining of a pressure tunnel in a linear elastic rock which is inhomogeneous within a thick ring around the liner. This inhomogeneity was characterized by a slight variation of the shear modulus around the opening. Postol'skaya (1986) performed a series of parametric investigations on the stresses in crack-resistant linings in different anisotropic media using the FEM. Kumar & Singh (1990) studied the effect of jointed rocks on reinforced concrete linings in pressure tunnels by means of the FEM. Their approach is particularly interesting as they introduced a reduction factor in the analytical expression for load-sharing between a lining and an isotropic and homogeneous rock mass to include the effect of joints. They used a continuous constitutive relation according to Singh (1973) to characterize the jointed rock mass. More recent analytical developments were carried out to compute stresses and deformations in unlined and lined tunnels in anisotropic rock subject to in situ loadings (e.g., Hefny & Lo 1999; Bobet 2011; Tran Manh *et al.* 2014).

Nevertheless, in these studies, the particular case of SLPT&S made of four layers with different properties and the assumption of cracked layers was not considered. To the authors' knowledge, there are neither analytical, experimental nor numerical published extensive parametric studies characterizing the influence of anisotropic rock behavior on stresses and deformations in SLPT&S under quasi-static internal water pressure.

2.5 High-strength steels for steel-lined pressure tunnels and shafts

2.5.1 High-strength steels (HSS)

For structural applications, steels can be roughly classified in three categories, namely *mild steels* ($f_y < 300$ MPa), *high-strength steels* (HSS, $300 < f_y < 600$ MPa) and *very high-strength steels* ($600 < f_y < 1100$ MPa) (Pijpers 2011). In general, high-strength steels exhibit a lower tensile to yield strength ratio f_u/f_y . Examples of stress–strain curves are shown in Fig. 2.3, plotted using the stress–strain relation of Ramberg & Osgood (1943). In this report, the term *high-strength steel* (HSS) refers to steel grades up to S960 for simplification.

The types of steel that are commonly used in hydropower construction are given in Table 2.1, particularly up to grade S700 M in Europe. Types S890 and S960 are also presented as they will be considered in this research project.

Although the mechanical performances of HSS allow for thinner and thus more economic steel

2.5. High-strength steels for steel-lined pressure tunnels and shafts

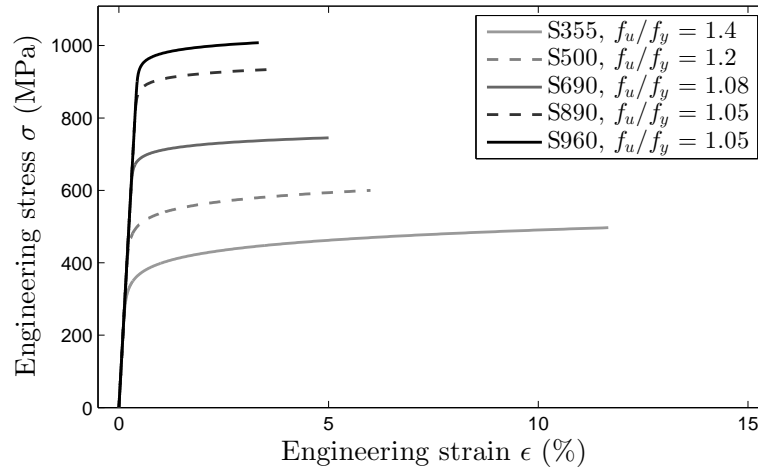


Figure 2.3: Qualitative examples of engineering stress–strain curves for different steel grades, with typical ultimate to yield strengths f_u/f_y ratios.

Table 2.1: Minimum yield strengths for different steel grades used in hydropower construction.

Grade	Standard	Yield strength f_y (MPa)	Thickness range (mm)
S355 J2/J2+N(*)	EN 10025-2 (2005)	355	$t_s \leq 16$ (**)
S355 N/NL(*)	EN 10025-3 (2005)	345	$16 < t_s \leq 40$ (**)
S355 M/ML(*)	EN 10025-4 (2005)	335	$40 < t_s \leq 63$ (**)
P355 N(**)	EN 10028-3 (2009)	325	$63 < t_s \leq 80$ (*)
		315	$60 < t_s \leq 100$ (**)
S500 ML	EN 10025-4 (2005)	500	$t_s \leq 16$
		490	$16 < t_s \leq 50$
		490	$50 < t_s \leq 75$
S690 QL	EN 10025-6 (2009)	690	$t_s \leq 50$
		650	$50 < t_s \leq 100$
S700 M (according to ALFORM®, Voestalpine)	EN 10149-2 (2013)	700	$8 < t_s \leq 15$
		680	$15 < t_s \leq 50$
		650	$50 < t_s \leq 60$
S890 QL	EN 10025-6 (2009)	890	$t_s \leq 50$
		830	$50 < t_s \leq 100$
S960 QL	EN 10025-6 (2009)	960	$t_s \leq 50$

liners with respect to the working stress criterion, welded HSS do not provide higher fatigue strength than lower welded grades (Nykänen *et al.* 2013). Indeed, the tensile strength has only little effects on the crack growth rate (Maddox 1991). As a consequence, if there is an initial crack-like flaw in the weld, the fatigue life is only determined by the crack propagation period and HSS does not provide an advantage.

Chapter 2. Steel-lined pressure tunnels and shafts

The combination of lean alloying concepts and thermomechanical treatment significantly enhanced the weldability of HSS, as well as ensured excellent strength and toughness properties (Cerjak *et al.* 2013a). However, although it has been drastically reduced, welded HSS are particularly subject to the risk of hydrogen induced cold cracking (HICC) (Cerjak *et al.* 2005; Cerjak 2008; Cerjak *et al.* 2013a,b, 2015; Enzinger & Cerjak 2006; Enzinger *et al.* 2006; Enzinger & Cerjak 2007, 2009; Enzinger *et al.* 2009; Roos *et al.* 2005). In the late 1950s when the application of quenched and tempered (Q+T) fine grain steels was initiated, HICC issue occurred in the heat-affected zone (HAZ) (Cerjak 2008; Cerjak *et al.* 2013b). With the development of grades S690 and S890 Q+T, the risk of HICC was shifted from the HAZ to the weld deposit (Cerjak 2008; Cerjak *et al.* 2013b). Despite the extensive research on welding procedures and the qualification programs used in practice, the HICC issue is still not satisfactorily solved today (Cerjak 2008). Although most cracks may appear transversally to the weld, some can also occur in the longitudinal direction, i.e., transversally to the major principal stress in pressurized steel liners. Examples of hydrogen induced cold cracks are shown in Figs. 2.4–2.5.

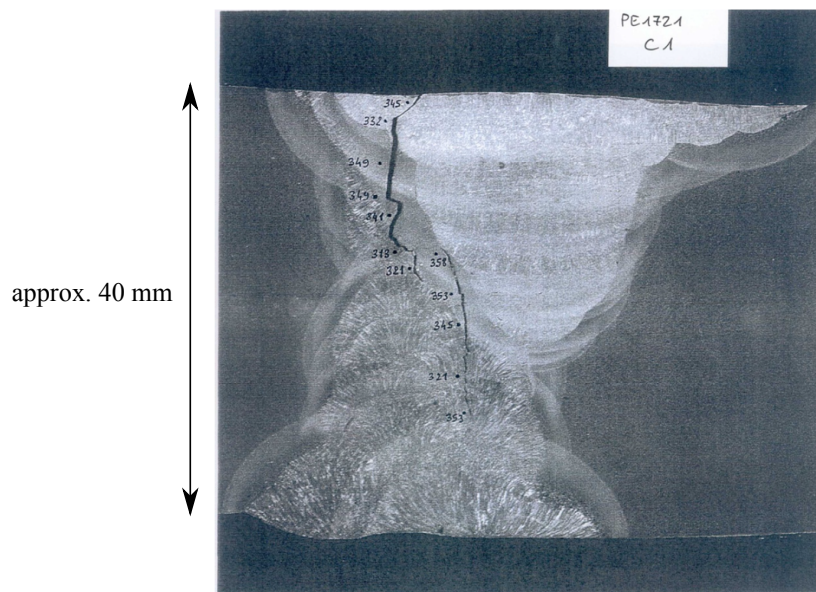
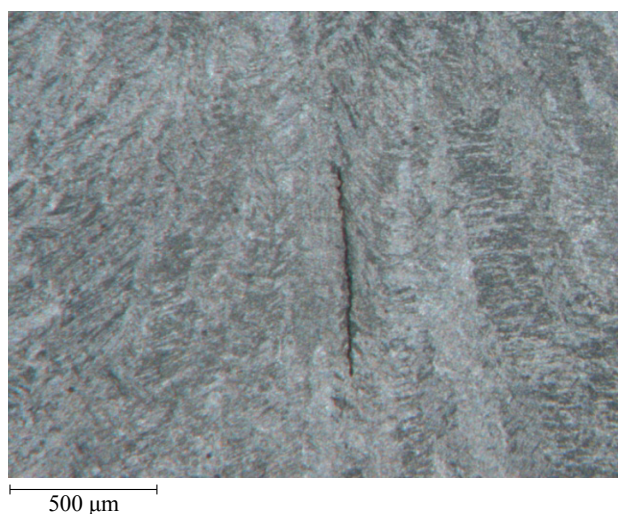


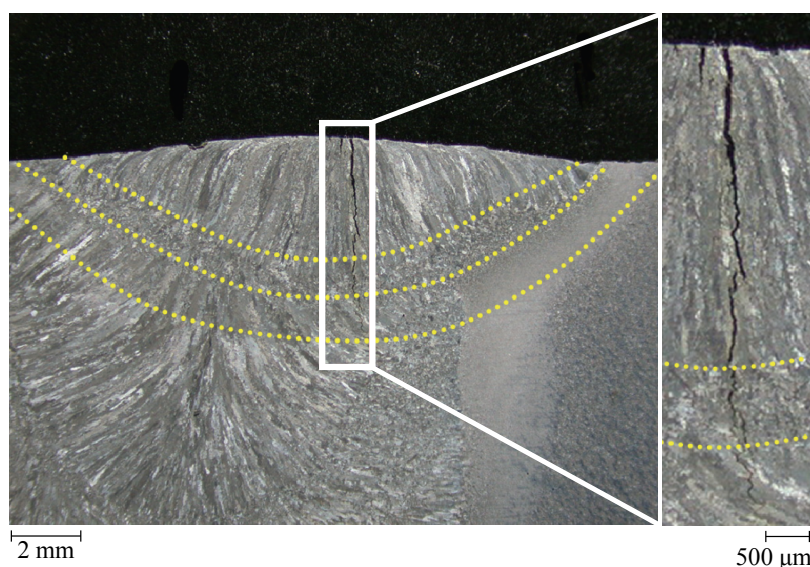
Figure 2.4: Cross section of longitudinal hydrogen induced cold crack in the weld deposit of steel grade S890 Q+T (modified after Cerjak *et al.* 2013a).

A tragic example of failure consequently to HICC occurred in December 2000, with the *accident* of the Cleuson–Dixence shaft, made of S890 (Cerjak *et al.* 2005). The release of high-pressure water into the surrounding rock mass provoked hydraulic jacking, resulting in a mudslide killing three people (see Fig. 2.6). S890 (see Table 2.1) was used for the first time in Europe for steel-lined pressure shafts. Although it was proved to fulfill the welding requirements, the rehabilitation of the shaft was then performed with lower grades (Cerjak *et al.* 2009).

2.5. High-strength steels for steel-lined pressure tunnels and shafts



(a) Embedded crack.

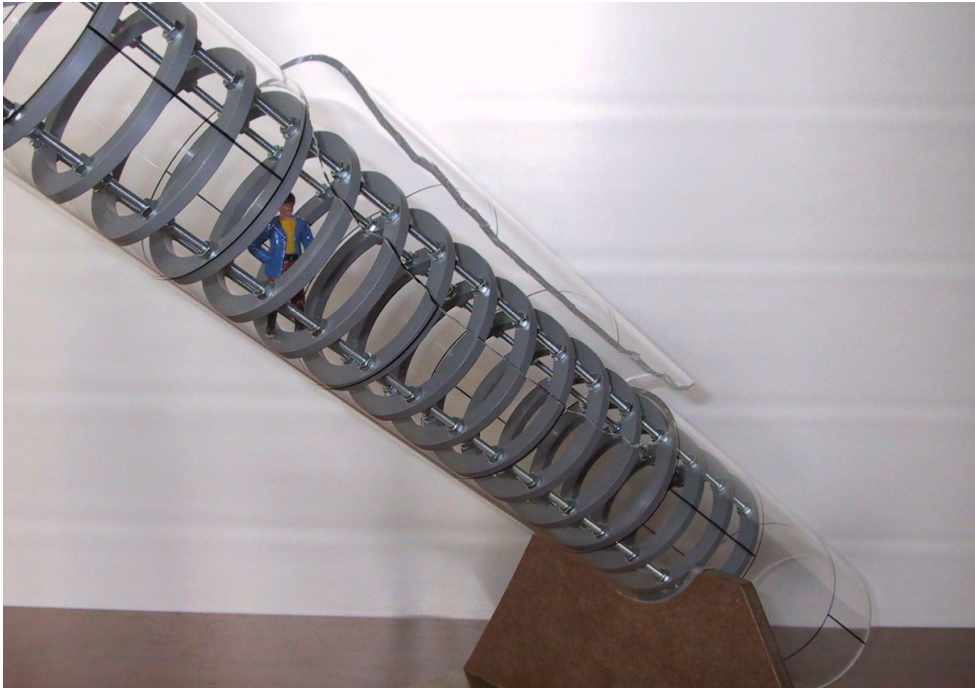


(b) Surface crack.

Figure 2.5: Examples of hydrogen induced cold cracks in the original material of the Cleuson–Dixence shaft (modified after Enzinger & Cerjak 2006, 2009).

2.5.2 Constructional aspects

Steel liners are straight-seam products manufactured from steel plates that are edge-broken (crimped), and rolled by means of a plate-bending roll in order to obtain a continuous and uniform curvature yielding a cylindrical shape (ASCE 2012). The crimped edges are then welded in the longitudinal direction (i.e., out-of-plane in Fig. 1.1, Section A-A). When manufactured from two rolled plates, a section may feature two longitudinal seams (see Fig. 2.7a). Once



(a) Scaled model reproducing the fracture in the steel liner.



(b) View on the mudslide after the failure.

Figure 2.6: Cleuson–Dixence: the accident of the 12th of December 2000 (from Hagin 2005).

welded longitudinally, the section is erected in the excavated shaft and welded circumferentially (girth weld) to the next reach. For the general quality level of the welds, the provisions of the European standard ISO 5817 (2014) are generally adopted, requiring class B, the highest. The acceptance levels for the non-destructive testing of the welds are given in the European standards EN ISO 11666 (2011) and EN ISO 23278 (2015) for ultrasonic and magnetic particle testing, respectively. The fabrication of the steel liners, from the plate manufacture to erection, including the welding procedures, must be performed in accordance with the relevant standards. In general, the choice of steel grades, filler materials and welding processes is assessed through extensive qualification programs (Cerjak *et al.* 2009; Chène 2009). Of particular interest in this research project, the C.E.C.T. (1980) recommendations give tolerances for the geometrical and weld imperfections. Some photographs taken on the construction site of the Nant de Drance project, in Switzerland, are presented in Fig. 2.7 and illustrate some selected constructional aspects. More details can be found, e.g., in Zerjeski (2007); ASCE (2012).

2.6 Transient pressure phenomena

Pressurized waterways are subject to transient phenomena. In hydroelectric power plants, these transients are due to an alteration of the flow velocity at any cross section, e.g., the sudden opening or closure of a valve, a sudden start-up or shutdown of a pump or turbine, etc. Such events generate a pressure wave propagating along the system with a high acoustic speed a . The induced dynamic forces are of primary importance on the design of the waterways. This pressure fluctuation is the so-called *water hammer*. Reviews of fluid-transients and water hammer theories are available in the literature, see, e.g., Jaeger (1977); Tijsseling (1996); Popescu *et al.* (2003); Ghidaoui *et al.* (2005). The usual dimensions of pipes justify a 1D-approach including the assumptions that flow properties such the pressure, velocity and density are uniform in a cross section. Assuming compressibility of water and neglecting the terms related to transport phenomena compared to propagating phenomena, the mass and momentum conservation equations yields the classical 1D-approach for water hammer flows, often solved by the *Methods of Characteristics* (MOC) (Popescu *et al.* 2003; Boillat & de Souza 2004; Ghidaoui *et al.* 2005; Kwon 2007; Bergant & Tijsseling 2008, other methods are also introduced, e.g., by Nicolet 2007). This classical theory predicts a quasi-static (i.e. without fluid-structure interaction) wave speed.

Fluid-Structure Interaction (FSI) characterizes the phenomenon when pressure waves in water produce dynamic forces in the steel liner and trigger vibrations, the latter causing water pressure waves in return (Hachem & Schleiss 2011c). According to Kuiken (1988), FSI may lead to higher or lower extreme dynamic pressures and so for the stresses in the liner, change in the natural frequencies of the system, more damping and dispersion of the waves. Numerous works have contributed to the comprehension of wave propagation in pressurized pipes considering FSI (see, e.g., Atabek 1968; Kuiken 1984, 1988; Lavooij & Tijsseling 1991; Heinsbroek 1997; Zhang 1999; Li *et al.* 2003; Tijsseling 2003; Kochupillai *et al.* 2005; Tijsseling 2007; Keramat *et al.* 2012; Moussou 2013).

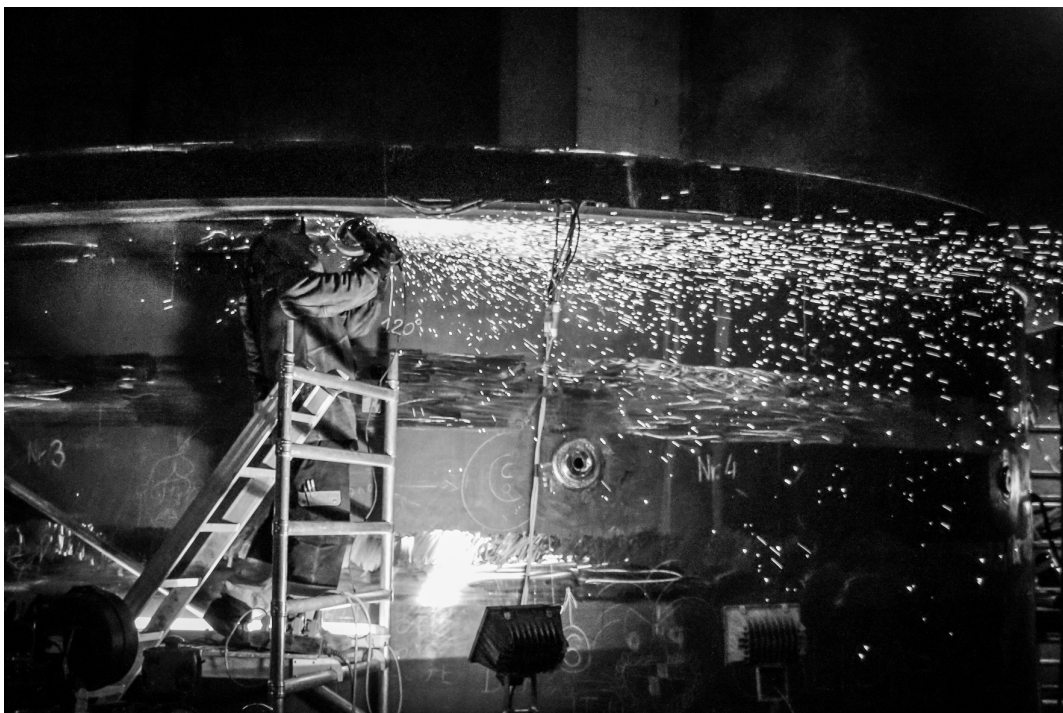


(a) Two rolled plates before welding and erection.



(b) Welding of an anchor ring.

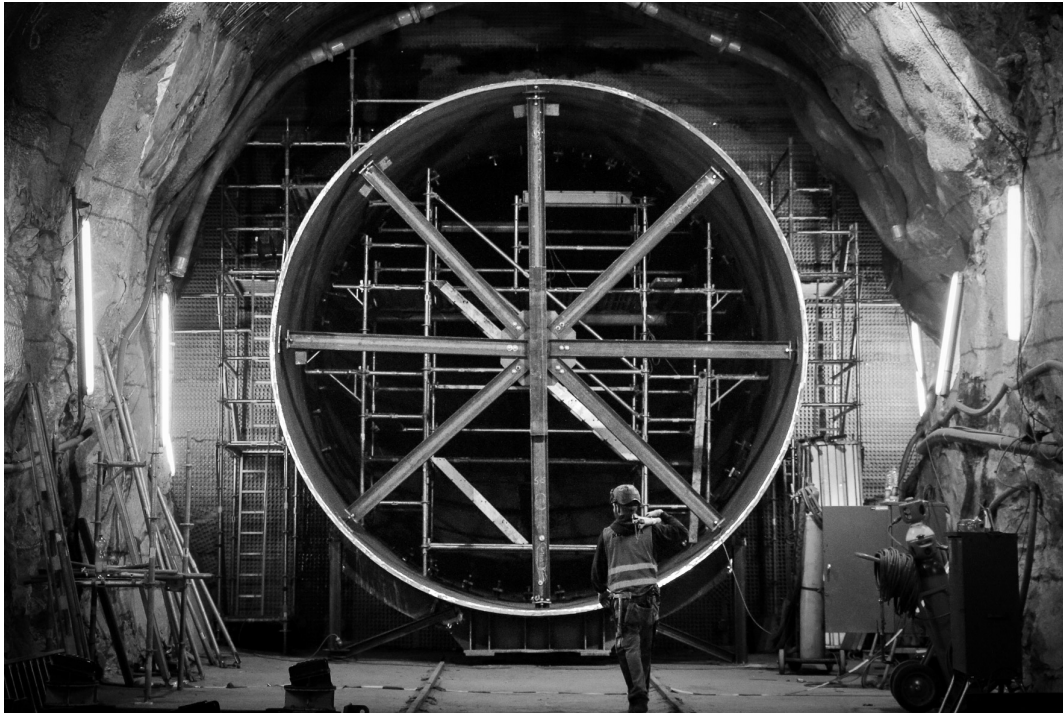
2.6. Transient pressure phenomena



(c) Grinding of the welded joints.



(d) Post-weld heat treatment of a grouting nipple.



(e) Steel liner with temporary bracing.



(f) Void between the steel liner and the surrounding rock (with shotcrete), before backfilling with concrete.

Figure 2.7: Photographs taken at the Nant de Drance project in Switzerland (©A. J. Pachoud, 2016). The author acknowledges the authorization provided by ANDRITZ and Nant de Drance to use these photographs herein.

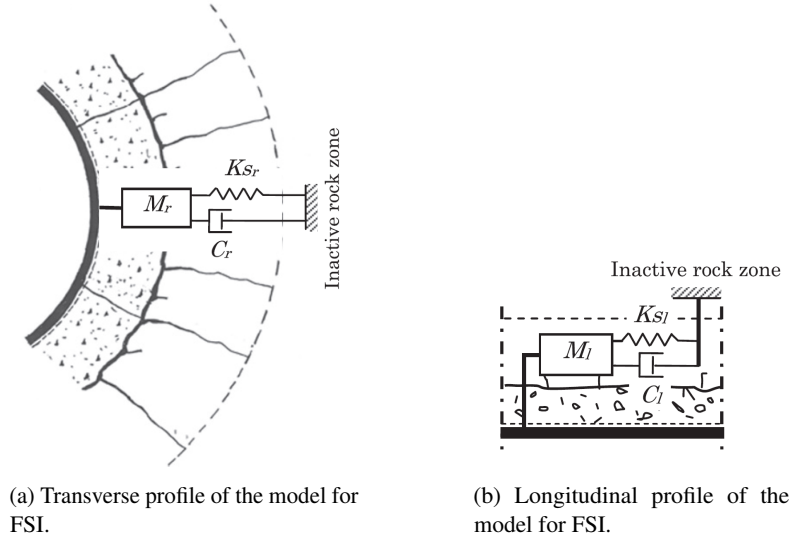


Figure 2.8: Computation model used for the frequency-dependent wave speed: (a) transverse profile and (c) longitudinal profile (figures from Hachem & Schleiss 2011c).

To model the steel–concrete–rock system of SLPT&S, Hachem & Schleiss (2011c) proposed a model shown in Fig. 2.8 for the computation of the frequency-dependent wave speed calculation, and thereby take into account FSI. In this model, the effect of backfill concrete and the surrounding rock mass is mechanically modeled by a spring, a dashpot and a lumped additional mass (Kelvin model). The spring stiffness (per unit area) is denoted K_{s_r} , the frictional coefficient of the dashpot C_r and the additional mass M_r . For the longitudinal interaction, an equivalent model is considered with coefficients K_{s_l} , C_l and M_l . It yields a six-equation (3-mode) model of the FSI problem, i.e., four equations for the fluid without body forces (two linearized equations of motion in axial and radial directions, equation of continuity and the thermodynamic constitutive equation for the density), and two equations of motion in an initially stressed field for the liner (axial and radial directions). The unknowns to be solved are u , v , p , u_l^s and u_r^s , i.e., the axial and radial water velocities, the water pressure, and the axial and radial displacement of the steel liner, respectively. Combining these equations yields a dispersion equation, and more specifically a quadratic dispersion by considering water as a compressible non-viscous fluid and by neglecting the initial longitudinal stress in the liner. The unknowns u , v , p , u_l^s and u_r^s are assumed to vary harmonically over the axial distance x and time t , with a real constant frequency ω . By denoting c the complex propagation velocity, and the *hat* superscript standing for the amplitude of the periodic quantities, the unknowns are expressed as:

$$[u, v, p] = [\hat{u}(r), \hat{v}(r), \hat{p}(r)] e^{i\omega(t-x/c)}, \quad (2.21)$$

$$[u_l^s, u_r^s] = [\hat{u}_l^s, \hat{u}_r^s] e^{i\omega(t-x/c)}. \quad (2.22)$$

The solutions of the dispersion equation yield two modes that can only propagate at low frequen-

cies (the so-called tube modes) and an infinite number of acoustic modes that propagate at high frequencies. The tube mode with the lowest velocity is the longitudinal compression mode in water (water hammer or Young mode), the tube mode with the highest velocity is the axial stress wave in the steel walls (called precursor or Lamb mode, resulting from the coupling of the radial expansion and contraction of the liner walls and the Poisson's ratio of the steel).

2.7 Changed operational conditions

High-head hydropower plants with storage and with/without pumping are increasingly being requested to provide ancillary services to the electrical grid. They guarantee that the network's frequencies remain within a narrow acceptable band around the standard frequency (e.g., 50 Hz in West and Central Europe). This is possible due to their ability to rapidly (within seconds–minutes) supply additional power to the grid, or in case of pumped-storage, absorb exceeding production in case of demand drop. From the infrastructure standpoint, this has led to the increase of the number of powerhouse starts per year, in particular for large-hydropower plants equipped with Francis groups, as depicted in Fig. 2.9.

Two major context changes of the last 30 years have contributed to the increase number of annual starts:

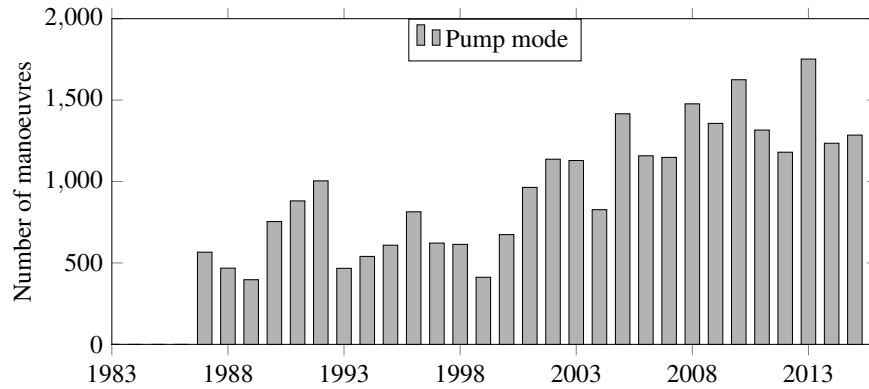
1. penetration of new renewable power plants using rapidly-varying natural resources (in time and space), like wind and solar radiation; and
2. the contractual mechanisms created by both Transmission System Operators (TSOs) and electricity market regulators to remunerate hydropower plants for their readiness to step-in (increase power supply).

The situation is not necessarily similar in hydropower plants equipped with Pelton groups, which can operate for a given head in a much larger range of discharges (and power) with acceptable efficiencies, than the Francis units can. Operators presently tend to keep Pelton units synchronized, varying the flow discharge and avoiding full stoppage if possible (and properly remunerated, e.g., secondary grid regulation), whereas Francis units are more often stopped and restarted.

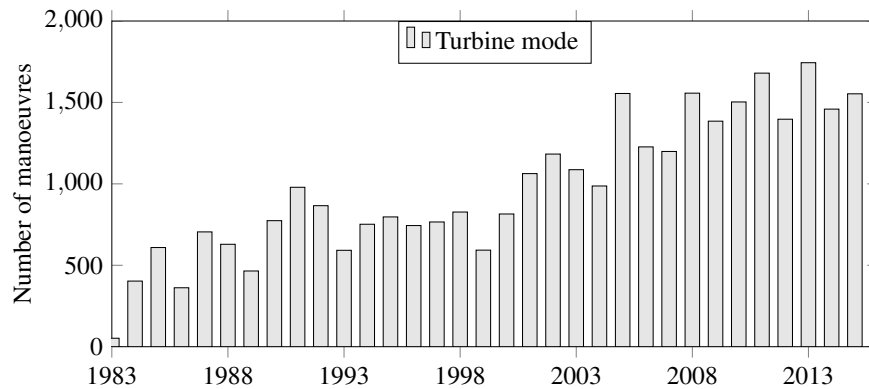
The increased number of starts raises several challenges to the operator in terms of long-term fitness-for-service of the assets. More maneuvers accelerate wear and fatigue, passing more often by unstable and unfavorable operation paths for the turbines. More rapid maneuvers may cut corners in terms of start and stop procedures. Steel-lined pressure tunnels and shafts are more frequently under operation transient loading conditions. Despite having lower amplitude than extreme transient load cases used for structural design of the steel lining, the cumulated number of load rejection cycles increases faster these last few years than before, raising doubts about the residual fatigue life of the steel-lined structures.

Different innovative solutions are being developed worldwide to mitigate load rejection pressure

2.8. New and innovative non-intrusive monitoring methods



(a) Start maneuvers in pump mode.



(b) Start maneuvers in turbine mode

Figure 2.9: Number of cumulated annual starts of a typical high-head storage hydropower plant in Switzerland equipped with Francis turbines and multistage pumps (after Manso *et al.* 2016a).

risers (Li *et al.* 2014) and mitigate instabilities during start/stop maneuvers (Manso *et al.* 2016b) by means of modified technologies or operation procedures.

In terms of steel-lined structures, however, the increased frequency of these maneuvers and the accelerated rise of cumulated loading cycles merits further research in terms of the corresponding structural stresses, crack propagation (if any) and residual fatigue life, both for mild as for high-strength steels.

2.8 New and innovative non-intrusive monitoring methods

Within the context of harsh operational conditions described in Sect. 2.7, non-intrusive monitoring techniques are of special interest for SLPT&S. The latest developments in this matter are presented

hereafter. Most of the content of this Section has been published in a scientific article entitled "Signal analysis of an actively generated cavitation bubble in pressurized pipes for detection of wall stiffness drops", by E. Mazzocchi, A. J. Pachoud, M. Farhat, F. E. Hachem, G. De Cesare and A. J. Schleiss, in the *Journal of Fluids and Structures* (Mazzocchi *et al.* 2016). The study was carried out in the framework of a Master thesis conducted by Mazzocchi (2014) at the Laboratory of Hydraulic Constructions (LCH, EPFL) in collaboration with the Laboratory for Hydraulic Machines (LMH, EPFL) within the scope of *HydroNet 2*. The author of the present report followed closely this Master thesis.

2.8.1 Historical development

Hydraulic assessment methods for pipelines failure and leak detection have been developed recently, especially in the fields of water-supply, gas and oil networks (see, e.g., Ferrante & Brunone 2003a,b; Covas *et al.* 2005; Beck *et al.* 2005; Misiunas *et al.* 2005; Shamloo & Haghighi 2009; Stephens *et al.* 2008). The general principle of these methods is based on the analysis of the system response to pressure transients. When a pressure wave is generated at a point of the pipeline, it propagates through the entire system. Each time it goes through features such as changes in section, resistances or junctions, the incident wave is partially reflected, partially transmitted and partially absorbed. Any new reflection boundary appearing in a network, is indicative of a new singularity.

2.8.2 Water hammer signals

Hachem (2011) developed a new non-intrusive monitoring method to detect and locate local drops of wall stiffness in SLPT&S. This method is based on the analysis of water hammer measurements, recorded by two pressure transducers placed at the ends of a steel test pipe, divided into several reaches. A local drop in the wall stiffness was modeled by replacing steel reaches with so-called *weak reaches*, made of aluminum or PVC. The water hammer waves were generated through closure maneuvers of a valve located at the downstream end of the pipe. When the incident wave encounters the weak reach, which is characterized by a lower propagation speed, it is partially reflected and partially transmitted (and partially absorbed in the case of viscoelastic materials, such as PVC).

Every time a rectangular pressure wave of magnitude $(h_i - h_0)$ goes through changes in the pipe wall stiffness or flow area, it is partially transmitted and partially reflected. For branching junctions, the theoretical transmission ratio of the incident wave through the n^{th} junction is given by (Wylie *et al.* 1993):

$$\frac{h_{in} - h_0}{h_i - h_0} = 2^n \prod_{j=i}^n \frac{1}{1 + \frac{a_{j+1}A_j}{a_jA_{j+1}}} \quad (2.23)$$

2.8. New and innovative non-intrusive monitoring methods

where, h_0 , h_i and h_{tr} are the piezometric heads of the steady-state, incident and transmitted waves, while a_j and A_j are the wave speed and flow area of each pipe reach j .

The experiments showed that the location and the stiffness of the weak reach can be estimated through the analysis of the reflected pressure signals. Nevertheless the analysis was proved to be effective only for significant stiffness reductions, around 98% (PVC reaches). When this value drops to approximately 63% (aluminum reaches), the location of the weak reach is no longer possible. Results of this research project were published in Hachem & Schleiss (2011a,b,d, 2012a,b).

2.8.3 Actively generated cavitation bubble signals

Hachem (2011) has shown in his work that the monitoring method could be significantly more effective when pressure waves characterized by a steep wavefront are analyzed. The objective of the study performed by Mazzocchi *et al.* (2016) was to improve the sensitivity and precision of the monitoring method by replacing water hammer with a more suitable pressure signal. An underwater spark generator was used to generate very steep shock waves, characterized by an extremely short wave period. These properties allowed for a much more precise estimation of the wave propagation celerity. A reduction of this wave celerity was clearly identified when a weak reach was introduced in the test pipe. This implies that the measure of the wave propagation speed, derived from hydrophones records at both ends of the pipe, can be used to detect changes in the overall wall stiffness. If a sufficiently powerful spark generator could be installed in a real pressure shaft, regular and precise measures of the wave speed could be recorded. Any significant deterioration of the structure should then be detected by a reduction of the measured wave celerity.

The spectral analysis of the signals was then carried out in order to estimate the position of the weak reach. The wave reflections caused by the aluminum reaches with a stiffness drop of 63.5% are relatively small and therefore the corresponding spectra are almost identical to those obtained from the steel pipe. In the case of the PVC reaches instead, the frequency content of the signal changes completely and two major peaks can be easily identified. Assuming that the corresponding frequencies are related to reflected waves, traveling back and forth between the weak reach and the pipe ends, the incident-reflection travel time can be derived. Using the estimated wave speed, it was therefore possible to compute the length of the reflection path. This analysis was showed to be able to locate the PVC reaches with a maximum relative error of 6.4% from the upstream sensor and 13.2% from the downstream one, with more explicit spectra than with the water hammer signal approach developed by Hachem (2011).

Spark-induced shock waves may represent a significantly more convenient pressure signal than water hammers. Remarkable precision improvements may be possible regarding both the detection and the location of local drops in the pipe wall stiffness. Nevertheless a challenge is still to generate cavitation bubbles in steel-lined conduits with several hundreds of meters internal

pressure.

2.8.4 Ranges of application

At the scale of SLPT&S, the objective of non-intrusive monitoring methods is to detect relatively small changes in the stiffness (and thus a small amount of damages) before a significant risk of failure occurs. According to Eq. 2.23, the wave reflection ratio is proportional to the drop of the wave speed inside the weak reach compared to the rest of the pipeline.

In order to estimate the wave speed reduction caused by local damages in a real SLPT&S, one can for instance study the effect of the modulus of elasticity of the rock mass on the wave speed. Substituting the backfill concrete, the near- and far-field rock masses with an equivalent homogeneous rock mass with an apparent modulus of elasticity E_{app} , and considering that the liner is in contact with the concrete–rock system, the wave speed can be expressed as follows (Hachem & Schleiss 2011c):

$$a = \left\{ \frac{1}{\rho_w \left[\frac{1}{K_w} + \frac{4(v_s^2 - 1)(1 + v_{rm})r_c r_i}{E_{app}(1 + v_s)[(2v_s - 1)r_c^2 - r_i^2] - E_s(1 + v_{rm})(r_c^2 - r_i^2)} \right]} \right\}^{1/2} \quad (2.24)$$

where ρ_w and K_w are the unit mass and the bulk modulus of water, respectively, and

$$E_{app} = \frac{E_{rm}E_{crm}}{E_{crm} - E_{rm}(1 - v_{rm}) \ln \left(\frac{r_c}{r_{rm}} \right)}. \quad (2.25)$$

The subscripts s , c , crm and rm refer to the steel-liner, backfill concrete, the near- and far-field rock zones, respectively, and $r_c = r_i + t_s$ (also see Fig. 2.1).

In the case of open-air penstock, the wave propagation speed is given by (Hachem & Schleiss 2011c):

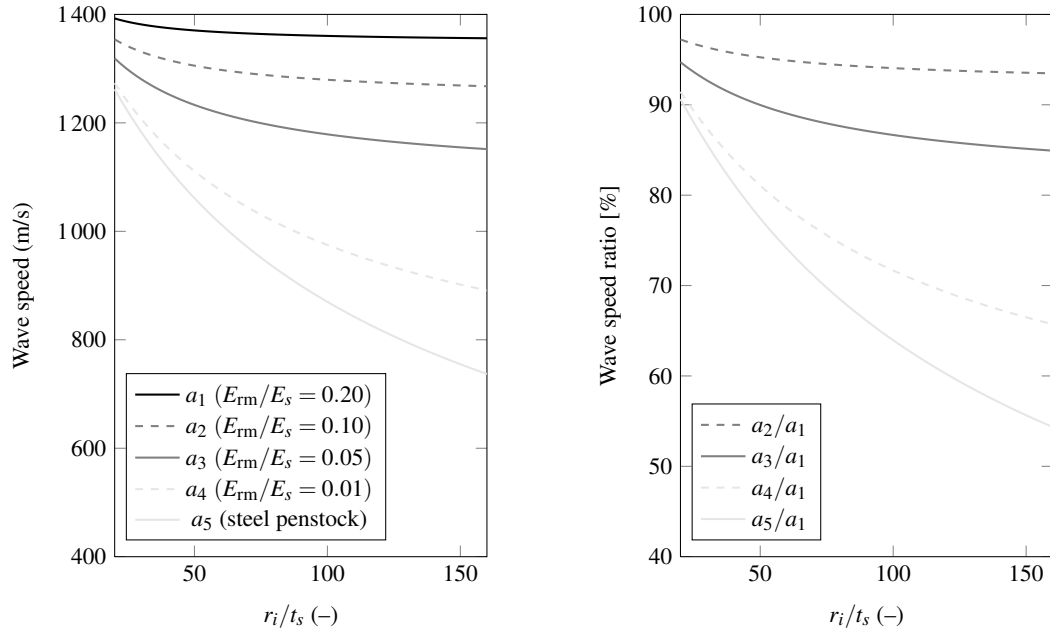
$$a = \left\{ \frac{1}{\rho_w \left(\frac{1}{K_w} + \frac{2r_i \lambda_3}{E_s t_s} \right)} \right\}^{1/2} \quad (2.26)$$

where E_s is the elastic modulus of steel, t_s is the steel thickness, and λ_3 is defined as:

$$\lambda_3 = \begin{cases} 1 - 0.5v_s & \text{if the penstock can freely slip in the longitudinal direction;} \\ 1 & \text{if the penstock has expansion joints over its entire length;} \\ 1 - v_s^2 & \text{if the penstock is blocked in the longitudinal direction;} \end{cases} \quad (2.27)$$

with ν_s the Poisson's ratio of steel.

Figure 2.10a gives the wave speed as a function of the ratio of the internal radius of the liner to the thickness of the liner for different levels of rock mass stiffness. The wave speed of an open-air steel penstock is also given (Eq. 2.26). The curves have been computed considering the parameters proposed by Hachem & Schleiss (2011c), namely $E_s = 2.1 \cdot 10^5$ MPa, $E_c = 2.1 \cdot 10^4$ MPa, $E_{crm} = 0.5E_{rm}$, $\nu_s = 0.3$, $\nu_c = 0.20$, $\nu_{rm} = 0.25$, $r_{crm} = 1.2 \cdot r_i$, $r_{rm} = 1.25 \cdot r_{crm}$, $K_w = 2.2 \cdot 10^3$ MPa and $\rho_w = 1 \cdot 10^3$ kg/m³.



(a) Wave speed as a function of the ratio of internal tunnel radius to steel liner's thickness for different values of E_{rm}/E_s and for open-air steel penstocks.

(b) Wave speed ratio of the four lower wave speed curves to the highest one as a function of the ratio of internal tunnel radius to steel liner's thickness.

Figure 2.10: Wave speeds in real SLPT&S (modified after Mazzocchi *et al.* 2016).

One could now consider a steel-lined pressure tunnel or shaft embedded in a very good quality rock mass (e.g., $E_{rm}/E_s = 0.20$) with local damage represented by a drop of the rock mass stiffness or, the extreme scenario of complete absence of rock mass participation (i.e., open-air steel penstock). Figure 2.10b gives the ratios between the wave speed inside the damaged zones and the rest of the pressure tunnel. As it can be seen, a very important local drop of the rock stiffness, in an overall good quality rock mass, can cause a wave speed reduction of up to around 55%. A more probable value would be from 85 to 95%.

Such damages can now be compared to the weak reaches used in the experimental pipeline by computing the wave reflection ratio as a function of the wave speed reduction inside the weak reach. As it can be seen from Fig. 2.11, the severity of the kind of damages that would occur in real SLPT&S are much better reproduced by the aluminum reaches (wall thickness of 5 mm)

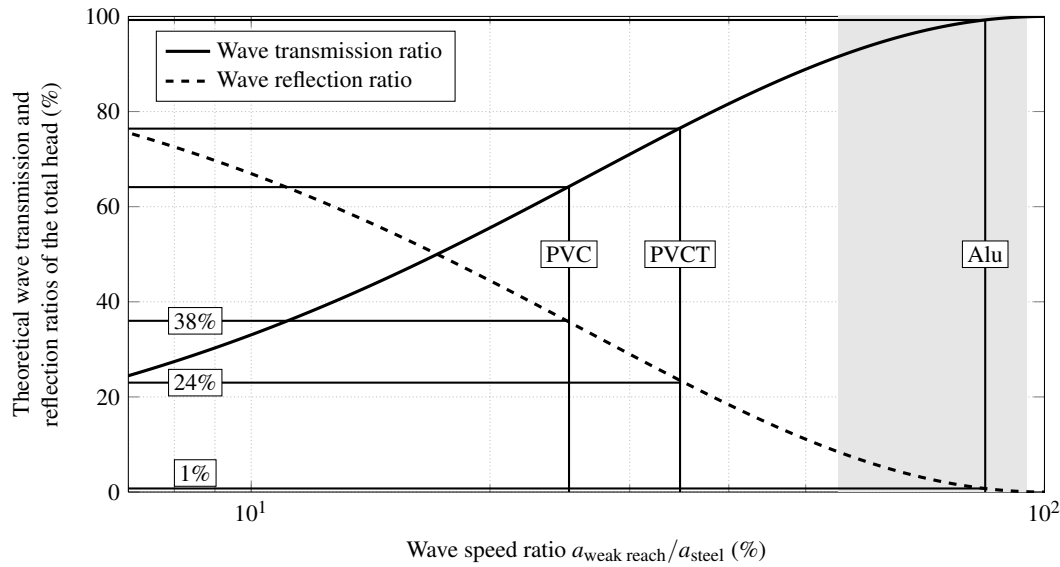


Figure 2.11: Theoretical ratios of wave transmission and reflection as a function of the ratio of the wave speed inside the weak reach $a_{\text{weak reach}}$ and the other stretches of the test pipe a_{steel} . The range of estimated possible values for SLPT&S are highlighted in gray (modified after Mazzocchi *et al.* 2016).

than the PVC (wall thickness of 5 mm) and PVCT (wall thickness of 10 mm) ones. In order to be effective, the sensitivity of the monitoring methods developed by Hachem (2011) and Mazzocchi *et al.* (2016) would therefore need to be improved for practical applications.

2.9 Conclusions

From the literature review on SLPT&S presented in this chapter, the following conclusions can be outlined.

1. The design of SLPT&S is normally done considering isotropic rock behavior with the lowest elastic modulus measured in situ.
2. There are neither analytical, experimental nor numerical published solutions to estimate the stresses in the steel liners of SLPT&S in anisotropic rock.
3. Hydropower plants, and particularly pumped-storage, operate presently under more frequent transients and thus faster cumulative number of cycles, raising the issue of fatigue at the welded joints of steel liners of SLPT&S.
4. The use of HSS, within the standard design procedure, allows reducing the liner's thickness and thus the economical costs. However, welded HSS do not provide a higher fatigue

strength than mild steels. As a consequence, for an optimized use of HSS, the issue of fatigue should be treated systematically.

5. Promising developments have been recently proposed for non-intrusive monitoring of SLPT&S, by means of water hammer transients and of actively generated cavitation bubble signals. These methods need to be further optimized, and a great technological challenge remains in their practical implementation.

In this research project, the gaps in knowledge related to the design of SLPT&S in anisotropic rock and the issue of fatigue will be addressed. However, the development of the non-intrusive monitoring methods is out of the scope of the project.

3 Fatigue and fracture assessment of welded joints

3.1 Introduction to fatigue

According to Maddox (1991),

in the context of engineering, fatigue is the process by which a crack can form and then grow under repeated or fluctuating loading. [...] The magnitude of the loading required to produce fatigue cracking in a component may be much less than needed to break the component in a single application of load.

Therefore, fatigue crack may initiate and propagate under applied loads lower than the ultimate strength because of stress concentration zones into a component, induced by geometrical features such as notches, or from initial defects located into the component. Welded joints are particularly sensitive to fatigue phenomenon, as the weld shape produces stress concentrations, and welding may introduce initial flaws into the welded component. Fatigue is a dangerous process leading to final fracture and failure as it generally happens under elastic nominal stress (at least from medium to very-high cycle fatigue), and the high localization of the damage (cracks) makes it difficult to observe.

The total number of cycles N_T during the fatigue life of a component is often assumed to the sum of the number of cycles to crack initiation N_i and the number of cycles during the crack propagation period N_p , as (Ho & Lawrence 1984; Pijpers 2011)

$$N_T = N_i + N_p. \quad (3.1)$$

Typically, the initiation stage is completed when the microcrack growth (dislocation, crack nucleation) is no longer dependent on the microstructure (Baptista 2016). The transition from microcrack to long crack regime (see also Fig. 3.3) typically occurs at crack depth $a \approx 0.1$ – 0.2 mm (Pijpers 2011; Baptista 2016). If an initial crack-like flaw is present in a welded

component (e.g., lack of fusion, undercuts, HICC, stress corrosion cracking), the fatigue life is generally dominated by the propagation stage (Borges 2008).

3.2 Fatigue assessment methods for welded steel structures

Fatigue assessment of welded steel structures is generally performed under two approaches, as enumerated hereafter (after, e.g., the reviews of Radaj 1996; Chryssanthopoulos & Righiniotis 2006; Radaj 2006; Fricke 2011, 2013).

1. **The so-called S – N approach**, where the S – N curves (or Wöhler curves) are based on statistics of experimental fatigue testing. S – N curves give a direct relationship between the fatigue life and constant amplitude load cycles N , in terms of nominal (Sect. 3.2.1) or local stresses (Sects. 3.2.2–3.2.3), S . For variable amplitude loading, the fatigue life is obtained indirectly using a damage accumulation law, e.g., the widespread Palmgren–Miner rule (Sect. 3.3). The S – N curves implicitly accounts for initiation and propagation stages.
2. **The crack propagation approach**, based on linear elastic fracture mechanics (LEFM) and the Paris–Erdogan law (Sect. 3.2.4). This approach assumes that an initial crack-like flaw is present (typically for welded joints), and thus estimate the propagation stage only. Initiation stage can be considered in combination with a local elastoplastic strain-based approach (Baptista 2016).

The main related approaches are introduced hereafter.

3.2.1 Nominal stress approach

The *nominal stress approach* (also called the *classification of structural details*) is the simplest and somehow *traditional* method, where the fatigue strength is obtained in terms of range of nominal stress. In this method, local stresses are disregarded and welded structural details are classified into different detail categories, associated to S – N curves. According to the recommendations of the International Institute of Welding (IIW, Hobbacher 2016), the S – N curves are characterized by their fatigue strength at $2 \cdot 10^6$ cycles with the probability of survival $p_s = 97.7\%$ (so-called FAT classes, in MPa), and a slope exponent $k = 3$ above and $k = 22$ below the knee point at $10 \cdot 10^6$ cycles for constant amplitude fatigue loading, as shown in Fig. 3.1. For variable amplitude fatigue loading (see also Sect. 3.3), S – N curves are modified with a slope exponent $k = 5$ below the knee point at $10 \cdot 10^6$. The modified S – N curves are plotted in Fig. 3.2.

The nominal stress approach is implemented in most structural codes for fatigue assessment, such as EN 1993-1-9 (2005) (Eurocode 3) in Europe. This approach is the easiest to use if the nominal stress can be defined. The S – N curves were derived experimentally in *as-welded* conditions, and the influence of geometrical imperfections such as linear misalignment are taken into account in the prescribed limits of the classification of the structural details.

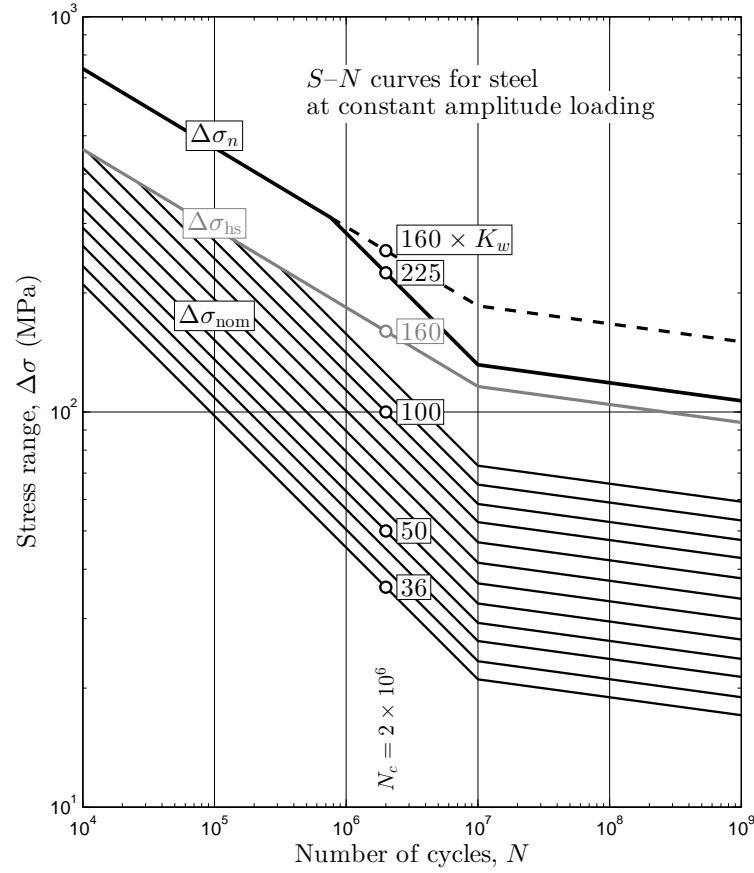


Figure 3.1: S – N curves for steel at constant amplitude loading (reproduced after Hobbacher 2016).

3.2.2 Structural hot-spot stress approach

The *structural hot-spot stress approach*, contrary to the nominal stress approach, includes the effect of the structural configuration, i.e., the stress increase caused by the *structure-related stress concentration* (Fricke 2013). This approach enables the treatment of weldments where a nominal stress cannot be defined meaningfully, and also reduces the number of FAT (Mann 2006), called hot-spot S – N curves (Niemi *et al.* 2006). Within this approach, the S – N curves are related to the type of weld (Hobbacher 2009). The structural hot-spot stress is a combination of membrane and bending stresses, excluding the nonlinear peaks induced by the weld shape, e.g., by the weld toes (see Fig. 3.9). The hot-spot S – N curves are therefore used in terms of range of structural hot-spot stress, that can be estimated by means finite element analysis (see Sect. 6.1.2) or analytical formulas provided in standards. Numerous application can be found in the literature, e.g., in Aygöl *et al.* (2012, 2013); Doerk *et al.* (2003); Lotsberg & Sigurdsson (2006a); Lotsberg (2006); Poutiainen *et al.* (2004); Stenberg *et al.* (2015).

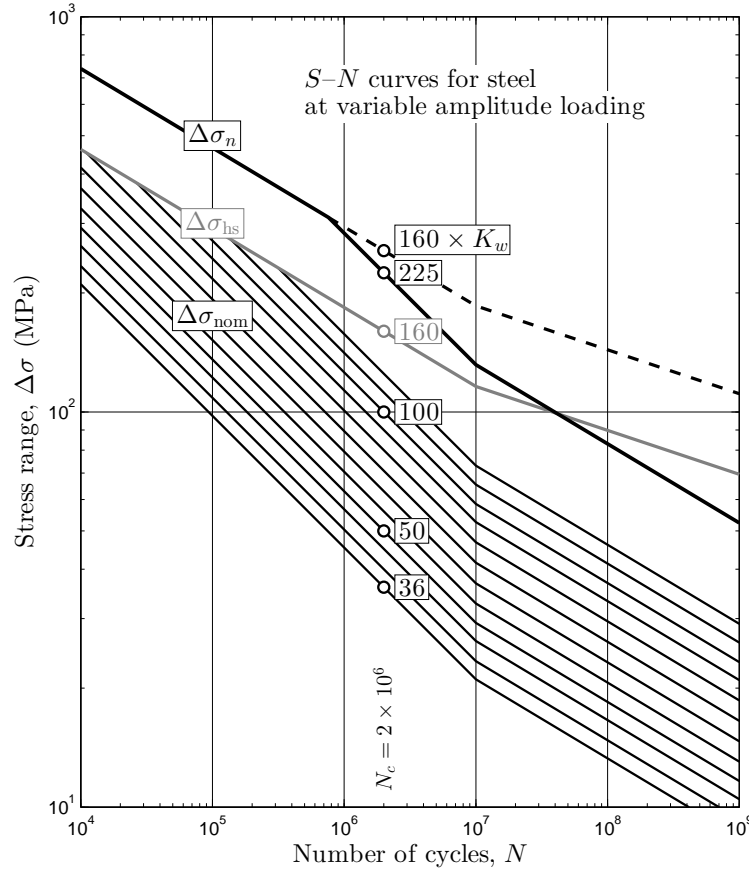


Figure 3.2: Modified S – N curves for steel at variable amplitude loading for Palmgren–Miner summation.

3.2.3 Effective notch stress approach

The so-called *notch stress approaches* add a degree of precision by considering the nonlinear peak induced by the presence of the weld, e.g., at weld toes or roots, which reduces the fatigue strength for high-cycle fatigue lives. The increase in local stress and its effect on fatigue strength can be expressed by a fatigue notch factor K_f , which can be determined from the elastic notch stress concentration factor K_t from different methods (Fricke 2012; Nykänen *et al.* 2013), e.g., the *stress averaging approach*, used under the form of fictitious notch rounding (Fricke 2012).

The notch rounding approach is based on the Neuber's concept of microsupport effect at notches, which consists in averaging the maximum notch stress in a small material volume by introducing an enlarged, fictitious radius ρ_f as (Fricke 2012; Radaj *et al.* 2013)

$$\rho_f = \rho + s\rho^* \quad (3.2)$$

3.2. Fatigue assessment methods for welded steel structures

where ρ is the actual notch radius, s is a factor for stress multiaxiality and strength criterion and ρ^* is the microsupport length. Radaj (1990) proposed, for structural steel welded joints, that $s \approx 2.5$ (plane strain conditions at notches combined with the von Mises multiaxial strength criterion for ductile materials), $\rho^* = 0.4$ mm (welded structural steels) and $\rho = 0$ mm (worst case scenario), yielding a so-called *reference radius* $\rho_f = r_{\text{ref}} = 1$ mm (Fricke 2012; Radaj *et al.* 2013). This results in a maximum possible fatigue notch factor $K_{f,\text{max}} \approx K_t(r_{\text{ref}} = 1 \text{ mm})$ (Nykänen *et al.* 2013). The related elastic notch stress is the fatigue-effective stress, from where the approach takes its name, so-called *effective notch stress approach*. In this approach, the fatigue strength in terms of range of effective notch stress is related to a single S – N curve of material, namely, for steel, FAT 225 limited¹ to FAT 160 $\times K_w$ with $K_w \geq 1.6$, under principal stress hypothesis (Sonsino 2009a; Radaj *et al.* 2009). The definition of K_w is given in Sect. 3.7.2. The FAT class is shown in Figs. 3.1 and 3.2 for fatigue assessment under constant and variable loading, respectively. This approach is described in the recommendations of the IIW (Hobbacher 2008, 2016), and applicable for structural steels up to $f_y = 960$ MPa. For ultra-high strength steels, the correspondence between K_f and K_t is no longer guaranteed (Nykänen *et al.* 2013). The notch rounding approach is also interesting as the effective notch stress can be estimated by means of finite element analysis (FEA), e.g., through the guidelines of the IIW (Fricke 2012). More details and applications of the method can be found in numerous publications see, e.g., Fricke (2011); Kranz & Sonsino (2010); Maddox (2011); Park & Miki (2008); Pedersen *et al.* (2010b); Schijve (2012); Sonsino (2009a); Sonsino *et al.* (2010); Sonsino (2011); Sonsino *et al.* (2012); Stenberg *et al.* (2015).

3.2.4 Fracture mechanics (crack propagation) approach

In the fracture mechanics approach, the behavior of fatigue crack growth in steels (and more generally in metals) can be depicted on a log-log plot of crack growth rate da/dN versus stress intensity range ΔK , as shown in Fig. 3.3. The propagation mainly occurs in accordance with the opening mode I (see Sect. 3.4), as superimposed modes II and III are negligible (Radaj 1990) if the crack grows perpendicularly to the principal tensile stress direction. In region I (also called *near-threshold behavior region*), cracks do not propagate below the threshold stress intensity factor range ΔK_{th} . In the region II, namely of *stable crack growth*, the linear part of the log-log plot can be described by the power law relation of Paris & Erdogan (1963)

$$\frac{da}{dN} = C \Delta K^m \quad (3.3)$$

¹This limitation comes from non-conservative results observed for mild weld notches, namely when $K_w \leq 1.6$. In those cases, the fatigue resistance of the weld notch is also limited to the resistance of the base material. This implies that both hot-spot and weld notch stresses σ_{hs} and σ_{n} , respectively, have to be evaluated in the effective notch stress approach. More details can be found, e.g., in Pedersen *et al.* 2010a; Hobbacher 2008, 2009, 2016; Fricke 2012; Stenberg *et al.* 2015. See the calculation example in Chapter 12.

Chapter 3. Fatigue and fracture assessment of welded joints

where C and m are material constants that can be determined experimentally. The stress intensity factor K is a linear elastic fracture parameters, that is described in Sect. 3.4. The Paris–Erdogan law is used within the framework of linear elastic fracture mechanics (LEFM). In region III, also called *unstable crack growth region*, the crack growth rate increases until failure.

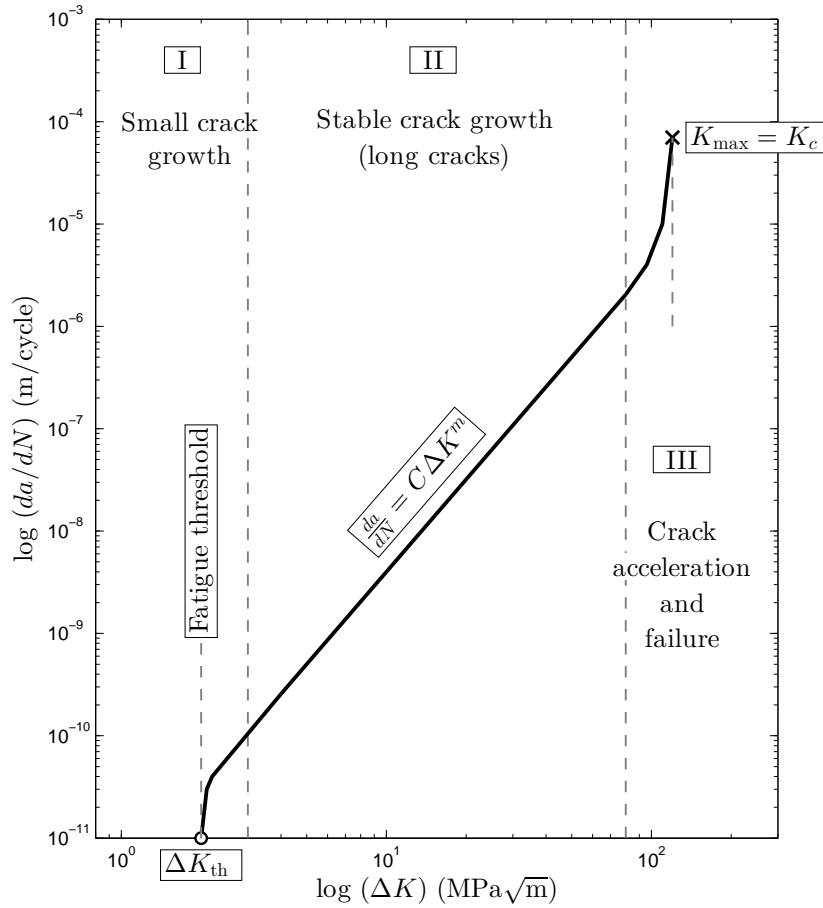


Figure 3.3: Typical behavior of fatigue crack growth in steels: log-log plot of crack growth rate da/dN versus stress intensity range ΔK .

The LEFM approach and the use of the Paris–Erdogan law is well suited to fatigue crack growth analysis of welded joints as the crack initiation period is negligible compared to the propagation period (Fricke 2013). Assuming an initial crack size, the LEFM approach can be used to model crack growth in region II, by integrating or summing Eq. 3.3 over the fatigue life. Compared to the local stresses approaches previously described, this is the highest level of analysis effort but generally provides the best fatigue life estimation when LEFM hypotheses are valid.

The Paris–Erdogan law has been modified by numerous authors to model a better fatigue behavior in regions I and III, as well as to consider the effects on crack growth rate of parameters such as

3.3. Damage and fatigue life calculation for variable amplitude loading

the stress intensity threshold ΔK_{th} , the fracture toughness K_C or the stress ratio $R = \sigma_{max}/\sigma_{min} = K_{max}/K_{min}$ (see, e.g., reviews such as Radaj 1990; Barsom & Rolfe 1999; Anderson 2005).

Variable amplitude loading and particularly overloads can also induce crack retardation, due to load interaction effects caused by plasticity-induced crack closure that influence the growth rate (Anderson 2005). Numerous crack retardation models have been proposed in the literature, based on the concept of effective stress intensity factor K_{eff} (see, e.g., Wheeler 1972; Willenborg *et al.* 1971; Borrego *et al.* 2003; Cui & Huang 2003; Huang & Moan 2007; Wang & Cui 2009).

Important feature of welded joints, the presence of residual stresses may also be of importance and have either a beneficial or detrimental effect depending on the studied case. The role of residual stresses is still a controversial issue, regularly discussed in the literature (Casavola & Pappalettere 2009). In the approaches based on $S-N$ curves derived in *as-welded* conditions, the influence of residual stresses is implicitly considered. In the fracture mechanics approach, considering the presence of residual stresses is a tedious task, particularly if their distribution is not known. In this work, residual stresses are disregarded when using the LEFM approach, i.e., assumed detrimental in tension and $\Delta K = \Delta K_{eff}$.

A large number of applications of the LEFM approach for fatigue crack growth, both in deterministic and probabilistic frameworks, can be found in, e.g., Lukić & Cremona (2001); Lassen & Sorensen (2002); Righiniotis & Chryssanthopoulos (2003, 2004); Nykänen *et al.* (2007); Barsom & Jonsson (2008); Liu & Mahadevan (2009); Chapetti & Jaureguizar (2012); Maljaars *et al.* (2012); Kocańda & Jasztal (2012); Leander *et al.* (2013); Mikkola *et al.* (2015); Baptista (2016). Guidelines for fatigue crack growth analysis are given, e.g., in the British Standard 7910 (2005) or in the IIW recommendations (Hobbacher 2008, 2016).

A more detailed theoretical background on fracture mechanics is proposed in Sect. 3.4.

3.3 Damage and fatigue life calculation for variable amplitude loading

For any procedure based on $S-N$ curves (namely nominal, structural hot-spot and notch stresses approaches) for variable amplitude loading, the fatigue verification in terms of stresses should be performed with a cumulative damage calculation such as the Palmgren–Miner rule as suggested in the IIW recommendations (Hobbacher 2008, 2016).

Assume a variable amplitude spectrum of \bar{N}_p cycles such as

$$\bar{N}_p = n_1 + n_2 + \dots + n_k, \quad (3.4)$$

where n_j is the number of cycles under stress range $\Delta\sigma_j$. Defining N_j as the number of cycles to

Chapter 3. Fatigue and fracture assessment of welded joints

failure at stress range $\Delta\sigma_j$ from the modified fatigue resistance S – N curve (Fig. 3.2), then the (linear) cumulative damage rule suggest that the calculated damage sum D_{calc} should remain below the specified damage sum D_{spec} as

$$D_{\text{calc}} = \frac{n_1}{N_1} + \frac{n_2}{N_2} + \dots + \frac{n_k}{N_k} = \sum_{j=1}^k \frac{n_j}{N_j} \leq D_{\text{spec}}. \quad (3.5)$$

For an assessment based on the major principal stress and a proportional loading, the IIW recommendations suggest, e.g., $D_{\text{spec}} = 1.0$ for constant amplitude, $D_{\text{spec}} = 0.5$ for variable amplitude loading, and D_{spec} possibly down to 0.2 for spectra with significant mean pressure fluctuations (thus R fluctuations). The values of D_{spec} are adapted on the load cases because the *conventional* value $D = 1.0$ was revealed to be unsafe in many investigations, when compared to the *real* damage sum D_{real} derived from experiments. More details can be found, e.g., in Sonsino (2004, 2007); Svensson *et al.* (2005); Zhang & Maddox (2009).

Consider that the stress intensity factor K_I , associated with the crack propagation leading to the same failure mode than the one observed experimentally for the derivation of the S – N , can be written as $K_I = Y\sigma\sqrt{\pi a}$ (see Sect. 3.9) with Y the shape and crack size correction factor, and a the crack size. The Palmgren–Miner rule can then be demonstrated by means of fracture mechanics (development after Gurney 2006). Rearranging and integrating Eq. 3.3 yields

$$\int_{a_{j-1}}^{a_j} \frac{da}{(Y\sqrt{\pi a})^m} = C(\Delta\sigma_j)^m n_j \quad (3.6)$$

where n_j is the number of cycles required for a crack to grow from size a_{j-1} until size a_j under constant amplitude $\Delta\sigma_j$. Let consider a spectrum defined by Eq. 3.4. Applying Eq. 3.6 to each cycles block n_j gives

$$\left\{ \begin{array}{l} \int_{a_i=a_0}^{a_1} \frac{da}{(Y\sqrt{\pi a})^m} = C(\Delta\sigma_1)^m n_1 \\ \int_{a_1}^{a_2} \frac{da}{(Y\sqrt{\pi a})^m} = C(\Delta\sigma_2)^m n_2 \\ \dots \\ \int_{a_{k-1}}^{a_f=a_k} \frac{da}{(Y\sqrt{\pi a})^m} = C(\Delta\sigma_k)^m n_k. \end{array} \right. \quad (3.7)$$

3.4. Theoretical background on fracture mechanics

Now, assuming different constant amplitude loadings leading to failure, one can write

$$\int_{a_i}^{a_f} \frac{da}{(Y\sqrt{\pi a})^m} = C(\Delta\sigma_1)^m N_1 = C(\Delta\sigma_2)^m N_2 = \dots = C(\Delta\sigma_k)^m N_k \quad (3.8)$$

Then, dividing for instance the first term of Eq. 3.7 by Eq. 3.8, one obtains

$$\frac{\int_{a_i}^{a_1} \frac{da}{(Y\sqrt{\pi a})^m}}{\int_{a_i}^{a_f} \frac{da}{(Y\sqrt{\pi a})^m}} = \frac{C(\Delta\sigma_1)^m n_1}{C(\Delta\sigma_1)^m N_1} = \frac{n_1}{N_1}. \quad (3.9)$$

Finally, applying Eq. 3.9 to all cycles blocks n_j and adding them yields

$$D_{\text{calc}} = \sum_{j=1}^k \frac{n_j}{N_j} = \frac{\sum_{j=1}^k \left\{ \int_{a_{j-1}}^{a_j} \frac{da}{(Y\sqrt{\pi a})^m} \right\}}{\int_{a_i}^{a_f} \frac{da}{(Y\sqrt{\pi a})^m}}. \quad (3.10)$$

This development shows the consistency of the Palmgren–Miner with fracture mechanics, under a certain number of assumptions, namely that the propagation period describes the entire fatigue life of the studied welded joint and that the loading sequence does not affect the result. The latter assumption may be a major source of non-validity of this development, leading to damage sums differing from 1.0.

Modifications of the Palmgren–Miner rule have been proposed in the literature see, e.g., Gurney (2006).

3.4 Theoretical background on fracture mechanics

3.4.1 Linear elastic fracture mechanics (LEFM)

Within the hypotheses of LEFM, the presence of a crack produces a $1/\sqrt{r}$ singularity in the stress field at the crack front, where r is the distance from the latter. The nomenclature of a 3D cracked body is shown in Fig. 3.4.

In 2D LEFM, the crack front is reduced to a so-called crack-tip. The $1/\sqrt{r}$ singularity is produced by each mode of loading, depicted in Fig. 3.5. The *opening* mode I is the most severe loading,

that makes cracks propagate (Karihaloo & Xiao 2003).

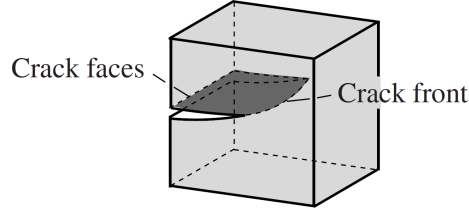


Figure 3.4: Some nomenclature in a cracked body (figure from Gross & Seelig 2011).

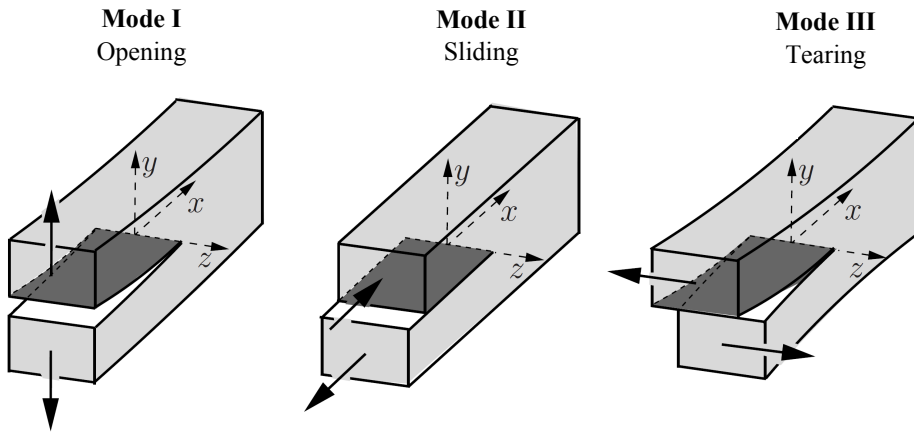


Figure 3.5: Fracture modes (adapted from Gross & Seelig 2011).

The intensity of the stress and displacement fields in the vicinity of a crack-tip can be approximated using the stress intensity factors (SIF), denoted K , depending on each mode of loading. The general expressions of these fields in the vicinity of the crack-tip (see Fig. 3.6) are given under the following form (see, e.g., Anderson 2005; Barsom & Rolfe 1999):

$$\sigma_{ij} = \frac{K_I}{\sqrt{2\pi r}} f_{ij}^I(\theta); \quad (3.11)$$

and

$$u_i = \frac{K_I}{2\mu} \sqrt{\frac{r}{2\pi}} g_i^I(\theta); \quad (3.12)$$

where σ_{ij} are the stresses, u_i the displacements, μ the shear modulus, r the distance from the crack-tip, and f and g are functions of θ in the local polar coordinates at the crack-tip, and of the considered mode.

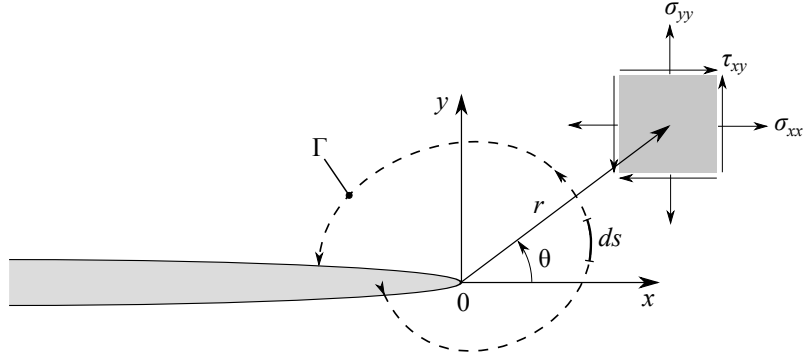


Figure 3.6: Local coordinate system at crack-tip and example of an arbitrary counterclockwise path Γ around the crack-tip.

Stress and displacement fields ahead of a crack-tip in Cartesian coordinates for Mode I are expressed as

$$\begin{aligned}\sigma_{xx} &= \frac{K_I}{\sqrt{2\pi r}} \cos\left(\frac{\theta}{2}\right) \left[1 - \sin\left(\frac{\theta}{2}\right) \sin\left(\frac{3\theta}{2}\right)\right]; \\ \sigma_{yy} &= \frac{K_I}{\sqrt{2\pi r}} \cos\left(\frac{\theta}{2}\right) \left[1 + \sin\left(\frac{\theta}{2}\right) \sin\left(\frac{3\theta}{2}\right)\right]; \\ \sigma_{xy} &= \frac{K_I}{\sqrt{2\pi r}} \cos\left(\frac{\theta}{2}\right) \sin\left(\frac{\theta}{2}\right) \cos\left(\frac{3\theta}{2}\right);\end{aligned}\tag{3.13}$$

and

$$\begin{aligned}u_x &= \frac{K_I}{2\mu} \sqrt{\frac{r}{2\pi}} \cos\left(\frac{\theta}{2}\right) \left[\kappa - 1 + 2\sin^2\left(\frac{\theta}{2}\right)\right]; \\ u_y &= \frac{K_I}{2\mu} \sqrt{\frac{r}{2\pi}} \sin\left(\frac{\theta}{2}\right) \left[\kappa + 1 - 2\cos^2\left(\frac{\theta}{2}\right)\right];\end{aligned}\tag{3.14}$$

with $\kappa = 3 - 4\nu$ in plane strain and $\kappa = (3 - \nu)/(1 + \nu)$ in plane stress, ν the Poisson ratio and μ the shear modulus. More information about LEFM can be found in monographs such as, e.g., Lawn (1993), Kanninen & Popelar (1985), Barsom & Rolfe (1999), Anderson (2005), Gross & Seelig (2011), or François *et al.* (2013).

3.4.2 Plasticity of the crack-tip

Linear elastic fracture mechanics predicts an asymptotic solution for stress fields at sharp crack-tips, with stresses tending toward infinity. However, in *real* materials, stresses are finite as yielding occurs. As the yielding zone extends, LEFM becomes inaccurate. Linear elastic fracture mechanics remains accurate within the hypothesis of small-scale yielding (SSY), i.e., when the

Chapter 3. Fatigue and fracture assessment of welded joints

size of the plastic zone is very small compared to crack size and the finite dimensions of the cracked components (see, e.g., Anderson 2005; Acevedo 2011). In the scope of LEFM, the fracture is governed by the K_{IC} (or G_{IC}) criterion.

The determination of the plastic zone ahead of a crack-tip (or front in 3D) in a nonlinear material is a complex task. However, as a first approximation, one can use the simplified approach proposed by Irwin. The redistribution of the asymptotic stress field is approximated assuming perfect plasticity (no strain hardening), i.e., the stress singularity is truncated by yielding in the vicinity of the crack-tip (see Fig. 3.7). In mode I, σ_{yy} at the crack plane is given by (σ_{yy} from Eq. 3.13 evaluated for $\theta = 0$):

$$\sigma_{yy} = \frac{K_I}{\sqrt{2\pi r}}. \quad (3.15)$$

Imposing Tresca's yield condition at the boundary between the plastic and the elastic zones (see Fig. 3.7), one obtains (Gross & Seelig 2011)

$$r_y = \frac{1}{2\pi} \left(\frac{K_I}{\alpha f_y} \right)^2, \quad (3.16)$$

called the first-order estimate of the plastic zone after Anderson (2005), where $1/\alpha = (1 - 2\nu)$ in plane strain, and $\alpha = 1$ in plane stress.

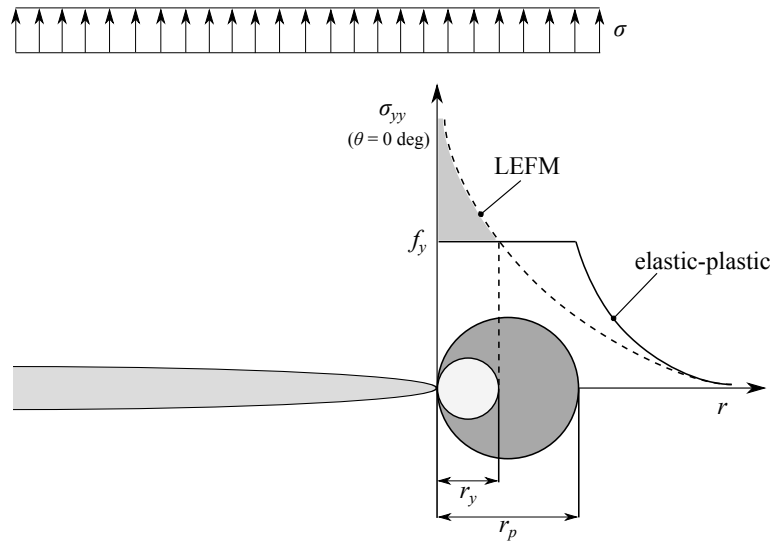


Figure 3.7: Crack-tip with first- and second-order estimates of plastic zone sizes r_y and r_p , respectively.

This calculation is not strictly correct as it is based on the linear elastic solution. The LEFM

3.4. Theoretical background on fracture mechanics

asymptotic stress field and the elastic–plastic stress distribution should ensure equilibrium, which is expressed as (Anderson 2005)

$$\alpha f_y r_p = \int_0^{r_y} \sigma_{yy} dr = \int_0^{r_y} \frac{K_I}{\sqrt{2\pi r}} dr, \quad (3.17)$$

where r_p is the second-order estimate size of the plastic zone, as depicted in Fig. 3.7. Integrating and solving for r_p in Eq. 3.17 yields

$$r_p = \frac{1}{\pi} \left(\frac{K_I}{\alpha f_y} \right)^2. \quad (3.18)$$

To account for the translation of the elastic stress field, Irwin defined an *effective crack length* a_{eff} , corrected by r_y as

$$a_{\text{eff}} = a + r_y. \quad (3.19)$$

One can observe that for the same loading, the plastic zone in plane strain is significantly smaller than in plane stress, due to the fact that $\alpha > 1$ in plane strain, e.g., $\alpha = 2.5$ with $\nu = 0.3$ for steels.

Anderson (2005) compared Irwin's correction with LEFM analysis. He roughly predicted that LEFM theory is applicable in mode I when the applied tension σ remains below half of the cracked material's yield strength, i.e., $\sigma \leq 0.5 f_y$ (see also, e.g., Schwalbe & Zerbst 2003). This is also in accordance with the correction from the more refined *Strip-Yield Model* proposed by Dugdale. In the scope of steel-lined pressure tunnels and shafts, this rule of thumb is generally verified due to the safety factors prescribed by the C.E.C.T. (1980) recommendations and the limitation of the rock mass participation, as it will be shown in Part V.

3.4.3 Elastic–plastic fracture mechanics (EPFM)

J-integral

The *J*-integral is a widely accepted parameter for elastic–plastic fracture mechanics (EPFM). Considering an arbitrary counterclockwise path Γ around the crack-tip, *J* is defined as (Rice 1968; Shih *et al.* 1986)

$$J = \int_{\Gamma} \left[w dy - \sigma_{ij} n_j \frac{\partial u_i}{\partial x} ds \right] \quad (3.20)$$

Chapter 3. Fatigue and fracture assessment of welded joints

where w and $T_i = \sigma_{ij}n_j$ are the strain energy density and the components of the traction vector respectively, σ_{ij} and u_i are the Cartesian components of the stress and displacement vector components, n_j is the unit vector normal to Γ and ds is the length increment along Γ (see Fig. 3.6). The value of J is independent of the path of integration (Rice 1968), and is thus called a *path-independent* integral.

SIF and J -integral

In a linear elastic cracked material, the J -integral represents the energy release rate and is associated to the SIF as

$$J = G = \frac{K_I^2}{E'} \quad (3.21)$$

where G is the energy-release rate, and $E' = E$ in plane stress conditions and $E' = E/(1 - \nu^2)$ in plane strain conditions.

HRR solution

Similarly to LEFM and the use of K to characterize the stress and strain fields, the J -integral characterizes the stress and strain fields in the vicinity of a crack-tip under yielding conditions. Assuming the small strain deformation theory of plasticity and a pure power stress–strain relation as

$$\frac{\varepsilon}{\varepsilon_0} = \alpha \left(\frac{\sigma}{\sigma_0} \right)^N \quad (3.22)$$

where σ_0 is the yield stress, ε_0 the yield strain and N the hardening exponent, Hutchinson (1968) and Rice & Rosengren (1968) proposed the so called HRR solution (also referred as fully plastic solution), which approximates the fields as

$$\sigma_{ij} = \sigma_0 \left(\frac{J}{\alpha \sigma_0 \varepsilon_0 I_N r} \right)^{1/(N+1)} \tilde{\sigma}_{ij}(\theta, N); \quad (3.23)$$

$$u_i = \alpha \varepsilon_0 \left(\frac{J}{\alpha \sigma_0 \varepsilon_0 I_N r} \right)^{N/(N+1)} \tilde{u}_i(\theta, N). \quad (3.24)$$

I_N is a dimensionless constant function of N , $\tilde{\sigma}_{ij}$ and \tilde{u}_i are functions of θ and N . More details can be found, e.g., in Karihaloo & Xiao (2003), Pineau & Pardoen (2007) or François *et al.* (2013).

Elastic–plastic solution

When crack problems are in the elastic–plastic regime, an estimation procedure is proposed by Kumar *et al.* (1981), interpolating over the range from small-scale yielding (SSY) to fully plastic conditions. For a material characterized by the Ramberg-Osgood stress–strain relation (Ramberg & Osgood 1943) as

$$\frac{\varepsilon}{\varepsilon_0} = \frac{\sigma}{\sigma_0} + \alpha \left(\frac{\sigma}{\sigma_0} \right)^N, \quad (3.25)$$

the interpolation to compute J combines the linear elastic and the fully plastic participations as

$$J = J_e(a_e) + J_p(a, N) \quad (3.26)$$

where J_e is the linear elastic contribution corrected for an adjusted crack length a_e , and J_p is the plastic contribution based on the hardening exponent N . In SSY, $J_e \gg J_p$ and J reduces to the linear elastic solution adjusted to a_e . In fully plastic conditions, $J_p \gg J_e$ and $J \approx J_p$.

The estimation procedure proposed by Kumar *et al.* (1981) is the so-called *EPRI Handbook*, and was later expanded to a (limited) number of additional configurations (Zahoor 1989, 1990, 1991). This procedure features some important limitations in its application, that were partly overcome by the development of the *Reference stress method* applied to EPFM (Zerbst *et al.* 2003). Further details on EPFM are out of the scope of the state-of-the-art of this research project.

3.4.4 Fracture strength

In traditional design, assuming the absence of flaws in steel structural members, the applied stress (e.g., in terms of the von Mises equivalent stress σ_{eq}) should remain below the appropriate material resistance (e.g., the yield strength f_y). As a structure may contain crack-like flaws, this failure criterion is not sufficient. In the early 1920s, Griffith (1920) already studied the difference between the theoretical tensile strength and the (lower) *real* strength in brittle materials containing flaws, such as *scratches*. In fracture mechanics, similarly to continuum mechanics, a simplified failure criterion states that the crack driving force should remain below *fracture toughness*, which represents the ability of a material to absorb energy prior to fracture.

Assuming, after Anderson (2005), that failure occurs locally at a crack-tip in a material, then crack propagation must occur at a *critical value* K_C , which measures the fracture toughness and is a material constant of a cracked body. Depending on crack-tip's conditions, K_C may not only depend on stress intensity.

Considering that the size of the plastic zone is small compared to the specimen's dimensions and the crack size, its size only depends on loading and material properties. The plastic zone thus only depends on K_I , although the linear elastic stress field does not apply within the yielding zone. Within the hypotheses of LEFM, the critical value of K_I beyond which a crack may propagate

Chapter 3. Fatigue and fracture assessment of welded joints

is referred to as *plane strain fracture toughness* and is denoted K_{IC} , which is a specimen-size independent material property (Anderson 2005). As a consequence, the plane strain fracture toughness can only be used as a fracture criterion within the framework of LEFM.

As the size of the plastic zone increases, the region with the $1/\sqrt{r}$ stress variation vanishes, and the K -characterization of the crack-tip conditions is no longer valid. In this case, the fracture toughness can be described by the J -integral, or the crack-tip opening displacement (CTOD) (Anderson 2005).

K_{IC} can be measured performing laboratory tests (see, e.g., Schwalbe *et al.* 2003), respecting the following *size condition*:

$$\min\{a, (t_s - a), B\} \geq 2.5 \left(\frac{K_{IC}}{f_y} \right)^2, \quad (3.27)$$

where B is the specimen's thickness in the direction of the crack front, and t_s the thickness in the direction of the crack propagation². The qualitative effect of the specimen's dimensions on K_C is illustrated in Fig. 3.8. In steels, K_{IC} typically stands in the range 25–100 MPa \sqrt{m} (Gross & Seelig 2011).

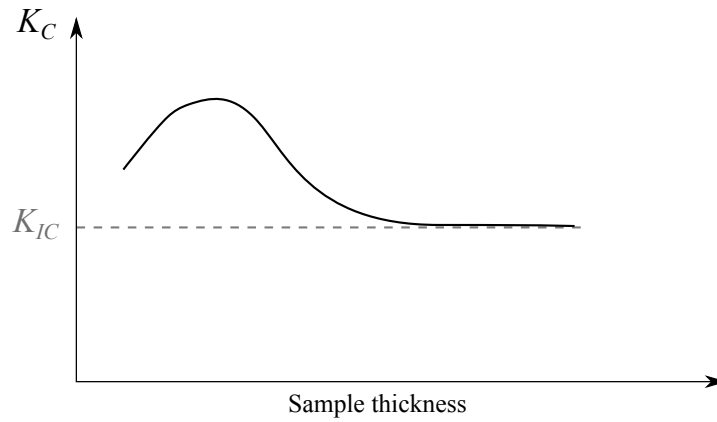


Figure 3.8: Qualitative representation of the effect of thickness on fracture toughness.

Within the framework of LEFM and after Gross & Seelig (2011), a rough estimation of the admissible size of the plastic zone can be assessed combining Eqs. 3.18 and 3.27, which yields

$$r_{y,c} \leq 0.02 \cdot \min\{a, (t_s - a), B\}. \quad (3.28)$$

²This dimension is often denoted W in the literature (see, e.g., Schwalbe *et al.* 2003; Anderson 2005; Gross & Seelig 2011). t_s was adopted herein for consistency with the nomenclature of steel liners.

This condition is naturally fulfilled by linear elastic materials, and in general also by high-strength elastoplastic metals such as HSS with a yield strength f_y greater than 500 MPa (Karihaloo & Xiao 2003). Indeed, these high-strength materials generally exhibit low plastic deformations.

3.5 Failure and fatigue assessment procedures

Beyond the brief development on fracture strength in the framework of LEFM in Sect. 3.4.4, engineering procedures for the assessment of structures containing crack-like flaws were developed. They often provide different levels of refinements considering elastoplasticity as well as features of weldments such as, for instance, secondary stresses and strength mismatch. There are two main approaches for failure assessment, namely the *Failure Assessment Diagram* (FAD) methods (Ainsworth 2003), and the *Crack Driving Force* (CDF) methods (Schwalbe & Zerbst 2003).

The FAD is an interaction diagram between the two principal failure criteria, namely LEFM and plastic collapse, proposing a failure line independent from components' geometries. Failure is assessed based on the relative location of the component-dependent point with respect to the failure line. Conversely to the FAD method, the CDF treats separately the crack driving force and the fracture resistance.

Some widespread engineering procedures are listed in Table 3.1. For each document, when available, references summarizing or detailing specific aspects of the corresponding procedure are proposed. Zerbst *et al.* (2003) reviews failure assessment methods, as well as their inclusion in codes and standards. An overview on some standards and codes for fatigue assessment is given in Table 3.2.

3.6 Reliability assessment

3.6.1 Probabilistic approaches in engineering

With the presence of uncertainties both on the demand and resistance sides of a structure, modern design methodologies tend to develop probabilistic approaches to assess reliability, instead of, for instance, using deterministic methods with empirically determined safety factors (Roos *et al.* 2011). Provan (1987) gives a general definition of reliability in structural engineering, that may be applied universally (nomenclature is adapted):

Reliability is the probability $P(T)$ that a component (or a system) will not fail in a time T . What is meant by the probability of failure-free operation is the probability that under definite operating conditions and within limits of operating duration, no failure will occur.

Table 3.1: Overview on some engineering procedures for **failure assessment** of structures containing flaws.

Document	Methods	Description	References
FITNET (Koçak <i>et al.</i> 2008)	FAD, CDF	Fitness-for-Service procedure within the framework of the European fitness-for-service network , unified engineering procedure for flaws in structures in the European community. This is an horizontal procedure.	Koçak <i>et al.</i> (2007a); Koçak (2007); Koçak <i>et al.</i> (2007b, 2008)
SINTAP (1999)	FAD, CDF	Outcome of a European project combining and unifying elements of the R6 procedure and the ETM method of GKSS. This is an horizontal procedure.	Ainsworth <i>et al.</i> (2000a,b); Webster & Bannister (2000)
British Standard 7910 (2005)	FAD	Comprehensive procedure for flaw assessment based on R6, developed in particular for the assessment of weld. This is an horizontal procedure.	Wiesner <i>et al.</i> (2000); Sharples <i>et al.</i> (2003); Muhammed (2007)
R6 (R6 Revision 4 2009)	FAD	This is an horizontal procedure, which had the greatest influence on the development of flaw assessment methods. It provides different levels of flaw assessments, with increasing complexity and thus decreasing conservatism. It was originally developed for the nuclear power generation industry.	Ainsworth & Hooton (2008); Budden <i>et al.</i> (2000); Milne <i>et al.</i> (1988a,b); Sharples <i>et al.</i> (2003)
EFAM-ETM (Schwalbe <i>et al.</i> 1997, 1998, for the analytical methods)	CDF	Engineering Flaw Assessment Method of GKSS (Germany). It consists of two sets of documents, namely the GTP referring to the experimental procedures (material side), and the Engineering Treatment Model (ETM), referring to the analytical procedures (applied side). This is an horizontal procedure.	Schwalbe (1998)
API 579 (API 2007)	FAD	Fitness-for-service assessment procedure, specially developed for petro-chemical and chemical industries by the American Petroleum Institute.	Anderson & Osage (2000); Muhammed (2007)
ASME Boiler and Pressure Vessel Code (ASME 2007)	FAD	Standard of the American Society of Mechanical Engineers, originally at the center of fracture assessment in the nuclear power generation industry. For SLPT&S, Section VIII, Division 1 and Section IX may be appropriate concerning welding procedures.	-

Table 3.2: Overview on some engineering procedures for **fatigue assessment** of structures.

Document	Methods	Description	References
EN 13445-3 (EN 13445-3 2014)	Nominal stress	European standard for the design of unfired pressure vessels.	-
EN 1993-1-9 (EN 1993-1-9 2005)	Nominal stress	Eurocode 3: European standard for the design of steel structures. The Part 1-9 is dedicated to fatigue.	Nussbaumer <i>et al.</i> (2011)
IIW recommendations (Hobbacher 2016)	Nominal stress, structural hot-spot stress, notch stress, LEFM	Recommendations of the International Institute of Welding on fatigue design of welded structures. This is the most scientifically up-to-date document.	Hobbacher (2008, 2009)
FKM Guideline 2003, 2005)	Nominal stress, structural hot-spot stress, notch stress, LEFM	German guidelines for fatigue and fracture assessment from the Research Committee Mechanical Engineering (FKM).	Pyttel <i>et al.</i> (2007)
FITNET (Koçak <i>et al.</i> 2008)	Nominal stress, structural hot-spot stress, notch stress, LEFM	Fitness-for-Service procedure within the framework of the European fitness-for-service network (see also Table 3.1).	Koçak <i>et al.</i> (2007a); Koçak (2007); Koçak <i>et al.</i> (2007b, 2008)
JSSC Fatigue Design Recommendations (JSSC 1995)	Nominal stress, structural hot-spot stress	Recommendations for fatigue design of steel structures from the Japanese Society of Steel Construction	-
VGB-Standard (VGB 2014)	-	This standard was elaborated at the initiative of the VGB Technical Committee for hydropower plants. It gives recommendations for fatigue life assessment of fatigue loaded components in hydropower plants. Several documents are summarized such as EN 13345-3, AD 2000, ASME, FKM, Eurocode 3, IIW, BS7910, and API 579.	Kofler <i>et al.</i> (2015)

Chapter 3. Fatigue and fracture assessment of welded joints

The time T is the time during which the probability of failure-free operation is determined, and is also named *lifespan* herein. Introducing t the time of operation until the first failure, then the above definition yields

$$P(T) = P(t > T). \quad (3.29)$$

Probabilistic approaches were developed at first for the needs of the nuclear power industry (Cameron *et al.* 1987; Wellein 1987; Bullough *et al.* 1999; Kanto *et al.* 2010), and aeronautics (Palmberg *et al.* 1987; Hooke 1987; Yang *et al.* 1987; Manning *et al.* 1987). It was then more and more extended to several fields of engineering such as, e.g., bridge engineering (Walbridge 2005; Kang *et al.* 2012; D'Angelo & Nussbaumer 2015), offshore engineering (Kirkemo 1988), pressure vessels and piping (Tsai & Wu 1994; Rahman 1997), or geomechanical engineering (Lü *et al.* 2011; Baecher 2003). To the author's best knowledge, a probabilistic approach for reliability assessment of SLPT&S was never published in the open literature.

3.6.2 Probabilistic fracture mechanics

Fatigue crack growth and fracture assessment particularly requires a large amount of inputs, which are rarely known with accuracy (Besuner & Tetelman 1977). Probabilistic approaches in fracture mechanics are thus very attractive, as evidenced by the prolificacy of the field in the scientific literature (see, e.g., reviews such as Johnston 1982; Besuner & Tetelman 1977; Dillström & Nilsson 2003). Welding components add even more uncertainties into the problem of fatigue and fracture analysis, particularly related to the geometrical and material parameters (Engesvik & Moan 1983). Uncertainties justifying the use of probabilistic fracture mechanics (PFM) can be enumerated after Besuner (1987) (non-exhaustive list):

1. Initial crack size:
 - (a) depth a ,
 - (b) length c ,
 - (c) location,
 - (d) orientation;
2. Probability of crack detection:
 - (a) probability of detection (POD),
 - (b) crack characterization;
3. Material properties:
 - (a) crack growth rate da/dN ,

- (b) fracture toughness (e.g., K_{IC}),
- (c) tensile properties;
- 4. Service conditions:
 - (a) loading (frequency, amplitude),
 - (b) environment;
- 5. Misdiagnosis of failure mode.

Assuming, for instance, a case where the failure mode is governed by K_{IC} , then the strength margin is defined as $Y = K_{IC} - K_I$, and the probability of failure p_f is expressed as

$$p_f = P(Y < 0). \quad (3.30)$$

3.6.3 Monte Carlo simulation technique

When a failure analysis problem is defined with several random (uncertain) variables, solving Eq. 3.30 is not trivial, if not impossible. The Monte Carlo simulation technique was developed to evaluate Eq. 3.30 numerically, by *trying* stochastic variables in a deterministic model (Provan 1987). The procedure can be summarized in six main steps (Haldar & Mahadevan 2000):

1. defining the random variables;
2. determining the distributions of the random variables in terms of their probability density functions;
3. generating the values of the random variables;
4. evaluating the problem (Y) through the deterministic model for each *trials*, i.e., for each set of the N_{MC} realizations of the random variables;
5. extracting the failure probability from the N_{MC} trials; and
6. determining the accuracy and efficiency of the simulation.

The probability of failure p_f can be estimated as

$$p_f = n_f / N_{MC}, \quad (3.31)$$

where n_f is the number of failures ($Y < 0$) observed among the N_{MC} trials. As N_{MC} tends to infinity, p_f converges to the *true* probability of failure p_f^{true} . One way to evaluate the accuracy

Chapter 3. Fatigue and fracture assessment of welded joints

of Eq. 3.31 is proposed, e.g., by Haldar & Mahadevan (2000) or Dillström & Nilsson (2003). Considering that each trial constitutes a Bernoulli trial, and thus n_f in N_{MC} trials can be considered to follow a binomial distribution and the error can be estimated as

$$\varepsilon \approx \frac{\sqrt{\frac{(1-p_f)p_f}{N_{MC}}}}{p_f}. \quad (3.32)$$

Equation 3.32 can be used to compute the error of a Monte Carlo analysis, or to estimate the necessary number of trials N_{MC} to reach a desired accuracy for a given probability of failure.

As a problem may require a large number of trials, Monte Carlo analysis may become inefficient due to the large associated computational time to ensure the convergence of p_f . Nevertheless, several methods are available to reduce N_{MC} by selective sampling. Other more efficient numerical methods were developed, e.g. the First-Order Reliability Methods (FORM) and the Second-Order Reliability Methods (SORM), but are more complex to implement than the Monte Carlo analysis (Brückner 1987; Dillström & Nilsson 2003).

3.7 Review of formulas for stress concentration factors at butt welded plates with linear misalignment

3.7.1 Decomposition of stress components

At the weld toe of a butt welded joint subject to membrane and bending stresses (due, e.g., to linear misalignment), the stress profile is nonlinear and composed of three components, namely the membrane stress σ_m , the bending stress σ_b and the nonlinear stress peak σ_{nl} . The decomposition of the notch stress σ_n is depicted in Fig. 3.9.

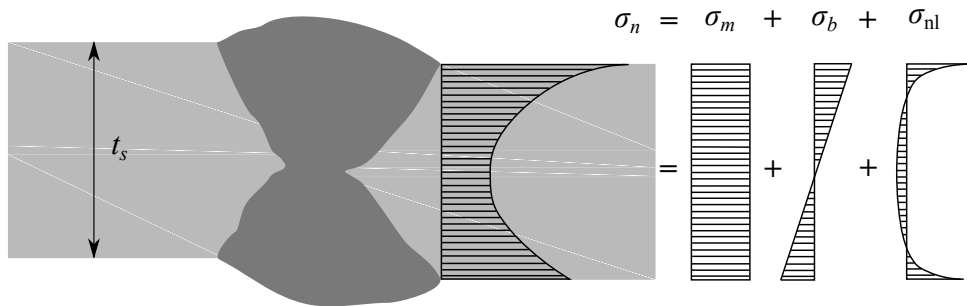


Figure 3.9: Decomposition of the nonlinear stress profile in a butt welded joint with linear misalignment.

3.7. Review of formulas for stress concentration factors at butt welded plates with linear misalignment

The structural stress σ_s is defined as the combination of the membrane and bending components (Niemi *et al.* 2006):

$$\sigma_s = \sigma_m + \sigma_b. \quad (3.33)$$

In this report, the so-called nominal stress σ_{nom} refers to the applied pure tension in the case of butt welded joints of straight plates. In the case of steel-lined pressure tunnels or shafts subject to internal water pressure, the nominal stress refers to the major principal stress computed at the internal fiber of the cylindrical steel liner.

3.7.2 Definition of the stress concentration factors (SCF)

The structural stress σ_s , due for example to a misalignment of the plate's axes, is related to the nominal σ_{nom} by the structural SCF denoted K_m as:

$$\sigma_s = K_m \sigma_{\text{nom}}. \quad (3.34)$$

The combination of several types of misalignments can be approximated as (see, e.g., Niemi *et al.* 2006; Remes & Varsta 2010; Chattopadhyay *et al.* 2011; Nykänen *et al.* 2013; Nykänen & Björk 2015):

$$\sigma_s = \left[1 + \sum_i (K_{m,i} - 1) \right] \sigma_{\text{nom}} \quad (3.35)$$

where i denotes a misalignment type. The weld SCF K_w considering the magnification of the weld shape is defined as the ratio between the notch stress σ_n and the structural stress σ_s as (Fricke 2012):

$$\sigma_n = K_w \sigma_s. \quad (3.36)$$

The notch SCF K_t considering all sources of magnifications relates the nominal stress σ_{nom} to the notch stress σ_n as (Fricke 2012):

$$\sigma_n = K_t \sigma_{\text{nom}}. \quad (3.37)$$

Without misalignment, $K_t = K_w$. An additional nomenclature for the general notch SCF $K_{t,m}$ (equivalent to K_t) is introduced for the analysis performed in Chapter 6. It can also be expressed as the following multiplicative combination of the structural SCF and the weld SCF (Remes & Varsta 2010; Nykänen *et al.* 2013), combining Eqs. 3.34 and 3.36:

$$\sigma_n = K_{t,m} \sigma_{\text{nom}} = K_m K_w \sigma_{\text{nom}}. \quad (3.38)$$

3.7.3 Structural SCF due to linear misalignment

The structural SCF due to linear misalignment can be derived from the classical plate theory (Cui *et al.* 1999). If the joint is unrestrained, in plane stress conditions K_m can be computed as (see, e.g., for welded plates, British Standard 7910 2005; Radaj 2006; Hobbacher 2008, 2009; Koçak *et al.* 2008; Lotsberg 2008, 2009a,b; Nussbaumer *et al.* 2011; Fricke 2013)

$$K_m = 1 + 3 \frac{e}{t_s}. \quad (3.39)$$

For axial misalignment at longitudinal welds in cylindrical shells, the following formula is proposed to compute the structural SCF (British Standard 7910 2005; Hobbacher 2008):

$$K_m = 1 + 3 \frac{e}{(1 - \nu_s^2) t_s}, \quad (3.40)$$

where t_s is the plate thickness and ν_s the Poisson's ratio of steel. To the best authors' knowledge, the presence of the factor $(1 - \nu_s^2)$ in Eq. 3.40 is no further explained in the literature.

3.7.4 Notch SCF due to weld shape

A notch factor for double-V butt welded joint was proposed by Lawrence *et al.* (1981):

$$K_t = 1 + A(t_s/\rho)^{0.5} \quad (3.41)$$

where ρ is the weld toe radius (see Fig. 6.2). A is a constant for a given flank angle β and a given edge preparation angle α (see Fig. 6.2). A similar approach is proposed by Cerit *et al.* (2010) for single-V butt welded joints:

$$K_t = 1 + A(t_s/\rho)^\alpha \quad (3.42)$$

3.7. Review of formulas for stress concentration factors at butt welded plates with linear misalignment

where α here depends on β and t_s/ρ . Another expression with a similar approach was proposed by Ho & Lawrence (1984) and Yung & Lawrence (1985):

$$K_t = 1 + 0.27 \tan(\beta)^{0.25} (t_s/\rho)^{0.5} \quad (3.43)$$

where the former coefficient A is a continuous function of β . This expression is for example used by Nykänen *et al.* (2013).

A more refined expression was proposed by Anthes *et al.* (1993) in the following form:

$$K_t = B(\beta) [1 + A(t_s/\rho)^\alpha] \quad (3.44)$$

with

$$B(\beta) = 1 + [B_0 + B_1 \sin(\beta) + B_2 \sin^2(\beta) + B_3 \sin^3(\beta)] \left(\frac{t_s}{\rho}\right)^{C(\beta)} \quad (3.45)$$

and

$$C(\beta) = \gamma_1 + \gamma_2 \sin(\beta + \gamma_3) \quad (3.46)$$

where A , α , the B_i and the γ_i are constant coefficients and exponents. This formula is for example used by Demofonti *et al.* (2001), Mecozzi *et al.* (2010) and Nykänen & Björk (2015). Reducing the range of application, the expression was simplified as (Anthes *et al.* 1993):

$$K_t = 1 + A \sin(\beta)^{\alpha_1} (t_s/\rho)^{\alpha_2} \quad (3.47)$$

where A and the α_i are constant coefficients.

A formula was proposed by Remes (2008) and Remes & Varsta (2010) for the notch factor at laser-based joints, where the weld bead is modeled as a trapezoidal protuberance:

$$K_t = 1 + \left(\frac{\delta}{t_s}\right)^{0.30} \left(\frac{l_w}{t_s}\right)^{0.30} \sin\left(\frac{\beta}{2}\right)^{0.30} \left(\frac{t_s}{\rho}\right)^{0.33} \quad (3.48)$$

where δ is the weld reinforcement height and l_w the weld length.

Chapter 3. Fatigue and fracture assessment of welded joints

Another formula was reported by Radaj (2006) after Lehrke for double-V butt welded joints as

$$K_t = \frac{4 \left[2 \cdot \tan \left(\frac{\beta}{2} \right) \right]^{1-2m}}{2\beta + \sin(2\beta)} \left(\frac{t_s}{4\rho} \right)^m. \quad (3.49)$$

The notch factor at a trapezoidal protuberance on a tension member that can be approximated to a weld bead was also proposed by Pilkey & Pilkey (2008) in a chart representing K_t as

$$K_t = 1 + f \left(\frac{\delta}{l_w}, \frac{t_s + 2\delta}{t_s}, \frac{\rho}{l_w}, \theta \right). \quad (3.50)$$

Finally, SCF at butt welded joints were also studied by He & Zhang (2011), where a parametric equation was proposed for a single thickness and a single weld toe radius only.

3.7.5 Comparison of published notch SCF equations

Some of the aforementioned formulas were evaluated against finite element analysis (FEA) performed with the FE model presented in Chapter 6, Sect. 6.1. The selected formulas were separated in two groups, depending on their behavior. Group 1 contains Eqs. 3.41, 3.42 and 3.43, while Group 2 gathers Eqs. 3.44–3.46, 3.47, 3.48 and 3.49.

The formulas were evaluated, when possible, for three plate thicknesses, namely 12, 30 and 60 mm, without linear misalignment, and for a constant weld toe radius $\rho = r_{\text{ref}} = 1$ mm. The flank angle β was varied, when possible, between 5° and 45° . The parameters of the FE model presented herein (see Sect. 6.1) were varied accordingly. However, as the FE model also includes variable weld reinforcement height δ (see Fig. 6.2a), it was varied correspondingly with β as reported in Table 3.3. The edge preparation angle α is set to 60° . The same weld reinforcements were chosen to evaluate Eq. 3.48, as well as α , yielding l_w (see Fig. 6.2a).

Table 3.3: Variation of the relative weld reinforcement δ/t_s accordingly to the flank angle β for the FEA results shown in Figs. 3.10 and 3.11.

β ($^\circ$)	5	10	15	20	25	30	35	40	45
δ/t_s (–)	0.015	0.030	0.040	0.050	0.060	0.070	0.080	0.090	0.100

The FEA performed with the proposed FE model (see Sect. 6.1) is compared with the estimation obtained by the equations of Group 1 in Fig. 3.10. The same FE results are plotted versus the estimation provided by the equations of Group 2 in Fig. 3.11. One can observe a large scatter in the estimation depending on the chosen formula. Considering the proposed hypotheses on the

3.8. Review of formulas for structural stress concentration factors in steel cylindrical structures

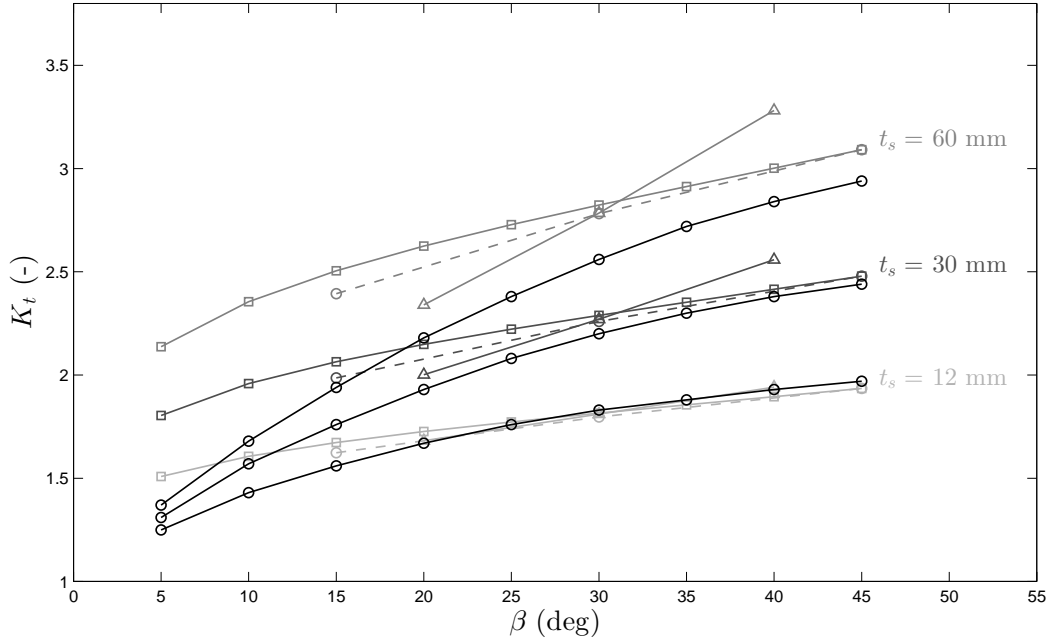


Figure 3.10: Notch SCF as a function of the flank angle β , estimated with the equations of Group 1. Legend: (—○—) FEA; (- -○- -) Eq. 3.41; (-△-) Eq. 3.42; and (-□-) Eq. 3.43.

geometry of the butt welded joint in this work (see Sect. 6.1), the equations of Group 1 seems more suited to estimate SCF with large flank angles, namely larger than $25\text{--}30^\circ$. Conversely, the equations of Group 2 show good agreement when estimating SCF with low flank angles. Also, all the reported formulas generally overestimate SCF compared with the proposed FEA. This trend becomes more significant with increasing thickness t_s .

One may note that the FE results presented in Figs. 3.10 and 3.11 depends on the variation of the weld reinforcement δ for each given flank angle β . However, Figs. 3.10 and 3.11 show that the published formulas are imprecise, as the influence of δ is not explicitly considered, except in Eq. 3.48. The influence of the weld length l_w is also not considered in most of the notch SCF formulas for standard butt-welded joints. The influence of these parameters will be studied in Sect. 6.2. One may note that in standards, the influence of l_w is related to the plate thickness reduction factor (Hobbacher 2016) when using the nominal or structural hot-spot stress approaches.

3.8 Review of formulas for structural stress concentration factors in steel cylindrical structures

Numerous analytical and empirical formulas for structural SCF at welded plates and shells have been published in the literature and included in standards (e.g., API 2007; British Standard 7910 2005; EN 13445-3 2014; Hobbacher 2008; Koçak *et al.* 2008). More specifically, numerous

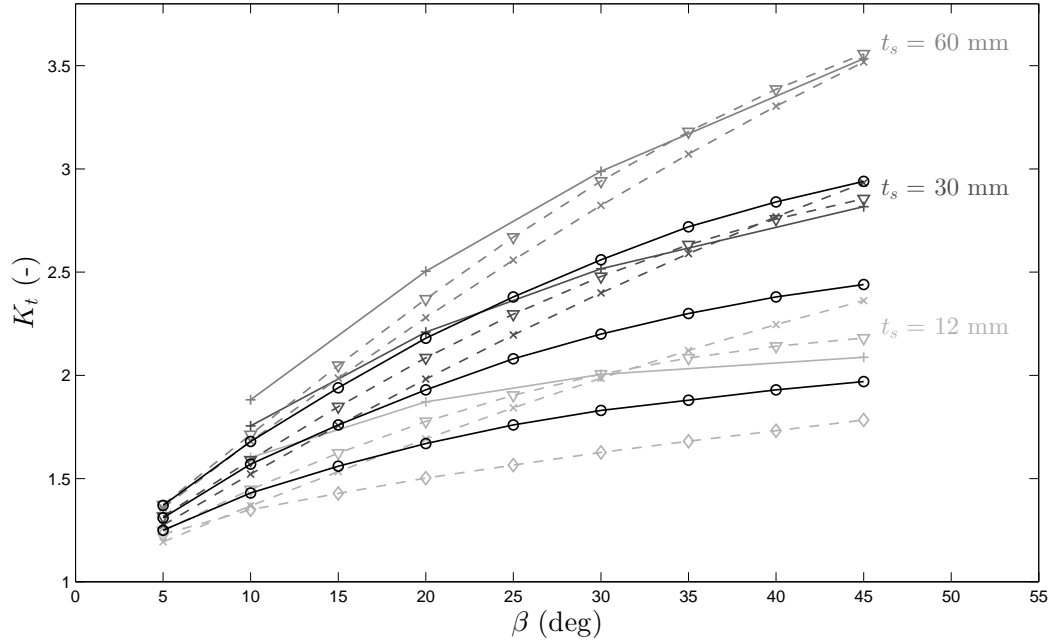


Figure 3.11: Notch SCF as a function of the flank angle β , estimated with the equations of Group 2. Legend: (—○—) FEA; (---×---) Eqs. 3.44–3.46; (---▽---) Eq. 3.47; (---◇---) Eq. 3.48; and (---+---) Eq. 3.49.

studies on SCF at longitudinally welded cylindrical shells can be found in the literature, see, e.g., Ohtani *et al.* (1991a,b); Böck & Zeman (1994); Zeman (1944); Ong & Hoon (1996); Schwarz & Zeman (1997). Selected formulas used in this work which can be applied to open-air penstock and pipelines are summarized in Table 3.4.

3.9 Review of formulas for stress intensity factors for cracks in plates and shells

3.9.1 General formulation

The general formulation for SIF under Mode I loading conditions K_I can be written as

$$K_I = Y \sigma \sqrt{\pi a} \quad (3.51)$$

where a is the minor semi-axis for an elliptical crack (crack depth for a semi-elliptical surface crack), σ the applied stress and Y is a general correction factor which depends on the structure

Table 3.4: Selected structural SCF at longitudinal butt welded joints in **cylindrical open-air penstocks** or **pipelines** published in literature (see the nomenclature in Fig. 7.1).

Imperfection type	SCF	References
Out-of-roundness of a cylindrical liner (the longitudinal butt welded joint is located at an angle Φ with respect to the largest radius)	$K_{m,\eta} = 1 + \frac{1.5(d_{\max} - d_{\min})\cos(2\Phi)}{t_s \left[1 + \frac{0.5p_i(1 - v_s^2)}{E_s} \left(\frac{d_{\max}}{t_s} \right)^3 \right]}$ <p>where d_{\max}, d_{\min} and d_{mean} are the maximum, minimum and mean diameters, respectively, and p_i the internal water pressure.</p>	British Standard 7910 (2005); Niemi <i>et al.</i> (2006); Hobbacher (2008); Koçak <i>et al.</i> (2008); Lotsberg (2008, 2009a)
Angular misalignment at the longitudinal butt welded joint in a cylindrical liner (peaking)	$K_{m,p} = 1 + \frac{3\Delta h}{t_s(1 - v_s^2)} \cdot \frac{\tanh(\phi/2)}{\phi/2}$ <p>(with fixed ends boundary conditions) where</p> $\phi = \frac{2l}{t_s} \sqrt{\frac{3(1 - v_s^2)\sigma_m}{E_s}}.$ <p>Δh is the distance of the roof-top from the perfect circle (or ellipse in the case of combination with out-of-roundness) and l is the length of the projected straight edge.</p>	British Standard 7910 (2005); Niemi <i>et al.</i> (2006); Hobbacher (2008); Koçak <i>et al.</i> (2008)
Liner misalignment (eccentricity) at the longitudinal butt welded joint in a cylindrical liner	$K_{m,e} = 1 + \frac{3e}{t_s(1 - v_s^2)}$ <p>where e is the eccentricity.</p>	British Standard 7910 (2005); Niemi <i>et al.</i> (2006); Hobbacher (2008); Koçak <i>et al.</i> (2008)

and crack geometries. For welded plated structures, Y can be detailed as

$$Y = \frac{M_w \cdot M_0}{\sqrt{Q}} \quad (3.52)$$

where M_0 is the correction factor not accounting for the weld and M_w is the correction factor accounting for the presence of the weld only. M_0 typically accounts for correction terms for finite thickness or free surface at the mouth of the crack, for semi-elliptical surface cracks for instance. Q is the complete elliptical integral of the second kind (Anderson 2003), also called flaw shape parameter, and is expressed as:

$$Q = \int_0^{\pi/2} \left[1 - \left(1 - \frac{a^2}{c^2} \right) \sin^2 \phi \right] d\phi. \quad (3.57)$$

Equation 3.57 does not have a closed-form solution, but can be approximated by Eq. B.2.

Published empirical solutions can be used to estimate SIF for cracks in plates (Anderson *et al.* 2002; Newman Jr 1973; Newman Jr & Raju 1981a,b, 1984; Raju & Newman Jr 1979; Shen *et al.* 1991; Shen & Glinka 1991; Wang & Lambert 1995b,a, 1997) and cylinders (Anderson *et al.* 2002; Newman Jr & Raju 1980; Raju & Newman Jr 1982; Li & Yang 2012; Wang & Lambert 1996). Some solutions are also available in fracture mechanics handbooks (Tada *et al.* 1985; Murakami 1987a,b) and reliability assessment standards (British Standard 7910 2005; API 2007; Koçak *et al.* 2008).

Hereafter, only the solutions considered herein are reported, namely for semi-elliptical surface cracks and embedded elliptical cracks in plates.

3.9.2 Axial semi-elliptical surface cracks in plates

Although parametric equations were published for axial semi-elliptical surface cracks in cylinders (see, e.g., Newman Jr & Raju 1980; Raju & Newman Jr 1982; Murakami 1987b), the solutions either cannot account for geometrical imperfections inducing bending stresses, or require knowing the stress distribution on the crack faces. As steel liners of SLPT&S typically have a high slenderness (high internal radii r_i and small relative thicknesses t_s/r_i), solutions for semi-elliptical surface cracks in plates can be considered. The solution chosen herein for its accuracy and widespread use is the one of Newman Jr & Raju (1981a), which can be expressed as

$$K_I = [M_m (\sigma_m + p_{cr}) + M_b \sigma_b] \sqrt{\frac{\pi a}{Q}} \quad (3.58)$$

3.9. Review of formulas for stress intensity factors for cracks in plates and shells

where M_m and M_b are the shape correction factors applied to membrane and bending stresses, respectively, and p_{cr} is the pressure applied on the crack face, equal to the internal pressure p_i in the case of internal surface cracks. The complete empirical solution is reported in Appendix B.1.

3.9.3 Axial embedded elliptical cracks in plates

Similarly to semi-elliptical surface cracks, a solution for embedded elliptical cracks in plates can be considered herein. The solution reported in the standard API 579 (API 2007) and attributed to an unpublished work of Anderson (2005) is chosen, and is expressed as

$$K_I = [M_m (\sigma_{me} + p_{cr}) + M_b \sigma_{be}] \sqrt{\frac{\pi a}{Q}}, \quad (3.59)$$

with

$$\sigma_{me} = \{\sigma_m + p_{cr}\} + \sigma_b \left(1 - \frac{2d_2}{t_s}\right) \quad (3.60)$$

where d_2 is defined in Fig. 8.3, and

$$\sigma_{be} = \sigma_b \left(\frac{2a}{t_s}\right). \quad (3.61)$$

The complete parametric equations for M_m and M_b are given in Appendix B.2.

3.9.4 Influence of the weld shape

In fracture mechanics of weldments literature, numerous studies have been published studying weld toe correction factors for cracked welded plates (Bowness & Lee 2000a,b; Brennan *et al.* 1999; Fu *et al.* 1993; Han *et al.* 2014; Hobbacher 1993; Lie *et al.* 2000, 2015; Niu & Glinka 1987, 1989; Wang & Lambert 1998). On the contrary, there are only few works assessing SIF for cracks in the weld deposit. Nykänen *et al.* (2005) studied SIF for root cracks in transverse penetration butt welds. Wang *et al.* (2012b) proposed parametric equations to estimate the SIF for 2D single-edge cracks at butt welded joints, and Wang *et al.* (2012a) proposed SIF solutions for 2D center cracks in undermatched butt joints. To the best author's knowledge, there is however no published work assessing the influence of the weld shape on SIF for 3D cracks in the weld material of butt welded joints with the specific features of SLPT&S.

3.10 Conclusions

From the literature review on fatigue and fracture assessment presented in this chapter, the following conclusions can be outlined.

1. The $S-N$ approaches are well established in standards and guidelines for fatigue assessment. In the case of fully penetrated welded joints, these methods account for fatigue crack initiation and propagation from notches, in particular weld toes for butt welded joints.
2. Among the $S-N$ approaches, the effective notch stress approach is the highest level of refinement. This method is still a subject of research, particularly concerning the parameters describing the curves after the knee point, namely in the high- to very-high cycle fatigue.
3. The fatigue crack growth analysis by means of LEFM is very widespread, particularly when the crack initiation period can be neglected because of the presence of an initial crack-like flaw.
4. To implement $S-N$ or LEFM approaches, structural and notch stress concentration factors are required. Some parametric solutions are available in the literature. If no appropriate solution does exist, they have to be determined by means of the FEM.
5. In the case of SLPT&S, the complex interaction between all geometrical imperfections and the contact between the steel liner and the backfill concrete–system has never been studied.
6. Probabilistic approaches in engineering can provide great advantages for the design, as they *measure* uncertainty. Although they are widely used in engineering fields such as in the nuclear power generation industry or in aeronautics, they are not commonly used in the scope of SLPT&S.

In this research study, parametric equations or correction factors will be derived by means of the FEM for an optimized application of the fatigue assessment engineering procedures to the specific case of SLPT&S. A probabilistic model for fatigue crack growth and fracture at the longitudinal butt welded joints of steel liners of SLPT&S will be developed, providing a framework for fatigue analyses in practice and therefore addressing the issues presented in Chapter 2.

Anisotropic rock behavior Part II

Anisotropy is everywhere. Isotropy is rare. Round stones are collectors' item, and any almost cubic blocks are photographed, as they are the exception.
– Barton & Quadros (2014)

Most of the content of this part (together with Sects. 2.1, 2.2, 2.3 and 2.4 of Chapter 2 in the literature review) has been published in a scientific article entitled "Stresses and displacements in steel-lined pressure tunnels and shafts in anisotropic rock under quasi-static internal water pressure" by Pachoud & Schleiss (2016) in *Rock Mechanics and Rock Engineering* 49(4), pp. 1263–1287. The finite element model, the parametric study (Chapter 4), the parametric correction factors (Chapter 5) and the respective analyses are original and were developed by the author of the present report.

4 Parametric study

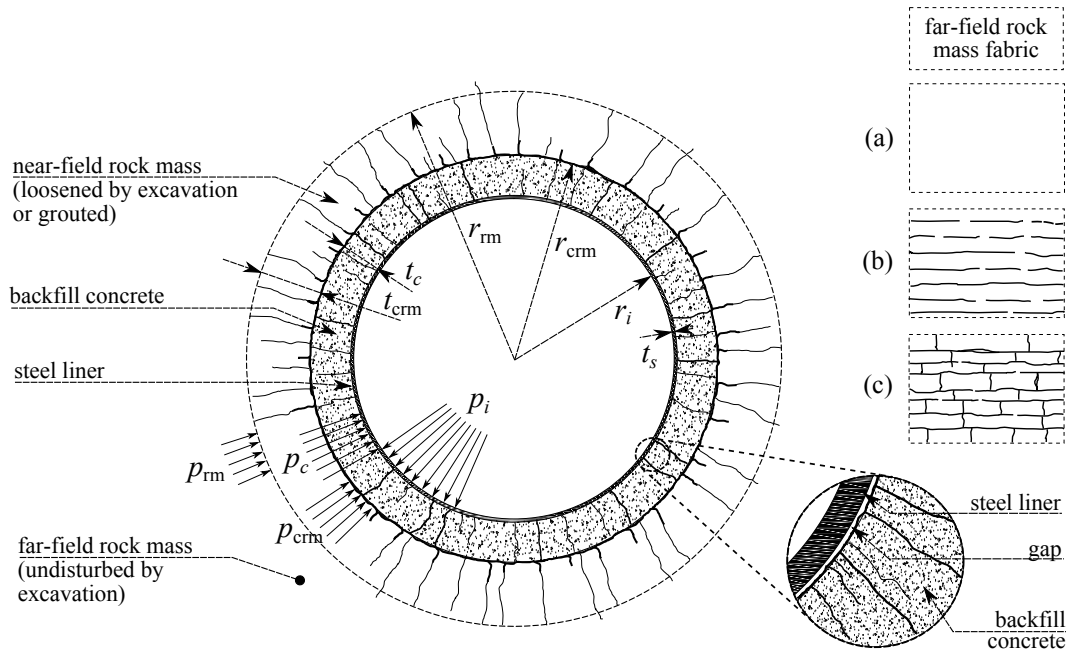


Figure 4.1: Definition sketch of the standard multilayer system for pressure tunnels and shafts embedded in: (a) elastic, isotropic rock mass (axisymmetrical case); (b) transversely isotropic, elastic rock mass; and (c) transversely isotropic, elastic rock mass with two sets of discontinuities.

4.1 Constitutive modeling of anisotropic rock

The definition sketch of steel-lined pressure tunnels and shafts in anisotropic rock is shown in Fig. 4.1. In engineering problems, when the rock is inhomogeneous or highly discontinuous, the latter is often modeled with a continuum approach (Jing 2003). A jointed rock mass is thus regarded as a continuum with equivalent properties taking into account the effects of the fabric patterns. In the particular cases of excavations in jointed rock masses, the continuum approach

Chapter 4. Parametric study

is justified when the opening diameter is large compared to the spacing of the discontinuities (Gerrard 1982; Jing 2003).

Amadei *et al.* (1987) states that the anisotropic behavior of rocks is often related to their fabric pattern in the form of bedding, stratification, layering, schistosity planes, foliation, fissuring or jointing. According to them, this is a general characteristic for rocks such as foliated metamorphic rocks, stratified sedimentary rocks and rocks cut by one or several regular and closely spaced joint sets. To model such discontinuities in rocks, one may consider an elastic transversely isotropic behavior for the constitutive law (Wittke 1990), i.e., with a plane of isotropy which is parallel to the foliation for example. Good introductions to transverse isotropy in rocks can be found in rock mechanics books, e.g., in Derski *et al.* (1989), Wittke (1990) or Brady & Brown (2006).

4.1.1 Definition of stress and strain vectors in the Cartesian coordinate system

In the Cartesian coordinate system, the stress and strain tensors are defined by nine components, respectively, at a given point (Lekhnitskii 1963):

$$\begin{bmatrix} \sigma_x & \tau_{xy} & \tau_{xz} \\ \tau_{yx} & \sigma_y & \tau_{yz} \\ \tau_{zx} & \tau_{zy} & \sigma_z \end{bmatrix} \quad (4.1)$$

and

$$\begin{bmatrix} \epsilon_x & \frac{1}{2}\gamma_{xy} & \frac{1}{2}\gamma_{xz} \\ \frac{1}{2}\gamma_{yx} & \epsilon_y & \frac{1}{2}\gamma_{yz} \\ \frac{1}{2}\gamma_{zx} & \frac{1}{2}\gamma_{zy} & \epsilon_z \end{bmatrix}. \quad (4.2)$$

These tensors are always symmetric. This implies $\tau_{ij} = \tau_{ji}$ and $\gamma_{ij} = \gamma_{ji}$. γ_{ij} are the engineering shear strains and are related to the strain tensor ϵ_{ij} as $\gamma_{ij} = 2\epsilon_{ij}$, ($i \neq j$). The following definition of stress and engineering strain vectors $\boldsymbol{\sigma}$ and $\boldsymbol{\epsilon}$ is considered in this work:

$$\boldsymbol{\sigma} = [\sigma_x, \sigma_y, \sigma_z, \tau_{yz}, \tau_{xz}, \tau_{xy}]^T \quad (4.3)$$

and

$$\boldsymbol{\epsilon} = [\epsilon_x, \epsilon_y, \epsilon_z, \gamma_{yz}, \gamma_{xz}, \gamma_{xy}]^T, \quad (4.4)$$

respectively.

4.1.2 Stress–strain relations in an orthotropic medium

A continuous elastic body is assumed to satisfy the generalized Hooke's law. For the most general anisotropic case in Cartesian coordinates, the relations between the components of stress and

strain are expressed in the so-called stiffness form as

$$\boldsymbol{\sigma} = [A_{ij}]\boldsymbol{\varepsilon}; \quad (4.5)$$

or in the so-called compliance form as

$$\boldsymbol{\varepsilon} = [a_{ij}]\boldsymbol{\sigma}, \quad (4.6)$$

where $[A_{ij}]$ is the matrix of elasticity and $[a_{ij}] = [A_{ij}]^{-1}$. They are (6×6) matrices. The 36 coefficients A_{ij} are called the moduli of elasticity, and the a_{ij} are called the elastic constants.

When studying problems of stability, stresses and deformations, the use of technical constants is convenient, i.e., the elastic moduli, the Poisson's ratios and the shear moduli.

A medium which has three orthogonal planes of elastic symmetry is called orthotropic. Assuming that the Cartesian axes are perpendicular to these planes, stress-strain relations are described with nine independent constants. The constitutive law for orthotropic materials can thus be written as (Lekhnitskii 1963)

$$\begin{Bmatrix} \varepsilon_x \\ \varepsilon_y \\ \varepsilon_z \\ \gamma_{yz} \\ \gamma_{xz} \\ \gamma_{xy} \end{Bmatrix} = \begin{bmatrix} \frac{1}{E_x} & -\frac{\nu_{yx}}{E_y} & -\frac{\nu_{zx}}{E_z} & 0 & 0 & 0 \\ -\frac{\nu_{xy}}{E_x} & \frac{1}{E_y} & -\frac{\nu_{zy}}{E_z} & 0 & 0 & 0 \\ -\frac{\nu_{xz}}{E_x} & -\frac{\nu_{yz}}{E_y} & \frac{1}{E_z} & 0 & 0 & 0 \\ 0 & 0 & 0 & \frac{1}{G_{yz}} & 0 & 0 \\ 0 & 0 & 0 & 0 & \frac{1}{G_{xz}} & 0 \\ 0 & 0 & 0 & 0 & 0 & \frac{1}{G_{xy}} \end{bmatrix} \begin{Bmatrix} \sigma_x \\ \sigma_y \\ \sigma_z \\ \tau_{yz} \\ \tau_{xz} \\ \tau_{xy} \end{Bmatrix} \quad (4.7)$$

where:

$$\frac{\nu_{ij}}{E_i} = \frac{\nu_{ji}}{E_j} \quad (4.8)$$

and the E_i are the moduli of elasticity, the G_{ij} are the shear moduli, and the ν_{ij} are the Poisson's ratios.

4.1.3 Stress-strain relations in a transversely isotropic medium

Transverse isotropy is a particular case of orthotropy, i.e., with a plane of isotropy. To characterize a transversely isotropic material, five independent constants denoted E , E' , ν , ν' and G' ($G = E/[2 + 2\nu]$) are required. E and E' are the elastic moduli in the plane of isotropy and perpendicular to it, respectively, ν and ν' are the Poisson's coefficients which characterize the reduction in

the plane of isotropy for the tension in the same plane and the tension in a direction normal to it respectively, and G and G' are the shear moduli for the planes parallel and normal to the plane of isotropy, respectively, (Amadei *et al.* 1987). G' is also called the cross-shear modulus. Assuming that the isotropic plane is parallel to the xz -coordinates plane, the stress–strain relation in Cartesian coordinates is expressed as (Lekhnitskii 1963)

$$\begin{Bmatrix} \varepsilon_x \\ \varepsilon_y \\ \varepsilon_z \\ \gamma_{yz} \\ \gamma_{xz} \\ \gamma_{xy} \end{Bmatrix} = \begin{bmatrix} \frac{1}{E} & -\nu' & -\nu & 0 & 0 & 0 \\ -\nu' & \frac{1}{E'} & -\nu' & 0 & 0 & 0 \\ \frac{E'}{E} & \frac{E'}{E'} & \frac{E'}{E} & 0 & 0 & 0 \\ \frac{-\nu}{E} & \frac{-\nu'}{E'} & \frac{1}{E} & 0 & 0 & 0 \\ 0 & 0 & 0 & \frac{1}{G'} & 0 & 0 \\ 0 & 0 & 0 & 0 & \frac{1}{G} & 0 \\ 0 & 0 & 0 & 0 & 0 & \frac{1}{G'} \end{bmatrix} \begin{Bmatrix} \sigma_x \\ \sigma_y \\ \sigma_z \\ \tau_{yz} \\ \tau_{xz} \\ \tau_{xy} \end{Bmatrix}. \quad (4.9)$$

4.1.4 Admissible values for the elastic constants

Thermodynamic considerations require that the strain energy of an elastic material is always positive definite. It implies conditions on the admissible elastic constants (Amadei *et al.* 1987, 1988):

$$\begin{aligned} E, E', G', G &> 0; \\ -1 < \nu < 1; \\ -\sqrt{\frac{E'}{E} \frac{1-\nu}{2}} < \nu' < \sqrt{\frac{E'}{E} \frac{1-\nu}{2}}. \end{aligned} \quad (4.10)$$

4.1.5 Ranges of properties of transversely isotropic rocks

The elastic properties of transversely isotropic rocks are usually assessed by in situ and laboratory tests, sometimes associated with numerical modeling (Hakala *et al.* 2007). However, despite the simplicity of the constitutive relations, the determination of these elastic properties is not simple due to the lack of standardization for the measurement methods (Gonzaga *et al.* 2008). The cross-shear modulus G' is the most difficult parameter to assess (Batugin & Nirenburg 1972; Homand *et al.* 1993).

Amadei *et al.* (1987) discuss the ranges of properties for transversely isotropic rocks which can be found in nature. For most transversely isotropic rocks, the values of the degree of anisotropy E/E' and the ratio of the shear moduli G/G' are between 1 and 3, the Poisson's ratio ν and ν' are between 0.15 and 0.35, and the value of $\nu'E/E'$ is between 0.1 and 0.7. However, in exceptional cases, E/E' may reach values between 4 and 6. Gerrard (1977) gathered a large bank

4.2. Constitutive modeling of the cracked layers

of published data of anisotropic rocks, including specific cases of transversely isotropic rocks. He also indicates, as it can be observed in numerous studies providing transversely isotropic rock properties, that the lowest stiffness is usually observed in the direction normal to the bedding, stratification, layering, foliation, schistosity planes, etc.

Gercek (2007) discusses in detail the Poisson's ratios' values for rocks. He outlines that for most rocks, the Poisson's ratios may be between 0.05 and 0.45. However, for most rock engineering applications with poor field data, most probable values between 0.2 and 0.3 are often assumed.

For the estimation of G' , the following empirical relation first introduced by Saint-Venant is widely considered in the literature:

$$G'_{S-V} = \frac{E'}{1 + E'/E + 2\nu'} \quad (4.11)$$

However, although most of the published data support the validity of this empirical equation, there are still major exceptions (Gonzaga *et al.* 2008) and measured values do not always correspond to G'_{S-V} (Hakala *et al.* 2007).

4.2 Constitutive modeling of the cracked layers

As assumed in Sect. 2.1, the backfill concrete and the near-field rock layers are radially cracked and thus cannot transfer tensile stresses in the tangential direction. A simple continuum damage-based approach is considered to model this effect of radial cracks in the backfill concrete and in the near-field rock. A scalar damage parameter D_i that measures the effect of damage is introduced (Cauvin & Testa 1999):

$$1 - D_i = R_i, \quad (4.12)$$

where the subscript i denotes a material parameter and R_i is a scalar factor to be applied to a material property. This approach does not aim at modeling an evolution of damage depending on the internal pressure. Instead it considers an already highly radially damaged material for a pseudo-static analysis. Due to the axisymmetrical nature of the problem, the stress-strain relations are considered in polar coordinates. In accordance with the assumption that the radially cracked materials do not transmit tangential tensile stresses, the elastic modulus in the tangential direction should be decreased as

$$R_{E_\theta} = \frac{\tilde{E}_\theta}{E_\theta}, \quad (4.13)$$

where \tilde{E}_θ is the elastic modulus of the damaged material in the tangential direction. Accordingly, other elastic parameters are also affected by the drop of stiffness in the tangential direction, and

Chapter 4. Parametric study

other scalar factors are defined to take into account the effect of damage:

$$R_{G_{\theta r}} = R_{G_{\theta z}} = \frac{\tilde{G}_{\theta r}}{G_{\theta r}} = \frac{\tilde{G}_{\theta z}}{G_{\theta r}}, \quad (4.14)$$

and

$$R_{v_{\theta r}} = R_{v_{\theta z}} = \frac{\tilde{v}_{\theta r}}{v_{\theta r}} = \frac{\tilde{v}_{\theta z}}{v_{\theta r}}. \quad (4.15)$$

The radially damaged materials are regarded as transversely isotropic materials in polar coordinates, i.e., with the plane of isotropy parallel to the rz -plane. The values of the degrees of damage R_i are discussed in Sect. 4.3.

4.3 Finite element model

4.3.1 Model

The 10 variables used in the FE model are presented in Table 4.1 and the parameters kept constant are given in Table 4.2.

Table 4.1: Variable parameters of the FE model.

Parameter	Definition
r_i	Internal radius of the steel liner
t_s	Thickness of the steel liner
t_{crm}	Thickness of the near-field rock zone
p_i	Internal quasi-static water pressure
E	Elastic modulus of the far-field rock in the plane of isotropy
E'	Elastic modulus of the far-field rock in the plane perpendicular to the plane of isotropy
G'	Cross-shear modulus of the far-field rock
ν	Poisson's ratio of the far-field rock related to the plane of isotropy
ν'	Poisson's ratio of the far-field rock related to the planes perpendicular to the plane of isotropy
E_{crm}	Elastic modulus of the near-field rock

Table 4.2: Constant parameters of the FE model.

Parameter	Unit	Value
E_s	GPa	210
ν_s	(–)	0.30
E_c	GPa	20
ν_c	(–)	0.20
t_c	m	0.5
ν_{crm}	(–)	0.20

The FE model (see Fig. 4.2) follows the same assumptions as the analytical solution in isotropic

rock (Sect. 2.2), and some additional hypotheses, namely:

1. the opening has a circular cross-section;
2. all the layers, including the backfill concrete and near-field rock zones have a circular cross-section;
3. 2D plane strain conditions;
4. high tunnel overburden, i.e., the dimensions of the far-field rock are large enough to be considered as infinite (equal to $r_{\text{rm}} + 30 \times r_i$ in this study) and thus full load transmission occurs through the layers;
5. tied contact between every layer, without initial gap Δr_0 ; and
6. all materials are linear elastic.

The constitutive laws for the far-field rock and cracked materials are implemented as described in Sect. 4.1 (Eq. 4.9) and in Sect. 4.2 respectively. R_{E_θ} , $R_{G_{\theta r}}$ and $R_{G_{\theta z}}$ are set equal to 10^{-4} which is the largest order of magnitude ensuring convergence toward the analytical solution for the isotropic cases. $R_{V_{\theta r}}$ and $R_{V_{\theta z}}$ are set to zero.

The elements used are PLANE183, 8-node squares for the steel liner and the beginning of the far-field rock (for post-processing convenience) and 6-node triangles for all the other zones of the model. The FE model, depending on the geometrical parameters, is meshed with a variable number of elements to ensure convergence toward the corresponding analytical solution in the isotropic case. The steel liner, for instance, is discretized by 400 elements along 90deg in the circumferential direction and 12 elements in the radial direction. An example of a mesh around the opening is shown in Fig. 4.2.

4.3.2 Nomenclature

The nomenclature used in this study is illustrated in Fig. 4.3. The plane of isotropy is along the xz -plane in Cartesian coordinates. E denotes the elastic moduli along the x - and z -axis (out-of-plane). E' denotes the elastic moduli along the y -axis. The angles of location $\theta = 0$ and 90deg in polar coordinates are shown, as well as the locations of the so-called internal and external fibers of the steel liner.

4.3.3 Validation in isotropic rock

Two thousands isotropic cases were generated and solved (see the ranges of variation of the parameters in Sect. 5.1.1). The relative error on the maximum major principal stress $\sigma_{1,\text{max}}^s$ and

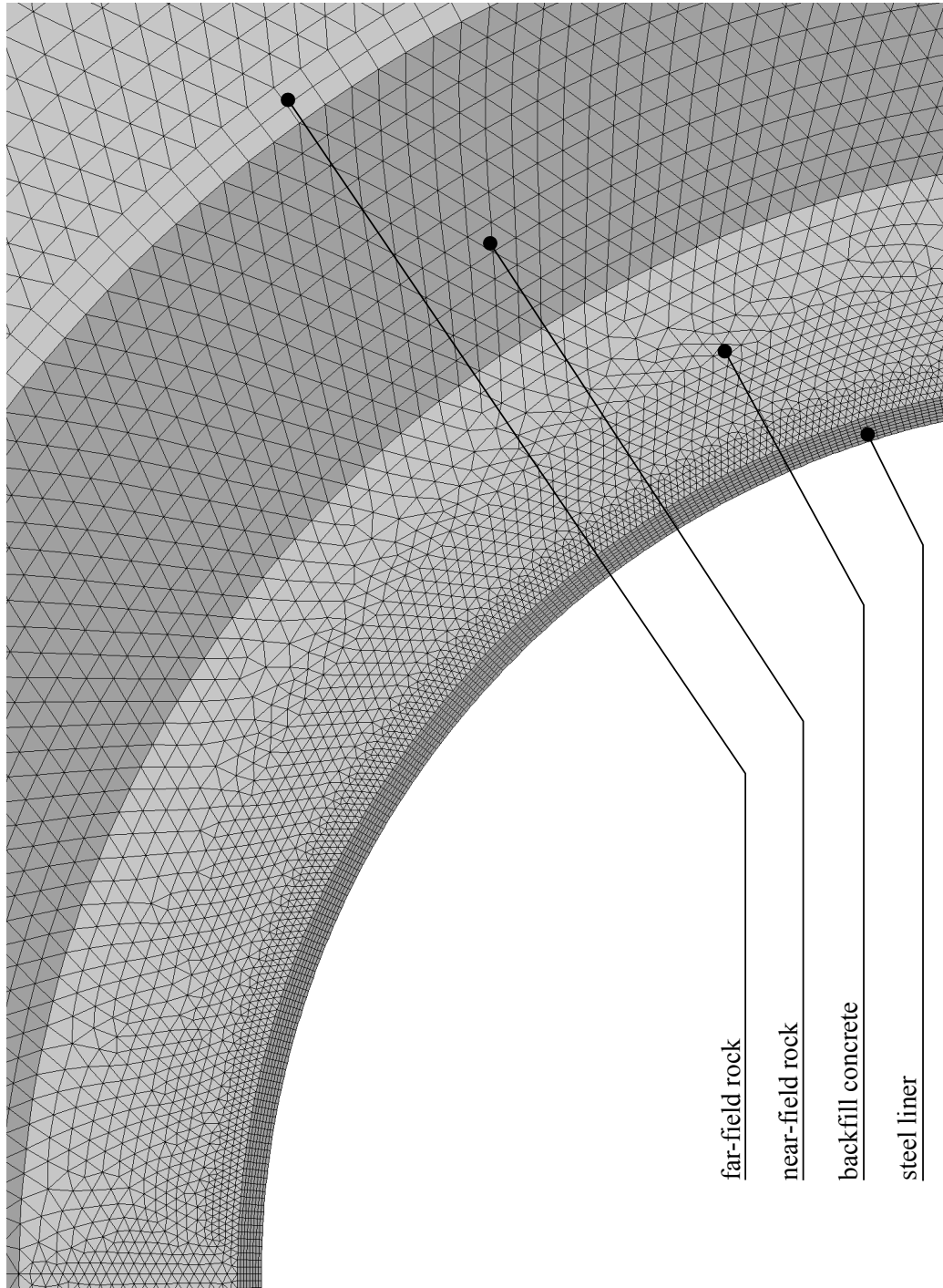


Figure 4.2: Example of a mesh of the FE model around the opening for $r_i = 2.0$ m, $t_s = 0.055$ m, $t_c = 0.50$ m and $t_{crn} = 0.70$ m.

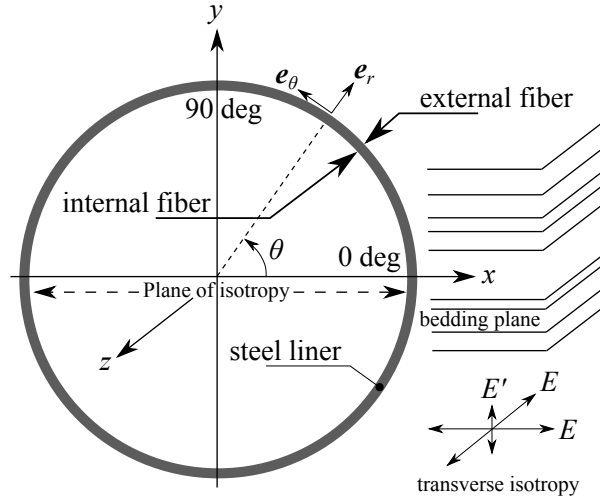


Figure 4.3: Nomenclature used for the discussion of the results.

the maximum radial displacement $u_{r,\max}^s$ in the steel liner (both at the internal fiber for $r = r_i$) was computed as

$$\text{Error} = \frac{\text{Numerical result} - \text{Analytical result}}{\text{Analytical result}} \cdot 100\% \quad (4.16)$$

where the numerical result was obtained with ANSYS and the theoretical result from the analytical solution (Sect. 2.2, Eqs. 2.8, 2.9, 2.10 and 2.14). The mean relative error on $\sigma_{i,\max}^s$ considering the two thousands simulations is -0.38% , with a minimum of -0.17% and a maximum of -0.81% . The mean relative error on $u_{r,\max}^s$ is -0.33% , with a minimum of -0.13% and a maximum of -0.78% . These results are in very good agreement with the analytical solution. In addition, results along paths in radial directions were studied for several cases and showed a very good behavior of the FE solution compared to the analytical solution.

4.4 Parametric study

4.4.1 Preliminary discussion on the parameters

Similarly to the methodology described in the following Sect. 4.4.2, preliminary systematic parametric studies, not detailed herein, were performed in order to assess the influence of the variable parameters of the problem. It was shown that material parameters such as E_{crm} , ν and ν' cause minor, if any, variations in the results. Concerning the geometrical parameters, for dimensional reasons the stresses and normalized displacements only depend on the ratio t_s/r_i . Finally, because of the assumption of elasticity, the internal pressure p_i is not investigated.

4.4.2 Set of calculation cases

Considering the aforementioned observations, a systematic parametric study was performed in order to assess the influence of the relevant variable parameters. A so-called *reference set of cases* was defined with fixed parameters presented in Table 4.3.

Table 4.3: Variation of the dimensionless parameters with respect to the reference set of cases.

Parameter	Reference value	Value 1	Value 2
t_{crm}/r_i	0.33	0.00	0.66
E/E_s	0.024	0.071	0.119
$G'/G'_{\text{S-V}}$	1.00	0.70	1.30

With respect to the reference set of cases, three dimensionless parameters were changed, namely:

1. the near-field rock thickness to steel liner's internal radius ratio t_{crm}/r_i ;
2. the rock mass elastic modulus to steel elastic modulus ratio E/E_s ; and
3. the cross-shear modulus to Saint-Venant empirical relation ratio $G'/G'_{\text{S-V}}$.

They are shown in Table 4.3. For each set of cases (reference and others), the liner's thickness to its internal radius ratio t_s/r_i and the degree of anisotropy E/E' were changed as reported in Table 4.4. For all the simulations, $r_i = 2$ m, $\nu = \nu' = 0.20$ and $E_{\text{crm}}/E' = 0.80$.

Table 4.4: Variation range of the variable dimensionless parameters for each set of cases.

Parameter	Min. value	Max. value	Increment
t_s/r_i	0.008	0.035	0.005 (from 0.010)
E/E'	1.00	3.50	0.25

As a consequence, there were seven sets of simulated cases (including the reference set), each one containing 77 cases, for a total of 1078 simulated cases in anisotropic rock. Every simulated case respected the following thermodynamic constraint and practical range of variation of the $\nu'E/E'$ term (see Sect. 4.1):

$$\begin{aligned} \nu' &< \sqrt{\frac{E'}{E} \frac{1-\nu}{2}}; \\ 0.1 &< \nu' \frac{E}{E'} < 0.7. \end{aligned} \tag{4.17}$$

4.4.3 Normalized results

All the results are normalized by the results obtained considering an isotropic rock with an elastic modulus equal to that prevailing perpendicularly to the bedding or schistosity plane. The latter

represents the most conservative isotropic model and is called hereafter as the *reference isotropic case*. For example, considering an anisotropic rock of parameters $E, E' < E, \nu, \nu' < \nu$ and G' , the reference isotropic case will be the case in isotropic rock of parameters E' and ν , i.e. $E_{rm} = E'$ and $\nu_{rm} = \nu$ correspondingly to Eqs. 2.8 and 2.9. Normalized results are denoted with a *caret* character, as for instance the major principal stress in the steel liner:

$$\hat{\sigma}_1^s = \frac{\sigma_{1,aniso}^s}{\sigma_{1,iso}^s} \quad (4.18)$$

where the subscript *aniso* refers to the results considering anisotropic rock behavior, and *iso* refers to the results in the corresponding reference isotropic case.

4.4.4 Stresses and displacements in the steel liner

Maximum stresses

Maximum normalized major principal stresses in the steel liner $\hat{\sigma}_{1,max}^s$ as a function of the degree of anisotropy E/E' are shown in Fig. 4.4. As $\hat{\sigma}_{1,max}^s$ always occurs at the internal fiber of the steel liner in the plane of isotropy (see Sect. 4.4.4), the normalized results are computed as

$$\hat{\sigma}_{1,max}^s = \frac{\sigma_{1,aniso}^s(r = r_i, \theta = 0)}{\sigma_{1,iso}^s(r = r_i)}. \quad (4.19)$$

Figure 4.4, in quadrant (a), shows the influence of the relative thickness of the near-field rock compared to the internal radius t_{crm}/r_i on $\hat{\sigma}_{1,max}^s$. The greater t_{crm}/r_i and the greater t_s/r_i , the lower the variation $\hat{\sigma}_{1,max}^s$. The influence of t_s/r_i can be explained by the notion of relative stiffness between the steel liner and the rest of the system. Indeed a stiff liner will limit the deformations induced by the internal pressure p_i , and will withstand large stresses. The influence of anisotropic behavior of the far-field rock compared to the reference isotropic case on $\hat{\sigma}_{1,max}^s$ is thus less significant if the relative stiffness of the liner is large compared to the rest of the system. The role of t_{crm}/r_i can be explained with similar considerations. An extended near-field rock zone (large t_{crm}/r_i) decreases the relative stiffness of the concrete-rock system compared to the steel liner and results in the same conclusions. One may also consider an additional effect due to the hypothesis of a cylindrical anisotropy in the cracked near-field zone with a constant elastic modulus in the radial direction. Such an axisymmetrical layer is thus expected to mitigate the effect of far-field anisotropy in terms of variations of $\hat{\sigma}_{1,max}^s$ in the steel liner.

In the quadrant (b) of Fig. 4.4, the influence of the relative stiffness of the far-field rock compared to the stiffness of the steel E/E_s is shown. The greater E/E_s , the lower $\hat{\sigma}_{1,max}^s$ compared to the corresponding reference isotropic case. These results depend on the relative stiffness between the steel liner and concrete-rock system. The stiffer the far-field rock (high relative stiffness E/E_s) the larger the part of p_i that the latter withstands, and thus considering anisotropic behavior yields a larger change in the estimation of $\hat{\sigma}_{1,max}^s$ in the steel liner. In other words, the lower the relative

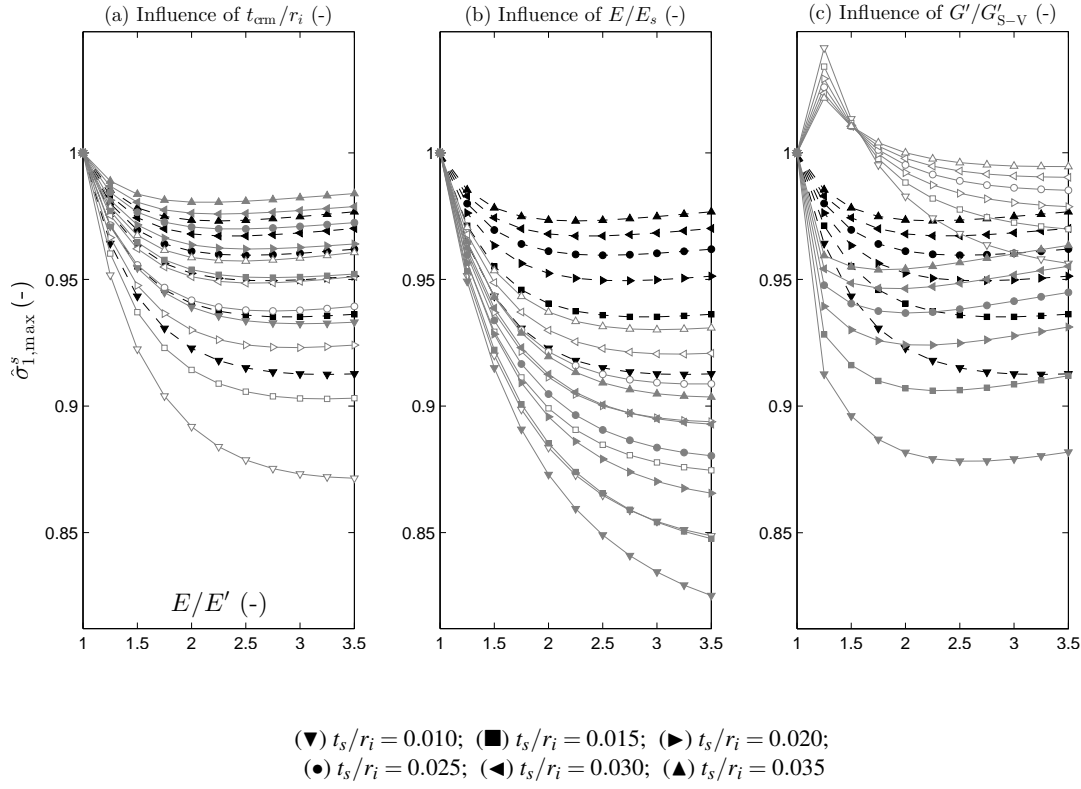


Figure 4.4: Maximum normalized major principal stresses in the steel liner $\hat{\sigma}_{1,max}^s$ as a function of the degree of anisotropy E/E' for different: (a) near-field rock thickness to steel liner's internal radius ratios t_{crm}/r_i ; (b) rock mass elastic modulus to steel elastic modulus ratios E/E_s ; and (c) cross-shear modulus to Saint-Venant empirical relation ratios G'/G'_{S-V} , and by varying the steel liner's thickness to the internal radius ratio t_s/r_i .

stiffness of the steel liner, the more conservative the consideration of the reference isotropic case in terms of $\hat{\sigma}_{1,max}^s$.

The third quadrant (c) of Fig. 4.4 represents the influence of the deviation of the cross-shear modulus G' from the empirical formula of Saint-Venant G'_{S-V} . The effect of G'/G'_{S-V} on $\hat{\sigma}_{1,max}^s$ has a different pattern, although the results may also depend on the concept of relative stiffness. For low values of E/E' , a low cross-shear modulus G' (i.e., lower than the value of G in an isotropic case), $\hat{\sigma}_{1,max}^s$ is larger than in the corresponding reference isotropic case. This is due to the fact that the far-field rock is globally softer than the corresponding reference isotropic case, and thus induces larger stresses in the steel liner to withstand p_i . This effect is canceled and even reversed for higher E/E' , where the influence of the latter becomes more significant. Conversely, a large cross-shear modulus G' for low degrees of anisotropy will increase the ability

of the far-field rock to attract stresses, and therefore $\hat{\sigma}_{1,\max}^s$ is lower than in the corresponding reference isotropic case. This effect is moderated for larger E/E' .

Major principal stresses and radial displacements

Normalized major principal stresses in the steel liner at the internal fiber $\hat{\sigma}_{1,\text{int}}^s$ and at the external fiber $\hat{\sigma}_{1,\text{ext}}^s$ as a function of the angle θ with respect to the plane of isotropy are shown in Fig. 4.5. For all the tested cases, $\hat{\sigma}_{1,\max}^s$ always occurs in the plane of isotropy ($\theta = 0$), at the internal fiber ($r = r_i$). The normalized results at internal and external fibers are computed with respect to the maximum major principal stress $\sigma_{1,\max}^s$ in the steel liner for the reference isotropic case as:

$$\hat{\sigma}_{1,\text{int}}^s(\theta) = \frac{\sigma_{1,\text{aniso}}^s(r = r_i, \theta)}{\sigma_{1,\text{iso}}^s(r = r_i)} \quad (4.20)$$

and

$$\hat{\sigma}_{1,\text{ext}}^s(\theta) = \frac{\sigma_{1,\text{aniso}}^s(r = r_i + t_s, \theta)}{\sigma_{1,\text{iso}}^s(r = r_i)}. \quad (4.21)$$

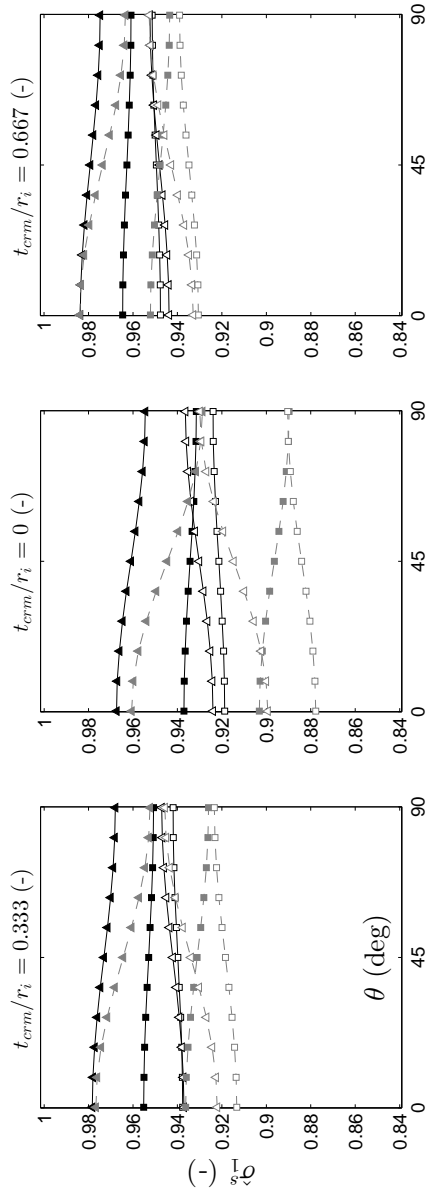
To illustrate the deformed shapes of the steel liners, the corresponding normalized radial displacements in the steel liner \hat{u}_r^s (at the internal fiber) are shown in Fig. 4.5. The normalized results are computed with respect to the maximum radial displacement of the corresponding reference isotropic case as

$$\hat{u}_r^s(\theta) = \frac{u_{r,\text{aniso}}^s(r = r_i, \theta)}{u_{r,\text{iso}}^s(r = r_i)}. \quad (4.22)$$

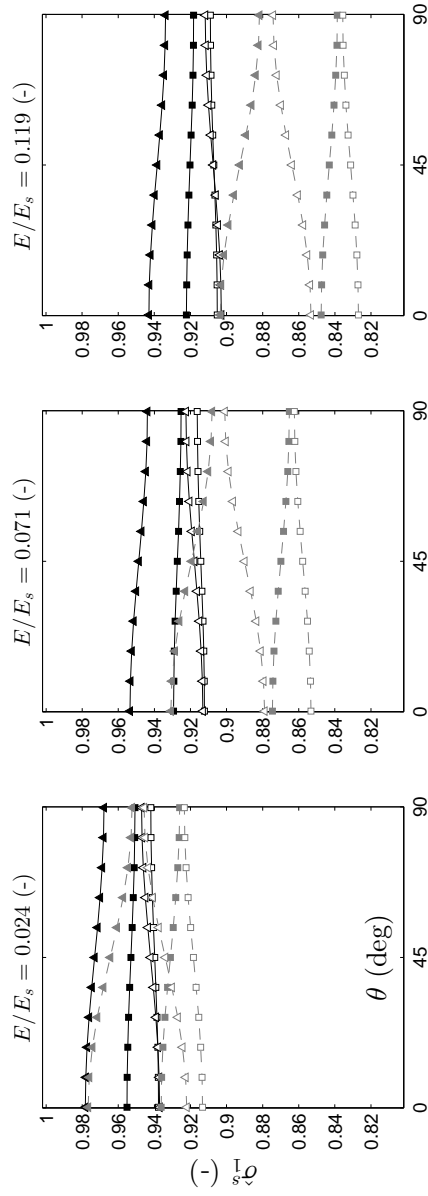
Figures 4.5a–4.5c shows the influence on $\hat{\sigma}_1^s$ of the relative thickness of the near-field rock compared to the internal radius t_{crm}/r_i , the relative stiffness of the far-field rock compared to the stiffness of the steel E/E_s , and the deviation of the cross-shear modulus G' from the empirical formula of Saint-Venant $G'_{\text{S-V}}$ respectively. Figure 4.6a–4.5c shows the influence of the dimensionless parameters on \hat{u}_r^s , respectively.

The same observations on the influence of each parameter on $\hat{\sigma}_{1,\max}^s$ as in Fig. 4.4 can be made. However as Fig. 4.5 shows the normalized major principal stresses on the perimeter of the steel liner both at the internal and external fibers, one can obtain information about the occurrence of bending in the steel liner. Some general observations can be made:

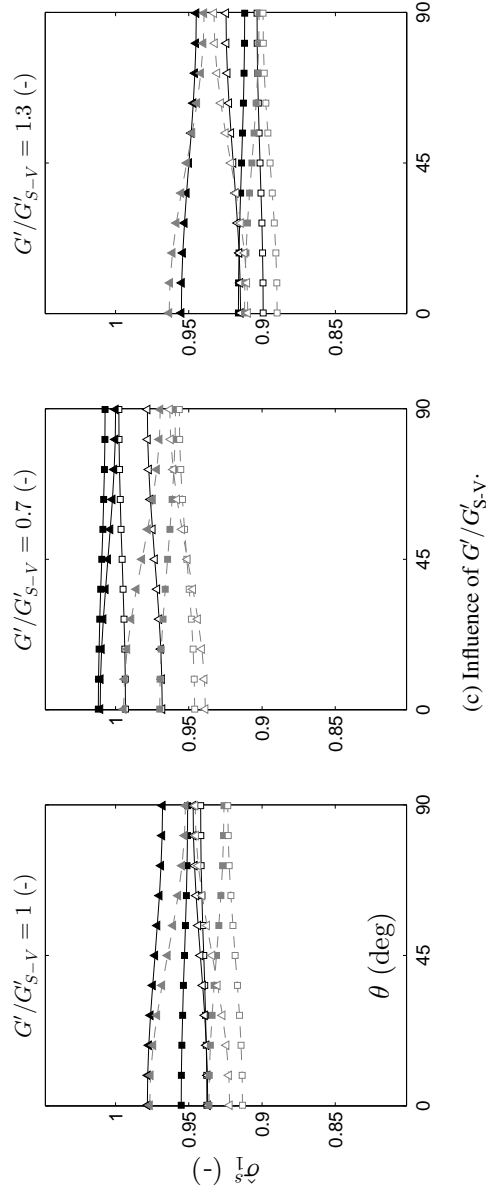
- the maximum major principal stress $\hat{\sigma}_{1,\max}^s$ always occurs at the internal fiber at $\theta = 0$ deg, along the springline (i.e., in the plane of isotropy of the far-field rock, see Fig. 4.5);
- the minimum major principal stress always occurs at the external fiber at $\theta = 90$ deg, along the crown (in the plane perpendicular to the plane of isotropy of the far-field rock, see



(a) Influence of t_{crm}/r_i .



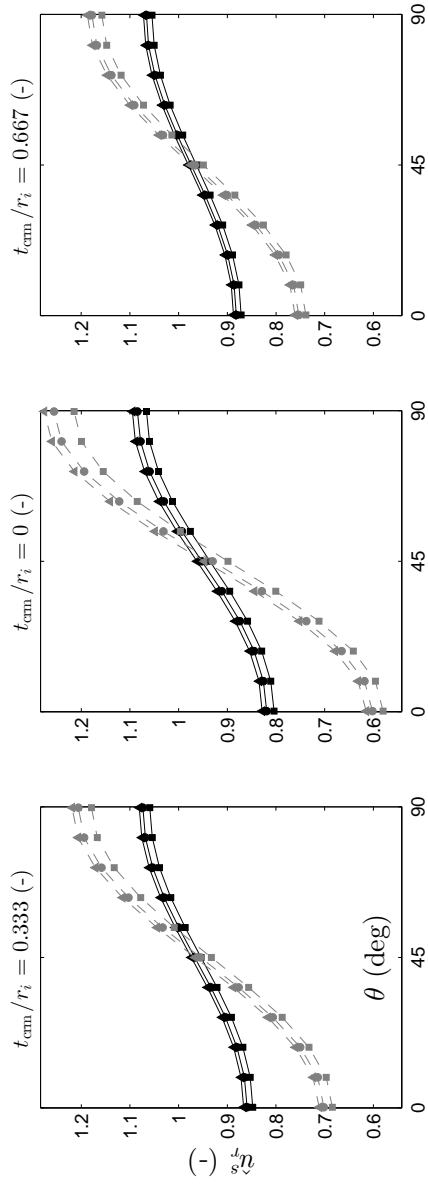
(b) Influence of E/E_s .



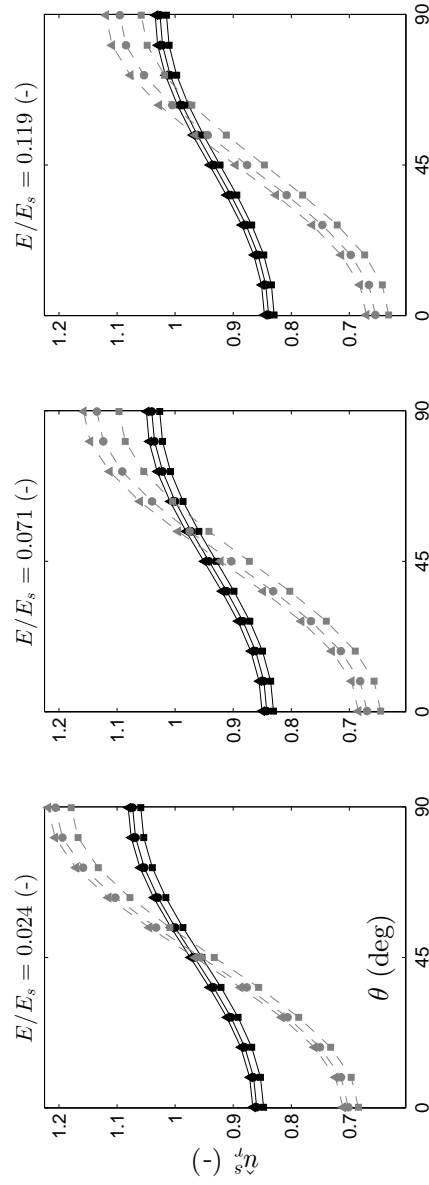
(■) $t_s/r_i = 0.015$; (▲) $t_s/r_i = 0.035$

Black solid lines (—): $E/E_s = 1.5$ Filled symbols: internal fiber
 Gray dashed lines (---): $E/E_s = 3.5$ Empty symbols: external fiber

Figure 4.5: Normalized major principal stresses in the steel liner $\hat{\sigma}_1^s$ at the internal and external fibers as a function of the angle θ with respect to the plane of isotropy for different: (a) near-field rock thickness to steel liner's internal radius ratios t_{cm}/r_i ; (b) rock mass elastic modulus to steel elastic modulus ratios E/E_s ; and (c) cross-shear modulus to Saint-Venant empirical relation ratios G'/G'_{S-V} , and by varying the steel liner's thickness to the internal radius ratio t_s/r_i and the degree of anisotropy E/E' .



(a) Influence of t_{crm}/r_i .



(b) Influence of E/E_s .

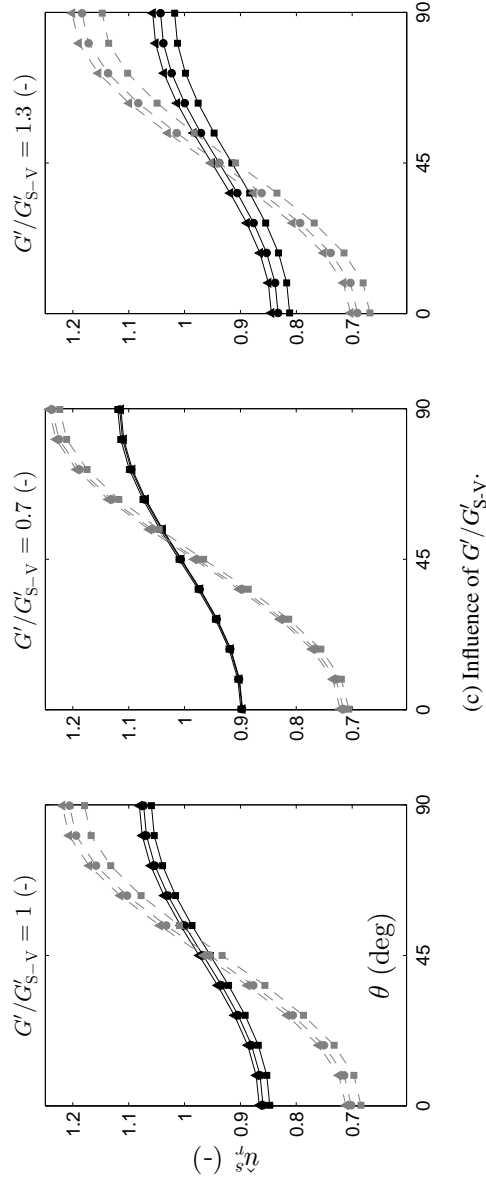


Figure 4.5: Normalized radial displacements at the internal fiber of the steel liner \hat{u}_r^s as a function of the angle θ with respect to the plane of isotropy for different: (a) near-field rock thickness to steel liner's internal radius ratios t_{cm}/r_i ; (b) rock mass elastic modulus to steel elastic modulus ratios E/E_s ; and (c) cross-shear modulus to Saint-Venant empirical relation ratios G'/G'_{S-V} , and by varying the steel liner's thickness to the internal radius ratio t_s/r_i and the degree of anisotropy E/E' .

Fig. 4.5);

- the liner is subject to bending which tends to increase the tension at the internal fiber at $\theta = 0$ deg and to decrease the tension at the internal fiber at $\theta = 90$ deg; and
- the larger E/E' , the larger the bending effect.

The aforementioned observations are consistent with the ellipse-like deformed shapes observed in Fig. 4.5, as the maximum radial displacement $\hat{u}_{r,\max}^s$ always occurs at $\theta = 90$ deg along the crown (the direction of the lowest modulus of elasticity E'), and the minimum radial displacement $\hat{u}_{r,\min}^s$ always occurs at $\theta = 0$ deg, along the springline (the stiffest direction with the modulus of elasticity E).

Figure 4.5a shows that an increasing thickness of the near-field rock zone attenuates the effect of the degree of anisotropy: the larger the extent of the near-field rock, the smaller the effect on anisotropy in terms of major principal stresses in the steel liner, and thus the effect of bending. This is in accordance with the radial displacements \hat{u}_r^s depicted in Fig. 4.6a and the observations made from the quadrant (a) of Fig. 4.4. This effect, although observable, is not significant.

One can observe in Fig. 4.5b that the relative stiffness of the far-field rock E/E_s have no or minor effect on bending. Only $\hat{\sigma}_{1,\max}^s$ is significantly affected, as discussed in Sect. 4.4.4. Indeed, Fig. 4.6b shows minor variations of \hat{u}_r^s for different values of E/E_s .

The influence of G'/G'_{S-V} depicted in Fig. 4.5c is also minor, if any, on the bending effect. This corresponds to the minor variations in the radial displacements \hat{u}_r^s in Fig. 4.5c.

4.4.5 Stresses in the far-field rock

Maximum stresses

Maximum normalized major principal stresses in the far-field rock $\hat{\sigma}_{1,\max}^{\text{rm}}$ as a function of the degree of anisotropy E/E' are shown in Fig. 4.6, at the interface between the near- and the far-field rock masses (at $r = r_{\text{rm}}$). Unlike in the steel liner, $\hat{\sigma}_{1,\max}^{\text{rm}}$ at $r = r_{\text{rm}}$ does not occur at a constant angle of location (see Sect. 4.4.5). The normalized results are thus computed as

$$\hat{\sigma}_{1,\max}^{\text{rm}} = \frac{\sigma_{1,\text{aniso}}^{\text{rm}}(r = r_{\text{rm}}, \theta = \tilde{\theta})}{\sigma_{1,\text{iso}}^{\text{rm}}(r = r_{\text{rm}})} \quad (4.23)$$

where $\tilde{\theta}$ is the angle of location of the maximum stress for each case. From Fig. 4.6 it can be seen that, contrary to $\hat{\sigma}_{1,\max}^s$ in most cases, $\hat{\sigma}_{1,\max}^{\text{rm}}$ is amplified compared to the reference isotropic case by considering the influence of the anisotropic rock behavior. The following analysis is complementary to the observations made on the variations of $\hat{\sigma}_{1,\max}^s$ in Sect. 4.4.4.

The quadrant (a) of Fig. 4.6 illustrates the influence of t_{crm}/r_i on $\hat{\sigma}_{1,\max}^{\text{rm}}$. It is shown that the lower

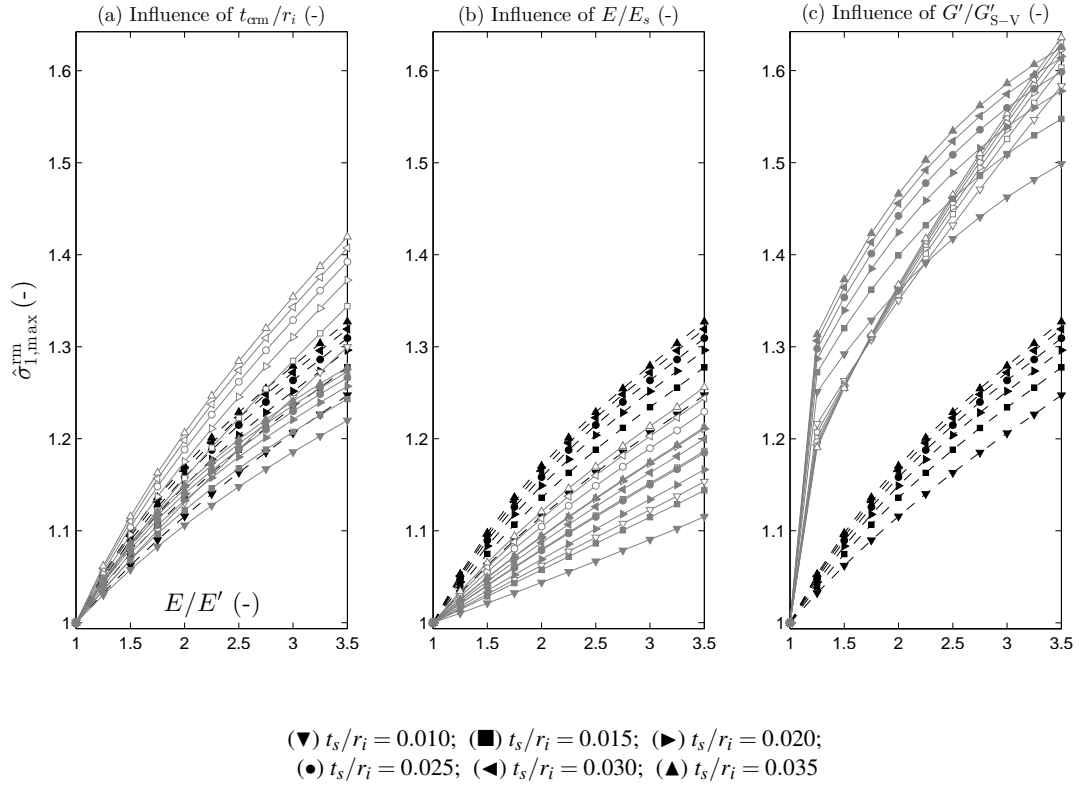


Figure 4.6: Maximum normalized major principal stresses in the far-field rock $\hat{\sigma}_{1,\text{max}}^{\text{rm}}$ as a function of the degree of anisotropy E/E' for different: (a) near-field rock thickness to steel liner's internal radius ratios t_{crm}/r_i ; (b) rock mass elastic modulus to steel elastic modulus ratios E/E_s ; and (c) cross-shear modulus to Saint-Venant empirical relation ratios $G'/G'_{\text{S-V}}$, and by varying the steel liner's thickness to the internal radius ratio t_s/r_i .

t_s/r_i and the larger t_{crm}/r_i , the smaller the increase of $\hat{\sigma}_{1,\text{max}}^{\text{rm}}$. The role of t_{crm}/r_i can be explained referring to the reference isotropic case. Considering Eqs. 2.4 and 2.6 yields $p_{\text{rm}} = (r_c/r_{\text{rm}})p_c$. As a consequence, the larger t_{crm} (and thus r_{rm}), the smaller the pressure transmitted to the far-field rock. The variation of $\hat{\sigma}_{1,\text{max}}^{\text{rm}}$ compared to the corresponding reference isotropic case is therefore smaller with a more extended cracked near-field rock, which mitigates the effect of the far-field anisotropy.

The influence of E/E_s on $\hat{\sigma}_{1,\text{max}}^{\text{rm}}$ is shown in the quadrant (b) of Fig. 4.6. One observes that the larger E/E_s and the smaller t_s/r_i , the smaller the variation of $\hat{\sigma}_{1,\text{max}}^{\text{rm}}$. Similarly to the analysis of the stresses in the steel liner, this phenomenon can be explained by the notion of relative stiffness. A relatively stiff far-field rock (high E/E_s ratio and low t_s/r_i ratio) attracts a larger part of the internal pressure p_i and therefore will be less affected by the consideration anisotropic behavior

compared to the reference isotropic case. Considering the far-field anisotropy introduces a larger elastic modulus E in the plane of isotropy which makes the rock withstand a larger part of p_i at the expense of larger $\hat{\sigma}_{1,\max}^{\text{rm}}$ compared to the reference isotropic case, and a smaller $\hat{\sigma}_{1,\max}^s$ consistently to the observations in Sect. 4.4.4.

The quadrant (c) of Fig. 4.6 illustrates the influence of $G'/G'_{\text{S-V}}$ on $\hat{\sigma}_{1,\max}^{\text{rm}}$. Some general observations can be made:

- The larger the deviation of the cross-shear modulus G' from the empirical formula of Saint-Venant $G'_{\text{S-V}}$ (either softer or stiffer), the more $\hat{\sigma}_{1,\max}^{\text{rm}}$ is underestimated considering the reference isotropic case;
- The lower t_s/r_i , the lower the change of $\hat{\sigma}_{1,\max}^{\text{rm}}$ (except for low E/E' and low $G'/G'_{\text{S-V}}$, although not significant), similarly to the previous observations of quadrants (a) and (b).

The explanation of the magnitude of the variations of $\hat{\sigma}_{1,\max}^{\text{rm}}$ due to high or low $G'/G'_{\text{S-V}}$ ratios would require further investigations, out of the scope of this research.

Major and minor principal stresses

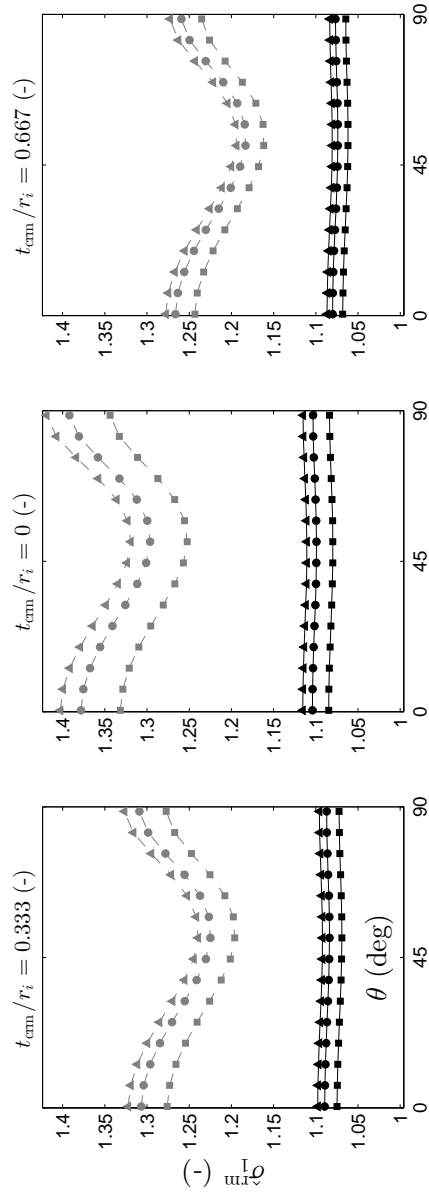
Normalized major and minor principal stresses in the far-field rock $\hat{\sigma}_1^{\text{rm}}$ and $\hat{\sigma}_3^{\text{rm}}$ as a function of the angle θ with respect to the plane of isotropy are shown in Figs. 4.6 and 4.6, respectively, at the interface between the near- and the far-field rock masses (at $r = r_{\text{rm}}$). Normalized stresses at $r = r_{\text{rm}}$ are computed as

$$\hat{\sigma}_1^{\text{rm}}(\theta) = \frac{\sigma_{1,\text{aniso}}^{\text{rm}}(r = r_{\text{rm}}, \theta)}{\sigma_{1,\text{iso}}^{\text{rm}}(r = r_{\text{rm}})} \quad (4.24)$$

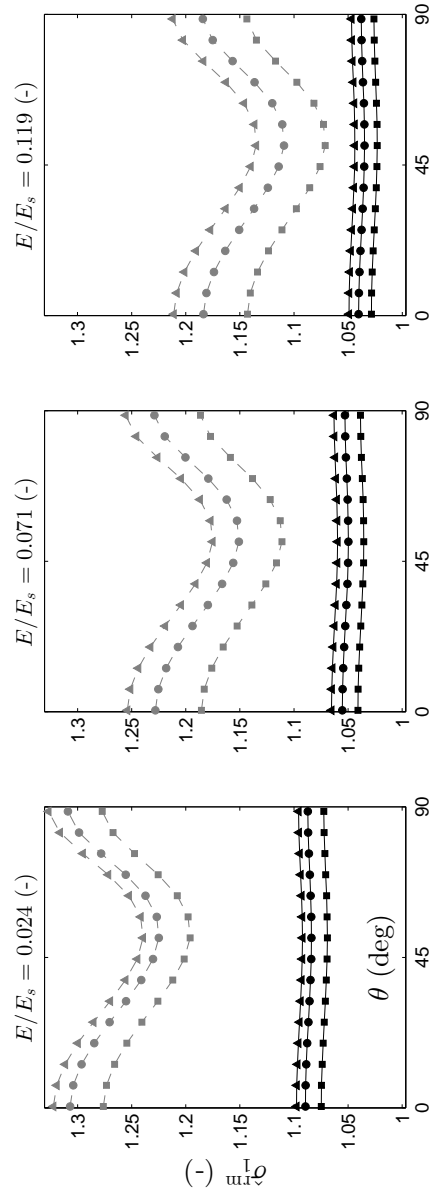
and

$$\hat{\sigma}_3^{\text{rm}}(\theta) = \frac{\sigma_{3,\text{aniso}}^{\text{rm}}(r = r_{\text{rm}}, \theta)}{\sigma_{3,\text{iso}}^{\text{rm}}(r = r_{\text{rm}})}. \quad (4.25)$$

The plots of $\hat{\sigma}_1^{\text{rm}}$ and $\hat{\sigma}_3^{\text{rm}}$ versus θ give more information on the stress repartition in the far-field rock. From Fig. 4.6 it can be seen that for all cases where $G' = G'_{\text{S-V}}$, $\hat{\sigma}_1^{\text{rm}}$ is maximum in the plane of isotropy along the springline and in the perpendicular direction of lowest stiffness along the crown, with minor differences. The higher the degree of anisotropy E/E' , the larger the variation along the perimeter at the near- and far-field interface compared to the reference isotropic case. For low values of G' (see Fig. 4.6c), $\hat{\sigma}_{1,\max}^{\text{rm}}$ occurs at $\theta = 0$ deg and there is a large variation of $\hat{\sigma}_1^{\text{rm}}$ along the perimeter, with the lowest major principal stress in the shear plane. Indeed, a low cross-shear modulus indicates that the rock attracts less stresses in this direction. Conversely, $\hat{\sigma}_{1,\max}^{\text{rm}}$ occurs in the shear plane when G' is larger than $G'_{\text{S-V}}$ (see Fig. 4.6c). This is illustrated in a xy -plane from $r = r_{\text{rm}}$ to $2r_{\text{rm}}$ in Fig. 4.7 for a specific configuration. The isotropic



(a) Influence of t_{crm}/r_i .



(b) Influence of E/E_s .

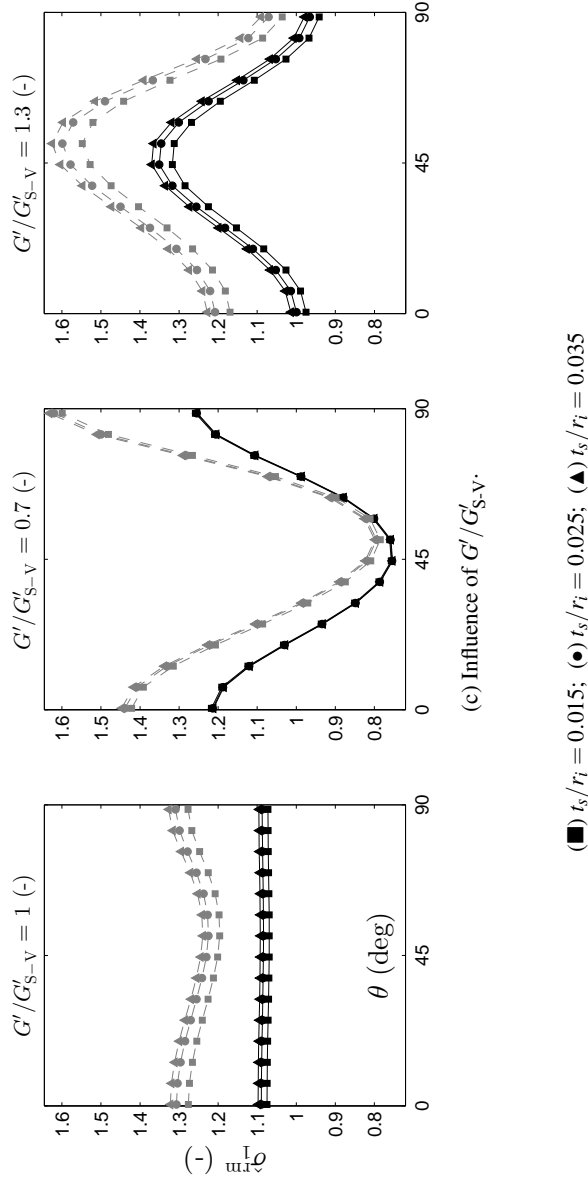
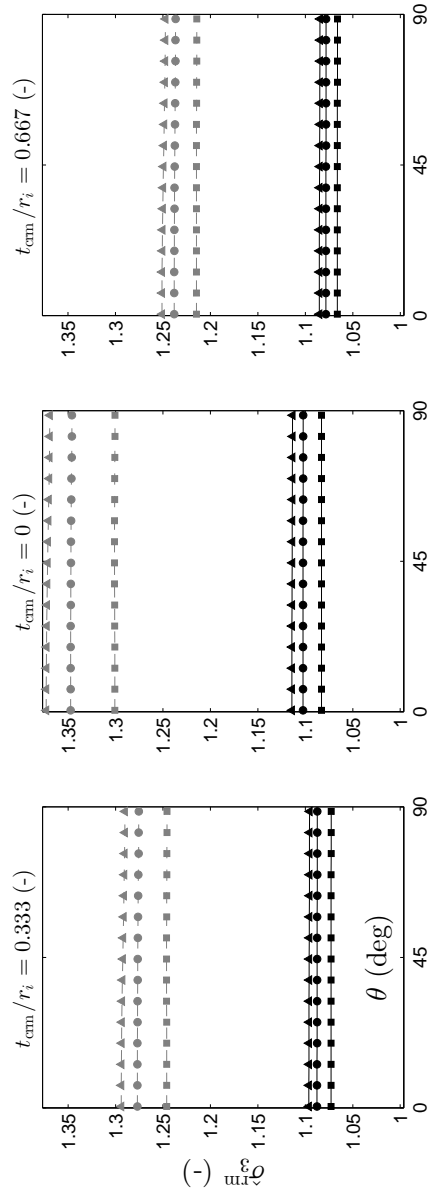
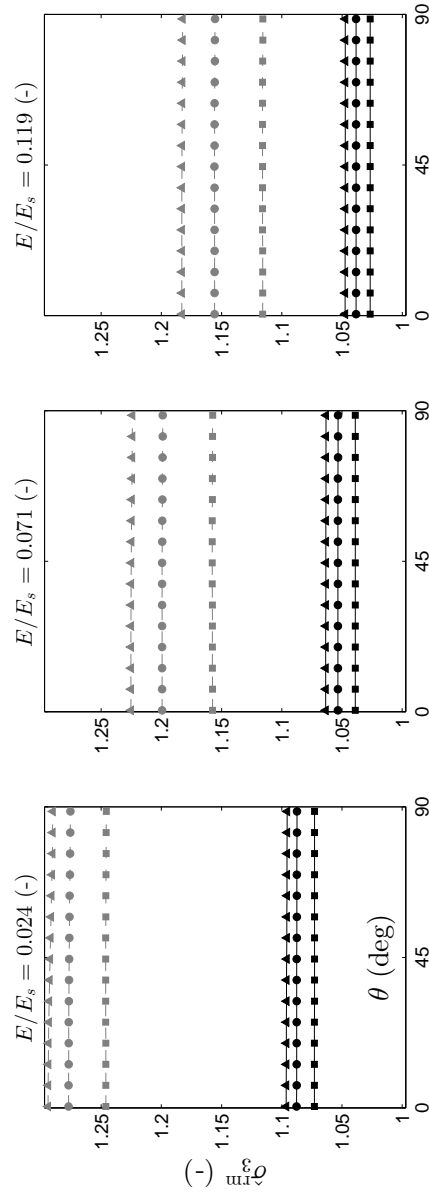


Figure 4.6: Normalized major principal stresses in the far-field rock σ_{rm}^m at radius r_{rm} as a function of the angle θ with respect to the plane of isotropy for different: (a) near-field rock thickness to steel liner's internal radius ratios t_{cm}/r_i ; (b) rock mass elastic modulus to steel elastic modulus ratios E/E_s ; and (c) cross-shear modulus to Saint-Venant empirical relation ratios G'/G'_{S-V} , and by varying the steel liner's thickness to the internal radius ratio t_s/r_i and the degree of anisotropy E/E' .



(a) Influence of t_{crm}/r_i .



(b) Influence of E/E_s .

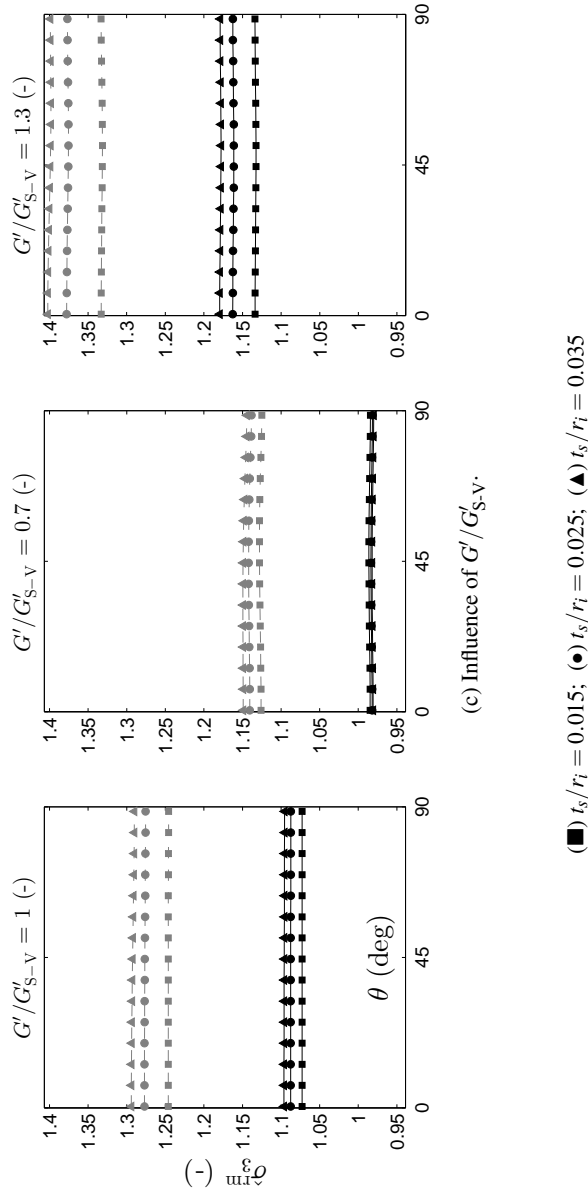
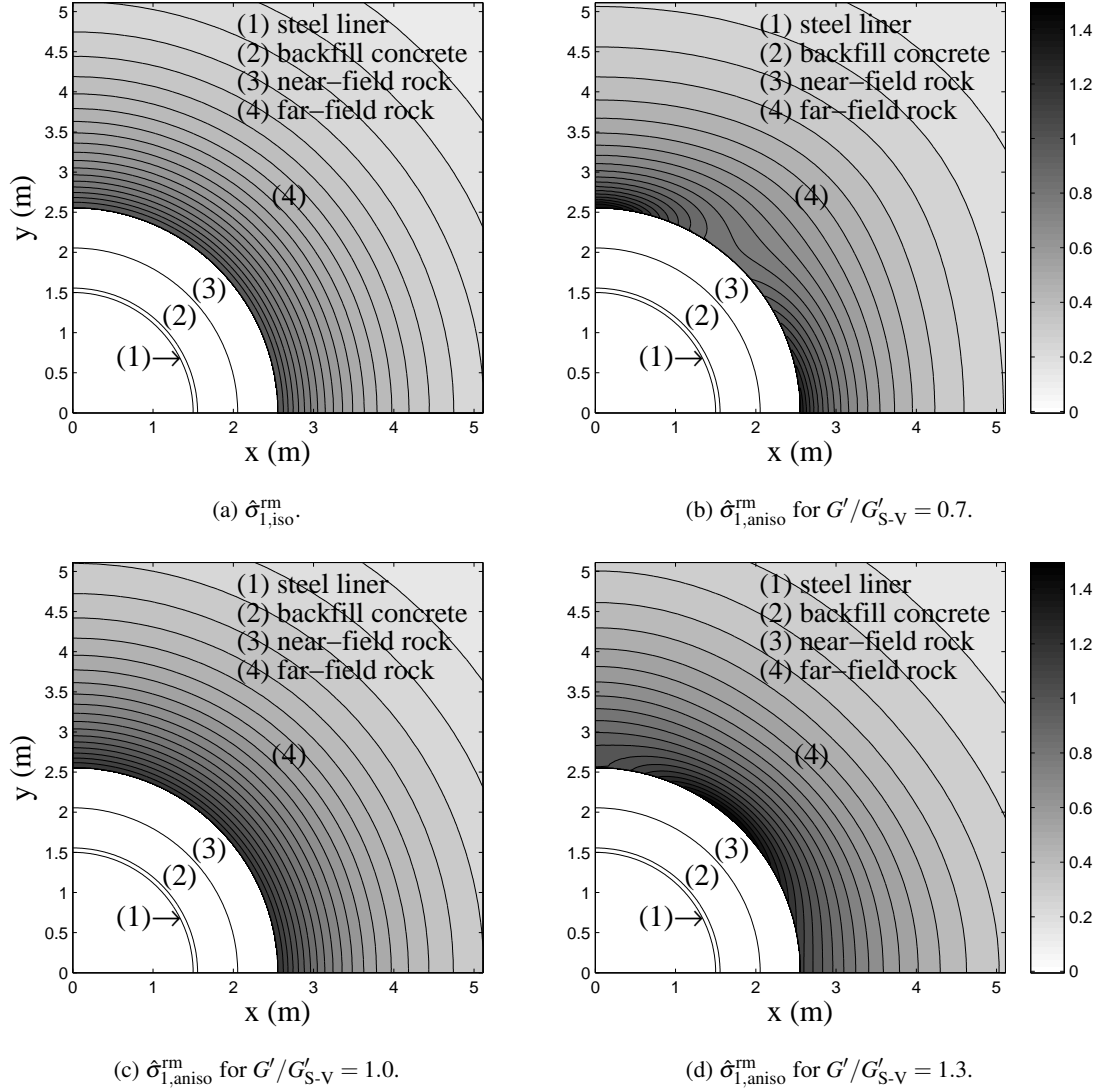


Figure 4.6: Normalized minor principal stresses in the far-field rock $\hat{\sigma}_3^{\text{rm}}$ at radius r_{rm} as a function of the angle θ with respect to the plane of isotropy for different: (a) near-field rock thickness to steel liner's internal radius ratios t_{cm}/r_i ; (b) rock mass elastic modulus to steel elastic modulus ratios E/E_s ; and (c) cross-shear modulus to Saint-Venant empirical relation ratios G'/G'_{S-V} , and by varying the steel liner's thickness to the internal radius ratio t_s/r_i and the degree of anisotropy E/E' .

case is shown in Fig. 4.7a, and the anisotropic cases with different G'/G'_{S-V} ratios are shown in Fig. 4.7b–4.7d.

Fig. 4.6 shows the corresponding normalized minor stresses in the far-field rock $\hat{\sigma}_3^{rm}$. One can only observe a minor variation around the perimeter. These results are given herein for completion.



Configuration: $r_i = 1.5$ m, $t_s = 0.055$ m, $t_{crm} = 0.5$ m, $p_i = 150$ bar, $E = 10$ GPa, $E' = 4$ GPa, $\nu = 0.2$, $\nu' = 0.15$ and $E_{crm} = 3.2$ GPa

Figure 4.7: Normalized major principal stresses in the far-field rock shown up to $2r_{rm}$: (a) $\hat{\sigma}_1$ in the isotropic case; $\hat{\sigma}_1$ in the anisotropic case for cross-shear moduli ratios of (b) $G'/G'_{S-V} = 0.7$; (c) $G'/G'_{S-V} = 1.0$; and (d) $G'/G'_{S-V} = 1.3$.

4.5 Discussion

The assumptions concerning the extent, shape and the characteristics of the loosened near-field rock zone (as a result of the excavation process) may be questionable in certain cases. In the isotropic case, the near-field rock zone is commonly assumed as circular, radially cracked with no tension transmitted in the tangential direction (see e.g., Schleiss 1988; USACE 1997; Sharma *et al.* 1997; Hachem & Schleiss 2009, 2011c; ASCE 2012), which was also considered herein for transversely isotropic rock. This was done considering a constant radial elastic modulus based on the weakest direction of the transversely isotropic rock. However, the damage may not be axisymmetrical considering the different characteristics of the far-field rock in the two principal directions of anisotropy, as the shape may not be circular. In addition, even if the damage would be radial, one may expect a varying stiffness with orientation, and a less conservative assumption on the tangential stiffness. Some discussions are enumerated below.

1. The latter point was for example treated analytically by Bobet (2009) in isotropic rock. The damaged zone was modeled with cylindrical transverse isotropy, as in this study, but with a tangential modulus of elasticity not equivalent to zero. It seems reasonable to state that considering a constant significant value for the damaged tangential elastic modulus in this work would probably mitigate the effect of anisotropy, as it was discussed in Sect. 4.4.4. The higher the tangential stiffness, the higher this effect would be expected.
2. Should a more complex constitutive law for the damaged near-field rock (e.g., non-radial cracks, varying stiffness) be considered, when the far-field is regarded as transversely isotropic, such a consideration would considerably increase the complexity of its definition. Cylindrical transverse isotropy defined via 5 constants could no longer be used, and 10 constants would be necessary to define such an anisotropic material in 2D (ANSYS Inc 2011), thus introducing new parameters to be varied independently.
3. The qualitative probable influence of these parameters can be discussed a priori. As mentioned previously, a significant damaged tangential modulus of elasticity should diminish the effect of anisotropy in terms of maximum major principal stresses in the steel liner. Conversely, varying radial stiffness in the near-field rock correspondingly to the principal directions of the far-field rock (within the hypothesis of radial cracks) would increase the effect of anisotropy on the steel liner. However, in the case of grouted near-field rock zone, the properties of the rock tend to be homogenized, and the aforementioned effects would be a less significant limitation.
4. It also seems reasonable to state that loosened near-field rock shapes with little variations from the circular shape may not induce significant effect on the results. However, discussing a priori the effects of a highly non circular loosened near-field rock zone due to the formation of plastic deformations during excavation may be controversial, and would require further investigation, e.g., nonlinear numerical analysis. Such considerations would have the serious drawbacks to make the systematic analysis very complicated. Nevertheless,

such extensive plastic zone has to be avoided with appropriated primary support measures during excavation.

The assumption of linear elasticity of the far-field rock also limits theoretically the applicability of the proposed approach. It requires that there are no plastic deformations further than the loosened near-field rock zone due to the excavation method. This does not have a strong limitation for good-quality rocks, i.e., if adequate primary support measures are implemented during excavation in weaker regions. Also, maximum stresses due to the internal water pressure in the far-field rock shall not exceed the in situ stresses surrounding the tunnel not to put the rock into tension. This requirement refers to the design criteria (2) in Sect. 2.3 regarding a minimum required overburden for steel-lined pressure shafts (Schleiss 1988). In most cases, the tangential stresses around the opening are compressive due to natural in situ stresses in the rock mass. At large depth, this requirement is therefore not a serious limitation.

4.6 Conclusions

For the design of steel-lined pressure tunnels and shafts, anisotropic rock behavior is rarely taken into account. Designers rather use a conservative model considering an unfavorable isotropic rock behavior in terms of maximum stresses in the steel liner. As a consequence, the mechanical behavior of the steel–concrete–rock system in anisotropic rock is still not fully understood. In this chapter, the behavior of steel-lined pressure tunnels and shafts in transversely isotropic rock was systematically studied by means of the FEM.

An extensive systematic parametric study was performed over a wide range of geometrical and material parameters, and significant results in terms of normalized stresses and displacements were investigated in the steel liner and the far-field rock mass. It was shown that the results mainly depend on the relative stiffness between the steel liner and the concrete–rock system.

In the steel liner, considering the reference isotropic case generally induces an overestimation of the maximum major principal stresses, except for low degrees of anisotropy when the cross-shear modulus is weaker than the empirical relation of Saint-Venant. It was also shown that in anisotropic rock, the steel liner is subject to bending (although this effect remains small, particularly for low degrees of anisotropy, e.g., $E/E' = 1.0\text{--}2.0$), which explains that the maximum stresses occur at the internal fiber of the steel liners in the plane of isotropy. Nevertheless, the main effect of anisotropy is to change the nominal tension in the steel liner.

In the far-field rock mass, it was observed that the maximum major principal stresses are underestimated compared to the isotropic solution, as a part of the stiffness is not taken into account.

5 Estimation of the maximum stresses

5.1 Derivation of correction factors to be included in the isotropic closed-form solution

5.1.1 Database

In order to calibrate and test the validity of the proposed correction factors, a large database of numerical results for anisotropic rock behavior was created by using the FE model described in Sect. 4.3 and the Probabilistic Design System in ANSYS. A user-defined-sampling of 2000 cases was generated accordingly to the ranges introduced in Table 5.1 for 9 geometrical and material parameters. The parameters of each case were randomly sampled with a uniform distribution of values under the constraints described by Eq. 4.17. Every sampled case not included in the aforementioned set of constraints was re-sampled until they were satisfied.

Table 5.1: Variation range of the parameters for the random user-defined sampling.

Parameter	Unit	Min. value	Max. value
r_i	m	1.00	3.50
t_s	m	0.010	0.080
t_{crm}/r_i	(-)	0.00	0.66
E	GPa	5.0	25.0
E/E'	(-)	1.1	3.5
$G'/G'_{\text{S-V}}$	(-)	0.70	1.30
ν	(-)	0.10	0.35
ν/ν'	(-)	1.0	3.5
E_{crm}/E'	(-)	0.60	1.00

5.1.2 Derivation of the correction factors

According to Eq. 2.9, the three terms in the expression for E_{eq}^{-1} refer, respectively, to the participation of the cracked backfill concrete, the cracked near-field rock and the far-field rock to

Chapter 5. Estimation of the maximum stresses

withstand the internal pressure p_i . As a consequence, the expression for p_c (Eq. 2.8) physically represents the ratio of the global stiffness of the system divided by the stiffness of the steel liner. Once p_c is known, the maximum stresses in the liner can be calculated with Eq. 2.14 for $r = r_i$.

From a physical insight, correction factors that multiply the term of the far-field rock participation in Eq. 2.9 were chosen in order to take into account the influence of the anisotropic behavior of the rock mass. The correction factors have to be physically correct, i.e., equal to unity in the isotropic cases, and were defined from dimensionless material parameters of the far-field rock mass. The so-called corrected E_{eq}^{-1} was introduced as

$$E_{eq,corr}^{-1} = \frac{1 - \nu_c^2}{E_c} \ln \left(\frac{r_{crm}}{r_c} \right) + \frac{1 - \nu_{crm}^2}{E_{crm}} \ln \left(\frac{r_{rm}}{r_{crm}} \right) + \prod_{i=1}^3 X_i^{\alpha_i} \cdot \frac{1 + \nu}{E'} \quad (5.1)$$

where the $X_i^{\alpha_i}$ are the correction factors; the X_i are the dimensionless parameters $X_1 = E/E'$, $X_2 = G/G'$, and $X_3 = (1 + \nu)/(1 + \nu')$; and the α_i are free exponents to be optimized. In this aim, the objective function was to minimize the fitness measure as

$$\hat{\alpha} = \underset{\alpha}{\operatorname{argmin}} \operatorname{MSE} [\hat{\sigma}_{1,num}^s, \hat{\sigma}_{1,corr}^s(\mathbf{X}, \alpha)] \quad (5.2)$$

where MSE is the mean squared error; $\hat{\alpha} = \{\alpha_1, \alpha_2, \alpha_3\}$ is the argument of the minimum; $\mathbf{X} = \{X_1, X_2, X_3\}$; $\hat{\sigma}_{1,num}^s$ is computed with the normalized numerical maximum major principal stresses in the steel liner in the isotropic and anisotropic cases; and $\hat{\sigma}_{1,corr}^s$ is computed with the normalized analytical solution including the corrected expression for E_{eq}^{-1} (Eq. 5.1).

The $\hat{\alpha}$ leading to the minimum mean squared error was determined using genetic algorithm. From the database, a training group containing 90% of the results was randomly sampled, and the rest of the samples were contained in a test group. The generation of the training and test groups and the optimization of $\hat{\alpha}$ was repeated 100 times, and the mean values of the α_i were computed as

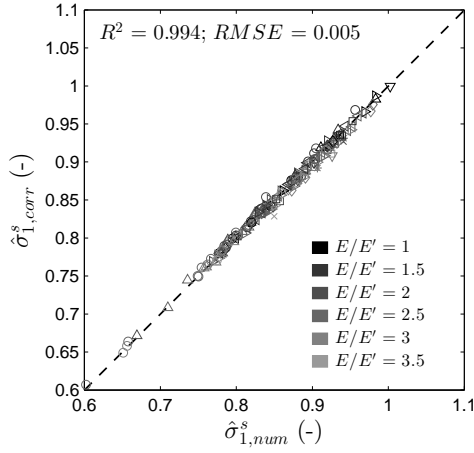
$$\hat{\alpha} = \{-0.65, +0.50, -0.56\}, \quad (5.3)$$

with standard deviations equal to 0.03, 0.04 and 0.07, respectively.

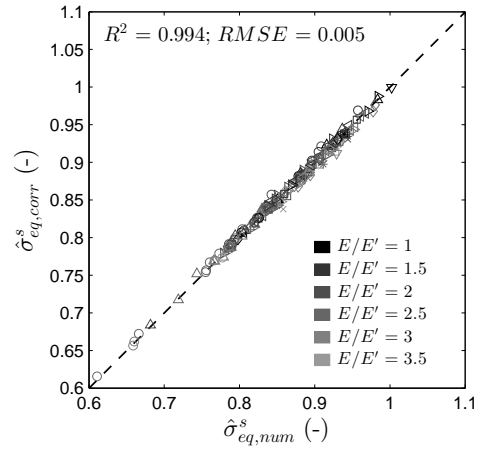
The regression between the normalized corrected maximum major principal stresses $\hat{\sigma}_{1,corr}^s$ and the normalized numerical maximum major principal stresses $\hat{\sigma}_{1,num}^s$ is plotted in Fig. 5.1a for one example of test group. A coefficient of determination $R^2 = 0.994$ and a root mean squared error RMSE = 0.005 were obtained.

When designing steel liners of pressure tunnels and shafts, the working stresses criterion usually suggests allowable equivalent stresses in steel liners according to the Hencky–Von Mises theory

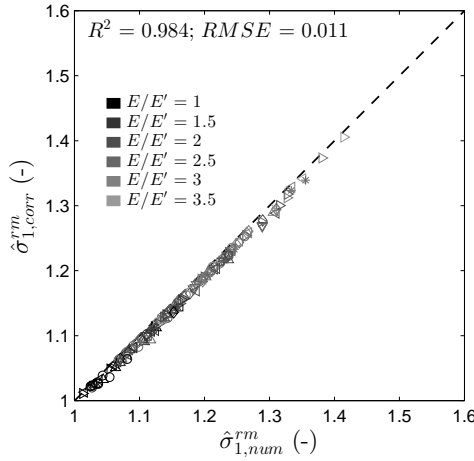
5.1. Derivation of correction factors to be included in the isotropic closed-form solution



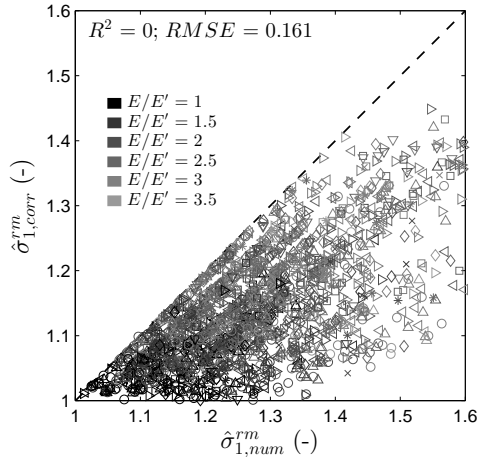
(a) Maximum major principal stresses in the steel liner.



(b) Maximum equivalent stresses in the steel liner.



(c) Maximum major principal stresses in the far-field rock (cases in which $G'/G'_{S-V} = 1$).



(d) Maximum major principal stresses in the far-field rock (all cases $0.7 \leq G'/G'_{S-V} \leq 1.3$).

(○)	$t_s/r_i < 0.010$	(◇)	$0.025 \leq t_s/r_i < 0.030$	(×)	$0.045 \leq t_s/r_i < 0.052$
(△)	$0.010 \leq t_s/r_i < 0.015$	(□)	$0.030 \leq t_s/r_i < 0.035$	(+)	$t_s/r_i > 0.052$
(◁)	$0.015 \leq t_s/r_i < 0.020$	(∇)	$0.035 \leq t_s/r_i < 0.040$		
(▷)	$0.020 \leq t_s/r_i < 0.025$	(*)	$0.040 \leq t_s/r_i < 0.045$	(- - -)	$f(x) = x$

Figure 5.1: Regression plots of the normalized corrected maximum stresses $\hat{\sigma}_{\text{corr}}$ vs. the normalized numerical maximum stresses $\hat{\sigma}_{\text{num}}$ with $\alpha = \{-0.65, +0.50, -0.56\}$. The maximum (a) major principal stresses $\hat{\sigma}_{1,\text{corr}}^s$ and (b) equivalent stresses $\hat{\sigma}_{\text{eq},\text{corr}}^s$ in the steel liner are represented for a test group of 10% of the 2000 cases. The maximum major principal stresses $\hat{\sigma}_{1,\text{corr}}^{\text{rm}}$ in the far-field rock are represented in (c) for all the 155 generated cases in which $G'/G'_{S-V} = 1$ and in (d) for all the 2000 cases.

in triaxial state of stresses, generally expressed as

$$\sigma_{eq}^s = \sqrt{\frac{1}{2}(\sigma_1^s - \sigma_2^s)^2 + \frac{1}{2}(\sigma_2^s - \sigma_3^s)^2 + \frac{1}{2}(\sigma_3^s - \sigma_1^s)^2}. \quad (5.4)$$

A corrected maximum equivalent stress in the steel liner considering anisotropy, denoted $\sigma_{eq,corr}^s$, would thus be useful for designers. It can be obtained from Eq. 5.4, by substituting:

- σ_1^s by the corrected value $\sigma_{1,corr}^s$ (Eq. 2.14, together with Eqs. 2.8 and 5.1);
- σ_3^s by its analytical value in the reference isotropic rock (Eq. 2.15, together with Eqs. 2.8 and 2.9); and
- σ_2^s by the corrected value denoted $\sigma_{2,corr}^s$ computed from Eq. 2.16 with $\sigma_{1,corr}^s$ and σ_3^s .

The regression between the normalized corrected maximum equivalent stresses $\hat{\sigma}_{eq,corr}^s$ and the normalized numerical maximum equivalent stresses $\hat{\sigma}_{eq,num}^s$ is plotted in Fig. 5.1b for the same test group than in Fig. 5.1a, and shows the same accuracy.

The applicability of these correction factors (Eq. 5.3) to estimate the normalized maximum major principal stresses in the far-field rock was investigated. The regression between the normalized corrected maximum major principal stresses $\hat{\sigma}_{1,corr}^{rm}$ (computed with Eqs. 2.19 and 5.1) and the normalized numerical maximum major principal stresses $\hat{\sigma}_{1,num}^{rm}$ is plotted in Fig. 5.1d for all the 2000 cases. It can be observed that the correction factors are only applicable to estimate the maximum major principal stresses in the cases where $G'/G'_{S-V} = 1$, plotted in Fig. 5.1c which shows a very good accuracy.

5.1.3 Synthesis

The conceptual formulas for the corrected maximum major principal stresses in the steel liner and in the far-field rock and the corrected maximum equivalent stresses in the steel liner with correction factors are summarized in Table 5.2. The proposed approach is therefore very efficient as it allows to assess maximum stresses in steel liners in anisotropic rock by introducing only three dimensionless correction factors multiplying the term related to the far-field rock participation in the analytical solution for isotropic rock. It is independent of the variable geometrical parameters and of the relative stiffness between the steel liner and the rest of the system. This approach, however, is not capable of representing the behavior of far-field rocks with a cross-shear modulus G' deviating from the empirical relation of Saint-Venant in terms of maximum major principal stresses in the far-field rock.

Table 5.2: Synthesis of the conceptual formulas derived to obtain some maximum stresses in steel-lined pressure tunnels and shafts in anisotropic rock.

Corrected value	Formula	Application ranges
Maximum major principal stress in the steel liner $\sigma_{1,\max}^s$	$\sigma_{1,\text{corr}}^s = \frac{1}{r_c^2 - r_i^2} [r_i^2 p_i - r_c^2 p_{c,\text{corr}} - r_c^2 (p_{c,\text{corr}} - p_i)]$ $p_{c,\text{corr}} = \frac{1 + \nu_s}{E_s} \frac{r_c}{r_c^2 - r_i^2} [(1 - 2\nu_s) p_i r_i^2 + p_i r_i^2]$ $E_{\text{eq,corr}}^{-1} = \frac{1 - \nu_c^2}{E_c} \ln \left(\frac{r_{\text{crm}}}{r_c} \right) + \frac{1 - \nu_{\text{crm}}^2}{E_{\text{crm}}} \ln \left(\frac{r_{\text{rm}}}{r_{\text{crm}}} \right) + \left[\left(\frac{E}{E'} \right)^{\alpha_1} \left(\frac{G}{G'} \right)^{\alpha_2} \left(\frac{1 + \nu}{1 + \nu'} \right)^{\alpha_3} \right] \frac{1 + \nu}{E'}$ $\alpha_1 = -0.65, \alpha_2 = 0.50 \text{ and } \alpha_3 = -0.56$	Table 5.1 constrained by Eq. 4.17
Maximum equivalent stress in the steel liner $\sigma_{\text{eq,max}}^s$	$\sigma_{\text{eq,corr}}^s = \sqrt{\frac{1}{2} (\sigma_{1,\text{corr}}^s - \sigma_{2,\text{corr}}^s)^2 + \frac{1}{2} (\sigma_{2,\text{corr}}^s - \sigma_3^s)^2 + \frac{1}{2} (\sigma_3^s - \sigma_{1,\text{corr}}^s)^2}$ $\sigma_{2,\text{corr}}^s = \nu_s (\sigma_{1,\text{corr}}^s + \sigma_3^s)$ <p>σ_3^s is obtained from the analytical solution in the reference isotropic rock (Eq. 2.15, together with Eqs. 2.8 and 2.9)</p>	Table 5.1 constrained by Eq. 4.17
Maximum major principal stress in the far-field rock $\sigma_{1,\max}^{r'm}$	$\sigma_{1,\text{corr}}^{r'm} = \frac{r_c}{r_{\text{rm}}} p_{c,\text{corr}}$	Table 5.1 constrained by Eq. 4.17 and restricted to $G'/G_{\text{S-V}} = 1$

5.2 Examples of application

In order to illustrate the applicability of the conceptual formulas, two examples are treated below.

5.2.1 Example 1

In this example, a transversely isotropic far-field rock with the elastic properties presented by Tonon & Amadei (2003) is considered, with $E = 7.80$ GPa, $E' = 2.40$ GPa, $G' = 0.83$ GPa, $\nu = 0.22$, $\nu' = 0.07$ and $G/G' = 3.85$. The degree of anisotropy is $E/E' = 3.25$. A steel-lined pressure tunnel is considered in this rock with the following characteristics: $r_i = 1.5$ m, $t_s = 0.030$ m, $t_{crm} = 0.5$ m, $p_i = 100$ bar, $E_{crm} = 2$ GPa. Other steel, backfill concrete and near-field rock characteristics are according to Table 4.2.

For comparison purposes, two other far-field rocks are considered: (1) the reference isotropic case with $E = 2.40$ GPa, $G = 0.98$ GPa and $\nu = 0.22$ correspondingly to the conventions of this study; and (2) the rock mass presented by Tonon & Amadei (2003) by substituting G' by $G'_{S-V} = 1.66$ GPa.

The numerical results and the results obtained with the conceptual formulas are presented in Table 5.3a. One can observe that the conceptual formulas estimate the maximum major principal stresses in the steel liner $\sigma_{1,corr}^s$ and in the far-field rock $\sigma_{1,corr}^{rm}$ with a high accuracy for the anisotropic rock with $G' = G'_{S-V}$. In the case where the rock is exactly the one presented by Tonon & Amadei (2003) however, the maximum stress in the far-field rock $\sigma_{1,max}^{rm}$ is underestimated by 27.5% by the conceptual formula for $\sigma_{1,corr}^{rm}$. In this case G' deviates from G'_{S-V} by 50%, thus this result is consistent with the analysis presented in Sect. 5.1.2. The maximum stresses in the steel liner $\sigma_{1,max}^s$ are estimated with accuracy for every case (error $< 1\%$). Since the cross-shear modulus is relatively low compared to the empirical relation of Saint-Venant in the rock described by Tonon & Amadei (2003), considering anisotropy does not affect significantly the maximum major principal stress in the steel liner $\sigma_{1,max}^s$ (lowered by 3%). Nevertheless, in the case with $G' = G'_{S-V}$, $\sigma_{1,max}^s$ is 10% lower than in the reference isotropic case.

5.2.2 Example 2

In this example, a transversely isotropic far-field rock with the elastic properties presented by Amadei (1996) is considered, with $E = 29.30$ GPa, $E' = 23.90$ GPa, $G' = 6.20$ GPa, $\nu = 0.18$, $\nu' = 0.13$ and $G/G' = 2$. The degree of anisotropy is $E/E' = 1.23$. A steel-lined pressure tunnel is considered in this rock with the following characteristics: $r_i = 2.5$ m, $t_s = 0.020$ m, $t_{crm} = 0.7$ m, $p_i = 150$ bar, $E_{crm} = 20$ GPa. Other steel, backfill concrete and near-field rock characteristics are according to Table 4.2.

Similarly to example 1, two other far-field rocks are considered: (1) the reference isotropic case with $E = 23.90$ GPa, $G = 10.13$ GPa and $\nu = 0.18$; and (2) the rock mass presented by Amadei

Table 5.3: Maximum major principal stresses in the steel liner and in the far-field rock for the cases of examples 1 and 2.

(a) Example 1.						
Cases	$\sigma_{I,max}^s$ (ANSYS) (MPa)	$\sigma_{I,corr}^s$ (Table 5.2) (MPa)	Error (%)	$\sigma_{I,max}^{rm}$ (ANSYS) (MPa)	$\sigma_{I,corr}^{rm}$ (Table 5.2) (MPa)	Error (%)
Reference isotropic case	373	374	< 1	1.51	1.53	1.4
Anisotropic rock from Tonon & Amadei (2003)	364	361	< 1	2.34	1.69	27.5
Anisotropic rock from Tonon & Amadei (2003) with $G' = G'_{S-V}$	334	332	< 1	2.00	2.03	1.1
(b) Example 2.						
Cases	$\sigma_{I,max}^s$ (ANSYS) (MPa)	$\sigma_{I,corr}^s$ (Table 5.2) (MPa)	Error (%)	$\sigma_{I,max}^{rm}$ (ANSYS) (MPa)	$\sigma_{I,corr}^{rm}$ (Table 5.2) (MPa)	Error (%)
Reference isotropic case	204	204	< 1	8.87	8.99	1.3
Anisotropic rock from Amadei (1996)	232	232	< 1	9.92	8.84	10.9
Anisotropic rock from Amadei (1996) with $G' = G'_{S-V}$	187	189	< 1	8.97	9.07	1.1

(1996) by substituting G' by $G'_{S-V} = 11.51$ GPa.

The numerical results and the results obtained with the conceptual formulas are presented in Table 5.3b. In the case where $G' = G'_{S-V}$, the maximum stresses in the steel liner $\sigma_{1,max}^s$ and in the far-field rock $\sigma_{1,max}^{rm}$ are estimated with a high accuracy. In the case where the rock is exactly the one reported by Amadei (1996) with G' 53% softer than G'_{S-V} , the maximum major principal stress in the far-field rock $\sigma_{1,corr}^{rm}$ is underestimated by 10.9%. Since the degree of anisotropy is low ($E/E' = 1.23$) and the cross-shear modulus is relatively soft, the maximum major principal stress in the steel liner $\sigma_{1,max}^s$ is underestimated (by 14%) in the reference isotropic case, which corresponds to the trend presented in Sect. 4.4.4. In the case where $G' = G'_{S-V}$, and despite the low degree of anisotropy, the maximum major principal stress in the steel liner $\sigma_{1,max}^s$ is significantly lower (by 8%) than in the isotropic case as the relative stiffness of the rock is high. This is in accordance with the trend observed in Sect. 4.4.4.

5.3 Discussion

No initial gap between the steel liner and the backfill concrete was considered in this study. However, before such a gap, if any, is closed, the steel liner takes solely a part of the internal pressure. Considering a linear elastic behavior of the materials and that the tangential displacements in the liner are very small, the proposed solution could be superimposed to the initial elastic stresses due to the presence of such a gap as a first approach.

The proposed method also relies on an accurate knowledge of the transversely isotropic rock mass properties, i.e., E , E' , G' , ν , and ν' . However, as outlined by Jing & Hudson (2002), *in rock mechanics and engineering design, having insufficient data is a way of life, rather than a local difficulty*. This lack of information may be due to economical factors (costs of measurements campaigns), lack of standard procedures for the estimation of the rock mass parameters, etc. When facing such issues, uncertainties on the rock mass parameters should be assessed and a sensitivity analysis should be performed on the proposed conceptual formulas. In practice, relatively high security factors are applied for the working stresses in the liner (see e.g., Schleiss 1988). Despite these uncertainties, in the case of a steel-lined pressure tunnel and shaft embedded in anisotropic rock, it may worth using a model closer to reality than the axisymmetrical assumption, which can in certain case either overestimate the stresses in the steel liner (which is the main element) and underestimate the stresses in the rock mass (whose participation is ensured by enough overburden).

5.4 Conclusions

Correction factors to be included in the analytical solution for isotropic rock conditions were derived. This conceptual approach allows a simple and fast estimation of the maximum major

principal stresses and the maximum equivalent stresses in the steel liner by a correction of the isotropic analytical solution with a high accuracy if the transversely isotropic rock parameters are known. These correction factors are also applicable to estimate the maximum major principal stresses in the far-field rock when the cross-shear modulus is equivalent to the empirical relation of Saint-Venant.

Although the assumption of linear elasticity and the hypothesis on the extent and the properties of the loosened near-field rock limit the applicability of the results presented in this study for certain conditions in practice, it has the strong advantage to propose a rational framework to carry out a systematic parametric analysis with the relevant parameters.

Further investigation is necessary to study the effects of parameters such as the shape and properties of the loosened near-field rock or nonlinear behaviors.

Geometrical imperfections and weld profile at longitudinal butt welded joints of steel liners

Part III

Universality is a hypothesis, capable of being falsified every time it is applied. Every time it survives falsification – a fancy way to say it gives good results – the justification for using it becomes a little stronger. If [as in the case of gravitational forces] it survives thousands of such tests, the justification becomes very strong indeed. However, the hypothesis can never be proved *true*: for all we know, the next experiment might produce incompatible results.

– Ian Stewart,
in *Seventeen Equations that Changed the World*, 2012.

Most of the content of Chapter 6 of this part (together with Sect. 3.7) has been published in a scientific article entitled "New parametric equations to estimate notch stress concentration factors at butt welded joints modeling the weld profile with splines" by Pachoud *et al.* (2017) in *Engineering Failure Analysis* 72(February), pp. 11–24. The finite element model, the parametric study, the proposed parametric equations and the respective analyses are original and were developed by the author of the present report.

6 Stress concentration at butt welded joints of straight plates

6.1 Finite element analysis

6.1.1 FE model description and hypotheses

The chosen static system is shown in Fig. 6.1. The butt welded joint is submitted to a nominal tension σ_{nom} , and the plates on both sides of the weld have a length of 20 times the thickness t_s . The material is isotropic linear elastic steel of elastic modulus of $E_s = 210$ GPa and Poisson's ratio $\nu_s = 0.3$. The self weight is not considered. The FEA assumes plane strain conditions, as recommended by Fricke (2012) for 2D models as a biaxial stress state occurs at the notch surface, where in 3D the high stress concentration at the notch is restrained in the out-of-plane direction (see Figs. 6.1–6.2).

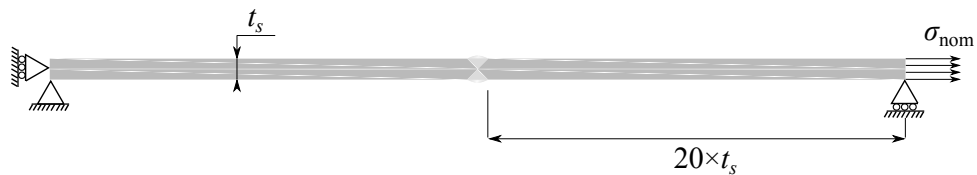
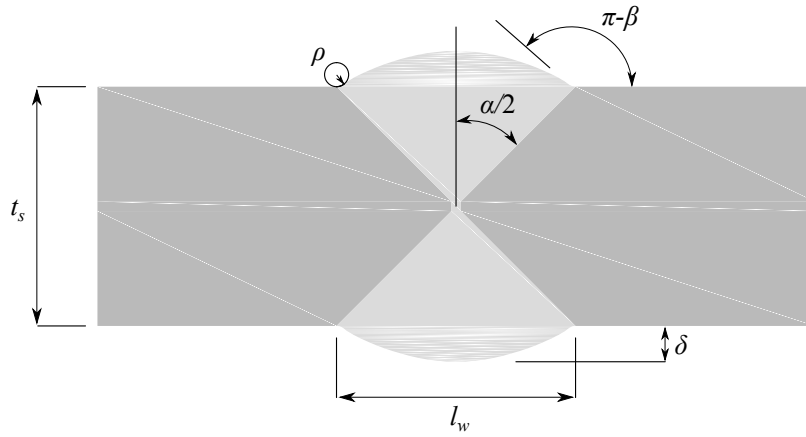


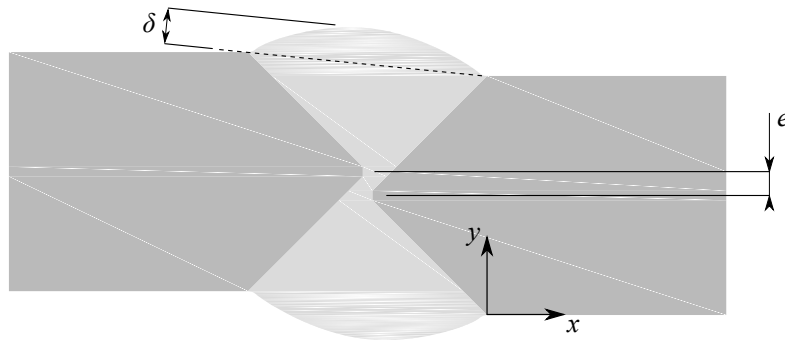
Figure 6.1: Static scheme of the model.

The geometry of the weld and the studied parameters are shown in Fig. 6.2. The parameters are listed as:

- t_s : plate thickness;
- ρ : weld toe radius;
- β : flank angle;
- α : edge preparation angle;



(a) Without misalignment.



(b) With misalignment e .

Figure 6.2: Definition sketch of butt welded joints (a) without linear misalignment and (b) with linear misalignment e .

- δ : weld reinforcement height;
- l_w : weld length (as a function of α , the gap between the plate edges is set to 3 mm, see, e.g., ISO 9692-1 2013);
- e : linear misalignment (eccentricity) between the two plates.

The geometry of the weld reinforcement was generated from a spline fit to three keypoints (see the command BSPLIN in ANSYS Inc 2015), namely the weld toes (extremities of the weld

toes arcs of radius ρ) and the crown point of the reinforcement. A tangent was imposed at each keypoint. At the weld toes, the spline has an angle with plate equal to the flank angle β . At the crown, the tangent is parallel to the plates in the case without linear misalignment, and is parallel to the segment linking the weld toes in the case with linear misalignment. More details on the mathematical modeling of the geometry are given in Appendix A. The FE model was built parametrically as a function of all the variables defined in Fig. 6.2. The geometry was split in different zones for the meshing. The convergence of the mesh was tested. In the case of $\rho = r_{\text{ref}} = 1 \text{ mm}$ for example, the mesh density was superior to what is recommended by Fricke (2012). Some mesh examples are shown in Fig. 6.3 without linear misalignment and in Fig. 6.4 with linear misalignment.

The integration of the aforementioned hypotheses on the geometrical parameters in the FE model are illustrated in Figs. 6.3–6.4. Figures 6.3a and 6.4a shows the example of a butt welded joint with a relatively low reinforcement and a low flank angle. The reinforcement in this case does not exhibit inflexion points in between the weld toes' arcs. Figures 6.3c and 6.4c presents the example of a relatively large reinforcement and of a low flank angle. In this case, the reinforcement may exhibit up to two inflexion points, on each side of the crown point. Finally, an example of a relatively large reinforcement associated to a large flank angle is shown in Figs. 6.3e and 6.4e. In this case, the reinforcement does not exhibit inflexion points. These three examples show the main types of geometries that can be covered by the approach presented in this chapter.

According to the principal stress hypothesis (see, e.g., Sonsino 2009a) the SCF are computed by dividing the maximum major principal stress by the applied nominal tension as (Terán *et al.* 2013):

$$\text{SCF} = \frac{\sigma_{\text{max}}}{\sigma_{\text{nom}}} \quad (6.1)$$

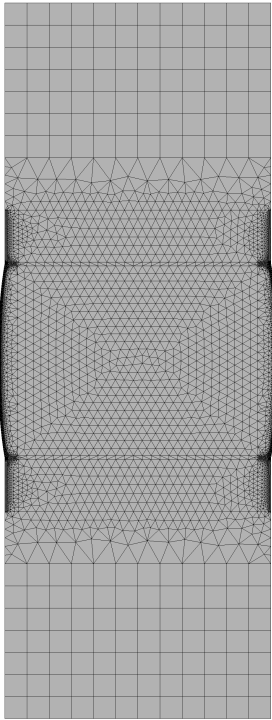
where σ_{max} is the maximum major principal stress. Notch SCF are computed with σ_{max} at the notch, while structural SCF are computed with the corresponding structural stress (see Sect. 6.1.2).

6.1.2 Validation of the FE model

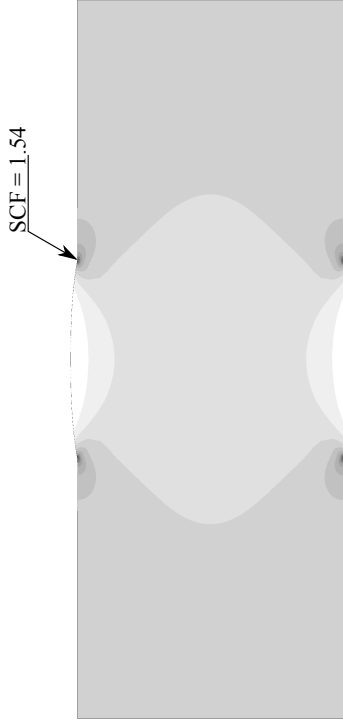
As there is no specific published solution for the notch SCF considering the hypotheses made in this chapter, the FE model was validated by its ability to reproduce structural SCF due to linear misalignments. Several methods of structural stress evaluation were considered.

1. The structural hot-spot stress evaluation by linear surface stress extrapolation (see, e.g., Niemi *et al.* 2006; Doerk *et al.* 2003):

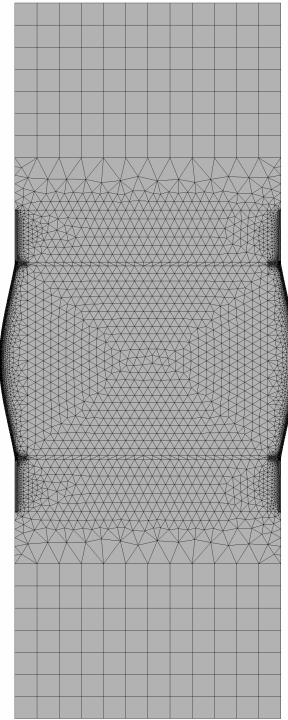
$$\sigma_{\text{hs}} = 1.5\sigma_{0.5t_s} - 0.5\sigma_{1.5t_s} \quad (6.2)$$



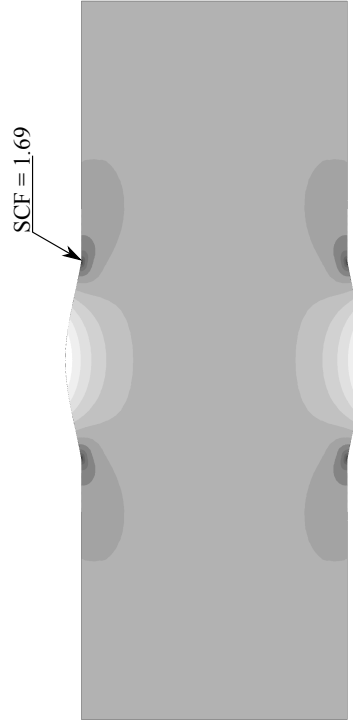
(a) Mesh 1 (parameters: $t_s = 30$ mm, $\rho = r_{\text{ref}} = 1$ mm, $\delta/t_s = 0.025$, $e/t_s = 0.00$, $\beta = 10^\circ$, and $l_w = 22.3$ mm).



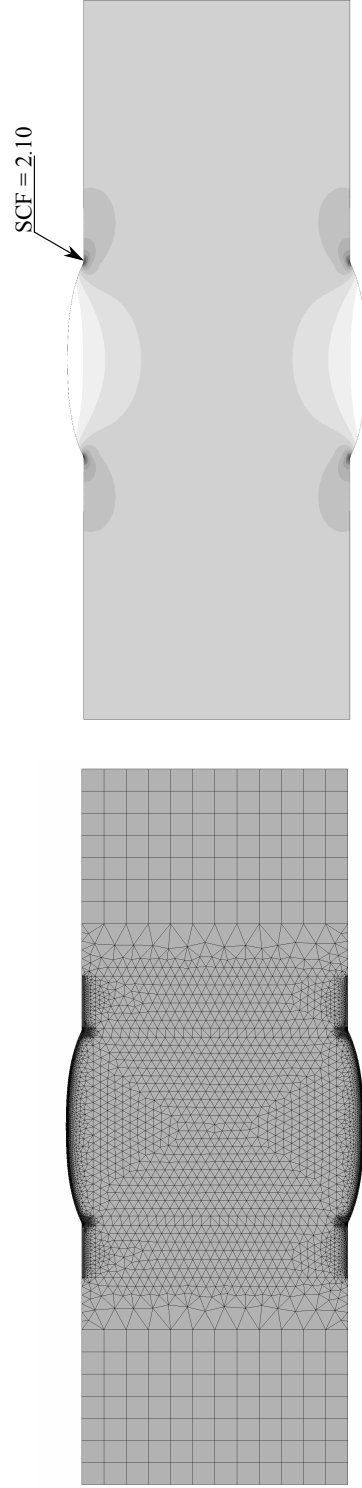
(b) Major principal stress contour and SCF.



(c) Mesh 2 (parameters: $t_s = 30$ mm, $\rho = r_{\text{ref}} = 1$ mm, $\delta/t_s = 0.070$, $e/t_s = 0.00$, $\beta = 10^\circ$, and $l_w = 22.3$ mm).



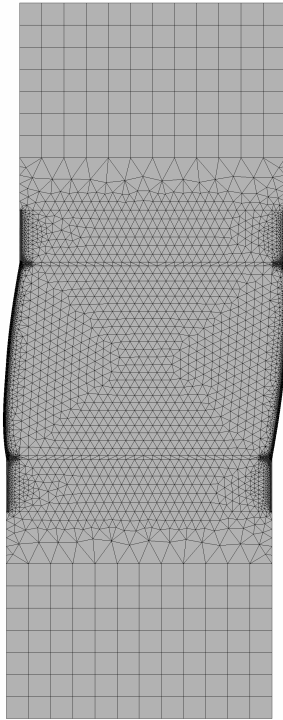
(d) Major principal stress contour and SCF.



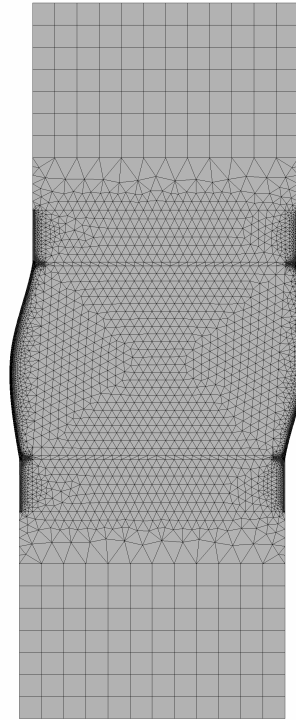
(e) Mesh 3 (parameters: $t_s = 30$ mm, $\rho = r_{\text{ref}} = 1$ mm, $\delta/t_s = 0.070$, $e/t_s = 0.00$, $\beta = 25^\circ$, and $l_w = 22.3$ mm).

(f) Major principal stress contour and SCF.

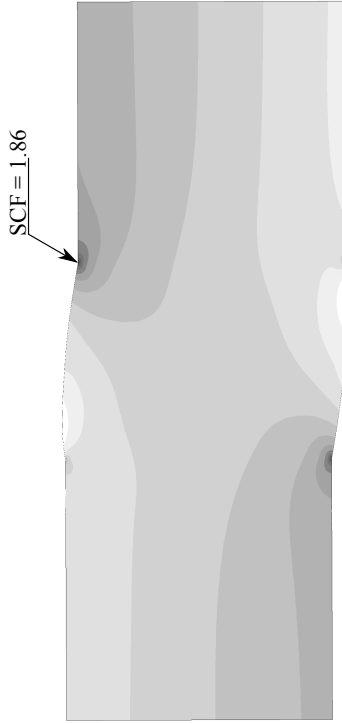
Figure 6.3: Three examples of butt welded joints without linear misalignment with (a)–(b): a relatively low reinforcement height and a low flank angle; (c)–(d): a relatively large reinforcement height and a low flank angle; and (e)–(f): a relatively large reinforcement height and a large flank angle.



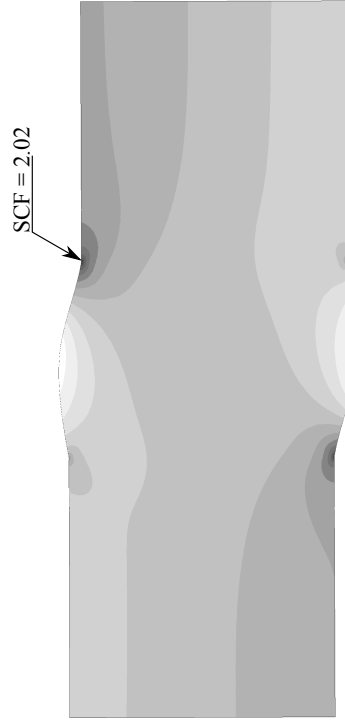
(a) Mesh 1 (parameters: $t_s = 30$ mm, $\rho = r_{\text{ref}} = 1$ mm, $\delta/t_s = 0.025$, $e/t_s = 0.05$, $\beta = 10^\circ$, and $l_w = 22.3$ mm).



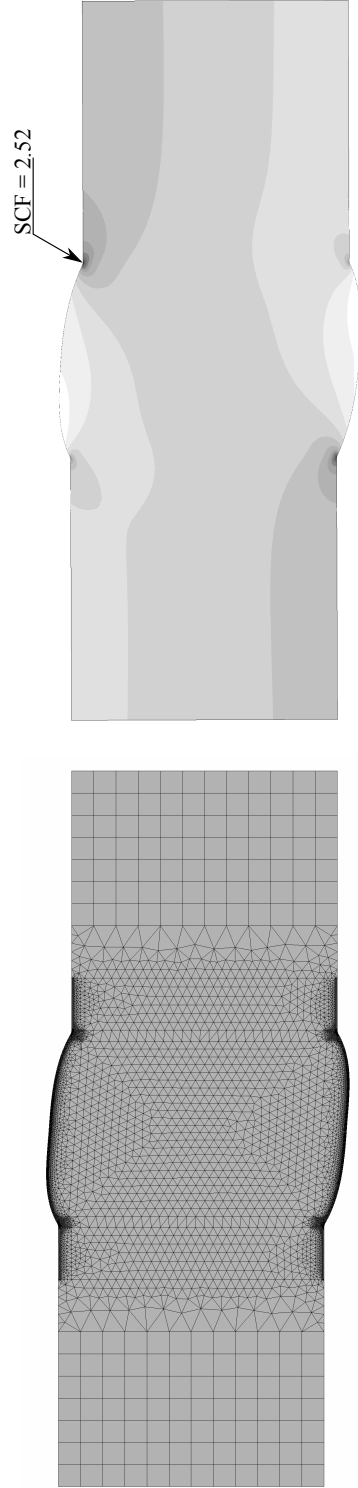
(c) Mesh 2 (parameters: $t_s = 30$ mm, $\rho = r_{\text{ref}} = 1$ mm, $\delta/t_s = 0.070$, $e/t_s = 0.05$, $\beta = 10^\circ$, and $l_w = 22.3$ mm).



(b) Major principal stress contour and SCF.



(d) Major principal stress contour and SCF.



(e) Mesh 3 (parameters: $t_s = 30$ mm, $\rho = r_{\text{ref}} = 1$ mm, $\delta/t_s = 0.070$, $e/t_s = 0.05$, $\beta = 25^\circ$, and $l_w = 22.3$ mm).

(f) Major principal stress contour and SCF.

Figure 6.4: Three examples of butt welded joints with linear misalignment with (a)–(b): a relatively low reinforcement height and a low flank angle; (c)–(d): a relatively large reinforcement height and a low flank angle; and (e)–(f): a relatively large reinforcement height and a large flank angle.

and

$$\sigma_{hs} = 1.67\sigma_{0.4t_s} - 0.67\sigma_{1.0t_s}, \quad (6.3)$$

where σ_{xt_s} is the major principal stress at the surface at a distance of $x \cdot t_s$ from the notch (i.e., the weld toe).

2. The structural stress evaluation according to Dong (2001):

$$\sigma_m = \frac{1}{t_s} \int_0^{t_s} \sigma_x(y) \cdot dy \quad (6.4)$$

and

$$\sigma_m \frac{t_s^2}{2} + \sigma_b \frac{t_s^2}{6} = \int_0^{t_s} \sigma_x(y) \cdot y \cdot dy + d \int_0^{t_s} \tau_{xy}(y) \cdot dy, \quad (6.5)$$

where σ_m and σ_b are the membrane and bending parts of the stress profile (see Fig. 3.9), respectively. In Eqs. 6.4 and 6.5, the x -axis is along the plate, i.e., parallel to the nominal tension, and the y -axis is through the section.

Structural stresses were evaluated for three thicknesses, namely $t_s = 20, 35$ and 50 mm, and for a relative eccentricity e/t_s from 0.00 to 0.07 (–). The other parameters were kept constant, namely $\beta = 30^\circ$, $\rho = 1$ mm, $\delta/t_s = 0.060$, and $\alpha = 60^\circ$. The analysis was linear elastic, without considering the effect of large deflections. In Fig. 6.5 a very good agreement with the theoretical solution given by Eq. 3.39 can be seen.

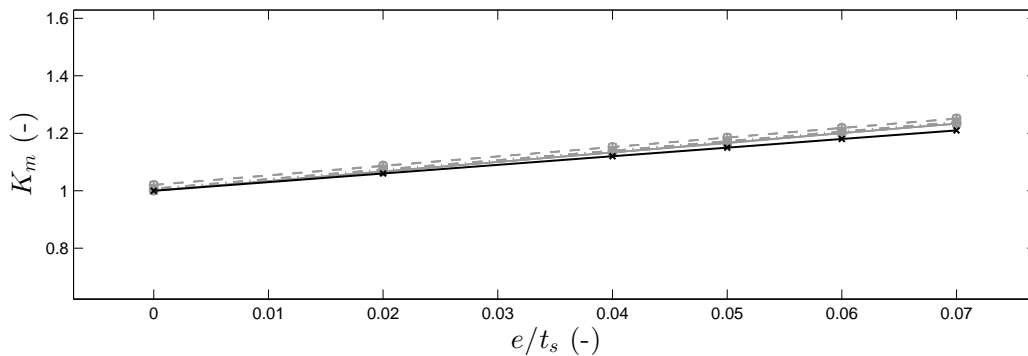


Figure 6.5: Evaluation of the structural SCF K_m for different relative eccentricities e/t_s according to Eq. 6.2 (– · –), Eq. 6.3 (– –) and Eqs. 6.4–6.5 (–); and for three different thicknesses $t_s = 20$ mm (○), $t_s = 35$ mm (+) and $t_s = 50$ mm (□). The theoretical values of K_m are evaluated according to Eq. 3.39 (– × –).

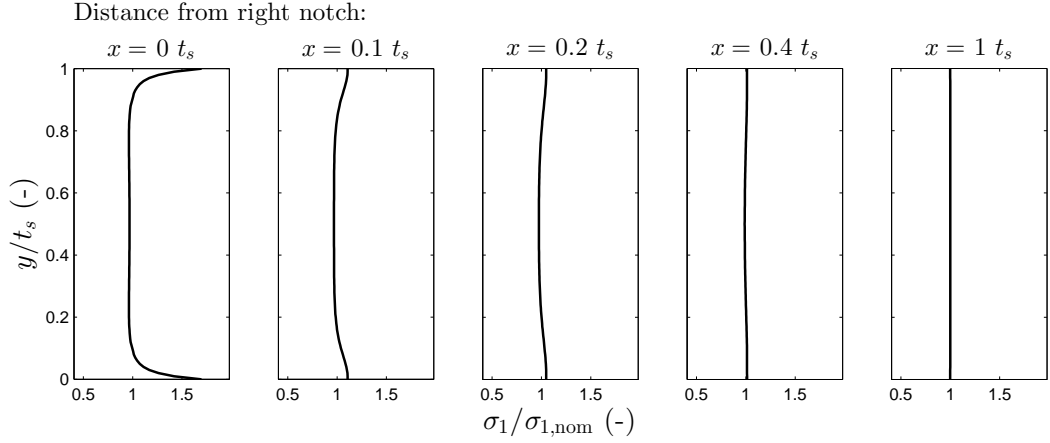
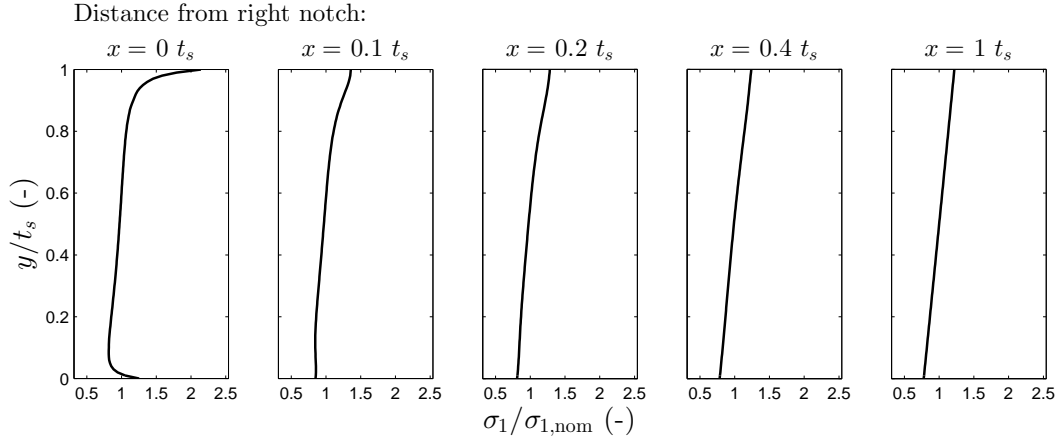

 (a) $e/t_s = 0.00$.

 (b) $e/t_s = 0.07$.

Figure 6.6: Major principal stress profiles at different distances from the right weld toe (accordingly to Fig. 6.2), for a butt welded joint (a) without misalignment and (b) with misalignment. Parameters: $t_s = 20$ mm, $\rho = r_{\text{ref}} = 1$ mm, $\delta/t_s = 0.060$, $\beta = 30^\circ$, and $l_w = 13$ mm.

Two examples of major stress profiles at different distances from the weld toe are shown in Fig. 6.6. Without linear misalignment (Fig. 6.6a), the nonlinear peaks of σ_1 at the upper and lower weld toes are symmetric. At approximately $0.5 \cdot t_s$, the influence of the notch vanishes and σ_1 is constant through the thickness and equal to σ_{nom} . Figure 6.6b shows the same results with a large linear misalignment. In this case, the nonlinear peak of σ_1 is larger at the upper right weld toe, as this part is subject to tensile structural stresses (see also Fig. 6.3). This is consistent with literature (see, e.g., Fricke 2011). At approximately $0.5 \cdot t_s$, the influence of the notch vanishes and a bending stress profile is observed. The maximum value of $\sigma_1/\sigma_{1,\text{nom}}$ at the upper surface is equal to the structural SCF of the weldment.

6.2 Parametric study

A systematic parametric study was performed to assess the influence of five geometrical parameters on the SCF at weld toes of butt welded joints, namely (see also Fig. 6.2):

1. the flank angle β (from 5° to 30°),
2. the weld toe radius ρ (from 0.4 to 1.9 mm),
3. the edge preparation angle α (from 60° to 100°) which gives the weld length l_w ,
4. the relative weld reinforcement height δ/t_s (from 0.04 to 0.1), and
5. the relative eccentricity e/t_s (from 0 to 0.07).

Each parameter was varied for three different thicknesses ($t_s = 20, 35$ and 50 mm), keeping the four others constant.

The notch SCF K_t as a function of β is plotted in Fig. 6.7. One can observe a great influence on the SCF. The greater β , the greater the SCF.

Figure 6.8 represents K_t as a function of the weld toe radius ρ . It also shows that ρ is a determinant parameter influencing the SCF. The smaller ρ , the greater K_t . Together with the flank angle β , the weld toe radius ρ is the most important parameter considered in the parametric equations found in the literature (Eqs. 3.41–3.49) since they greatly influence the SCF (see Sect. 3.7.4). This observation is also reported, e.g., by Teng *et al.* (2002).

Figure 6.9 represents K_t as a function of the relative weld reinforcement height δ/t_s . The greater δ/t_s , the greater the SCF. This is a somewhat interesting result as δ is rarely taken into account the parametric equations for SCF found in the literature. As β and ρ , it acts as a significant stress concentration raiser.

The influence of α on K_t is presented in Fig. 6.10. One can observe a slight influence on the SCF as a stress raising parameter. The weld length l_w (directly linked to α) is not commonly considered in parametric equations in the literature. According to Teng *et al.* (2002), the influence of l_w is mainly related to residual stresses. However, the influence of l_w on the fatigue life is claimed to be insignificant compared to the aforementioned parameters by Teng *et al.* (2002).

Finally, Fig. 6.11 represents K_t as a function of the relative eccentricity e/t_s . The greater e/t_s , the greater the SCF. This is largely due to the increase of the structural SCF. Indeed, one may note that the use of splines with imposed tangents to describe the weld reinforcement surface also introduces a role of the misalignment in slightly changing the weld geometry. The corresponding structural SCF K_m were shown in Fig. 6.5.

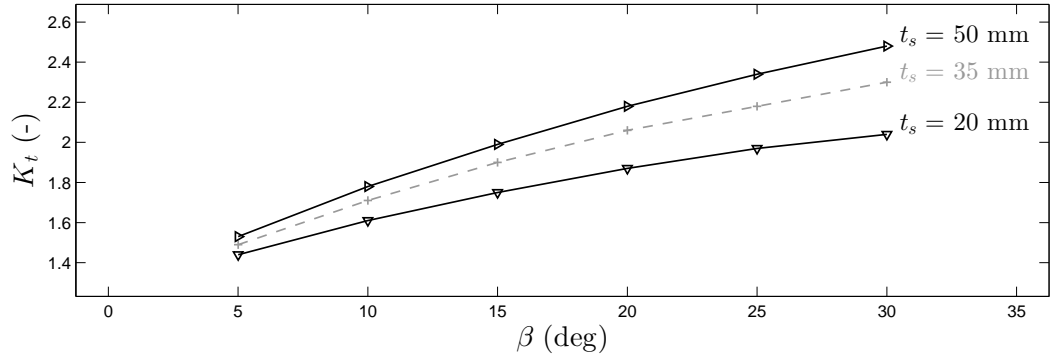


Figure 6.7: Notch SCF K_t as a function of flank angle β for three thicknesses t_s . Constant parameters: $\rho = r_{\text{ref}} = 1$ mm, $\delta/t_s = 0.060$, $e/t_s = 0.00$, and $\alpha = 90^\circ$.

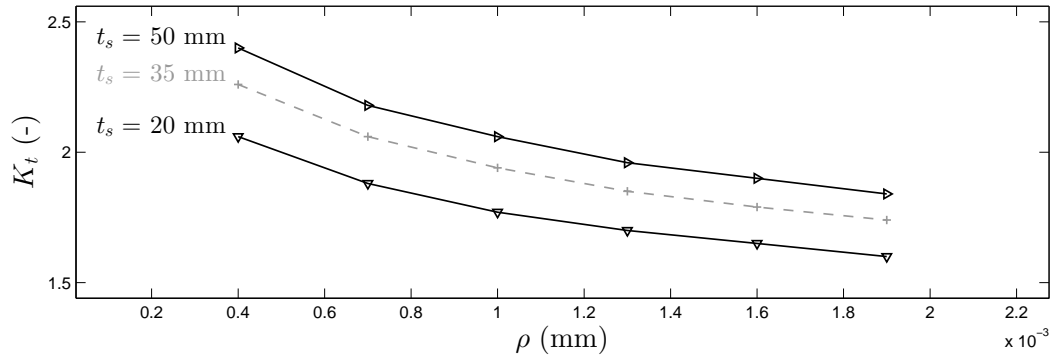


Figure 6.8: Notch SCF K_t as a function of the weld toe radius ρ for three thicknesses t_s . Constant parameters: $\beta = 20^\circ$, $\delta/t_s = 0.040$, $e/t_s = 0.00$, and $\alpha = 60^\circ$.

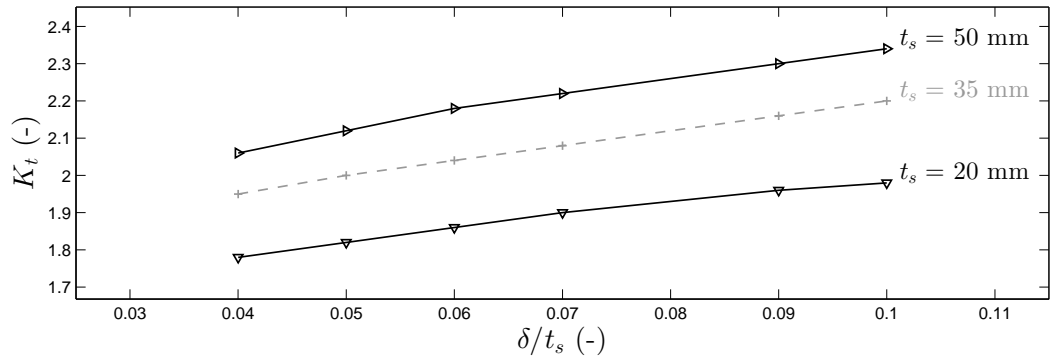


Figure 6.9: Notch SCF K_t as a function of the relative weld reinforcement height δ/t_s for three thicknesses t_s . Constant parameters: $\beta = 20^\circ$, $\rho = r_{\text{ref}} = 1$ mm, $e/t_s = 0.00$ and $\alpha = 70^\circ$.

6.3 Parametric equations

Simple parametric equations were published in the literature (e.g., Radaj & Zhang 1991; Radaj 2006; Remes 2008; Remes & Varsta 2010) for notch SCF at welded plates under the form of

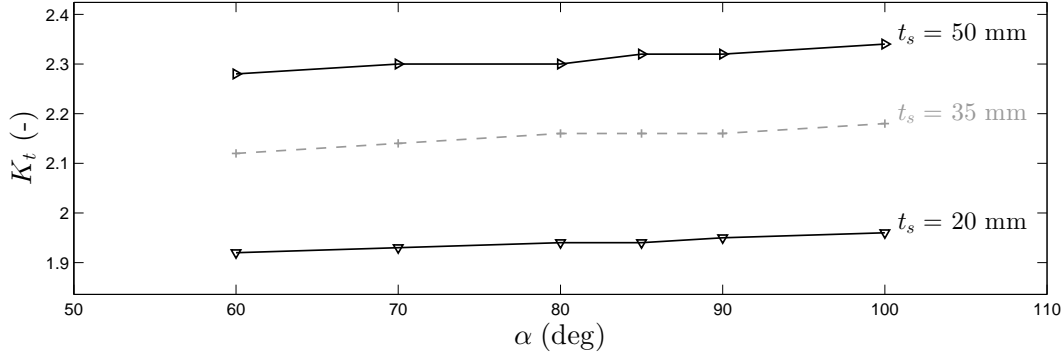


Figure 6.10: Notch SCF K_t as a function of the edge preparation angle α for three thicknesses t_s . Constant parameters: $\beta = 25^\circ$, $\rho = r_{\text{ref}} = 1$ mm, $\delta/t_s = 0.055$ and $e/t_s = 0.00$.

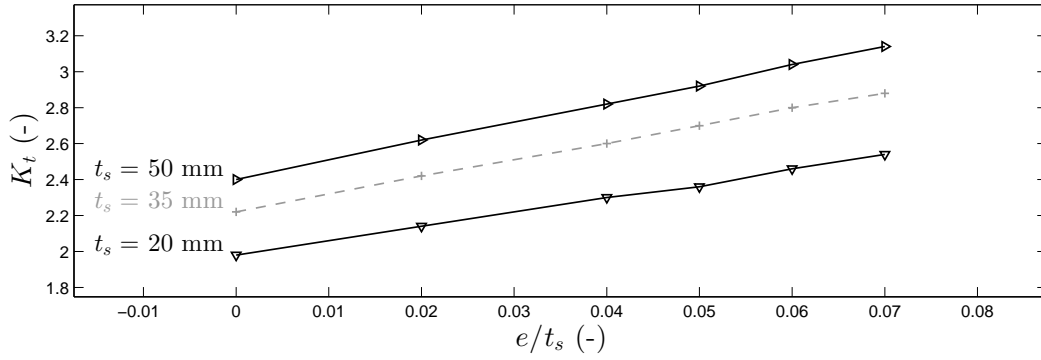


Figure 6.11: Notch SCF K_t as a function of the relative eccentricity e/t_s for three thicknesses t_s . Constant parameters: $\beta = 30^\circ$, $\rho = r_{\text{ref}} = 1$ mm, $\delta/t_s = 0.50$ and $\alpha = 60^\circ$. The corresponding structural SCF K_m are shown in Fig. 6.5.

products of dimensionless parameters with constant coefficient and exponents as

$$K_t = 1 + \alpha_0 \prod_{i=1}^n \lambda_i^{\alpha_i}, \quad (6.6)$$

where the λ_i are dimensionless parameters and the α_i are constant coefficient and exponents to be fitted. This approach is also considered herein for its simplicity and efficiency. Four new parametric equations for notch SCF are proposed hereafter:

- for SCF at butt welded joints considering linear misalignment $K_{t,m}$, under the form

$$K_{t,m} = K_m K_w; \quad (6.7)$$

- for SCF at butt welded joints without linear misalignment K_t ;
- for SCF at butt welded joints considering only a constant $\rho = r_{\text{ref}} = 1$ mm and linear misalignment $K_{t,m}^{\rho=r_{\text{ref}}}$ under the form

$$K_{t,m}^{\rho=r_{\text{ref}}} = K_m K_w^{\rho=r_{\text{ref}}}; \quad (6.8)$$

and

- for SCF at butt welded joints considering only a constant $\rho = r_{\text{ref}} = 1$ mm without linear misalignment $K_t^{\rho=r_{\text{ref}}}$.

The influence of misalignment is accounted by means of Eq. 3.39 for K_m . Concerning the influence of the weld geometry, the general form of Eq. 6.6 was considered for K_w . The four proposed parametric equations have the following forms:

$$K_{t,m} = \left[1 + 3 \frac{e}{t_s} \right] \left[1 + \alpha_0 \left(\frac{\delta}{t_s} \right)^{\alpha_1} \left(\frac{\rho}{t_s} \right)^{\alpha_2} \tan \left(\frac{\beta}{2} \right)^{\alpha_3} \right]; \quad (6.9)$$

$$K_t = 1 + \alpha_0 \left(\frac{\delta}{t_s} \right)^{\alpha_1} \left(\frac{\rho}{t_s} \right)^{\alpha_2} \tan \left(\frac{\beta}{2} \right)^{\alpha_3}; \quad (6.10)$$

$$K_{t,m}^{\rho=r_{\text{ref}}} = \left[1 + 3 \frac{e}{t_s} \right] \left[1 + \alpha_0 \left(\frac{\delta}{t_s} \right)^{\alpha_1} \left(\frac{r_{\text{ref}}}{t_s} \right)^{\alpha_2} \tan \left(\frac{\beta}{2} \right)^{\alpha_3} \right]; \quad (6.11)$$

and

$$K_t^{\rho=r_{\text{ref}}} = 1 + \alpha_0 \left(\frac{\delta}{t_s} \right)^{\alpha_1} \left(\frac{r_{\text{ref}}}{t_s} \right)^{\alpha_2} \tan \left(\frac{\beta}{2} \right)^{\alpha_3}. \quad (6.12)$$

In order to fit the constant coefficient and exponents α_i , four series of FEA were performed, each composed of 138 cases of butt welded joints. The design of the variation of t_s , δ/t_s , β and α (and thus l_w) remained unchanged for all series, and was performed arbitrarily to cover a large extent of cases. The design of the variation of ρ remained unchanged for the series of $K_{t,m}$ and K_t , as the variation of e/t_s for $K_{t,m}$ and $K_{t,m}^{\rho=r_{\text{ref}}}$, correspondingly.

Considering the aforementioned method to construct the geometry of the weld, not any pair of values for β and δ were allowed. For instance, a large value of β with a relatively low value of δ

Chapter 6. Stress concentration at butt welded joints of straight plates

may induce undesired weld profiles (e.g., with a local cavity at the crown). A visual inspection of all the cases was performed. When such a combination was detected, the values were adapted arbitrarily. The ranges of variation of the parameters are presented in Table 6.1.

Table 6.1: Ranges of variation of the parameters in the series of simulations used to derive the parametric equations.

Parameter	Unit	Minimum value	Maximum value	Increment
t_s	(mm)	15	60	1
ρ	(mm)	0.2	2.0	0.1
δ/t_s	(–)	0.010	0.100	0.010
e/t_s	(–)	0.00	0.07	0.01
β	(°)	3	45	1
α	(°)	60	100	5

To fit the constant coefficient and exponents α_i an objective function was defined, for each series, as:

$$\hat{\alpha} = \underset{\alpha}{\operatorname{argmin}} \operatorname{MSE}[\mathbf{SCF}^{\text{num}}, \mathbf{SCF}^{\text{emp}}(\mathbf{\Lambda}, \alpha)] \quad (6.13)$$

where MSE is the mean squared error; $\hat{\alpha} = \{\alpha_i\}$ is the argument of the minimum; $\mathbf{\Lambda} = \{\mathbf{\Lambda}_i\}$ contains the dimensionless parameters; $\mathbf{SCF}^{\text{num}}$ contains the values of SCFs obtained by FEA (namely 138 cases per series); and $\mathbf{SCF}^{\text{emp}}$ contains the corresponding values computed via the corresponding proposed parametric equations, i.e., Eqs 6.9–6.12. The sets of α_i , for each equation, were determined by means of genetic algorithm (GA) with a *training group* containing 90% of the database. The other 10% were used as a *test group* to test the results. The obtained α_i are presented in Table 6.2 for $K_{t,m}$ and K_t and in Table 6.3 for $K_{t,m}^{\rho=r_{\text{ref}}}$ and $K_t^{\rho=r_{\text{ref}}}$.

Table 6.2: Coefficient and exponents α_i for the parametric equations for the notch SCF $K_{t,m}$ and K_t .

SCF	α_0	α_1	α_2	α_3
$K_{t,m}$	1.16	0.23	-0.38	0.46
K_t	0.81	0.11	-0.40	0.59

Table 6.3: Coefficient and exponents α_i for the parametric equations for the notch SCF $K_{t,m}^{\rho=r_{\text{ref}}}$ and $K_t^{\rho=r_{\text{ref}}}$.

SCF	α_0	α_1	α_2	α_3
$K_{t,m}^{\rho=r_{\text{ref}}}$	0.95	0.06	-0.35	0.56
$K_t^{\rho=r_{\text{ref}}}$	0.99	0.06	-0.34	0.59

The regression between the numerical SCF and the empirical SCF for the training and test groups are plotted in Fig. 6.12 for $K_{t,m}$ and K_t , and in Fig. 6.13 for $K_{t,m}^{\rho=r_{\text{ref}}}$ and $K_t^{\rho=r_{\text{ref}}}$. One can observe

good coefficients of determination R^2 for all the expressions, with relatively low root mean squared error RMSE.

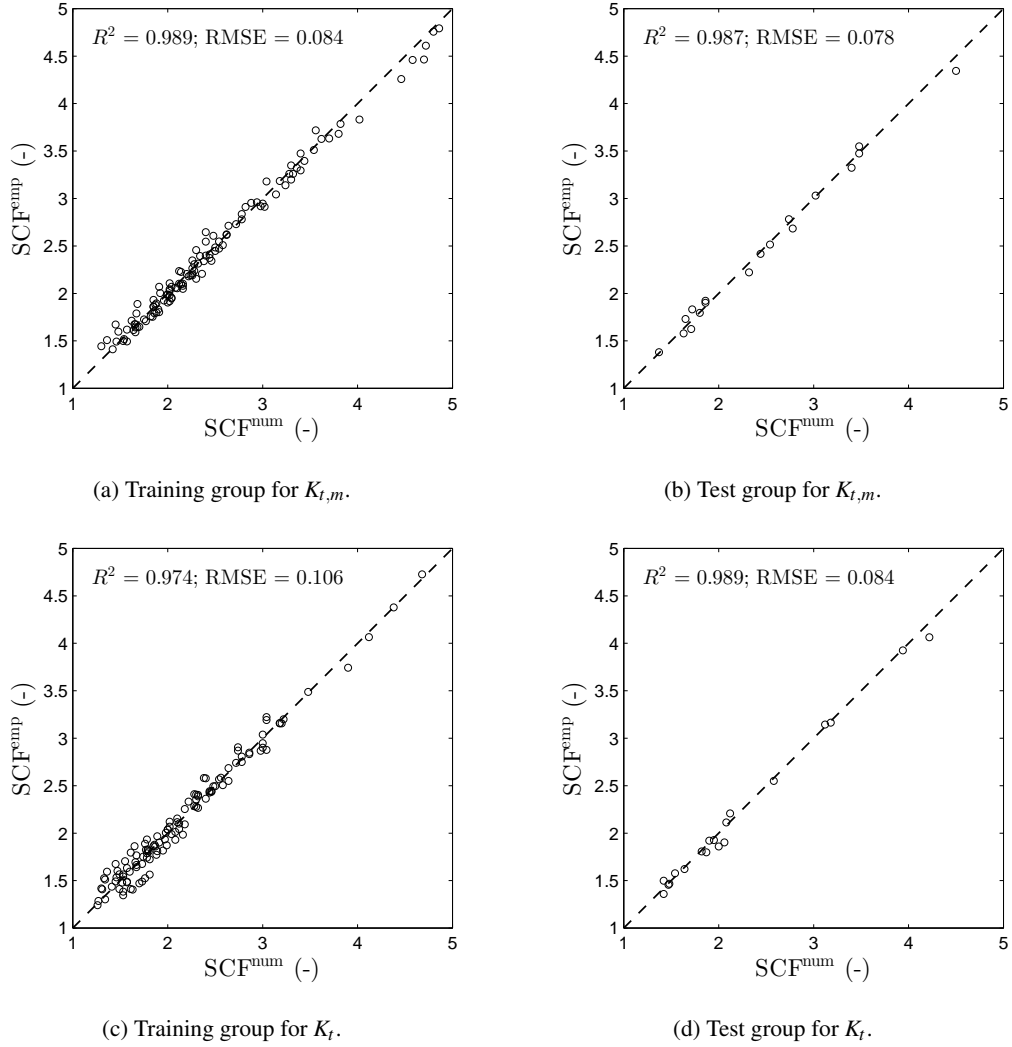
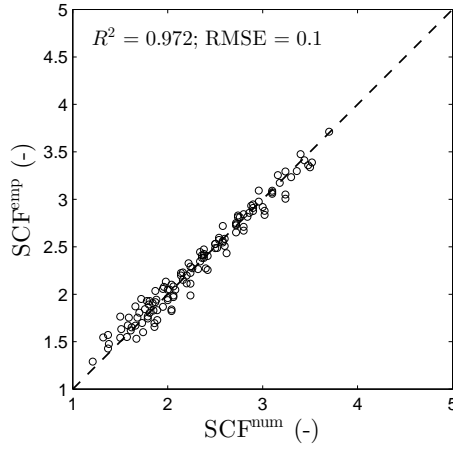


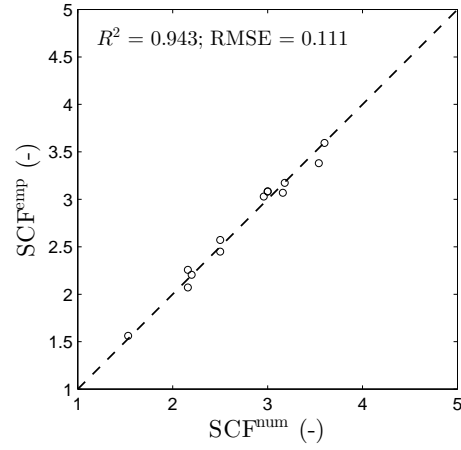
Figure 6.12: Regression plots of the numerical SCF $K_{t,m}$ and K_t obtained by FEA vs. the empirical SCF fitted by GA.

6.4 Conclusions

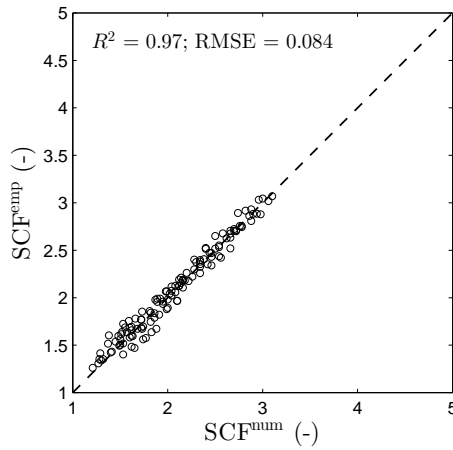
In Sect. 3.7, notch SCF were estimated by means of some published formulas and a significant scatter was observed. New and detailed hypotheses on the geometry of the weld were presented in this chapter, i.e., modeled with splines, and a parametrically-built FE model was used. This model is able to model different types of weld geometries that were shown by means of selected examples.



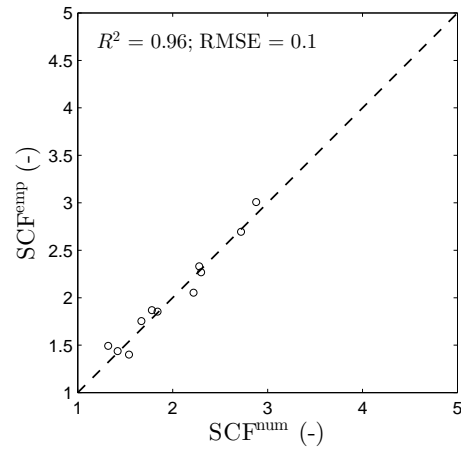
(a) Training group for $K_{t,m}^{p=r_{ref}}$.



(b) Test group for $K_{t,m}^{p=r_{ref}}$.



(c) Training group for $K_t^{p=r_{ref}}$.



(d) Test group for $K_t^{p=r_{ref}}$.

Figure 6.13: Regression plots of the numerical SCF $K_{t,m}^{p=r_{ref}}$ and $K_t^{p=r_{ref}}$ obtained by FEA vs. the empirical SCF fitted by GA.

A parametric study was performed by means of FEA and outlined the importance of the influence of the reinforcement height of the weld δ , which is often absent in the parametric equations as found in the literature.

Finally, four new parametric equations were derived which allow to estimate SCF at butt welded joints, namely without and without linear misalignment, and with variable weld toe radius ρ , or set to $\rho = r_{\text{ref}} = 1$ mm for a straight forward use within the effective notch stress approach.

The hypotheses adopted in this chapter to model the weld shape as well as the derived parametric equations will be considered in the subsequent Chapters 7 and 8.

7 Stress concentration at longitudinal butt welded joints of steel liners

7.1 Conceptual model

7.1.1 Types of geometrical imperfections

Out-of-roundness

Out-of-roundness (or ovality) is characterized by a deviation η of the steel liner from the circular shape, i.e., with a no longer constant diameter. This defect is illustrated in Fig. 7.1 and may have various origins (erection, transportation, welding). To maintain roundness within tolerances, temporary bracing may be installed during the erection of the steel liner, as shown in Fig. 2.7e. C.E.C.T. (1980) recommend that the out-of-roundness parameter η should not exceed 1% of the internal radius r_i . The tolerated η is thus defined herein as

$$\eta_{\text{tol}} = 0.01 \cdot r_i. \quad (7.1)$$

Peaking

Peaking (or roof-topping) is a deviation from the circular shape which is local to the longitudinal welded joints and induced by two straight edges of length l_u (which are thus unrolled), inherent to the rolling process. It may result in a radial deviation Δh from the circular shape as illustrated in Fig. 7.1. C.E.C.T. (1980) recommend a tolerance that can be related to this defect. The harshest is given for joints of Class I, as (dimensions in mm)

$$\Delta h_{\text{tol}} = \left(\frac{2r_i}{1000} + \frac{20}{t_s} + 0.5 \right). \quad (7.2)$$

It is the tolerance considered herein.

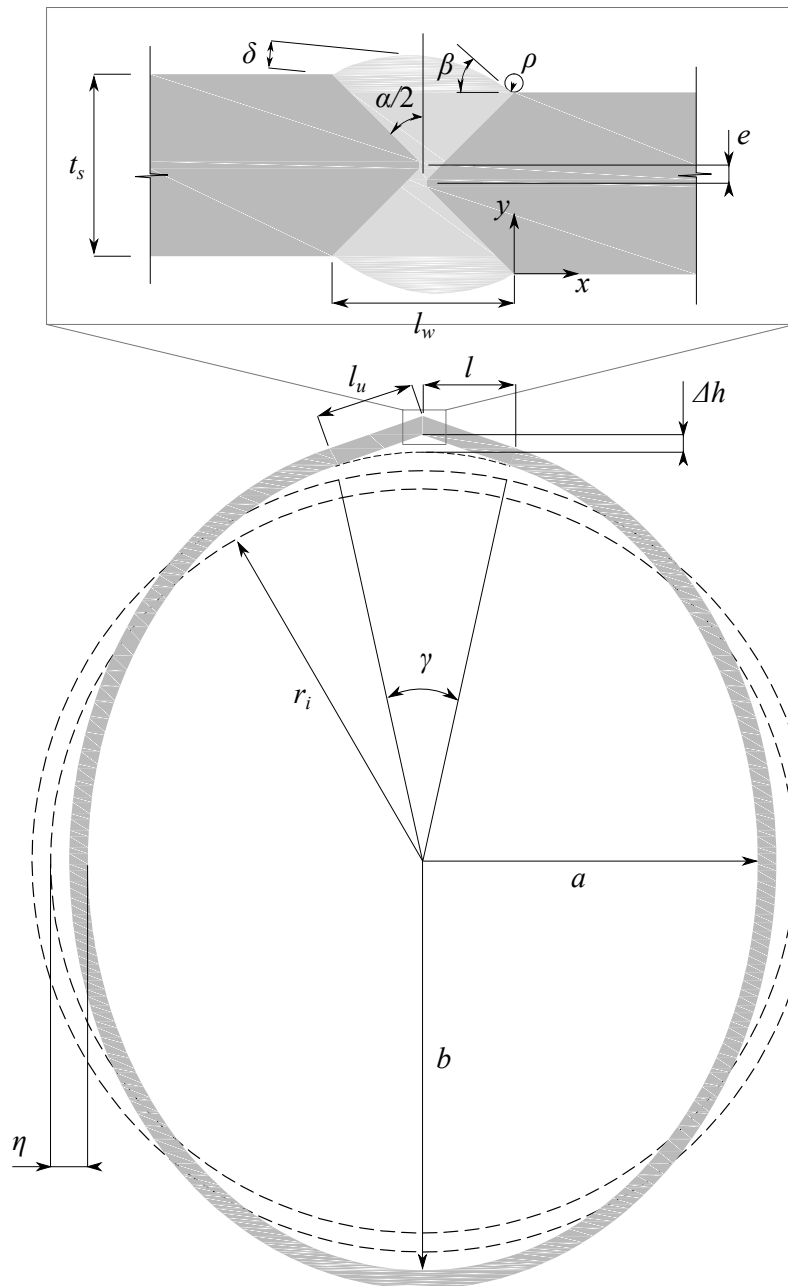


Figure 7.1: Definition sketch of the geometrical imperfections and the local butt welded joints' geometry at steel liners of pressure tunnels and shafts. The geometrical imperfections and the thickness of the liner are magnified for presentation purposes.

Axial misalignment

Axial misalignment (or eccentricity) is a common misalignment for butt welded plates or shells. It is characterized by an eccentricity e between the mean axes of the welded plates. It is illustrated at the top of Fig. 7.1, in the detail of the longitudinal weld. For joints of Class I, C.E.C.T. (1980) recommend a tolerance as (dimensions in mm)

$$e_{\text{tol}} = \left(\frac{t_s}{50} + 1 \right). \quad (7.3)$$

7.1.2 Global geometry

To model the global geometry of the steel liner, the following assumptions are made (also see Fig. 7.1, and more details are given in Appendix A).

1. To model the out-of-roundness, the shape of the steel liner is modeled by an ellipse of minimum axis $a = r_{i,\min} = r_i - \eta$ and maximum axis $b = r_{i,\max} = r_i + \eta$.
2. The peaking is modeled by two straight edges of length l_u that are tangent to the elliptic parts of the liner. The so-called angular misalignment angle γ is approximated as $\gamma = 2l_u/r_i$ in radians.
3. The linear misalignment at the butt welded joint is modeled by separating the ellipse in two, with respect to a vertical axis passing by the longitudinal butt welded joint. The axes of the left ellipse are increased by $e/4$. For the right ellipse, the axes are decreased by $e/4$ and the vertical coordinate of the center of the ellipse is displaced by $e/2$ in the opposite direction of the joint. This way a linear misalignment e occurs at the longitudinal butt welded joint, and the origin of the defect is thus apportioned over all the liner. The straight edges can remain tangent to the elliptic parts. To keep the presentation simple, this feature is not represented on the global geometry in Fig. 7.1.

Some nomenclature is introduced hereafter in order to relate the values of the geometrical imperfections to the tolerance values given by C.E.C.T. (1980) or to the relevant physical parameter. The length of the straight edges l_u is defined relatively to the thickness of the steel liner t_s by the factor ψ_u as

$$l_u = \psi_u t_s. \quad (7.4)$$

Chapter 7. Stress concentration at longitudinal butt welded joints of steel liners

The linear misalignment e is defined proportionally to the tolerance value by the factor ψ_e as

$$e = \psi_e e_{\text{tol}}. \quad (7.5)$$

Similarly, the out-of-roundness η is defined through the factor ψ_η as

$$\eta = \psi_\eta \eta_{\text{tol}}. \quad (7.6)$$

These definitions are useful for a comprehensive and systematic description of the forthcoming analyses.

7.1.3 Local geometry of the longitudinal butt welded joints

The local geometry of the longitudinal joints is presented in the upper part of Fig. 7.1. The parameters are listed as follows:

- the weld toe radius ρ ;
- the flank angle β ;
- the edge preparation angle α ; and
- the weld reinforcement height δ .

The weld length l_w is related to α as (dimensions in mm)

$$l_w = 2b_w = \frac{t_s}{2} \sin(\alpha/2) + 1.5 \quad (7.7)$$

where b_w is the half-length of the weld and $1.5 \cdot 2 = 3$ mm is the separation between the welded edges. The tolerance for the weld reinforcement height is defined in C.E.C.T. (1980) for Class I joints as (dimensions in mm)

$$\delta_{\text{tol}} = \left[1 + \frac{3}{100} (t_s + l_w) \right]. \quad (7.8)$$

Similarly to the geometrical imperfections, the factor ψ_δ is introduced as

$$\delta = \psi_\delta \delta_{\text{tol}}. \quad (7.9)$$

The construction of the geometry of the weld reinforcement is given in Sect. 7.2.

7.2 Finite element model

7.2.1 Assumptions

The finite element (FE) model follows the assumptions of the conceptual model described in Sect. 7.1. Some additional hypotheses are listed below.

1. The internal interface of the backfill concrete perfectly fits the geometry of the external fiber of the steel liner, shifted by the initial gap Δr_0 .
2. All the other layers' interfaces are circular.
3. 2D plane strain conditions are assumed given the large dimension of SLPT&S in the axis of the tunnel.
4. The tunnel is at great depth and thus has a high overburden. The far-field rock dimensions are regarded as infinite ($30 \times r_i$ ensures convergence of the results in this study) and full load transmission can occur.
5. All materials are linear elastic.
6. The constitutive model for the crack layers is according to previously described in Chapter 4, Sect. 4.2, using a scalar damage parameter R_i . In Chapter 4 R_i was set to 10^{-4} . In this chapter R_i was set to 10^{-3} for convergence issues with the contact technology. This value still ensure a behavior of the cracked layer that reproduces very well the theoretical assumptions.
7. Large-deflection effects are considered.
8. Surface-to-surface contact technology was used to model the contact between the steel liner and the backfill concrete. Ranges for the friction coefficient μ between steel and concrete can be found, e.g., in Rabbat & Russell (1985); Baltay & Gjelsvik (1990); Johansson & Gylltoft (2002); Anderson (2008). In this model, changing μ from 0 to 0.7 did not have any influence on the results, probably due to the very low circumferential displacements and the fact that the backfill concrete cannot transmit circumferential stresses. μ was thus fixed to 0.6.
9. The local weld geometry was modeled with the approach described in Chapter 6. The weld reinforcement was generated from a spline (BSPLIN command in ANSYS Inc 2015) with three tangents imposed at three keypoints, namely the two weld toes where the tangent is defined by the flank angle β , and the crown of the reinforcement where the tangent is defined parallel to the segment linking the two weld toes (also see Fig. 7.1).

10. The boundary conditions (BC) are shown in Fig. 7.2a. In order to verify that the BC on the steel liner shown in Fig. 7.2a were appropriate, comparative open-air penstock simulations were performed with an alternative set of BC, as shown in Fig. 7.2b, i.e., considering an horizontal displacement restriction at the inner fiber and a vertical displacement restriction on the outer fiber at the invert level. Both sets of BC gave the same results at the longitudinal butt-welded joints. The first above-mentioned BC (Fig. 7.2a) were retained since they are the only set compatible with the physics involved in embedded liners: in fact, restraining a vertical displacement would not allow for load sharing with the rock mass.

The FE model was built parametrically. For all the simulations of this study, some parameters remained constant, namely $E_s = 210$ GPa, $\nu_s = 0.3$, $E_c = 20$ GPa, $\nu_c = 0.2$, $t_c = 0.5$ m, and $\nu_{crm} = 0.2$.

7.2.2 Mesh

8-node squares and 6-node triangles elements PLANE183 were used to mesh the materials. The surface-to-surface contact was modeled via the target elements TARGE169 and the contact elements CONTA172 (ANSYS Inc 2015). The contact stiffness was set to 0.6 after the validation process conducted in a Master thesis performed in the framework of the present research project (Senn 2014). The contact stiffness is highly dependent on the mesh density. In this case however, as the refinement of the mesh is relatively high, the determination of the contact stiffness is not very sensitive. The mesh density was parametrized with respect to the geometrical dimensions. Most importantly, for the notch stresses convergence, the dimension of the elements at the fictitious rounding of the weld toes was set to 0.05 mm, which is, for the considered values of ρ and β , finer than the recommendations of Fricke (2012) for $\rho = r_{ref} = 1$ mm. An example of a mesh in the vicinity of the longitudinal butt welded joint is given in Fig. 7.3.

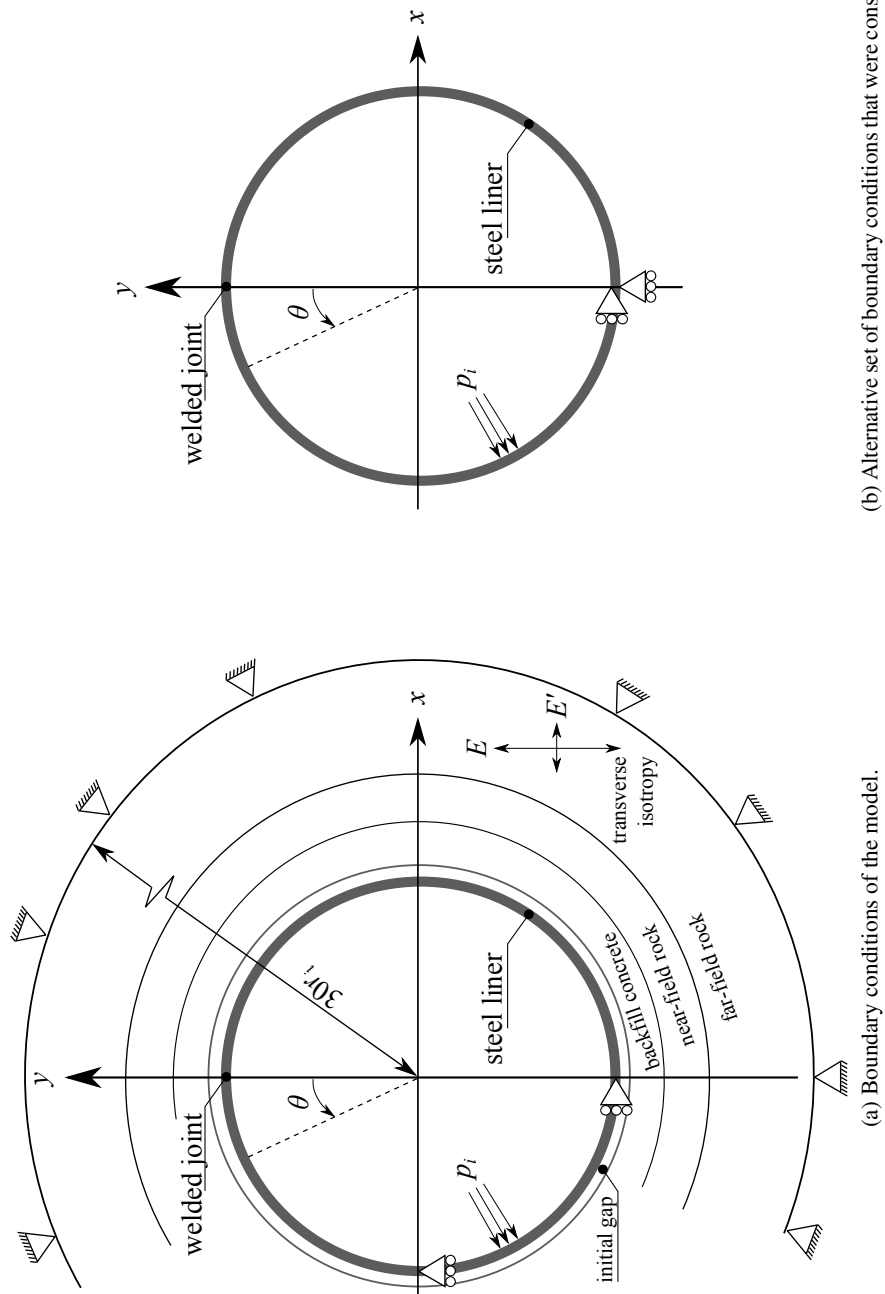
7.2.3 Validation for open-air steel liners (penstocks)

Stresses and displacements in SLPT&S in isotropic rock

To validate the global behavior of the multilayer system and the FE contact technology, results on radial paths through the thicknesses of the layer were analyzed and compared with analytical solutions presented in Chapter 2. The FE model was successfully validated, but the results are skipped herein for the sake of concision.

Methods for structural stresses evaluation

Several methods are available to evaluate structural stresses, such as the linear stress extrapolation methods (see, e.g., Doerk *et al.* 2003; Poutiainen *et al.* 2004; Niemi *et al.* 2006) and the approach proposed by Dong (2001) (see Sect. 6.1.2). In this study, the approach of Dong (2001) is used



(b) Alternative set of boundary conditions that were considered in the open-air penstock model for comparison

(a) Boundary conditions of the model.

Figure 7.2: Sketches illustrating the boundary conditions of the model.

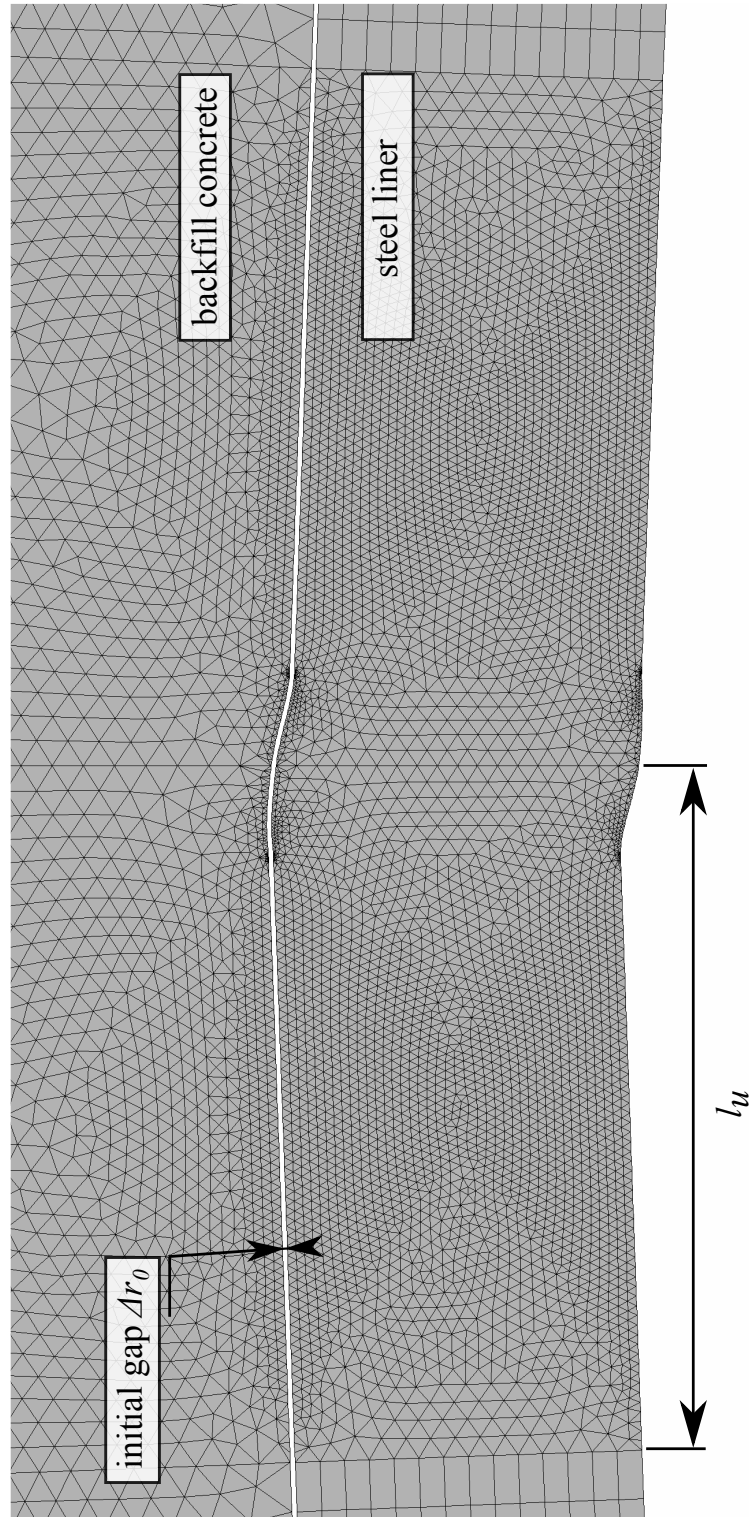


Figure 7.3: Example of a mesh in the vicinity of the longitudinal butt welded joint ($r_i = 2$ m, $t_s = 35$ mm, $\rho = 1$ mm, $\psi_\eta = 1.25$, $\psi_u = 2.00$, $\delta/t_s = 0.030$, $e/t_s = 0.061$, $\beta = 5^\circ$, $\alpha = 50^\circ$ and $\Delta r_0 = 0.025\% \cdot r_i$).

for all the calculations. For the structural stresses at the weld toes of the longitudinal joints, the method of Dong is applied directly to the through-thickness stress profile between the internal and external weld toes.

Structural SCF at longitudinal butt welded joints in open-air steel liners (penstocks)

The implementation of the geometrical imperfections in the steel liner was validated through the study of open-air steel liners (penstocks), thus neglecting the surrounding concrete and rock. Three slenderness ratios were considered, namely $r_i/t_s = 100, 60$ and 43 (–) for two radii $r_i = 1.5$ and 2.5 m. The weld geometry was fixed to $\rho = r_{\text{ref}} = 1$ mm, $\psi_\delta = 0.40$, $\beta = 10^\circ$ and $\alpha = 90^\circ$. The results are plotted in Fig. 7.4 and compared with the corresponding analytical solutions presented in Table 3.4. The BC on the steel liner were the same than the ones shown in Fig. 7.2a.

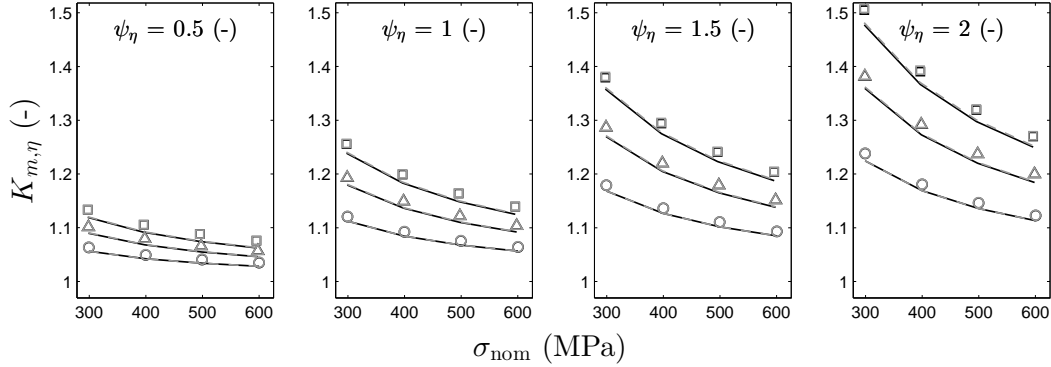
Fig. 7.4a shows the influence of the out-of-roundness factor ψ_η on the structural SCF $K_{m,\eta}$. The weld is located at the largest radius, the worst case. The analytical solution is given by Eq. 3.53, where $d_{\text{max}} - d_{\text{min}} = 4\eta$, and $\Phi = 0$. One can observe a very good agreement between the FE model and the analytical solution, and therefore a good reproduction of the nonlinear geometrical behavior as a function of the nominal stress σ_{nom} , even until an out-of-roundness of 200% of the tolerance given by C.E.C.T. (1980).

The influence of the peaking factor ψ_u on $K_{m,p}$ is plotted in Fig. 7.4b. The analytical solution is evaluated with the approximation $l \approx l_u$ in Eqs. 3.54–3.55 and Δh was computed directly from the geometry of the FE model, and was verified to correspond to $\Delta h = r_i [1/\cos(\gamma/2) - 1]$ proposed by Böck & Zeman (1994). Until $\psi_u = 2$ (and thus $l_u = 2 \cdot t_s$), the FE model and Eqs. 3.54–3.55 gives sensibly the same results. For larger peaking as $l_u = 3 \cdot t_s$, there is a slight divergence of the FE model from the proposed analytical solution. However, one may expect that the FE model is a better representation of the problem studied herein. Indeed, the BC considered to derive Eqs. 3.54–3.55 are less representative of the real structure and thus yield inaccuracies, as pointed out by Ong & Hoon (1996).

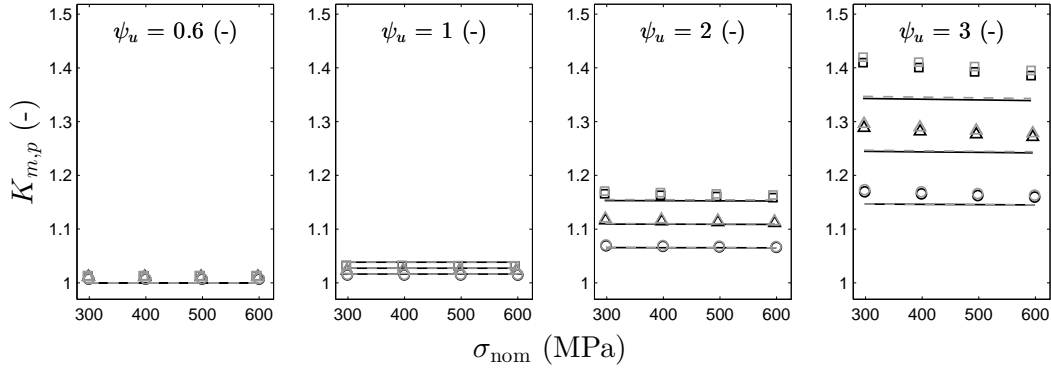
Finally, Fig. 7.4c presents the influence of the relative eccentricity e/t_s on the structural SCF $K_{m,e}$. The analytical solution corresponds to Eq. 3.56. The agreement is very good, and the slight overestimation of $K_{m,e}$ by Eq. 3.56 for large e/t_s ratios can be explained because it does not consider the nonlinear geometrical effects.

Maximum stresses in SLPT&S in anisotropic rock

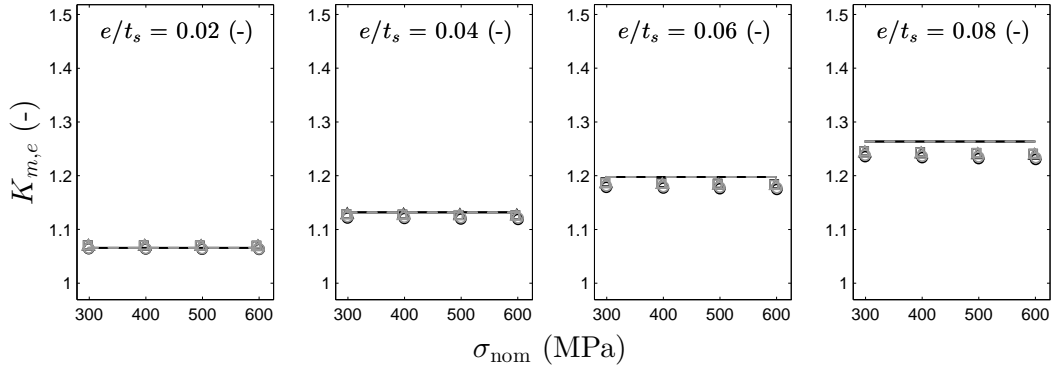
The ability of the model including the FE contact technology to reproduce the effect of the anisotropic rock behavior obtained in Chapter 5 is also investigated. A new correction coefficient describing the influence of the anisotropic rock mass on the nominal stresses in the steel liner



(a) Influence of out-of-roundness ψ_η on $K_{m,\eta}$.



(b) Influence of peaking ψ_u on $K_{m,p}$.



(c) Influence of relative eccentricity e/t_s on $K_{m,e}$.

(○) $r_i/t_s = 100$ (△) $r_i/t_s = 60$ (□) $r_i/t_s = 43$; Black symbols: $r_i = 1.5$ m; Gray symbols: $r_i = 2.5$ m
 Black solid lines (—): analytical solutions of Table 3.4 for $r_i = 1.5$ m
 Gray dashed lines (---): analytical solutions of Table 3.4 for $r_i = 2.5$ m

Figure 7.4: Structural SCF $K_{m,i}$ for open-air penstocks as a function of the nominal stress σ_{nom} for different: (a) out-of-roundness factors ψ_η ; (b) peaking factors ψ_u ; and (c) relative eccentricities e/t_s .

(i.e., the maximum stress at the internal fiber) is defined as

$$K_{rm,aniso}^* = \frac{\sigma_{nom,aniso}}{\sigma_{nom,iso}} \quad (7.10)$$

where $\sigma_{nom,iso}$ is the nominal stress considering isotropic rock (i.e., of parameters E' and ν) and $\sigma_{nom,aniso}$ is the maximum stress considering transversely isotropic rock (i.e., of parameters E , E' , G' , ν and ν'). The superscript $*$ stands for the interaction with the rock mass.

Two slenderness ratios were considered, namely $r_i/t_s = 100$ and 43 (–) for two radii $r_i = 1.5$ and 2.5 m. The weld geometry was fixed as aforementioned (in Sect. 7.2.1), and the initial gap was reduced to zero (set to $\Delta r_0 = 10^{-6} \cdot r_i$ in the FE model). The influence of the degree of anisotropy E/E' on $K_{rm,aniso}^*$ is shown in Fig. 7.5. The empirical solution proposed in Chapter 5 is also plotted. One can observe a very good agreement.

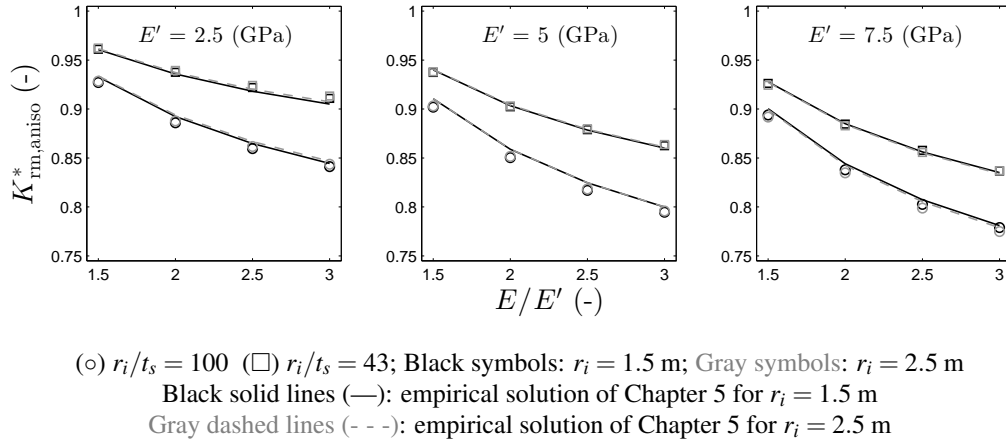


Figure 7.5: Correction coefficient $K_{rm,aniso}^*$ for embedded steel liners as a function of the degree of anisotropy E/E' for different lowest rock moduli E' , and for $\sigma_{nom} = 300$ MPa.

7.3 Parametric study

The influence of the interaction between the steel liner and the concrete–rock system on the structural SCF due to geometrical imperfections was first assessed through a systematic parametric analysis.

7.3.1 Parameters

The three geometrical imperfections, namely out-of-roundness, peaking and linear misalignment, were considered, each interacting with three different isotropic rocks of elastic modulus $E = 2.5$, 5.0 and 7.5 GPa and Poisson's ratio $\nu = 0.2$. The elastic modulus of the near-field rock was

defined as $E_{\text{crm}} = 0.8 \cdot E$ and the Poisson's ratio as $\nu_{\text{crm}} = 0.20$. The ranges of variations of ψ_η , ψ_u and e/t_s were the same than in Sect. 7.2 for the validation of open-air steel liners for comparison purposes. The weld geometry was fixed as aforementioned, and the initial gap was reduced to zero (set to $\Delta r_0 = 10^{-6} \cdot r_i$ in the FE model).

7.3.2 Structural SCF in the steel liner

The influence of the interaction with the concrete–rock system on steel liners with out-of-roundness imperfections is plotted in Fig. 7.6a. One can observe that the confinement induced by the concrete–rock system completely eliminates the SCF yielded by the out-of-roundness in open-air steel liners. This effect can be explained by the fact that the confinement completely avoids the flattening of the deformed shape at the largest radii of the elliptic steel liner. As a consequence, no additional bending stresses occur at the longitudinal butt welded joint. This effect, however, comes at the price of larger stresses in the far-field rock (see Sect. 7.3.3). Figure 7.7 represents the through-thickness major principal stress σ_1 profiles at the weld toes of the longitudinal butt welded joint. In Figs. 7.7a–7.7d, the stresses are represented in open-air steel liners, while in Figs. 7.7e–7.7h, in steel liners embedded in the concrete–rock system. One can see that the higher ψ_η , the higher additional tension is induced at the internal fiber of the steel liner in open-air. On the contrary, unchanging σ_1 profiles are observed in the embedded steel liners.

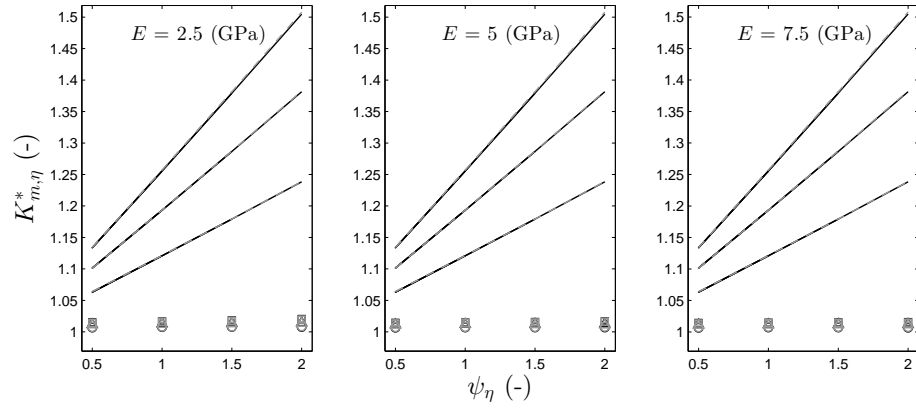
Figure 7.6b presents the effect in steel liners with peaking imperfections¹. Compared to open-air penstocks, one can observe a mitigation effect on the structural SCF $K_{m,p}^*$ when embedded in the concrete–rock system. This effect remains the same for all tested rock elastic moduli. This effect may be due to the fact that confinement reduces the flattening of roof-topping, that creates larger bending stresses in open-air, as the internal pressure ensure full contact with the surrounding materials.

Finally, the effect of linear misalignment is shown in Fig. 7.6c. It can be seen that the structural SCF $K_{m,e}^*$ is only slightly mitigated compared to $K_{m,e}$ in open-air. This effect is constant for all the tested elastic moduli. This slight mitigation can be explained by the constraint that the contact with the backfill concrete induces at the longitudinal butt welded joint.

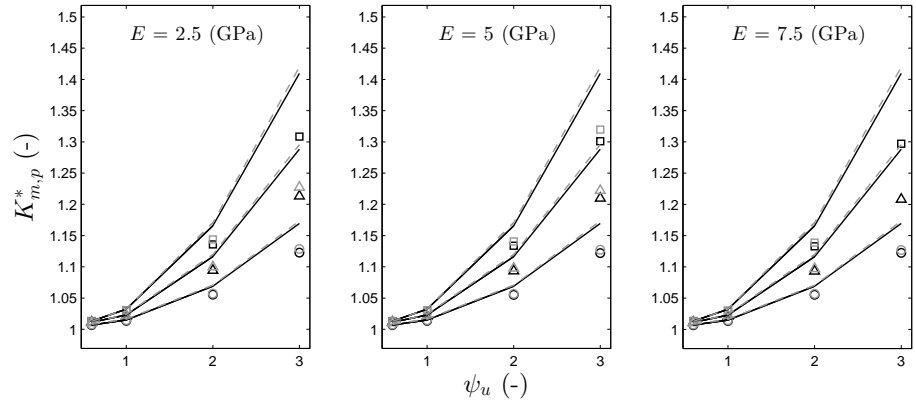
Figure 7.8 presents the major principal stress σ_1 profiles at the weld toes of the longitudinal butt welded joint of steel liners embedded in the concrete–rock system are presented. In the subplots of the left column, one can observe the results in steel liners with peaking imperfections. The larger is ψ_u , the larger are the bending stresses yielding additional tension at the internal fiber. Unlike peaking and out-of-roundness, linear misalignment does not induce a symmetrical effect on the stress profiles at the weld toes, as shown on the subplots of the right column. The larger e/t_s , the larger the additional tensile stresses at the left weld toe at the internal fiber, where the maximum major principal stress occur with the geometrical convention adopted herein.

¹Two symbols for $\psi_u = 3$ are missing because of convergence issues of the FE model that were not resolved in the scope of this study.

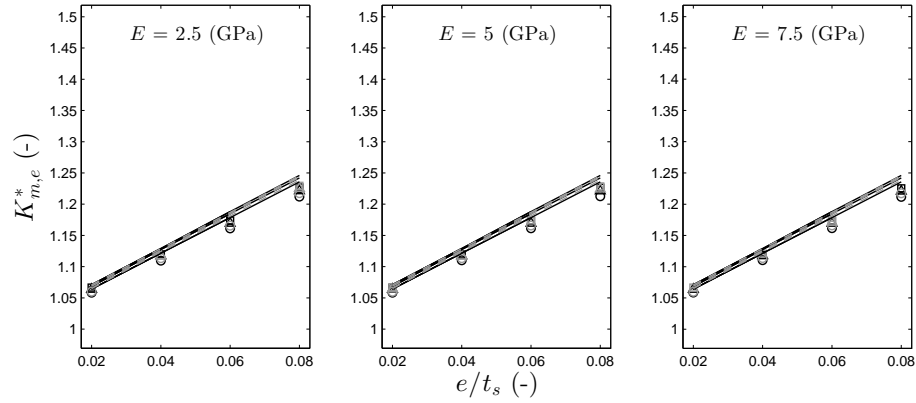
7.3. Parametric study



(a) Structural SCF $K_{m,\eta}^*$ as a function of the out-of-roundness factor ψ_η .



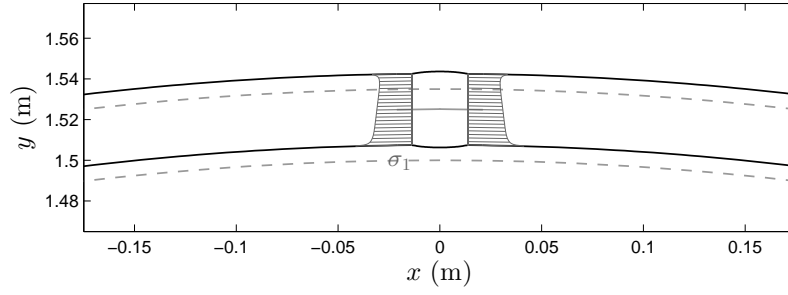
(b) Structural SCF $K_{m,p}^*$ as a function of the peaking factor ψ_u .



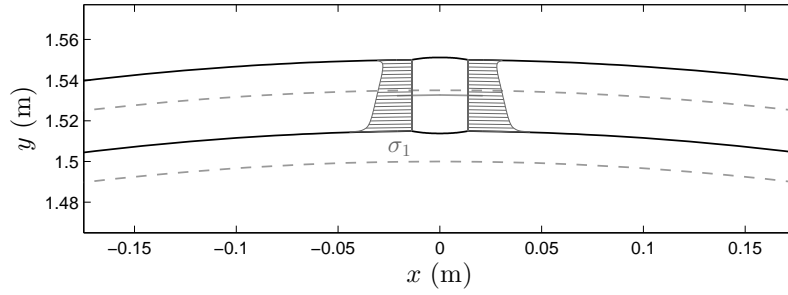
(c) Structural SCF $K_{m,e}^*$ as a function of the relative eccentricity e/t_s .

Embedded steel liner: (○) $r_i/t_s = 100$ (△) $r_i/t_s = 60$ (□) $r_i/t_s = 43$;
 Black symbols: $r_i = 1.5$ m; Gray symbols: $r_i = 2.5$ m
 Black solid lines (—): FE results in open-air steel liners for $r_i = 1.5$ m
 Gray dashed lines (---): FE results in open-air steel liner for $r_i = 2.5$ m

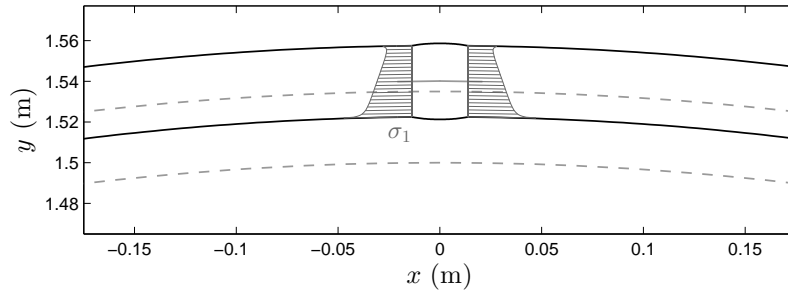
Figure 7.6: Structural SCF from FEA as a function of the magnitude of the corresponding geometrical imperfections for different lowest rock moduli E' , and for $\sigma_{\text{nom}} = 300$ MPa.



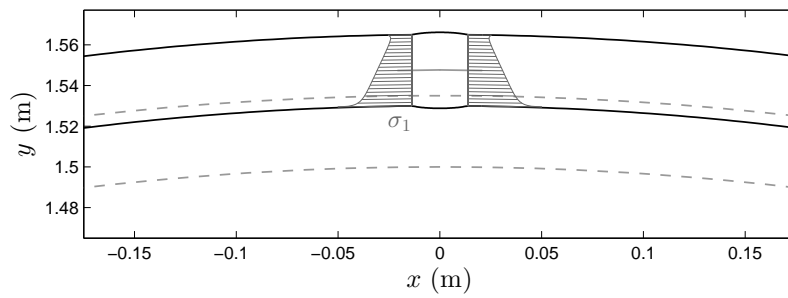
(a) $\psi_\eta = 0.5$ (open-air steel liner).



(b) $\psi_\eta = 1.0$ (open-air steel liner).



(c) $\psi_\eta = 1.5$ (open-air steel liner).



(d) $\psi_\eta = 2.0$ (open-air steel liner).

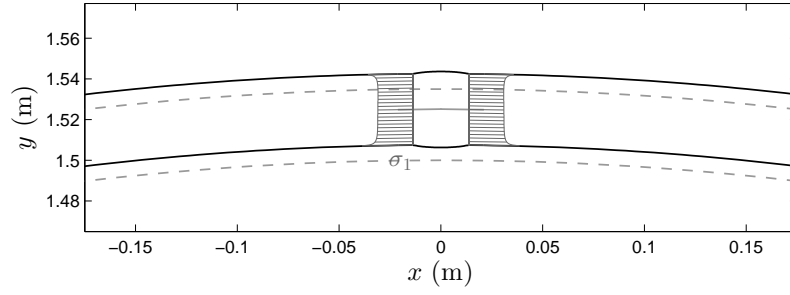
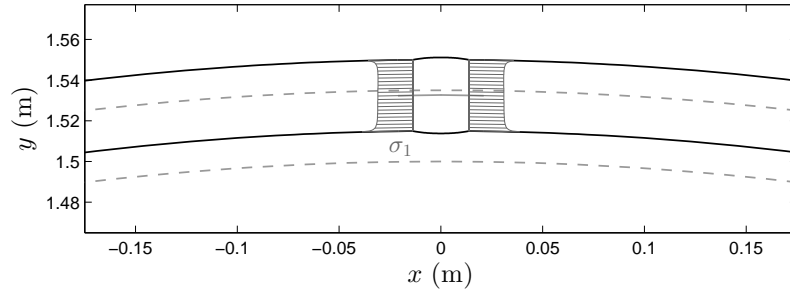
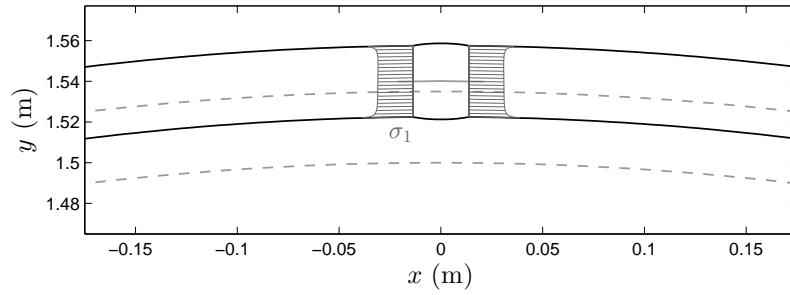
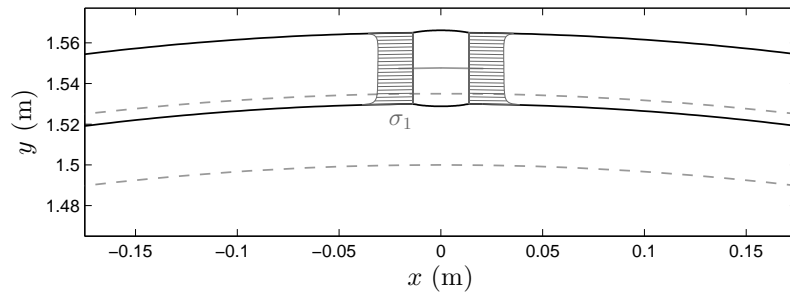
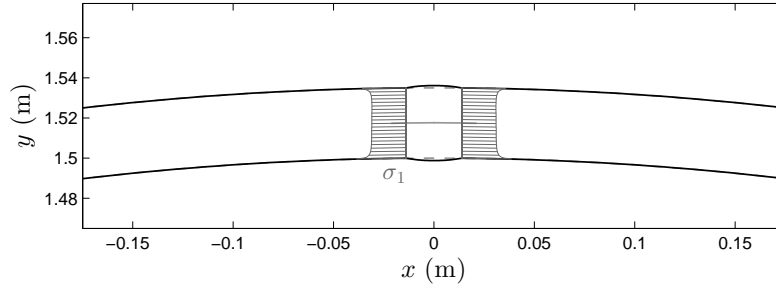
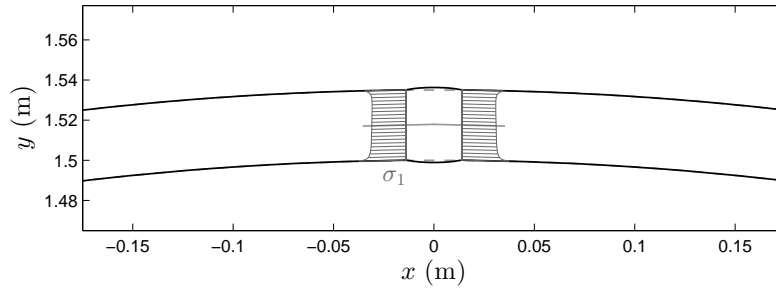

(e) $\psi_\eta = 0.5$ (steel-lined pressure tunnel).

(f) $\psi_\eta = 1.0$ (steel-lined pressure tunnel).

(g) $\psi_\eta = 1.5$ (steel-lined pressure tunnel).

(h) $\psi_\eta = 2.0$ (steel-lined pressure tunnel).

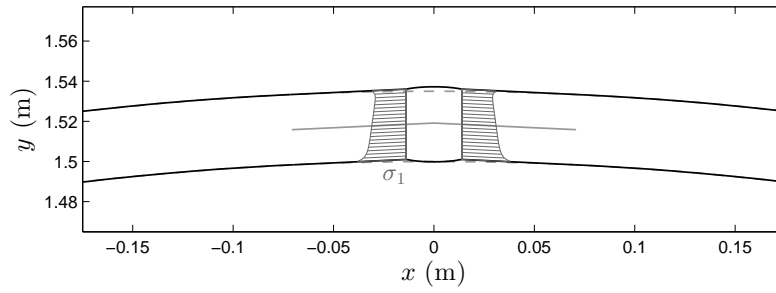
Figure 7.7: Major principal stress profiles at weld toes in steel liners ($r_i = 1.5$ m and $t_s = 35$ mm) with out-of-roundness in open-air (a, b, c, d) and embedded in isotropic rock of elastic modulus $E = 5$ GPa (e, f, g, h). The gray solid lines (—) on the mean axis of the steel liners represent the length of the straight edges, and the gray dashed lines (---) are the circular internal and external fibers. The stress profiles are scaled so that $t_s/2$ represents the magnitude of the membrane stress σ_m in the xy plan.



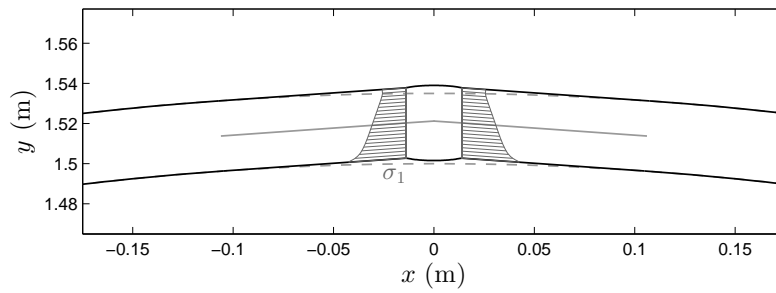
(a) $\psi_u = 0.6$.



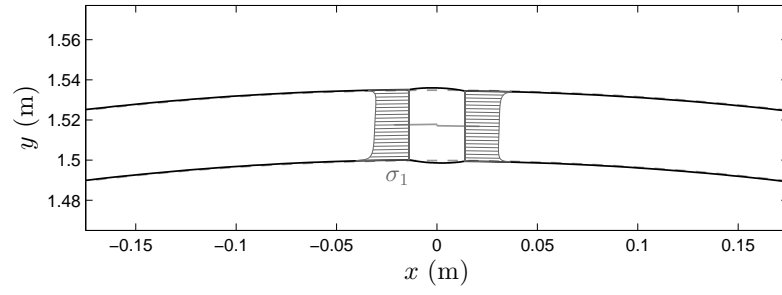
(b) $\psi_u = 1.0$.



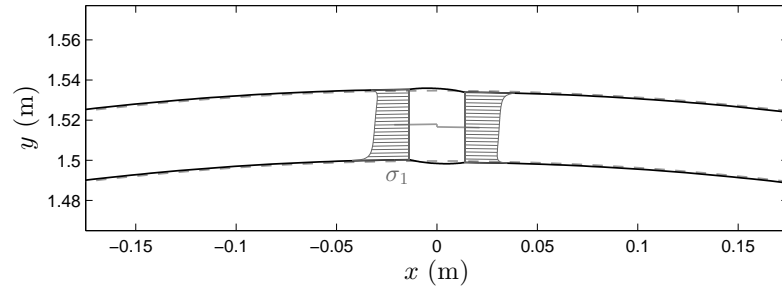
(c) $\psi_u = 2.0$.



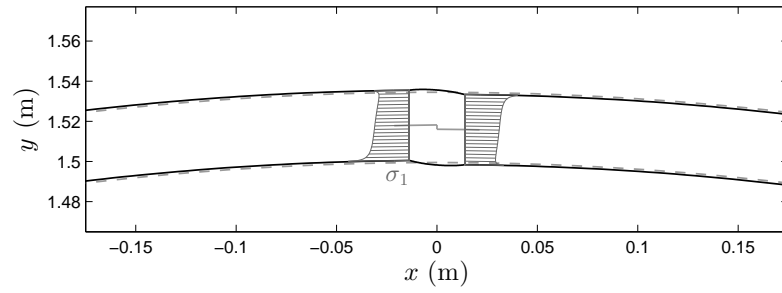
(d) $\psi_u = 3.0$.



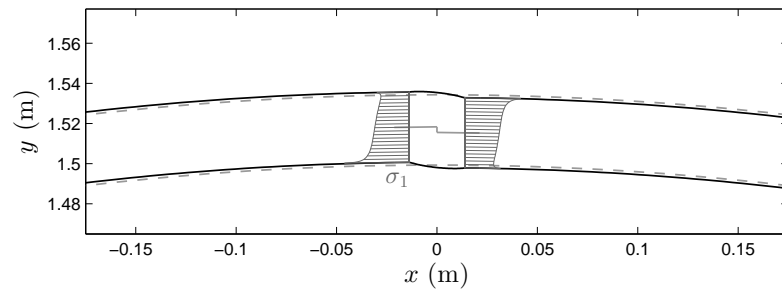
(e) $e/t_s = 0.020$ ($\psi_e = 0.41$).



(f) $e/t_s = 0.040$ ($\psi_e = 0.82$).



(g) $e/t_s = 0.060$ ($\psi_e = 1.24$).



(h) $e/t_s = 0.080$ ($\psi_e = 1.65$).

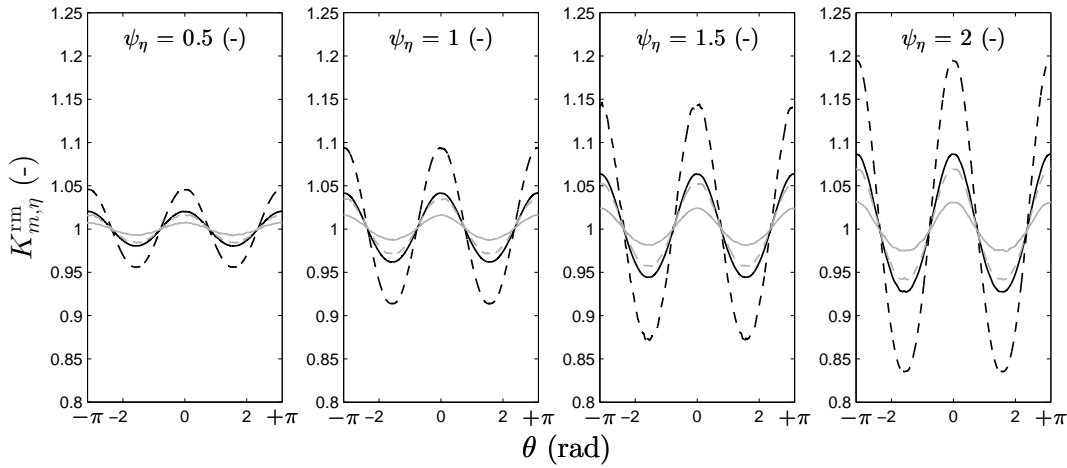
Figure 7.8: Major principal stress profiles at weld toes in steel liners ($r_i = 1.5$ m and $t_s = 35$ mm) with peaking defects (a, b, c, d) and linear misalignment defects (e, f, g, h) considering the interaction with isotropic rock of elastic modulus $E = 5$ GPa. The gray solid lines (—) on the mean axis of the steel liners represent the length of the straight edges, and the gray dashed lines (---) are the circular internal and external fibers. The stress profiles are scaled so that $t_s/2$ represents the magnitude of the membrane stress σ_m in the xy plan.

7.3.3 Pressure transmitted to the far-field surrounding rock mass

The mitigation of the effects of the embedment on the geometrical imperfections on the structural SCF in the steel liners has the counter effect of increasing the stresses transmitted to the far-field rock.

For peaking and linear misalignment, an increase of the major principal stresses in the far-field rock at $r = r_{rm}$ is observed only locally, in the same circumferential location than the longitudinal welded joint. They are not presented herein for the sake of concision. For $\psi_u = 3$ or $e/t_s = 0.08$, the local increase can be up to 10%.

Figure 7.9 presents the influence of the out-of-roundness of the steel liner on the correction coefficient $K_{m,\eta}^{rm}$ at the circumference of the far-field rock mass at $r = r_{rm}$. It can be observed that the far-field rock has to withstand increased major principal stresses at the circumferential location of the largest radii of the elliptic steel liners, up to 20% for $\psi_u = 2$.



Black solid lines (—): $r_i/t_s = 100$, $E = 2.5$ GPa; Gray solid lines (—): $r_i/t_s = 100$, $E = 7.5$ GPa
Black dashed lines (- -): $r_i/t_s = 43$, $E = 2.5$ GPa; Gray dashed lines (- -): $r_i/t_s = 43$, $E = 7.5$ GPa

Figure 7.9: Correction coefficient at far-field rock $K_{m,\eta}^{rm}$ as a function of the circumferential location θ for different out-of-roundness factors ψ_η .

7.3.4 Remarks on the initial gap

As aforementioned, the systematic parametric study was performed with a closed initial gap $\Delta r_0 = 10^{-6} \cdot r_i$. This choice was made in order to reach a faster convergence and thus reasonable time consuming simulations in the scope of this study. However, several simulations were run changing the initial gap to values as observed in practice such as $\Delta r_0 = 0.010\text{--}0.025\%$ of r_i , adapting p_i to obtain the same nominal stress σ_{nom} . No difference has been obtained in the SCF, either in isotropic or anisotropic rocks, for every type of imperfections. As a consequence, the

initial gap can be included directly in the computation of σ_{nom} if assumed constant along the circumference.

7.4 Derivation of parametric equations

This section aims at deriving parametric equations for both structural and notch SCF at longitudinal butt welded joints of SLPT&S, that can be used by designers for fatigue life estimation by means of local approaches as well as for estimating the maximum equivalent stress to be considered for the working stress criterion in the steel liner (Schleiss 1988). To fit the coefficients and exponents of the parametric equations proposed in the following, a database of 161 simulations' results was built. Only the worst combinations of geometrical imperfections and rock anisotropy were considered, i.e., the longitudinal welded joints are located at the circumferential direction of the largest axis of the elliptic liner ($\Psi = 0$ in Eq. 3.53) and the isotropic plane is in the yz plan (see also Fig. 7.2a). This assumption was verified a posteriori in some cases to exclude some unexpected behavior leading to higher SCF.

The design of the simulations was performed varying 15 parameters covering arbitrarily a large extent of cases. The ranges of variation of the parameters are detailed in Table 7.1. One can see that the out-of-roundness, the linear misalignment and the weld reinforcement were tested until 150% of the tolerance given by C.E.C.T. (1980). The peaking Δh induced by ψ_u , however, was not tested compared to the tolerance as it does not produce per se a significant amount of roof-topping. As a consequence, straight edges' lengths l_u were tested until $\psi_u = 2.0$ only, which is already quite large in practical applications.

Table 7.1: Variation ranges (minimum and maximum values) of the parameters for the 161 simulations used to derive structural and notch SCF at longitudinal butt welded joints of SLPT&S.

r_i (m)	t_s (mm)	ψ_δ (-)	ψ_e (-)	ψ_η (-)	ψ_u (-)	β (deg)	α (deg)
1.5	15	0.1	0.0	0.0	0.6	5	45
2.5	45	1.5	1.5	1.5	2.0	30	80

E (GPa)	ν (-)	E/E' (-)	G'/G'_{S-V} (-)	E_{crm}/E' (-)	t_{crm}/r_i (-)	σ_{nom} (MPa)
2	0.10	1.00	0.80	0.60	0.33	200
20	0.35	3.00	1.20	1.00	0.66	630

The initial gap was set to $\Delta r_0 = 10^{-6} \cdot r_i$ for faster convergence as it does not have any influence on the results, and the Poisson's coefficient ν' of the anisotropic rock was a function of ν as $\nu' = \nu E'/E$. The weld toes' radius was fixed to the so-called *reference radius* $\rho = r_{\text{ref}} = 1$ mm, effective radius for steels according to the Neuber concept of fictitious notch rounding (Radaj *et al.* 2013) and current recommendation of the IIW for the application of the notch stress approach

Chapter 7. Stress concentration at longitudinal butt welded joints of steel liners

for fatigue assessment (Hobbacher 2008, 2016; Fricke 2012). The other parameters were kept constant as aforementioned. The conceptual models and the results are presented in the following sections.

7.4.1 Structural SCF at the longitudinal butt welded joints for major principal stresses

A structural SCF denoted K_m^* is defined, characterizing the structural stress concentration at the longitudinal butt welded joints considering the interaction with the concrete–rock system. The structural stress σ_s is thus related to the nominal stress σ_{nom} as

$$\sigma_s = K_m^* \sigma_{\text{nom}} \quad (7.11)$$

where

$$\sigma_{\text{nom}} = \sigma_{\text{nom,iso}} K_{\text{rm,aniso}}^* \quad (7.12)$$

and

$$K_m^* = [1 + (K_{m,e}^* - 1) + (K_{m,p}^* - 1)] . \quad (7.13)$$

One may note that although the out-of-roundness was simulated, the influence of η is not considered in the proposed conceptual model, accordingly to the observations made in Sect. 7.3. $K_{m,p}^*$ and $K_{m,e}^*$ are defined by introducing a constraint coefficient α_i in Eqs. 3.54 and 3.56 as

$$K_{m,p}^* = 1 + \frac{3\alpha_1 \Delta h}{t_s(1 - \nu_s^2)} \cdot \frac{\tanh(\phi/2)}{\phi/2} \quad (7.14)$$

and

$$K_{m,e}^* = 1 + \frac{3\alpha_2 e}{t_s(1 - \nu_s^2)} . \quad (7.15)$$

The constraint coefficients α_1 and α_2 were fitted by means of genetic algorithm (GA), with a *training group* of 80% of the results and a *test group* with the other 20%. The separation was

performed by random sampling. The objective function was defined as

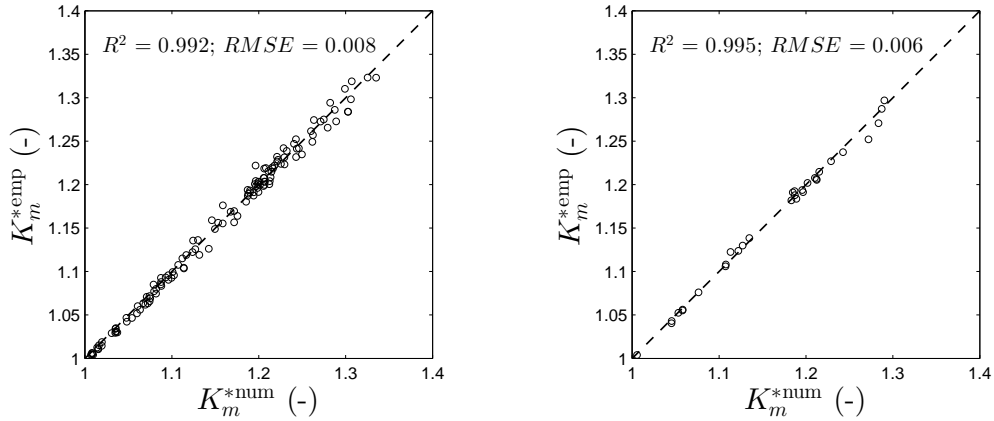
$$\hat{\alpha} = \underset{\alpha}{\operatorname{argmin}} \operatorname{MSE} [K_m^{*\text{num}}, K_m^{*\text{emp}}(\alpha)] \quad (7.16)$$

where MSE is the mean squared error, and $\hat{\alpha} = \{\alpha_1, \alpha_2\}$ is the argument of the minimum. $K_m^{*\text{num}}$ contains the values of the structural SCF obtained by finite elements analysis (FEA), and $K_m^{*\text{emp}}$ contains the corresponding values computed via Eq. 7.11. The following α_i coefficients were obtained:

$$\hat{\alpha} = \{1.05, 0.87\}. \quad (7.17)$$

Although the derived α_i coefficients do not characterize a significant change, one may note that their values does not correspond to the trend depicted in Sect. 7.3 (see also Fig. 7.6). This result could be due to the interaction effect between the studied geometrical imperfections (which have been studied separately in Sect. 7.3). A more extensive parametric study considering interactions between the geometrical imperfections should be conducted, but it was out of the scope of this project.

The regression between the empirical and the numerical structural SCF K_m^* are shown in Fig. 7.10a for the training group, and in Fig. 7.10b for the test group. One can observe very good coefficients of determination R^2 , with low root mean squared error RMSE.



(a) Numerical structural SCF $K_m^{*\text{num}}$ obtained by FEA vs. the empirical $K_m^{*\text{emp}}$ fitted by GA ($\alpha_1 = 1.05$ and $\alpha_2 = 0.87$) (training group).

(b) Numerical structural SCF $K_m^{*\text{num}}$ obtained by FEA vs. the empirical $K_m^{*\text{emp}}$ fitted by GA ($\alpha_1 = 1.05$ and $\alpha_2 = 0.87$) (test group).

Figure 7.10: Regression plots of the numerical results vs. the empirical results fitted by GA.

7.4.2 Notch SCF at longitudinal butt welded joints for major principal stresses

Similarly to the structural SCF, a notch SCF K_t^* is defined, characterizing the maximum notch stress concentration at the longitudinal butt welded joints' toes considering the interaction with the concrete–rock system, relating the notch stress σ_n to σ_{nom} as

$$\sigma_n = K_t^* \sigma_{nom} \quad (7.18)$$

with

$$K_t^* = K_m^* K_w \quad (7.19)$$

where K_w is the notch SCF due to the weld geometry. It is defined under the form of Eq. 6.6, and as presented in Chapter 6 using the same approach to model the weld geometry:

$$K_w = 1 + \alpha_0 \left(\frac{\delta}{t_s} \right)^{\alpha_1} \left(\frac{\rho}{t_s} \right)^{\alpha_2} \tan \left(\frac{\beta}{2} \right)^{\alpha_3} \quad (7.20)$$

where the α_i are coefficients that were fitted using the same procedure than previously described, yielding:

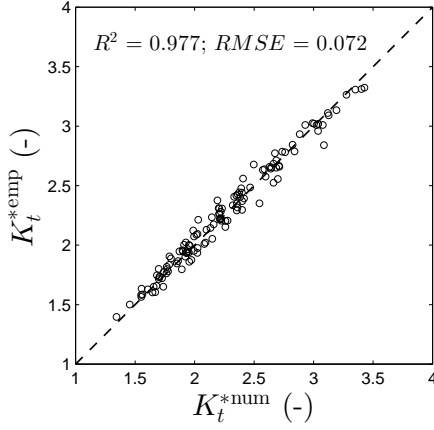
$$\hat{\alpha} = \{1.08, 0.24, -0.41, 0.41\}. \quad (7.21)$$

The regression plots are shown in Figs. 7.11a and 7.11c for the training groups. The test groups are in Figs. 7.11b and 7.11d. A very good correlation between the FEA and the empirical formula can be observed.

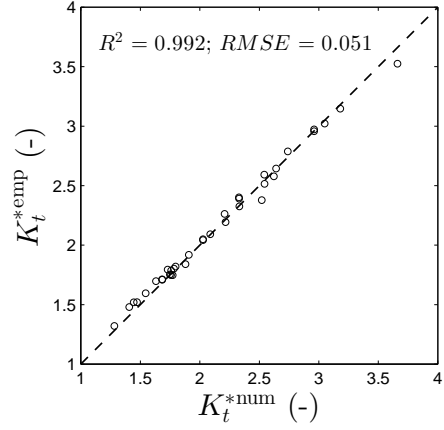
7.4.3 Extrapolation to equivalent stresses

The equivalent stresses concentrations at longitudinal butt welded joints may also be of interest. The SCF K_t^* previously defined can be applied to obtain the equivalent notch stress $\sigma_{n,eq}$ as

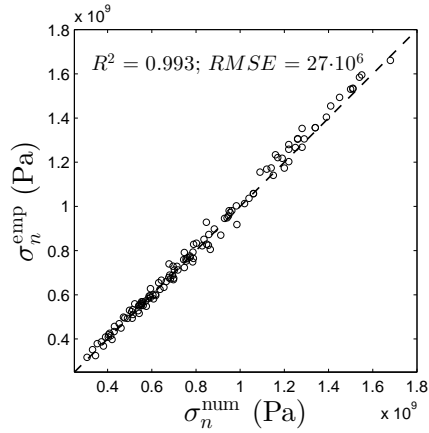
$$\sigma_{n,eq} = K_t^* \sigma_{nom,eq}. \quad (7.22)$$



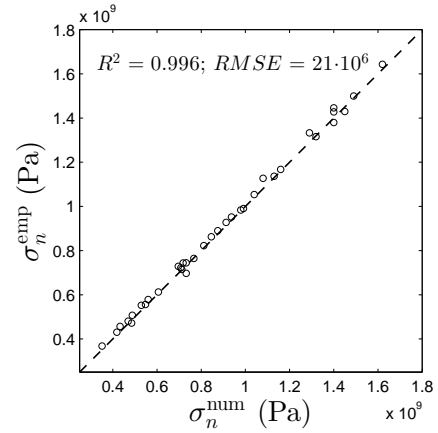
(a) Numerical notch SCF K_t^{*num} obtained by FEA vs. the empirical K_t^{*emp} fitted by GA ($\alpha_0 = 1.08$, $\alpha_1 = 0.24$, $\alpha_2 = -0.41$ and $\alpha_3 = 0.41$) (training group).



(b) Numerical notch SCF K_t^{*num} obtained by FEA vs. the empirical K_t^{*emp} fitted by GA ($\alpha_0 = 1.08$, $\alpha_1 = 0.24$, $\alpha_2 = -0.41$ and $\alpha_3 = 0.41$) (test group).



(c) Numerical notch stresses σ_n^{num} obtained by FEA vs. the empirical σ_n^{emp} fitted by GA ($\alpha_0 = 1.08$, $\alpha_1 = 0.24$, $\alpha_2 = -0.41$ and $\alpha_3 = 0.41$) (training group).



(d) Numerical notch stresses σ_n^{num} obtained by FEA vs. the empirical σ_n^{emp} fitted by GA ($\alpha_0 = 1.08$, $\alpha_1 = 0.24$, $\alpha_2 = -0.41$ and $\alpha_3 = 0.41$) (test group).

Figure 7.11: Regression plots of the numerical results vs. the empirical results fitted by GA.

Chapter 7. Stress concentration at longitudinal butt welded joints of steel liners

In Eq. 7.22, K_t^* is defined by Eq. 7.19, with the same fitted coefficients. The nominal equivalent stress $\sigma_{\text{nom,eq}}$ can be computed as

$$\sigma_{\text{nom,eq}} = \sigma_{\text{nom,eq,iso}} K_{\text{rm,eq,aniso}}^* \quad (7.23)$$

where

$$K_{\text{rm,eq,aniso}}^* = \frac{\sigma_{\text{nom,eq,aniso}}}{\sigma_{\text{nom,eq,iso}}}, \quad (7.24)$$

which can be computed by the empirical equation proposed in Chapter 5. Eq. 7.22 was applied to all the results obtained by FEA. The regression is shown in Fig. 7.12, where a very good agreement can be observed between the FE results and the empirical equation.

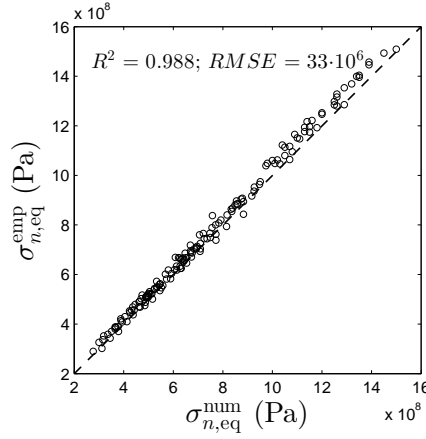


Figure 7.12: Numerical equivalent notch stresses $\sigma_{n,\text{eq}}^{\text{num}}$ obtained by FEA vs. the empirical $\sigma_{n,\text{eq}}^{\text{emp}}$ obtained via Eq. 7.22.

7.4.4 Application examples

The application of the proposed parametric equations is illustrated through four examples with realistic parameters as shown in Table 7.2a. The relevant results are presented in Table 7.2b, where the errors e are computed as

$$e_{\text{SCF}} = \frac{\text{SCF}^{\text{num}} - \text{SCF}^{\text{emp}}}{\text{SCF}^{\text{num}}}. \quad (7.25)$$

One can observe the good accuracy of the proposed parametric equations. Particular attention may be paid to cases 3 and 4, which are identical except for the initial gap Δr_0 , which does not

Table 7.2: (a) Parameters and (b) results for the application examples.

(a) Parameters of the application examples. For all cases, $\rho = r_{\text{ref}} = 1 \text{ mm}$, $G'/G'_{S,V} = 1.00$, $\nu = 0.10$, $\nu' = \nu E'/E$ and $E_{\text{erm}}/E' = 0.80$.

Case n°	r_i (m)	t_s (mm)	ψ_η (-)	ψ_u (-)	δ/t_s (-)	e/t_s (-)	β (deg)	α (deg)	E (GPa)	E/E' (-)	t_{erm}/r_i (-)	$\Delta r_0/r_i$ (%)	p_i (MPa)
1	2.25	35	0.00	1.80	0.030	0.039	10	50	8.00	2.00	0.33	0.000	9.50
2	2.00	30	1.00	1.50	0.041	0.059	18	60	12.00	2.50	0.50	0.000	10.00
3	1.50	25	0.00	1.20	0.027	0.000	8	60	8.00	2.00	0.33	0.010	8.00
4	1.50	25	0.00	1.20	0.027	0.000	8	60	8.00	2.00	0.33	0.000	8.00

(b) Results of the application examples.

Case n°	$\sigma_{\text{nom}}^{\text{num}}$ (MPa)	$K_m^{\text{*num}}$ (-)	$K_m^{\text{*emp}}$ (-)	$K_f^{\text{*num}}$ (-)	$K_f^{\text{*emp}}$ (-)	σ_s^{num} (MPa)	σ_s^{emp} (MPa)	σ_n^{num} (MPa)	σ_n^{emp} (MPa)	$e_{K_f^*}$ (%)	e_{σ_s} (%)	e_{σ_n} (%)
1	310	1.21	1.20	2.13	2.08	367	371	645	644	1.0	2.5	-1.2
2	311	1.23	1.23	2.46	2.39	378	381	757	744	0.2	2.8	-0.9
3	262	1.05	1.04	1.57	1.63	269	272	405	427	0.5	-4.1	-1.2
4	252	1.05	1.04	1.58	1.63	258	262	388	411	0.5	-3.4	-1.7

influence the accuracy of the prediction.

7.5 Application limits

Some assumptions made in this chapter are discussed hereafter.

1. Three geometrical imperfections were investigated, namely the out-of-roundness, peaking and linear misalignment. Peaking was considered due to straight edges at the longitudinal butt welded joints, resulting from the rolling process. However, the tolerance given by C.E.C.T. (1980) (Eq. 7.2) can also refer to flattening imperfections adjacent to the welds, inducing a shift of the mean axis of the steel liner inward the perfectly circular shape. Although this is an important issue for buckling analysis, this geometrical defect was not treated herein. Under internal pressure, it is expected to create bending stresses yielding compression at the internal fiber of the steel liner, where all maximum SCF occur for the studied imperfections. For future research, the influence of this defect at the external fiber of the longitudinal welded joints, relatively to the other imperfections, should be investigated. Some cases may shift the maximum SCF at the external fiber, which could become critical for fatigue life estimation.
2. Notch SCF were only proposed for constant weld toe radii $\rho = r_{\text{ref}} = 1 \text{ mm}$. If one needs to evaluate K_t^* for other radii (e.g., for the use of other local approaches, or future refinements of the notch stress approach), K_w in Eq. 7.19 can be substituted by the parametric equations proposed in Chapter 6 as a reasonable approximation.

7.6 Conclusions

Several published formulas for SCF in steel-lined structures were reported in Sect. 3.8. Geometrical imperfections such as linear misalignment, peaking or out-of-roundness are treated, but the interaction with surrounding materials, to the best author's knowledge, was never studied. In this chapter, the influence of the contact with the backfill concrete–rock system on the SCF at the longitudinal butt welded joints of steel liners was investigated.

The main result is that the effect of out-of-roundness is completely vanished under the effect of embedment. Therefore, only the effects of peaking and linear misalignment remain. To provide designers with fast computational tools to estimate SCF at the longitudinal butt welded joints of SLPT&S, some published expressions have been modified to compute structural and notch SCF accounting for the interaction with the concrete–rock system.

Crack-like flaws at longitudinal butt welded joints of steel liners

Part IV

Iron may be stronger than a tree, but this impression of strength may be misleading since the products of the art of forging are not as safe as the trees produced by mother nature.

– Cristopher Polhem (1661–1751),
reported by Jonsson (2011).

8 Stress intensity factors (SIF) for axial cracks in the weld material

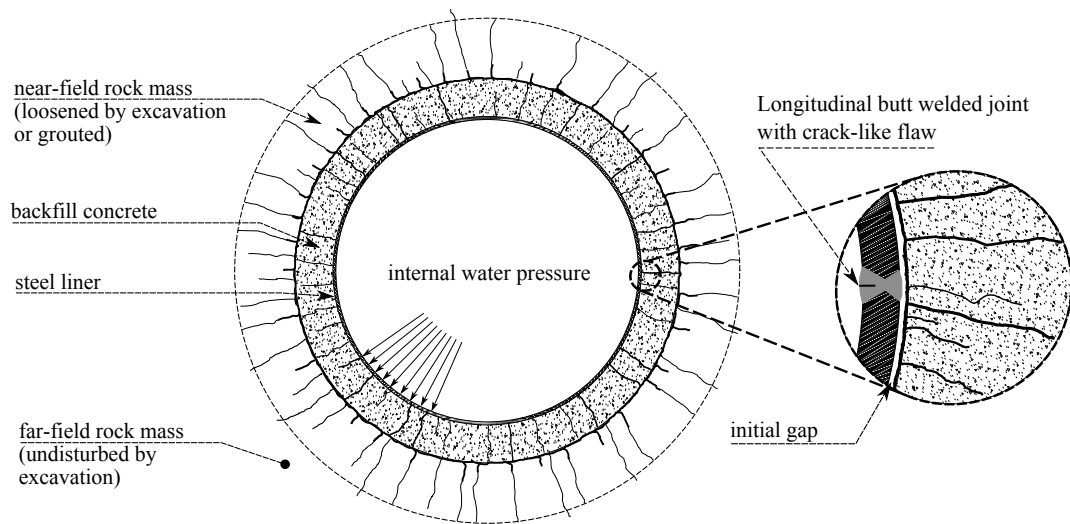


Figure 8.1: Definition sketch of the standard multilayer system for SLPT&S. The longitudinal butt welded joint is emphasized in the upper right corner, with an axial surface crack in the weld material.

8.1 Types of studied cracks

In this chapter, SIF are studied by means of the finite element method (FEM) for two types of cracks at the longitudinal butt welded joints of steel liners (see Fig. 8.1), namely:

1. semi-elliptical surface cracks (Fig. 8.2); and
2. embedded elliptical cracks (with $d_1 = d_2 = t_s/2$, see Fig. 8.3).

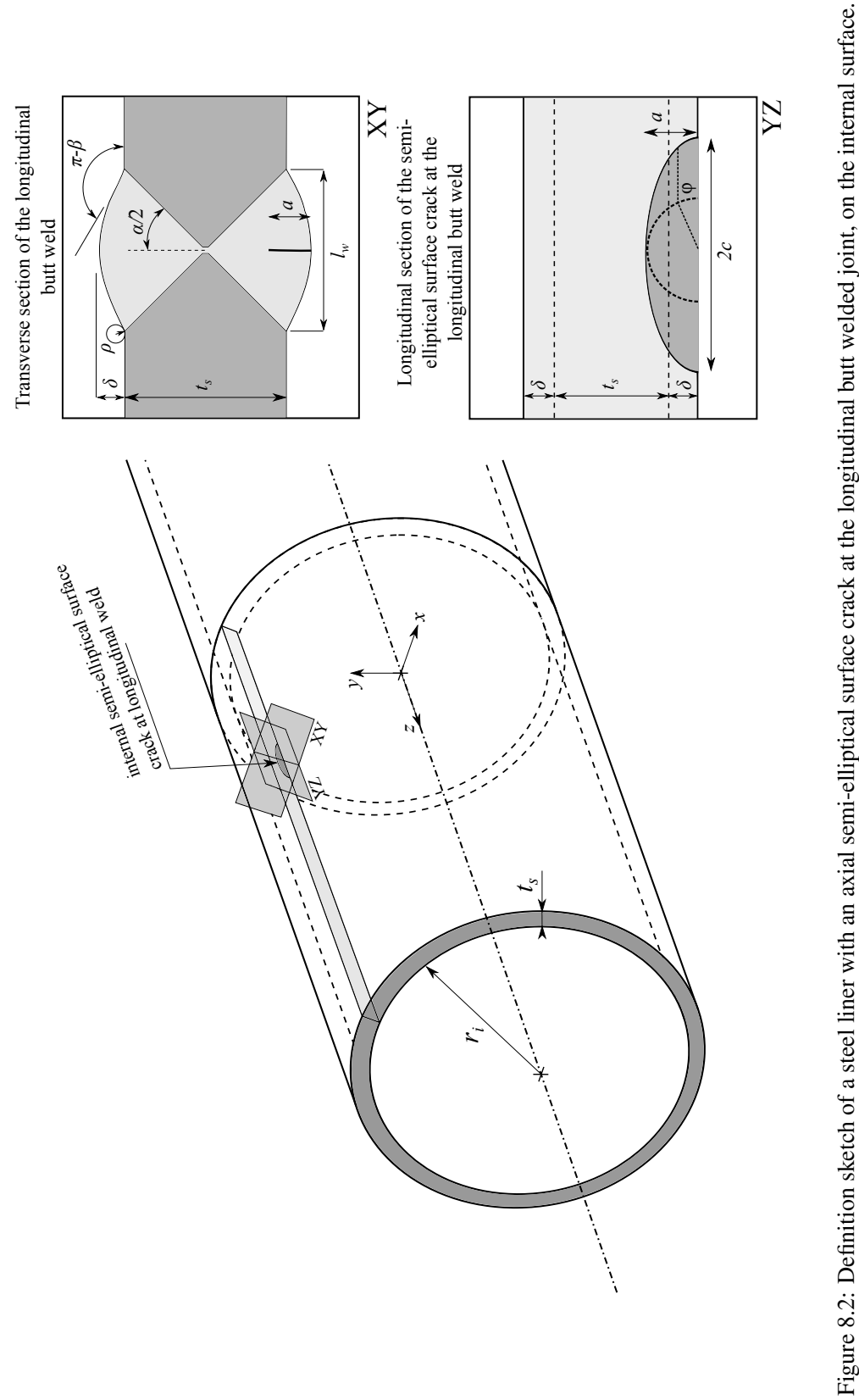


Figure 8.2: Definition sketch of a steel liner with an axial semi-elliptical surface crack at the longitudinal butt welded joint, on the internal surface.

8.2. Definition of weld shape correction factor M_w for axial cracks at longitudinal butt welded joints of SLPT&S

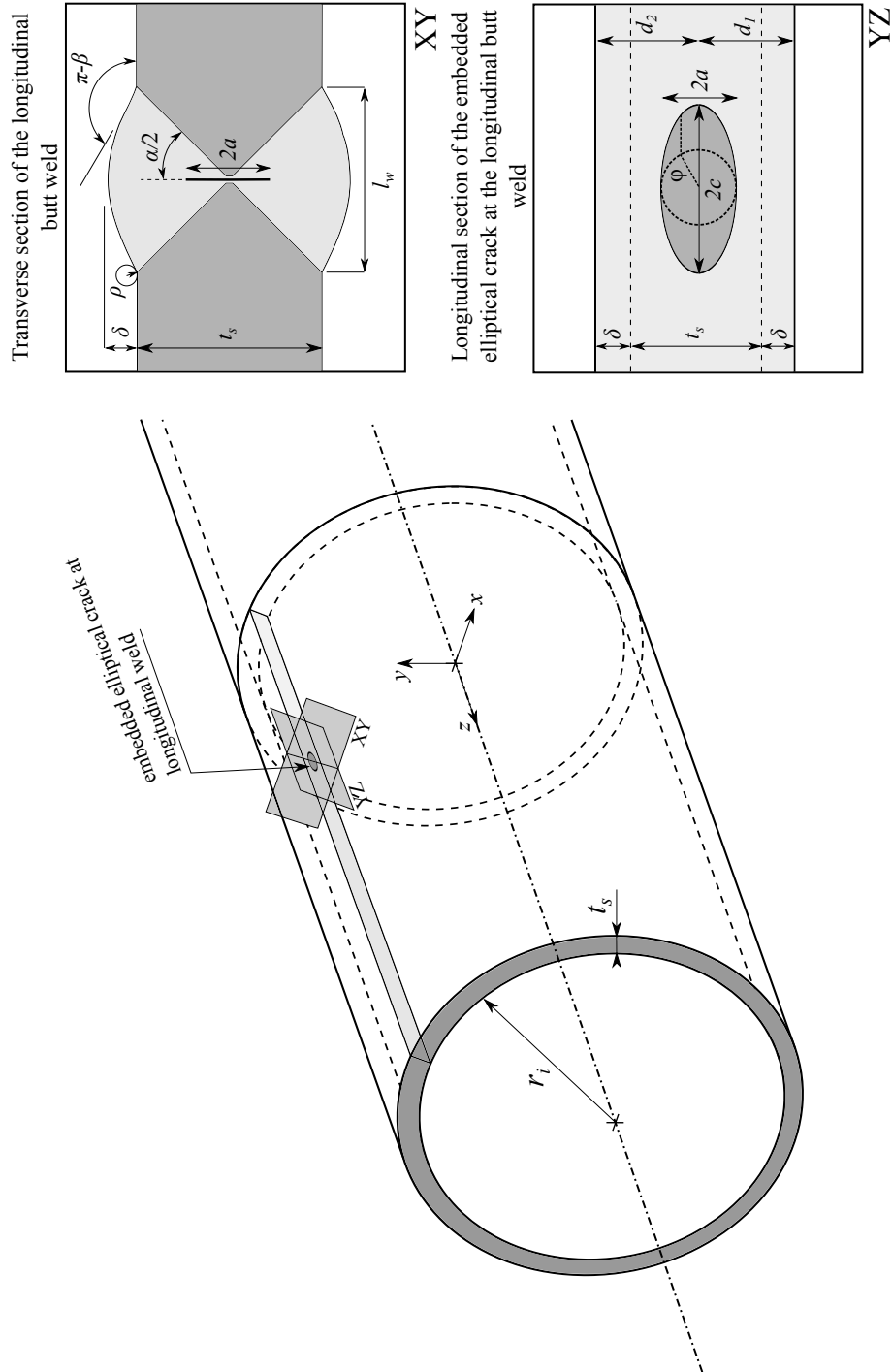


Figure 8.3: Definition sketch of a steel liner with an axial embedded elliptical crack at the longitudinal butt welded joint.

8.2 Definition of weld shape correction factor M_w for axial cracks at longitudinal butt welded joints of SLPT&S

8.2.1 Membrane and bending stresses in steel liners of pressure tunnels and shafts

Nominal stress in anisotropic rock

SLPT&S embedded in anisotropic rock (in the special case of transverse isotropy) were studied in Part II. Empirical correction factors included in the analytical closed-form solution in isotropic rock were derived, allowing to estimate maximum major principal stresses in the steel liners. It was found that the influence of transversally isotropic rock on steel liners is mainly to change the nominal stress, inducing negligible bending stresses. The latter can be neglected when studying SCF at the longitudinal butt welded joints in the worst case scenario when the joint is located in the area of maximum major principal stresses, as considered in Chapter 7.

In Chapter 7, a correction coefficient denoted $K_{rm,aniso}^*$ accounting for the change of nominal stress due to anisotropic rock behavior was defined and expressed as

$$\sigma_{nom,aniso} = K_{rm,aniso}^* \sigma_{nom,iso} \quad (8.1)$$

where $\sigma_{nom,aniso}$ is the corrected nominal stress when the steel liner is in anisotropic rock, and $\sigma_{nom,iso}$ is the nominal stress obtained through the analytical closed-form solution in isotropic rock (with the steel liner considered with the thick-walled pipe theory, i.e., the nominal stress is defined as the maximum stress at the internal fiber). The superscript * stands for the interaction with the rock mass.

Geometrical imperfections

As described in detail in Chapter 7, steel liners of SLPT&S are subject to unavoidable geometrical imperfections that may raise stress concentrations, particularly at the welds. The most important are recalled hereafter.

1. *Out-of-roundness* (or ovality), which is characterized by a deviation η from the perfectly circular shape due to the erection process, transportation or welding methods. The resulting elliptical shape of the liner is illustrated in Fig. 8.4.
2. *Peaking* (or roof-topping), which is induced by two straight edges of length l_u inherent to the rolling process of the original manufactured plates. It yields a radial deviation Δh from the perfectly circular shape at the longitudinal butt welded joint, as shown in Fig. 8.4.
3. *Axial misalignment* (or eccentricity), which is characterized by an eccentricity between the mean axes of the welded plates.

8.2. Definition of weld shape correction factor M_w for axial cracks at longitudinal butt welded joints of SLPT&S

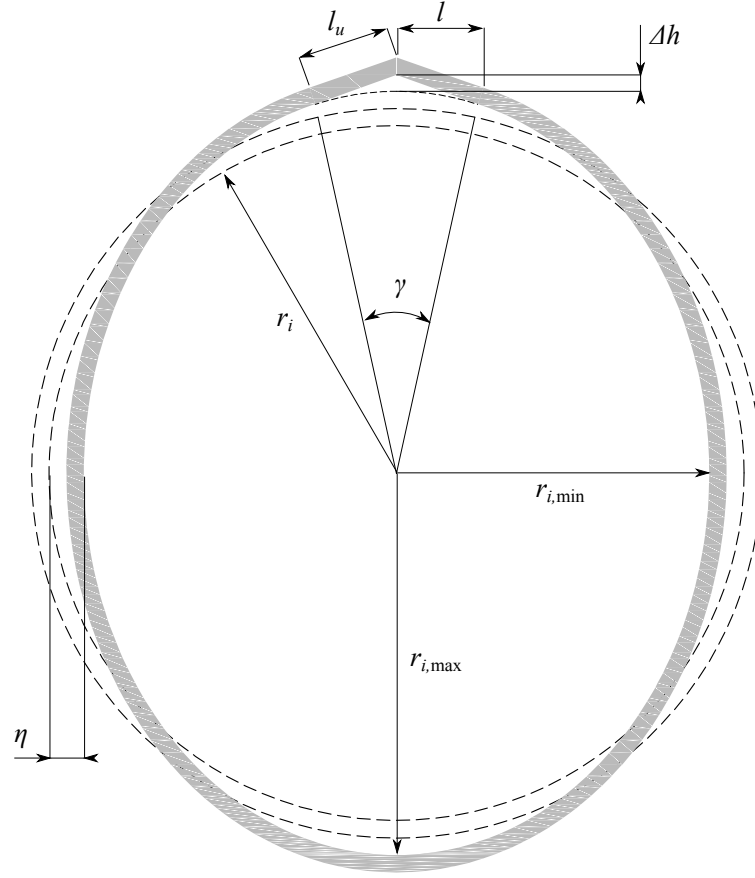


Figure 8.4: Definition sketch of the geometrical imperfections of pressure tunnels and shafts. The geometrical imperfections and the thickness of the liner are magnified for presentation purposes.

Influence of the concrete–rock system

The structural SCF at longitudinal butt welded joints of steel liners considering the interaction with the surrounding concrete–rock system was studied in Chapter 7. It was found that the structural stress concentration due to the out-of-roundness vanishes because of the embedment, while the influence of peaking and linear misalignment remains. Empirical constraint coefficients to be included in published solutions for SCF accounting for the embedment effect were proposed. The obtained structural SCF was denoted K_m^* .

8.2.2 Definition of weld shape correction factor M_w

As aforementioned, structural stresses at longitudinal butt welded joints of steel liners embedded in rock can be estimated by SCF empirical developed in the preceding chapters. The remaining lack of knowledge is thus the weld shape correction factor M_w . As it will be presented below,

Chapter 8. Stress intensity factors (SIF) for axial cracks in the weld material

empirical equations to estimate SIF will only be derived for semi-elliptical surface cracks.

Even if linear misalignment has a great influence on notch SCF at the weld toes and thus on the fatigue growth of cracks emanating from these notches (Ferreira & Branco 1991), it is not expected to have a strong influence on a crack located in the vicinity of the edges of the welded plates in the weld deposit (see Figs. 8.2 and 8.3), as outlined, e.g., by Ho & Lawrence (1984). Indeed, structural stresses induced by an eccentricity between the mean axes of the plates change sign through the weld (see Fig. 7.8). As a consequence, only peaking will be accounted for in this study. For this case, it is proposed to rewrite and complete Eq. 3.58 as

$$K_I = M_w [M_m (\sigma_m + p_{cr}) + M_b \sigma_b] \sqrt{\frac{\pi a}{Q}} \quad (8.2)$$

$$= M_w [M_m (\sigma_{m,iso} K_{rm,aniso}^* + p_{cr}) + M_b \sigma_{m,iso} K_{rm,aniso}^* (K_{m,p}^* - 1)] \sqrt{\frac{\pi a}{Q}}, \quad (8.3)$$

where:

- M_w is the weld shape correction factor to be determined;
- $K_{m,p}^*$ is the structural SCF due to peaking accounting for the interaction with the concrete–rock system (see Chapter 7); and
- the membrane component $\sigma_{m,iso}$ is approximated by the analytical solution in isotropic rock considering the thin-walled pipe theory.

8.3 Finite element model

8.3.1 Conceptual model

Consequently to the discussion conducted in Sect. 8.2, solely the steel liner was modeled herein in order to study semi-elliptical surface cracks and embedded elliptical cracks. Moreover, only peaking was considered, and modeled by two straight edges of length l_u that are tangent to the circular parts of the liner. The so-called angular misalignment angle γ is approximated as $\gamma = 2l_u/r_i$ (rad) to construct the model (see Fig. 8.4). The parameter ψ_u defined in Chapter 7 is used to relate the length of the straight edges l_u to the liner's thickness t_s as

$$l_u = \psi_u t_s. \quad (8.4)$$

For practical applications, ψ_u may typically vary between 0 and 2 with good workmanship. One may note that in this study, no imperfection is approximated to $\psi = 0.6$, because of the weld length.

The geometry of the longitudinal butt welded joints is depicted in Figs. 8.2 and 8.3. The main

parameters are the weld reinforcement height δ , the flank angle β , the edge preparation angle α and the weld toe radius ρ . The weld length l_w is related to the edge preparation angle as (dimensions in mm)

$$l_w = t_s \sin(\alpha/2) + 3 \text{ (mm)} \quad (8.5)$$

where the 3 mm in the right-hand end is the separation between the crimped edges. The geometry of the weld was modeled according to the approach proposed in Part III, namely by the use of splines (BSPLIN command in ANSYS) for the weld reinforcement. Three tangents are imposed at three keypoints, i.e., at the weld toes with an imposed flank angle β , and at the highest point of the reinforcement where the tangent is parallel to the segment linking the two weld toes. More details are given in Appendix A.

8.3.2 Assumptions of the FE model

The geometry of the FE model follows the aforementioned conceptual model. Additional hypotheses are undertaken and listed hereafter.

1. The constitutive law for steel is linear elastic with an elastic modulus $E_s = 210$ GPa and a Poisson's ratio $\nu_s = 0.3$, following the requirement of LEFM to compute SIF.
2. The symmetrical conditions allow modeling only half of the steel liner, as shown in Fig. 8.5.
3. Large-deflections effects are considered when necessary (see Tables 8.1 and 8.2), namely for large surface cracks inducing a deflection at the longitudinal butt welded joint, or for a large geometrical imperfection, in order to avoid inconsistent results.
4. The boundary conditions are shown in Fig. 8.5 (also used, e.g., by Kou & Burdekin 2006). As SLPT&S are very long structures in the z direction, plane strain conditions are assumed. To impose pseudo-plane strain conditions in 3D, the nodes on the xy planes of the two extreme sections of the steel liner were constrained in the z direction.
5. The length of the FE model along the z direction should be large enough so that there is no length effects on the results along the crack. Newman Jr & Raju (1980) and Raju & Newman Jr (1982) used for instance $10 \times c$. In this study several cases were tested and it was found that $3 \times c$ already ensures a satisfying convergence (threshold at 1%). For the sake of fast computational time, the dimension of the model along the z direction was thus set to $3 \times c$.

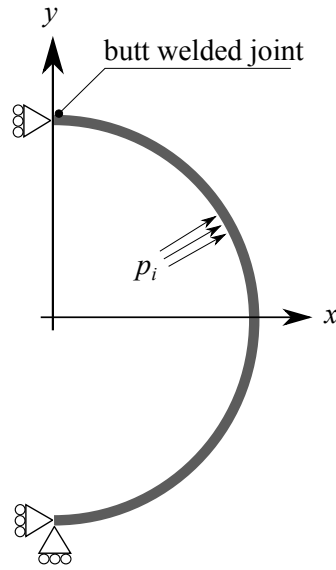
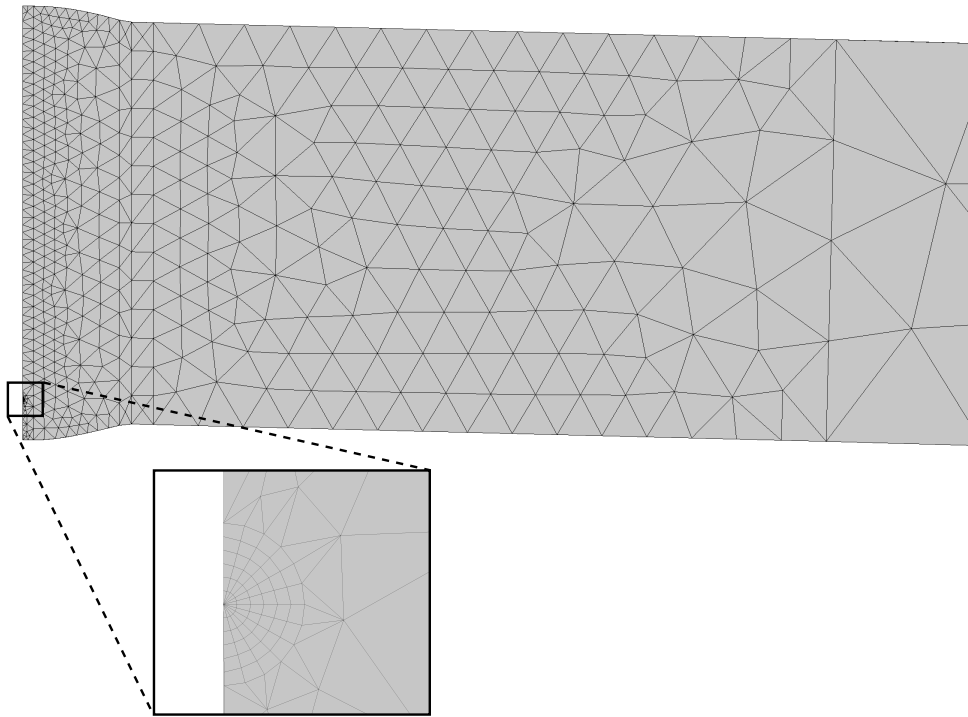


Figure 8.5: Boundary conditions of the model.

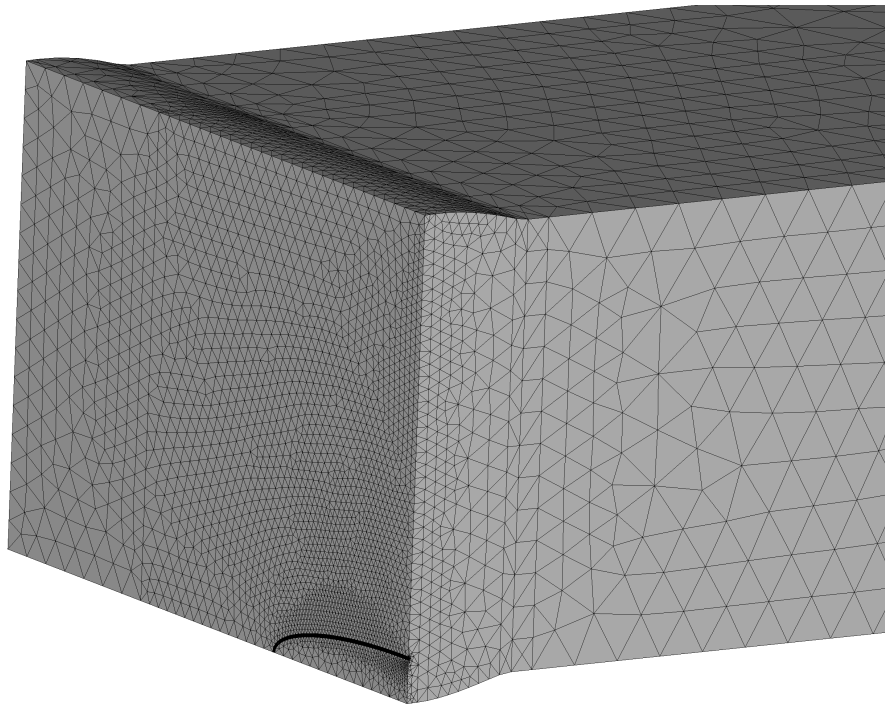
8.3.3 Mesh

In LEFM, the presence of a crack front produces a $1/\sqrt{r}$ singularity in the stress field (where r is the distance from the crack front). To capture this asymptotic behavior, Barsoum (1976) developed singular elements, namely quadratic isoparametric elements with mid-side nodes shifted to the quarter points. These elements are widely used in LEFM, and are available in ANSYS by skewing 2D quadratic elements (PLANE183). To mesh the crack front, a torus volume is created along the crack front (see Figs. 8.6d and 8.7d), and meshed with 3D 20-node quadratic solid elements (SOLID186, as recommended in ANSYS Inc 2015). The 1st row of elements in contact with the crack front are skewed using the generation of volume elements from skewed PLANE183. The remaining volumes in the steel liner are meshed with high order 3D 10-node quadratic elements (SOLID187). The length of the elements along the crack front varied between 0.10 to 1.00 mm depending on the crack length. This is a very dense refinement with respect to most published studies in computational LEFM.

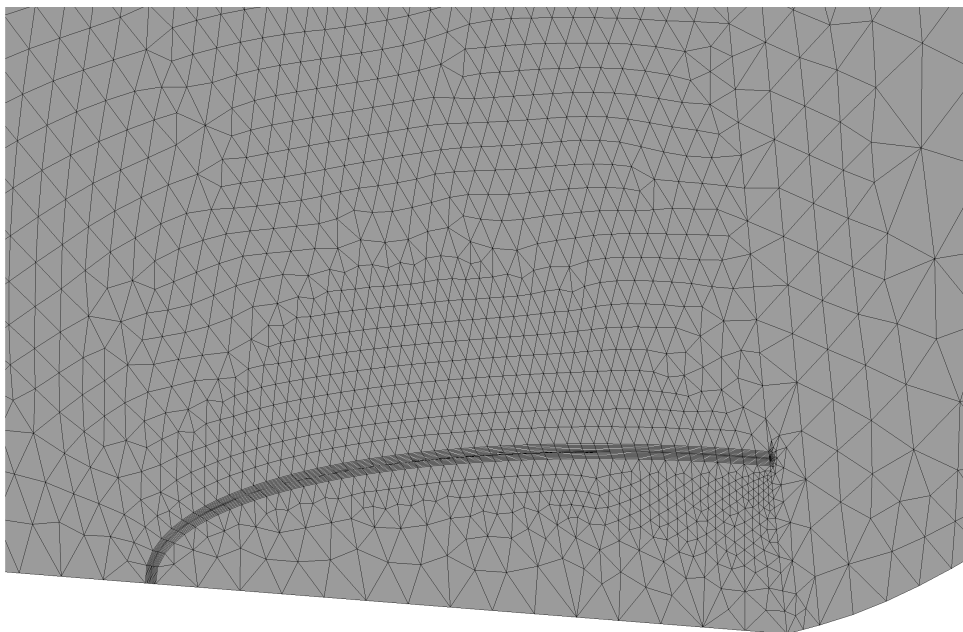
A mesh example of a steel liner with a semi-elliptical surface crack is presented in Figs. 8.6a–8.6d. Under internal pressure p_i inducing circumferential major principal stresses in the steel liner and $p_{cr} = p_i$ on the crack face, the crack is loaded in mode I. The deformed mesh is shown in Figs. 8.6e–8.6f. Similarly, a mesh example for an embedded elliptical crack is shown in Figs. 8.7a–8.7d, and the deformed mesh in Figs. 8.7e–8.7f.



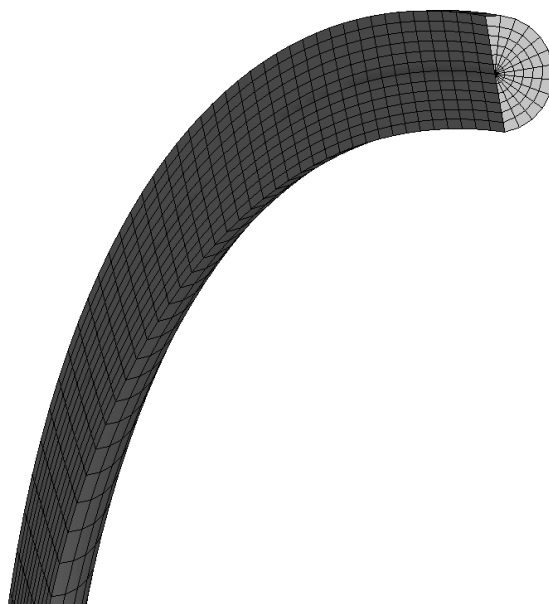
(a) Mesh: section of the welded joint.



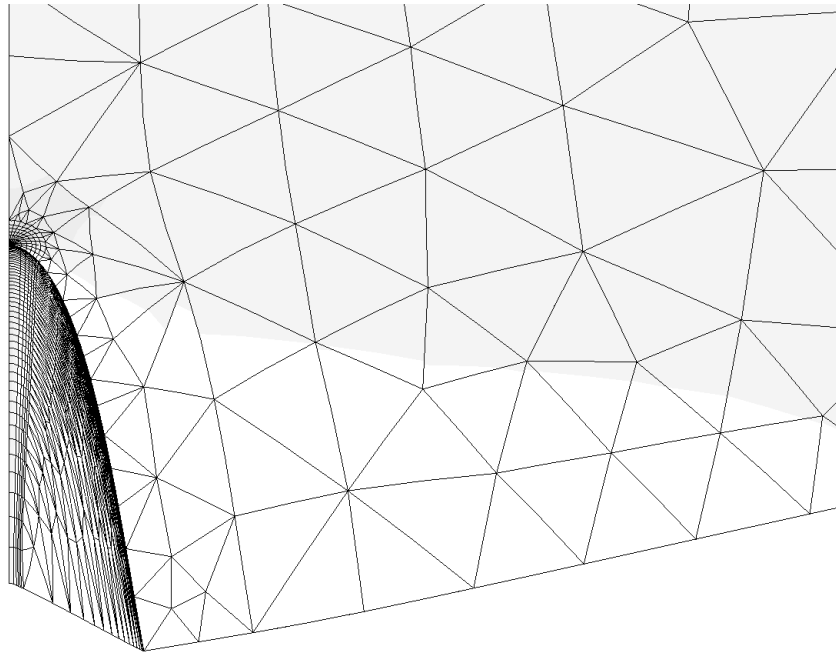
(b) Mesh: 3D view focused on the butt welded joint with semi-elliptical surface crack.



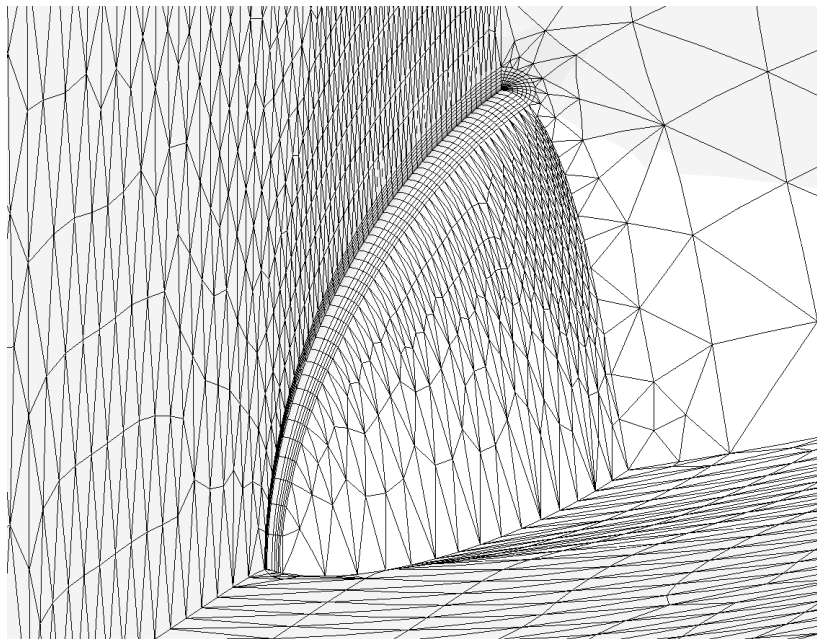
(c) Mesh: 3D view focused on the crack face and front.



(d) Mesh: torus around crack front, meshed with quadratic isoparametric elements.

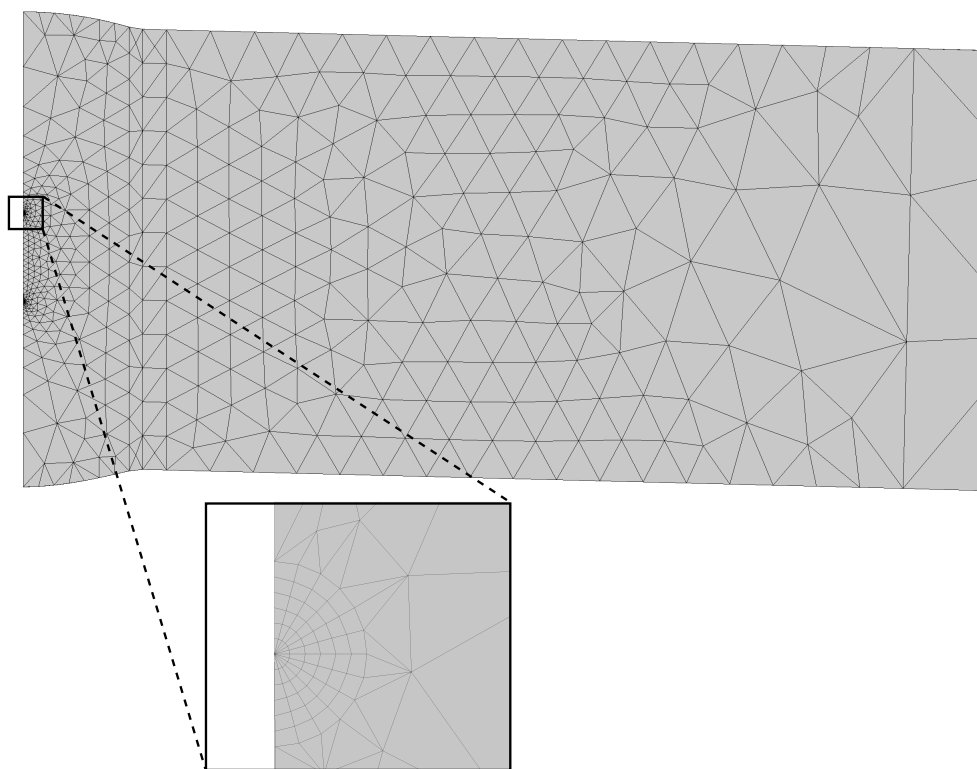


(e) Deformed mesh: sectional view.

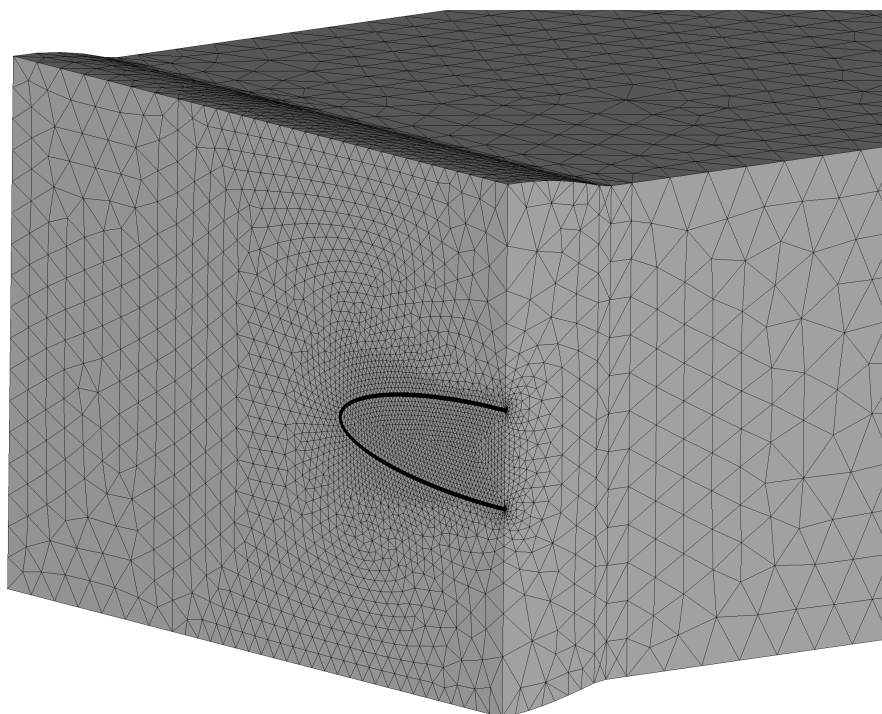


(f) Deformed mesh: 3D view of crack face and front.

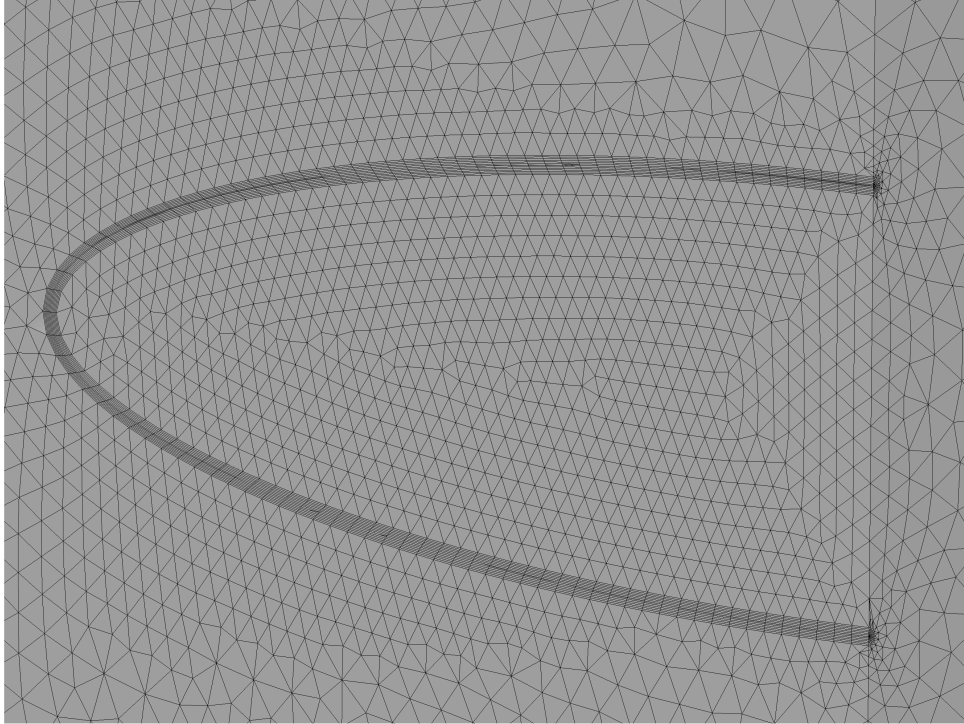
Figure 8.6: FE mesh and deformed mesh of a steel liner with a semi-elliptical surface crack in the weld material of the welded joint.



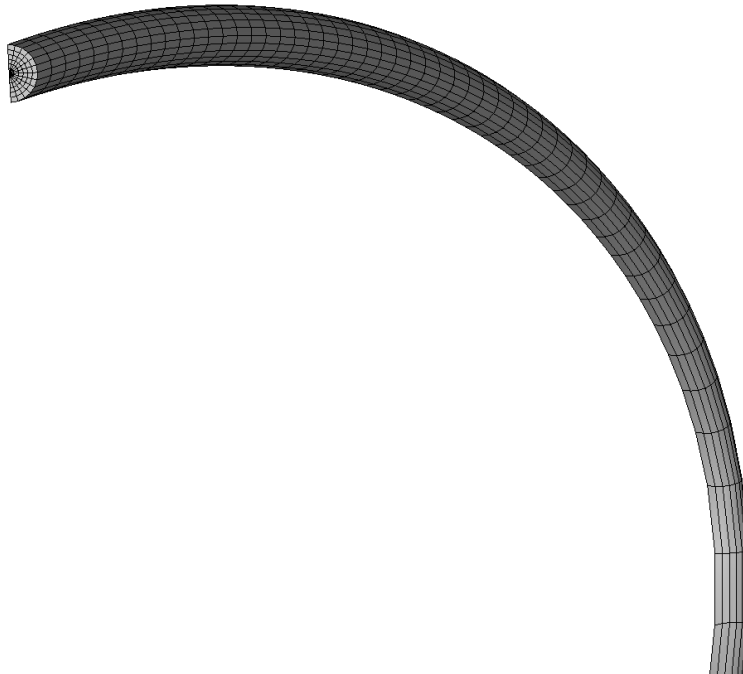
(a) Mesh: section of the welded joint.



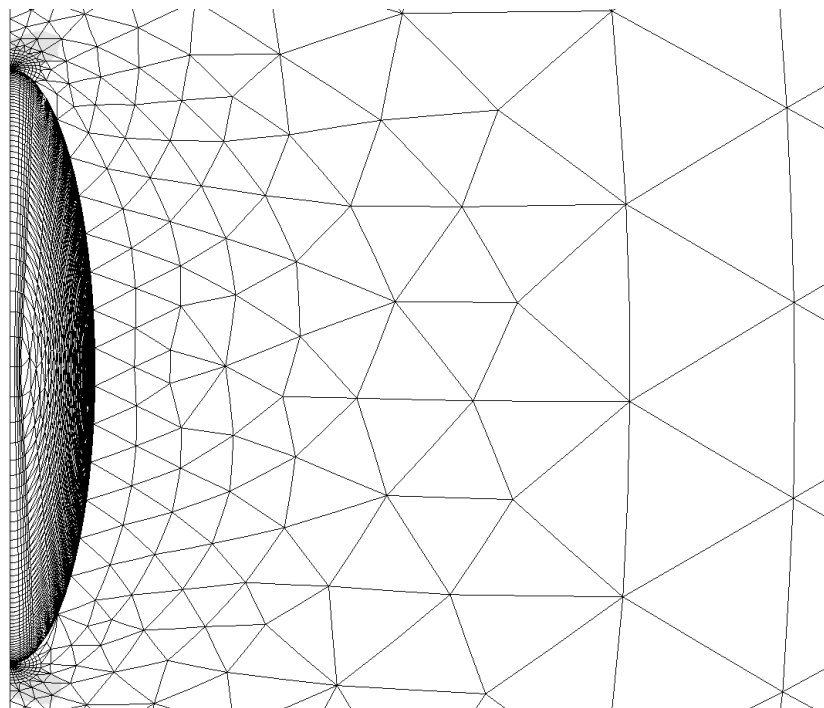
(b) Mesh: 3D view focused on the butt welded joint with embedded elliptical crack.



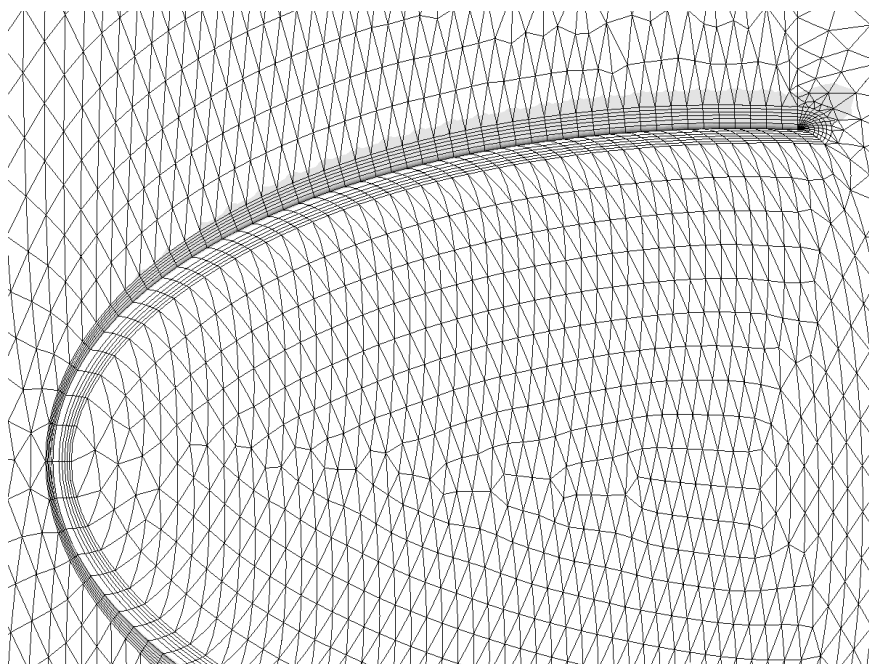
(c) Mesh: 3D view focused on the crack face and front.



(d) Mesh: torus around crack front, meshed with quadratic isoparametric elements.



(e) Deformed mesh: sectional view.



(f) Deformed mesh: 3D view of crack face and front.

Figure 8.7: FE mesh and deformed mesh of a steel liner with an embedded elliptical crack in the weld material of the welded joint.

8.3.4 Evaluation of stress intensity factors

As described in Sect. 3.4, in LEFM the SIF can be calculated from the J -integral (Rice 1968; Shih *et al.* 1986) as

$$J = \frac{K_I^2}{E'} \quad (8.6)$$

where $E' = E_s$ in plane stress and $E' = E_s/(1 - \nu_s^2)$ in plane strain conditions (Anderson 2005). In ANSYS, the J -integral is computed via a discretization (on the elements) of the domain integral representation given by Shih *et al.* (1986).

The chosen FE code offers two approaches to compute the SIF, namely the *Interaction Integrals Method* (Walters *et al.* 2005) computing J , and the *Displacement Extrapolation Method* (Guinea *et al.* 2000) computing directly K_I . In this study, both were implemented and compared. It was verified that they gave the same results using Eq. 8.6 in plane strain from the 2nd to the 4th contours. The 1st contour was omitted consistently with other studies (see, e.g., Bowness & Lee 2000a), giving slightly different results. It was also observed that both methods gave constant results through the 3 studied contours. In the following, the results from the Displacement Extrapolation Method are used, averaged on the 3 contours (although negligible variation was observed).

This agreement between the two methods is better than sometimes reported in other studies (see, e.g., Bowness & Lee 2000a). This might be due to the high mesh density that was implemented herein, or the ranges of variation of the crack sizes. This was not further investigated.

8.3.5 Normalization

The forthcoming analyses are performed with normalized results. The normalized SIF denoted \hat{K}_I is computed as

$$\hat{K}_I = \frac{K_I^{\text{num}}}{K_I^0} \quad (8.7)$$

where K_I^{num} is obtained from the finite element analysis (FEA) and K_I^0 is the analytical solution obtained from Eqs. B.1–B.16 for surface cracks and from Eqs. B.17–B.31 for embedded cracks. The choice of where to evaluate K_I^0 along the crack front differs with respect to the performed analysis, and will be specified when needed.

8.3.6 Validation

The FE models were validated against the corresponding analytical solutions of Newman Jr & Raju (1981a) (Eqs. B.1–B.16) and Anderson (2005) (reported in API 2007, Eqs. B.17–B.31). The validation was performed in so-called *base studies* (see Tables 8.1–8.2). The error was computed as

$$\text{error} = \frac{K_I^{\text{num}} - K_I^0}{K_I^0}, \quad (8.8)$$

at the deepest point of the crack for surface cracks ($\phi = \pi/2$), and at the point of maximum SIF for the embedded crack ($\phi = -\pi/2$, i.e., at the inner side of the steel liner).

The bending stresses σ_b to be inserted in the analytical solutions were computed using the following SCF (British Standard 7910 2005; Hobbacher 2008; Koçak *et al.* 2008):

$$K_{m,p} = 1 + \frac{3\Delta h}{t_s(1 - \nu_s^2)} \cdot \frac{\tanh(\phi/2)}{\phi/2} \quad (8.9)$$

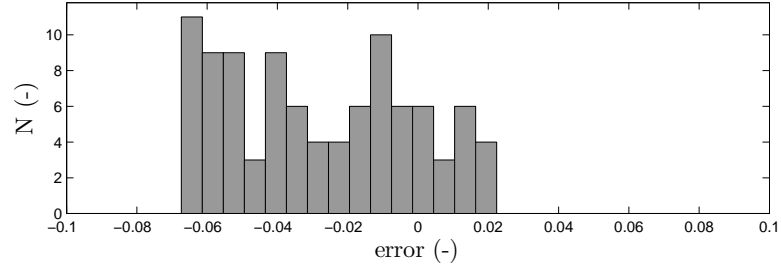
with fixed ends boundary conditions where

$$\phi = \frac{2l}{t_s} \sqrt{\frac{3(1 - \nu_s^2)\sigma_m}{E_s}}. \quad (8.10)$$

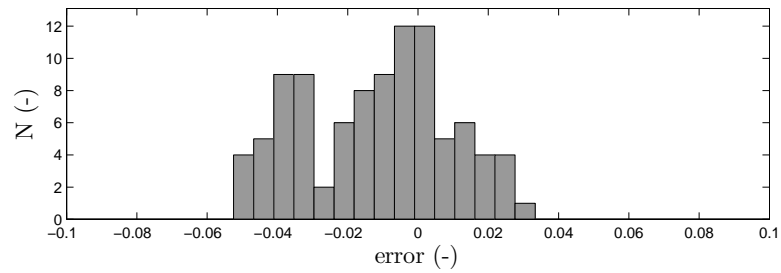
The length l is the projection of the straight edge as shown in Fig. 8.4. This equation was proved to estimate correctly the bending stresses in open-air steel liners (penstocks) until $\psi_u = 2.0$ in Chapter 7.

The errors of prediction of the FE model of the surface crack are plotted in Figs. 8.8a–8.8b. One can observe a good agreement, within the claimed range of accuracy of the analytical solution. It was found that the largest errors correspond to the smallest tested cracks. Although the agreement is fairly good, this can partly be due to the fact that the FE models of the base studies already include a small relative weld reinforcement $\delta/t_s = 0.005$ influencing the results with the same trend that will be outlined in Sect. 8.4. Some examples of normalized SIF along crack fronts are presented in Fig. 8.9, where \hat{K}_I was computed with the maximum analytical SIF K_I^0 along crack front. One can observe that the FE model reproduces the variation of the SIF with a good accuracy along the crack front.

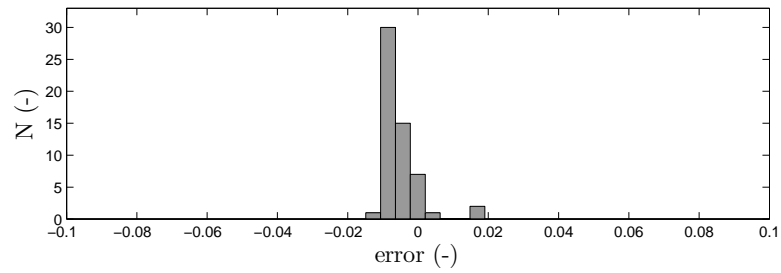
Figures 8.8c–8.8d present the errors of prediction of the FE model of the embedded crack, and Fig. 8.10 shows some examples of variation of normalized SIF along crack fronts. A good agreement is also observed.



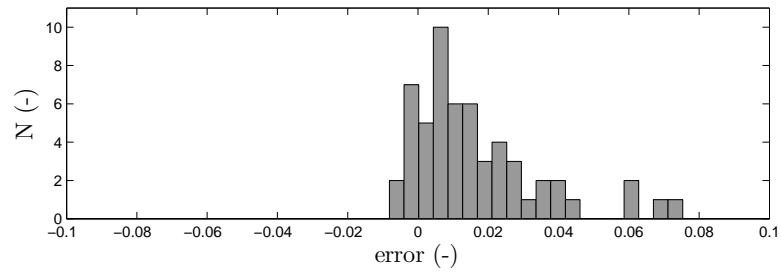
(a) Semi-elliptical surface cracks, $\psi_u = 0.6$.



(b) Semi-elliptical surface cracks, $\psi_u = 2.0$.

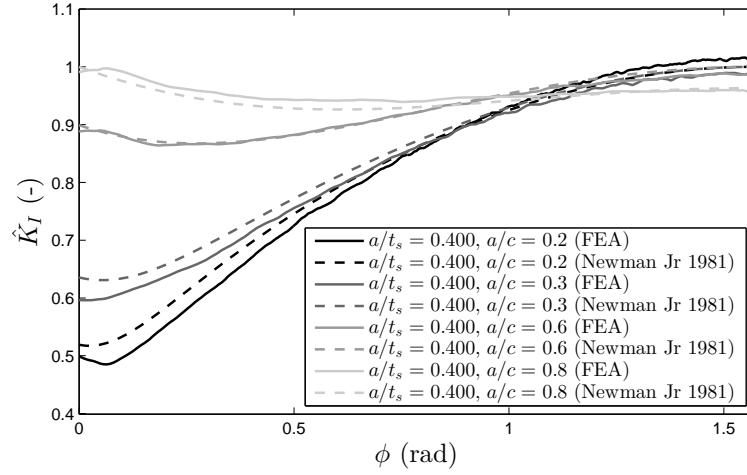


(c) Embedded elliptical cracks, $\psi_u = 0.6$.

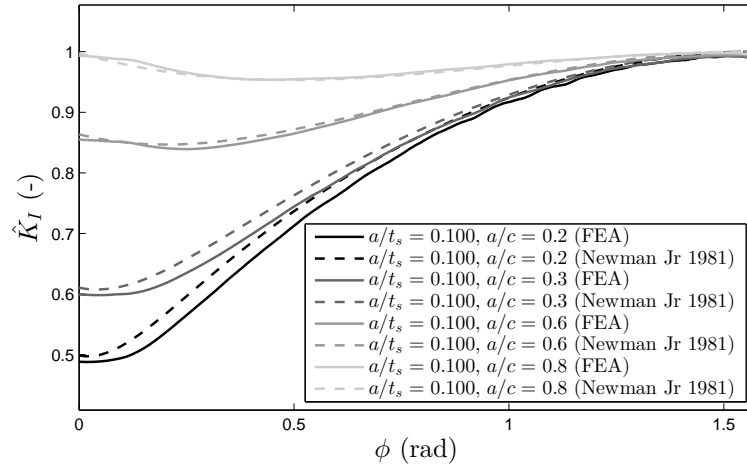


(d) Embedded elliptical cracks, $\psi_u = 2.0$.

Figure 8.8: Error histograms of the prediction of the FE models compared to the corresponding analytical solutions.

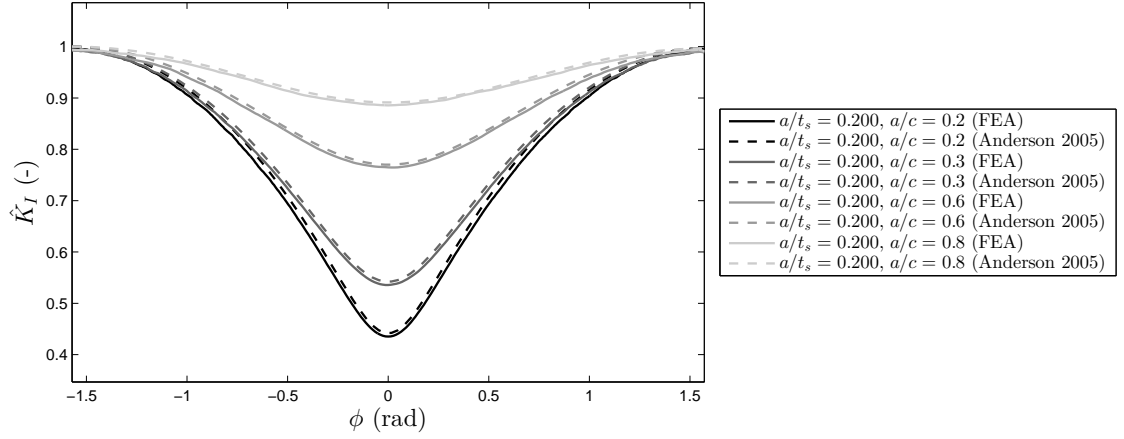


(a) $\psi_u = 0.6$ ($r_i = 2$ m, $t_s = 40$ mm, $\rho = 10$ mm, $\delta/t_s = 0.005$, $\beta = 2$ deg, $\alpha = 50$ deg).

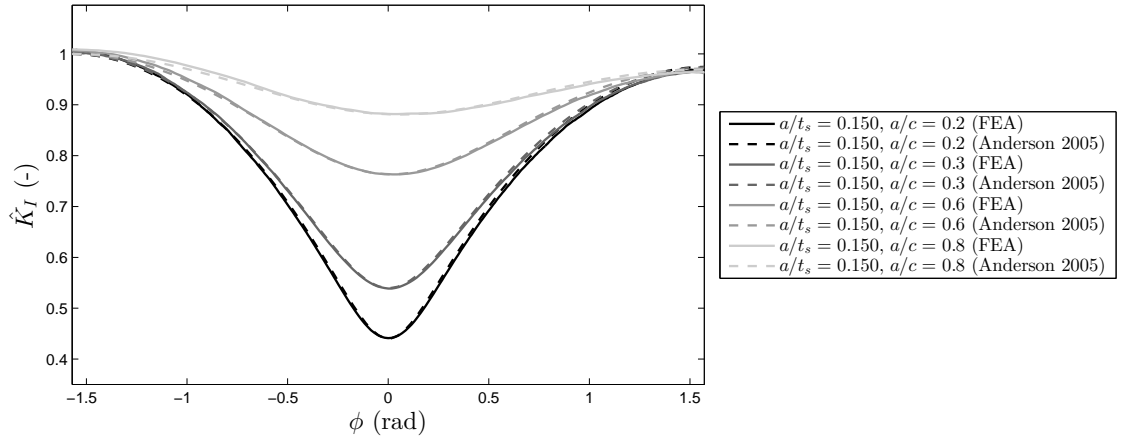


(b) $\psi_u = 2.0$ ($r_i = 2$ m, $t_s = 40$ mm, $\rho = 10$ mm, $\delta/t_s = 0.005$, $\beta = 2$ deg, $\alpha = 50$ deg).

Figure 8.9: Normalized SIF \hat{K}_I along the crack front of semi-elliptical surface cracks.



(a) $\psi_u = 0.6$ ($r_i = 2$ m, $t_s = 25$ mm, $\rho = 10$ mm, $\delta/t_s = 0.005$, $\beta = 2$ deg, $\alpha = 50$ deg).



(b) $\psi_u = 2.0$ ($r_i = 2$ m, $t_s = 25$ mm, $\rho = 10$ mm, $\delta/t_s = 0.005$, $\beta = 2$ deg, $\alpha = 50$ deg).

Figure 8.10: Normalized SIF \hat{K}_I along the crack front of embedded elliptical cracks.

8.3.7 Applicability of the analytical solutions

The results presented previously show that the analytical solutions of Newman Jr & Raju (1981a) and Anderson (2005) are well suited to estimate SIF at surface and embedded cracks, respectively, in the longitudinal butt welded joints of steel liners where the bending stresses can be estimated with the SCF proposed by in Chapter 7 for SLPT&S.

8.4 Parametric study

The influence of the weld shape parameters such as the relative weld reinforcement δ/t_s , the flank angle β and edge preparation angle α (and thus the weld length l_w) was assessed by means of systematic parametric FEA for both surface and embedded cracks. The radius ρ of the weld toes were not included in this parametric study as preliminary simulations showed that it has a negligible influence, if any, as far as it remains a short transition (i.e., only considered to model the notch), not changing significantly the global shape of the weld reinforcement described by the splines. Therefore the local notch stress concentration does not influence a crack in the weld material. This observation is consistent with the tendency presented by Wang *et al.* (2012b), although in their case the circle of radius ρ was used to model a longer transition between the base plate and the weld reinforcement that one may not consider as a notch in terms of local stresses approaches in fatigue assessment.

8.4.1 Semi-elliptical surface cracks

Approximately 2100 cases of steel liners with semi-elliptical surface cracks were simulated according to the matrix of simulations presented in Table 8.1. The weld toe's radius ρ was adapted to the variation of the flank angle β to allow a reasonable meshing as well as not to influence the weld shape as aforementioned. The FE model may present two sources of geometrical nonlinearities that require running nonlinear analyses, namely deep cracks or large roof-topping. After preliminary tests, it was concluded that all simulations with relative crack depth $a/t_s \geq 0.5$ or with roof-topping with $\psi_u \geq 1.0$ required to consider large-deflections effects. They are marked with the superscript * in Table 8.1.

In the following, the normalized SIF \hat{K}_I (thus equivalent to the weld shape correction factor M_w) are computed at the deepest point of the cracks as

$$\hat{K}_I = \frac{K_I^{\text{num}}(\phi = \pi/2)}{K_I^0(\phi = \pi/2)} = M_w. \quad (8.11)$$

The influence of the relative weld reinforcement height δ/t_s is shown in Fig. 8.11a. One can observe that the larger δ/t_s , the smaller the weld shape correction factor M_w (i.e., the SIF

8.4. Parametric study

Table 8.1: Matrix of performed simulations for steel liners with axial semi-elliptical surface cracks at longitudinal butt welded joints (total of approximately 2100 simulations). The so-called base studies are highlighted in **bold**. The superscript * indicates that large-deflections effects were considered.

ψ_u (-)	α (deg)	δ/t_s (-)	β (deg)	ρ (mm)	a/t_s (-)	r_i/t_s (-)	a/c (-)
0.6	50	0.005	2	10	0.025, 0.05, 0.1, 0.2, 0.4, 0.5*, 0.6*	50, 80, 86, 100	0.2, 0.3, 0.6, 0.8
		0.010	2	10	0.025, 0.05, 0.1, 0.2, 0.4, 0.5*, 0.6*	50, 80, 86, 100	0.2, 0.3, 0.6, 0.8
		0.010	5	10	0.025, 0.05, 0.1, 0.2, 0.4, 0.5*, 0.6*	100	0.2, 0.3, 0.6, 0.8
		0.020	2	10	0.025, 0.05, 0.1, 0.2, 0.4, 0.5*, 0.6*	50, 80, 86, 100	0.2, 0.3, 0.6, 0.8
		0.020	5	10	0.025, 0.05, 0.1, 0.2, 0.4, 0.5*, 0.6*	100	0.2, 0.3, 0.6, 0.8
		0.020	10	5	0.5*, 0.6*	80, 100	0.2, 0.3, 0.6, 0.8
		0.040	2	10	0.025, 0.05, 0.1, 0.2, 0.4, 0.5*, 0.6*	50, 80, 100	0.2, 0.3, 0.6, 0.8
		0.040	5	10	0.025, 0.05, 0.1, 0.2, 0.4, 0.5*, 0.6*	100	0.2, 0.3, 0.6, 0.8
		0.040	10	5	0.5*, 0.6*	80, 100	0.2, 0.3, 0.6, 0.8
		0.040	15	3	0.5*, 0.6*	80, 100	0.2, 0.3, 0.6, 0.8
		0.060	2	10	0.025, 0.05, 0.1, 0.2, 0.4, 0.5*, 0.6*	50, 80, 100	0.2, 0.3, 0.6, 0.8
		0.060	5	10	0.025, 0.05, 0.1, 0.2, 0.4, 0.5*, 0.6*	100	0.2, 0.3, 0.6, 0.8
		0.060	10	5	0.025, 0.05, 0.1, 0.2, 0.5*, 0.6*	80	0.2, 0.3, 0.6, 0.8
		0.060	15	3	0.025, 0.05, 0.1, 0.2, 0.5*, 0.6*	80	0.2, 0.3, 0.6, 0.8
		0.060	20	2	0.025, 0.05, 0.1, 0.2, 0.4, 0.5*, 0.6*	50, 80	0.2, 0.3, 0.6, 0.8
		0.080	2	10	0.025, 0.05, 0.1, 0.2, 0.4, 0.5*, 0.6*	50, 80, 100	0.2, 0.3, 0.6, 0.8
		0.080	5	10	0.5*, 0.6*	80, 100	0.2, 0.3, 0.6, 0.8
		0.080	10	5	0.025, 0.05, 0.1, 0.2, 0.5*, 0.6*	100	0.2, 0.3, 0.6, 0.8
		0.080	15	3	0.5*, 0.6*	80, 100	0.2, 0.3, 0.6, 0.8
		0.080	20	2	0.025, 0.05, 0.1, 0.2, 0.4, 0.5*, 0.6*	50, 80, 86, 100	0.2, 0.3, 0.6, 0.8
		0.080	25	1	0.025, 0.05, 0.1, 0.2, 0.5*, 0.6*	100	0.2, 0.3, 0.6, 0.8
		0.080	30	1	0.025, 0.05, 0.1, 0.2, 0.5*, 0.6*	100	0.2, 0.3, 0.6, 0.8
	60, 70	0.040	5	10	0.025, 0.05, 0.1, 0.2	100	0.2, 0.3, 0.6, 0.8
		0.060	5	10	0.025, 0.05, 0.1, 0.2	100	0.2, 0.3, 0.6, 0.8
		0.060	10	5	0.025, 0.05, 0.1, 0.2	80	0.2, 0.3, 0.6, 0.8
		0.060	15	3	0.025, 0.05, 0.1, 0.2	80	0.2, 0.3, 0.6, 0.8
		0.060	20	2	0.025, 0.05, 0.1, 0.2	80	0.2, 0.3, 0.6, 0.8
1.0	50	0.005	2	10	0.025*, 0.05*, 0.1*, 0.2*, 0.4*, 0.5*, 0.6*	50, 80, 100	0.2, 0.3, 0.6, 0.8
		0.010	5	10	0.025*, 0.05*, 0.1*, 0.2*, 0.4*, 0.6*	50, 80	0.2, 0.3, 0.6, 0.8
		0.020	10	5	0.025*, 0.05*, 0.1*, 0.2*, 0.4*, 0.6*	50	0.2, 0.3, 0.6, 0.8
	60, 70	0.010	5	10	0.025*, 0.05*, 0.1*, 0.2*	50	0.2, 0.3, 0.6, 0.8
		0.020	10	5	0.025*, 0.05*, 0.1*, 0.2*	50	0.2, 0.3, 0.6, 0.8
1.5	50	0.005	2	10	0.025*, 0.05*, 0.1*, 0.2*, 0.4*, 0.5*, 0.6*	50, 80, 100	0.2, 0.3, 0.6, 0.8
		0.010	5	10	0.025*, 0.05*, 0.1*, 0.2*, 0.4*, 0.6*	50, 100	0.2, 0.3, 0.6, 0.8
		0.020	10	5	0.025*, 0.05*, 0.1*, 0.2*, 0.4*	50	0.2, 0.3, 0.6, 0.8
	60, 70	0.010	5	10	0.025*, 0.05*, 0.1*, 0.2*	50	0.2, 0.3, 0.6, 0.8
		0.020	10	5	0.025*, 0.05*, 0.1*, 0.2*	50	0.2, 0.3, 0.6, 0.8
2.0	50	0.005	2	10	0.025*, 0.05*, 0.1*, 0.2*, 0.4*, 0.5*, 0.6*	50, 80, 86, 100	0.2, 0.3, 0.6, 0.8
		0.010	5	10	0.025*, 0.05*, 0.1*, 0.2*, 0.4*, 0.6*	50, 80, 100	0.2, 0.3, 0.6, 0.8
		0.020	10	5	0.025*, 0.05*, 0.1*, 0.2*, 0.4*, 0.6*	50, 80, 100	0.2, 0.3, 0.6, 0.8
		0.040	15	3	0.025*, 0.05*, 0.1*, 0.2*, 0.4*, 0.6*	50, 100	0.2, 0.3, 0.6, 0.8
		0.060	20	2	0.025*, 0.05*, 0.1*, 0.2*, 0.4*, 0.6*	50, 100	0.2, 0.3, 0.6, 0.8
		0.080	30	1	0.025*, 0.05*, 0.1*, 0.2*, 0.4*, 0.6*	100	0.2, 0.3, 0.6, 0.8
	60, 70	0.040	15	3	0.025*, 0.05*, 0.1*, 0.2*	100	0.2, 0.3, 0.6, 0.8
		0.060	20	2	0.025*, 0.05*, 0.1*, 0.2*	100	0.2, 0.3, 0.6, 0.8
		0.080	30	1	0.025*, 0.05*, 0.1*, 0.2*, 0.4*	100	0.2, 0.3, 0.6, 0.8

decreases compared to the analytical solution). The decrease of M_w is approximately linear with respect to δ/t_s . Also, the aspect ratio has no influence for small cracks ($a/t_s \leq 0.2$) and a not significant influence for larger cracks ($a/t_s > 0.2$). To explain these observations, the major principal stress σ_1 profiles are plotted in Fig. 8.13. The influence of δ/t_s is depicted in Figs. 8.13a, 8.13b, 8.13c, and 8.13d. It can be seen that the greater δ/t_s , the smaller σ_1 in the weld reinforcement area, due to the enlargement of the thickness of the steel liner. The influence of δ/t_s on two crack sizes along the crack fronts is shown in Fig. 8.12.

Figure 8.11b presents the influence of the edge preparation angle α (and thus the weld length l_w). It can be observed that the greater α , the greater M_w (and thus the smaller the influence of the weld shape). The increase of M_w is approximately linear with respect to α . This can be explained by the fact that a larger weld length allows for a smoother stress gradient through the weld material, and thus a more homogeneous stress profile through the thickness and the weld reinforcement. This is illustrated in Figs. 8.13i, 8.13j, 8.13k, and 8.13l.

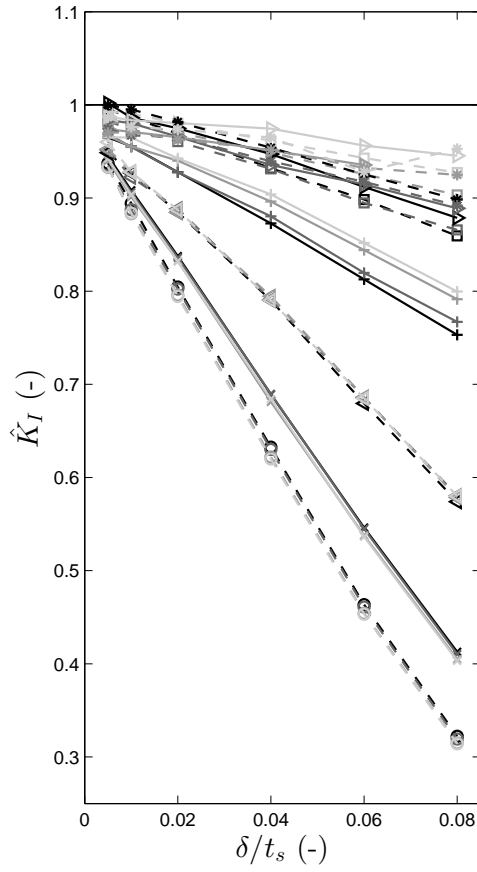
Finally, the influence of the flank angle β is plotted in Fig. 8.11c. Similarly to the influence of α , one can see that the greater β , the greater M_w . A great β indeed yields more weld material (for a fixed δ and l_w), allowing a more homogeneous stress profile and thus a smoother stress gradient. This effect is also illustrated in Figs. 8.13e, 8.13f, 8.13g and 8.13h.

8.4.2 Embedded elliptical cracks

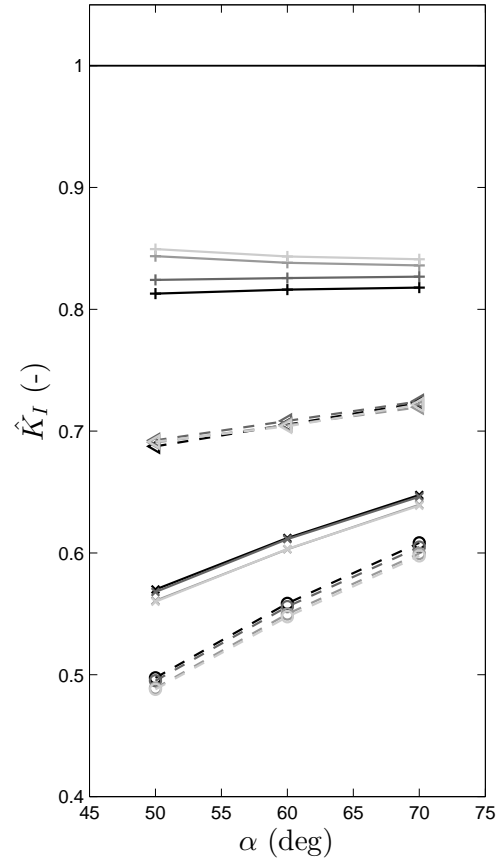
For steel liners with embedded elliptical cracks, approximately 330 cases were simulated according to the matrix of simulations given in Table 8.2. As for the semi-elliptical surface cracks, the influence of the weld shape parameters were studied as shown in Fig. 8.14 (Eq. 8.11 was evaluated for $\phi = -\pi/2$ in this case). One can observe that for the studied ranges of relative crack depths a/t_s , the influence of the weld shape is negligible. This observation is consistent with the analysis performed previously. Indeed, in the case of embedded cracks with $d_1 = d_2$ (cracks centered on the mean axis of the welded plates), the crack front is located in a zone where the major principal stress profile is not affected by the weld shape (see Fig. 8.13).

8.4.3 Commentaries on the results

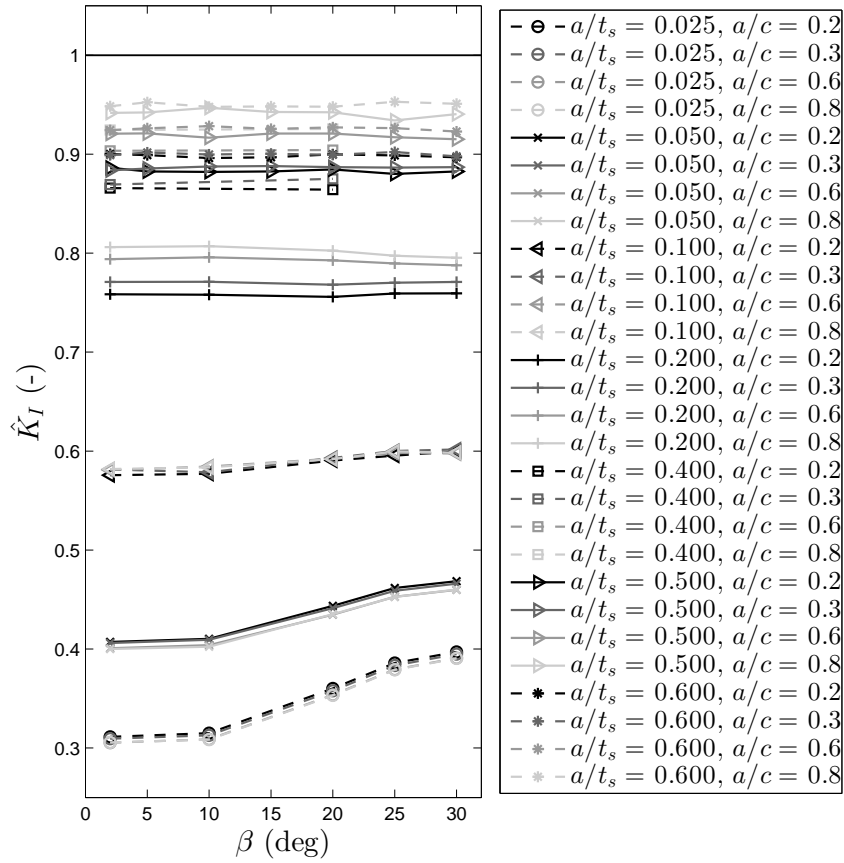
The parametric study has shown that the weld reinforcement mitigates SIF by diminishing the major principal stresses acting on crack fronts located in the region near the reinforcement surface. This effect is mitigated with increasing weld length l_w or flank angle β . Therefore it strongly affects semi-elliptical surface cracks at early stages of growth. The further the crack front advances through the thickness, the less the influence of the weld shape. For the simulated embedded elliptical cracks centered to the mean axis of the plates, the weld shape has a negligible influence as the crack front remains in regions where the stress profile is not affected. This may not be true for very long cracks reaching the weld reinforcement region. However, in the scope of fatigue crack growth analysis by means of LEFM approach, the influence of the weld shape on



(a) Influence of relative weld reinforcement height δ/t_s ($r_i = 2$ m, $t_s = 25$ mm, $\rho = 10$ mm, $\beta = 2$ deg, $\alpha = 50$ deg).

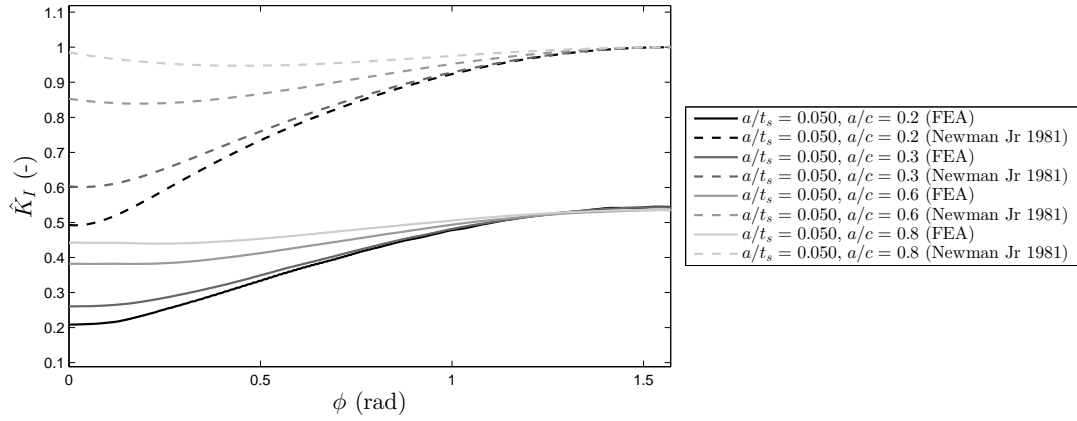


(b) Influence of weld preparation angle α ($r_i = 2$ m, $t_s = 25$ mm, $\rho = 3$ mm, $\delta/t_s = 0.060$, $\beta = 15$ deg).

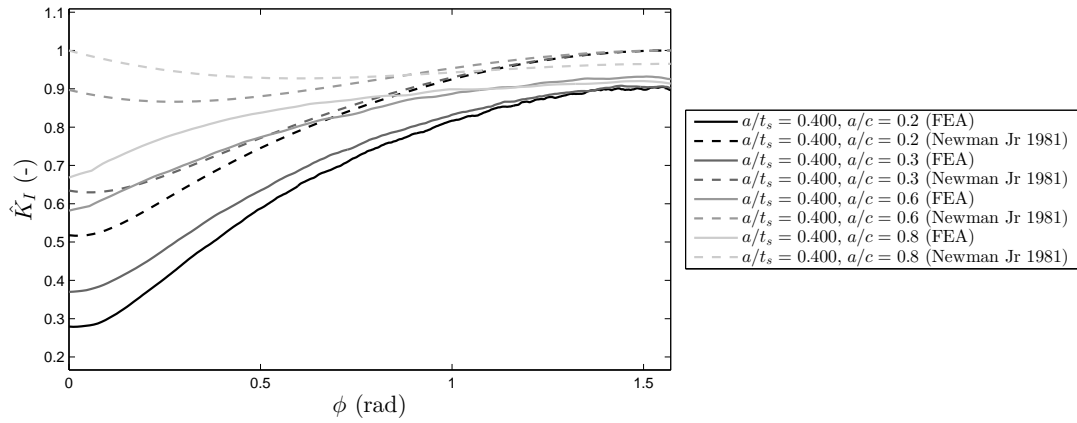


(c) Influence of flank angle β ($r_i = 3$ m, $t_s = 30$ mm, $\delta/t_s = 0.080$, $\alpha = 50$ deg).

Figure 8.11: Normalized SIF \hat{K}_I at the deepest point of semi-elliptical surface cracks.

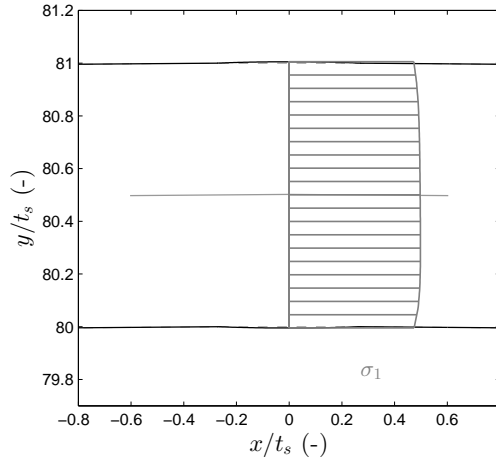


(a) $a/t_s = 0.050$ ($r_i = 3$ m, $t_s = 30$ mm, $\rho = 10$ mm, $\delta/t_s = 0.060$, $\beta = 2$ deg, $\alpha = 50$ deg).

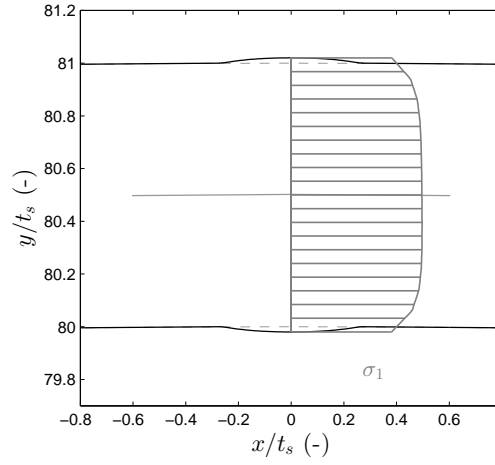


(b) $a/t_s = 0.400$ ($r_i = 3$ m, $t_s = 30$ mm, $\rho = 10$ mm, $\delta/t_s = 0.060$, $\beta = 2$ deg, $\alpha = 50$ deg).

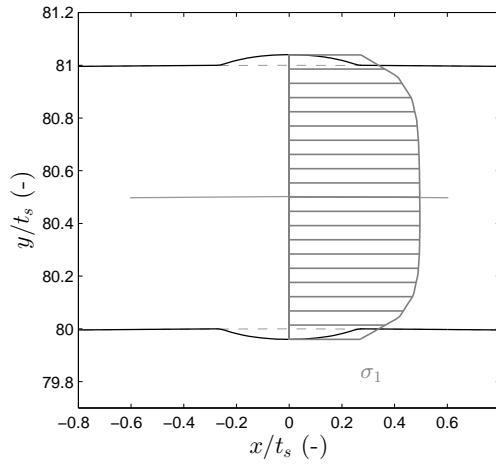
Figure 8.12: Influence of relative weld reinforcement on the normalized SIF \hat{K}_I along the crack front of semi-elliptical surface cracks.



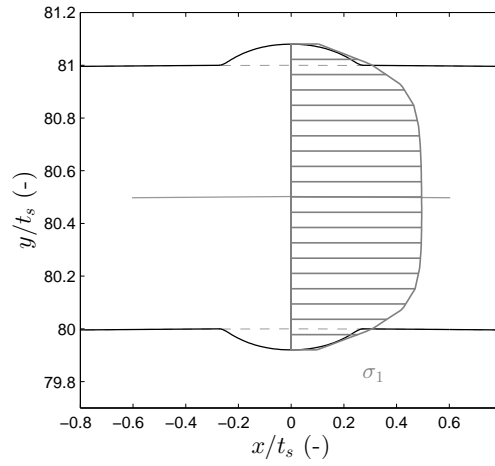
(a) $\delta/t_s = 0.005$.



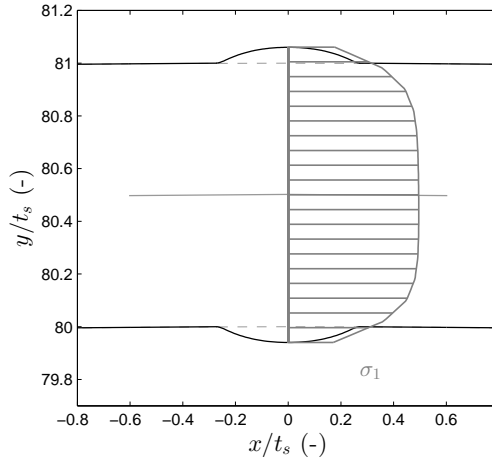
(b) $\delta/t_s = 0.020$.



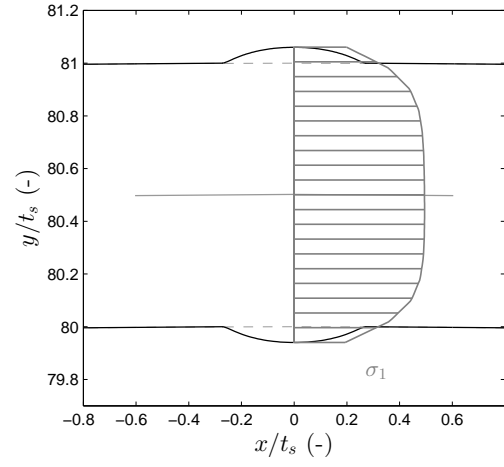
(c) $\delta/t_s = 0.040$.



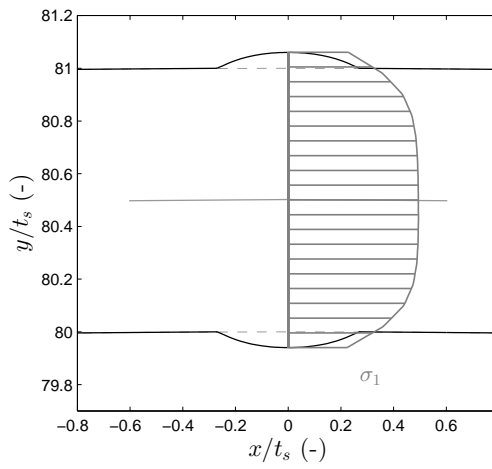
(d) $\delta/t_s = 0.080$.



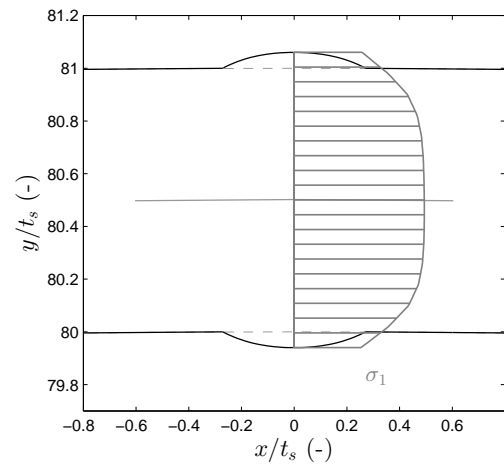
(e) $\beta = 2 \text{ deg.}$



(f) $\beta = 10 \text{ deg.}$



(g) $\beta = 20 \text{ deg.}$



(h) $\beta = 30 \text{ deg.}$

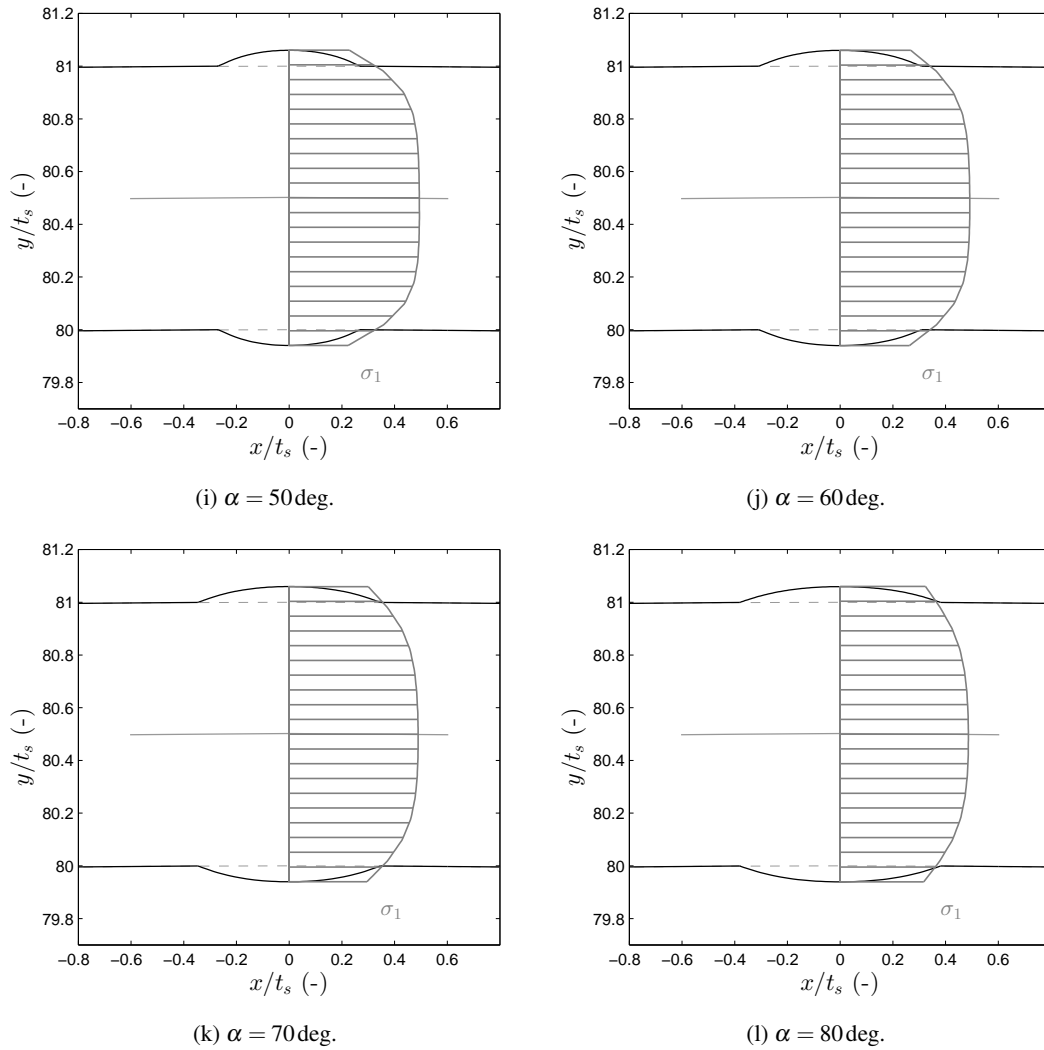
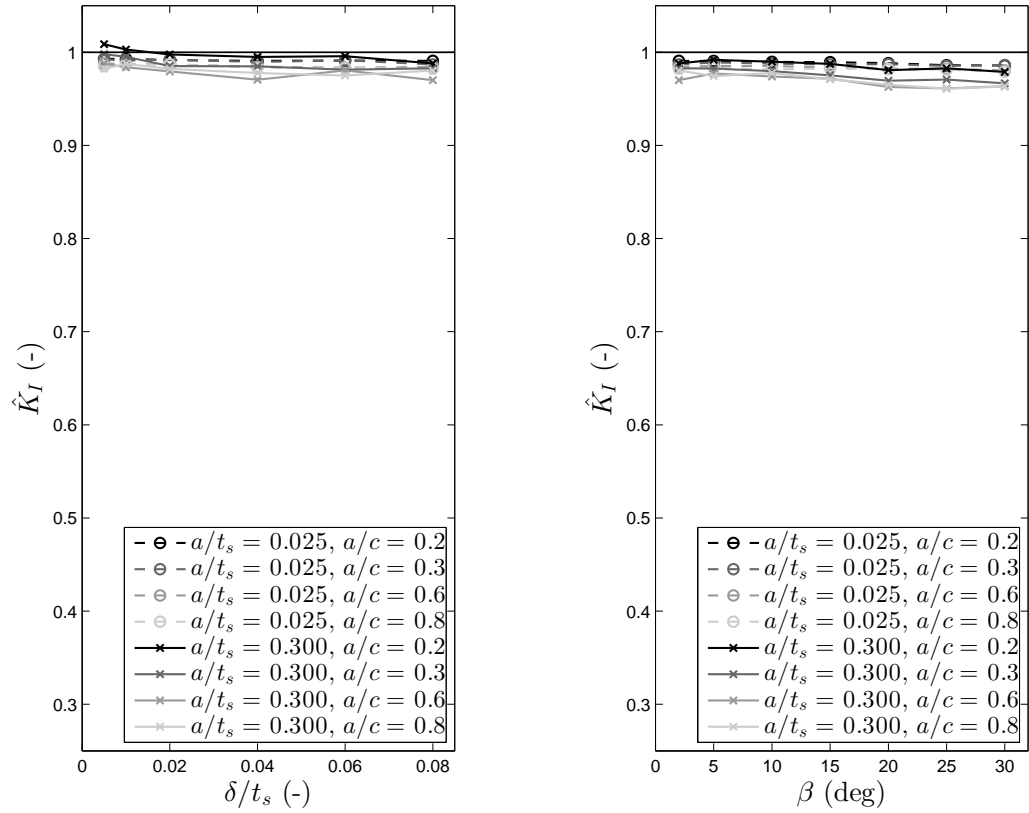


Figure 8.13: Major principal stress profiles in the weld material ($r_i = 2$ m, $t_s = 25$ mm, $\rho = 1$ mm): (a,b,c,d) influence of the relative weld reinforcement δ/t_s ($\beta = 2$ deg, $\alpha = 50$ deg); (e,f,g,h) influence of the flank angle β ($\delta/t_s = 0.060$, $\alpha = 50$ deg); and (i,j,k,l) influence of the edge preparation angle α ($\delta/t_s = 0.060$, $\beta = 20$ deg). The stress profiles are scaled so that $t_s/2$ represents the magnitude of the membrane stress.



(a) Influence of relative weld reinforcement height δ/t_s ($r_i = 2$ m, $t_s = 25$ mm, $\rho = 10$ mm, $\beta = 2$ deg, $\alpha = 50$ deg).

(b) Influence of flank angle β ($r_i = 2$ m, $t_s = 25$ mm, $\delta/t_s = 0.080$, $\alpha = 50$ deg).

Figure 8.14: Maximum normalized SIF \hat{K}_I (at $\phi = -\pi/2$) of embedded elliptical cracks.

Chapter 8. Stress intensity factors (SIF) for axial cracks in the weld material

Table 8.2: Matrix of performed simulations for steel liners with axial embedded elliptical cracks at longitudinal butt welded joints (total of approximately 330 simulations). The so-called base studies are highlighted in **bold**. The superscript * indicates that large-deflections effects were considered.

ψ_{it} (-)	α (deg)	δ/t_s (-)	β (deg)	ρ (mm)	a/t_s (-)	r_i/t_s (-)	a/c (-)
0.6	50	0.005	2	10	0.025, 0.05, 0.075, 0.1, 0.15, 0.2, 0.3	50, 80	0.2, 0.3, 0.6, 0.8
		0.010	2	10	0.025, 0.3	80	0.2, 0.3, 0.6, 0.8
		0.020	2	10	0.025, 0.3	80	0.2, 0.3, 0.6, 0.8
		0.040	2	10	0.025, 0.3	80	0.2, 0.3, 0.6, 0.8
		0.040	5	10	0.025, 0.3	80	0.2, 0.3, 0.6, 0.8
		0.040	10	5	0.025, 0.3	80	0.2, 0.3, 0.6, 0.8
		0.040	15	3	0.025, 0.3	80	0.2, 0.3, 0.6, 0.8
		0.060	2	10	0.025, 0.3	80	0.2, 0.3, 0.6, 0.8
		0.080	2	10	0.025, 0.3	80	0.2, 0.3, 0.6, 0.8
		0.080	5	10	0.025, 0.3	80	0.2, 0.3, 0.6, 0.8
		0.080	10	5	0.025, 0.3	80	0.2, 0.3, 0.6, 0.8
		0.080	15	3	0.025, 0.3	80	0.2, 0.3, 0.6, 0.8
		0.080	20	2	0.025, 0.3	80	0.2, 0.3, 0.6, 0.8
		0.080	25	1	0.025, 0.3	80	0.2, 0.3, 0.6, 0.8
		0.080	30	1	0.025, 0.3	80	0.2, 0.3, 0.6, 0.8
	60, 70	0.040	10	5	0.025, 0.3	80	0.2, 0.3, 0.6, 0.8
		0.080	10	5	0.025, 0.3	80	0.2, 0.3, 0.6, 0.8
		0.080	20	2	0.025, 0.3	80	0.2, 0.3, 0.6, 0.8
		0.080	30	1	0.025, 0.3	80	0.2, 0.3, 0.6, 0.8
2.0	50	0.005	2	10	0.025*, 0.05*, 0.075*, 0.1*, 0.15*, 0.2*, 0.3*	50, 80	0.2, 0.3, 0.6, 0.8
		0.010	5	10	0.025*, 0.3 *	80	0.2, 0.3, 0.6, 0.8
		0.020	10	5	0.025*, 0.3 *	80	0.2, 0.3, 0.6, 0.8
		0.040	15	3	0.025*, 0.3 *	80	0.2, 0.3, 0.6, 0.8
		0.060	20	2	0.025*, 0.3 *	80	0.2, 0.3, 0.6, 0.8
		0.080	30	1	0.025*, 0.3 *	80	0.2, 0.3, 0.6, 0.8

SIF for embedded cracks can be neglected, as most of the fatigue life would be consumed before the cracks reach sizes which may be influenced by the weld shape.

8.5 Parametric equation to estimate the weld shape correction factor M_w for semi-elliptical surface cracks

In order to derive a parametric equation to estimate M_w for SIF at the deepest point of semi-elliptical surface cracks in steel liners of SLPT&S, all the data generated in the parametric study (see Table 8.1) are considered, i.e., 2100 cases. Based on the observations made in the parametric study (see Fig. 8.11), it is proposed to express the weld shape correction factor M_w as a combination of three functions f_i describing the influence of δ/t_s , β and α , as

$$M_w = f_1 \left(\frac{a}{t_s}, \frac{\delta}{t_s} \right) f_2 \left(\frac{a}{t_s}, \frac{l_w}{t_s}, \frac{\delta}{t_s} \right) + f_3 \left(\frac{a}{t_s}, \frac{l_w}{t_s}, \frac{\delta}{t_s}, \beta \right), \quad (8.12)$$

8.5. Parametric equation to estimate the weld shape correction factor M_w for semi-elliptical surface cracks

where f_1 is a linear function of δ/t_s with a slope depending on the crack depth a/t_s , f_2 is a linear function of l_w/t_s with a slope depending on a/t_s and δ/t_s , and f_3 is part a trigonometric function of β , with an amplitude depending on a/t_s , δ/t_s and l_w/t_s . The f_i are defined as

$$f_1 = 1 + \chi_1 g_{11} \left(\frac{\delta}{t_s} \right), \quad (8.13)$$

$$f_2 = 1 + \chi_3 g_{21} g_{22} \left(\frac{l_w}{t_s} \right), \quad (8.14)$$

$$f_3 = \frac{\chi_6 g_{31} g_{32} g_{33}}{2} [1 + \cos(\pi + 6\beta)]; \quad (8.15)$$

with the following functions g_{ij} :

$$g_{11} = \left(\frac{a}{t_s} \right)^{\chi_2}; \quad (8.16)$$

$$g_{21} = \left(\frac{a}{t_s} \right)^{\chi_4}, \quad (8.17)$$

$$g_{22} = \left(\frac{\delta}{t_s} \right)^{\chi_5}; \quad (8.18)$$

and

$$g_{31} = \left(\frac{a}{t_s} \right)^{\chi_7}, \quad (8.19)$$

$$g_{32} = \left(\frac{\delta}{t_s} \right)^{\chi_8}, \quad (8.20)$$

$$g_{33} = \left(\frac{l_w}{t_s} \right)^{\chi_9}. \quad (8.21)$$

The 9 coefficients and exponents χ_i are to be fitted against the results obtained by FEA. One should note that Eq. 8.12 tends toward unity when δ and β tend to zero, which has a meaningful physical sense.

The coefficients and exponents χ_i were fitted by means of genetic algorithm (GA), with a so-called *training group* of 80% of the results from FEA, and a *test group* regrouping the other 20%. The groups were constituted by random sampling. The objective function was defined as:

$$\hat{\chi} = \underset{\chi}{\operatorname{argmin}} \operatorname{MSE} \left[\hat{\mathbf{K}}_I^{\text{num}}, \hat{\mathbf{K}}_I^{\text{emp}}(\chi) \right] \quad (8.22)$$

where MSE is the mean squared error function, $\hat{\chi} = \{\chi_1, \dots, \chi_9\}$ is the argument of the minimum, $\hat{\mathbf{K}}_I^{\text{num}}$ is a vector containing the results from FEA normalized with the analytical solution of New-

Chapter 8. Stress intensity factors (SIF) for axial cracks in the weld material

man Jr (1981) and \hat{K}_I^{emp} contains the results to be fitted with the proposed empirical parametric equation for M_w . The obtained coefficients and exponents χ_i are given in Table 8.3.

Table 8.3: Coefficients and exponents χ_i for the parametric equation of M_w fitted by GA.

χ_1	χ_2	χ_3	χ_4	χ_5	χ_6	χ_7	χ_8	χ_9
-1.79	-0.45	2.63	1.08	0.79	0.37	-1.10	0.88	4.84

The regression between the normalized results from FEA and the proposed empirical parametric equation for M_w is presented in Fig. 8.15, both for training and test groups. One can observe a good coefficient of determination R^2 and a low root mean squared error (RMSE), as well as a good agreement between both groups. The errors computed as

$$\text{error} = \frac{\hat{K}_I^{\text{emp}} - \hat{K}_I^{\text{num}}}{\hat{K}_I^{\text{num}}} \quad (8.23)$$

are presented in histograms in Fig. 8.16. One can observe a fairly good prediction of the proposed parametric equation. Most of the predictions are in the range of an underestimation and an overestimation of -10% and +10%, respectively, with a mean absolute error of 2.7%. The extreme underestimations and overestimations can reach -20% and +20% for few cases.

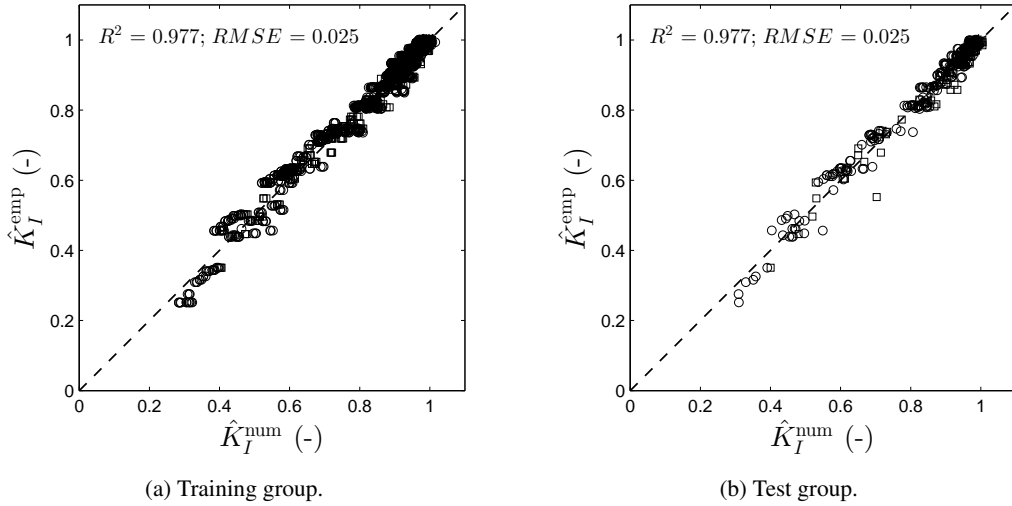


Figure 8.15: Regression plots of the empirical results against the numerical results fitted by GA.

8.6 Application limits

To consider the weld shape correction factor to estimate SIF for semi-elliptical surface cracks, it was proposed herein to derive a global factor M_w to be applied to the equation of Newman Jr &

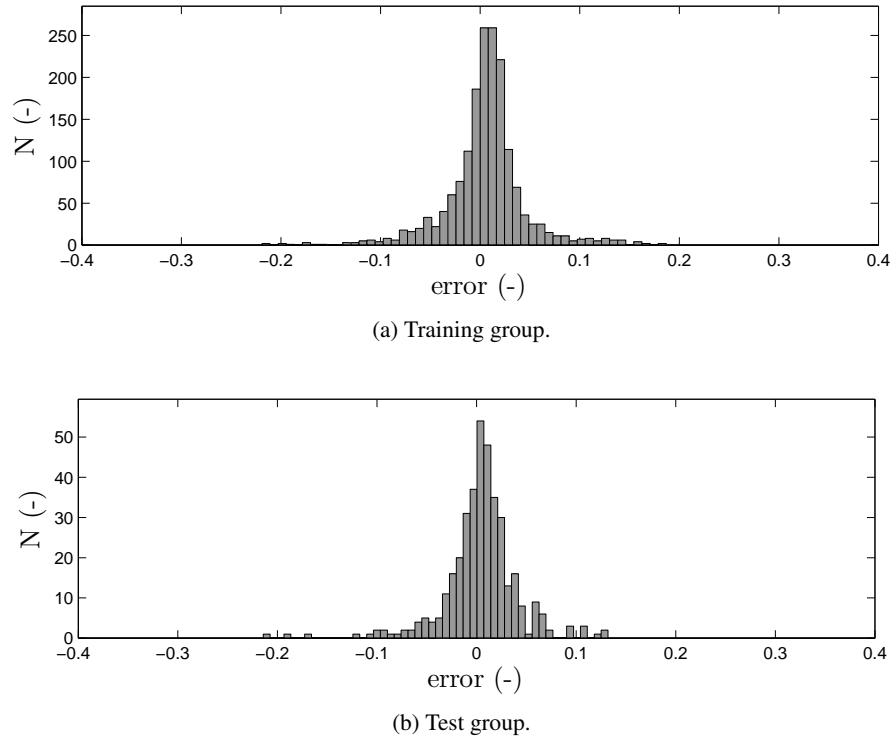


Figure 8.16: Error histograms of the predictions of the parametric equation compared to the FE results.

Raju (1981a), as described by Eq. 8.2. In literature, correction factors are often derived separately for membrane and bending stresses. In this study, no significantly enhanced accuracy could be reached for the tested parametric equations by applying specific factors to membrane and bending stresses. This can be explained by the relatively low degree of bending (DOB) that is applied to the longitudinal butt welded joints of steel liners of SLPT&S. By defining the DOB as

$$\text{DOB} = \frac{\sigma_b}{\sigma_m + \sigma_b}, \quad (8.24)$$

and by considering a roof-topping varying from $\psi_u = 0.6$ to 2.0, the maximum tested DOB was of 12%, with a mean value of 3.1% over the 2100 tested cases (see Table 8.1). As consequence, the proposed parametric equation specifically applies to longitudinal butt welded joints of SLPT&S featuring roof-topping in typical ranges found in practice. The derivation of a weld shape correction factor for semi-elliptical surface cracks at butt welded plates with a high DOB would require further investigations.

One may also note that the tested crack aspect ratios are in the range $a/c = 0.2$ to 0.8. Although

this range is often representative of the cracks found in practical applications and studied in the literature, probabilistic approaches for fatigue crack growth by means of LEFM requires probability density functions for a/c that may be defined beyond these limits (Lukić & Cremona 2001; Maljaars *et al.* 2012), e.g., from 0 to 1. To confirm the applicability of the proposed parametric equations, further analysis would be required, and in particular the implementation of a 2D FE model to simulate $a/c = 0$, i.e., edge cracks.

However, the parametric study performed herein indicated that for low relative crack depth a/t_s (the most affected by the weld shape), the crack aspect ratio in the studied range does not have an influence. For larger cracks (less affected), the influence is less clear but remains low. Moreover, when plotting the solution of Newman Jr & Raju (1981a) against the solution of Newman Jr (1973) in Fig. 8.17, one can see that the solution for $a/c = 0.8$ has already almost converged to the solution for $a/c = 1.0$ (by 11%), and the solution for $a/c = 0.2$ toward the single-edge crack (by 8%). In the light of these observations, the use of the proposed parametric equations could be extended to $a/c = 0$ to 1 as a first approximation.

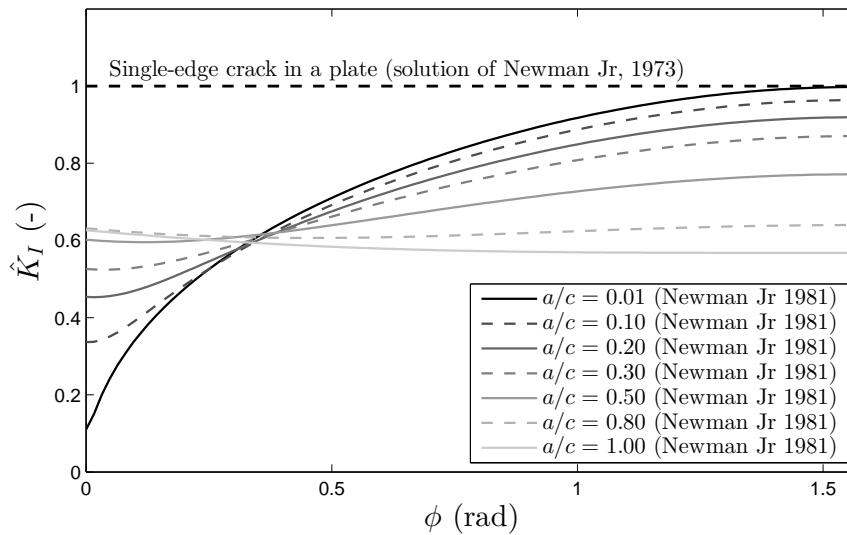


Figure 8.17: Convergence of the 3D solution for normalized SIF \hat{K}_I along semi-elliptical surface crack for different aspect ratios a/c toward the 2D single-edge crack solution in a plate.

8.7 Conclusions

For an accurate engineering fatigue and fracture assessment of the longitudinal butt welded joints of steel liners of SLPT&S by means of LEFM, the SIF for typical axial cracks such as semi-elliptical surface cracks and embedded elliptical cracks should be known.

In this chapter, it was first verified that the solutions for surface and embedded cracks in plated structures could be used for steel liners of SLPT&S, including the SCF due to geometrical

imperfections studied in the previous chapters. In order to determine the influence of the weld shape on the SIF, a parametric study was then performed over the main weld shape parameters, namely the weld reinforcement height δ , the flank angle β and the edge preparation angle α (and thus the weld length l_w). It was found that the weld shape has a major influence on small semi-elliptical surface cracks relative depth a/t_s , i.e., when they are located in the weld reinforcement region. It results in a mitigation of the SIF due to the local distribution of major principal stresses (i.e., $M_w \leq 1$). On the contrary, embedded elliptical cracks were not significantly affected by the weld shape within the relative crack sizes of interest for fatigue crack growth in the scope of LEFM.

Finally, an empirical parametric equation was derived to estimate weld shape correction factors for SIF at the deepest point of axial semi-elliptical surface cracks at longitudinal butt welded joints of steel liners of SLPT&S that can be used for engineering fatigue and fracture assessment with the LEFM approach, given crack aspect evolution curves. The proposed equation has the advantage to be easy to implement and is physically meaningful.

Fatigue assessment of steel liners

under variable amplitude loading

Part V

Inherent variability is relative to a level of refinement of the model. Except for quantum mechanical phenomena inherent variability is reducible by more detailed modeling combined with corresponding gathering of information. For example, this is the case for material properties like stress–strain relationships. Thus, the inherent variability of material properties in structural reliability is relative to the "usual" level of modeling material behavior. The same applies to the loads. For example, the inherent variability of the wind load on a structure can in principle be reduced as the abilities of meteorologists to predict wind velocities from geophysical models become better and better. Philosophically it does not make sense to claim that wind velocities are random. Randomness is not a property of nature but a property of the model.

– Ove Ditlevsen,
in a correspondence with Arman Der Kiureghian in 1988,
reported by the latter in Der Kiureghian (2008).

9 Loading spectra

9.1 Introduction

Real structures are rarely subject to constant amplitude loading, which would allow the direct use of $S-N$ curves for fatigue-life assessment (Gurney 2006). On the contrary, they may be subject to rather complex variable amplitude loadings, raising the tedious task of determining the spectra under normal operation conditions.

Pressure tunnels and shafts are typically subject to random variable amplitude loadings (Hachem & Giovanola 2013). They are caused by frequent pressure fluctuations in the system (also called water hammers), e.g., induced by pump and turbine start-up and shut-down in pumped-storage hydroelectric power plants (HPP), or by any rapid change of flow velocity causing pressure surges.

The estimation of load cycles can either be done a priori, if the normal operation conditions can be forecast and the load cycles simulated with a model (analytical or numerical), or measured directly on prototype. In the scope of online monitoring of steel-lined pressure tunnels and shafts (SLPT&S), Hachem & Schleiss (2012c) have equipped the pressure shaft of the Grimsel II pumped-storage HPP with high sensitivity pressure sensors allowing to capture water hammer transients generated during the course of one week under normal operation conditions. In subsequent research, Hachem & Giovanola (2013) extended the use of these data by deriving a pressure amplitudes series with a cycle-counting method for fatigue-life assessment of SLPT&S.

The aim of this chapter is to re-analyze these data and to propose a normalized loading spectrum, that may be extrapolated to other HPP with different static heads. In the absence of site-specific data, the proposed approach can then be considered as a preliminary hypothesis for fatigue-life assessment of any HPP whose normal operation conditions may be considered similar to the ones at the origin of these data, thus yielding new spectra scaled with respect to the mean pressure. Nevertheless, the proposed loading spectrum remains specific to the pumped-storage power plant Grimsel II, equipped with ternary groups with Francis turbines.

The analysis presented in this chapter is based on a Master thesis conducted in the framework of the present research project (Muller 2016).

9.2 Prototype measurements under normal operation conditions

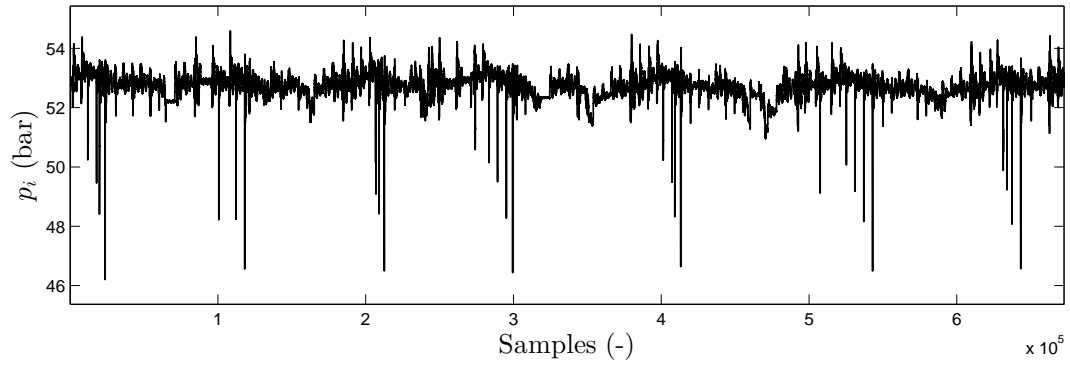
The measurement campaign of Hachem & Schleiss (2012c) was performed on the Grimsel II pumped-storage HPP, owned by Kraftwerke Oberhasli AG (KWO), located in the Canton of Bern, Switzerland. The pressure fluctuations were recorded at the downstream reach of the shaft, i.e., at the location with maximum mean static pressure. The detailed description of the measurement site, the instrumentation and the data acquisition system can be found in Hachem (2011) and Hachem & Schleiss (2012c). Based on the data collected during a typical week of operation, Hachem & Giovanola (2013) filtered and assembled all the records triggered by maneuvers repeated many times per day according to the grid's demand, namely pump and turbine start-up and shut-down. The absolute pressure history in bar is shown in Fig. 9.1a, and the pressure history normalized with the mean internal pressure $p_{i,\text{mean}}$ computed from the series is presented in Fig. 9.1b. It represents 672'600 samples.

9.3 Cycle-counting

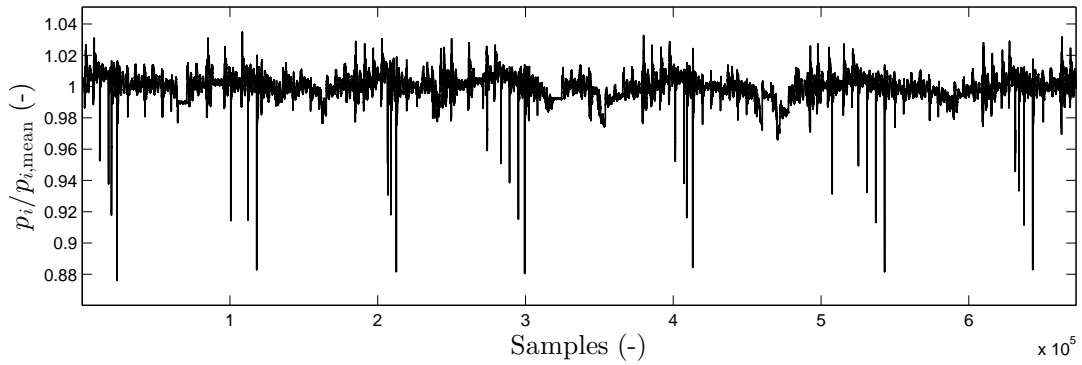
A load cycle is defined as a closed hysteresis loop in a stress (σ)–strain (ϵ) diagram (Kondo 2003; Klemenc & Fajdiga 2004). The goal of cycle-counting is to reduce a loading history into elementary load cycles. There are several cycle-counting methods available for variable amplitude loading, such as the *rainflow counting*¹ (RFC), *peak counting*, *range counting* and the *range-pair counting* (Kondo 2003). The RFC is the most widely used and accepted method (Amzallag *et al.* 1994), as the extracted load cycles correspond to the closed hysteresis loop in a σ – ϵ diagram, closely related to the fatigue damage mechanism (Kondo 2003). The peak and range methods result in a conservative (largest damage) and nonconservative evaluation, respectively, due to a different definition of the load cycle. The range-pair method is similar to the RFC in the definition of the load cycle, with the feature of discarding the small amplitude load cycles which do not produce damage. In this study, the RFC is used for the wide consensus on its applicability and its ease of implementation. As mentioned in the introduction, the RFC is applied to the normalized pressure history, shown in Fig. 9.1b. The principle of cycle extraction of the RFC is not illustrated herein for the sake of concision. One may refer, e.g., to Downing & Socie (1982) or Amzallag *et al.* (1994) for a didactic description of the principle.

The RFC method requires only the *peaks* and *valleys* of the analyzed signal. The first step of the analysis is thus to discard the pressure samples between the peaks and valleys of the normalized pressure history presented in Fig. 9.1b. From 672'600 samples, only 167'774 remain.

¹According to Gurney (2006), the rainflow counting technique gets its name from an analogy with the flow of drops of rain down a pagoda roof.



(a) Pressure history assembled by Hachem & Giovanola (2013).

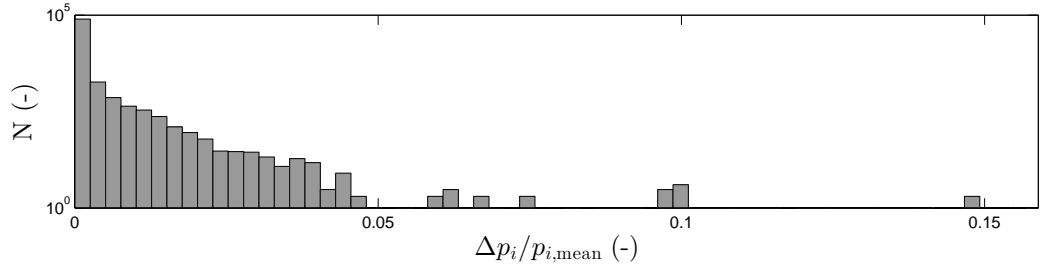


(b) Normalized pressure history.

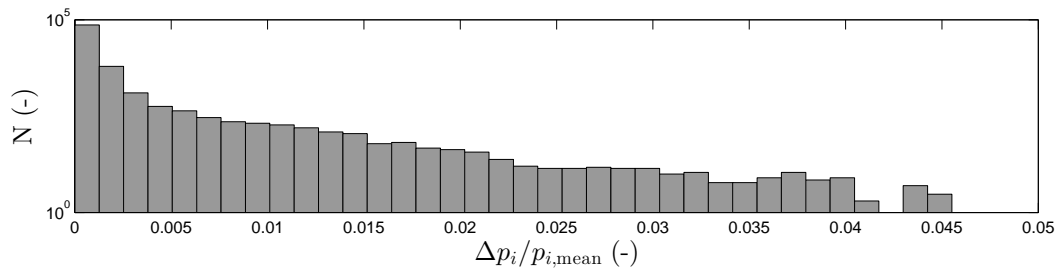
Figure 9.1: Pressure history for a normal week of operation.

In this study, the RFC so-called *Algorithm I* proposed by Downing & Socie (1982) was implemented into the MATLAB® (2012) numerical calculation software. The obtained normalized loading spectrum is shown in Fig. 9.2. A total number of 83'887 cycles (closed hysteresis loops) has been counted during the course of a week under normal operation conditions.

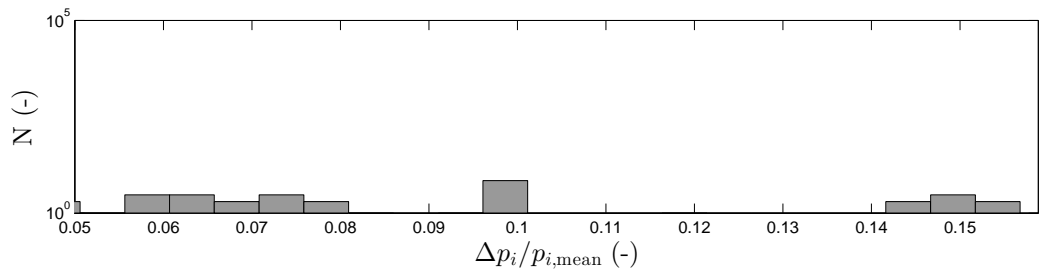
Although HPP are all site specific (general lay-out, head, role in the electric grid, type of electromechanical units), their procedures for maneuvers are subject to constraints from the electric grid (e.g., unit inertia) as well as from design considerations (e.g., maximum allowable overpressure to be withstood by the steel liner in case of SLPT&S, overspeed of the hydraulic machines). As a consequence, in a large majority of cases the ratio between fluctuating parts of the pressure history and the mean static pressure is similar. This allows the extrapolation of the spectrum presented in Fig. 9.2, scaled with respect to the mean pressure.



(a) Entire spectrum.



(b) Part of the spectrum between 0 to 5% of relative pressure amplitude.



(c) Part of the spectrum between 5 to 16% of relative pressure amplitude.

Figure 9.2: Loading spectrum histogram obtained with RFC. The ordinates axis representing the number of occurrences N is in logarithmic scale for presentation purposes.

9.4 Conclusions

The pressure fluctuations were measured by Hachem & Schleiss (2012c) at the downstream reach of a steel-lined pressure shaft of pumped-storage HPP in Switzerland during the course of a week under normal operation conditions. The assembled sample data from Hachem & Giovanola (2013) were re-analyzed and the RFC method was applied in order to obtain a normalized loading spectrum with respect to the mean static pressure that may be extended to hydroelectric power plants with different heads, as a preliminary hypothesis, for fatigue-life analyses. One has to keep in mind that the derived loading spectrum remains specific to the pumped-storage hydropower plant of Grimsel II, equipped with ternary groups with Francis turbines.

10 Fatigue assessment with the effective notch stress approach

10.1 Effective notch stress approach

10.1.1 S – N curves

As described in Sect. 3.2.3, the effective notch stress approach refers to a single FAT value related to a material, namely FAT 225 for steel. However, FAT 225 is limited to $\text{FAT } 160 \times K_w$ with $K_w \geq 1.6$ under principal stress hypothesis (to avoid underestimation in the case of mild weld notches), and to the resistance of the parent material, i.e., related to FAT 160 for steel (Hobbacher 2008, 2016; Sonsino 2009a; Radaj *et al.* 2009; Fricke 2012). As a consequence, both structural hot-spot¹ and notch stresses (with weld toe radius set to $\rho = r_{\text{ref}} = 1 \text{ mm}$) have to be computed, and the minimum N_j given by the aforementioned FAT values is retained to evaluate the linear damage sum (see Eq. 10.5). The S – N curves under consideration are shown in Fig. 10.1.

10.1.2 Stress ranges

Maximum and minimum values of the transient loading

For each cycle, the maximum and minimum values are computed as

$$\begin{cases} p_{i,\text{max}} = p_{i,\text{mean}} + 0.5 \cdot \Delta p_i \\ p_{i,\text{min}} = p_{i,\text{mean}} - 0.5 \cdot \Delta p_i \end{cases} \quad (10.1)$$

where Δp_i is given by the spectrum derived in Chapter 9, scaled to the assumed mean internal water pressure $p_{i,\text{mean}}$. As a consequence, for each cycle, the absolute maximum and minimum pressures are approximated by adding and subtracting 50% of positive variation to the mean

¹For this verification, it is assumed herein that the hot-spot stress is equivalent to the structural stress.

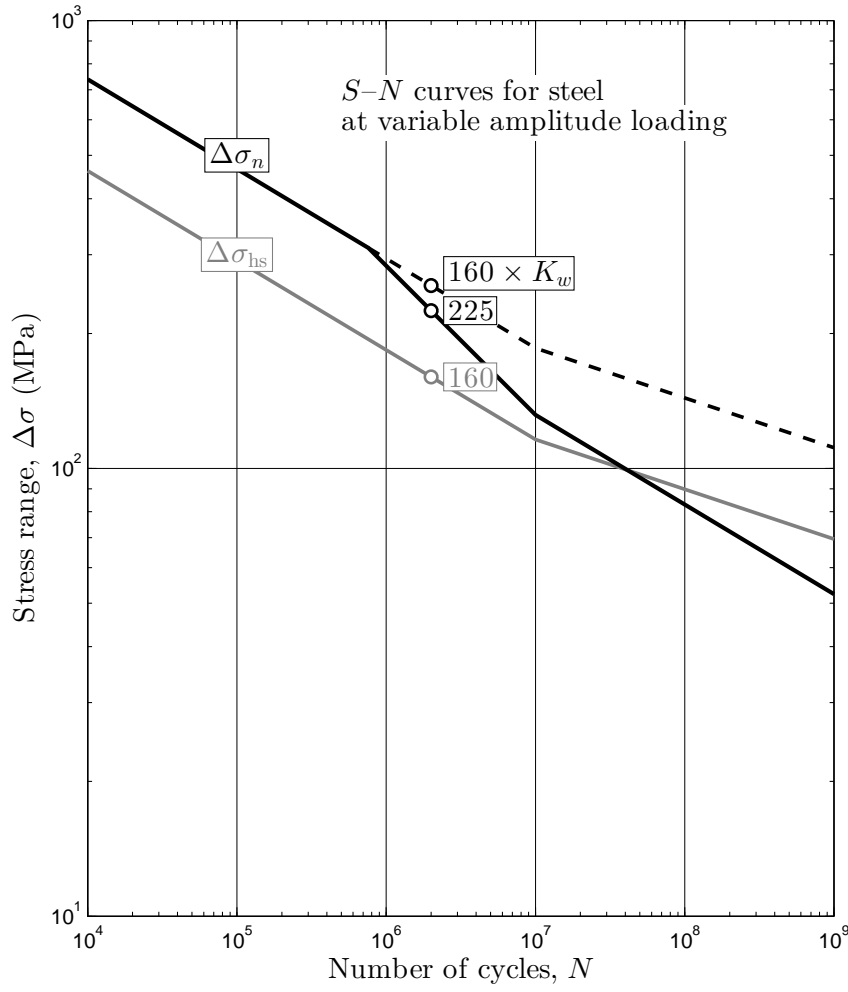


Figure 10.1: Modified S – N curves for steel at variable amplitude loading for Palmgren–Miner summation using the effective notch stress approach.

pressure, respectively. In the S – N approaches, this assumption of symmetric variation with respect to the mean pressure does not influence the result as the stress range is not affected.

Structural stress range

From the maximum and minimum internal water pressures $p_{i,\max}$ and $p_{i,\min}$, the structural stresses are computed as

$$\begin{cases} \sigma_{s,\text{aniso},\max} = K_{m,\max}^* K_{rm,\text{aniso}}^* \sigma_{\text{nom},\text{iso},\max} \\ \sigma_{s,\text{aniso},\min} = K_{m,\min}^* K_{rm,\text{aniso}}^* \sigma_{\text{nom},\text{iso},\min} \end{cases} \quad (10.2)$$

where²

$$\begin{cases} K_{m,\max}^* = [1 + (K_{m,p,\max}^* - 1) + (K_{m,e}^* - 1)] \\ K_{m,\min}^* = [1 + (K_{m,p,\min}^* - 1) + (K_{m,e}^* - 1)] \end{cases} \quad (10.3)$$

The factor $K_{m,\text{aniso}}^*$ transforming the nominal stress computed in the isotropic case is defined by Eq. 7.24, the structural stress concentration factor (SCF) $K_{m,\max}^*$ considering the interaction with the backfill concrete–rock system is defined by Eq. 7.13. The nominal stresses are computed assuming full load sharing between the layers, i.e., that the rock cover is sufficient with a safety factor of 2.0 (see Fig. 2.2). As described in Chapter 7, the worst combinations of geometrical imperfections and rock anisotropy were considered, i.e., the longitudinal welded joints are located at the circumferential direction of the largest nominal stress in the liner, namely in the direction of the plane of isotropy.

Notch stress range

From the maximum and minimum structural stresses obtained above, the notch stresses are computed as

$$\begin{cases} \sigma_{n,\text{aniso},\max} = K_w \sigma_{s,\text{aniso},\max} \\ \sigma_{n,\text{aniso},\min} = K_w \sigma_{s,\text{aniso},\min} \end{cases} \quad (10.4)$$

where the weld SCF is described by Eq. 7.20.

10.1.3 Linear damage calculation by means of the Palmgren–Miner rule

The damage sum D_{calc} is calculated according to the Palmgren–Miner rule

$$D_{\text{calc}} = \frac{n_1}{N_1} + \frac{n_2}{N_2} + \dots + \frac{n_k}{N_k} = \sum_{j=1}^k \frac{n_j}{N_j} \leq 0.5 \quad (10.5)$$

²The structural stress concentration due to peaking $K_{m,p}$ is computed for the maximum and minimum membrane stresses (approximated by the nominal stresses), according to Eq. 3.54, whence the differentiation between maximum and minimum values. However, one may note that as the elastic modulus of steel is greater than the nominal stress in steel liners typically by a factor of 10^3 (see Eqs. 3.54–3.55). As a consequence, $K_{m,p}$ could be considered as constant and computed, e.g., with $p_{i,\max}$.

where n_j is the number of cycles under stress range $\Delta\sigma_j$, and N_j is the number of cycles to failure at stress range $\Delta\sigma_j$ from the limiting modified fatigue resistance S – N curve (see Fig. 10.1). According to the IIW recommendations (Hobbacher 2008, 2016), D_{calc} should remain below 0.5 for variable amplitude loading and proportional loading.

10.2 Parametric study

A parametric study is performed to assess the influence of the parameters enumerated below.

- The mean head of the hydropower plant (3 values from 5 to 15 MPa, i.e., 50 to 150 bar), defining the mean internal water pressure $p_{i,\text{mean}}$ at the lowest point of the shaft. This pressure is directly the one considered to use the loading spectrum proposed in Chapter 9. In reality, this pressure would represent the static head minus the linear and local head losses along the pressurized waterways. It may also vary through the weeks/seasons, but this is not considered herein.
- The steel grades used for the design, from S355 to S960, as defined in Table 10.1.
- The safety factor SF to be considered for the design of the thickness t_s according to the working stress criterion (see Sect. 2.3 and Fig. 2.2). The C.E.C.T. (1980) recommendations suggest $\text{SF} = 2.0$ if the rock mass participation is considered. Three values were tested, namely $\text{SF} = 1.8, 2.0$ and 2.2 . Herein the rock mass participation was limited to 50% for the design³, but the *real* participation was used to compute the stresses for fatigue assessment. The thickness t_s was computed according to a simplified criterion $\sigma_1 \leq f_y/\text{SF}$ in this chapter. This is slightly conservative compared to the criteria recommended by the C.E.C.T. (1980) with the equivalent stress. The rock cover is assumed to be sufficient in all cases.
- The far-field rock mass elastic modulus $E' = 5.0$ and 10.0 GPa.
- The degree of anisotropy $E/E' = 1.0$ to 2.0 (considering transverse isotropy). The design of t_s was performed considering the isotropic case with the lowest elastic modulus E' .
- Two loading spectra are tested, namely the spectrum proposed in Chapter 9, and a so-called *magnified* loading spectrum, by defining a frequency factor γ_{freq} and an amplitude factor γ_{ampl} . Denoting n_{wl} the number of weeks in the lifespan of 100 years, then the magnified loading spectrum is repeated $n_{\text{wl}} \cdot \gamma_{\text{freq}}$ times in the lifespan. The amplitude factor γ_{ampl} applies directly on Δp_i , and it is always verified that the maximum range remains below the overpressure used for the design Δp^+ (see Table 10.2). One should also note that only the part of the spectrum above the threshold $[\Delta p_i/p_{i,\text{mean}}]_{\text{th}} = 1\%$ was considered for the cumulative damage sum, as D_{calc} already converged. Approximately 1080 cycles per week remain in the loading spectra.

³This is an arbitrary rule used in practice, so that the worst case scenario where the rock participation would be inexistent would not cause stresses beyond the yield strength.

10.2. Parametric study

Table 10.1: Minimum yield strengths for different steel grades used in hydropower construction considered for the parametric analysis of fatigue assessment by means of the effective notch stress approach.

Grade	Standard	Yield strength f_y (MPa)	Thickness range (mm)
S355 M/ML	EN 10025-4 (2005)	355	$t_s \leq 16$
		345	$16 < t_s \leq 40$
		335	$40 < t_s \leq 63$
		325	$63 < t_s \leq 80$
S500 ML	EN 10025-4 (2005)	500	$t_s \leq 16$
		490	$16 < t_s \leq 50$
		490	$50 < t_s \leq 75$
S690 QL	EN 10025-6 (2009)	690	$t_s \leq 50$
		650	$50 < t_s \leq 100$
S890 QL	EN 10025-6 (2009)	890	$t_s \leq 50$
		830	$50 < t_s \leq 100$
S960 QL	EN 10025-6 (2009)	960	$t_s \leq 50$

Table 10.2: Constant parameters (or depending on constants) of the parametric analysis of fatigue assessment by means of the effective notch stress approach.

Parameter	Definition	Value	Unit
r_i	Internal radius of the steel liner	1.5	(m)
$\Delta p^+ / p_{i,\text{mean}}$	Maximum overpressure ratio considered for the design	0.10	(-)
Δr_0	Initial gap between steel liner and backfill concrete	$0.025\% \cdot r_i$	(m)
ψ_u	Straight edge factor (inducing peaking)	2.0	(-)
ψ_e	Linear misalignment factor	1.0	(-)
ψ_δ	Weld reinforcement factor	1.0	(-)
β	Flank angle	30	(deg)
α	Edge preparation angle	50	(deg)
E_s	elastic modulus of steel	210	(GPa)
ν_s	Poisson's ratio of steel	0.3	(-)
t_c	Thickness of the backfill concrete layer	0.5	(m)
E_c	Elastic modulus of the backfill concrete	20	(GPa)
ν_c	Poisson's ratio of backfill concrete	0.2	(-)
ν	Poisson's ratio of the far-field rock related to the plane of isotropy	0.2	(-)
ν'	Poisson's ratio of the far-field rock related to the planes perpendicular to the plane of isotropy	0.2	(-)
G'	Cross-shear modulus of the far-field rock	Eq. 4.11	(GPa)
E_{crm}	Elastic modulus of the near-field rock	$0.8 \cdot E'$	(GPa)
ν_{crm}	Poisson's ratio of the near-field rock	0.2	(-)
t_{crm}	Thickness of the near-field rock layer	0.5	(m)

The constant parameters of the study are given in Table 10.2. It should be mentioned that the weld reinforcement and the linear misalignment are set to 100% to the tolerances recommended by the C.E.C.T. (1980) ($\psi_e = \psi_\delta = 1.0$). The peaking was modeled by considering $\psi_u = 2.0$, maximum value studied in Chapter 7. The out-of-roundness is not considered as it was shown in Chapter 7 that its effect is vanished with embedment (in terms of SCF at the longitudinal butt

weld). Finally, the flank angle β was set to 30 deg, as recommended by the IIW for butt welded joints when no other value is specified.

10.3 Results

The results with the *normal* and *magnified* loading spectra are presented in Tables 10.3 and 10.4, respectively. The load sharing considered for the design (either the *real* or limited to 50% of the internal water pressure) is indicated by p_c/p_i . The *real* concrete–rock system participation is indicated by $p_{c,real}/p_i$.

Table 10.3: Results from the effective notch stress approach ($\gamma_{\text{freq}} = 1.0$, $\gamma_{\text{ampl}} = 1.0$).

$p_{i,\text{mean}}$ (MPa)	f_y (MPa)	SF (–)	E (GPa)	$\frac{E}{E'}$ (–)	t_s (mm)	$\frac{p_c}{p_i}$ (%)	$\frac{p_{c,\text{real}}}{p_i}$ (%)	ψ_u (–)	ψ_e (–)	ψ_δ (–)	β (deg)	D_{calc} (–)
5	355	1.8	5.0	1.0	28.0	34	34	2.0	1.0	1.0	30	0.000178
				2.0	28.0	34	37	2.0	1.0	1.0	30	0.000138
			10.0	1.0	21.0	50	55	2.0	1.0	1.0	30	0.0000449
				2.0	21.0	50	58	2.0	1.0	1.0	30	0.0000319
		2.0	5.0	1.0	33.6	29	29	2.0	1.0	1.0	30	0.000127
				2.0	33.6	29	32	2.0	1.0	1.0	30	0.000120
		2.2	5.0	1.0	39.3	25	25	2.0	1.0	1.0	30	0.0000962
				2.0	26.5	48	48	2.0	1.0	1.0	30	0.0000352
	500	1.8	5.0	1.0	14.4	50	53	2.0	1.0	1.0	30	0.000596
				2.0	14.4	50	56	2.0	1.0	1.0	30	0.000404
			10.0	1.0	14.4	50	65	2.0	1.0	1.0	30	0.0000673
				2.0	14.4	50	68	2.0	1.0	1.0	30	0.000045
		2.0	5.0	1.0	17.1	48	48	2.0	1.0	1.0	30	0.000437
				2.0	16.3	50	62	2.0	1.0	1.0	30	0.0000585
		2.2	5.0	1.0	21.0	42	42	2.0	1.0	1.0	30	0.000301
				2.0	18.0	50	60	2.0	1.0	1.0	30	0.0000527
	690	1.8	5.0	1.0	10.4	50	61	2.0	1.0	1.0	30	-
				2.0	x	-	-	2.0	1.0	1.0	30	-
			10.0	1.0	x	-	-	2.0	1.0	1.0	30	-
				2.0	x	-	-	2.0	1.0	1.0	30	-
		2.0	5.0	1.0	11.5	50	58	2.0	1.0	1.0	30	-
				2.0	x	-	-	2.0	1.0	1.0	30	-
		2.2	5.0	1.0	x	-	-	2.0	1.0	1.0	30	-
				2.0	x	-	-	2.0	1.0	1.0	30	-
	10	1.8	5.0	1.0	24.8	41	41	2.0	1.0	1.0	30	0.00616
				2.0	24.8	41	45	2.0	1.0	1.0	30	0.00485
			10.0	1.0	21.0	50	60	2.0	1.0	1.0	30	0.00143
				2.0	21.0	50	63	2.0	1.0	1.0	30	0.000932
		2.0	5.0	1.0	30.0	36	36	2.0	1.0	1.0	30	0.00481
				2.0	23.0	50	57	2.0	1.0	1.0	30	0.00128
		2.2	5.0	1.0	35.2	32	32	2.0	1.0	1.0	30	0.00371
				2.0	25.7	50	55	2.0	1.0	1.0	30	0.00116

10.3. Results

15	890	1.8	5.0	1.0	16.2	50	53	2.0	1.0	1.0	30	0.0106
				2.0	16.2	50	56	2.0	1.0	1.0	30	0.00783
			10.0	1.0	16.2	50	66	2.0	1.0	1.0	30	0.00189
				2.0	16.2	50	69	2.0	1.0	1.0	30	0.00118
		2.0	5.0	1.0	18.3	49	49	2.0	1.0	1.0	30	0.00906
				2.0	18.0	50	63	2.0	1.0	1.0	30	0.00168
		2.2	5.0	1.0	22.3	44	44	2.0	1.0	1.0	30	0.00703
				2.0	19.9	50	62	2.0	1.0	1.0	30	0.00152
	690	1.8	5.0	1.0	46.8	27	27	2.0	1.0	1.0	30	0.0113
				2.0	46.8	27	31	2.0	1.0	1.0	30	0.0096
			10.0	1.0	31.6	50	51	2.0	1.0	1.0	30	0.00615
				2.0	31.6	50	55	2.0	1.0	1.0	30	0.00465
		2.0	5.0	1.0	54.6	24	24	2.0	1.0	1.0	30	0.00937
				2.0	37.6	47	47	2.0	1.0	1.0	30	0.00542
		2.2	5.0	1.0	62.4	21	21	2.0	1.0	1.0	30	0.00799
				2.0	45.7	41	41	2.0	1.0	1.0	30	0.00469
	890	1.8	5.0	1.0	31.2	37	37	2.0	1.0	1.0	30	0.0191
				2.0	31.2	37	41	2.0	1.0	1.0	30	0.0152
			10.0	1.0	24.5	50	58	2.0	1.0	1.0	30	0.0074
				2.0	24.5	50	61	2.0	1.0	1.0	30	0.00546
		2.0	5.0	1.0	37.2	33	33	2.0	1.0	1.0	30	0.0152
				2.0	27.0	50	55	2.0	1.0	1.0	30	0.00685
		2.2	5.0	1.0	43.1	29	29	2.0	1.0	1.0	30	0.0125
				2.0	29.9	50	53	2.0	1.0	1.0	30	0.00639
	960	1.8	5.0	1.0	27.3	40	40	2.0	1.0	1.0	30	0.0224
				2.0	27.3	40	44	2.0	1.0	1.0	30	0.0178
			10.0	1.0	22.7	50	60	2.0	1.0	1.0	30	0.00782
				2.0	22.7	50	63	2.0	1.0	1.0	30	0.00571
		2.0	5.0	1.0	32.8	36	36	2.0	1.0	1.0	30	0.0179
				2.0	25.2	50	57	2.0	1.0	1.0	30	0.00724
		2.2	5.0	1.0	38.3	32	32	2.0	1.0	1.0	30	0.0146
				2.0	27.7	50	55	2.0	1.0	1.0	30	0.00675

Table 10.4: Results from the effective notch stress approach with magnified loading spectra ($\gamma_{\text{freq}} = 1.2$, $\gamma_{\text{ampl}} = 1.2$).

$p_{i,\text{mean}}$ (MPa)	f_y (MPa)	SF (-)	E (GPa)	$\frac{E}{E'}$ (-)	t_s (mm)	$\frac{p_c}{p_i}$ (%)	$\frac{p_{c,\text{real}}}{p_i}$ (%)	ψ_u (-)	ψ_e (-)	ψ_δ (-)	β (deg)	D_{calc} (-)
5	355	1.8	5.0	1.0	28.0	34	34	2.0	1.0	1.0	30	0.000531
				2.0	28.0	34	37	2.0	1.0	1.0	30	0.000411
			10.0	1.0	21.0	50	55	2.0	1.0	1.0	30	0.000134
				2.0	21.0	50	58	2.0	1.0	1.0	30	0.0000951
		2.0	5.0	1.0	33.6	29	29	2.0	1.0	1.0	30	0.000381
				2.0	33.6	29	32	2.0	1.0	1.0	30	0.00306
		2.2	5.0	1.0	39.3	25	25	2.0	1.0	1.0	30	0.000287
				2.0								

Chapter 10. Fatigue assessment with the effective notch stress approach

			10.0	2.0	26.5	48	48	2.0	1.0	1.0	30	0.000105
	500	1.8	5.0	1.0	14.4	50	53	2.0	1.0	1.0	30	0.00178
				2.0	14.4	50	56	2.0	1.0	1.0	30	0.00121
			10.0	1.0	14.4	50	65	2.0	1.0	1.0	30	0.000201
				2.0	14.4	50	68	2.0	1.0	1.0	30	0.000134
		2.0	5.0	1.0	17.1	48	48	2.0	1.0	1.0	30	0.00131
			10.0	2.0	16.3	50	62	2.0	1.0	1.0	30	0.000175
		2.2	5.0	1.0	21.0	42	42	2.0	1.0	1.0	30	0.000898
			10.0	2.0	18.0	50	60	2.0	1.0	1.0	30	0.000157
	690	1.8	5.0	1.0	10.4	50	61	2.0	1.0	1.0	30	-
				2.0	x	-	-	2.0	1.0	1.0	30	-
			10.0	1.0	x	-	-	2.0	1.0	1.0	30	-
				2.0	x	-	-	2.0	1.0	1.0	30	-
		2.0	5.0	1.0	11.5	50	58	2.0	1.0	1.0	30	-
			10.0	2.0	x	-	-	2.0	1.0	1.0	30	-
		2.2	5.0	1.0	x	-	-	2.0	1.0	1.0	30	-
			10.0	2.0	x	-	-	2.0	1.0	1.0	30	-
10	690	1.8	5.0	1.0	24.8	41	41	2.0	1.0	1.0	30	0.014
				2.0	24.8	41	45	2.0	1.0	1.0	30	0.011
			10.0	1.0	21.0	50	60	2.0	1.0	1.0	30	0.00427
				2.0	21.0	50	63	2.0	1.0	1.0	30	0.00278
		2.0	5.0	1.0	30.0	36	36	2.0	1.0	1.0	30	0.0109
			10.0	2.0	23.0	50	57	2.0	1.0	1.0	30	0.00383
		2.2	5.0	1.0	35.2	32	32	2.0	1.0	1.0	30	0.00889
			10.0	2.0	25.7	50	55	2.0	1.0	1.0	30	0.00347
	890	1.8	5.0	1.0	16.2	50	53	2.0	1.0	1.0	30	0.0241
				2.0	16.2	50	56	2.0	1.0	1.0	30	0.0179
			10.0	1.0	16.2	50	66	2.0	1.0	1.0	30	0.00549
				2.0	16.2	50	69	2.0	1.0	1.0	30	0.00351
		2.0	5.0	1.0	18.3	49	49	2.0	1.0	1.0	30	0.0207
			10.0	2.0	18.0	50	63	2.0	1.0	1.0	30	0.00496
		2.2	5.0	1.0	22.3	44	44	2.0	1.0	1.0	30	0.016
			10.0	2.0	19.9	50	62	2.0	1.0	1.0	30	0.00451
15	690	1.8	5.0	1.0	46.8	27	27	2.0	1.0	1.0	30	0.0257
				2.0	46.8	27	31	2.0	1.0	1.0	30	0.022
			10.0	1.0	31.6	50	51	2.0	1.0	1.0	30	0.014
				2.0	31.6	50	55	2.0	1.0	1.0	30	0.0106
		2.0	5.0	1.0	54.6	24	24	2.0	1.0	1.0	30	0.0214
			10.0	2.0	37.6	47	47	2.0	1.0	1.0	30	0.0123
		2.2	5.0	1.0	62.4	21	21	2.0	1.0	1.0	30	0.0182
			10.0	2.0	45.7	41	41	2.0	1.0	1.0	30	0.0107
	890	1.8	5.0	1.0	31.2	37	37	2.0	1.0	1.0	30	0.0413
				2.0	31.2	37	41	2.0	1.0	1.0	30	0.0337
			10.0	1.0	24.5	50	58	2.0	1.0	1.0	30	0.0169
				2.0	24.5	50	61	2.0	1.0	1.0	30	0.0124
		2.0	5.0	1.0	37.2	33	33	2.0	1.0	1.0	30	0.0336
			10.0	2.0	27.0	50	55	2.0	1.0	1.0	30	0.0156
		2.2	5.0	1.0	43.1	29	29	2.0	1.0	1.0	30	0.0282
			10.0	2.0	29.9	50	53	2.0	1.0	1.0	30	0.0146

960	1.8	5.0	1.0	27.3	40	40	2.0	1.0	1.0	30	0.0484
			2.0	27.3	40	44	2.0	1.0	1.0	30	0.0388
		10.0	1.0	22.7	50	60	2.0	1.0	1.0	30	0.0179
			2.0	22.7	50	63	2.0	1.0	1.0	30	0.013
	2.0	5.0	1.0	32.8	36	36	2.0	1.0	1.0	30	0.0389
		10.0	2.0	25.2	50	57	2.0	1.0	1.0	30	0.0165
	2.2	5.0	1.0	38.3	32	32	2.0	1.0	1.0	30	0.0324
		10.0	2.0	27.7	50	55	2.0	1.0	1.0	30	0.0154

The first general observation that can be made is that all the tested cases, for both normal and magnified spectra, exhibit very low damage sums compared to the limit $D_{\text{calc}} \leq 0.5$. Beside this observation, one can assess the influence of each parameter.

The parameter that has the most significant influence is the mean internal water pressure $p_{i,\text{mean}}$. Indeed, one can observe that for the normal spectra, D_{calc} is roughly of the order of 10^{-4} for $p_{i,\text{mean}} = 5$ MPa, 10^{-3} for $p_{i,\text{mean}} = 10$ MPa and 10^{-2} for $p_{i,\text{mean}} = 15$ MPa. For the magnified spectra, the cumulative damage sums are of the same order of magnitude, approximately multiplied by a factor of 3. This can be explained because of the fact that although the relative variation of pressure with respect to $p_{i,\text{mean}}$ is similar for all cases, the resulting variation of absolute pressure ranges (and thus stress ranges in the steel liner) increases with increasing $p_{i,\text{mean}}$. It can be illustrated by selecting four cases with the same SF = 2.0. The variation of nominal pressure with respect to the yield strength is shown in Fig. 10.2 and is identical for the 4 cases. This is true only as the rock participation remains below 50% of p_i for all 4 cases.

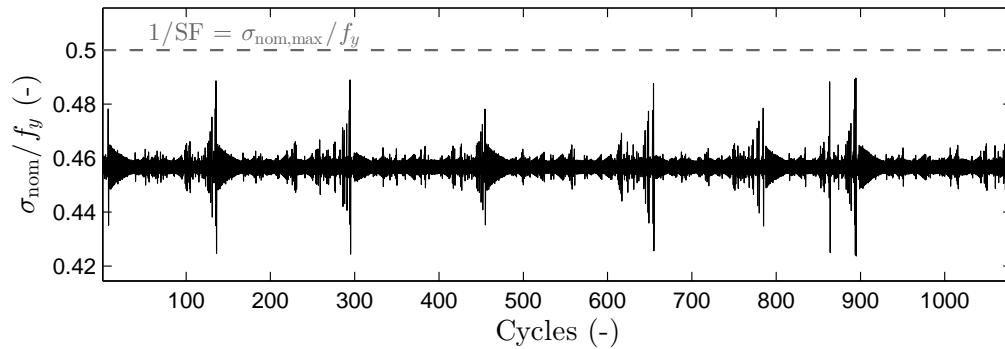


Figure 10.2: Variation of the nominal stress during one week under normal loading spectrum with $[\Delta p_i / p_{i,\text{mean}}]_{\text{th}} = 1\%$, representative of all cases presented in Figs. 10.3 and 10.4.

Figure 10.3 presents the relative variation of the notch stress σ_n with respect to the mean nominal stress $\sigma_{\text{nom},\text{mean}}$. The mean value of the variation in each subplot indicates the notch stress concentration factor $K_t^* = K_m^* K_w$ in each case. One can observe that the thicker the steel liner, the greater K_t^* . For a given weld toe radius $\rho = r_{\text{ref}} = 1$ mm, this is explained by the induced

stress gradient at the fictitious rounding, increasing with thickness. The weld reinforcement height δ also influences this result, as the tolerance suggested by the C.E.C.T. (1980) is not linear, but this is not further investigated in the scope of this analysis. Beside this observation, it can be seen that for the same $p_{i,\text{mean}}$, the damage sum is greater for higher steel grade. As a consequence, although great thickness increases the notch concentration, higher yield strength induces a smaller thickness which increases the stresses variation in the steel liner, which seems to be the most significant effect. This is confirmed by plotting the variation of the notch stress ranges in Fig. 10.4. The influence of $p_{i,\text{mean}}$ is also depicted in Fig. 10.4.

The influence of the other parameters results from the aforementioned observations. Greater rock elastic modulus induces more rock participation, and thus smaller stress variation in the steel liner. The same effect is observed when anisotropy is considered, as extra rock participation is neglected when the design is performed with the lowest elastic modulus E' . Finally, increasing SF also reduces the damage sum, as it reduces the stress variation in the steel liner.

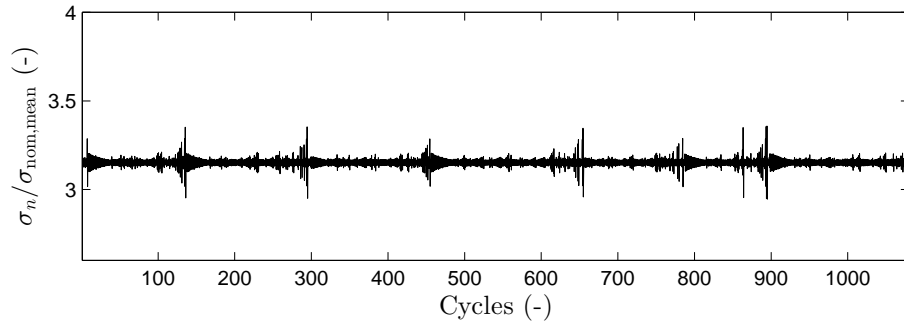
The influence of the loading spectra can also be analyzed. According to Eq. 10.5, the number of cycles characterized by γ_{freq} has a linear influence on the result. This is not the case for γ_{ampl} . The factor 3 between the results of both spectra is thus mostly due to the increase of γ_{ampl} from 1.0 to 1.2. With the calculated damage sums D_{calc} of both Tables 10.3 and 10.4, one can calculate the critical $\gamma_{\text{freq,c}}$ with respect to the normal spectrum to reach the critical damage sum as

$$\gamma_{\text{freq,c}} = \frac{0.5}{\gamma_{\text{freq}} \cdot D_{\text{calc}}}. \quad (10.6)$$

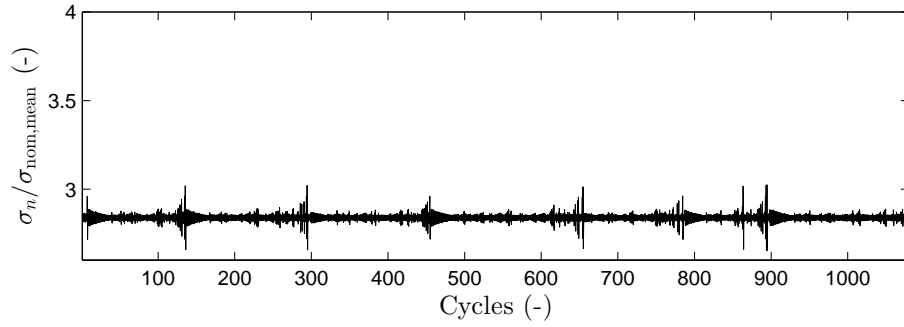
For the normal spectrum, $p_{i,\text{mean}} = 15$ MPa and using S960, $\gamma_{\text{freq,c}}$ is of the order of 20–100. In the corresponding cases with the magnified spectrum, $\gamma_{\text{freq,c}}$ is of the order of 10–30.

10.4 Commentaries on the results

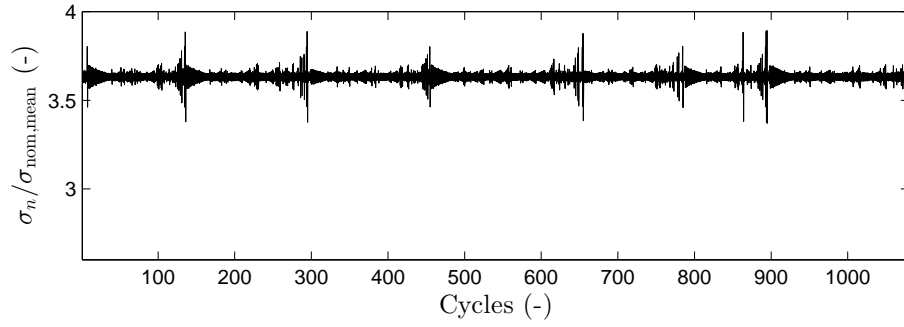
Demal & Moser (2013) also presented a fatigue assessment study of a penstock using the effective notch stress approach. In their study, the cumulative damage sum could reach the critical value of 0.5 in some cases, which is a major difference with the results presented herein. In Demal & Moser (2013), a single case study was presented, namely a penstock (in open-air) with $p_{i,\text{mean}} = 1.7$ MPa, using S690 QL, a radius $r_i = 1.85$ m and a thickness $t_s = 14$ mm. Considering SF = 1.7 according to the C.E.C.T. (1980), one can roughly assume that this penstock was designed to withstand a water hammer inducing $\Delta p^+ \approx 50\%$ of $p_{i,\text{mean}}$ (or limited by another criterion). Within this context, the fatigue assessment was performed with a loading spectrum that is described quantitatively but its origin is not detailed. With notch concentrations very similar to the one computed herein, the notch stress ranges induced by the loading spectrum used by Demal & Moser (2013) goes up to $\Delta\sigma_n = 500$ MPa, with significantly more occurrences of ranges from 100 to 400 MPa than in the loading spectrum considered herein. This explains



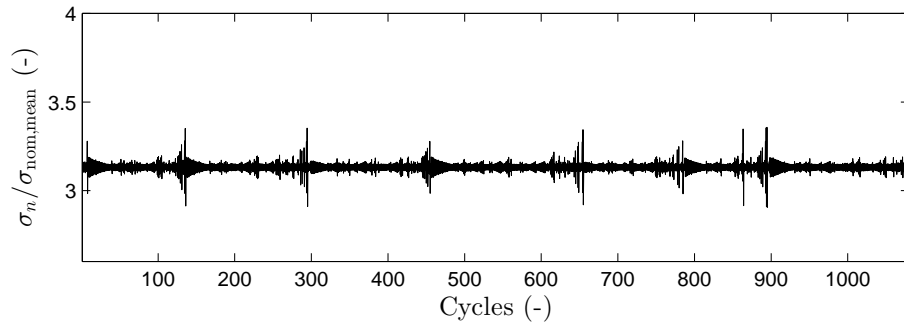
(a) $p_{i,\text{mean}} = 5 \text{ MPa}$, S355 ML, $t_s = 33.6 \text{ mm}$, $D_{\text{calc}} = 0.000127$.



(b) $p_{i,\text{mean}} = 5 \text{ MPa}$, S500 ML, $t_s = 17.1 \text{ mm}$, $D_{\text{calc}} = 0.000437$.

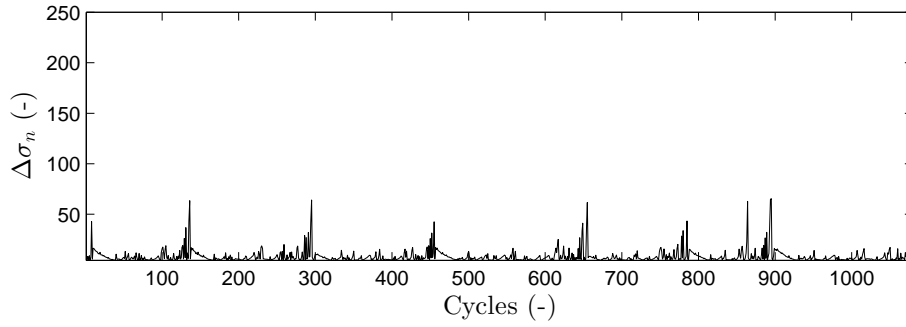


(c) $p_{i,\text{mean}} = 15 \text{ MPa}$, S690 QL, $t_s = 54.6 \text{ mm}$, $D_{\text{calc}} = 0.000937$.

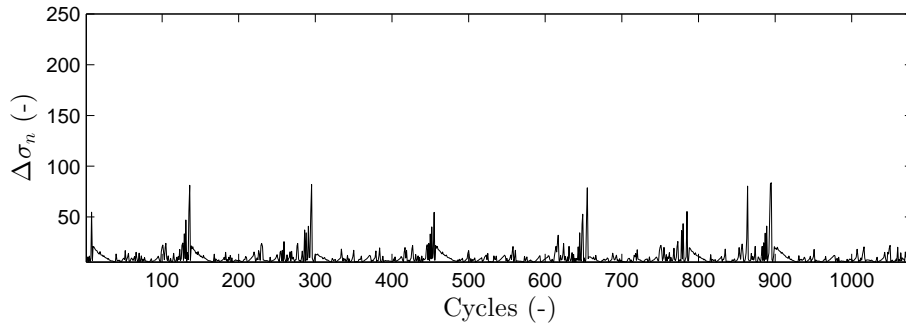


(d) $p_{i,\text{mean}} = 15 \text{ MPa}$, S960 QL, $t_s = 32.8 \text{ mm}$, $D_{\text{calc}} = 0.0179$.

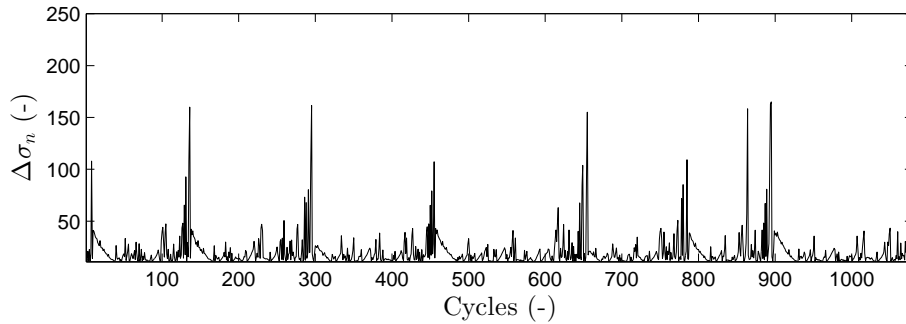
Figure 10.3: Variation of the notch stress during one week under normal loading spectrum with $[\Delta p_i / p_{i,\text{mean}}]_{\text{th}} = 1\%$. In all cases, $\text{SF} = 2.0$, $E' = 5 \text{ MPa}$, and $E/E' = 1.0$.



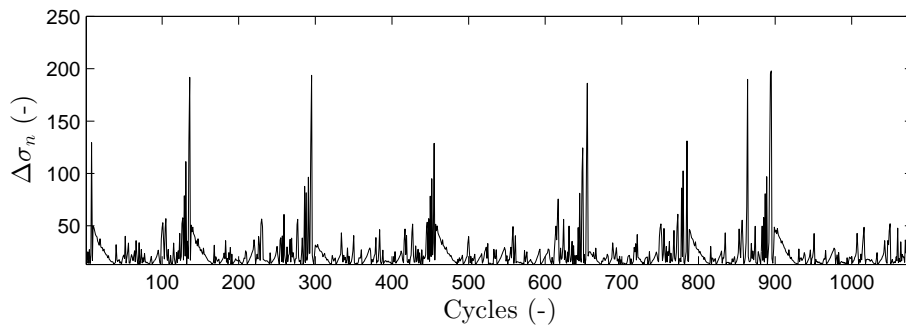
(a) $p_{i,\text{mean}} = 5 \text{ MPa}$, S355 ML, $t_s = 33.6 \text{ mm}$, $D_{\text{calc}} = 0.000127$.



(b) $p_{i,\text{mean}} = 5 \text{ MPa}$, S500 ML, $t_s = 17.1 \text{ mm}$, $D_{\text{calc}} = 0.000437$.



(c) $p_{i,\text{mean}} = 15 \text{ MPa}$, S690 QL, $t_s = 54.6 \text{ mm}$, $D_{\text{calc}} = 0.000937$.



(d) $p_{i,\text{mean}} = 15 \text{ MPa}$, S960 QL, $t_s = 32.8 \text{ mm}$, $D_{\text{calc}} = 0.0179$.

Figure 10.4: Variation of notch stress ranges during one week under normal loading spectrum with $[\Delta p_i/p_{i,\text{mean}}]_{\text{th}} = 1\%$. In all cases, $\text{SF} = 2.0$, $E' = 5 \text{ MPa}$ and $E/E' = 1.0$.

the major differences with the results presented in the present chapter. This is also illustrated in Fig. 10.5, where the maximum N_{\max} in Eq. 10.5 is found with the maximum notch stress range $\Delta\sigma_n^{\max}$ observed in the case characterized by $p_{i,\text{mean}} = 15$ MPa, S960 QL, SF = 2.0, $E' = 5$ MPa, $E/E' = 1.0$ and $t_s = 32.8$ mm, yielding $D_{\text{calc}} = 0.0179$. Considering the corresponding spectrum shown at the bottom of Fig. 10.4, one can rapidly see that the damage sum 0.5 cannot be reached within the hypothesis made herein, as more than 2 millions cycles would be required at this level over the lifespan.

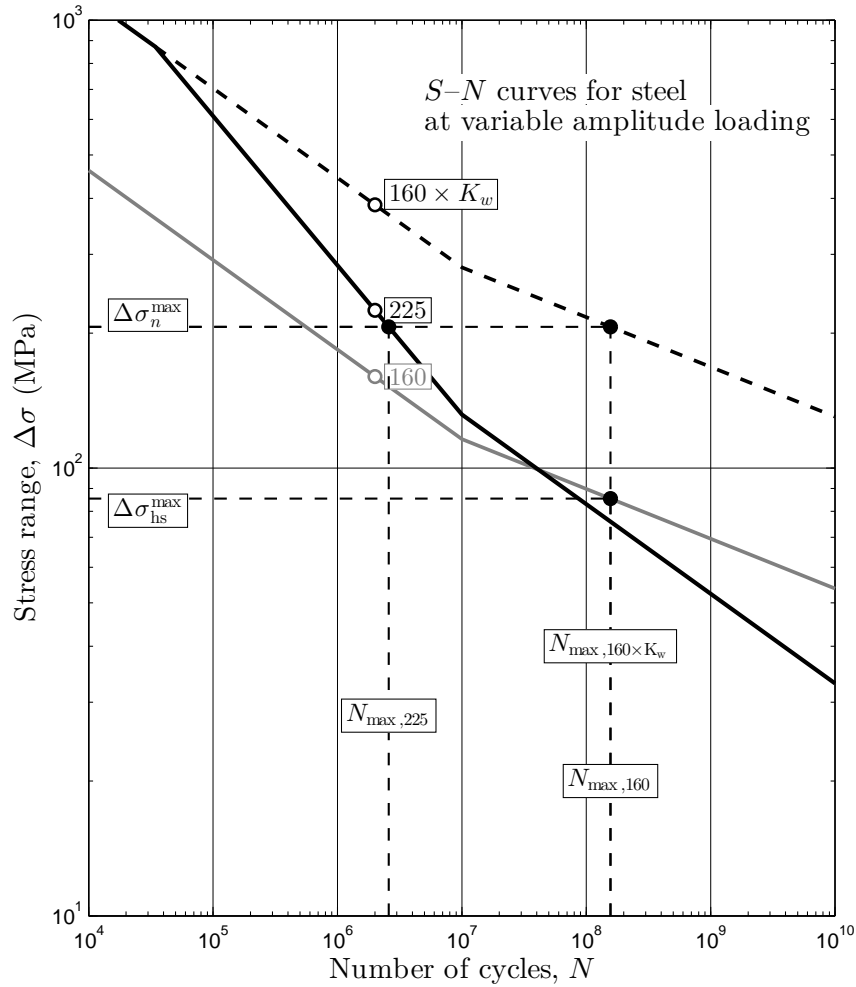


Figure 10.5: Maximum number of cycles to failure N_{\max} associated to the maximum notch stress range $\Delta\sigma_n^{\max}$ for the case characterized by $p_{i,\text{mean}} = 15$ MPa, S960 QL, SF = 2.0, $E' = 5$ MPa, $E/E' = 1.0$ and $t_s = 32.8$ mm.

This brief comparison also outlines the major influence of the loading spectrum, which should be case specific in practice.

10.5 Conclusions

In this chapter, fatigue assessment of longitudinal butt welded joints of steel-lined pressure tunnels and shafts was performed by means of the effective notch stress approach. This procedure thus assesses the failure from crack initiation and propagation from the weld toe. A parametric study was performed for a large range of high-head hydropower plants where the participation of the rock mass is considered. It could be shown that the cumulative damage sum, calculated with the Palmgren–Miner rule and the parametric equations proposed in Chapters 5 and 7 for the notch SCF, is only a few percents of the critical value of 0.5 recommended by the IIW recommendations (Hobbacher 2008, 2016) for variable amplitude loading.

With the pressure amplitudes of the spectrum proposed in Chapter 10, the critical value could be reached for occurrences 10 to 100 times higher, in the worst cases with high mean pressures and the highest steel grades. However, it was also discussed that the results highly depend on the loading spectrum. One has to keep in mind that the spectrum was derived from measurements on the pumped-storage power plant Grimsel II, with specific hydraulic machines (ternary groups with Francis turbines), and might not be representative of weekly transients occurring, e.g., in a very high-head hydropower plant with Pelton turbines.

11 Probabilistic model for fatigue crack growth and fracture

11.1 LEFM approach for fatigue crack growth and fracture

11.1.1 Fatigue crack growth

The fatigue crack growth is modeled by the Paris–Erdogan law, expressing the crack growth rate da/dN as a function of the stress intensity factor range ΔK in mode I as (see also Sect. 3.2.4)

$$\frac{da}{dN} = \begin{cases} 0 & \text{for } \Delta K \leq \Delta K_{th} \\ C(\Delta K)^m & \text{for } \Delta K > \Delta K_{th} \end{cases} \quad (11.1)$$

where C and m are material parameters and ΔK_{th} is the stress intensity factor threshold below which propagation does not occur. In this study, an initial crack-like flaw of minor semi-axis a_i is assumed, due, e.g., to hydrogen induced cold cracking. Under variable amplitude loading, the final crack size after $N_{lifespan}$ cycles over the defined lifespan is thus calculated by the nonlinear summation of all the crack increments yielding

$$a_f = a_i + \sum_{j=1}^{N_{lifespan}} \left(\frac{da}{dN} \right)_j \quad (11.2)$$

where $(da/dN)_j$ is equivalent to an increment Δa_j under the j^{th} cycle.

11.1.2 Types of studied cracks

In this chapter, the fatigue propagation of two types of cracks is studied, namely semi-elliptical surface cracks (Fig. 11.1) and embedded elliptical cracks (with $d_1 = d_2 = t_s/2$, see Fig. 11.2).

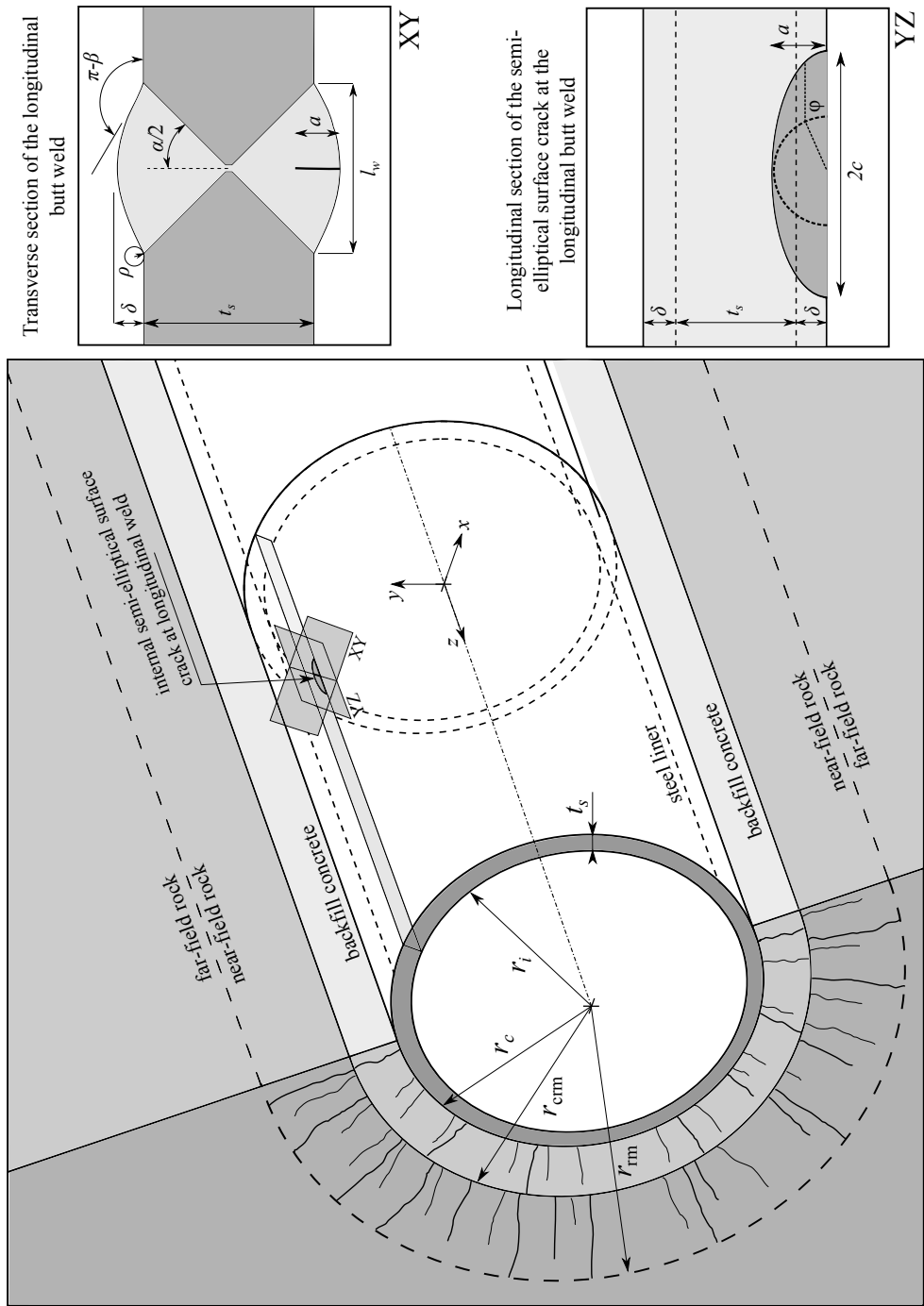


Figure 11.1: Definition sketch of a steel-lined pressure tunnel or shaft with an axial semi-elliptical surface crack at the longitudinal butt welded joint, on the internal surface. The slenderness of the steel liner is distorted for the sake of presentation.

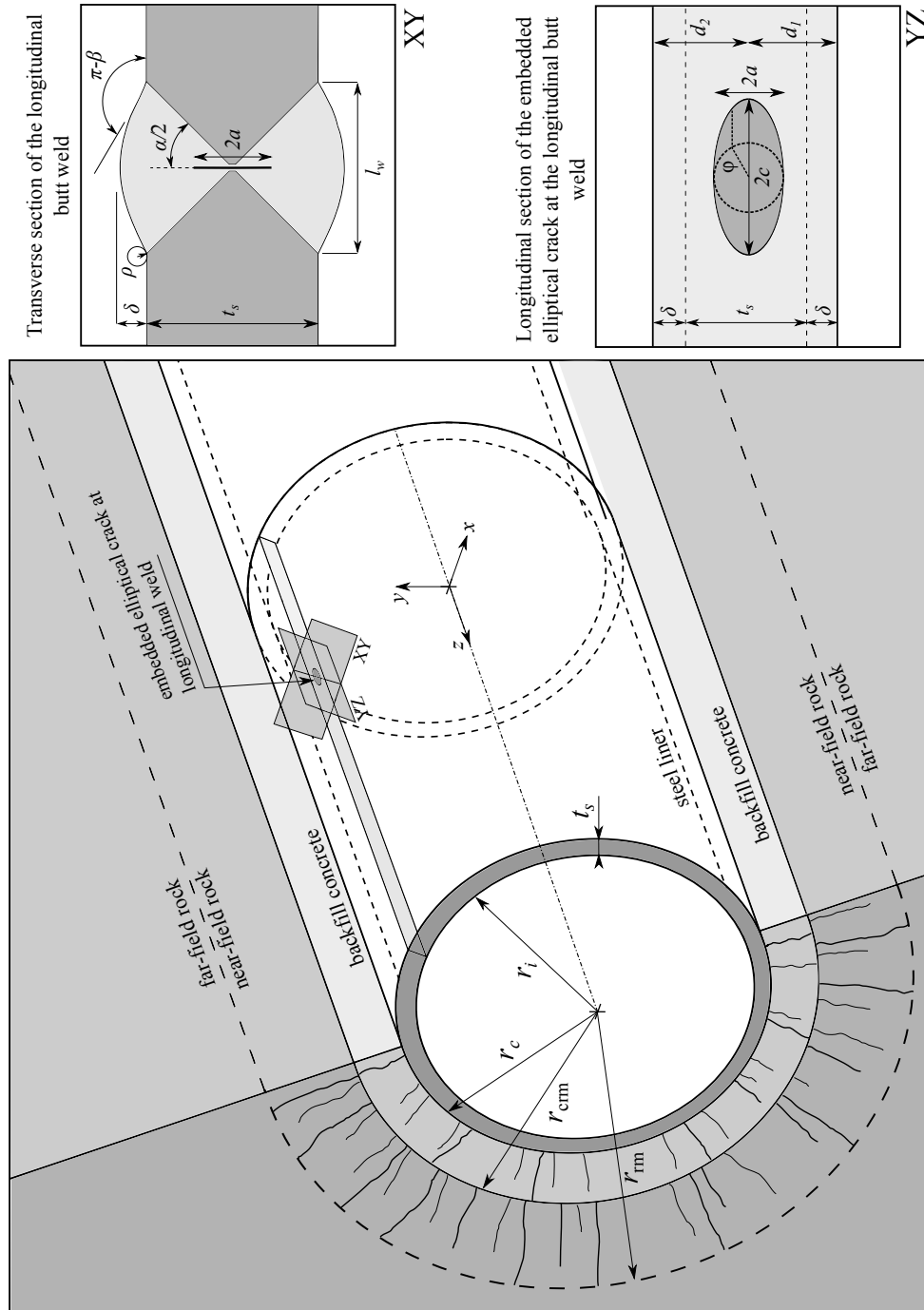


Figure 11.2: Definition sketch of a steel-lined pressure tunnel or shaft with an axial embedded elliptical crack at the longitudinal butt welded joint. The slenderness of the steel liner is distorted for the sake of presentation.

11.1.3 Failure criteria

Two failure criteria are considered, namely:

1. failure associated with fracture; and
2. failure associated with the crack length reaching a size equal to the liner's thickness, i.e., through-thickness crack.

At cycle N , the first criterion is verified if the maximum crack driving force remains below the fracture toughness K_{IC} (see Sect. 11.1.4), i.e., that

$$K_{I,max}^N < K_{IC}. \quad (11.3)$$

The second criterion is verified if

$$a_N < t_s. \quad (11.4)$$

11.1.4 Fracture toughness

Due to the absence of fracture mechanics data in the scope of this research project allowing an estimate of the fracture toughness for each tested case, it is chosen to adopt the true plane strain fracture toughness K_{IC} as a fracture criterion, thus remaining in the framework of linear elastic fracture mechanics. Based on the *size condition* imposed in the experimental procedure to measure K_{IC} (Schwalbe *et al.* 2003)

$$t_s \geq 2.5 \left(\frac{K_{IC}}{f_y} \right)^2, \quad (11.5)$$

for each tested case the fracture toughness K_{IC} is assumed to be expressed as

$$K_{IC} = f_y \sqrt{\frac{t_s}{2.5}}, \quad (11.6)$$

which represents the maximum plane strain fracture toughness that can be validated for a given thickness t_s , and should be a conservative assumption. It yields fracture toughness values from approximately 40 to 120 MPa \sqrt{m} within the tested cases. The values obtained by Hachem & Giovanola (2013) from a deterministic correlation formula converting notch impact energy K_V are of the same order of magnitude.

Some data from Charpy V-notch impact tests performed by an undisclosed swiss hydroelectric company on steel welded joints were used to assess the aforementioned hypothesis. The test were performed according to EN ISO 148-1 (2011) for steels S500 ML, S690 QL and ALFORM 700 M. Three different values for the absorbed energy K_V were measured at different temperatures in the weld material for each type of joints. The fracture toughness was estimated from the Charpy V-notch tests by means of the procedure described in SINTAP (Bannister 1998) and in the British Standard 7910 (2005). It was verified that the proposed hypothesis to estimate K_{IC} is a conservative assumption when compared to the probabilistic distributions of the fracture toughness obtained from this procedure (Muller 2016).

Moreover, with the failure criteria adopted in Sect. 11.1.3, the choice of the fracture toughness value may only have a limited influence on the fatigue life, if any, as the crack growth rate increases exponentially with crack size before failure (Maljaars *et al.* 2012).

11.2 Monte Carlo procedure

The preliminary development of the probabilistic model presented in this chapter was performed in a Master thesis in the framework of the present research project (Muller 2016).

11.2.1 Stochastic variables

Crack shape ratio a/c

In welded joints, one can consider that the crack shape ratio a/c (see Figs. 11.1–11.2) varies from 0 to 1 (Lukić & Cremona 2001). During fatigue life, the crack shape may evolve depending on parameters such as the weld geometry, the crack size, the loading spectrum or the effect of coalescence between several flaws. For the sake of simplicity, some authors assume a constant crack shape ratio during crack propagation. Other approaches may be to study the crack propagation along the two axes of the 3D plane crack, or to assume a crack shape evolution function, e.g., as a function of a .

In this study, the simple approach of a constant a/c ratio during the crack propagation is adopted both for semi-elliptical surface cracks and embedded elliptical cracks, following the lognormal distribution proposed by Yamada & Nagatsu (1989). The proposed distribution is truncated so that the crack shape ratio a/c remains below 1 as (Dillström & Nilsson 2003)

$$F_{a/c}^t(x) = \begin{cases} 0 & \text{for } x > 1 \\ cF_{a/c}(x) & \text{for } x \leq 1 \end{cases} \quad (11.7)$$

with

$$c = \frac{1}{F_{a/c}(x_t = 1)}, \quad (11.8)$$

where $F_{a/c}$ is the cumulative density function of a/c . The probability density function (PDF) and the cumulative density function (CDF) of a/c are plotted in Fig. 11.3. Following the nomenclature of the lognormal distribution presented in Appendix C, a/c is thus distributed as

$$a/c \sim \text{lognormal}(\mu = -1.01; \sigma = 0.40). \quad (11.9)$$

Threshold stress intensity factor ΔK_{th}

For deterministic analyses, the recommendations of the International Institute of Welding (IIW, Hobbacher 2008, 2016) and the British Standard 7910 (2005) suggest the use of $\Delta K_{th} = 63 \text{ Nmm}^{-3/2}$, or $\Delta K_{th} = 2 \text{ MPa}\sqrt{\text{m}}$. In this study, the distribution proposed by Walbridge (2005) is adopted, i.e.,

$$\Delta K_{th}(\text{Nmm}^{-3/2}) \sim \text{lognormal}(\mu = 4.6044; \sigma = 0.0387). \quad (11.10)$$

The lognormal random ΔK_{th} is thus characterized by the mean value $m = 100 \text{ Nmm}^{-3/2}$ and the variance $v = 15 \text{ Nmm}^{-3/2}$. The distributions in $(\text{Nmm}^{-3/2})$ and in $(\text{MPa}\sqrt{\text{m}})$ are plotted in Fig. 11.4.

Paris law parameter C

According to Maddox (1991), the crack growth rate da/dN is quasi-independent from the material tensile strength, and Baptista (2016) reports, after the same author in a previous study, that it does not significantly vary through the different regions of the welded joint, namely the base material, the heat-affected zone (HAZ) or the weld material. The exponent m in Eq. 11.1 is commonly assumed as deterministic, and the uncertainty in the crack growth rate da/dN is considered by assuming a lognormal distribution for the coefficient C (see, e.g., Lassen & Sorensen 2002; Righiniotis & Chryssanthopoulos 2003, 2004; Maljaars *et al.* 2012; Baptista 2016). The following distribution is adopted herein for C in inert environment after Baptista (2016):

$$C(\text{Nmm}^{-3/2}) \sim \text{lognormal}(\mu = 29.84; \sigma = 0.55), \quad (11.11)$$

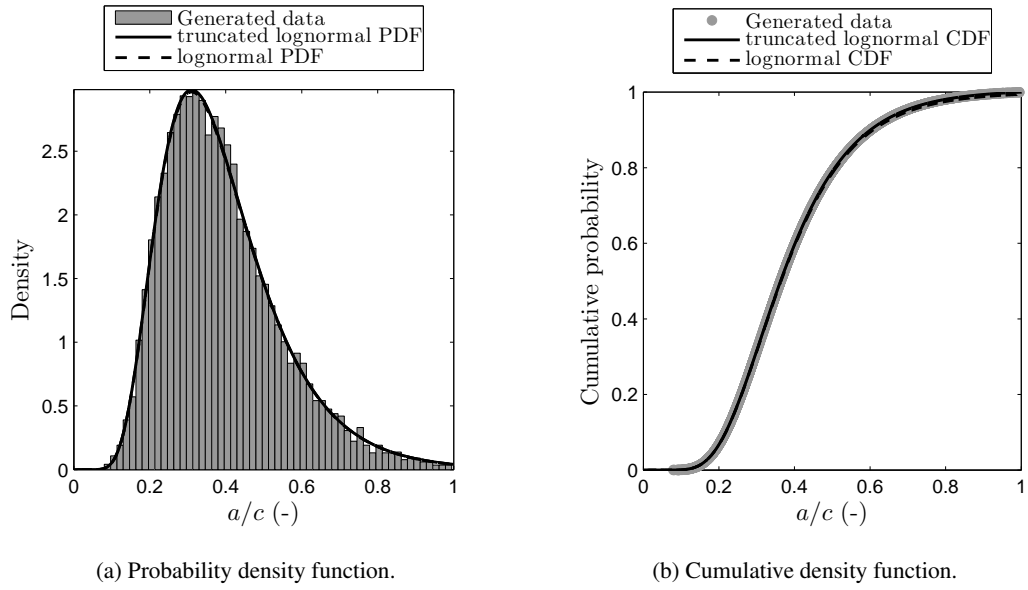


Figure 11.3: Truncated lognormal distribution for the crack shape ratio a/c . The histogram was generated from a sampling of 10^4 values, and its number of bins was defined according to the Freedman & Diaconis (1981) rule for the sake of presentation.

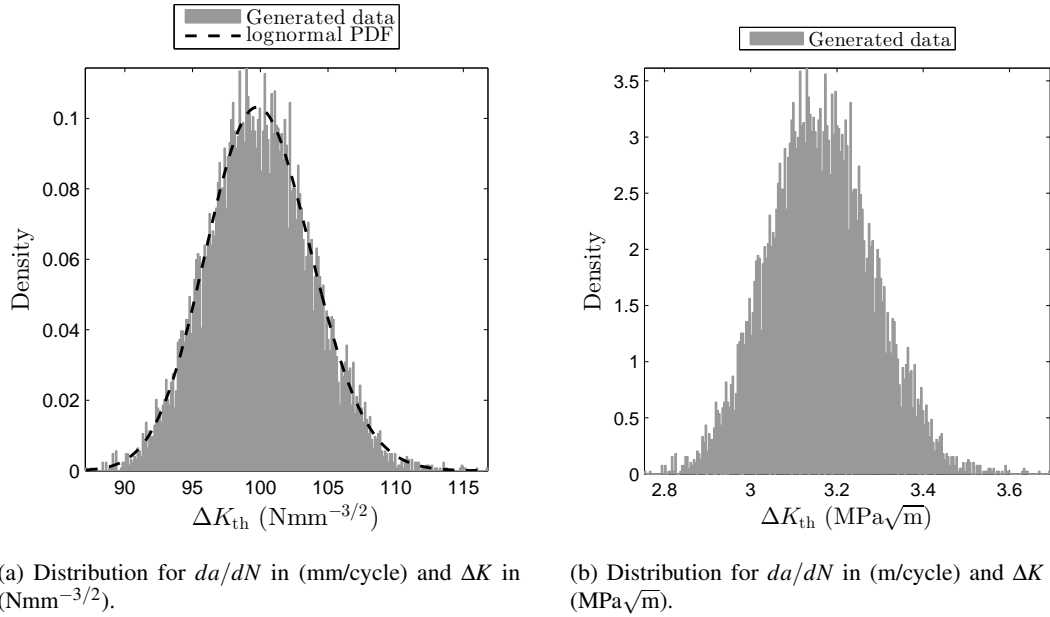


Figure 11.4: Lognormal distribution for the threshold stress intensity factor ΔK_{th} of the Paris–Erdogan law. The histograms were generated from a sampling of 10^4 values, and their number of bins was defined according to the Freedman & Diaconis (1981) rule for the sake of presentation. The unit change is performed as $\Delta K_{\text{th}}(\text{MPa}, \text{m}) = 1/31.62 \cdot \Delta K_{\text{th}}(\text{N}, \text{mm})$.

Chapter 11. Probabilistic model for fatigue crack growth and fracture

yielding a mean value $m = 1.2785 \cdot 10^{-13} \text{ Nmm}^{-3/2}$ of C . The deterministic value for the exponent is assumed to be $m = 3$.

At longitudinal butt welded joints of steel-lined pressure and shafts, a semi-elliptical surface crack might be subject to aggressive environment because of the presence of water, although the coating of the internal surface of the steel liner aims at protecting the latter from corrosion. To assess the eventual effect of an aggressive environment on the fatigue crack growth, a more detrimental distribution of C is proposed as

$$C(\text{Nmm}^{-3/2}) \sim 5 \cdot \text{lognormal}(\mu = 29.84; \sigma = 0.55), \quad (11.12)$$

yielding a mean value $m = 6.3599 \cdot 10^{-13} \text{ Nmm}^{-3/2}$ of C . This assumption was made based on engineering judgment after the British Standard 7910 (2005), which recommends deterministic values for C in both inert and aggressive (marine) environments, differing by a factor of the order of 5. The exponent m remains equal to 3 in both environments. The aforementioned distributions for C in both inert and aggressive environments are shown in Fig. 11.5. Beside its simplicity, this hypothesis has to be considered with care, as it is not physically meaningful. Indeed, the multiplicative factor of 5 should have been applied only to the mean value of the distribution. The distribution proposed in Eq. 11.12 also enlarges the variance with respect to the distribution in inert environment, which may not be realistic in nature.

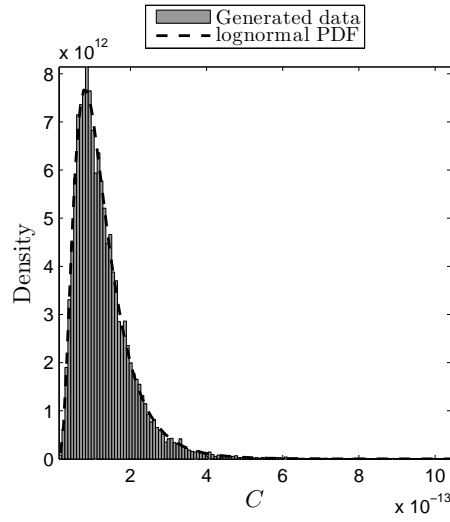
11.2.2 Deterministic model to compute ΔK

Maximum and minimum values of the transient loading

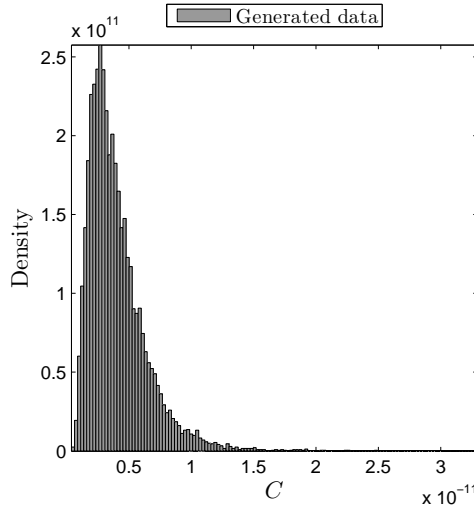
The loading spectrum proposed in Chapter 9 is adopted. Similarly to Chapter 10, the maximum and minimum pressures for each cycle are computed as

$$\begin{cases} p_{i,\max} = p_{i,\text{mean}} + 0.5 \cdot \Delta p_i \\ p_{i,\min} = p_{i,\text{mean}} - 0.5 \cdot \Delta p_i. \end{cases} \quad (11.13)$$

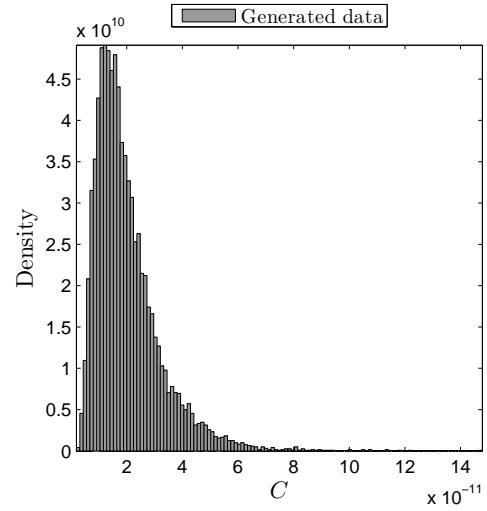
Unlike the S – N approach, the absolute values of $p_{i,\max}$ does have an effect on the fracture criterion. One can note that this assumption of the repartition of Δp_i around $p_{i,\text{mean}}$ is conservative. Within the framework of LEFM, the crack growth rate is not affected.



(a) Inert environment, for da/dN in (mm/cycle) and ΔK in ($\text{Nmm}^{-3/2}$).



(b) Inert environment, for da/dN in (m/cycle) and ΔK in ($\text{MPa}\sqrt{\text{m}}$).



(c) Aggressive environment, for da/dN in (m/cycle) and ΔK in ($\text{MPa}\sqrt{\text{m}}$).

Figure 11.5: Lognormal distributions for the parameter C of the Paris–Erdogan law in inert and aggressive environments. The histograms were generated from a sampling of 10^4 values, and their number of bins was defined according to the Freedman & Diaconis (1981) rule for the sake of presentation. The unit change is performed as $C(\text{MPa}, \text{m}) = 31.62 \cdot C(\text{N}, \text{mm})$, valid only for $m = 3$.

Membrane stress in the steel liner

Similarly to Chapter 10, the membrane stress (here equivalent to the nominal stress) acting at the longitudinal butt welded joint is computed by means of $K_{rm,aniso}^*$ (see Chapter 7) as

$$\sigma_{m,aniso} = K_{rm,aniso}^* \sigma_{m,iso}, \quad (11.14)$$

assuming the worst case in which the joint is located in the direction of maximum major principal stress in the steel liner in the case of anisotropic rock behavior.

Stress concentration at longitudinal butt welded joints

After the discussion conducted in Sect. 8.2, only the structural stress concentration due to peaking is expected to induce a bending stress across the longitudinal butt welded joint, thus estimated as

$$\sigma_{b,aniso} = (K_{m,p}^* - 1) \sigma_{m,aniso} \quad (11.15)$$

considering the effect of the interaction with the concrete–rock system.

Stress intensity factors for semi-elliptical surface cracks

With the previously computed membrane and bending stresses, the stress intensity factors for semi-elliptical surface cracks can be computed as

$$K_I = M_w [M_m (\sigma_{m,aniso} + p_{cr}) + M_b \sigma_{b,aniso}] \sqrt{\frac{\pi a}{Q}} \quad (11.16)$$

where M_m and M_b are the shape correction factors applied to membrane and bending stresses, respectively (see Appendix B.1), and p_{cr} is the pressure applied on the crack face, equal to the applied internal pressure. As the longitudinal butt welded joints are normally ground flush at the internal surface of the steel liner, mostly to facilitate coating, the weld shape correction factor M_w derived in Chapter 8 is taken equal to 1.0. This is a conservative assumption, as it was shown that the weld reinforcement mitigates the stress intensity factors for semi-elliptical surface cracks in the weld material.

Stress intensity factors for embedded elliptical cracks

The stress intensity factors for embedded elliptical cracks can be computed as

$$K_I = [M_m (\sigma_{me} + p_{cr}) + M_b \sigma_{be}] \sqrt{\frac{\pi a}{Q}}, \quad (11.17)$$

with

$$\sigma_{me} = \{\sigma_{m,aniso} + p_{cr}\} + \sigma_{b,aniso} \left(1 - \frac{2d_2}{t_s}\right) \quad (11.18)$$

where d_2 is defined in Fig. 11.2, and

$$\sigma_{be} = \sigma_{b,aniso} \left(\frac{2a}{t_s}\right). \quad (11.19)$$

The shape correction factors applied to the stress components are given in Appendix B.2.

The complete development of the deterministic model is presented in Chapter 12 for practical implementation. For the sake of concision, it is only summarized in the present chapter.

11.2.3 Flowchart of the procedure

The proposed Monte Carlo procedure is described in Fig. 11.6 by means of a flowchart. For each *trial*, the random variables are sampled and the fatigue crack propagation is simulated through the deterministic model until failure, or until the end of the lifespan. An important parameter to optimize the computational time is the relative pressure range threshold $[\Delta p_i / p_{i,mean}]_{th}$. Indeed, the loading spectrum derived in Chapter 9 approximately contains 84'000 cycles. However, it appeared through preliminary studies that only a little fraction of the highest cycles can cause crack propagation according to Eq. 11.1. For the studied cases, $[\Delta p_i / p_{i,mean}]_{th} = 0.04$, namely 4% of the mean water pressure, is generally a good assumption to begin with. However, it has to be verified a posteriori that no cycle were neglected. Defining N_w the number of cycles per week that are kept into the loading spectrum and $N_{w,p}$ the number of cycles causing crack propagation each week, the ratio $N_{w,p} / N_w$ has to remain below 1.0 each week of lifespan. If this condition is not fulfilled, an unknown number of propagating cycles has been neglected and the result may be nonconservative. However, in some cases this criterion is too harsh and would induce too much computational time with lower thresholds, without influencing, or in a negligible manner, the probability of failure. The reliability of a Monte Carlo simulation exhibiting some $N_{w,p} / N_w$ ratios equal to unity at the end of the lifespan can, e.g., be assessed by assuming the worst case

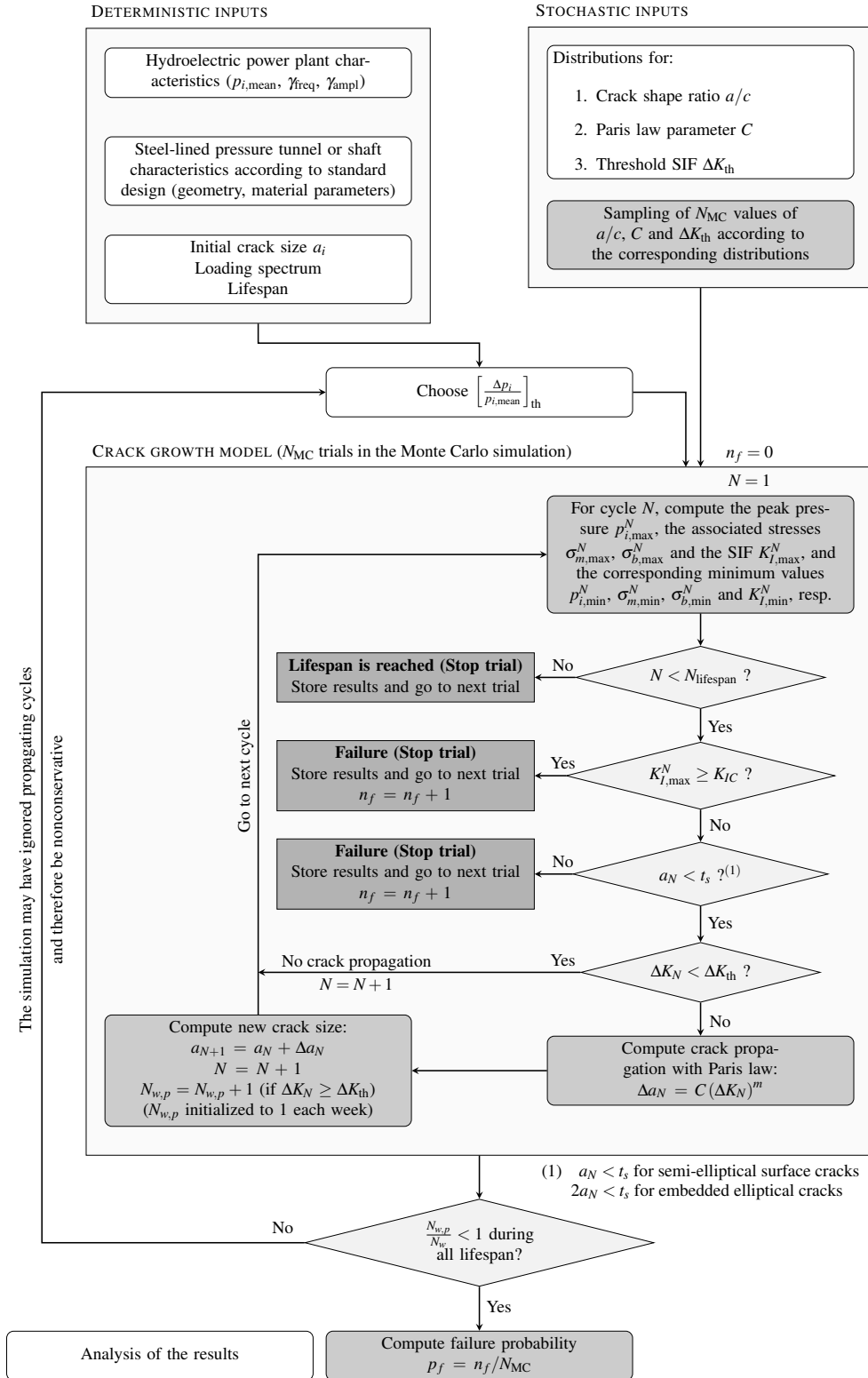


Figure 11.6: Flowchart of the proposed Monte Carlo simulation procedure.

scenario in which each trial resulting in failure is not a trial with $N_{w,p}/N_w = 1$. If the order of magnitude of the n trials with $N_{w,p}/N_w = 1$ is lower than the number of failure n_f by an order of magnitude, the result can be considered as reliable. Moreover, one can note that in most of the observed trials where $N_{w,p}/N_w = 1$, it occurs only the last few weeks/months of life due to the exponential crack growth leading to failure.

11.2.4 Probability of failure and accuracy

Defining N_{MC} as the total number of trials in one Monte Carlo simulation and n_f the number of observed failures, the probability of failure p_f is finally computed as

$$p_f = \frac{n_f}{N_{MC}}. \quad (11.20)$$

Moreover, the accuracy of each Monte Carlo simulation is quantified using Eq. 3.32 with respect to p_f as

$$\varepsilon_{p_f} \approx \frac{\sqrt{\frac{(1-p_f)p_f}{N_{MC}}}}{p_f}, \quad (11.21)$$

and with respect to 10^{-5} (very severe target probability of failure for non-redundant component according to the British Standard 7910 2005, and commonly adopted in Switzerland) as

$$\varepsilon_{10^{-5}} \approx \frac{\sqrt{\frac{(1-10^{-5})10^{-5}}{N_{MC}}}}{10^{-5}}. \quad (11.22)$$

For an accuracy $\varepsilon = 1\%$ with respect to a probability of failure of 10^{-5} , it is required to perform 10^9 simulations. However, performing such a number of trials was not realistic in the scope of this project. The Monte Carlo procedure presented in Fig. 11.6 was implemented into the MATLAB® (2012) numerical calculation software. To provide an order of magnitude, performing one Monte Carlo simulation of 10^6 trials required a computational time of 24 hours with parallel computing on a personal computer equipped with an Intel® Core™ i7-3770 CPU @ 3.40 GHz processor, and considering $[\Delta p_i / p_{i,\text{mean}}]_{\text{th}} = 0.04$. As a consequence, the number of trials N_{MC} was estimated for each case based on preliminary analyses, previous complete analyses, and/or engineering judgment.

11.3 Parametric study

The design of the parametric study is identical to the one performed in Chapter 10, with the exception that a new parameter is included, namely the initial crack size a_i . The parameters are briefly repeated and completed hereafter.

- The mean head of the hydropower plant, defining the mean internal water pressure $p_{i,\text{mean}}$ at the lowest point of the shaft for the loading spectrum.
- The initial crack size a_i , tested for the values 2 and 4 mm. This parameter is a fundamental hypothesis in fatigue crack growth analyses by means of the LEFM approach. The initial crack size a_i is often defined as the threshold crack size under which a crack cannot be detected by the nondestructive testing procedures adopted in a project.
- The steel grades characterized by their yield strength f_y as defined in Table 11.1.

Table 11.1: Minimum yield strengths for different steel grades used in hydropower construction considered for the parametric analysis of fatigue assessment by means of linear elastic fracture mechanics approach.

Grade	Standard	Yield strength f_y (MPa)	Thickness range (mm)
S355 M/ML	EN 10025-4 (2005)	355	$t_s \leq 16$
		345	$16 < t_s \leq 40$
		335	$40 < t_s \leq 63$
		325	$63 < t_s \leq 80$
S500 ML	EN 10025-4 (2005)	500	$t_s \leq 16$
		490	$16 < t_s \leq 50$
		490	$50 < t_s \leq 75$
S690 QL	EN 10025-6 (2009)	690	$t_s \leq 50$
		650	$50 < t_s \leq 100$
S890 QL	EN 10025-6 (2009)	890	$t_s \leq 50$
		830	$50 < t_s \leq 100$
S960 QL	EN 10025-6 (2009)	960	$t_s \leq 50$

- The safety factor SF to be considered for the design of the thickness t_s according to a simplified criterion $\sigma_1 \leq f_y/\text{SF}$, which is slightly conservative compared to the criteria recommended by the C.E.C.T. (1980) with the equivalent stress. The rock cover is assumed to be sufficient in all cases.
- The far-field rock mass elastic modulus E' and the degree of anisotropy E/E' . The design of t_s was performed considering the isotropic case with the lowest elastic modulus E' .

The loading spectra are generated from the normalized spectrum proposed in Chapter 9, without magnifying factors. The constant parameters (or depending on other constants) of the study are

given in Table 11.2. The out-of-roundness is not considered as it was shown in Chapter 7 that its effect is vanished with embedment (in terms of SCF at the longitudinal butt welded joint). Finally, the flank angle β and the weld reinforcement height factor ψ_δ are set to zero as the longitudinal butt welded joints are assumed to be flush ground.

11.4 Results

The results from the Monte Carlo simulations are reported in Appendix D, in Tables D.1, D.2 and D.3 for semi-elliptical surface cracks in inert and aggressive environments, and for embedded elliptical cracks in inert environment, respectively. From the results presented in Appendix D, some general observations are made hereafter.

- The most detrimental crack type is the semi-elliptical surface crack, particularly in aggressive environment.
- For all the tested cases, embedded elliptical cracks never led to failure, i.e., $p_f = 0$ after a 100 years lifespan.
- For semi-elliptical surface cracks, aggressive environment drastically increase the probability of failure, from 1 to 3–4 orders of magnitude.
- The thickness t_s of the steel liner is a fundamental parameter. Indeed, thinner liners will be more sensitive to the presence of initial cracks as the relative crack depth ratio a/t_s has a major influence on the stress intensity factor within the scope of the hypotheses made herein. Thicker liners induce smaller initial relative crack depth, and larger critical sizes with respect to the fracture toughness criterion¹. In all tested cases, it was observed that the larger SF (and thus t_s), the smaller p_f .
- Another determinant parameter is the range of variation of the stresses in the steel liner, and thus the range of variation of the stress intensity factor ΔK . The greater the amplitudes of ΔK , the faster the crack propagation. Regarding the Paris–Erdogan law, this statement is trivial. However, the combinations of parameters leading to large stress amplitudes in the steel liner are not evident to determine prior to calculation. For instance, large rock elastic modulus allows for thinner steel liners, which tends to be detrimental for fatigue, but load sharing reduces the liner’s participation at the same time, which is favorable in terms of stress variations. The following remarks are related to this point.
- In general, the risk of failure increases with the mean internal water pressure, as the pressure variation is relative to the latter. As a consequence, high head induces larger absolute stress ranges, as shown in Chapter 10.

¹These observations have to be considered with care, as they are only meaningful in the scope of the hypotheses made in this study, namely that the initial crack sizes take absolute values, independently from the thickness of the steel liner, and that the fracture toughness is expressed by Eq. 11.6. In practical applications, the risk of occurrence of initial crack-like flaws may, e.g., be larger in thicker welded joints. Also, the hypothesis made on the fracture toughness is particularly detrimental for small thicknesses and low steel grades.

Table 11.2: Constant parameters (or depending on constants) of the parametric analysis performed with the probabilistic model for fatigue crack growth and fracture.

Parameter	Definition	Value	Unit
r_i	Internal radius of the steel liner	1.5	(m)
$\Delta p^+ / p_{i,\text{mean}}$	Maximum overpressure ratio considered for the design	0.10	(-)
Δr_0	Initial gap between steel liner and backfill concrete	$0.025\% \cdot r_i$	(m)
ψ_u	Straight edge factor (inducing peaking)	2.0	(-)
ψ_δ	Weld reinforcement factor	0.0	(-)
β	Flank angle	0	(deg)
α	Edge preparation angle	50	(deg)
E_s	Elastic modulus of steel	210	(GPa)
ν_s	Poisson's ratio of steel	0.3	(-)
t_c	Thickness of the backfill concrete layer	0.5	(m)
E_c	Elastic modulus of the backfill concrete	20	(GPa)
ν_c	Poisson's ratio of backfill concrete	0.2	(-)
ν'	Poisson's ratio of the far-field rock related to the plane of isotropy	0.2	(-)
ν''	Poisson's ratio of the far-field rock related to the planes perpendicular to the plane of isotropy	0.2	(-)
G'	Cross-shear modulus of the far-field rock	Eq. 4.11	(GPa)
E_{crm}	Elastic modulus of the near-field rock	$0.8 \cdot E'$	(GPa)
ν_{crm}	Poisson's ratio of the near-field rock	0.2	(-)
t_{crm}	Thickness of the near-field rock layer	0.5	(m)
K_{IC}	Plane strain fracture toughness	Eq. 11.6	(MPa $\sqrt{\text{m}}$)
N_{lifespan}	Number of cycles considered during a lifespan of 100 years, which depends on $[\Delta p_i / p_{i,\text{mean}}]_{\text{th}}$	-	(-)

- The risk of failure increases with the steel yield strength, allowing thinner liners according to the design criterion, and larger stress ranges.
- The risk of failure decreases with good rock quality, namely with increasing elastic modulus, as a larger part of p_i is shared with the concrete–rock system. The limitation of the rock participation to 50% of the design pressure is particularly favorable in cases where full load sharing is beyond this limitation, as computations were performed considering the *real* rock participation.
- Inherently to the isotropic assumption for the design, the presence of rock anisotropy is also favorable as stresses are overestimated in the standard design procedure.
- One should also note that within the assumption made for K_{IC} in the present study, thinner thicknesses induce lower fracture toughnesses. For instance, the series of simulations with $p_{i,\text{mean}} = 10$ MPa, $a_i = 4$ mm and $f_y = 980$ MPa exhibit numerous failures before the crack growths at an exponential rate. In those cases, the failure criterion with respect to fracture toughness may have a significant influence on p_f .

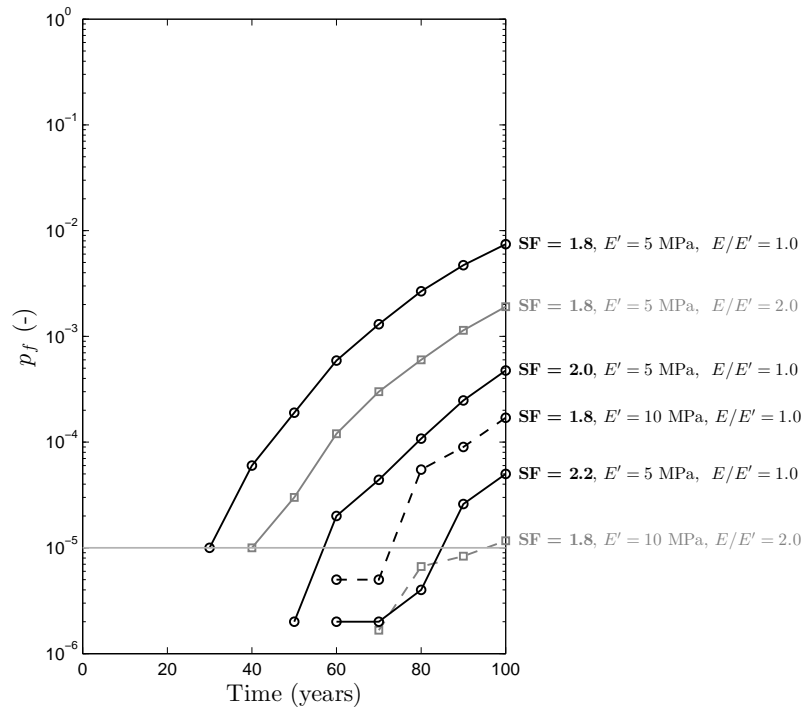
To illustrate some of the aforementioned observations and the model's behavior, the series of simulations of steel liners made of S890 QL and S960 QL with semi-elliptical surface cracks in aggressive environment for $p_{i,\text{mean}} = 15$ MPa and $a_i = 4$ mm (see results in Table D.2) are analyzed more into detail hereafter. The evolution of the probability of failure over the lifespan is shown in Fig. 11.7 for all the tested cases. One can observe that by increasing SF, the probability of failure decreases (as t_s increases), although the rock participation diminishes (compare Figs. 11.8, 11.9 and 11.10). Also, good quality rocks are favorable in terms of fatigue behavior for the tested cases. Although it allows thinner liners, the increase in rock participation seems to be more efficient as it reduces the stress amplitude in the steel liner (compare Figs. 11.8 and 11.11).

The rock anisotropy, inherently to the isotropic model considered for the design, has a similar favorable effect as shown in Fig. 11.7. Figures 11.8–11.10, although quite representative of the selected cases, represent the results from the associated Monte Carlo simulations performed with 1000 trials only, for presentation purposes.

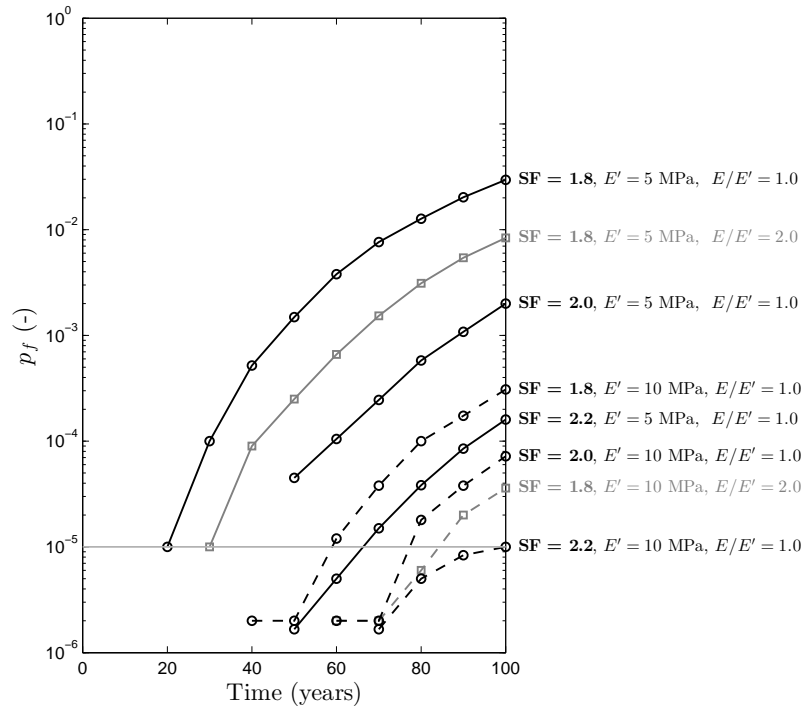
11.5 Discussion

Although quantitative, the results presented herein should be considered with care. Several remarks can be made, both concerning the model and the interpretation of the results.

- As the model is not calibrated with experimental or prototype data, the probabilities of failure obtained in the present chapter are only rough estimates. In order to tend toward the *real* probability of failure, more variables should be considered as stochastic, e.g., the

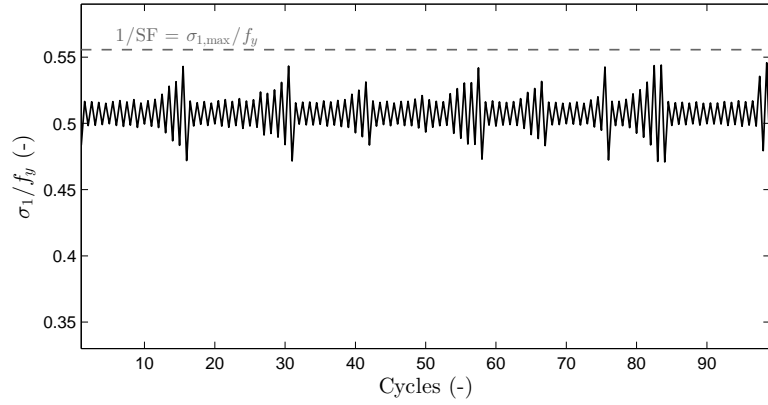


(a) S890 QL.

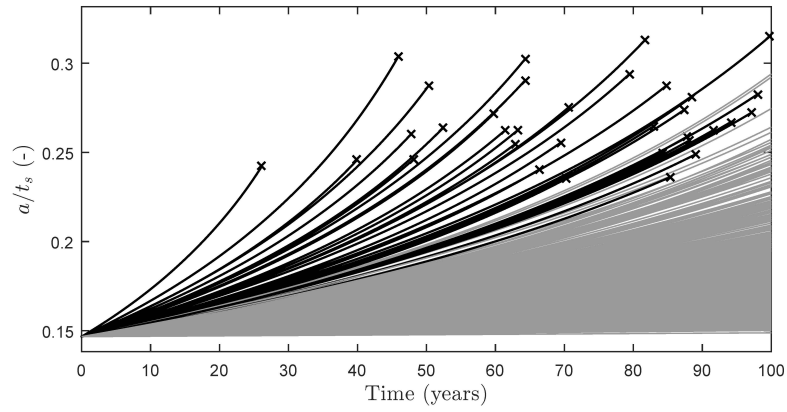


(b) S960 QL.

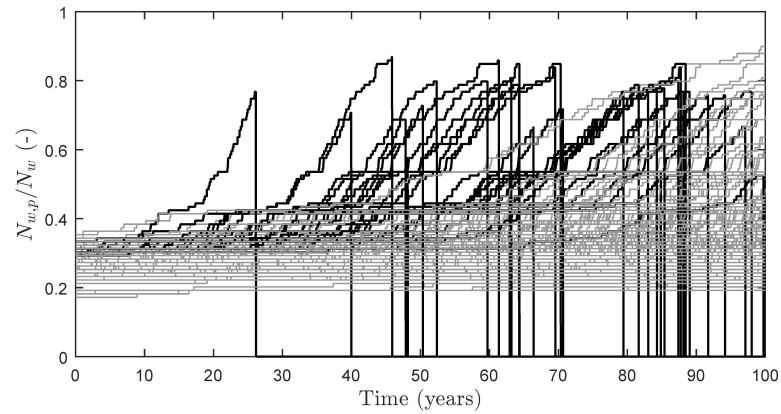
Figure 11.7: Probability of failure along lifespan of steel liners with semi-elliptical surface cracks in aggressive environment for $p_{i,\text{mean}} = 15$ MPa and $a_i = 4$ mm.



(a) Weekly variation of the major principal stress with respect to the yield strength σ_1/f_y at the longitudinal butt welded joint (threshold of $\Delta p_i/p_{i,mean}$ set to 3.2%).

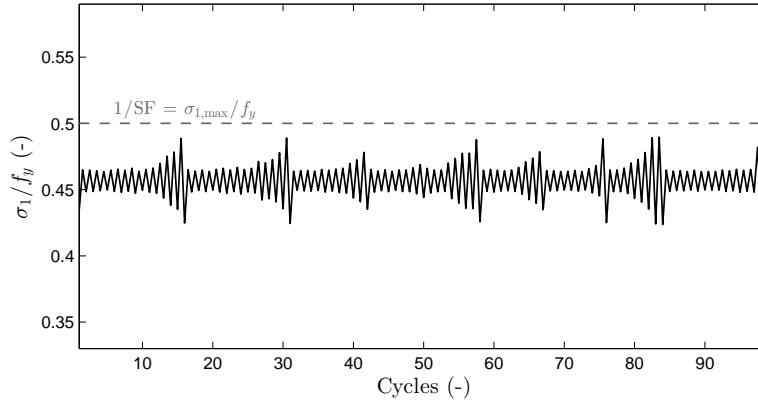


(b) Relative crack a/t_s growth as a function of time (\times = failure).

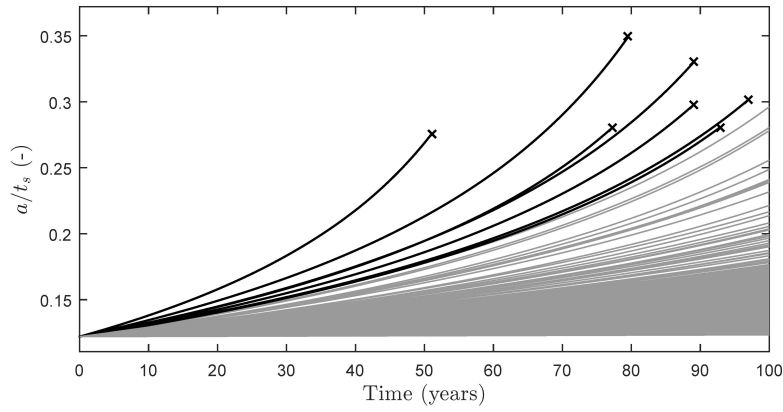


(c) Ratio of weekly propagating cycles $N_{w,p}/N_w$ as a function of time.

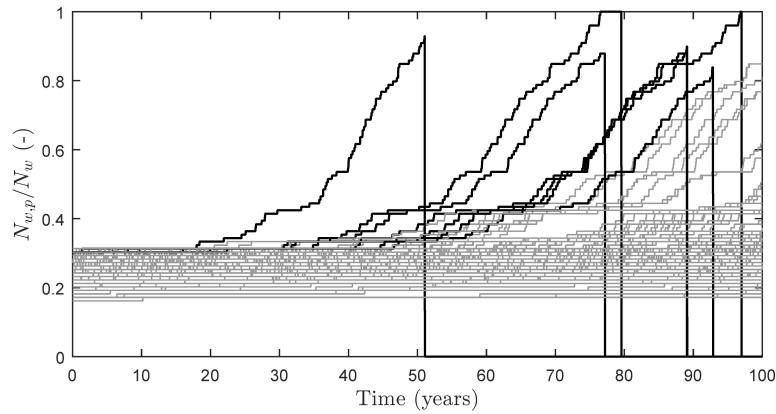
Figure 11.8: Results from the probabilistic fatigue crack growth and fracture model (for random 1000 trials) of semi-elliptical surface cracks in aggressive environment for $p_{i,mean} = 15$ MPa, $t_s = 27.3$ mm, $a_i = 4$ mm, $f_y = 960$ MPa, $SF = 1.8$, $E' = 5.0$ GPa and $E/E' = 1$.



(a) Weekly variation of the major principal stress with respect to the yield strength σ_1/f_y at the longitudinal butt welded joint (threshold of $\Delta p_i/p_{i,\text{mean}}$ set to 3.2%).

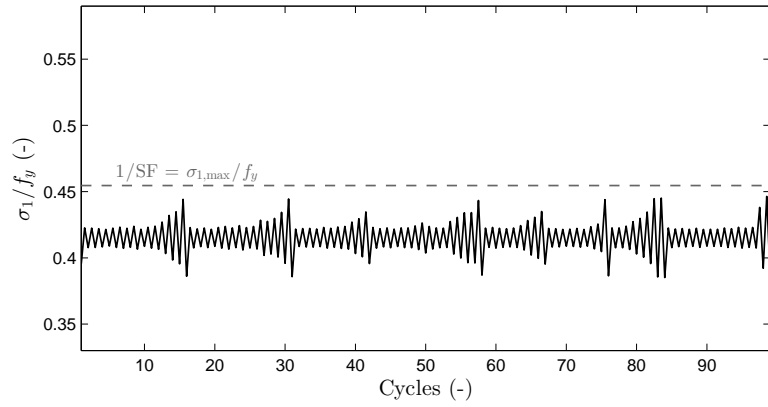


(b) Relative crack a/t_s growth as a function of time (\times = failure).

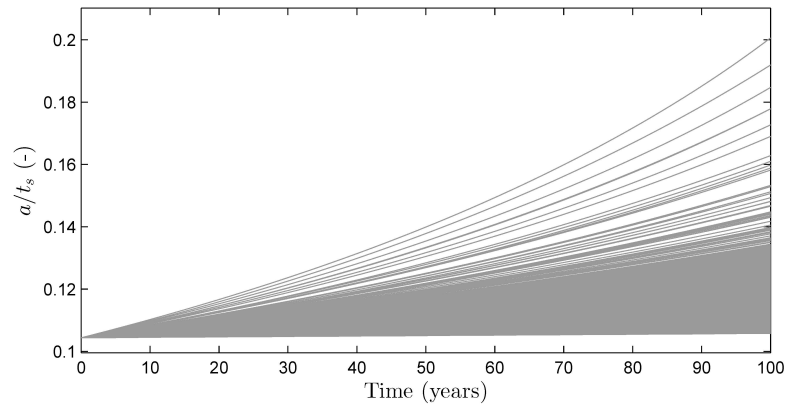


(c) Ratio of weekly propagating cycles $N_{w,p}/N_w$ as a function of time.

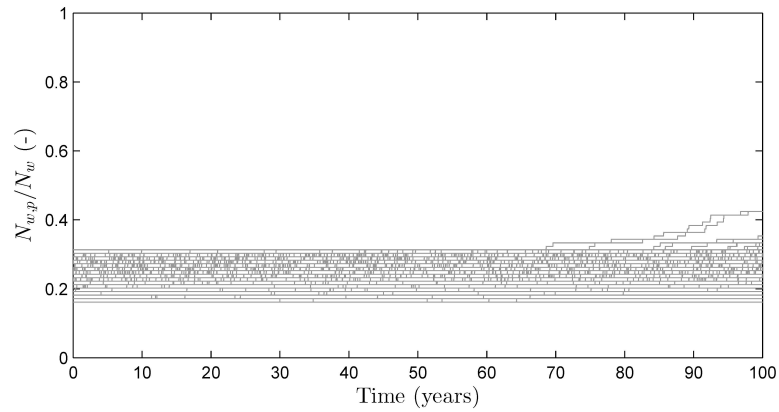
Figure 11.9: Results from the probabilistic fatigue crack growth and fracture model (for random 1000 trials) of semi-elliptical surface cracks in aggressive environment for $p_{i,\text{mean}} = 15$ MPa, $t_s = 32.8$ mm, $a_i = 4$ mm, $f_y = 960$ MPa, $SF = 2.0$, $E' = 5.0$ GPa and $E/E' = 1$.



(a) Weekly variation of the major principal stress with respect to the yield strength σ_1/f_y at the longitudinal butt welded joint (threshold of $\Delta p_i/p_{i,\text{mean}}$ set to 3.2%).



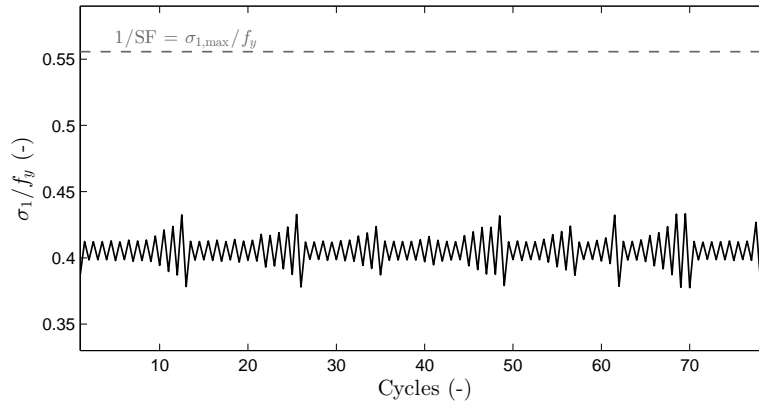
(b) Relative crack a/t_s growth as a function of time (\times = failure).



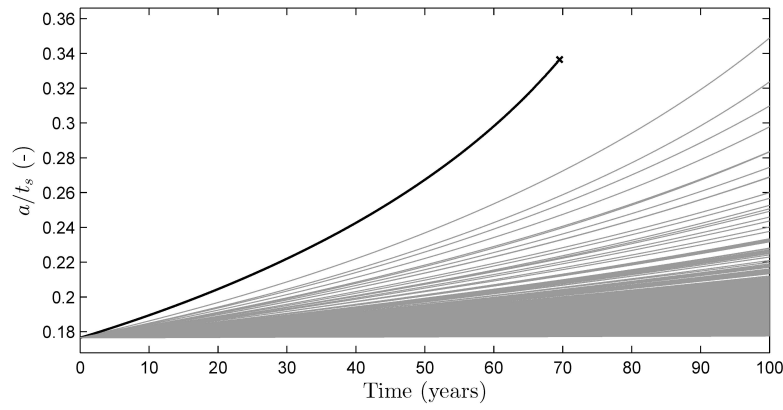
(c) Ratio of weekly propagating cycles $N_{w,p}/N_w$ as a function of time.

Figure 11.10: Results from the probabilistic fatigue crack growth and fracture model (for random 1000 trials) of semi-elliptical surface cracks in aggressive environment for $p_{i,\text{mean}} = 15$ MPa, $t_s = 38.3$ mm, $a_i = 4$ mm, $f_y = 960$ MPa, $SF = 2.2$, $E' = 5.0$ GPa and $E/E' = 1$.

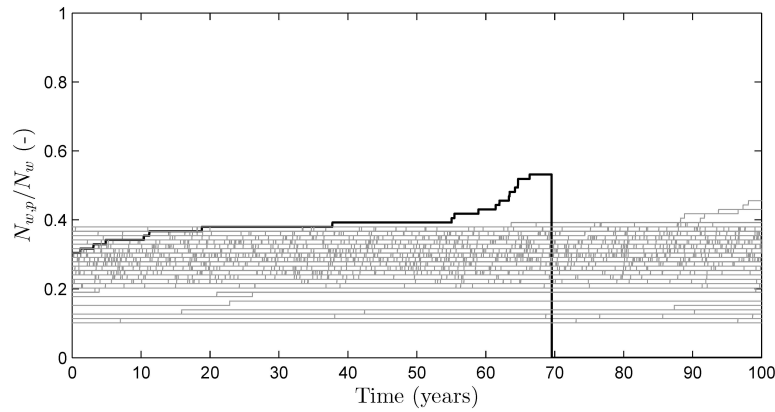
Chapter 11. Probabilistic model for fatigue crack growth and fracture



(a) Weekly variation of the major principal stress with respect to the yield strength σ_1/f_y at the longitudinal butt welded joint (threshold of $\Delta p_i/p_{i,mean}$ set to 3.5%).



(b) Relative crack a/t_s growth as a function of time (\times = failure).



(c) Ratio of weekly propagating cycles $N_{w,p}/N_w$ as a function of time.

Figure 11.11: Results from the probabilistic fatigue crack growth and fracture model (for random 1000 trials) of semi-elliptical surface cracks in aggressive environment for $p_{i,mean} = 15$ MPa, $t_s = 22.7$ mm, $a_i = 4$ mm, $f_y = 960$ MPa, $SF = 1.8$, $E' = 10.0$ GPa and $E/E' = 1$.

material parameters, the fracture toughness, the loading spectrum, the effect of corrosion on the thickness of the steel liner, the accuracy of the deterministic model, or the initial crack sizes (also in relation with the probability of detection, POD). Also, the distributions adopted herein were taken from reasonable assumptions from the literature, but not from actual data specific to SLPT&S. Particularly, the distribution of a/c was derived from flawed at weld toes of welded joints.

- The failure criterion adopted herein is very conservative. If hydraulic jacking is prevented by rock cover, a crack propagating through the thickness does not necessarily deteriorates the short-term service operations of the hydropower plant. The through-crack may continue to propagate along the the longitudinal joint before service operations are threatened. This more realistic failure criterion would have required a more complex model and experimental data for the fracture toughness, which was out of the scope of this project.
- The obtained probabilities of failure highly depend on the loading spectrum, which may not be transferable to other operational conditions than those in which it was derived. It remains an hypothesis allowing to run the proposed probabilistic model through parametric studies in this project.
- The accuracy of the Monte Carlo simulations was only estimated for the probability of failure p_f at the end of the lifespan. One should keep in mind that it actually evolves along lifespan. For an increasing probability of failure along lifespan, the accuracy of p_f at, e.g., 30 years, will be typically lower than the accuracy at 100 years.

11.6 Conclusions

In this chapter, a probabilistic model for fatigue crack growth and fracture of initial axial cracks in the weld material of longitudinal butt welded joints of SLPT&S was proposed. The parametric equations developed along Parts II to IV to compute ranges of stress intensity factors for surface and embedded cracks was implemented in the framework of the Monte Carlo simulation procedure. Possible distributions for the assumed stochastic parameters, particularly for the crack shape ratio a/c and the parameters of the Paris–Erdogan law C and ΔK_{th} , were discussed and adopted from reasonable hypotheses taken from the literature. The loading spectra were derived from the normalized spectrum proposed in Chapter 9.

By means of a parametric study, it was shown that semi-elliptical surface cracks in aggressive environment (i.e., with harsher growth rates) can become the leading limit state for SLPT&S made of HSS in high-head hydropower plants. Although the proposed probabilistic model cannot be calibrated against experimental or prototype data, it gives valuable quantitative results that can be incorporated into a fitness-for-service philosophy for the design of SLPT&S when fatigue phenomena arise.

12 Case study

12.1 Case description

The studied case is presented in Fig. 12.1. The mean head is $H_{\text{mean}} = 1300$ m, thus inducing a mean internal water pressure $p_{i,\text{mean}} = 13$ MPa (130 bar), at the lowest point of the steel-lined pressure shaft. The deterministic parameters of the case study are given in Table 12.1. The loading spectrum is derived from the normalized spectrum derived in Chapter 9, without any magnification factor. It is assumed that the thickness is preliminarily designed with respect to the working stress criterion using the allowable equivalent stress in steel liners according to the Hencky–Von Mises theory in triaxial state of stresses as suggested in the C.E.C.T. (1980) recommendations (see Sect. 12.2).

The aim is to study the crack propagation (semi-elliptical internal surface cracks and embedded elliptical cracks) from three different initial crack sizes, namely $a_i = 2, 3$ and 4 mm, for different designs depending on the use of the three different types of high-strength steels given in Table 12.2, and on varying the global safety factor to assess the influence on the thickness of the steel liner on the failure probability. For the design of steel liners embedded in concreted tunnels or shafts, the C.E.C.T. (1980) recommend $\text{SF} = 1.1$ if no load sharing is considered, and $\text{SF} = 2.0$ if load sharing is assumed. Moreover, the practical rule stating that the rock mass load sharing is limited to 50% of the internal water pressure is adopted.

Chapters 10 and 11 focused on developing a framework for the use of fatigue assessment engineering procedures to steel liners of pressure tunnels and shafts and on comparing the relative results obtained through a parametric study. On the contrary, the objective of the present chapter is to present in detail all the calculation procedures using the model developed along Parts II to IV to estimate the stress concentration factors and the stress intensity factors for cracks at the longitudinal butt welded joints of steel-lined pressure tunnels and shafts. For completion, the detailed calculation procedure to apply the effective notch stress approach is also presented. This synthesis aims at guaranteeing the transfer of these developments toward practical implementation.

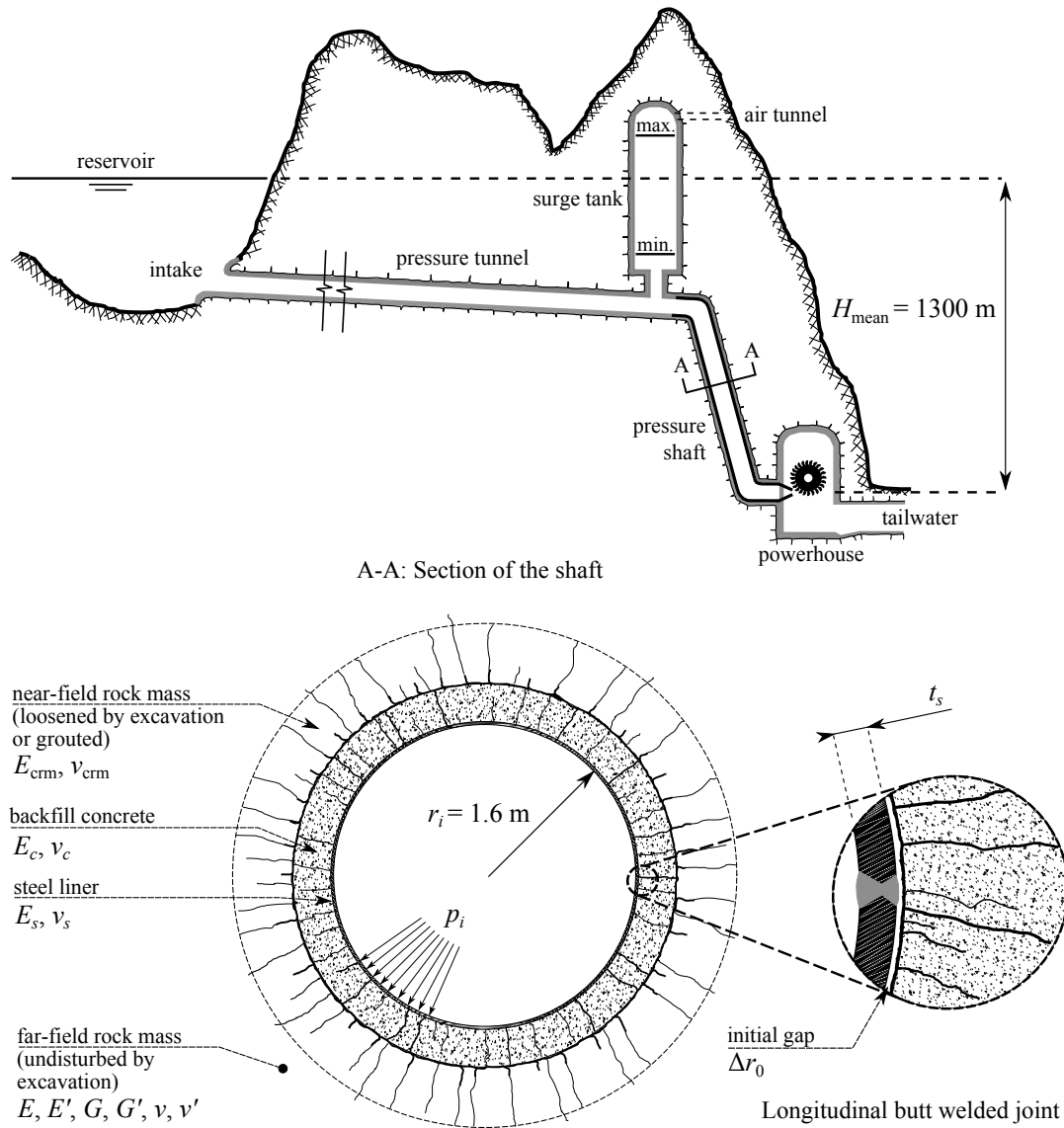


Figure 12.1: Longitudinal schematic view of the studied alpine high-head power plant and sectional view of the steel-lined pressure shaft. The relative dimensions are adapted for the sake of presentation.

Table 12.1: Deterministic parameters of the case study.

Parameter	Definition	Value	Unit
$p_{i,\text{mean}}$	Mean internal water pressure	13	(MPa)
r_i	Internal radius of the steel liner	1.6	(m)
$\Delta p^+ / p_{i,\text{mean}}$	Maximum overpressure ratio considered for the design	0.10	(-)
Δr_0	Initial gap between steel liner and backfill concrete	$0.025\% \cdot r_i$	(m)
ψ_u	Straight edge factor (inducing peaking)	2.0	(-)
ψ_δ	Weld reinforcement factor (for fatigue assessment by means of the notch stress approach)	1.0	(-)
ψ_δ	Weld reinforcement factor (for crack propagation by means of LEFM)	0.0	(-)
β	Flank angle (for fatigue assessment by means of the notch stress approach)	30	(deg)
β	Flank angle (for crack propagation by means of LEFM)	0	(deg)
α	Edge preparation angle	50	(deg)
E_s	Elastic modulus of steel	210	(GPa)
ν_s	Poisson's ratio of steel	0.3	(-)
t_c	Thickness of the backfill concrete layer	0.5	(m)
E_c	Elastic modulus of the backfill concrete	20	(GPa)
ν_c	Poisson's ratio of backfill concrete	0.2	(-)
E	Elastic modulus of the far-field rock in the plane of isotropy	7.5	(GPa)
E'	Elastic modulus of the near-field rock in the plane perpendicular to the plane of isotropy	6	(GPa)
ν	Poisson's ratio of the far-field rock related to the plane of isotropy	0.2	(-)
ν'	Poisson's ratio of the far-field rock related to the planes perpendicular to the plane of isotropy	0.2	(-)
G'	Cross-shear modulus of the far-field rock	Eq. 4.11	(GPa)
E_{crn}	Elastic modulus of the near-field rock	$0.8 \cdot E'$	(GPa)
ν_{crn}	Poisson's ratio of the near-field rock	0.2	(-)
t_{crn}	Thickness of the near-field rock layer	0.5	(m)
K_{IC}	Plane strain fracture toughness	Eq. 11.6	(MPa $\sqrt{\text{m}}$)
N_{frespan}	Number of cycles considered during a lifespan of 100 years, which depends on $[\Delta p_i / p_{i,\text{mean}}]_{\text{th}}$	-	(-)

Table 12.2: Minimum yield strengths for the different studied steel grades.

Grade	Standard	Yield strength f_y (MPa)	Thickness range (mm)
S690 QL	EN 10025-6 (2009)	690	$t_s \leq 50$
		650	$50 < t_s \leq 100$
S890 QL	EN 10025-6 (2009)	890	$t_s \leq 50$
		830	$50 < t_s \leq 100$
S960 QL	EN 10025-6 (2009)	960	$t_s \leq 50$

12.2 Standard design with the working stress criterion

In this study, only the working stress criterion is regarded for the design. The equivalent stress in the steel liner, under the maximum allowable internal water pressure, has to remain below the steel yield strength corrected by SF as

$$\sigma_{eq} \leq \frac{f_y}{SF}. \quad (12.1)$$

Buckling and crack bridging criteria (see Sect. 2.3) are assumed to be non determining. The thickness of the steel liner is designed with respect to the maximum allowable overpressure characterized by $\Delta p^+ / p_{i,mean} = 0.10$ for this case study. As a consequence, the maximum allowable internal water pressure is calculated as

$$p_{i,max} = \left(1 + \frac{\Delta p^+}{p_{i,mean}} \right) \cdot p_{i,mean}. \quad (12.2)$$

According to Hencky–Von Mises yield criterion,

$$\sigma_{eq,max} = \sqrt{\frac{1}{2}(\sigma_{1,max} - \sigma_{2,max})^2 + \frac{1}{2}(\sigma_{2,max} - \sigma_{3,max})^2 + \frac{1}{2}(\sigma_{3,max} - \sigma_{1,max})^2} \quad (12.3)$$

where:

1. the maximum major principal stress is computed considering the lowest elastic modulus of the anisotropic rock E' (transverse isotropy) as

$$\sigma_{1,max} = \frac{1}{r_c^2 - r_i^2} [r_i^2 p_{i,max} - r_c^2 p_{c,max} - r_c^2 (p_{c,max} - p_{i,max})] \quad (12.4)$$

with

$$p_{c,\max} = \frac{\frac{1+\nu_s}{E_s} \frac{r_c}{r_c^2 - r_i^2} [(1-2\nu_s)p_{i,\max}r_i^2 + p_{i,\max}r_i^2] - \Delta r_0}{\frac{1+\nu_s}{E_s} \frac{r_c}{r_c^2 - r_i^2} [(1-2\nu_s)r_c^2 + r_i^2] + r_c \frac{1}{E_{\text{eq}}}} \quad (12.5)$$

and

$$\frac{1}{E_{\text{eq}}} = \frac{1-\nu_c^2}{E_c} \ln\left(\frac{r_{\text{crm}}}{r_c}\right) + \frac{1-\nu_{\text{crm}}^2}{E_{\text{crm}}} \ln\left(\frac{r_{\text{rm}}}{r_{\text{crm}}}\right) + \frac{1+\nu}{E'}; \quad (12.6)$$

2. the maximum minor principal stress is computed as

$$\sigma_{3,\max} = \frac{1}{r_c^2 - r_i^2} \left[r_i^2 p_{i,\max} - r_c^2 p_{c,\max} + \frac{r_i^2 r_c^2}{r_i^2} (p_{c,\max} - p_{i,\max}) \right]; \quad (12.7)$$

3. and the stress in the second principal direction is computed as

$$\sigma_{2,\max} = \nu_s [\sigma_{1,\max} + \sigma_{3,\max}] = \frac{2\nu_s}{r_c^2 - r_i^2} (r_i^2 p_{i,\max} - r_c^2 p_{c,\max}). \quad (12.8)$$

12.3 Fatigue assessment

Fatigue crack growth and fracture is studied according to the linear elastic fracture mechanics (LEFM) approach with the Paris–Erdogan law, using the probabilistic model presented in Chapter 11 (see particularly Fig. 11.6). The stochastic variables are as described in the latter chapter.

12.4 Detailed example of the calculation of the crack growth for the k^{th} cycle

In this example, let's assume a crack size a_k resulting from the propagation due to the $(k-1)$ preceding cycles from an initial crack size a_i :

$$a_k = a_i + \sum_{j=1}^{k-1} \left(\frac{da}{dN} \right)_j. \quad (12.9)$$

From the k^{th} cycle of the loading spectrum (Chapter 9), the associated maximum and minimum

pressures $p_{i,\max}^k$ and $p_{i,\min}^k$ are computed as

$$\begin{cases} p_{i,\max}^k = p_{i,\text{mean}} + 0.5 \cdot \Delta p_i^k \\ p_{i,\min}^k = p_{i,\text{mean}} - 0.5 \cdot \Delta p_i^k. \end{cases} \quad (12.10)$$

12.4.1 Compute $K_{\text{rm},\text{aniso}}^*$ (Chapter 5)

In this case study, the rock exhibits transverse isotropy. In order to compute the greatest nominal stress at each cycle in the steel liner, the $K_{\text{rm},\text{aniso}}^*$ factor is approximated for the mean internal water pressure $p_{i,\text{mean}}$. Because of the presence of the initial gap, Δr_0 , $K_{\text{rm},\text{aniso}}^*$ varies with pressure. However, this variation can be neglected.

Considering an isotropic model with the lowest rock elastic modulus E' , the part of the internal water pressure taken by the concrete–rock system can be computed as

$$p_{c,\text{iso},\text{mean}} = \frac{\frac{1+\nu_s}{E_s} \frac{r_c}{r_c^2 - r_i^2} [(1-2\nu_s)p_{i,\text{mean}}r_i^2 + p_{i,\text{mean}}r_i^2] - \Delta r_0}{\frac{1+\nu_s}{E_s} \frac{r_c}{r_c^2 - r_i^2} [(1-2\nu_s)r_c^2 + r_i^2] + r_c \frac{1}{E_{\text{eq}}}}, \quad (12.11)$$

where

$$\frac{1}{E_{\text{eq}}} = \frac{1-\nu_c^2}{E_c} \ln\left(\frac{r_{\text{crm}}}{r_c}\right) + \frac{1-\nu_{\text{crm}}^2}{E_{\text{crm}}} \ln\left(\frac{r_{\text{rm}}}{r_{\text{crm}}}\right) + \frac{1+\nu}{E'}. \quad (12.12)$$

Then, the mean major principal stress at the internal fiber of the steel liner is computed as

$$\sigma_{\text{iso},\text{mean}} = \frac{1}{r_c^2 - r_i^2} \left[r_i^2 p_{i,\text{mean}} - r_c^2 p_{c,\text{iso},\text{mean}} - \frac{r_i^2 r_c^2}{r_i^2} (p_{c,\text{iso},\text{mean}} - p_{i,\text{mean}}) \right]. \quad (12.13)$$

Similarly, considering rock anisotropy by means of the correction factors proposed in Chapter 5 gives the following expression for $p_{c,\text{aniso},\text{mean}}$:

$$p_{c,\text{aniso},\text{mean}} = \frac{\frac{1+\nu_s}{E_s} \frac{r_c}{r_c^2 - r_i^2} [(1-2\nu_s)p_{i,\text{mean}}r_i^2 + p_{i,\text{mean}}r_i^2] - \Delta r_0}{\frac{1+\nu_s}{E_s} \frac{r_c}{r_c^2 - r_i^2} [(1-2\nu_s)r_c^2 + r_i^2] + r_c \frac{1}{E_{\text{eq},\text{corr}}}}, \quad (12.14)$$

12.4. Detailed example of the calculation of the crack growth for the k^{th} cycle

with

$$\begin{aligned} \frac{1}{E_{\text{eq,corr}}} = & \frac{1 - \nu_c^2}{E_c} \ln \left(\frac{r_{\text{crm}}}{r_c} \right) + \frac{1 - \nu_{\text{crm}}^2}{E_{\text{crm}}} \ln \left(\frac{r_{\text{rm}}}{r_{\text{crm}}} \right) \dots \\ & \dots + \left[\left(\frac{E}{E'} \right)^{-0.65} \left(\frac{G}{G'} \right)^{0.50} \left(\frac{1 + \nu}{1 + \nu'} \right)^{-0.56} \right] \frac{1 + \nu}{E'}. \end{aligned} \quad (12.15)$$

The corresponding mean major principal stress is computed as

$$\sigma_{\text{aniso,mean}} = \frac{1}{r_c^2 - r_i^2} \left[r_i^2 p_{i,\text{mean}} - r_c^2 p_{c,\text{aniso,mean}} - \frac{r_i^2 r_c^2}{r_i^2} (p_{c,\text{aniso,mean}} - p_{i,\text{mean}}) \right]. \quad (12.16)$$

Finally, $K_{\text{rm,aniso}}^*$ is defined by the ratio of the mean stresses calculated above as

$$K_{\text{rm,aniso}}^* = \frac{\sigma_{\text{aniso,mean}}}{\sigma_{\text{iso,mean}}}. \quad (12.17)$$

12.4.2 Compute maximum and minimum membrane and bending stresses (Chapter 7)

The membrane stresses (equivalent to the nominal stresses herein) in anisotropic rock associated with cycle k can be approximated as

$$\begin{cases} \sigma_{m,\text{aniso,max}}^k = K_{\text{rm,aniso}}^* \sigma_{m,\text{iso,max}}^k \\ \sigma_{m,\text{aniso,min}}^k = K_{\text{rm,aniso}}^* \sigma_{m,\text{iso,min}}^k \end{cases} \quad (12.18)$$

As previously, $\sigma_{m,\text{iso,max}}^k$ and $\sigma_{m,\text{iso,min}}^k$ are computed from

$$\begin{cases} p_{c,\text{iso,max}}^k = \frac{\frac{1 + \nu_s}{E_s} \frac{r_c}{r_c^2 - r_i^2} \left[(1 - 2\nu_s) p_{i,\text{max}}^k r_i^2 + p_{i,\text{max}}^k r_i^2 \right] - \Delta r_0}{\frac{1 + \nu_s}{E_s} \frac{r_c}{r_c^2 - r_i^2} \left[(1 - 2\nu_s) r_c^2 + r_i^2 \right] + r_c \frac{1}{E_{\text{eq}}}} \\ p_{c,\text{iso,min}}^k = \frac{\frac{1 + \nu_s}{E_s} \frac{r_c}{r_c^2 - r_i^2} \left[(1 - 2\nu_s) p_{i,\text{min}}^k r_i^2 + p_{i,\text{min}}^k r_i^2 \right] - \Delta r_0}{\frac{1 + \nu_s}{E_s} \frac{r_c}{r_c^2 - r_i^2} \left[(1 - 2\nu_s) r_c^2 + r_i^2 \right] + r_c \frac{1}{E_{\text{eq}}}} \end{cases} \quad (12.19)$$

with

$$\frac{1}{E_{eq}} = \frac{1 - \nu_c^2}{E_c} \ln \left(\frac{r_{crm}}{r_c} \right) + \frac{1 - \nu_{crm}^2}{E_{crm}} \ln \left(\frac{r_{rm}}{r_{crm}} \right) + \frac{1 + \nu}{E'}, \quad (12.20)$$

allowing to compute

$$\begin{cases} \sigma_{m,iso,max}^k = \frac{1}{r_c^2 - r_i^2} \left[r_i^2 p_{i,max}^k - r_c^2 p_{c,iso,max}^k - \frac{r_i^2 r_c^2}{r_i^2} (p_{c,iso,max}^k - p_{i,max}^k) \right] \\ \sigma_{m,iso,min}^k = \frac{1}{r_c^2 - r_i^2} \left[r_i^2 p_{i,min}^k - r_c^2 p_{c,iso,min}^k - \frac{r_i^2 r_c^2}{r_i^2} (p_{c,iso,min}^k - p_{i,min}^k) \right]. \end{cases} \quad (12.21)$$

To compute the bending stresses, only peaking is considered, as discussed in Sect. 8.2.2. The maximum and minimum bending stresses $\sigma_{b,aniso,max}^k$ and $\sigma_{b,aniso,min}^k$ at cycle k can be computed as

$$\begin{cases} \sigma_{b,aniso,max}^k = (K_{m,p}^{*k} - 1) \sigma_{m,aniso,max}^k \\ \sigma_{b,aniso,min}^k = (K_{m,p}^{*k} - 1) \sigma_{m,aniso,min}^k \end{cases} \quad (12.22)$$

with

$$K_{m,p}^{*k} = 1 + \frac{3 \cdot 1.05 \cdot \Delta h}{t_s (1 - \nu_s^2)} \cdot \frac{\tanh(\phi_{mean}/2)}{\phi_{mean}/2} \quad (12.23)$$

where ϕ_{mean} can be computed with $\sigma_{aniso,mean}$ as suggested in Sect. 10.1.2 and thus

$$\phi_{mean} = \frac{2l}{t_s} \sqrt{\frac{3(1 - \nu_s^2) \sigma_{m,aniso,mean}}{E_s}}. \quad (12.24)$$

12.4.3 Compute maximum and minimum stress intensity factors (Chapter 8)

Once maximum and minimum membrane and bending stresses are known for cycle k , one can compute the range of stress intensity factor (SIF) for cycle k .

12.4. Detailed example of the calculation of the crack growth for the k^{th} cycle

For semi-elliptical surface crack

The pressure acting on the crack faces is

$$\begin{cases} p_{\text{cr,max}}^k = p_{i,\text{max}}^k \\ p_{\text{cr,min}}^k = p_{i,\text{min}}^k \end{cases} \quad (12.25)$$

The maximum and minimum SIF $K_{I,\text{max}}^k$ and $K_{I,\text{min}}^k$, respectively, are computed according to the following expressions:

$$\begin{cases} K_{I,\text{max}}^k = M_w^k \left[M_m^k \left(\sigma_{m,\text{aniso,max}}^k + p_{\text{cr,max}}^k \right) + M_b^k \sigma_{b,\text{aniso,max}}^k \right] \sqrt{\frac{\pi a_k}{Q}} \\ K_{I,\text{min}}^k = M_w^k \left[M_m^k \left(\sigma_{m,\text{aniso,min}}^k + p_{\text{cr,min}}^k \right) + M_b^k \sigma_{b,\text{aniso,min}}^k \right] \sqrt{\frac{\pi a_k}{Q}} \end{cases} \quad (12.26)$$

Q is approximated as

$$Q = 1.0 + 1.464 \left(\frac{a_k}{c_k} \right)^{1.65} \quad (12.27)$$

As a/c is constant in each trial, the terms only function of a_k/c_k are independent from the cycle k .

The membrane correction factor is expressed as

$$M_m^k = \left[M_1 + M_2 \left(\frac{a_k}{t_s} \right)^2 + M_3 \left(\frac{a_k}{t_s} \right)^4 \right] g^k f_\phi f_w, \quad (12.28)$$

where

$$M_1 = 1.13 - 0.09 \left(\frac{a_k}{c_k} \right) \quad (12.29)$$

$$M_2 = \frac{0.89}{0.2 + \frac{a_k}{c_k}} - 0.54 \quad (12.30)$$

Chapter 12. Case study

$$M_3 = 0.5 - \frac{1}{0.65 + \frac{a_k}{c_k}} + 14 \left[1 - \frac{a_k}{c_k} \right]^{24} \quad (12.31)$$

and (with $\phi = \pi/2$, i.e., deepest point of the crack)

$$g^k = 1 + \left[0.1 + 0.35 \left(\frac{a_k}{t_s} \right)^2 \right] (1 - \sin \phi)^2 \quad (12.32)$$

$$f_\phi = \left[\left(\frac{a_k}{c_k} \right)^2 \cos^2 \phi + \sin^2 \phi \right]^{0.25} \quad (12.33)$$

$$f_w = 1. \quad (12.34)$$

The bending correction factor is calculated as

$$M_b^k = M_m^k H^k \quad (12.35)$$

where

$$H^k = H_1^k + (H_2^k - H_1^k)(\sin \phi)^{q^k}; \quad (12.36)$$

$$H_1^k = 1 - 0.34 \left(\frac{a_k}{t_s} \right) - 0.11 \left(\frac{a_k}{c_k} \right) \left(\frac{a_k}{t_s} \right) \quad (12.37)$$

$$H_2^k = 1 + G_1 \left(\frac{a_k}{t_s} \right) + G_2 \left(\frac{a_k}{t_s} \right)^2 \quad (12.38)$$

$$q^k = 0.2 + \left(\frac{a_k}{c_k} \right) + 0.6 \left(\frac{a_k}{t_s} \right); \quad (12.39)$$

and

$$G_1 = -1.22 - 0.12 \left(\frac{a_k}{c_k} \right); \quad (12.40)$$

$$G_2 = 0.55 - 1.05 \left(\frac{a_k}{c_k} \right)^{0.75} + 0.47 \left(\frac{a_k}{c_k} \right)^{1.5}. \quad (12.41)$$

Finally, the weld shape correction factor, if it is to be considered, is calculated as

$$M_w^k = f_1^k \left(\frac{a_k}{t_s}, \frac{\delta}{t_s} \right) f_2^k \left(\frac{a_k}{t_s}, \frac{l_w}{t_s}, \frac{\delta}{t_s} \right) + f_3^k \left(\frac{a_k}{t_s}, \frac{l_w}{t_s}, \frac{\delta}{t_s}, \beta \right) \quad (12.42)$$

12.4. Detailed example of the calculation of the crack growth for the k^{th} cycle

where the f_i^k are given by

$$f_1^k = 1 - 1.79 \cdot g_{11}^k \left(\frac{\delta}{t_s} \right) \quad (12.43)$$

$$f_2^k = 1 + 2.63 \cdot g_{21}^k g_{22}^k \left(\frac{l_w}{t_s} \right) \quad (12.44)$$

$$f_3^k = \frac{0.37 \cdot g_{31}^k g_{32}^k g_{33}^k}{2} [1 + \cos(\pi + 6\beta)]; \quad (12.45)$$

and the g_{ij}^k by

$$g_{11}^k = \left(\frac{a_k}{t_s} \right)^{-0.45}; \quad (12.46)$$

$$g_{21}^k = \left(\frac{a_k}{t_s} \right)^{1.08} \quad (12.47)$$

$$g_{22}^k = \left(\frac{\delta}{t_s} \right)^{0.79}; \quad (12.48)$$

and

$$g_{31}^k = \left(\frac{a_k}{t_s} \right)^{-1.10} \quad (12.49)$$

$$g_{32}^k = \left(\frac{\delta}{t_s} \right)^{0.88} \quad (12.50)$$

$$g_{33}^k = \left(\frac{l_w}{t_s} \right)^{4.84}. \quad (12.51)$$

For embedded elliptical crack

Similarly to surface cracks, the maximum and minimum SIF for embedded elliptical cracks, $K_{I,\max}^k$ and $K_{I,\min}^k$, respectively, are computed as

$$\begin{cases} K_{I,\max}^k = \left[M_m^k (\sigma_{\text{me},\max}^k + 0) + M_b^k \sigma_{\text{be},\max}^k \right] \sqrt{\frac{\pi a_k}{Q}} \\ K_{I,\min}^k = \left[M_m^k (\sigma_{\text{me},\min}^k + 0) + M_b^k \sigma_{\text{be},\min}^k \right] \sqrt{\frac{\pi a_k}{Q}} \end{cases} \quad (12.52)$$

where there is no pressure on the crack faces, as they are not in contact with internal water pressure.

Chapter 12. Case study

The maximum and minimum values of σ_{me}^k and σ_{be}^k are computed from the membrane and bending stresses as

$$\begin{cases} \sigma_{me,max}^k = \{\sigma_{m,aniso,max}^k + 0\} + \sigma_{b,aniso,max}^k \left(1 - \frac{2t_s/2}{t_s}\right) \\ \sigma_{me,min}^k = \{\sigma_{m,aniso,min}^k + 0\} + \sigma_{b,aniso,min}^k \left(1 - \frac{2t_s/2}{t_s}\right) \end{cases} \quad (12.53)$$

and

$$\begin{cases} \sigma_{be,max}^k = \sigma_{b,aniso,max}^k \left(\frac{2a_k}{t_s}\right) \\ \sigma_{be,min}^k = \sigma_{b,aniso,min}^k \left(\frac{2a_k}{t_s}\right). \end{cases} \quad (12.54)$$

Assuming that

$$\begin{cases} \alpha = a_k/c_k \\ \beta_1^k = a_k/d_1 \\ \beta_2^k = a_k/d_2, \end{cases} \quad (12.55)$$

the membrane correction factor can be computed as

$$M_m^k = H_\phi^k f_\phi f_w \quad (12.56)$$

where (with $\phi = -\pi/2$, i.e., most detrimental point along crack front toward the internal fiber)

$$H_\phi^k = \frac{1}{2} \sin^2 \phi \left[H_{90}^k (1 + \sin \phi) + H_{270}^k (1 - \sin \phi) \right] + H_0^k \cos^2 \phi, \quad (12.57)$$

$$f_\phi = \left[\left(\frac{a_k}{c_k} \right)^2 \cos^2 \phi + \sin^2 \phi \right]^{0.25}, \quad (12.58)$$

$$f_w = 1; \quad (12.59)$$

$$H_{90}^k = h_1^k(\alpha, \beta_1^k) h_3^k(\alpha, \beta_2^k), \quad (12.60)$$

$$H_0^k = h_2^k(\alpha, \beta_1^k) h_2^k(\alpha, \beta_2^k), \quad (12.61)$$

$$H_{270}^k = h_3^k(\alpha, \beta_1^k) h_1^k(\alpha, \beta_2^k); \quad (12.62)$$

12.4. Detailed example of the calculation of the crack growth for the k^{th} cycle

and

$$h_1^k(\alpha, \beta_i^k) = 1 + \left(-0.04 + \frac{0.085}{0.34 + \alpha} \right) (\beta_i^k)^2 + (0.05 - 0.03\alpha) (\beta_i^k)^4, \quad (12.63)$$

$$h_2^k(\alpha, \beta_i^k) = 1 + \left(-0.03 + \frac{0.075}{0.30 + \alpha} \right) (\beta_i^k)^2 + \left(0.08 - \frac{0.024}{0.1 + \alpha} \right) (\beta_i^k)^4, \quad (12.64)$$

$$h_3^k(\alpha, \beta_i^k) = 1 + \left(-0.06 + \frac{0.070}{0.25 + \alpha} \right) (\beta_i^k)^2 + (0.643 - 0.343\alpha) (\beta_i^k)^4; \quad (12.65)$$

and the bending correction factor is expressed as

$$M_b^k = - \left[0.5 + 0.2591\alpha^{1.5} - 0.09189\alpha^{2.5} \right] f_\phi f_w f_\beta^k \sin \phi \quad (12.66)$$

where

$$f_\beta^k = \frac{f_{270}^k + f_{90}^k}{2} - \frac{f_{270}^k - f_{90}^k}{2} \sin \phi, \quad (12.67)$$

$$f_{90}^k = 1 + \exp \left[-1.9249 - 3.9087\alpha^{0.5} + 4.1067(\beta_2^k)^3 \right], \quad (12.68)$$

$$f_{270}^k = 1 + \exp \left[-1.9249 - 3.9087\alpha^{0.5} + 4.1067(\beta_1^k)^3 \right]. \quad (12.69)$$

12.4.4 Compute the new crack size

Finally, for both crack types, the crack increment at cycle k is computed using the range of SIF

$$\Delta K^k = K_{I,\max}^k - K_{I,\min}^k, \quad (12.70)$$

and from the Paris–Erdogan law one obtains

$$\left(\frac{da}{dN} \right)_k = \Delta a_k = C \left(\Delta K^k \right)^m. \quad (12.71)$$

The crack size for the $(k+1)^{\text{th}}$ cycle is then

$$a_{k+1} = a_k + \Delta a_k. \quad (12.72)$$

12.5 Detailed example of the calculation of the k^{th} term of the cumulative damage sum

At the k^{th} cycle, the damage sum is expressed according to the Palmgren–Miner rule as

$$D_{\text{calc}} = \frac{n_1}{N_1} + \frac{n_2}{N_2} + \dots + \frac{n_j}{N_j} + \dots + \frac{n_k}{N_k} = \sum_{j=1}^k \frac{n_j}{N_j}. \quad (12.73)$$

Similarly to Sect. 12.4, the maximum and minimum nominal stresses $\sigma_{\text{nom,aniso,max}}^k$ and $\sigma_{\text{nom,aniso,min}}^k$ at cycle k are computed as¹

$$\begin{cases} \sigma_{\text{nom,aniso,max}}^k = K_{\text{rm,aniso}}^* \sigma_{\text{nom,iso,max}}^k \\ \sigma_{\text{nom,aniso,min}}^k = K_{\text{rm,aniso}}^* \sigma_{\text{nom,iso,min}}^k \end{cases} \quad (12.74)$$

From the nominal stresses, the structural stresses are calculated as

$$\begin{cases} \sigma_{s,\text{aniso,max}}^k = K_m^* \sigma_{\text{nom,aniso,max}}^k \\ \sigma_{s,\text{aniso,min}}^k = K_m^* \sigma_{\text{nom,aniso,min}}^k \end{cases} \quad (12.75)$$

where

$$K_m^* = [1 + (K_{m,p}^* - 1) + (K_{m,e}^* - 1)]. \quad (12.76)$$

The peaking stress concentration factor (SCF) can be computed as

$$K_{m,p}^* = 1 + \frac{3 \cdot 1.05 \cdot \Delta h}{t_s(1 - \nu_s^2)} \cdot \frac{\tanh(\phi_{\text{mean}}/2)}{\phi_{\text{mean}}/2} \quad (12.77)$$

¹The nominal stress $\sigma_{\text{nom,aniso}}^k$ defined herein is equivalent to $\sigma_{m,\text{aniso}}^k$ used in Sect. 12.4. The nomenclature difference is only related to the conventions adopted through the related chapters.

12.5. Detailed example of the calculation of the k^{th} term of the cumulative damage sum

with

$$\phi_{\text{mean}} = \frac{2l}{t_s} \sqrt{\frac{3(1 - \nu_s^2) \sigma_{\text{nom, aniso, mean}}}{E_s}}; \quad (12.78)$$

and the linear misalignment SCF as

$$K_{m,e}^* = 1 + \frac{3 \cdot 0.87 \cdot e}{t_s(1 - \nu_s^2)}. \quad (12.79)$$

From the structural stresses, one can obtain the notch stresses as

$$\begin{cases} \sigma_{n, \text{aniso, max}}^k = K_t^* \sigma_{\text{nom, aniso, max}}^k = K_m^* K_w \sigma_{\text{nom, aniso, max}}^k \\ \sigma_{n, \text{aniso, min}}^k = K_t^* \sigma_{\text{nom, aniso, min}}^k = K_m^* K_w \sigma_{\text{nom, aniso, min}}^k \end{cases} \quad (12.80)$$

where the weld SCF is expressed as

$$K_w = 1 + 1.08 \left(\frac{\delta}{t_s} \right)^{0.24} \left(\frac{\rho}{t_s} \right)^{-0.41} \tan \left(\frac{\beta}{2} \right)^{0.41}. \quad (12.81)$$

Finally, the structural hot-spot² and notch stresses ranges at cycle k are calculated as

$$\begin{cases} \Delta \sigma_{\text{hs}}^k = \sigma_{s, \text{aniso, max}}^k - \sigma_{s, \text{aniso, min}}^k \\ \Delta \sigma_n^k = \sigma_{n, \text{aniso, max}}^k - \sigma_{n, \text{aniso, min}}^k. \end{cases} \quad (12.82)$$

The determination of $N_k = \min \{N_{k,225}; N_{k,160 \times K_w}; N_{k,160}\}$ is illustrated in Fig. 12.2 according to the recommendations of the IIW (Hobbacher 2008, 2016).

²For this verification, it is assumed herein that the hot-spot stress is equivalent to the structural stress.

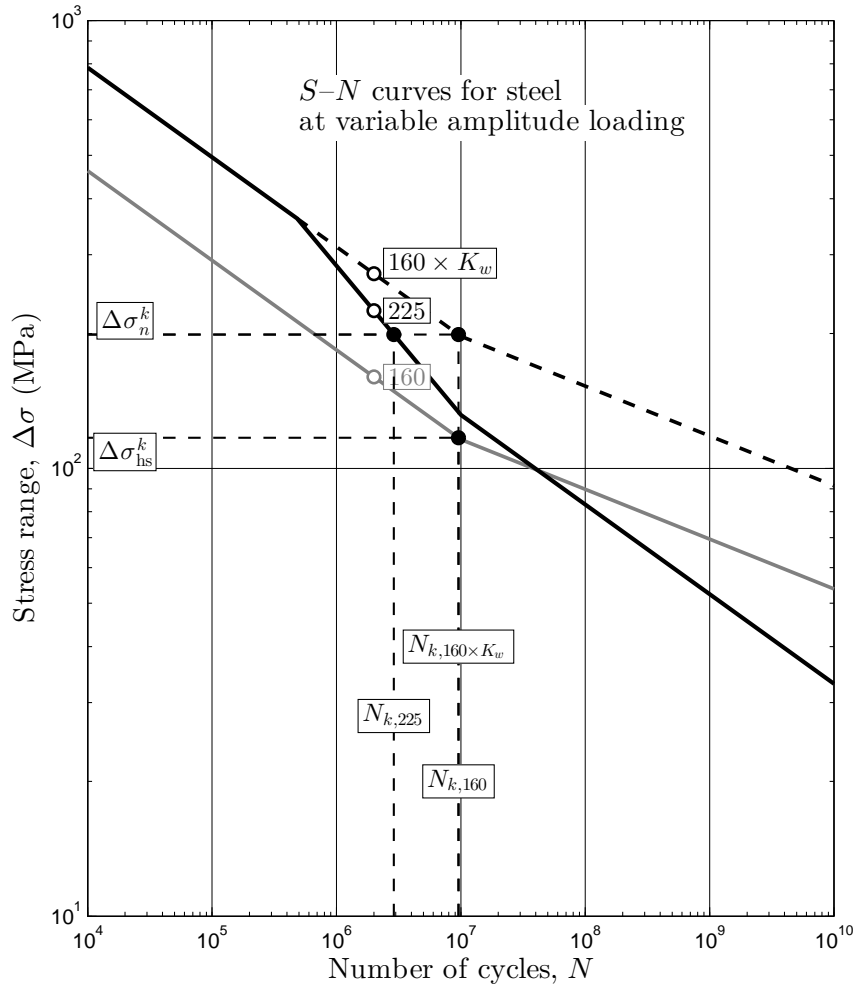


Figure 12.2: Determination of $N_k = \min \{N_{k,225}; N_{k,160 \times K_w}; N_{k,160}\}$ for a given $\Delta\sigma_n^k$ (and $\Delta\sigma_{hs}^k$) with modified $S-N$ curves for steel at variable amplitude loading within the effective notch stress approach. In this example, $K_m^* = 1.3$, $K_w = 1.7$, and $\Delta\sigma_{nom}^k = 90$ MPa.

12.6 Results from the LEFM approach for fatigue propagation of cracks in the weld material

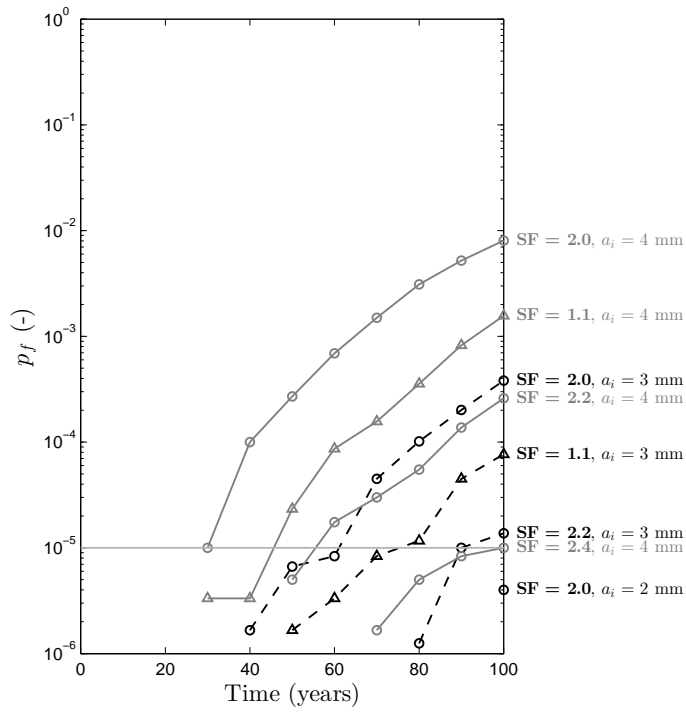
The results from the Monte Carlo simulations are reported in Appendix E, in Tables E.1, E.2 and E.3 for semi-elliptical surface cracks in inert and aggressive environments, and for embedded elliptical cracks in inert environment, respectively. One can see that with respect to the target probability of failure $p_f = 10^{-5}$, only semi-elliptical surface cracks within the hypothesis of aggressive environment exhibit a significant risk of failure. The evolution of the probability of failure along lifespan is presented in Fig. 12.3 for all the tested cases. The design choice would depend on the nondestructive testing capabilities and on the adopted fitness-for-service

philosophy. Assuming no inspection plan during lifespan, and that the hypothesis of aggressive environment cannot be avoided, the acceptable designs in terms of surface crack propagation are summarized hereafter according with Fig. 12.3 and Table E.2.

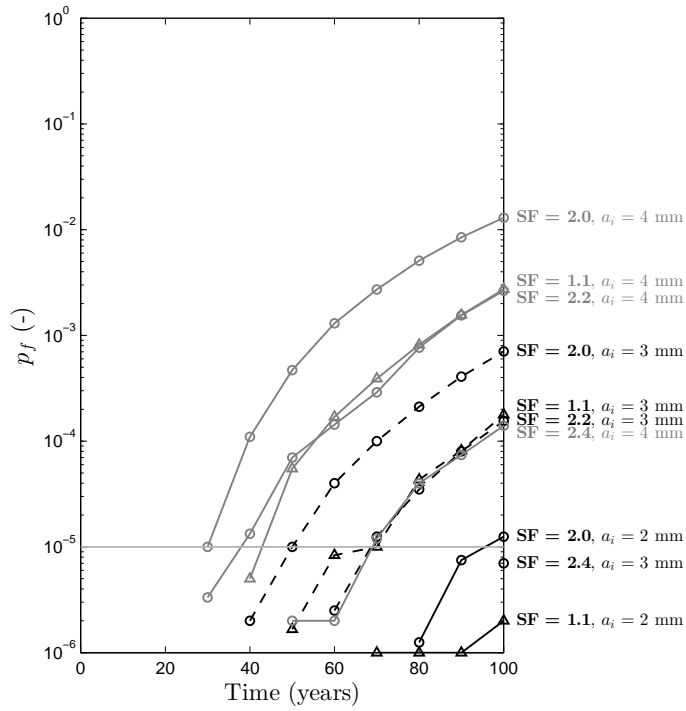
- If S890 QL is used:
 - SF = 2.0 if $a_i = 2$ mm;
 - SF = 2.2 if $a_i = 3$ mm;
 - SF = 2.4 if $a_i = 4$ mm.
- If S960 QL is used:
 - SF = 2.0 or 1.1 without rock participation if $a_i = 2$ mm;
 - SF = 2.4 if $a_i = 3$ mm;
 - $a_i = 4$ mm is not acceptable or larger SF has to be assessed.
- S690 QL is adequate at least for $a_i \leq 4$ mm.

12.7 Conclusions

This chapter aimed at detailing the calculation procedures in the model developed in this research project within the framework of the Monte Carlo simulation method. The probabilistic model for fatigue crack growth and fracture was then applied to a case study, an hypothetic high-head hydropower plant with $H_{\text{mean}} = 1300$ m. The application of the model in order to determine acceptable undetected initial crack sizes depending on the design (steel grade, SF) was presented, for an easier transfer toward practical implementation.



(a) S890 QL.



(b) S960 QL.

Figure 12.3: Probability of failure considering initial semi-elliptical surface cracks in aggressive environment.

Conclusions **Part VI**

13 Conclusions

13.1 Summary and conclusions

The literature review has emphasized that for the design of steel-lined pressure tunnels and shafts (SLPT&S), when made of high-strength steel (HSS) and subject to harsher transient loading, the issue of fatigue behavior arises. An accurate use of engineering fatigue assessment methods requires to estimate local stresses at the welded joints of the steel liners, which normally requires finite element analysis (FEA) if empirical or analytical equations are not known.

The main objectives of this research project were:

1. the enhancement of the comprehension of the mechanical behavior of SLPT&S accounting for rock anisotropy, geometrical imperfections in the steel liners, and the presence of crack-like flaws in the weld material; and
2. the construction of a crack propagation and fracture model based on the first objective, using the linear elastic fracture mechanics (LEFM) approach combined with the Paris–Erdogan law in a probabilistic framework by means of the Monte Carlo simulation procedure.

These objectives have been fulfilled through the following steps.

Anisotropic behavior

The influence of anisotropic rock behavior, and more particularly transverse isotropy, was studied by means of FEA. It was shown that considering an isotropic case for the design with the lowest elastic modulus measured in situ is a conservative assumption. The extent of this result mainly depends on the relative stiffness between the steel liner and the concrete–rock system. The maximum major principal stress in a steel liner in transversely isotropic rock occurs in the direction of the plane of isotropy. It was also shown that the main change when considering anisotropy is a shift of the nominal stress in the steel liner, up to 15–20% lower than in isotropic

Chapter 13. Conclusions

cases with realistic material and geometrical parameters. Finally, correction factors to be included in the analytical solution in isotropic rock to account for the influence of anisotropy were derived. One may note that this study was already extended by Bobet & Yu (2016), who analytically solved the stress and displacement fields in SLPT&S in transversely isotropic rock. The proposed approach remains highly relevant for practical engineering applications where only the maximum stresses are required. Furthermore, the proposed empirical solution highlights clearly the relative importance of the involved parameters.

Geometrical imperfections

The influence of geometrical imperfections in the steel liners was studied by means of FEA, considering rock anisotropy and the contact between the external fiber of the steel liner and the backfill concrete–rock system. Imperfections such as out-of-roundness, peaking and linear misalignment were considered. The main result is that embedment completely vanishes the effect of the out-of-roundness, while the effect of peaking and linear misalignment remains. To estimate the stress concentration factors at the longitudinal butt welded joints of SLPT&S in anisotropic rock, correction factors were derived to be included in widespread empirical equations for SCF in welded plates and shells. With these correction factors, membrane and bending stresses at the longitudinal joints considering anisotropic rock behavior, geometrical imperfections and the initial gap between steel and concrete can be estimated.

Crack-like flaws in the weld material of the longitudinal butt welded joints

When using the LEFM approach for fatigue assessment, stress intensity factors (SIF) for the studied cracks must be known. Two types of cracks in the weld material of the longitudinal butt welded joints of SLPT&S were studied by means of FEA, namely axial semi-elliptical surface cracks and axial embedded elliptical cracks. At first, the applicability of SIF solutions in cracked plated structures to steel liners was verified using the previously developed parametric equations to estimate membrane and bending stresses at the longitudinal joints. Finally, the influence of the weld shape on the SIF for axial cracks was studied. It could be shown that the weld reinforcement has a mitigation effect on the SIF for semi-elliptical surface cracks, while it has no effect for embedded elliptical cracks in the tested ranges. This mitigation effect is particularly large for small cracks, i.e., with crack depth within the weld reinforcement height. A new parametric equation was derived for the weld shape correction factor. However, weld shape correction factors were not considered for crack propagation as the internal surface of the longitudinal joints may be flush ground in some cases, and considering this mitigation effect is not conservative.

Fatigue assessment

A probabilistic model for fatigue crack growth and fracture was established, using the previously developed deterministic model in the framework of the Monte Carlo simulation technique.

Parameters such as the crack shape ratio a/c , the material parameter C characterizing the crack growth rate in the Paris–Erdogan law and the threshold stress intensity factor range ΔK_{th} were considered as stochastic. Reasonable hypotheses on their distributions were made based on the literature of probabilistic fracture mechanics of welded joints. A normalized loading spectrum was derived based on the measurements during a week of normal operation performed by Hachem & Schleiss (2012c) and Hachem & Giovanola (2013) on a pumped-storage hydropower plant (HPP) in Switzerland, namely Grimsel II, equipped with ternary groups with Francis turbines. Although loading spectra may be case specific (general waterway lay-out, head, role in the electric grid, type of electromechanical units), it was assumed to be transferable and scaled to other HPP in this study.

Although there were no data available to calibrate the model in the scope of this research study, the proposed probabilistic approach can provide very informative quantitative results, relatively to the hypotheses adopted for the deterministic parameters. An extensive parametric study was performed considering steel liners designed under the so-called basic criteria herein (i.e., isotropic case, rock participation limited to 50% of the internal pressure, use of global safety factor SF for the steel resistance as recommended in the C.E.C.T. 1980 recommendations). It could be shown that high heads and the use of high-strength steels (i.e., allowing thinner steel liners with respect to the working stress criterion) yields a higher risk of failure in case of the presence of initial cracks below detection limits in the weld material. However, the results may highly depend on the loading spectra, which should be determined case by case.

Initiation and propagation of cracks from notches (weld toes) of the longitudinal butt welded joints was assessed by means of the effective notch stress approach, which is an $S-N$ based engineering procedure. Within the hypotheses made herein, the calculated damage sums by means of the Palmgren–Miner rule have shown a considerable margin of security with respect to the recommendations of the IIW (Hobbacher 2008, 2016). To reach the critical damage sum, the main peaks of the proposed loading spectrum would require to occur at least 10–20 times more frequently for the worst tested cases. However, a probability of rupture is not assessed when using the effective notch stress approach and the cumulative damage sum, and as a consequence the risk of failure from the latter verification is not directly comparable with the results from the LEFM approach for the analysis of the fatigue propagation of initial flaws in the weld material. The application of the LEFM approach to cracks emanating from weld toes would allow such a comparison.

In the light of the application of these engineering fatigue assessment procedures, one can conclude that when HSS are considered for the design and particularly if harsh operational conditions are expected, the *Good Workmanship* philosophy should be substituted by the *Fitness-for-Service* philosophy, based on fracture mechanics. This work is a first attempt to develop a framework for this design philosophy specific to steel-lined pressure tunnels and shafts.

13.2 Recommendations

Based on the conclusions of this research project, it is recommended to complete the standard design procedure presented in Sect. 2.3, Fig. 2.2. In cases where fatigue phenomena may arise, a third criterion should be included, namely the fatigue resistance of the longitudinal butt welded joints. The completed standard design flowchart is presented in Fig. 13.1, where the so-called Condition III is added. The latter condition could also be implemented in a deterministic framework.

For instance, Condition III could be implemented in the scope of a *Damage Tolerant Design* philosophy, as shown in Fig. 13.2, modified after Zerbst *et al.* (2007). In the scope of this design philosophy, the proposed probabilistic approach can also provide a quantitative basis for the planning of the nondestructive testing (NDT) inspections, and for the assessment of the acceptability of the cracks detected during lifespan.

13.3 Future research

The discussions driven in the present research project enable to propose an outlook for future research in the scope of the design of SLPT&S subject to fatigue phenomenon.

Loading spectra

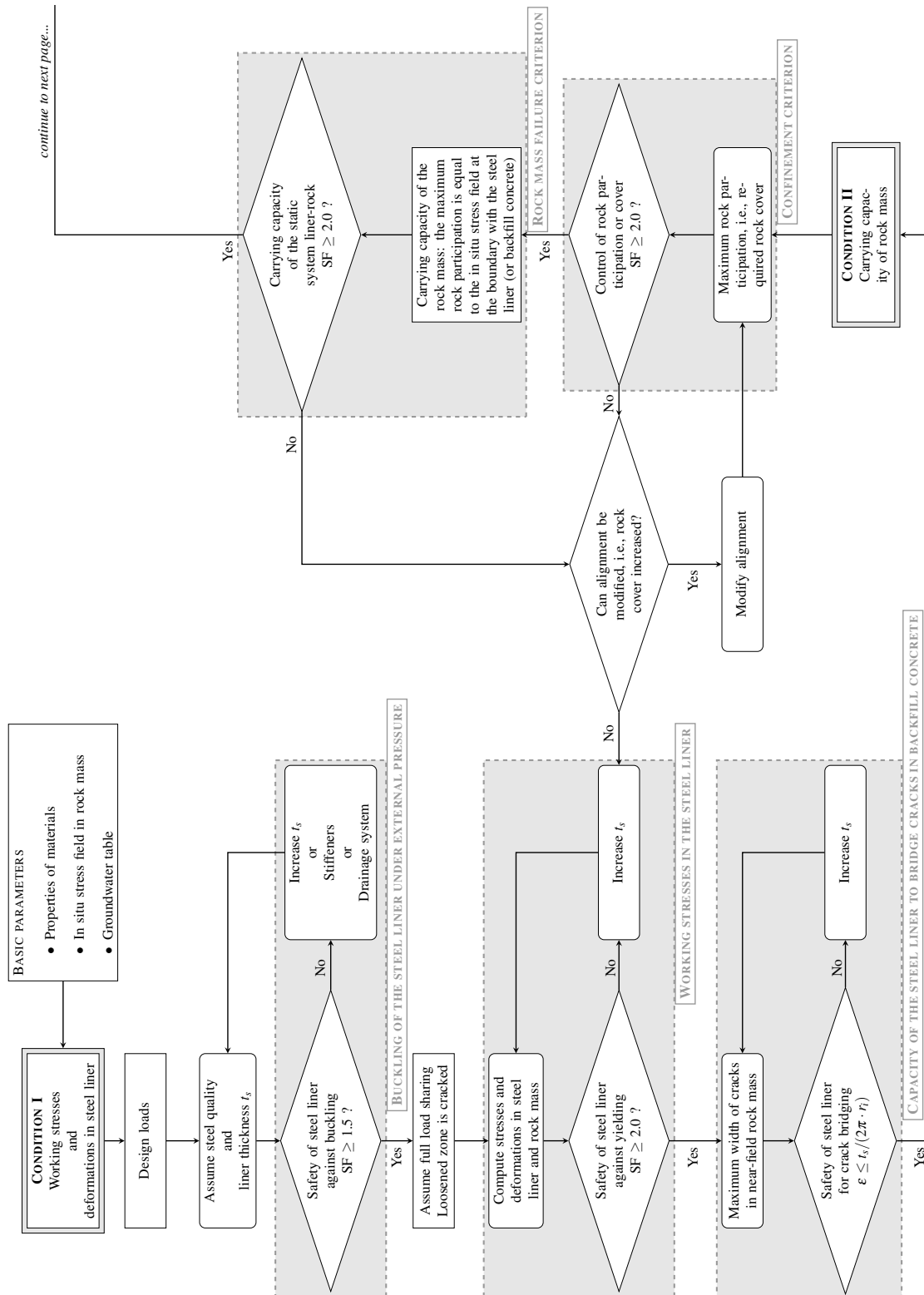
- Loading spectra are a fundamental input for fatigue assessment procedures. In the case of storage and pumped-storage hydropower plants, very few data are available. For a wider and more accurate application of the proposed methodology, more data should be acquired from prototypes.
- When stress cycles vary in a random manner, it may also be beneficial to describe their distribution by a continuous probability distribution function (PDF) (Klemenc & Fajdiga 2004). The normalized spectrum based on the original measurements of Hachem & Schleiss (2012c), although it can be scaled to different mean pressures, has the drawback neither to be able to predict different relative pressure amplitudes (either larger or within unobserved ranges during the measurement period) nor to change the weekly frequency of load cycles. To allow reasonable modifications of the original spectrum and a wider use in practical applications, modeling the distribution of the load cycles with the best-fitting continuous PDF can address these issues.

Online and non-intrusive monitoring

- As outlined in Sect. 2.8, the development of non-intrusive monitoring techniques based on the analysis of pressure transients in SLPT&S is very promising but still faces great

scientific and technological challenges. Further research should be conducted in order to detect damage evolution (e.g., loss of stiffness in one or several layers, through-thickness crack in the steel liner) in the waterways with accuracy.

- The proposed methodology for fatigue crack propagation could be implemented in combination with online monitoring (providing real loading history) in order to assess the remaining lifetime of SLPT&S of HPP, based on forecast.



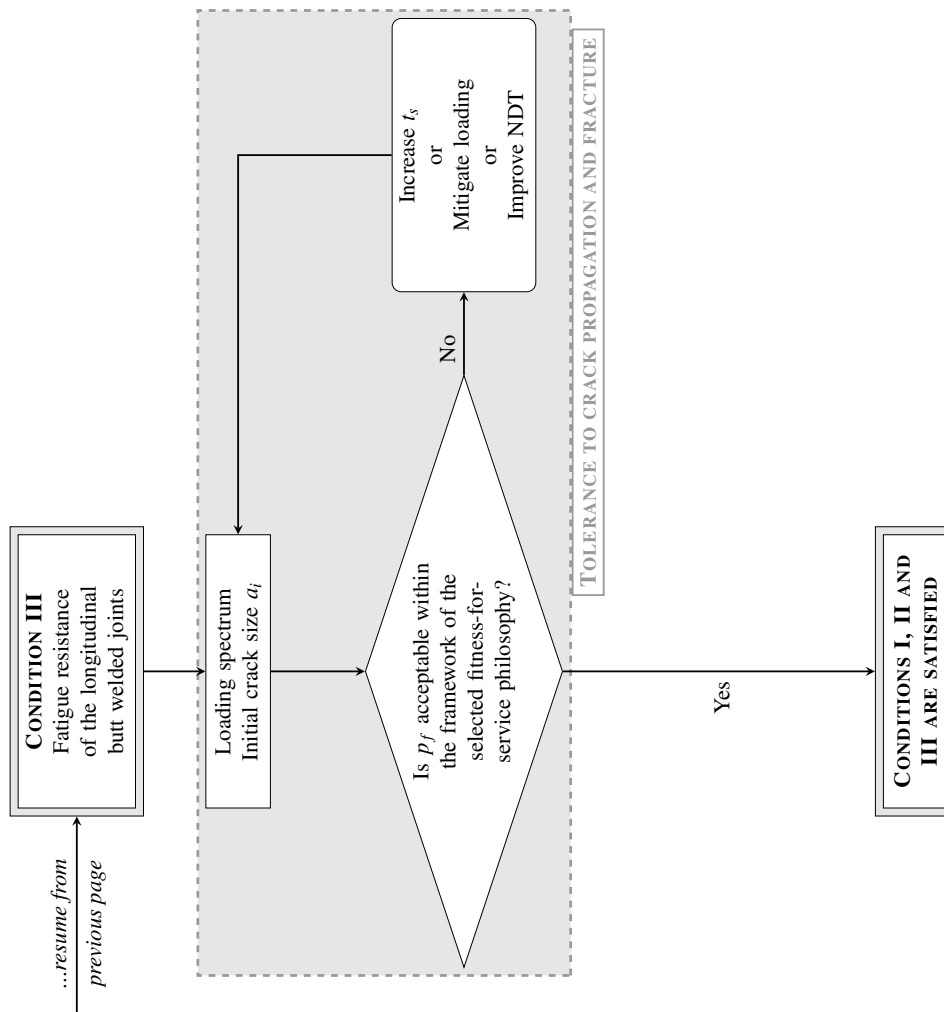


Figure 13.1: Recommended design procedure, extended after Schleiss (1988) to the consideration of fatigue crack propagation and fracture.

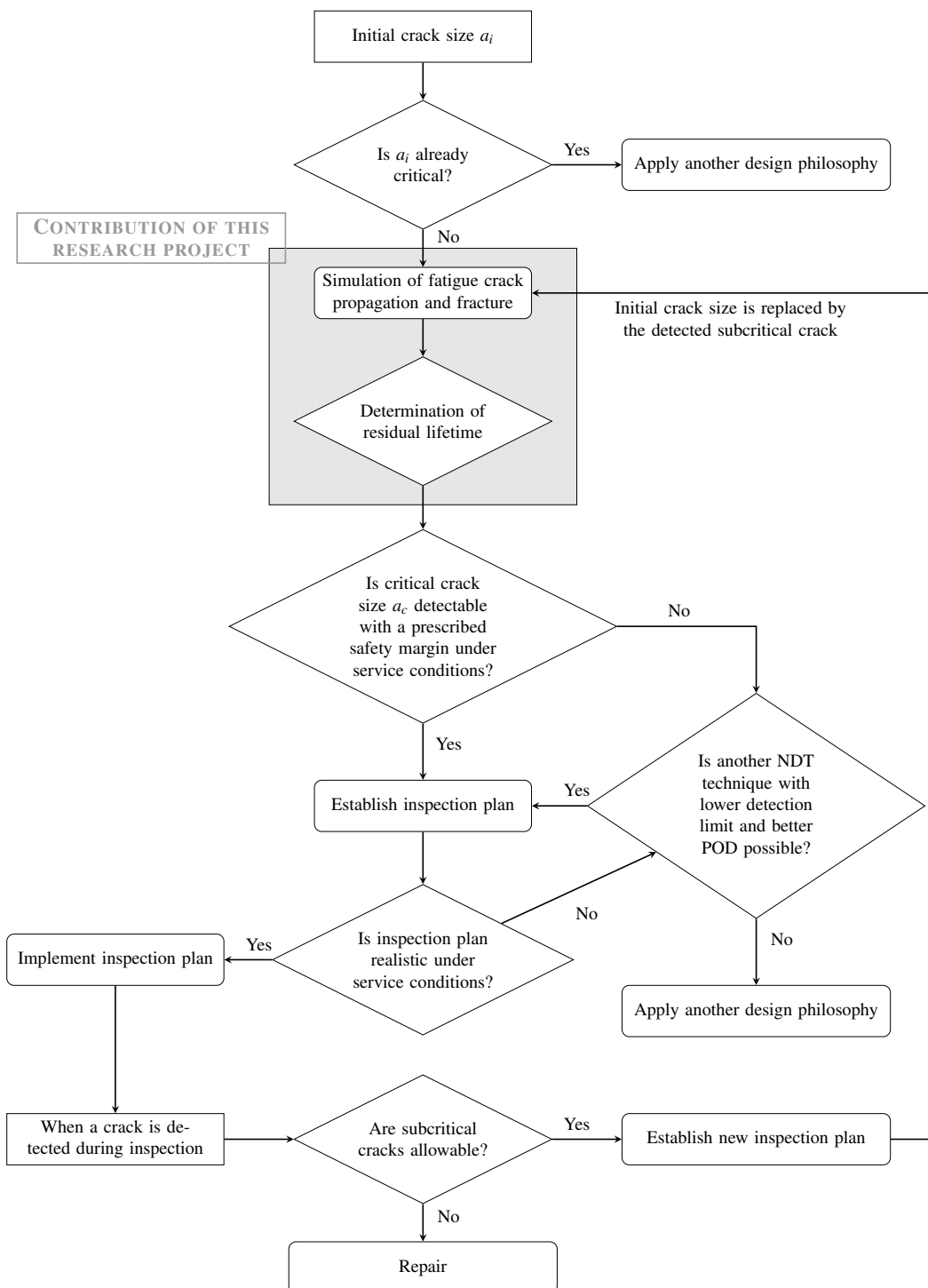


Figure 13.2: Fatigue and fracture analysis within the framework of Damage Tolerant Design (modified after Zerbst *et al.* 2007). POD: probability of detection; NDT: nondestructive testing.

A Mathematical model for geometrical imperfections of steel liners

This Appendix presents the mathematical model for the geometry of the steel liners. At first the parameters of the model firstly used in Part III are recalled and completed. The coordinates of the points used to construct the model are described mathematically. The approach described hereafter is also used for the FE models used in Part IV.

A.1 Parameters and nomenclature

The variable parameters of the model are listed hereafter:

- r_i : internal radius (m);
- t_s : liner's thickness (m);
- ψ_η : factor for out-of-roundness η (-);
- ψ_u : factor for straight edge's length¹ (-) ;
- ψ_e : factor for linear misalignment (-);
- ψ_δ : factor for weld reinforcement/concavity (-);
- β : weld flank angle (deg);
- α : edge preparation angle (deg).

The calculated or constant parameters of the model are itemized hereafter:

¹This parameter controls the peaking, i.e., the deviation Δh from the circular shape.

Appendix A. Mathematical model for geometrical imperfections of steel liners

- b_w : half weld reinforcement length (m), expressed as (dimensions in m):

$$b_w = \frac{t_s}{2} \sin(\alpha/2) + 0.0015 \quad (\text{A.1})$$

where the angle α results from the fact that the plates are edge-broken (crimped) prior to welding (ASCE 2012), and 0.0015 m is half of the gap between the plates recommended, e.g., in ISO 9692-1 (2013);

- $l_w = 2b_w$: weld reinforcement length (m);
- Δh_{tol} : C.E.C.T. (1980) tolerance for the roof-topping (m);

$$\Delta h_{\text{tol}} = \left(\frac{2r_i}{1000} + \frac{20}{t_s} + 0.5 \right) / 10^3 \text{ (input in mm)} \quad (\text{A.2})$$

- e_{tol} : C.E.C.T. (1980) tolerance for linear misalignment (m);

$$e_{\text{tol}} = \left(\frac{t_s}{50} + 1 \right) / 10^3 \text{ (input in mm)} \quad (\text{A.3})$$

- δ_{tol} : C.E.C.T. (1980) tolerance for weld reinforcement/concavity (m);

$$\delta_{\text{tol}} = \left[1 + \frac{3}{100}(t_s + l_w) \right] / 10^3 \text{ if } \psi_d \geq 0 \text{ (input in mm)} \quad (\text{A.4})$$

$$\delta_{\text{tol}} = \left(\frac{t_s + l_w}{100} \right) / 10^3 \text{ if } \psi_d < 0 \text{ (input in mm)} \quad (\text{A.5})$$

- η_{tol} : C.E.C.T. (1980) tolerance for out-of-roundness (m);

$$\eta_{\text{tol}} = 0.01r_i \quad (\text{A.6})$$

- $l_u = \psi_u t_s$: length of straight edges (m);
- $\gamma = 2l_u/r_i$: angular misalignment (rad);
- $e = \psi_e e_{\text{tol}}$: linear misalignment (m);
- $\eta = \psi_\eta \eta_{\text{tol}}$: out-of-roundness (m);
- $\delta = \psi_\delta \delta_{\text{tol}}$: weld reinforcement/concavity (m);
- $r_{\text{max}} = r_i + \eta$: maximum axis of the liner (ellipse) (m);
- $r_{\text{min}} = r_i - \eta$: minimum axis of the liner (ellipse) (m);
- $x_{0,l} = 0$: x -coordinate of the center of the ellipse representing the *left* part of the liner (m);

- $y_{0,l} = 0$: y-coordinate of the center of the ellipse representing the *left* part of the liner (m);
- $x_{0,r} = 0$: x-coordinate of the center of the ellipse representing the *right* part of the liner (m);
- $y_{0,r} = -e/2$: y-coordinate of the center of the ellipse representing the *right* part of the liner (m);
- $a_l = r_{\min} + e/4$: horizontal internal axis of the left ellipse (m);
- $b_l = r_{\max} + e/4$: vertical internal axis of the left ellipse (m);
- $a_r = r_{\min} - e/4$: horizontal internal axis of the right ellipse (m);
- $b_r = r_{\max} - e/4$: vertical internal axis of the right ellipse (m).

A point located by coordinates x_i and y_i is denoted \mathbf{P}_i . The geometry of the steel liners described by the mathematical model developed hereafter is presented in Fig. A.1, where the main points are shown.

A.2 Rolled plates

In order to combine both the out-of-roundness and the linear misalignment at the longitudinal butt welds, the left and right *circular* (or *elliptical*) parts of the steel liner are modeled with four ellipses (two for the internal fiber and two for the external fiber, see Fig. A.1) whose points' coordinates are functions of θ as

$$\begin{cases} x_{r,\text{int},l} = x_{0,l} + a_l \cos(\theta_l) \\ y_{r,\text{int},l} = y_{0,l} + b_l \sin(\theta_l) \end{cases} \quad (\text{A.7})$$

$$\begin{cases} x_{r,\text{ext},l} = x_{0,l} + (a_l + t_s) \cos(\theta_l) \\ y_{r,\text{ext},l} = y_{0,l} + (b_l + t_s) \sin(\theta_l) \end{cases} \quad (\text{A.8})$$

with $\theta_l \in [\pi/2 + \gamma/2, 3/2\pi]$ for the left part and

$$\begin{cases} x_{r,\text{int},r} = x_{0,r} + a_r \cos(\theta_r) \\ y_{r,\text{int},r} = y_{0,r} + b_r \sin(\theta_r) \end{cases} \quad (\text{A.9})$$

$$\begin{cases} x_{r,\text{ext},r} = x_{0,r} + (a_r + t_s) \cos(\theta_r) \\ y_{r,\text{ext},r} = y_{0,r} + (b_r + t_s) \sin(\theta_r) \end{cases} \quad (\text{A.10})$$

with $\theta_r \in [-\pi/2, \pi/2 - \gamma/2]$ for the right part.

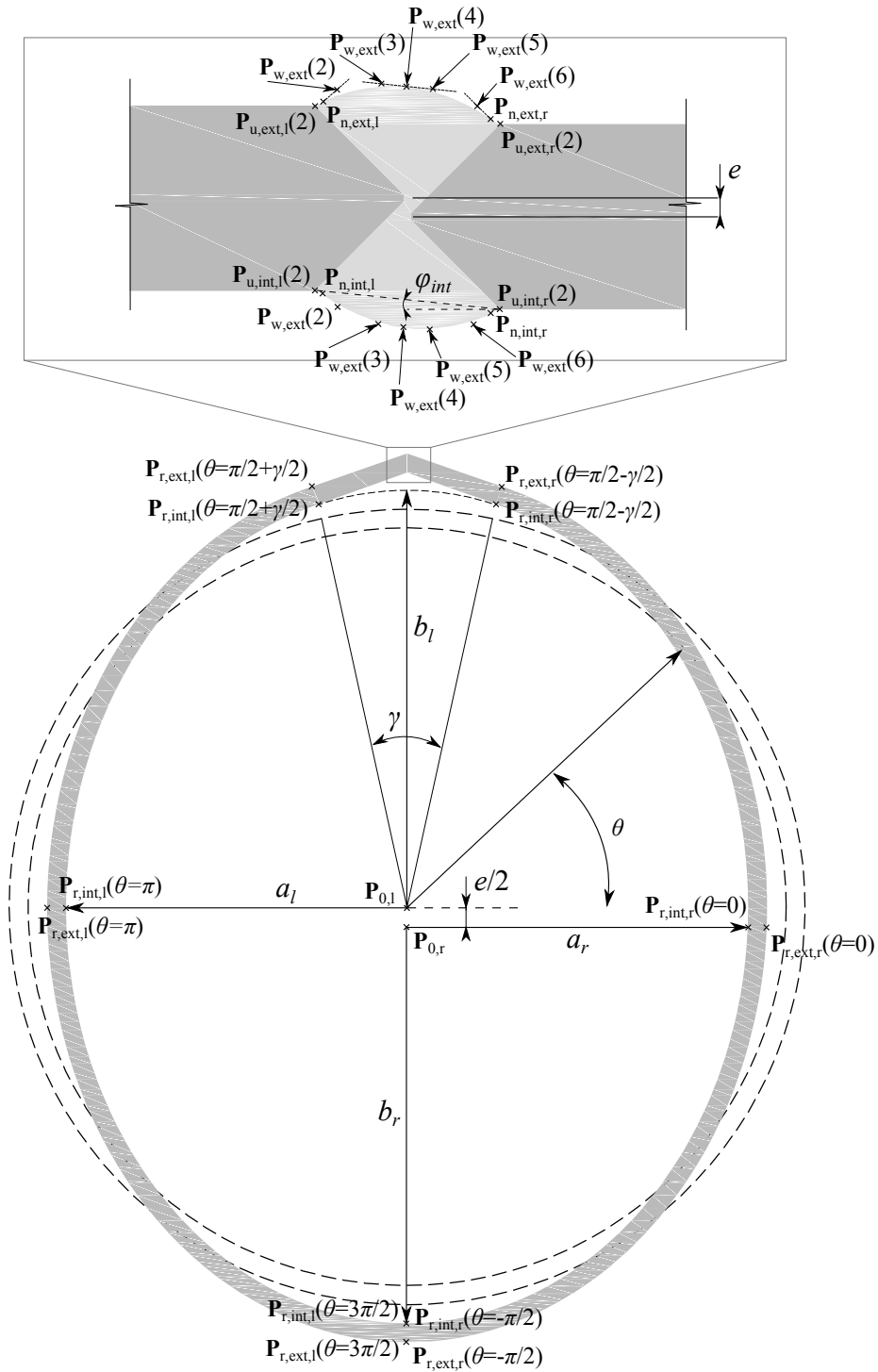


Figure A.1: Definition sketch of the geometrical imperfections and the local butt welded joint's geometry at steel liners presenting the main points of the mathematical model for the geometry. The geometrical imperfections and the thickness of the liner are distorted for presentation purposes.

A.3 Straight edges

The straight edges of the steel plates are inherent to the rolling process and are considered as tangential to the respective ellipses. As a consequence, the internal and external fibers are assumed to follow the equations of the tangents to the respective ellipses, until $x = -b_w$ for the left edge and until $x = b_w$ for the right edge. The left edge is thus modeled by two straight lines between the following coordinates both for internal and external fibers:

$$\left\{ \begin{array}{l} \mathbf{X}_{u,\text{int},l} = [x_{r,\text{int},l}(\pi/2 + \gamma/2), -b_w] \\ \mathbf{Y}_{u,\text{int},l}(1) = \frac{b_l^2}{(y_{r,\text{int},l}(\pi/2 + \gamma/2) - y_{0,l})} \cdots \\ \quad \cdots - \frac{b_l^2}{a_l^2} \cdot \frac{x_{r,\text{int},l}(\pi/2 + \gamma/2) - x_{0,l}}{y_{r,\text{int},l}(\pi/2 + \gamma/2) - y_{0,l}} \cdot [\mathbf{X}_{u,\text{int},l}(1) - x_{0,l}] + y_{0,l} \\ \mathbf{Y}_{u,\text{int},l}(2) = \frac{b_l^2}{(y_{r,\text{int},l}(\pi/2 + \gamma/2) - y_{0,l})} \cdots \\ \quad \cdots - \frac{b_l^2}{a_l^2} \cdot \frac{x_{r,\text{int},l}(\pi/2 + \gamma/2) - x_{0,l}}{y_{r,\text{int},l}(\pi/2 + \gamma/2) - y_{0,l}} \cdot [\mathbf{X}_{u,\text{int},l}(2) - x_{0,l}] + y_{0,l}, \end{array} \right. \quad (\text{A.11})$$

and

$$\left\{ \begin{array}{l} \mathbf{X}_{u,\text{ext},l} = [x_{r,\text{ext},l}(\pi/2 + \gamma/2), -b_w] \\ \mathbf{Y}_{u,\text{ext},l}(1) = \frac{(b_l + t_s)^2}{(y_{r,\text{ext},l}(\pi/2 + \gamma/2) - y_{0,l})} \cdots \\ \quad \cdots - \frac{(b_l + t_s)^2}{(a_l + t_s)^2} \cdot \frac{x_{r,\text{ext},l}(\pi/2 + \gamma/2) - x_{0,l}}{y_{r,\text{ext},l}(\pi/2 + \gamma/2) - y_{0,l}} \cdot [\mathbf{X}_{u,\text{ext},l}(1) - x_{0,l}] + y_{0,l} \\ \mathbf{Y}_{u,\text{ext},l}(2) = \frac{(b_l + t_s)^2}{(y_{r,\text{ext},l}(\pi/2 + \gamma/2) - y_{0,l})} \cdots \\ \quad \cdots - \frac{(b_l + t_s)^2}{(a_l + t_s)^2} \cdot \frac{x_{r,\text{ext},l}(\pi/2 + \gamma/2) - x_{0,l}}{y_{r,\text{ext},l}(\pi/2 + \gamma/2) - y_{0,l}} \cdot [\mathbf{X}_{u,\text{ext},l}(2) - x_{0,l}] + y_{0,l}. \end{array} \right. \quad (\text{A.12})$$

For the right edge, similarly:

$$\left\{ \begin{array}{l} \mathbf{X}_{u,\text{int},r} = [x_{r,\text{int},r}(\pi/2 - \gamma/2), b_w] \\ \mathbf{Y}_{u,\text{int},r}(1) = \frac{b_r^2}{(y_{r,\text{int},r}(\pi/2 - \gamma/2) - y_{0,r})} \cdots \\ \quad \cdots - \frac{b_r^2}{a_r^2} \cdot \frac{x_{r,\text{int},r}(\pi/2 - \gamma/2) - x_{0,r}}{y_{r,\text{int},r}(\pi/2 - \gamma/2) - y_{0,r}} \cdot [\mathbf{X}_{u,\text{int},r}(1) - x_{0,r}] + y_{0,r} \\ \mathbf{Y}_{u,\text{int},r}(2) = \frac{b_r^2}{(y_{r,\text{int},r}(\pi/2 - \gamma/2) - y_{0,r})} \cdots \\ \quad \cdots - \frac{b_r^2}{a_r^2} \cdot \frac{x_{r,\text{int},r}(\pi/2 - \gamma/2) - x_{0,r}}{y_{r,\text{int},r}(\pi/2 - \gamma/2) - y_{0,r}} \cdot [\mathbf{X}_{u,\text{int},r}(2) - x_{0,r}] + y_{0,r}, \end{array} \right. \quad (\text{A.13})$$

and

$$\left\{ \begin{array}{l} \mathbf{X}_{u,\text{ext},r} = [x_{r,\text{ext},r}(\pi/2 - \gamma/2), b_w] \\ \mathbf{Y}_{u,\text{ext},r}(1) = \frac{(b_r + t_s)^2}{(y_{r,\text{ext},r}(\pi/2 - \gamma/2) - y_{0,r})} \cdots \\ \quad \cdots - \frac{(b_r + t_s)^2}{(a_r + t_s)^2} \cdot \frac{x_{r,\text{ext},r}(\pi/2 - \gamma/2) - x_{0,r}}{y_{r,\text{ext},r}(\pi/2 - \gamma/2) - y_{0,r}} \cdot [\mathbf{X}_{u,\text{ext},r}(1) - x_{0,r}] + y_{0,r} \\ \mathbf{Y}_{u,\text{ext},r}(2) = \frac{(b_r + t_s)^2}{(y_{r,\text{ext},r}(\pi/2 - \gamma/2) - y_{0,r})} \cdots \\ \quad \cdots - \frac{(b_r + t_s)^2}{(a_r + t_s)^2} \cdot \frac{x_{r,\text{ext},r}(\pi/2 - \gamma/2) - x_{0,r}}{y_{r,\text{ext},r}(\pi/2 - \gamma/2) - y_{0,r}} \cdot [\mathbf{X}_{u,\text{ext},r}(2) - x_{0,r}] + y_{0,r}. \end{array} \right. \quad (\text{A.14})$$

A.4 Notches

A.4.1 Weld reinforcement $\delta > 0$

Left notch

The angle ϕ_l between the straight edge and the horizontal is expressed as

$$\phi_l = \text{atan} \left[\frac{\mathbf{Y}_{u,\text{int},l}(2) - \mathbf{Y}_{u,\text{int},l}(1)}{\mathbf{X}_{u,\text{int},l}(2) - \mathbf{X}_{u,\text{int},l}(1)} \right]. \quad (\text{A.15})$$

According to the fictitious notch rounding definition at weld toes (Hobbacher 2008; Radaj *et al.* 2013), the notches are modeled by arcs of radius ρ . The coordinates of the center of the left internal notch are expressed as

$$\left\{ \begin{array}{l} x_{0,n,\text{int},l} = \mathbf{X}_{u,\text{int},l}(2) + \rho \sin(\phi_l) \\ y_{0,n,\text{int},l} = \mathbf{Y}_{u,\text{int},l}(2) - \rho \cos(\phi_l). \end{array} \right. \quad (\text{A.16})$$

The equation of the notch's points is then expressed as

$$\left\{ \begin{array}{l} x_{n,\text{int},l} = x_{0,n,\text{int},l} + \rho \cos(\theta) \\ y_{n,\text{int},l} = y_{0,n,\text{int},l} + \rho \sin(\theta) \end{array} \right. \quad (\text{A.17})$$

with $\theta \in [\pi/2 + \phi_l, \pi/2 + \phi_l - \beta]$. Similarly, for the external notch:

$$\left\{ \begin{array}{l} x_{0,n,\text{ext},l} = \mathbf{X}_{u,\text{ext},l}(2) - \rho \sin(\phi_l) \\ y_{0,n,\text{ext},l} = \mathbf{Y}_{u,\text{ext},l}(2) + \rho \cos(\phi_l) \end{array} \right. \quad (\text{A.18})$$

and

$$\left\{ \begin{array}{l} x_{n,\text{ext},l} = x_{0,n,\text{ext},l} + \rho \cos(\theta) \\ y_{n,\text{ext},l} = y_{0,n,\text{ext},l} + \rho \sin(\theta) \end{array} \right. \quad (\text{A.19})$$

with $\theta \in [-\pi/2 + \phi_l, -\pi/2 + \phi_l + \beta]$.

Right notch

The angle ϕ_r between the straight edge and the horizontal is expressed as

$$\phi_r = \text{atan} \left[\frac{\mathbf{Y}_{u,\text{int},r}(2) - \mathbf{Y}_{u,\text{int},r}(1)}{-\mathbf{X}_{u,\text{int},r}(2) + \mathbf{X}_{u,\text{int},r}(1)} \right]. \quad (\text{A.20})$$

The coordinates of the center of the right internal notch are expressed as

$$\begin{cases} x_{0,n,\text{int},r} = \mathbf{X}_{u,\text{int},r}(2) - \rho \sin(\phi_r) \\ y_{0,n,\text{int},r} = \mathbf{Y}_{u,\text{int},r}(2) - \rho \cos(\phi_r). \end{cases} \quad (\text{A.21})$$

The equation of the notch's points is then expressed as

$$\begin{cases} x_{n,\text{int},r} = x_{0,n,\text{int},r} + \rho \cos(\theta) \\ y_{n,\text{int},r} = y_{0,n,\text{int},r} + \rho \sin(\theta) \end{cases} \quad (\text{A.22})$$

with $\theta \in [\pi/2 - \phi_r, \pi/2 - \phi_r + \beta]$. Similarly, for the external notch:

$$\begin{cases} x_{0,n,\text{ext},r} = \mathbf{X}_{u,\text{ext},r}(2) + \rho \sin(\phi_r) \\ y_{0,n,\text{ext},r} = \mathbf{Y}_{u,\text{ext},r}(2) + \rho \cos(\phi_r), \end{cases} \quad (\text{A.23})$$

and

$$\begin{cases} x_{n,\text{ext},r} = x_{0,n,\text{ext},r} + \rho \cos(\theta) \\ y_{n,\text{ext},r} = y_{0,n,\text{ext},r} + \rho \sin(\theta) \end{cases} \quad (\text{A.24})$$

with $\theta \in [-\pi/2 - \phi_r, -\pi/2 - \phi_r - \beta]$.

A.4.2 Weld reinforcement $\delta = 0$

The angles between the internal and external fibers of the welds (represented as a straight line between left and right notches when $\delta = 0$) with the horizontal are given by:

$$\phi_{\text{ext}} = \text{atan} \left[\frac{\mathbf{Y}_{u,\text{ext},l}(2) - \mathbf{Y}_{u,\text{ext},r}(2)}{-\mathbf{X}_{u,\text{ext},l}(2) + \mathbf{X}_{u,\text{ext},r}(2)} \right] \quad (\text{A.25})$$

and

$$\phi_{\text{int}} = \text{atan} \left[\frac{\mathbf{Y}_{u,\text{int},l}(2) - \mathbf{Y}_{u,\text{int},r}(2)}{-\mathbf{X}_{u,\text{int},l}(2) + \mathbf{X}_{u,\text{int},r}(2)} \right]. \quad (\text{A.26})$$

Appendix A. Mathematical model for geometrical imperfections of steel liners

Left notch

The angle ϕ_l between the straight edge and the horizontal is expressed as

$$\phi_l = \text{atan} \left[\frac{\mathbf{Y}_{u,\text{int},l}(2) - \mathbf{Y}_{u,\text{int},l}(1)}{\mathbf{X}_{u,\text{int},l}(2) - \mathbf{X}_{u,\text{int},l}(1)} \right]. \quad (\text{A.27})$$

The coordinates of the center of the left internal notch are expressed as

$$\begin{cases} x_{0,n,\text{int},l} = \mathbf{X}_{u,\text{int},l}(2) + \rho \sin(\phi_l) \\ y_{0,n,\text{int},l} = \mathbf{Y}_{u,\text{int},l}(2) - \rho \cos(\phi_l). \end{cases} \quad (\text{A.28})$$

The equation of the notch's points is then expressed as

$$\begin{cases} x_{n,\text{int},l} = x_{0,n,\text{int},l} + \rho \cos(\theta) \\ y_{n,\text{int},l} = y_{0,n,\text{int},l} + \rho \sin(\theta) \end{cases} \quad (\text{A.29})$$

with $\theta \in [\pi/2 + \phi_l, \pi/2 - \phi_{\text{int}}]$. Similarly, for the external notch:

$$\begin{cases} x_{0,n,\text{ext},l} = \mathbf{X}_{u,\text{ext},l}(2) + \rho \sin(\phi_l) \\ y_{0,n,\text{ext},l} = \mathbf{Y}_{u,\text{ext},l}(2) - \rho \cos(\phi_l), \end{cases} \quad (\text{A.30})$$

and

$$\begin{cases} x_{n,\text{ext},l} = x_{0,n,\text{ext},l} + \rho \cos(\theta) \\ y_{n,\text{ext},l} = y_{0,n,\text{ext},l} + \rho \sin(\theta) \end{cases} \quad (\text{A.31})$$

with $\theta \in [\pi/2 + \phi_l, \pi/2 - \phi_{\text{ext}}]$.

Right notch

The angle ϕ_r between the straight edge and the horizontal is expressed as

$$\phi_r = \text{atan} \left[\frac{\mathbf{Y}_{u,\text{int},r}(2) - \mathbf{Y}_{u,\text{int},r}(1)}{-\mathbf{X}_{u,\text{int},r}(2) + \mathbf{X}_{u,\text{int},r}(1)} \right]. \quad (\text{A.32})$$

1. If $\phi_{\text{ext}} \geq \phi_r$:

The coordinates of the center of the right internal notch are expressed as

$$\begin{cases} x_{0,n,\text{int},r} = \mathbf{X}_{u,\text{int},r}(2) + \rho \sin(\phi_r) \\ y_{0,n,\text{int},r} = \mathbf{Y}_{u,\text{int},r}(2) + \rho \cos(\phi_r). \end{cases} \quad (\text{A.33})$$

The equation of the notch's points is then expressed as

$$\begin{cases} x_{n,\text{int},r} = x_{0,n,\text{int},r} + \rho \cos(\theta) \\ y_{n,\text{int},r} = y_{0,n,\text{int},r} + \rho \sin(\theta) \end{cases} \quad (\text{A.34})$$

with $\theta \in [-\pi/2 - \phi_r, -\pi/2 - \phi_{\text{int}}]$. Similarly, for the external notch:

$$\begin{cases} x_{0,n,\text{ext},r} = \mathbf{X}_{u,\text{ext},r}(2) + \rho \sin(\phi_r) \\ y_{0,n,\text{ext},r} = \mathbf{Y}_{u,\text{ext},r}(2) + \rho \cos(\phi_r), \end{cases} \quad (\text{A.35})$$

and

$$\begin{cases} x_{n,\text{ext},r} = x_{0,n,\text{ext},r} + \rho \cos(\theta) \\ y_{n,\text{ext},r} = y_{0,n,\text{ext},r} + \rho \sin(\theta) \end{cases} \quad (\text{A.36})$$

with $\theta \in [-\pi/2 - \phi_r, -\pi/2 - \phi_{\text{ext}}]$.

2. Else if $\phi_{\text{ext}} < \phi_r$:

The coordinates of the center of the right internal notch are expressed as

$$\begin{cases} x_{0,n,\text{int},r} = \mathbf{X}_{u,\text{int},r}(2) - \rho \sin(\phi_r) \\ y_{0,n,\text{int},r} = \mathbf{Y}_{u,\text{int},r}(2) - \rho \cos(\phi_r). \end{cases} \quad (\text{A.37})$$

The equation of the notch's points is then expressed as

$$\begin{cases} x_{n,\text{int},r} = x_{0,n,\text{int},r} + \rho \cos(\theta) \\ y_{n,\text{int},r} = y_{0,n,\text{int},r} + \rho \sin(\theta) \end{cases} \quad (\text{A.38})$$

with $\theta \in [\pi/2 - \phi_r, \pi/2 - \phi_{\text{int}}]$. Similarly, for the external notch:

$$\begin{cases} x_{0,n,\text{ext},r} = \mathbf{X}_{u,\text{ext},r}(2) - \rho \sin(\phi_r) \\ y_{0,n,\text{ext},r} = \mathbf{Y}_{u,\text{ext},r}(2) - \rho \cos(\phi_r), \end{cases} \quad (\text{A.39})$$

and

$$\begin{cases} x_{n,\text{ext},r} = x_{0,n,\text{ext},r} + \rho \cos(\theta) \\ y_{n,\text{ext},r} = y_{0,n,\text{ext},r} + \rho \sin(\theta) \end{cases} \quad (\text{A.40})$$

with $\theta \in [\pi/2 - \phi_r, \pi/2 - \phi_{\text{ext}}]$.

A.4.3 Weld reinforcement $\delta < 0$

Left notch

The angle ϕ_l between the straight edge and the horizontal is expressed as

$$\phi_l = \text{atan} \left[\frac{\mathbf{Y}_{u,\text{int},l}(2) - \mathbf{Y}_{u,\text{int},l}(1)}{\mathbf{X}_{u,\text{int},l}(2) - \mathbf{X}_{u,\text{int},l}(1)} \right]. \quad (\text{A.41})$$

The coordinates of the center of the left internal notch are expressed as

$$\begin{cases} x_{0,n,\text{int},l} = \mathbf{X}_{u,\text{int},l}(2) - \rho \sin(\phi_l) \\ y_{0,n,\text{int},l} = \mathbf{Y}_{u,\text{int},l}(2) + \rho \cos(\phi_l). \end{cases} \quad (\text{A.42})$$

The equation of the notch's points is then expressed as

$$\begin{cases} x_{n,\text{int},l} = x_{0,n,\text{int},l} + \rho \cos(\theta) \\ y_{n,\text{int},l} = y_{0,n,\text{int},l} + \rho \sin(\theta) \end{cases} \quad (\text{A.43})$$

with $\theta \in [-\pi/2 + \phi_l, -\pi/2 + \phi_l + \beta]$. Similarly, for the external notch:

$$\begin{cases} x_{0,n,\text{ext},l} = \mathbf{X}_{u,\text{ext},l}(2) + \rho \sin(\phi_l) \\ y_{0,n,\text{ext},l} = \mathbf{Y}_{u,\text{ext},l}(2) - \rho \cos(\phi_l), \end{cases} \quad (\text{A.44})$$

and

$$\begin{cases} x_{n,\text{ext},l} = x_{0,n,\text{ext},l} + \rho \cos(\theta) \\ y_{n,\text{ext},l} = y_{0,n,\text{ext},l} + \rho \sin(\theta) \end{cases} \quad (\text{A.45})$$

with $\theta \in [\pi/2 + \phi_l, \pi/2 + \phi_l - \beta]$.

Right notch

The angle ϕ_r between the straight edge and the horizontal is expressed as

$$\phi_r = \text{atan} \left[\frac{\mathbf{Y}_{u,\text{int},r}(2) - \mathbf{Y}_{u,\text{int},r}(1)}{-\mathbf{X}_{u,\text{int},r}(2) + \mathbf{X}_{u,\text{int},r}(1)} \right]. \quad (\text{A.46})$$

The coordinates of the center of the right internal notch are expressed as

$$\begin{cases} x_{0,n,\text{int},r} = \mathbf{X}_{u,\text{int},r}(2) + \rho \sin(\phi_r) \\ y_{0,n,\text{int},r} = \mathbf{Y}_{u,\text{int},r}(2) + \rho \cos(\phi_r). \end{cases} \quad (\text{A.47})$$

The equation of the notch's points is then expressed as

$$\begin{cases} x_{n,\text{int},r} = x_{0,n,\text{int},r} + \rho \cos(\theta) \\ y_{n,\text{int},r} = y_{0,n,\text{int},r} + \rho \sin(\theta) \end{cases} \quad (\text{A.48})$$

with $\theta \in [-\pi/2 - \phi_r, -\pi/2 - \phi_r + \beta]$. Similarly, for the external notch:

$$\begin{cases} x_{0,n,\text{ext},r} = \mathbf{X}_{u,\text{ext},r}(2) - \rho \sin(\phi_r) \\ y_{0,n,\text{ext},r} = \mathbf{Y}_{u,\text{ext},r}(2) - \rho \cos(\phi_r), \end{cases} \quad (\text{A.49})$$

and

$$\begin{cases} x_{n,\text{ext},r} = x_{0,n,\text{ext},r} + \rho \cos(\theta) \\ y_{n,\text{ext},r} = y_{0,n,\text{ext},r} + \rho \sin(\theta) \end{cases} \quad (\text{A.50})$$

with $\theta \in [\pi/2 - \phi_r, \pi/2 - \phi_r + \beta]$.

A.5 Control points for the weld profile

For the sake of concision, some nomenclature is introduced hereafter.

1. If weld reinforcement $\delta > 0$:

- Left notch:

$$\begin{cases} \theta_{\text{int},l} = +\pi/2 + \phi_l - \beta \\ \theta_{\text{ext},l} = -\pi/2 + \phi_l + \beta; \end{cases} \quad (\text{A.51})$$

- Right notch:

$$\begin{cases} \theta_{\text{int},r} = +\pi/2 - \phi_r + \beta \\ \theta_{\text{ext},r} = -\pi/2 - \phi_r - \beta. \end{cases} \quad (\text{A.52})$$

2. If weld reinforcement $\delta = 0$:

- Left notch:

$$\begin{cases} \theta_{\text{int},l} = \pi/2 - \phi_{\text{int}} \\ \theta_{\text{ext},l} = \pi/2 - \phi_{\text{ext}}; \end{cases} \quad (\text{A.53})$$

- Right notch:

(a) if $\phi_{\text{ext}} \geq \phi_r$:

$$\begin{cases} \theta_{\text{int},r} = -\pi/2 - \phi_{\text{int}} \\ \theta_{\text{ext},r} = -\pi/2 - \phi_{\text{ext}}; \end{cases} \quad (\text{A.54})$$

(b) if $\phi_{\text{ext}} < \phi_r$:

$$\begin{cases} \theta_{\text{int},r} = \pi/2 - \phi_{\text{int}} \\ \theta_{\text{ext},r} = \pi/2 - \phi_{\text{ext}}. \end{cases} \quad (\text{A.55})$$

3. If weld reinforcement $\delta < 0$:

• Left notch:

$$\begin{cases} \theta_{\text{int},l} = -\pi/2 + \phi_l + \beta \\ \theta_{\text{ext},l} = +\pi/2 + \phi_l - \beta; \end{cases} \quad (\text{A.56})$$

• Right notch:

$$\begin{cases} \theta_{\text{int},r} = -\pi/2 - \phi_r - \beta \\ \theta_{\text{ext},r} = +\pi/2 - \phi_r + \beta. \end{cases} \quad (\text{A.57})$$

A.5.1 Internal weld surface

The distance between the two internal notches is expressed as

$$l_{w,\text{int}} = \left\{ [x_{n,\text{int},l}(\theta_{\text{int},l}) - x_{n,\text{int},r}(\theta_{\text{int},r})]^2 + [y_{n,\text{int},l}(\theta_{\text{int},l}) - y_{n,\text{int},r}(\theta_{\text{int},r})]^2 \right\}^{1/2}. \quad (\text{A.58})$$

The coordinates of the arbitrarily defined control points for the B-splines are defined as follows:

$$\begin{aligned} \mathbf{X}_{w,\text{int}} = & [x_{n,\text{int},l}(\theta_{\text{int},l}), \\ & x_{n,\text{int},l}(\theta_{\text{int},l}) + 0.02 \cdot l_{w,\text{int}} \cos \left\{ \text{atan} \left[\frac{x_{n,\text{int},l}(\theta_{\text{int},l})}{y_{n,\text{int},l}(\theta_{\text{int},l})} \right] \right\}, \\ & \frac{\mathbf{X}_{u,\text{int},l}(2) + \mathbf{X}_{u,\text{int},r}(2)}{2} - 0.05 \cdot [x_{n,\text{int},r}(\theta_{\text{int},r}) - x_{n,\text{int},l}(\theta_{\text{int},l})] \dots \\ & \dots - \delta \sin \left\{ \text{atan} \left[\frac{y_{n,\text{int},l}(\theta_{\text{int},l}) - y_{n,\text{int},r}(\theta_{\text{int},r})}{x_{n,\text{int},r}(\theta_{\text{int},r}) - x_{n,\text{int},l}(\theta_{\text{int},l})} \right] \right\}, \\ & \frac{\mathbf{X}_{u,\text{int},l}(2) + \mathbf{X}_{u,\text{int},r}(2)}{2} - \delta \sin \left\{ \text{atan} \left[\frac{y_{n,\text{int},l}(\theta_{\text{int},l}) - y_{n,\text{int},r}(\theta_{\text{int},r})}{x_{n,\text{int},r}(\theta_{\text{int},r}) - x_{n,\text{int},l}(\theta_{\text{int},l})} \right] \right\}, \\ & \frac{\mathbf{X}_{u,\text{int},l}(2) + \mathbf{X}_{u,\text{int},r}(2)}{2} + 0.05 \cdot [x_{n,\text{int},r}(\theta_{\text{int},r}) - x_{n,\text{int},l}(\theta_{\text{int},l})] \dots \\ & \dots - \delta \sin \left\{ \text{atan} \left[\frac{y_{n,\text{int},l}(\theta_{\text{int},l}) - y_{n,\text{int},r}(\theta_{\text{int},r})}{x_{n,\text{int},r}(\theta_{\text{int},r}) - x_{n,\text{int},l}(\theta_{\text{int},l})} \right] \right\}, \\ & x_{n,\text{int},r}(\theta_{\text{int},r}) - 0.02 \cdot l_{w,\text{int}} \cos \left\{ \text{atan} \left[\frac{x_{n,\text{int},r}(\theta_{\text{int},r})}{y_{n,\text{int},r}(\theta_{\text{int},r})} \right] \right\}, \\ & x_{n,\text{int},r}(\theta_{\text{int},r})], \end{aligned} \quad (\text{A.59})$$

and

$$\begin{aligned}
 \mathbf{Y}_{w,int} = & [y_{n,int,l}(\theta_{int,l}), \\
 & y_{0,n,int,l} + \frac{\rho^2}{y_{n,int,l}(\theta_{int,l}) - y_{0,n,int,l}} - \frac{x_{n,int,l}(\theta_{int,l}) - x_{0,n,int,l}}{y_{n,int,l}(\theta_{int,l}) - y_{0,n,int,l}} \cdot [\mathbf{X}_{w,int}(2) - x_{0,n,int,l}], \\
 & \frac{\mathbf{Y}_{u,int,l}(2) + \mathbf{Y}_{u,int,r}(2)}{2} + 0.05 \cdot [y_{n,int,l}(\theta_{int,l}) - y_{n,int,r}(\theta_{int,r})] \dots \\
 & \dots - \delta \cos \left\{ \text{atan} \left[\frac{y_{n,int,l}(\theta_{int,l}) - y_{n,int,r}(\theta_{int,r})}{x_{n,int,r}(\theta_{int,r}) - x_{n,int,l}(\theta_{int,l})} \right] \right\}, \\
 & \frac{\mathbf{Y}_{u,int,l}(2) + \mathbf{Y}_{u,int,r}(2)}{2} - \delta \cos \left\{ \text{atan} \left[\frac{y_{n,int,l}(\theta_{int,l}) - y_{n,int,r}(\theta_{int,r})}{x_{n,int,r}(\theta_{int,r}) - x_{n,int,l}(\theta_{int,l})} \right] \right\}, \\
 & \frac{\mathbf{Y}_{u,int,l}(2) + \mathbf{Y}_{u,int,r}(2)}{2} - 0.05 \cdot [y_{n,int,l}(\theta_{int,l}) - y_{n,int,r}(\theta_{int,r})] \dots \\
 & \dots - \delta \cos \left\{ \text{atan} \left[\frac{y_{n,int,l}(\theta_{int,l}) - y_{n,int,r}(\theta_{int,r})}{x_{n,int,r}(\theta_{int,r}) - x_{n,int,l}(\theta_{int,l})} \right] \right\}, \\
 & y_{0,n,int,r} + \frac{\rho^2}{y_{n,int,r}(\theta_{int,r}) - y_{0,n,int,r}} - \frac{x_{n,int,r}(\theta_{int,r}) - x_{0,n,int,r}}{y_{n,int,r}(\theta_{int,r}) - y_{0,n,int,r}} \cdot [\mathbf{X}_{w,int}(6) - x_{0,n,int,r}], \\
 & y_{n,int,r}(\theta_{int,r})].
 \end{aligned} \tag{A.60}$$

A.5.2 External weld surface

The distance between the two external notches is expressed as

$$l_{w,ext} = \left\{ [x_{n,ext,l}(\theta_{ext,l}) - x_{n,ext,r}(\theta_{ext,r})]^2 + [y_{n,ext,l}(\theta_{ext,l}) - y_{n,ext,r}(\theta_{ext,r})]^2 \right\}^{1/2}. \tag{A.61}$$

Appendix A. Mathematical model for geometrical imperfections of steel liners

The coordinates of the arbitrarily defined control points for the B-splines are defined as follows:

$$\begin{aligned}
 \mathbf{X}_{w,\text{ext}} = & [x_{n,\text{ext},l}(\theta_{\text{ext},l}), \\
 & x_{n,\text{ext},l}(\theta_{\text{ext},l}) + 0.02 \cdot l_{w,\text{ext}} \cos \left\{ \text{atan} \left[\frac{x_{n,\text{ext},l}(\theta_{\text{ext},l})}{y_{n,\text{ext},l}(\theta_{\text{ext},l})} \right] \right\}, \\
 & \frac{\mathbf{X}_{u,\text{ext},l}(2) + \mathbf{X}_{u,\text{ext},r}(2)}{2} - 0.05 \cdot [x_{n,\text{ext},r}(\theta_{\text{ext},r}) - x_{n,\text{ext},l}(\theta_{\text{ext},l})] \dots \\
 & \dots - \delta \sin \left\{ \text{atan} \left[\frac{y_{n,\text{ext},l}(\theta_{\text{ext},l}) - y_{n,\text{ext},r}(\theta_{\text{ext},r})}{x_{n,\text{ext},r}(\theta_{\text{ext},r}) - x_{n,\text{ext},l}(\theta_{\text{ext},l})} \right] \right\}, \\
 & \frac{\mathbf{X}_{u,\text{ext},l}(2) + \mathbf{X}_{u,\text{ext},r}(2)}{2} - \delta \sin \left\{ \text{atan} \left[\frac{y_{n,\text{ext},l}(\theta_{\text{ext},l}) - y_{n,\text{ext},r}(\theta_{\text{ext},r})}{x_{n,\text{ext},r}(\theta_{\text{ext},r}) - x_{n,\text{ext},l}(\theta_{\text{ext},l})} \right] \right\}, \quad (\text{A.62}) \\
 & \frac{\mathbf{X}_{u,\text{ext},l}(2) + \mathbf{X}_{u,\text{ext},r}(2)}{2} + 0.05 \cdot [x_{n,\text{ext},r}(\theta_{\text{ext},r}) - x_{n,\text{ext},l}(\theta_{\text{ext},l})] \dots \\
 & \dots - \delta \sin \left\{ \text{atan} \left[\frac{y_{n,\text{ext},l}(\theta_{\text{ext},l}) - y_{n,\text{ext},r}(\theta_{\text{ext},r})}{x_{n,\text{ext},r}(\theta_{\text{ext},r}) - x_{n,\text{ext},l}(\theta_{\text{ext},l})} \right] \right\}, \\
 & x_{n,\text{ext},r}(\theta_{\text{ext},r}) - 0.02 \cdot l_{w,\text{ext}} \cos \left\{ \text{atan} \left[\frac{x_{n,\text{ext},r}(\theta_{\text{ext},r})}{y_{n,\text{ext},r}(\theta_{\text{ext},r})} \right] \right\}, \\
 & x_{n,\text{ext},r}(\theta_{\text{ext},r})],
 \end{aligned}$$

and

$$\begin{aligned}
 \mathbf{Y}_{w,\text{ext}} = & [y_{n,\text{ext},l}(\theta_{\text{ext},l}), \\
 & y_{0,n,\text{ext},l} + \frac{\rho^2}{y_{n,\text{ext},l}(\theta_{\text{ext},l}) - y_{0,n,\text{ext},l}} - \frac{x_{n,\text{ext},l}(\theta_{\text{ext},l}) - x_{0,n,\text{ext},l}}{y_{n,\text{ext},l}(\theta_{\text{ext},l}) - y_{0,n,\text{ext},l}} \cdot [\mathbf{X}_{w,\text{ext}}(2) - x_{0,n,\text{ext},l}], \\
 & \frac{\mathbf{Y}_{u,\text{ext},l}(2) + \mathbf{Y}_{u,\text{ext},r}(2)}{2} + 0.05 \cdot [y_{n,\text{ext},l}(\theta_{\text{ext},l}) - y_{n,\text{ext},r}(\theta_{\text{ext},r})] \dots \\
 & \dots + \delta \cos \left\{ \text{atan} \left[\frac{y_{n,\text{ext},l}(\theta_{\text{ext},l}) - y_{n,\text{ext},r}(\theta_{\text{ext},r})}{x_{n,\text{ext},r}(\theta_{\text{ext},r}) - x_{n,\text{ext},l}(\theta_{\text{ext},l})} \right] \right\}, \\
 & \frac{\mathbf{Y}_{u,\text{ext},l}(2) + \mathbf{Y}_{u,\text{ext},r}(2)}{2} + \delta \cos \left\{ \text{atan} \left[\frac{y_{n,\text{ext},l}(\theta_{\text{ext},l}) - y_{n,\text{ext},r}(\theta_{\text{ext},r})}{x_{n,\text{ext},r}(\theta_{\text{ext},r}) - x_{n,\text{ext},l}(\theta_{\text{ext},l})} \right] \right\}, \\
 & \frac{\mathbf{Y}_{u,\text{ext},l}(2) + \mathbf{Y}_{u,\text{ext},r}(2)}{2} - 0.05 \cdot [y_{n,\text{ext},l}(\theta_{\text{ext},l}) - y_{n,\text{ext},r}(\theta_{\text{ext},r})] \dots \\
 & \dots + \delta \cos \left\{ \text{atan} \left[\frac{y_{n,\text{ext},l}(\theta_{\text{ext},l}) - y_{n,\text{ext},r}(\theta_{\text{ext},r})}{x_{n,\text{ext},r}(\theta_{\text{ext},r}) - x_{n,\text{ext},l}(\theta_{\text{ext},l})} \right] \right\}, \\
 & y_{0,n,\text{ext},r} + \frac{\rho^2}{y_{n,\text{ext},r}(\theta_{\text{ext},r}) - y_{0,n,\text{ext},r}} - \frac{x_{n,\text{ext},r}(\theta_{\text{ext},r}) - x_{0,n,\text{ext},r}}{y_{n,\text{ext},r}(\theta_{\text{ext},r}) - y_{0,n,\text{ext},r}} \cdot [\mathbf{X}_{w,\text{ext}}(6) - x_{0,n,\text{ext},r}], \\
 & y_{n,\text{ext},r}(\theta_{\text{ext},r})]. \quad (\text{A.63})
 \end{aligned}$$

A.6 Splines for weld's profile in ANSYS® Mechanical™

In the FE models of this project, the weld's profile is built using the command BSPLIN (ANSYS Inc 2011). For the internal weld's fiber, the spline is generated to fit the keypoints $\mathbf{P}_{w,int}(1)$, $\mathbf{P}_{w,int}(4)$ and $\mathbf{P}_{w,int}(7)$ (see Fig. A.1). Tangents are imposed at each keypoint. At $\mathbf{P}_{w,int}(1)$, the tangent vector is defined by $\mathbf{P}_{w,int}(1)$ and $\mathbf{P}_{w,int}(2)$, at $\mathbf{P}_{w,int}(4)$ by $\mathbf{P}_{w,int}(3)$ and $\mathbf{P}_{w,int}(5)$, and at $\mathbf{P}_{w,int}(7)$ by $\mathbf{P}_{w,int}(6)$ and $\mathbf{P}_{w,int}(7)$.

Similarly, for the external fiber, the spline is generated to fit the keypoints $\mathbf{P}_{w,ext}(1)$, $\mathbf{P}_{w,ext}(4)$ and $\mathbf{P}_{w,ext}(7)$ (see Fig. A.1), with the tangents imposed correspondingly.

A.7 Splines for weld's in MATLAB® for presentation purposes, using the NURBS Libraries (based on Dedè 2015 and Cottrell *et al.* 2009)

For presentation purposes, some figures herein were plotted with MATLAB® (2012), using the NURBS Libraries, as described below.

Both internal and external weld fibers are plotted with NURBS curves in \mathbb{R}^d as:

$$\mathbf{C}(\xi) = \sum_{i=1}^n R_{i,p}(\xi) \mathbf{P}_i \quad (\text{A.64})$$

where:

- $R_{i,p}(\xi) = \text{NURBS basis functions in } \mathbb{R}$;
- $\mathbf{P}_i = \text{control points in } \mathbb{R}^d \text{ which define a control polygon.}$

NURBS basis functions are built from B-spline basis functions $N_{i,p}(\xi)$ by associating to each of them weights $w_i \in \mathbb{R}$ (assuming $w_i > 0$) as

$$\mathbf{R}_{i,p}(\xi) = \frac{N_{i,p}(\xi) w_i}{\sum_{j=1}^n N_{j,p}(\xi) w_j}, \quad i = 1, \dots, n. \quad (\text{A.65})$$

The B-spline basis functions $N_{i,p}(\xi)$, $i = 1, \dots, n$, are built with the Cox - de Boor recursion formula:

Appendix A. Mathematical model for geometrical imperfections of steel liners

- for $p' = 0$:

$$N_{i,0}(\xi) = \begin{cases} 1 & \text{if } \xi_i \leq \xi \leq \xi_{i+1} \\ 0 & \text{otherwise} \end{cases} \quad (\text{A.66})$$

- for $p' = 1, 2, 3, \dots, p$:

$$N_{i,p'}(\xi) = \frac{\xi - \xi_i}{\xi_{i+p'} - \xi_i} N_{i,p'-1}(\xi) + \frac{\xi_{i+p'+1} - \xi}{\xi_{i+p'+1} - \xi_{i+1}} N_{i+1,p'-1}(\xi) \quad (\text{A.67})$$

The knot vector, for both internal and external surfaces, is chosen as

$$\Xi = \left\{ 0, 0, 0, \frac{1}{10}, \frac{1}{2}, \frac{1}{2}, \frac{9}{10}, 1, 1, 1 \right\}. \quad (\text{A.68})$$

The control points are defined as

$$\mathbf{P}_{i,\text{int}} = [\mathbf{X}_{w,\text{int}}(i), \mathbf{Y}_{w,\text{int}}(i)] \quad (\text{A.69})$$

for the internal weld surface and as

$$\mathbf{P}_{i,\text{ext}} = [\mathbf{X}_{w,\text{ext}}(i), \mathbf{Y}_{w,\text{ext}}(i)]. \quad (\text{A.70})$$

In this case, $p = 2$ and $n = 7$. The physical domain is \mathbb{R}^2 ($d = 2$). The weights w_i are all equal to 1 (i.e., the NURBS reduces to a B-spline).

B Stress intensity factors solutions

This appendix presents the analytical solutions published by Newman Jr & Raju (1981a) and Anderson (2005) (reported in API 2007) for stress intensity factors for axial semi-elliptical surface crack and embedded elliptical cracks in plates. These solutions are used and extended to compute stress intensity factors for cracks at the longitudinal butt welded joints of steel-lined pressure tunnels and shafts in Parts IV and V.

B.1 Axial semi-elliptical surface crack in plates subject to membrane and bending stresses ($a/c \leq 1$)

The SIF for semi-elliptical surface cracks in plates can be computed according to Newman Jr & Raju (1981a) as

$$K_I = [M_m(\sigma_m + p_{cr}) + M_b\sigma_b] \sqrt{\frac{\pi a}{Q}} \quad (\text{B.1})$$

where the flaw shape parameters Q can be approximated as

$$Q = 1.0 + 1.464 \left(\frac{a}{c}\right)^{1.65}. \quad (\text{B.2})$$

B.1.1 Membrane correction factor

The membrane correction factor is expressed as

$$M_m = \left[M_1 + M_2 \left(\frac{a}{t_s}\right)^2 + M_3 \left(\frac{a}{t_s}\right)^4 \right] g f_\phi f_w \quad (\text{B.3})$$

Appendix B. Stress intensity factors solutions

where:

$$M_1 = 1.13 - 0.09 \left(\frac{a}{c} \right); \quad (\text{B.4})$$

$$M_2 = \frac{0.89}{0.2 + \frac{a}{c}} - 0.54; \quad (\text{B.5})$$

$$M_3 = 0.5 - \frac{1}{0.65 + \frac{a}{c}} + 14 \left[1 - \frac{a}{c} \right]^{24}; \quad (\text{B.6})$$

and

$$g = 1 + \left[0.1 + 0.35 \left(\frac{a}{t_s} \right)^2 \right] (1 - \sin \phi)^2; \quad (\text{B.7})$$

$$f_\phi = \left[\left(\frac{a}{c} \right)^2 \cos^2 \phi + \sin^2 \phi \right]^{0.25}; \quad (\text{B.8})$$

$$f_w = 1. \quad (\text{B.9})$$

The finite width correction factor have been set to $f_w = 1$ because of the assumed infinite dimension along the tunnel axis.

B.1.2 Bending correction factor

The bending correction factor is expressed as

$$M_b = M_m H \quad (\text{B.10})$$

with

$$H = H_1 + (H_2 - H_1) \sin^q \phi \quad (\text{B.11})$$

where:

$$H_1 = 1 - 0.34 \left(\frac{a}{t_s} \right) - 0.11 \left(\frac{a}{c} \right) \left(\frac{a}{t_s} \right); \quad (\text{B.12})$$

$$H_2 = 1 + G_1 \left(\frac{a}{t_s} \right) + G_2 \left(\frac{a}{t_s} \right)^2; \quad (\text{B.13})$$

$$q = 0.2 + \left(\frac{a}{c} \right) + 0.6 \left(\frac{a}{t_s} \right); \quad (\text{B.14})$$

B.2. Axial embedded elliptical crack in plates subject to membrane and bending stresses $(a/c \leq 1)$

and

$$G_1 = -1.22 - 0.12 \left(\frac{a}{c} \right); \quad (\text{B.15})$$

$$G_2 = 0.55 - 1.05 \left(\frac{a}{c} \right)^{0.75} + 0.47 \left(\frac{a}{c} \right)^{1.5}. \quad (\text{B.16})$$

B.2 Axial embedded elliptical crack in plates subject to membrane and bending stresses $(a/c \leq 1)$

The SIF for embedded elliptical cracks in plates can be computed according to Anderson (2005) (reported in API 2007) as

$$K_I = [M_m(\sigma_{me} + p_{cr}) + M_b\sigma_{be}] \sqrt{\frac{\pi a}{Q}} \quad (\text{B.17})$$

where Q is approximated by Eq. B.2.

B.2.1 Membrane correction factor

Defining $\alpha = a/c$, $\beta_1 = a/d_1$ and $\beta_2 = a/d_2$, the membrane correction factor is expressed as

$$M_m = H_\phi f_\phi f_w \quad (\text{B.18})$$

with

$$H_\phi = \frac{1}{2} \sin^2 \phi [H_{90}(1 + \sin \phi) + H_{270}(1 - \sin \phi)] + H_0 \cos^2 \phi; \quad (\text{B.19})$$

$$f_\phi = \left[\left(\frac{a}{c} \right)^2 \cos^2 \phi + \sin^2 \phi \right]^{0.25}; \quad (\text{B.20})$$

$$f_w = 1. \quad (\text{B.21})$$

where:

$$H_{90} = h_1(\alpha, \beta_1) h_3(\alpha, \beta_2); \quad (\text{B.22})$$

$$H_0 = h_2(\alpha, \beta_1) h_2(\alpha, \beta_2); \quad (\text{B.23})$$

$$H_{270} = h_3(\alpha, \beta_1) h_1(\alpha, \beta_2); \quad (\text{B.24})$$

and

$$h_1(\alpha, \beta_i) = 1 + \left(-0.04 + \frac{0.085}{0.34 + \alpha} \right) \beta_i^2 + (0.05 - 0.03\alpha) \beta_i^4; \quad (\text{B.25})$$

Appendix B. Stress intensity factors solutions

$$h_2(\alpha, \beta_i) = 1 + \left(-0.03 + \frac{0.075}{0.30 + \alpha} \right) \beta_i^2 + \left(0.08 - \frac{0.024}{0.1 + \alpha} \right) \beta_i^4; \quad (\text{B.26})$$

$$h_3(\alpha, \beta_i) = 1 + \left(-0.06 + \frac{0.070}{0.25 + \alpha} \right) \beta_i^2 + (0.643 - 0.343\alpha) \beta_i^4. \quad (\text{B.27})$$

B.2.2 Bending correction factor

The bending correction factor is expressed as

$$M_b = - \left[0.5 + 0.2591\alpha^{1.5} - 0.09189\alpha^{2.5} \right] f_\phi f_w f_\beta \sin \phi \quad (\text{B.28})$$

where

$$f_\beta = \frac{f_{270} + f_{90}}{2} - \frac{f_{270} - f_{90}}{2} \sin \phi; \quad (\text{B.29})$$

$$f_{90} = 1 + \exp \left[-1.9249 - 3.9087\alpha^{0.5} + 4.1067\beta_2^3 \right]; \quad (\text{B.30})$$

$$f_{270} = 1 + \exp \left[-1.9249 - 3.9087\alpha^{0.5} + 4.1067\beta_1^3 \right]. \quad (\text{B.31})$$

C Lognormal distribution

This appendix introduces the lognormal distribution used to characterize some of the stochastic variables in Chapters 11 and 12. The nomenclature used in this report for the parameters is therefore clarified, allowing a straight forward interpretation.

The lognormal distribution is often used in engineering stochastic applications where a random variable X cannot have a negative value, considering the natural logarithm of X (Haldar & Mahadevan 2000). The normal and lognormal distributions are closely related as if a random variable X follows a lognormal distribution, then $\ln X$ has a normal distribution. The lognormal probability density function is expressed as

$$f_X(x) = \frac{1}{x\sigma\sqrt{2\pi}} \exp\left[-\frac{(\ln x - \mu)^2}{2\sigma^2}\right] \quad (\text{C.1})$$

where μ and σ are the mean and standard deviation, respectively, of the associated normal distribution. The mean m and the variance v of the lognormal random variable can be calculated as

$$m = \exp\left(\mu + \frac{\sigma^2}{2}\right) \quad (\text{C.2})$$

and

$$v = \exp(2\mu + \sigma^2) [\exp(\sigma^2) - 1], \quad (\text{C.3})$$

Appendix C. Lognormal distribution

respectively. From the above equations, one can also express the parameters μ and σ as functions of m and v , as

$$\mu = \ln \left[\frac{m^2}{\sqrt{v + m^2}} \right], \quad (\text{C.4})$$

and

$$\sigma = \sqrt{\ln \left[\frac{v}{m^2} + 1 \right]}. \quad (\text{C.5})$$

D Results from the Monte Carlo simulations conducted in Chapter 11

Table D.1: Results from the Monte Carlo simulations of semi-elliptical internal surface cracks in inert environment.

$p_{i,\text{mean}}$	a_i	f_y	SF	E'	$\frac{E}{E'}$	t_s	$\frac{p_c}{p_i}$	$\frac{p_{c,\text{real}}}{p_i}$	N_{MC}	p_f	$\epsilon_{10^{-5}}$	ϵ_{pf}	$\left[\frac{\Delta p_i}{p_{i,\text{mean}}} \right]_{\text{th}}$	Occurrences of $\frac{N_{w,p}}{N_p} = 1$
(MPa)	(mm)	(MPa)	(-)	(GPa)	(-)	(mm)	(%)	(%)	(-)	(-)	(%)	(%)	(%)	(-)
5	2	355	1.8	5.0	1.0	-	-	-	-	-	-	-	-	-
		2.0	5.0	1.0	-	-	-	-	-	-	-	-	-	-
		2.2	5.0	1.0	-	-	-	-	-	-	-	-	-	-
500	2	355	1.8	5.0	1.0	14.4	50	53	$5 \cdot 10^5$	0.00	45	∞	4.0	0
		2.0	5.0	1.0	-	-	-	-	-	-	-	-	-	-
		2.2	5.0	1.0	-	-	-	-	-	-	-	-	-	-
690	2	355	1.8	5.0	1.0	-	-	-	-	-	-	-	-	-
		2.0	5.0	1.0	-	-	-	-	-	-	-	-	-	-
		2.2	5.0	1.0	-	-	-	-	-	-	-	-	-	-
4	2	355	1.8	5.0	1.0	28.0	34	34	$5 \cdot 10^5$	0.00	45	∞	4.0	0
		2.0	5.0	1.0	-	-	-	-	-	-	-	-	-	-
		2.2	5.0	1.0	-	-	-	-	-	-	-	-	-	-

Table D.2: Results from the Monte Carlo simulations of semi-elliptical internal surface cracks in aggressive environment.

$p_{i,\text{mean}}$	a_i	f_y	SF	E'	$\frac{E}{E'}$	t_s	$\frac{p_c}{p_i}$	$\frac{p_{c,\text{real}}}{p_i}$	N_{MC}	p_f	$\varepsilon_{10^{-5}}$	ε_{p_f}	$\left[\frac{\Delta p_i}{p_{i,\text{mean}}} \right]_{\text{th}}$	Occurrences of $\frac{N_{w,p}}{N_p} = 1$
(MPa)	(mm)	(MPa)	(-)	(GPa)	(-)	(mm)	(%)	(%)	(-)	(-)	(%)	(%)	(%)	(-)
5	2	355	1.8	5.0	1.0	14.4	50	53	$5 \cdot 10^5$	0.00	45	∞	4.0	0
		2.0	5.0	1.0	2.0	10.0	34	34	$5 \cdot 10^5$	0.00	45	∞	5.0	0
		2.2	5.0	1.0	2.0	10.0	34	34	$5 \cdot 10^5$	0.00	45	∞	5.0	0
690	2	355	1.8	5.0	1.0	14.4	50	53	$5 \cdot 10^5$	0.00	45	∞	4.0	0
		2.0	5.0	1.0	2.0	10.0	34	34	$5 \cdot 10^5$	0.00	45	∞	5.0	0
		2.2	5.0	1.0	2.0	10.0	34	34	$5 \cdot 10^5$	0.00	45	∞	5.0	0

[illegible]

	2.2	5.0	1.0	43.1	29	29	6·10 ⁵	0.00	41	∞	3.5	0
		10.0	2.0	-	-	-	-	-	-	-	-	-
960	1.8	5.0	1.0	27.3	40	40	1·10 ⁵	1.80·10 ⁻⁴	100	24	4.0	34
			2.0	27.3	40	44	5·10 ⁵	4.20·10 ⁻⁵	45	22	4.0	35
		10.0	1.0	22.7	50	60	5·10 ⁵	0.00	45	∞	4.0	0
			2.0	-	-	-	-	-	-	-	-	-
	2.0	5.0	1.0	32.8	36	36	1·10 ⁶	8.00·10 ⁻⁶	32	35	4.0	11
		10.0	2.0	25.2	50	57	6·10 ⁵	0.00	41	∞	4.0	0
	2.2	5.0	1.0	-	-	-	-	-	-	-	-	-
		10.0	2.0	-	-	-	-	-	-	-	-	-
4	1.8	5.0	1.0	46.8	27	27	5·10 ⁵	5.00·10 ⁻⁵	45	20	3.5	0
			2.0	46.8	27	31	6·10 ⁵	8.33·10 ⁻⁶	41	45	3.5	0
		10.0	1.0	31.6	50	51	1·10 ⁶	1.50·10 ⁻⁵	32	26	3.5	0
			2.0	-	-	-	-	-	-	-	-	-
	2.0	5.0	1.0	54.6	24	24	8·10 ⁵	0.00	35	∞	3.5	0
		10.0	2.0	-	-	-	-	-	-	-	-	-
	2.2	5.0	1.0	-	-	-	-	-	-	-	-	-
		10.0	2.0	-	-	-	-	-	-	-	-	-
890	1.8	5.0	1.0	31.2	37	37	1·10 ⁵	7.45·10 ⁻³	100	4	3.5	237
			2.0	31.2	37	41	1·10 ⁵	1.91·10 ⁻³	100	8	3.5	59
		10.0	1.0	24.5	50	58	2·10 ⁵	1.70·10 ⁻⁴	71	17	3.5	0
			2.0	24.5	50	61	6·10 ⁵	1.17·10 ⁻⁵	41	38	3.2	0
	2.0	5.0	1.0	37.2	33	33	5·10 ⁵	4.76·10 ⁻⁴	45	6	3.5	372
		10.0	2.0	27.2	50	59	1·10 ⁶	0.00	32	∞	3.5	0
	2.2	5.0	1.0	43.2	29	29	5·10 ⁵	5.00·10 ⁻⁵	45	20	3.5	41
		10.0	2.0	-	-	-	-	-	-	-	-	-
960	1.8	5.0	1.0	27.3	40	40	1·10 ⁵	2.96·10 ⁻²	100	2	3.2	11
			2.0	27.3	40	44	1·10 ⁵	8.37·10 ⁻³	100	3	3.5	360
		10.0	1.0	22.7	50	60	5·10 ⁵	3.08·10 ⁻⁴	45	8	3.5	0
			2.0	22.7	50	63	5·10 ⁵	3.60·10 ⁻⁵	45	24	3.5	0
	2.0	5.0	1.0	32.8	36	36	2·10 ⁵	2.00·10 ⁻³	71	5	3.2	158
		10.0	2.0	25.2	50	57	5·10 ⁵	7.20·10 ⁻⁵	45	17	3.5	0
	2.2	5.0	1.0	38.3	32	32	6·10 ⁵	1.60·10 ⁻⁴	100	7	3.2	139
		10.0	2.0	27.7	50	55	6·10 ⁵	1.00·10 ⁻⁵	41	41	3.2	0

Table D.3: Results from the Monte Carlo simulations of embedded elliptical cracks in inert environment.

$p_{i,\text{mean}}$	a_i	f_y	SF	E'	$\frac{E}{E'}$	t_s	$\frac{p_c}{p_i}$	$\frac{p_{c,\text{real}}}{p_i}$	N_{MC}	p_f	$\epsilon_{10^{-5}}$	ϵ_{pf}	$\left[\frac{\Delta p_i}{p_{i,\text{mean}}} \right]_{\text{th}}$	Occurrences of $\frac{N_{w,p}}{N_p} = 1$
(MPa)	(mm)	(MPa)	(-)	(GPa)	(-)	(mm)	(%)	(%)	(-)	(-)	(%)	(%)	(%)	(-)
5	2	355	1.8	5.0	1.0	-	-	-	-	-	-	-	-	-
		500	1.8	5.0	1.0	14.4	50	53	-	-	-	-	-	-
		690	1.8	5.0	1.0	-	-	-	-	-	-	-	-	-
4		355	1.8	5.0	1.0	28.0	34	34	-	-	-	-	-	-

Table 1: Material properties and test parameters for the concrete specimens														
$p_{i,\text{mean}}$ (MPa)	a_i (mm)	f_y	SF	E'	$\frac{E}{E'}$	t_s (mm)	$\frac{P_c}{P_i}$	$\frac{P_{c,\text{real}}}{P_i}$	N_{MC}	P_f	$\epsilon_{10^{-5}}$	ϵ_{P_f}	$\left[\frac{\Delta p_i}{p_{i,\text{mean}}}\right]_{\text{th}}$	Occurrences of $\frac{N_{w,p}}{N_p} = 1$ (-)
10	2	690	1.8	5.0	1.0	24.8	41	41	$1 \cdot 10^5$	0.00	100	∞	4.0	0
				10.0	1.0	21.0	50	60	-	-	-	-	-	-
				2.0	2.0	-	-	-	-	-	-	-	-	-
		2.0	5.0	1.0	1.0	-	-	-	-	-	-	-	-	-
		10.0	10.0	2.0	2.0	-	-	-	-	-	-	-	-	-
		2.2	5.0	1.0	1.0	-	-	-	-	-	-	-	-	-
		10.0	10.0	2.0	2.0	-	-	-	-	-	-	-	-	-
Table 2: Material properties and test parameters for the concrete specimens														
890	1.8	5.0	1.0	16.2	50	53	$5 \cdot 10^5$	0.00	45	∞	4.0	0	-	-
		10.0	1.0	-	-	-	-	-	-	-	-	-	-	-
		2.0	2.0	-	-	-	-	-	-	-	-	-	-	-
		18.3	49	49	49	49	-	-	-	-	-	-	-	-
		2.0	5.0	1.0	1.0	-	-	-	-	-	-	-	-	-
		10.0	10.0	2.0	2.0	-	-	-	-	-	-	-	-	-

[illegible]

	2.2	5.0	1.0	43.1	29	29	-	-	-	-	-	-
		10.0	2.0	-	-	-	-	-	-	-	-	-
960	1.8	5.0	1.0	27.3	40	40	-	-	-	-	-	-
			2.0	27.3	40	44	-	-	-	-	-	-
		10.0	1.0	22.7	50	60	-	-	-	-	-	-
			2.0	-	-	-	-	-	-	-	-	-
	2.0	5.0	1.0	32.8	36	36	-	-	-	-	-	-
		10.0	2.0	25.2	50	57	-	-	-	-	-	-
	2.2	5.0	1.0	-	-	-	-	-	-	-	-	-
		10.0	2.0	-	-	-	-	-	-	-	-	-
4	690	1.8	5.0	1.0	46.8	27	27	-	-	-	-	-
			2.0	-	-	-	-	-	-	-	-	-
		10.0	1.0	-	-	-	-	-	-	-	-	-
			2.0	-	-	-	-	-	-	-	-	-
	2.0	5.0	1.0	54.6	24	24	-	-	-	-	-	-
		10.0	2.0	-	-	-	-	-	-	-	-	-
	2.2	5.0	1.0	-	-	-	-	-	-	-	-	-
		10.0	2.0	-	-	-	-	-	-	-	-	-
890	1.8	5.0	1.0	31.2	37	37	4 · 10 ⁵	0.00	50	∞	4.0	0
			2.0	31.2	37	41	-	-	-	-	-	-
		10.0	1.0	24.5	50	58	-	-	-	-	-	-
			2.0	-	-	-	-	-	-	-	-	-
	2.0	5.0	1.0	37.2	33	33	-	-	-	-	-	-
		10.0	2.0	-	-	-	-	-	-	-	-	-
	2.2	5.0	1.0	43.2	29	29	-	-	-	-	-	-
		10.0	2.0	-	-	-	-	-	-	-	-	-
960	1.8	5.0	1.0	27.3	40	40	1 · 10 ⁵	0.00	100	∞	4.0	0
			2.0	27.3	40	44	-	-	-	-	-	-
		10.0	1.0	22.7	50	60	-	-	-	-	-	-
			2.0	22.7	50	63	-	-	-	-	-	-
	2.0	5.0	1.0	32.8	36	36	-	-	-	-	-	-
		10.0	2.0	-	-	-	-	-	-	-	-	-
	2.2	5.0	1.0	38.3	32	32	-	-	-	-	-	-
		10.0	2.0	27.7	50	55	-	-	-	-	-	-

E Results from the Monte Carlo simulations conducted in Chapter 12

Appendix E. Results from the Monte Carlo simulations conducted in Chapter 12

Table E.1: Results from the Monte Carlo simulations of **semi-elliptical internal surface cracks in inert environment**.

a_i	f_y	SF	t_s	$\frac{p_c}{p_i}$	$\frac{p_{c,real}}{p_i}$	N_{MC}	p_f	$\epsilon_{10^{-5}}$	ϵ_{p_f}	$\left[\frac{\Delta p_i}{p_{i,mean}} \right]_{th}$	Occurrences of $\frac{N_{w,p}}{N_p} = 1$
(mm)	(MPa)	(-)	(mm)	(%)	(%)	(-)	(-)	(%)	(%)	(%)	(-)
2	690	1.1	-	-	-	-	-	-	-	-	-
		2.0	-	-	-	-	-	-	-	-	-
		2.2	-	-	-	-	-	-	-	-	-
		2.4	-	-	-	-	-	-	-	-	-
	890	1.1	-	-	-	-	-	-	-	-	-
		2.0	22.9	50.0	51.7	-	-	-	-	-	-
		2.2	-	-	-	-	-	-	-	-	-
		2.4	-	-	-	-	-	-	-	-	-
	960	1.1	23.4	0.0	51.1	-	-	-	-	-	-
		2.0	21.2	50.0	53.7	-	-	-	-	-	-
		2.2	23.6	49.5	50.9	-	-	-	-	-	-
		2.4	-	-	-	-	-	-	-	-	-
3	690	1.1	-	-	-	-	-	-	-	-	-
		2.0	37.9	37.1	38.4	-	-	-	-	-	-
		2.2	-	-	-	-	-	-	-	-	-
		2.4	-	-	-	-	-	-	-	-	-
	890	1.1	25.3	0.0	49.0	-	-	-	-	-	-
		2.0	22.9	50.0	51.7	-	-	-	-	-	-
		2.2	27.8	45.2	46.6	-	-	-	-	-	-
		2.4	33.1	40.6	42.0	-	-	-	-	-	-
	960	1.1	23.4	0.0	51.1	-	-	-	-	-	-
		2.0	21.2	50.0	53.7	$1 \cdot 10^6$	0.00	32	∞	3.8	0
		2.2	23.6	49.5	50.9	-	-	-	-	-	-
		2.4	28.5	44.6	46.0	-	-	-	-	-	-
4	690	1.1	-	-	-	-	-	-	-	-	-
		2.0	37.9	37.1	38.4	$6 \cdot 10^5$	0.00	41	∞	3.8	0
		2.2	-	-	-	-	-	-	-	-	-
		2.4	-	-	-	-	-	-	-	-	-
	890	1.1	25.3	0.0	49.0	-	-	-	-	-	-
		2.0	22.9	50.0	51.7	$6 \cdot 10^5$	$1.67 \cdot 10^{-6}$	41	100	3.8	0
		2.2	27.8	45.2	46.6	-	-	-	-	-	-
		2.4	33.1	40.6	42.0	-	-	-	-	-	-
	960	1.1	23.4	0.0	51.1	$6 \cdot 10^5$	0.00	41	∞	3.8	0
		2.0	21.2	50.0	53.7	$5 \cdot 10^5$	$2.00 \cdot 10^{-6}$	45	100	3.8	0
		2.2	23.6	49.5	50.9	-	-	-	-	-	-
		2.4	28.5	44.6	46.0	-	-	-	-	-	-

Table E.2: Results from the Monte Carlo simulations of **semi-elliptical internal surface cracks in aggressive environment**.

a_i	f_y	SF	t_s	$\frac{p_c}{p_i}$	$\frac{p_{c,real}}{p_i}$	N_{MC}	p_f	$\varepsilon_{10^{-5}}$	ε_{p_f}	$\left[\frac{\Delta p_i}{p_{i,mean}} \right]_{th}$	Occurrences of $\frac{N_{w,p}}{N_p} = 1$ (-)
(mm)	(MPa)	(-)	(mm)	(%)	(%)	(-)	(-)	(%)	(%)	(%)	
2	690	1.1	-	-	-	-	-	-	-	-	-
		2.0	-	-	-	-	-	-	-	-	-
		2.2	-	-	-	-	-	-	-	-	-
		2.4	-	-	-	-	-	-	-	-	-
	890	1.1	-	-	-	-	-	-	-	-	-
		2.0	22.9	50.0	51.7	$1 \cdot 10^6$	$4.00 \cdot 10^{-6}$	32	50	3.8	0
		2.2	-	-	-	-	-	-	-	-	-
		2.4	-	-	-	-	-	-	-	-	-
	960	1.1	23.4	0.0	51.1	$1 \cdot 10^6$	$2.00 \cdot 10^{-6}$	32	71	3.8	0
		2.0	21.2	50.0	53.7	$8 \cdot 10^5$	$1.25 \cdot 10^{-5}$	35	32	3.8	0
		2.2	23.6	49.5	50.9	$1 \cdot 10^6$	0.00	32	∞	3.8	0
		2.4	-	-	-	-	-	-	-	-	-
	690	1.1	-	-	-	-	-	-	-	-	-
		2.0	37.9	37.1	38.4	$5 \cdot 10^5$	0.00	45	∞	3.8	0
		2.2	-	-	-	-	-	-	-	-	-
		2.4	-	-	-	-	-	-	-	-	-
	890	1.1	25.3	0.0	49.0	$6 \cdot 10^5$	$7.67 \cdot 10^{-5}$	41	15	3.8	2
		2.0	22.9	50.0	51.7	$6 \cdot 10^5$	$3.82 \cdot 10^{-4}$	41	7	3.8	0
		2.2	27.8	45.2	46.6	$8 \cdot 10^5$	$1.38 \cdot 10^{-5}$	35	30	3.8	4
		2.4	33.1	40.6	42.0	$1 \cdot 10^6$	0.00	32	∞	3.8	0
	960	1.1	23.4	0.0	51.1	$6 \cdot 10^5$	$1.78 \cdot 10^{-4}$	41	10	3.8	25
		2.0	21.2	50.0	53.7	$5 \cdot 10^5$	$7.06 \cdot 10^{-4}$	45	5	3.8	7
		2.2	23.6	49.5	50.9	$8 \cdot 10^5$	$1.55 \cdot 10^{-4}$	35	9	3.8	36
		2.4	28.5	44.6	46.0	$1 \cdot 10^6$	$7.00 \cdot 10^{-6}$	32	38	3.8	10
4	690	1.1	-	-	-	-	-	-	-	-	-
		2.0	37.9	37.1	38.4	$5 \cdot 10^5$	$6.00 \cdot 10^{-6}$	45	58	3.8	0
		2.2	-	-	-	-	-	-	-	-	-
		2.4	-	-	-	-	-	-	-	-	-
	890	1.1	25.3	0.0	49.0	$3 \cdot 10^5$	$1.57 \cdot 10^{-3}$	58	5	3.8	14
		2.0	22.9	50.0	51.7	$1 \cdot 10^5$	$8.04 \cdot 10^{-3}$	100	4	3.8	0
		2.2	27.8	45.2	46.6	$4 \cdot 10^5$	$2.60 \cdot 10^{-4}$	50	10	3.8	39
		2.4	33.1	40.6	42.0	$6 \cdot 10^5$	$1.00 \cdot 10^{-5}$	41	41	3.8	14
	960	1.1	23.4	0.0	51.1	$2 \cdot 10^5$	$2.74 \cdot 10^{-3}$	70	4	3.8	134
		2.0	21.2	50.0	53.7	$1 \cdot 10^5$	$1.30 \cdot 10^{-2}$	100	3	3.8	32
		2.2	23.6	49.5	50.9	$3 \cdot 10^5$	$2.64 \cdot 10^{-3}$	58	4	3.8	231
		2.4	28.5	44.6	46.0	$5 \cdot 10^5$	$1.40 \cdot 10^{-4}$	45	12	3.8	100

Appendix E. Results from the Monte Carlo simulations conducted in Chapter 12

Table E.3: Results from the Monte Carlo simulations of **embedded elliptical cracks in inert environment**.

a_i	f_y	SF	t_s	$\frac{p_c}{p_i}$	$\frac{p_{c,real}}{p_i}$	N_{MC}	p_f	$\varepsilon_{10^{-5}}$	ε_{p_f}	$\left[\frac{\Delta p_i}{p_{i,mean}} \right]_{th}$	Occurrences of $\frac{N_{w,p}}{N_p} = 1$
(mm)	(MPa)	(-)	(mm)	(%)	(%)	(-)	(-)	(%)	(%)	(%)	(-)
2	690	1.1	-	-	-	-	-	-	-	-	-
		2.0	-	-	-	-	-	-	-	-	-
		2.2	-	-	-	-	-	-	-	-	-
		2.4	-	-	-	-	-	-	-	-	-
	890	1.1	-	-	-	-	-	-	-	-	-
		2.0	22.9	50.0	51.7	-	-	-	-	-	-
		2.2	-	-	-	-	-	-	-	-	-
		2.4	-	-	-	-	-	-	-	-	-
	960	1.1	23.4	0.0	51.1	-	-	-	-	-	-
		2.0	21.2	50.0	53.7	-	-	-	-	-	-
		2.2	23.6	49.5	50.9	-	-	-	-	-	-
		2.4	-	-	-	-	-	-	-	-	-
3	690	1.1	-	-	-	-	-	-	-	-	-
		2.0	37.9	37.1	38.4	-	-	-	-	-	-
		2.2	-	-	-	-	-	-	-	-	-
		2.4	-	-	-	-	-	-	-	-	-
	890	1.1	25.3	0.0	49.0	-	-	-	-	-	-
		2.0	22.9	50.0	51.7	-	-	-	-	-	-
		2.2	27.8	45.2	46.6	-	-	-	-	-	-
		2.4	33.1	40.6	42.0	-	-	-	-	-	-
	960	1.1	23.4	0.0	51.1	-	-	-	-	-	-
		2.0	21.2	50.0	53.7	-	-	-	-	-	-
		2.2	23.6	49.5	50.9	-	-	-	-	-	-
		2.4	28.5	44.6	46.0	-	-	-	-	-	-
4	690	1.1	-	-	-	-	-	-	-	-	-
		2.0	37.9	37.1	38.4	$1 \cdot 10^6$	0.00	32	∞	3.5	0
		2.2	-	-	-	-	-	-	-	-	-
		2.4	-	-	-	-	-	-	-	-	-
	890	1.1	25.3	0.0	49.0	-	-	-	-	-	-
		2.0	22.9	50.0	51.7	-	-	-	-	-	-
		2.2	27.8	45.2	46.6	-	-	-	-	-	-
		2.4	33.1	40.6	42.0	-	-	-	-	-	-
	960	1.1	23.4	0.0	51.1	-	-	-	-	-	-
		2.0	21.2	50.0	53.7	$1 \cdot 10^6$	0.00	32	∞	3.5	0
		2.2	23.6	49.5	50.9	-	-	-	-	-	-
		2.4	28.5	44.6	46.0	-	-	-	-	-	-

Bibliography

- ACEVEDO, C. (2011). *Influence of residual stresses on fatigue response of welded tubular K-joints*. Ph.D. thesis, Ecole Polytechnique Fédérale de Lausanne.
- AINSWORTH, R. A. (2003). 7.03 - Failure assessment diagram methods. In: *Comprehensive Structural Integrity*, vol. 7. Pergamon, pp. 89–132.
- AINSWORTH, R. A., BANNISTER, A. C. & ZERBST, U. (2000a). An overview of the European flaw assessment procedure SINTAP and its validation. *International Journal of Pressure Vessels and Piping* **77**(14-15), 869–876.
- AINSWORTH, R. A., GUTIERREZ-SOLANA, F. & RUIZ OCEJO, J. (2000b). Analysis levels within the SINTAP defect assessment procedures. *Engineering Fracture Mechanics* **67**(6), 515–527.
- AINSWORTH, R. A. & HOOTON, D. G. (2008). R6 and R5 procedures: The way forward. *International Journal of Pressure Vessels and Piping* **85**(3), 175–182.
- ALAWADHI, E. M. (2010). *Finite Element Simulations Using ANSYS*. CRC Press, United States.
- AMADEI, B. (1996). Importance of anisotropy when estimating and measuring in situ stresses in rock. *International Journal of Rock Mechanics and Mining Sciences* **33**(3), 293–325.
- AMADEI, B., SAVAGE, W. Z. & SWOLFS, H. S. (1987). Gravitational stresses in anisotropic rock masses. *International Journal of Rock Mechanics and Mining Sciences* **24**(1), 5–14.
- AMADEI, B., SWOLFS, H. S. & SAVAGE, W. Z. (1988). Gravity-induced stresses in stratified rock masses. *Rock Mechanics and Rock Engineering* **21**(1), 1–20.
- AMZALLAG, C., GEREY, J. P., ROBERT, J. L. & BAHUAUD, J. (1994). Standardization of the rainflow counting method for fatigue analysis. *International Journal of Fatigue* **16**(4), 287–293.
- ANDERSON, P. (2008). Concentration of plastic strains in steel liners due to concrete cracks in the containment wall. *International Journal of Pressure Vessels and Piping* **85**(10), 711–719.
- ANDERSON, T. L. (2003). 7.06 - Flaw characterization. In: *Comprehensive Structural Integrity*, vol. 7. Pergamon, pp. 227–243.

Bibliography

- ANDERSON, T. L. (2005). *Fracture Mechanics: Fundamentals and Applications*. CRC Press.
- ANDERSON, T. L. & OSAGE, D. A. (2000). API 579: a comprehensive fitness-for-service guide. *International Journal of Pressure Vessels and Piping* **77**(14-15), 953–963.
- ANDERSON, T. L., THORWALD, G., REVELLE, D. J., OSAGE, D. A., JANELLE, J. L. & FUHRY, M. E. (2002). Development of stress intensity factor solutions for surface and embedded cracks in API 579. Bulletin 471, Welding Research Council, Inc., NY, USA.
- ANSYS INC (2011). *ANSYS® Academic Research, Help System, Documentation, Release 14.0*. ANSYS, Inc.
- ANSYS INC (2015). *ANSYS® Academic Research, Help System, Documentation, Release 16.1*. ANSYS, Inc.
- ANTHES, R. J., KÖTTGEN, V. B. & SEEGER, T. (1993). Notch shape factors of butt joints and double-T joints. *Schweißen und Schneiden* **45**(12), 685–688.
- API (2007). *Fitness-for-service*. American Petroleum Institute, second ed. API 579-1/ASME FFS-1.
- ASCE (2012). *Steel Penstocks*, vol. 79 of *Manuals and Reports on Engineering Practice*. American Society of Civil Engineers, Reston, Virginia.
- ASME (2007). *ASME Boiler and Pressure Vessel Code, Section VIII, Division 2: Alternative Rules*. The American Society of Mechanical Engineers (ASME), New York, NY.
- ATABEK, H. B. (1968). Wave propagation through a viscous fluid contained in a tethered, initially stressed, orthotropic elastic tube. *Biophysical Journal* **8**(5), 626–649.
- AYGÜL, M., AL-EMRANI, M. & URUSHADZE, S. (2012). Modelling and fatigue life assessment of orthotropic bridge deck details using FEM. *International Journal of Fatigue* **40**, 129–142.
- AYGÜL, M., BOKESJÖ, M., HESHMATI, M. & AL-EMRANI, M. (2013). A comparative study of different fatigue failure assessments of welded bridge details. *International Journal of Fatigue* **49**, 62–72.
- BAECHER, G. B. (2003). *Reliability and statistics in geotechnical engineering*. John Wiley & Sons Ltd, Chichester, England.
- BALTAY, P. & GJELSVIK, A. (1990). Coefficient of friction for steel on concrete at high normal stress. *Journal of Materials in Civil Engineering* **2**(1), 46–49.
- BANNISTER, A. C. (1998). SINTAP–Sub-task 3.3 report: Final issue determination of fracture toughness from Charpy impact energy: procedure and validation. Document SINTAP/BS/17, British Steel, Rotherham, United Kingdom. Brite-Euram Project No. BE95-1426.
- BAPTISTA, C. (2016). *Multiaxial and variable amplitude fatigue in steel bridges*. Ph.D. thesis, Ecole Polytechnique Fédérale de Lausanne, Switzerland.

- BARSON, J. M. & ROLFE, S. T. (1999). *Fracture and Fatigue Control in Structures*. American Society for Testing and Materias (ASTM), West Conshohocken, PA, United States.
- BARSOUM, R. S. (1976). On the use of isoparametric finite elements in linear fracture mechanics. *International Journal for Numerical Methods in Engineering* **10**(1), 25–37.
- BARSOUM, Z. & JONSSON, B. (2008). Fatigue assessment and LEFM analysis of cruciform joints fabricated with different welding processes. *Welding in the World* **52**(7-8), 93–105.
- BARTON, N. & QUADROS, E. (2014). Anisotropy is everywhere, to see, to measure, and to model. *Rock Mechanics and Rock Engineering* **48**(4), 1323–1339.
- BASLAVSKII, I. A. (1973). Stresses in the lining of a pressure tunnel driven in an inhomogeneous rock mass. *Soviet Mining* **9**(6), 613–617.
- BATHE, K. J. (1996). *Finite Element Procedures*. New Jersey: Prentice-Hall.
- BATUGIN, S. A. & NIRENBURG, R. K. (1972). Approximate relation between the elastic constants of anisotropic rocks and the anisotropy parameters. *Soviet Mining* **8**(1), 5–9.
- BECK, S. B. M., CURREN, M. D., SIMS, N. D. & STANWAY, R. (2005). Pipeline network features and leak detection by cross-correlation analysis of reflected waves. *Journal of Hydraulic Engineering* **131**(8), 715–723.
- BENSON, R. (1989). Design of unlined and lined pressure tunnels. *Tunnelling and Underground Space Technology* **4**(2), 155–170.
- BERGANT, A. & TIJSSELING, A. (2008). Parameters affecting water hammer wave attenuation, shape and timing - Part 1: Mathematical tools. *Journal of Hydraulic Research* **46**(3), 373–381.
- BESUNER, P. M. (1987). Probabilistic fracture mechanics. In: *Probabilistic Fracture Mechanics and Reliability* (PROVAN, J. W., ed.). Martinus Nijhoff Publishers, Dordrecht, The Netherlands.
- BESUNER, P. M. & TETELMAN, A. S. (1977). Probabilistic fracture mechanics. *Nuclear Engineering and Design* **43**, 99–114.
- BOBET, A. (2009). Elastic solution for deep tunnels. application to excavation damage zone and rockbolt support. *Rock Mechanics and Rock Engineering* **42**(2), 147–174.
- BOBET, A. (2011). Lined circular tunnels in elastic transversely anisotropic rock at depth. *Rock Mechanics and Rock Engineering* **44**(2), 149–167.
- BOBET, A. & NAM, S. W. (2007). Stresses around pressure tunnels with semi-permeable liners. *Rock Mechanics and Rock Engineering* **40**(3), 287–315.
- BOBET, A. & YU, H. (2016). Full stress and displacement fields for steel-lined deep pressure tunnels in transversely anisotropic rock. *Tunnelling and Underground Space Technology* **56**(June), 125–135.

Bibliography

- BÖCK, N. & ZEMAN, J. L. (1994). On bending stresses at longitudinal weld joints of cylindrical shells due to peaking. *International Journal of Pressure Vessels and Piping* **60**(1), 103–106.
- BOILLAT, J.-L. & DE SOUZA, P. (2004). *Hydraulic System – Modélisation des systèmes hydrauliques à écoulements transitoires en charge*, vol. 16 of *Communications du Laboratoire de Constructions Hydrauliques, Ecole Polytechnique Fédérale de Lausanne*.
- BORGES, L. A. (2008). *Size effects in the fatigue behaviour of tubular bridge joints*. Ph.D. thesis, Ecole Polytechnique Fédérale de Lausanne, Switzerland.
- BORREGO, L. P., FERREIRA, J. M., PINHO DA CRUZ, J. M. & COSTA, J. M. (2003). Evaluation of overload effects on fatigue crack growth and closure. *Engineering Fracture Mechanics* **70**(11), 1379–1397.
- BOWLING, A. J. (2010). Performance of steel liners in the power tunnel of the King River Power Development, Tasmania. *Australian Journal of Civil Engineering* **6**(1), 71–80.
- BOWNESS, D. & LEE, M. M. K. (2000a). Prediction of weld toe magnification factors for semi-elliptical cracks in T-butt joints. *International Journal of Fatigue* **22**(5), 369–387.
- BOWNESS, D. & LEE, M. M. K. (2000b). Weld toe magnification factors for semi-elliptical cracks in T-butt joints – comparison with existing solutions. *International Journal of Fatigue* **22**(5), 389–396.
- BRADY, B. H. G. & BROWN, E. T. (2006). *Rock Mechanics For Underground Mining*. Springer, Dordrecht, The Netherlands, third ed.
- BREKKE, T. L. & RIPLEY, B. D. (1987). Design guidelines for pressure tunnels and shafts. Final report, University of California at Berkeley, Department of Civil Engineering, Berkeley, California 94707. EPRI AP-5273, Project 1745-17.
- BRENNAN, F. P., DOVER, W. D., KARÉ, R. F. & HELLIER, A. K. (1999). Parametric equations for T-butt weld toe stress intensity factors. *International Journal of Fatigue* **21**(10), 1051–1062.
- BRITISH STANDARD 7910 (2005). *Guide to methods for assessing the acceptability of flaws in metallic structures*. British Standards Institution (BSi). BS7910:2005.
- BRÜCKNER, A. (1987). Numerical methods in probabilistic fracture mechanics. In: *Probabilistic Fracture Mechanics and Reliability* (PROVAN, J. W., ed.). Martinus Nijhoff Publishers, Dordrecht, The Netherlands.
- BUDDEN, P. J., SHARPLES, J. K. & DOWLING, A. R. (2000). The R6 procedure: recent developments and comparison with alternative approaches. *International Journal of Pressure Vessels and Piping* **77**(14-15), 895–903.
- BULLOUGH, R., GREEN, V. R., TOMKINS, B., WILSON, R. & WINTLE, J. B. (1999). A review of methods and applications of reliability analysis for structural integrity assessment of UK nuclear plant. *International Journal of Pressure Vessels and Piping* **76**(13), 909–919.

- CAMERON, R. F., JOHNSTON, G. O. & LIDIARD, A. B. (1987). The reliability of pressurized water reactor vessels. In: *Probabilistic Fracture Mechanics and Reliability* (PROVAN, J. W., ed.). Martinus Nijhoff Publishers, Dordrecht, The Netherlands.
- CASAVOLA, C. & PAPPALETTERE, C. (2009). Discussion on local approaches for the fatigue design of welded joints. *International Journal of Fatigue* **31**(1), 41–49.
- CAUVIN, A. & TESTA, R. B. (1999). Damage mechanics: basic variables in continuum theories. *International Journal of Solids and Structures* **36**(5), 747–761.
- C.E.C.T. (1980). *Recommendations for the design, manufacture and erection of steel penstocks of welded construction for hydroelectric installations*. European Committee of Boiler, Vessel and Pipe Work Manufacturers.
- CERIT, M., KOKUMER, O. & GENEL, K. (2010). Stress concentration effects of undercut defect and reinforcement metal in butt welded joint. *Engineering Failure Analysis* **17**(2), 571–578.
- CERJAK, H. (2008). The role of welding in the power generation industry. In: *Proceedings IIW International Conference on Safety and Reliability of Welded Components in Energy and Processing Industry*. Graz, Austria.
- CERJAK, H., CHÈNE, O., ENZINGER, N. & ROOS, E. (2009). Qualification program for the rehabilitation of Cleuson-Dixence: requirements and results. In: *Proceedings of the Conference on High Strength Steels for Hydropower Plants*. Takasaki, Japan.
- CERJAK, H., DIMMLER, G. & ENZINGER, N. (2005). Steel S890 for pressurized shaft CD: review of the metallurgical investigations. In: *Proceedings of the Conference on High Strength Steels for Hydropower Plants*. Graz, Austria: Graz University of Technology.
- CERJAK, H., ENZINGER, N. & PUDAR, M. (2013a). Development, experience and qualification of steel grades for hydropower conduits. *Steel Construction* **6**(4), 265–270.
- CERJAK, H., ENZINGER, N. & PUDAR, M. (2013b). Development, experiences and qualifications of steel grades for hydro power conduits. In: *Proceedings of the Conference on High Strength Steels for Hydropower Plants*. Graz, Austria: Graz University of Technology.
- CERJAK, H., ENZINGER, N. & PUDAR, M. (2015). Development, experiences and qualification of steel grades for hydro power conduits. *WasserWirtschaft* **1**, 109–113.
- CHAPETTI, M. D. & JAUREGUIZHAR, L. F. (2012). Fatigue behavior prediction of welded joints by using an integrated fracture mechanics approach. *International Journal of Fatigue* **43**(October), 43–53.
- CHATTOPADHYAY, A., GLINKA, G., EL-ZEIN, M., QIAN, J. & FORMAS, R. (2011). Stress analysis and fatigue of welded structures. *Welding in the World* **55**(7-8), 2–21.
- CHÈNE, O. (2009). Welding processes for the Cleuson-Dixence shaft. In: *Proceedings of the Conference on High Strength Steels for Hydropower Plants*. Takasaki, Japan.

Bibliography

- CHÈNE, O. (2013). In-situ deformation measurement of the Hongrin-Léman shaft. In: *Proceedings of the Conference on High Strength Steels for Hydropower Plants*. Graz, Austria: Graz University of Technology.
- CHRYSSANTHOPOULOS, M. K. & RIGHINIOTIS, T. D. (2006). Fatigue reliability of welded steel structures. *Journal of Constructional Steel Research* **62**(11), 1199–1209.
- COTTRELL, J. A., HUGHES, T. J. R. & BAZILEVS, Y. (2009). *Isogeometric analysis—toward integration of CAD and FEA*. John Wiley & Sons, Ltd, Chichester, West Sussex, United Kingdom.
- COVAS, D., RAMOS, H. & BETÂMIO DE ALMEIDA, A. (2005). Standing wave difference method for leak detection in pipeline systems. *Journal of Hydraulic Engineering* **131**(12), 1106–1116.
- CUI, W., WAN, Z. & MANSOUR, A. E. (1999). Stress concentration factor in plates with transverse butt-weld misalignment. *Journal of Constructional Steel Research* **52**(2), 159–170.
- CUI, W. C. & HUANG, X. P. (2003). A general constitutive relation for fatigue crack growth analysis of metal structures. *Acta Metallurgica Sinica (English Letters)* **16**(5), 342–354.
- D'ANGELO, L. & NUSSBAUMER, A. (2015). Reliability based fatigue assessment of existing motorway bridge. *Structural Safety* **57**, 35–42.
- DE JESUS, A. M. P., MATOS, R., FONTOURA, B. F. C., REBELO, C., DA SILVA, L. S. & VELJKOVIC, M. (2012). A comparison of the fatigue behavior between S355 and S690 steel grades. *Journal of Constructional Steel Research* **79**, 140–150.
- DEDÈ, L. (2015). B-spline and NURBS curves. Lecture notes of the course EDMA: MATH-782 Computational Mechanics by Isogeometric Analysis.
- DEMAL, R. & MOSER, C. (2013). Fatigue assessment of hydropower plants - penstocks using IIW-notch stress concept. In: *Proceedings of the Conference on High Strength Steels for Hydropower Plants*. Graz, Austria: Graz University of Technology.
- DEMOFONTI, G., RISCIFULI, S., SONSINO, C. M., KAUFMANN, H., SEDLACEK, G., MÜLLER, C., HANUS, F. & WEGMANN, H. G. (2001). High-strength steels in welded state for lightweight constructions under high and variable stress peaks. Tech. Rep. EUR 19989 EN, European Commission, Technical steel research.
- DER KIUREGHIAN, A. (2008). Analysis of structural reliability under parameter uncertainties. *Probabilistic Engineering Mechanics* **23**(4), 351–358.
- DERSKI, W., IZBICKI, R., KISIEL, I. & MRÓZ, Z. (1989). *Rock and Soil Mechanics*, vol. 48 of *Developments in Geotechnical Engineering*. Elsevier, Amsterdam, The Netherlands.
- DILL, E. H. (2012). *The Finite Element Method for Mechanics of Solids with ANSYS Applications*. CRC Press.

- DILLSTRÖM, P. & NILSSON, F. (2003). 7.11 - Probabilistic fracture mechanics. In: *Comprehensive Structural Integrity*, vol. 7. Pergamon, pp. 465–489.
- DOERK, O., FRICKE, W. & WEISSENBORN, C. (2003). Comparison of different calculation methods for structural stresses at welded joints. *International Journal of Fatigue* **25**(5), 359–369.
- DONG, P. (2001). A structural stress definition and numerical implementation for fatigue analysis of welded joints. *International Journal of Fatigue* **23**(10), 865–876.
- DOWNING, S. D. & SOCIE, D. F. (1982). Simple rainflow counting algorithms. *International Journal of Fatigue* **4**(1), 31–40.
- DUPARCHY, F., CHAMBAS, P.-A., MARIN, H. & PEREIRA, T., F. AND COMBAZ (2013). Impact of pressure fluctuation on the fatigue life of high pressure penstocks. In: *Proceedings of the Conference on High Strength Steels for Hydropower Plants*. Graz, Austria: Graz University of Technology.
- EN 10025-2 (2005). *Hot rolled products of structural steels – Part 2: Technical delivery conditions for non-alloy structural steels*. European Committee for Standardization, Brussels. NF EN 10025-2.
- EN 10025-3 (2005). *Hot rolled products of structural steels – Part 3: Technical delivery conditions for normalized/normalized rolled weldable fine grain structural steels*. European Committee for Standardization, Brussels. NF EN 10025-3.
- EN 10025-4 (2005). *Hot rolled products of structural steels – Part 4: Technical delivery conditions for thermomechanical rolled weldable fine grain structural steels*. European Committee for Standardization, Brussels. NF EN 10025-4.
- EN 10025-6 (2009). *Hot rolled products of structural steels – Part 6: Technical delivery conditions for flat products of high yield strength structural steels in the quenched and tempered condition*. European Committee for Standardization, Brussels. NF EN 10025-6+A1.
- EN 10028-3 (2009). *Flat products made of steels for pressure purposes – Part 3: Weldable fine grain steels, normalized*. European Committee for Standardization, Brussels. NF EN 10028-3.
- EN 10149-2 (2013). *Hot rolled flat products made of high yield strength steels for cold forming – Part 2: Technical delivery conditions for thermomechanically rolled steels*. European Committee for Standardization, Brussels. NF EN 10149-2.
- EN 13445-3 (2014). *Unfired pressure vessels – Part 3: Design*. European Committee for Standardization, Brussels. NF EN 13445-3 V1.
- EN 1993-1-9 (2005). *Eurocode 3: Design of steel structures - Part 1-9: Fatigue*. European Committee for Standardization, Brussels. NF EN 1993-1-9.

Bibliography

- ENGESVIK, K. M. & MOAN, T. (1983). Probabilistic analysis of the uncertainty in the fatigue capacity of welded joints. *Engineering Fracture Mechanics* **18**(4), 743–762.
- EN ISO 11666 (2011). *Non-destructive testing of welds–Ultrasonic testing–Acceptance levels*. European Committee for Standardization, Brussels. NF EN ISO 11666.
- EN ISO 148-1 (2011). *Charpy pendulum impact test – Part 1: Test method*. European Committee for Standardization, Brussels. NF EN ISO 148-1.
- EN ISO 23278 (2015). *Non-destructive testing of welds–Magnetic particle testing–Acceptance levels*. European Committee for Standardization, Brussels. NF EN ISO 23278.
- ENZINGER, N. & CERJAK, H. (2006). Investigation of cracks in original material of Cleuson-Dixence shaft. *Science and Technology of Welding and Joining* **11**(3), 347–351.
- ENZINGER, N. & CERJAK, H. (2007). Characterisation of cracks in high strength steel weldments. *Welding in the World* **51**(11-12), 29–33.
- ENZINGER, N. & CERJAK, H. (2009). Welding of high strength steel in hydropower applications – the Cleuson-Dixence case. In: *Proceedings of the 8th International Conference on Trends in Welding Research*. Pine Mountain, Georgia, USA: ASM International, Materials Park, Ohio.
- ENZINGER, N., CERJAK, H., ROOS, E. & EISELE, U. (2006). Fracture mechanical investigation of steel grade S890 used in Cleuson-Dixence hydropower plant shaft. *Science and Technology of Welding and Joining* **11**(4), 422–428.
- ENZINGER, N., HEBER, S. J., GUBELJAK, N., MAYRHUBER, J. & CERJAK, H. (2009). Investigation of watergas welded joints for future decisions concerning old hydropower stations. *Welding in the World* **53**(3-4), R52–R56.
- ÉRISTOV, V. S. (1967a). Computation of pressure tunnel linings in anisotropic rocks. *Hydrotechnical Construction* **1**(5), 436–442.
- ÉRISTOV, V. S. (1967b). Experimental studies of pressure-tunnel linings in anisotropic formations. *Hydrotechnical Construction* **1**(12), 1054–1057.
- FERRANTE, M. & BRUNONE, B. (2003a). Pipe system diagnosis and leak detection by unsteady-state tests. 1. Harmonic analysis. *Advances in Water Resources* **26**(1), 95–105.
- FERRANTE, M. & BRUNONE, B. (2003b). Pipe system diagnosis and leak detection by unsteady-state tests. 2. Wavelet analysis. *Advances in Water Resources* **26**(1), 107–116.
- FERREIRA, J. M. & BRANCO, C. M. (1991). Influence of misalignment on the fatigue strength of butt welds. *International Journal of Fatigue* **13**(5), 405–409.
- FKM-GUIDELINE (2003). FKM-Guideline–Analytical strength assessment of components in mechanical engineering. Tech. rep., Forschungskuratorium Maschinenbau (FKM), Frankfurt.

- FKM-GUIDELINE (2005). FKM-Guideline–Fracture mechanics proof of strength for engineering components. Tech. rep., Forschungskuratorium Maschinenbau (FKM), Frankfurt.
- FRANÇOIS, D., PINEAU, A. & ZAOUI, A. (2013). *Mechanical Behavior of Materials. Volume 2: Fracture Mechanics and Damage*, vol. 191 of *Solid Mechanics and its Applications*. Springer, Dordrecht Heidelberg London New York.
- FREEDMAN, D. & DIACONIS, P. (1981). On the histogram as a density estimator: l_2 theory. *Zeitschrift für Wahrscheinlichkeitstheorie und Verwandte Gebiete* **57**(4), 453–476.
- FREY, F. (2006). *Mécanique des structures: Analyse des structures et milieux continus*, vol. 2 of *Traité de Génie Civil de l'Ecole Polytechnique Fédérale de Lausanne*. Presses polytechniques et universitaires romandes (PPUR), Lausanne. In French.
- FRICKE, W. (2011). Fatigue strength assessment of local stresses in welded joints. In: *Fracture and fatigue of welded joints and structures* (MACDONALD, K. A., ed.). Woodhead Publishing Limited, Cambridge.
- FRICKE, W. (2012). *IIW Recommendations for the Fatigue Assessment of Welded Structures By Notch Stress Analysis: IIW-2006-09*. International Institute of Welding. Woodhead Publishing, Cambridge.
- FRICKE, W. (2013). IIW guideline for the assessment of weld root fatigue. *Welding in the World* **57**(6), 753–791.
- FU, B., HASWELL, J. V. & BETTESS, P. (1993). Weld magnification factors for semi-elliptical surface cracks in fillet welded T-butt joint models. *International Journal of Fracture* **63**(2), 155–171.
- GERCEK, H. (2007). Poisson's ratio values for rocks. *International Journal of Rock Mechanics & Mining Sciences* **44**(1), 1–13.
- GERRARD, C. M. (1977). Background to mathematical modelling in geomechanics: the roles of fabric and stress history. In: *Finite Elements in Geomechanics* (GUDEHUS, G., ed.). John Wiley & Sons, London New York Sydney Toronto.
- GERRARD, C. M. (1982). Equivalent elastic moduli of a rock mass consisting of orthorhombic layers. *International Journal of Rock Mechanics and Mining Sciences* **19**, 9–14.
- GHIDAOU, M. S., ZHAO, M., MCINNIS, D. A. & AXWORTHY, D. H. (2005). A review of water hammer theory and practice. *Applied Mechanics Reviews* **58**(1), 49–76.
- GMÜR, T. (2007). *Méthode des éléments finis en mécanique des structures*. Mécanique. Presses polytechniques et universitaires romandes (PPUR), Lausanne. In French.
- GMÜR, T. (2008). *Analyse modale numérique des systèmes mécaniques*. Mécanique. Presses polytechniques et universitaires romandes (PPUR), Lausanne. In French.

Bibliography

- GONZAGA, G. G., LEITE, M. H. & CORTHÉSY, R. (2008). Determination of anisotropic deformability parameters from a single standard rock specimen. *International Journal of Rock Mechanics & Mining Sciences* **45**, 1420–1438.
- GREINER, R., INNERHOFER, G. & STERING, W. (2013a). New design aspects for steel linings made of high-strength steel for pressure shafts. *Steel Construction* **6**(4), 280–286.
- GREINER, R., INNERHOFER SEN., G. & STERING, W. (2013b). New design aspects for steel linings of pressure shafts made of high strength steel. In: *Proceedings of the Conference on High Strength Steels for Hydropower Plants*. Graz, Austria: Graz University of Technology.
- GREINER, R. & LECHNER, A. (2013a). Fatigue strength of high strength steel-linings with different types of grouting openings. In: *Proceedings of the Conference on High Strength Steels for Hydropower Plants*. Graz, Austria: Graz University of Technology.
- GREINER, R. & LECHNER, A. (2013b). Fatigue strength of high strength steel-linings with different types of grouting openings. *Steel Construction* **6**(4), 287–293.
- GREINER, R., UNTERWEGER, H., LECHNER, A., KETTLER, M., STERING, W., MAYRHUBER, J., STERING, P., KIRILOWITSCH, C., MALDET, R., HAMMER, A., MEUSBURGER, P., MONSCHEIN, M., WERLE, L., HOFFMANN, W., MAYR, J. & NEUFELD, F. (2013c). Innovation in construction of steel linings of pressure shafts for pumped storage plants. FFG – Research Project 824592, 831613 and 836105, Österreichs E-Wirtschaft Forschung & Innovation, Österreichische Forschungsförderungsgesellschaft mbH (FFG).
- GRIFFITH, A. A. (1920). The phenomena of rupture and flow in solids. *Philosophical Transactions of the Royal Society of London. Series A, Containing Papers of a Mathematical or Physical Character* **221**, 163–198.
- GROSS, D. & SEELIG, T. (2011). *Fracture Mechanics—With an Introduction to Micromechanics*. Mechanical Engineering Series. Springer-Verlag Berlin Heidelberg, second ed.
- GUINEA, G. V., PLANAS, J. & ELICES, M. (2000). K_I evaluation by the displacement extrapolation technique. *Engineering Fracture Mechanics* **66**(3), 243–255.
- GURNEY, T. R. (2006). *Cumulative damage of welded joints*. Woodhead Publishing Ltd, Cambridge.
- HACHEM, F. & GIOVANOLA, F. (2013). Fatigue cracks propagation in steel-lined pressure shaft of pumped-storage power plants under normal operation conditions. In: *Proceedings of the Conference on High Strength Steels for Hydropower Plants*. Graz, Austria: Graz University of Technology.
- HACHEM, F. E. (2011). *Monitoring of steel-lined pressure shafts considering water-hammer wave signals and fluid-structure interaction*. Ph.D. thesis, Ecole Polytechnique Fédérale de Lausanne, Switzerland. And Vol. 49 of Communication of Laboratory of Hydraulic Constructions (LCH), EPFL, Ed. A. J. Schleiss, ISSN 1661-1179.

- HACHEM, F. E. & SCHLEISS, A. J. (2009). The design of steel-lined pressure tunnels and shafts. *International Journal on Hydropower and Dams* **16**(3), 142–151.
- HACHEM, F. E. & SCHLEISS, A. J. (2011a). Monitoring of steel-lined pressure shafts and tunnels. *Hydropower and Dams*, 74–77.
- HACHEM, F. E. & SCHLEISS, A. J. (2011b). Physical tests for estimating the water-hammer wave speed in pipes and tunnels with local weak wall stiffness. In: *Proceedings of the 2011 World Environmental and Water Resources Congress*. Palm Springs, California.
- HACHEM, F. E. & SCHLEISS, A. J. (2011c). A review of wave celerity in frictionless and axisymmetrical steel-lined pressure tunnels. *Journal of Fluids and Structures* **27**(2), 311–328.
- HACHEM, F. E. & SCHLEISS, A. J. (2012a). Detection of local wall stiffness drop in steel-lined pressure tunnels and shafts of hydroelectric power plants using steep pressure wave excitations and wavelet decomposition. *Journal of Hydraulic Engineering* **138**(1), 35–45.
- HACHEM, F. E. & SCHLEISS, A. J. (2012b). Effect of drop in pipe wall stiffness on water-hammer speed and attenuation. *Journal of Hydraulic Research* **50**(2), 218–227.
- HACHEM, F. E. & SCHLEISS, A. J. (2012c). Online monitoring of steel-lined pressure shafts by using pressure transient signals under normal operation conditions. *Journal of Hydraulic Engineering* **138**(12), 1110–1118.
- HACHEM, F. H. & SCHLEISS, A. J. (2011d). A model based approach for pipeline monitoring and leak locating. In: *Proceedings of the 34th IAHR World Congress*. Brisbane, Australia.
- HAGIN, B. (2005). Project Cleuson–Dixence and the accident on Dec. 12th, 2000. In: *Proceedings of the Conference on High Strength Steels for Hydropower Plants*. Graz, Austria: Graz University of Technology.
- HAKALA, M., KUULA, H. & HUDSON, J. (2007). Estimating the transversely isotropic elastic intact rock properties for in situ stress measurement data reduction: A case study of the Olkiluoto mica gneiss, Finland. *International Journal of Rock Mechanics and Mining Sciences* **44**(1), 14–46.
- HALDAR, A. & MAHADEVAN, S. (2000). *Probability, reliability, and statistical methods in engineering design*. John Wiley & Sons, Inc., New York.
- HAN, J. W., HAN, D. K. & HAN, S. H. (2014). Stress intensity factors for three-dimensional weld toe cracks using weld toe magnification factors. *Fatigue and Fracture of Engineering Materials and Structures* **37**(2), 146–156.
- HE, B. & ZHANG, X. (2011). Finite element calculation about stress concentration coefficient of welded butt joints based on the ABAQUS. *Applied Mechanics and Materials* **80–81**, 807–811.

Bibliography

- HEFNY, A. M. & LO, K. Y. (1999). Analytical solutions for stresses and displacements around tunnels driven in cross-anisotropic rocks. *International Journal for Numerical and Analytical Methods in Geomechanics* **23**(2), 161–177.
- HEINSBROEK, A. G. T. J. (1997). Fluid-structure interaction in non-rigid pipeline systems. *Nuclear Engineering and Design* **172**(1-2), 123–135.
- HO, N.-J. & LAWRENCE, F. V. (1984). Constant amplitude and variable load history fatigue test results and predictions for cruciform and lap welds. *Theoretical and Applied Fracture Mechanics* **1**(1), 3–21.
- HOBACHER, A. F. (1993). Stress intensity factors of welded joints. *Engineering Fracture Mechanics* **46**(2), 173–182.
- HOBACHER, A. F. (2008). Recommendations for fatigue design of welded joints and components. Recommendations IIW document IIW-1823-07 ex XIII-2151r4-07/XV-1254r4-07, International Institute of Welding, Paris, France.
- HOBACHER, A. F. (2009). The new IIW recommendations for fatigue assessment of welded joints and components – A comprehensive code recently updated. *International Journal of Fatigue* **31**(1), 50–58.
- HOBACHER, A. F. (2016). *Recommendations for fatigue design of welded joints and components*. IIW Collection. Springer International Publishing.
- HOMAND, F., MOREL, E., HENRY, J. P., CUXAC, P. & HAMMADE, E. (1993). Characterization of the moduli of elasticity of an anisotropic rock using dynamic and static methods. *International Journal of Rock Mechanics and Mining Sciences* **30**(5), 527–535.
- HOOKE, F. H. (1987). Aircraft structural reliability and risk analysis. In: *Probabilistic Fracture Mechanics and Reliability* (PROVAN, J. W., ed.). Martinus Nijhoff Publishers, Dordrecht, The Netherlands.
- HUANG, X. & MOAN, T. (2007). Improved modeling of the effect of r -ratio on crack growth rate. *International Journal of Fatigue* **29**(4), 591–602.
- HUGHES, T. J. R. (1987). *The Finite Element Method*. Prentice-Hall, Inc., Englewood Cliffs, New Jersey.
- HUTCHINSON, J. W. (1968). Singular behavior at the end of a tensile crack in a hardening material. *Journal of the Mechanics and Physics of Solids* **16**, 13–31.
- ISO 5817 (2014). *Welding – Fusion-welded joints in steel, nickel, titanium and their alloys (beam welding excluded) – Quality levels for imperfections*. European Committee for Standardization. ISO 5817:2014.

- ISO 9692-1 (2013). *Welding and allied processes – Types of joint preparation – Part 1: Manual metal-arc welding, gas-shielded metal-arc welding, gas welding, TIG welding and beam welding of steels*. European Committee for Standardization, Brussels. NF EN ISO 9692-1.
- JAEGER, C. (1977). *Fluid transients in Hydro-Electric Engineering Practice*. Blackie & Son Limited, Glasgow and London.
- JING, L. (2003). A review of techniques, advances and outstanding issues in numerical modelling for rock mechanics and rock engineering. *International Journal of Rock Mechanics & Mining Sciences* **40**(3), 283–353.
- JING, L. & HUDSON, J. A. (2002). Numerical methods in rock mechanics. *International Journal of Rock Mechanics & Mining Sciences* **39**(4), 409–427.
- JOHANSSON, M. & GYLLTOFT, K. (2002). Mechanical behavior of circular steel–concrete composite stub columns. *Journal of Structural Engineering* **128**(8), 1073–1081.
- JOHNSTON, G. O. (1982). A review of probabilistic fracture mechanics literature. *Reliability Engineering* **3**(6), 423–448.
- JONSSON, B. (2011). Improving weld class systems in assessing the fatigue life of different welded joint designs. In: *Fracture and fatigue of welded joints and structures* (MACDONALD, K. A., ed.). Woodhead Publishing Limited, Cambridge.
- JSSC (1995). Fatigue design recommendations for steel structures. English version, Japanese Society of Steel Construction, Tokyo.
- KANG, D.-H., JANG, C., PARK, Y.-S., HAN, S.-Y. & KIM, J. H. (2012). Fatigue reliability assessment of steel member using probabilistic stress-life method. *Advances in Mechanical Engineering* **2012**, 10 pages.
- KANNINEN, M. F. & POPELAR, C. H. (1985). *Advanced Fracture Mechanics*, vol. 15 of *Oxford Engineering Science Series*. Oxford University Press.
- KANTO, Y., ONIZAWA, K., MACHIDA, H., ISOBE, Y. & YOSHIMURA, S. (2010). Recent Japanese research activities on probabilistic fracture mechanics for pressure vessel and piping of nuclear power plant. *International Journal of Pressure Vessels and Piping* **87**(1), 11–16.
- KARIHALOO, B. & XIAO, Q. Z. (2003). 2.03 - Linear and nonlinear fracture mechanics. In: *Comprehensive Structural Integrity*, vol. 2. Pergamon, pp. 81–212.
- KAUFMANN, H., SONSINO, C. M., DEMOFONTI, G. & RISCIFULI, S. (2008). High-strength steels in welded state for light-weight constructions under high and variable stress peaks. *Steel Research International* **79**(5), 382–389.
- KERAMAT, A., TIJSSELING, A. S., HOU, Q. & AHMADI, A. (2012). Fluid-structure interaction with pipe-wall viscoelasticity during water hammer. *Journal of Fluids and Structures* **28**, 434–455.

Bibliography

- KIRKEMO, F. (1988). Applications of probabilistic fracture mechanics to offshore structures. *Applied Mechanics Reviews* **41**(2), 61–84.
- KLEMENC, J. & FAJDIGA, M. (2004). An improvement to the methods for estimating the statistical dependencies of the parameters of random load states. *International Journal of Fatigue* **26**(2), 141–154.
- KOCAŃDA, D. & JASZTAL, M. (2012). Probabilistic predicting the fatigue crack growth under variable amplitude loading. *International Journal of Fatigue* **39**(June), 68–74.
- KOÇAK, M. (2007). FITNET fitness-for-service procedure: an overview. *Welding in the World* **51**(5), 94–105.
- KOÇAK, M., SEIB, E. & MOTARJEMI, A. (2007a). Treatments of structural welds using FITNET fitness-for-service assessment procedure. *Welding in the World* **51**(5/6), 106–118.
- KOÇAK, M., WEBSTER, S. & HADLEY, I. (2007b). Fracture assessment of flaws in weldments using FITNET FFS procedure: an overview. *Key Engineering Materials* **345-346**, 401–409.
- KOÇAK, M., WEBSTER, S., JANOSCH, J. J., AINSWORTH, R. A. & KOERS, R. (2008). FITNET Fitness-for-Service (FFS) Procedure. Tech. rep. Revision MK8.
- KOCHUPILLAI, J., GANESAN, N. & PADMANABHAN, C. (2005). A new finite element formulation based on the velocity of flow for water hammer problems. *International Journal of Pressure Vessels and Piping* **82**(1), 1–14.
- KOFLER, W., SCHNEIDER, K. & SCHULER, X. (2015). Guideline for the assessment of fatigue loaded components in hydropower plants. *WasserWirtschaft* **1**, 99–103.
- KONDO, Y. (2003). 4.10 - Fatigue under variable amplitude loading. In: *Comprehensive Structural Integrity*, vol. 4. Pergamon, pp. 253–279.
- KOU, K. P. & BURDEKIN, F. M. (2006). Stress intensity factors for a wide range of long-deep semi-elliptical surface cracks, partly through-wall cracks and fully through-wall cracks in tubular members. *Engineering Fracture Mechanics* **73**(2), 1693–1710.
- KRANZ, B. & SONSINO, C. M. (2010). Verification of FAT values for the application of the notch stress concept with the reference radii $r_{\text{ref}} = 1.00$ and 0.05 mm. *Welding in the World* **54**(7/8), R218–224.
- KUIKEN, G. D. C. (1984). Wave propagation in fluid lines. *Applied Scientific Research* **41**(2), 69–91.
- KUIKEN, G. D. C. (1988). Amplification of pressure fluctuations due to fluid-structure interaction. *Journal of Fluids and Structures* **2**(5), 425–435.
- KUMAR, P. & SINGH, B. (1990). Design of reinforced concrete lining in pressure tunnels, considering thermal effects and jointed rockmass. *Tunnelling and Underground Space Technology* **5**(1/2), 91–101.

- KUMAR, V., GERMAN, M. D. & SHIH, C. F. (1981). An engineering approach for elastic-plastic fracture analysis. EPRI-Report NP-1931, Electric Power Research Institute (EPRI), Palo Alto, CA.
- KWON, H. J. (2007). Analysis of transient flow in a piping system. *KSCE Journal of Civil Engineering* **11**(4), 209–214.
- LASSEN, T. & SORENSEN, J. D. (2002). A probabilistic damage tolerance concept for welded joints. Part 1: data base and stochastic modelling. *Marine Structures* **15**(6), 599–613.
- LAVOOIJ, C. S. W. & TIJSSELING, A. S. (1991). Fluid-structure interaction in liquid-filled piping systems. *Journal of Fluids and Structures* **5**(5), 573–595.
- LAWN, B. R. (1993). *Fracture of Brittle Solids*. Cambridge Solid State Science, 2nd ed.
- LAWRENCE, F. V., HO, N.-J. & MAZUMDAR, P. K. (1981). Predicting the fatigue resistance of welds. *Annual Review of Materials Science* **11**(1), 401–425.
- LEANDER, J., AYGÜL, M. & NORLIN, B. (2013). Refined fatigue assessment of joints with welded in-plane attachments by LEFM. *International Journal of Fatigue* **56**, 25–32.
- LEKHNITSKII, S. G. (1963). *Theory of elasticity of an anisotropic elastic body*. Holden-Day, Inc., San Francisco.
- LI, C. Q. & YANG, S. T. (2012). Stress intensity factors for high aspect ratio semi-elliptical internal surface cracks in pipes. *International Journal of Pressure Vessels and Piping* **96-97**(August-September), 13–23.
- LI, Q. S., YANG, K. & ZHANG, L. (2003). Analytical solution for fluid-structure interaction in liquid-filled pipes subjected to impact-induced water hammer. *Journal of Engineering Mechanics* **129**(12), 1408–1417.
- LI, X., CHANG, J. & LI, C. (2014). Guide vane asynchronous closure mode for improving the transient quality of hydroturbine. *Chinese Journal of Hydroelectric Engineering* **33**(1), 202–206.
- LIE, S. T., VIPIN, S. P. & LI, T. (2015). New weld toe magnification factors for semi-elliptical cracks in double-sided T-butt joints and cruciform X-joints. *International Journal of Fatigue* **80**(November), 178–191.
- LIE, S. T., ZHAO, Z. & YAN, S. H. (2000). Two-dimensional and three-dimensional magnification factors, M_k , for non-load-carrying fillet welds cruciform joints. *Engineering Fracture Mechanics* **65**(4), 435–453.
- LIU, Y. & MAHADEVAN, S. (2009). Probabilistic fatigue life prediction using an equivalent initial flaw size distribution. *International Journal of Fatigue* **31**(3), 476–487.

Bibliography

- LOTSBERG, I. (2006). Fatigue design of plated structures using finite element analysis. *Ships and Offshore Structures* **1**(1), 45–54.
- LOTSBERG, I. (2008). Stress concentration factors at welds in pipelines and tanks subjected to internal pressure and axial force. *Marine Structures* **21**(2-3), 138–159.
- LOTSBERG, I. (2009a). Stress concentrations at butt welds in pipelines. *Marine Structures* **22**(2), 335–337.
- LOTSBERG, I. (2009b). Stress concentrations due to misalignment at butt welds in plated structures and at girth welds in tubulars. *International Journal of Fatigue* **31**(8-9), 1337–1345.
- LOTSBERG, I. & SIGURDSSON, G. (2006a). Hot spot stress S-N curve for fatigue analysis of plated structures. *Journal of Offshore Mechanics and Arctic Engineering* **128**(November), 330–336.
- LÜ, Q., SUN, H.-Y. & LOW, B. K. (2011). Reliability analysis of ground-support interaction in circular tunnels using the response surface method. *International Journal of Rock Mechanics & Mining Sciences* **48**(8), 1329–1343.
- LUKIĆ, M. & CREMONA, C. (2001). Probabilistic assessment of welded joints versus fatigue and fracture. *Journal of Structural Engineering* **127**(2), 211–218.
- MADDOX, S. J. (1991). *Fatigue strength of welded structures*. Abington Publishing.
- MADDOX, S. J. (2011). Fatigue design rules for welded structures. In: *Fracture and fatigue of welded joints and structures* (MACDONALD, K. A., ed.). Woodhead Publishing Limited, Cambridge.
- MADENCI, E. & GUVEN, I. (2006). *The Finite Element Method and Applications in Engineering using ANSYS*. Springer.
- MALJAARS, J., STEENBERGEN, H. M. G. M. & VROUWENVELDER, A. C. W. M. (2012). Probabilistic model for fatigue crack growth and fracture of welded joints in civil engineering structures. *International Journal of Fatigue* **38**, 108–117.
- MANN, T. (2006). *Fatigue assessment methods for welded structures and their application to an aluminium T-joint*. Ph.D. thesis, Norwegian University of Science and Technology, Trondheim, Norway.
- MANNING, S. D., YANG, J. N. & RUDD, J. L. (1987). Durability of aircraft structures. In: *Probabilistic Fracture Mechanics and Reliability* (PROVAN, J. W., ed.). Martinus Nijhoff Publishers, Dordrecht, The Netherlands.
- MANSO, P. A., SCHAEFLI, B. & SCHLEISS, A. J. (2016a). Adaptation of Swiss hydropower infrastructure to meet future electricity needs. *Renewable Energy* (Submitted in 2016, under review process).

- MANSO, P. A., SCHLEISS, A. J., STÄHLY, M. & AVELLAN, F. (2016b). Electricity supply and hydropower development in Switzerland. *International Journal of Hydropower and Dams* (5).
- MATLAB® (2012). *version 8.0.0.783 (R2012b)*. Natick, Massachusetts: The MathWorks Inc.
- MAZZOCCHI, E. (2014). Monitoring of steel-lined pressure tunnels and shafts by active pressure signal analysis. Master thesis, Ecole Polytechnique Fédérale de Lausanne, Switzerland.
- MAZZOCCHI, E., PACHOUD, A. J., FARHAT, M., E., H. F., DE CESARE, G. & SCHLEISS, A. J. (2016). Signal analysis of an actively generated cavitation bubble in pressurized pipes for detection of wall stiffness drops. *Journal of Fluids and Structures* **65**(August), 60–75.
- MCFADYEN, N. B., BELL, R. & VOSIKOVSKY, O. (1990). Fatigue crack growth of semi-elliptical surface cracks. *International Journal of Fatigue* **12**(1), 43–50.
- MECOZZI, E., LECCA, M., SORRENTINO, S., LARGE, M., DAVIES, C., GOUVEIA, H., MAIA, C., ERDELEN-PEPPLER, M., KARAMANOS, S. & PERDIKARIS, P. (2010). Fatigue behaviour of high-strength steel-welded joints in offshore and marine systems (FATHOMS). Tech. Rep. EUR 24214 EN, European Commission, Research Fund for Coal and Steel.
- MIKKOLA, E., MURAKAMI, Y. & MARQUIS, G. (2015). Equivalent rack approach for fatigue life assessment of welded joints. *Engineering Fracture Mechanics* **149**(November), 144–155.
- MILNE, I., AINSWORTH, R. A., R., D. A. & T., S. A. (1988a). Assessment of the integrity of structures containing defects. *International Journal of Pressure Vessels and Piping* **32**(1-4), 3–104.
- MILNE, I., AINSWORTH, R. A., R., D. A. & T., S. A. (1988b). Background to and validation of CEBG Report R/H/R6–Revision 3. *International Journal of Pressure Vessels and Piping* **32**(1-4), 105–196.
- MISIUNAS, D., VITKOVSKY, J., OLSSON, G., SIMPSON, A. & LAMBERT, M. (2005). Pipeline break detection using pressure transient monitoring. *Journal of Water Resources Planning and Management* **131**(4), 316–325.
- MOUSSOU, P. (2013). On the coincidence of the acoustical and mechanical natural frequencies of a pressure vessel. *Journal of Pressure Vessel Technology* **135**(3), 030902.
- MUHAMMED, A. (2007). Background to the derivation of partial safety factors for BS 7910 and API 579. *Engineering Failure Analysis* **14**(3), 481–488.
- MULLER, G. (2016). Design of steel-lined pressure tunnels and shafts: new and innovative probabilistic approaches for reliability assessment. Master thesis, Ecole Polytechnique Fédérale de Lausanne, Switzerland.
- MURAKAMI, Y. (1987a). *Stress Intensity Factors Handbook*, vol. 1. Pergamon Press, New York.
- MURAKAMI, Y. (1987b). *Stress Intensity Factors Handbook*, vol. 2. Pergamon Press, New York.

Bibliography

- NAKASONE, Y., YOSHIMOTO, S. & STOLARSKI, T. A. (2006). *Engineering Analysis With ANSYS Software*. Elsevier Butterworth-Heinemann.
- NEWMAN JR, J. C. (1973). Fracture analysis of surface- and through-cracked sheets and plates. *Engineering Fracture Mechanics* **5**(3), 667–689.
- NEWMAN JR, J. C. & RAJU, I. S. (1980). Stress-intensity factors for internal surface cracks in cylindrical pressure vessels. *Journal of Pressure Vessel Technology* **102**(4), 342–346.
- NEWMAN JR, J. C. & RAJU, I. S. (1981a). An empirical stress-intensity factor equation for the surface crack. *Engineering Fracture Mechanics* **15**(1-2), 185–192.
- NEWMAN JR, J. C. & RAJU, I. S. (1981b). Stress intensity factor equations for cracks in three-dimensional finite bodies. NASA Technical Memorandum 83200, NASA.
- NEWMAN JR, J. C. & RAJU, I. S. (1984). Stress intensity factor equations for cracks in three-dimensional finite bodies subjected to tension and bending loads. NASA Technical Memorandum 85793, NASA.
- NICOLET, C. (2007). *Hydroacoustic modeling and numerical simulation of unsteady operation of hydroelectric systems*. Ph.D. thesis, Ecole Polytechnique Fédérale de Lausanne, Switzerland.
- NICOLET, C., BERTHOD, R., RUCHONNET, N. & AVELLAN, F. (2010). Evaluation of possible penstock fatigue resulting from secondary control for the grid. In: *Proceedings of HYDRO 2010*. Lisbon, Portugal.
- NIEMI, E., FRICKE, W. & MADDOX, S. J. (2006). *Fatigue analysis of welded components—Designer's guide to the structural hot-spot stress approach: IIW-1430-00*. International Institute of Welding. Woodhead Publishing, Cambridge.
- NIU, X. & GLINKA, G. (1987). The weld profile effect on stress intensity factors in weldments. *International Journal of Fracture* **35**(1), 3–20.
- NIU, X. & GLINKA, G. (1989). Stress-intensity factors for semi-elliptical surface cracks in welded joints. *International Journal of Fracture* **40**(4), 255–270.
- NUSSBAUMER, A., BORGES, L. & DAVAINÉ, L. (2011). *Fatigue design of steel and composite structures*. ECCS Eurocode design manuals. European Convention for Constructional Steelwork.
- NYKÄNEN, T. & BJÖRK, T. (2015). Assessment of fatigue strength of steel butt-welded joints in as-welded condition—Alternative approaches for curve fitting and mean stress effect analysis. *Marine Structures* **44**(December), 288–310.
- NYKÄNEN, T., BJÖRK, T. & LAITINEN, R. (2013). Fatigue strength prediction of ultra high strength steel butt-welded joints. *Fatigue and Fracture of Engineering Materials and Structures* **36**(6), 469–482.

- NYKÄNEN, T., LI, X., BJÖRK, T. & MARQUIS, G. (2005). A parametric fracture mechanics study of welded joints with toe cracks and lack of penetration. *Engineering Fracture Mechanics* **72**(10), 1580–1609.
- NYKÄNEN, T., MARQUIS, G. & BJÖRK, T. (2007). Fatigue analysis of non-load-carrying fillet welded cruciform joints. *Engineering Fracture Mechanics* **74**(3), 399–415.
- OHTANI, Y., KOGUCHI, H. & YADA, T. (1991a). Non-linear analysis of strain concentration occurring at welded joint with initial distortion in a spherical pressure vessel. *International Journal of Pressure Vessels and Piping* **45**(1), 3–21.
- OHTANI, Y., KOGUCHI, H. & YADA, T. (1991b). Nonlinear stress analysis for thin spherical vessels with local non-axisymmetric imperfections. *International Journal of Pressure Vessels and Piping* **45**(3), 289–299.
- OLSSON, R., LINDBLOM, U. & GLAMHEDEN, R. (1997). Design of pressure shafts in recognition of rock structure and stress. In: *Tunnelling Asia '97*. New Delhi, India.
- ONG, L. S. & HOON, K. H. (1996). Bending stresses at longitudinal weld joints of pressurized cylindrical shells due to angular distortion. *Journal of Pressure Vessel Technology* **118**(3), 369–373.
- PACHOUD, A. J., MANSO, P. A. & SCHLEISS, A. J. (2017). New parametric equations to estimate notch stress concentration factors at butt welded joints modeling the weld profile with splines. *Engineering Failure Analysis* **72**(February), 11–24.
- PACHOUD, A. J. & SCHLEISS, A. J. (2016). Stresses and displacements in steel-lined pressure tunnels and shafts in anisotropic rock under quasi-static internal water pressure. *Rock Mechanics and Rock Engineering* **49**(4), 1263–1287.
- PALMBERG, B., BLOM, A. F. & EGGWERTZ, S. (1987). Probabilistic damage tolerance analysis of aircraft structures. In: *Probabilistic Fracture Mechanics and Reliability* (PROVAN, J. W., ed.). Martinus Nijhoff Publishers, Dordrecht, The Netherlands.
- PARIS, P. & ERDOGAN, F. (1963). A critical analysis of crack propagation laws. *Journal of Basic Engineering* **85**(4), 528–533.
- PARK, W. & MIKI, C. (2008). Fatigue assessment of large-size welded joints based on the effective notch stress approach. *International Journal of Fatigue* **30**(9), 1556–1568.
- PEDERSEN, M. M., MOURITSEN, O. O., HANSEN, M. R., ANDERSEN, J. G. & WENDERBY, J. (2010a). Re-analysis of fatigue data for welded joints using the notch stress approach. *International Journal of Fatigue* **32**(10), 1620–1626.
- PEDERSEN, M. M., MOURITSEN, O. O., HANSEN, M. R. & ANDERSEN, J. G. (2010b). Experience with the notch stress approach for fatigue assessment of welded joints. In: *Proceedings of Swedish Conference on Lightweight Optimised Welded Structures, LOST*. Borlänge, Sweden.

Bibliography

- PIJPERS, R. J. M. (2011). *Fatigue strength of welded connections made of very high strength cast and rolled steels*. Ph.D. thesis, Technische Universiteit Delft, Netherlands.
- PIJPERS, R. J. M., KOLSTEIN, M. H., ROMEIJN, A. & BIJLAARD, F. S. K. (2009). Fatigue experiments on very high strength steel base material and transverse butt welds. *Advanced Steel Construction* **5**(1), 14–32.
- PILKEY, W. D. & PILKEY, D. F. (2008). *Peterson's stress concentration factors*. John Wiley & Sons, Inc., Hoboken, New Jersey, third ed.
- PINEAU, A. & PARDOEN, T. (2007). 2.06 - Failure of metals. In: *Comprehensive Structural Integrity*, vol. 2. Pergamon, pp. 684–797.
- POPESCU, M., ARSENIE, D. & VLASE, P. (2003). *Applied Hydraulic Transients*. A.A. Balkema Publishers, Lisse, The Netherlands.
- POSTOL'SKAYA, O. K. (1986). Effect of the structure of a rock mass and properties of rocks on the stress state of hydraulic pressure tunnels. *Hydrotechnical Construction* **20**(1), 25–30.
- POUTIAINEN, I., TANSKANEN, P. & MARQUIS, G. (2004). Finite element methods for structural hot spot stress determination—a comparison of procedures. *International Journal of Fatigue* **26**(11), 1147–1157.
- PROVAN, J. W. (1987). Probabilistic approaches to the material-related reliability of fracture-sensitive structures. In: *Probabilistic Fracture Mechanics and Reliability* (PROVAN, J. W., ed.). Martinus Nijhoff Publishers, Dordrecht, The Netherlands.
- PYTTEL, B., VARFOLOMEYEV, I., LUKE, M., BERGER, C. & SIEGELE, D. (2007). Fkm guideline "fracture mechanics proof of strength for engineering components"—Overview and extension topics. *Welding in the World* **51**(5), 85–93.
- R6 REVISION 4 (2009). Assessment of the integrity of structures containing defects. Tech. Rep. Amendment 7, British Energy Generation Limited, Gloucester, UK.
- RABBAT, B. G. & RUSSELL, H. G. (1985). Friction coefficient of steel on concrete or grout. *Journal of Structural Engineering* **111**(3), 505–515.
- RADAJ, D. (1990). *Design and analysis of fatigue resistant welded structures*. Abington Publishing, Cambridge.
- RADAJ, D. (1996). Review of fatigue strength assessment of nonwelded and welded structures based on local parameters. *International Journal of Fatigue* **18**(3), 153–170.
- RADAJ, D. (2006). *Fatigue assessment of welded joints by local approaches*. Woodhead Publishing Limited, Cambridge, 2nd ed.
- RADAJ, D., LAZZARIN, P. & BERTO, F. (2013). Generalised Neuber concept of fictitious notch rounding. *International Journal of Fatigue* **51**(June), 105–115.

- RADAJ, D., SONSINO, C. M. & FRICKE, W. (2009). Recent developments in local concepts of fatigue assessment of welded joints. *International Journal of Fatigue* **31**(1), 2–11.
- RADAJ, D. & ZHANG, S. (1991). Multiparameter design optimisation in respect of stress concentrations. In: *Engineering Optimization in Design Processes*, vol. 63 of *Lecture Notes in Engineering*. Springer Berlin Heidelberg, pp. 181–189.
- RAHMAN, S. (1997). Probabilistic fracture analysis of cracked pipes with circumferential flaws. *International Journal of Pressure Vessels and Piping* **70**(3), 223–236.
- RAJU, I. S. & NEWMAN JR, J. C. (1979). Stress-intensity factors for a wide range of semi-elliptical surface cracks in finite-thickness plates. *Engineering Fracture Mechanics* **11**(4), 817–829.
- RAJU, I. S. & NEWMAN JR, J. C. (1982). Stress-intensity factors for internal and external surface cracks in cylindrical vessels. *Journal of Pressure Vessel Technology* **104**(4), 293–298.
- RAMBERG, W. & OSGOOD, W. R. (1943). Description of stress-strain curves by three parameters. Technical Note No. 902, National Advisory Committee For Aeronautics, Washington DC.
- REMES, H. (2008). *Strain-based approach to fatigue strength assessment of laser-welded joints*. Ph.D. thesis, Helsinki University of Technology (TKK), Espoo, Finland.
- REMES, H. & VARSTA, P. (2010). Statistics of weld geometry for laser-hybrid welded joints and its application within notch stress approach. *Welding in the World* **54**(7), R189–R207.
- RIBORDY, L. (1998). Le puits blindé et le répartiteur de l'aménagement Cleuson-Dixence. *Wasser, Energie, Luft - Eau, Energie, Air* (3/4), 53–60.
- RICE, J. R. (1968). A path independent integral and the approximate analysis of strain concentration by notches and cracks. *Journal of Applied Mechanics* **35**(2), 379–386.
- RICE, J. R. & ROSENGREN, G. F. (1968). Plane strain deformation near a crack tip in a power-law hardening material. *Journal of the Mechanics and Physics of Solids* **16**(1), 1–12.
- RIGHINIOTIS, T. D. & CHRYSSANTHOPOULOS, M. K. (2003). Probabilistic fatigue analysis under constant amplitude loading. *Journal of Constructional Steel Research* **59**(7), 867–886.
- RIGHINIOTIS, T. D. & CHRYSSANTHOPOULOS, M. K. (2004). Fatigue and fracture simulation of welded bridge details through a bi-linear crack growth law. *Structural Safety* **26**(2), 141–158.
- ROOS, E., STADTMÜLLER, W., CERJAK, H. & DIMMLER, G. (2005). Results of fracture mechanics investigations on steel S890 and its weldments. In: *Proceedings of the Conference on High Strength Steels for Hydropower Plants*. Graz, Austria: Graz University of Technology.
- ROOS, E., WACKENHUT, G., LAMMERT, R. & SCHULER, X. (2011). Probabilistic safety assessment of components. *International Journal of Pressure Vessels and Piping* **88**(1), 19–25.

Bibliography

- SCHIJVE, J. (2012). Fatigue predictions of welded joints and the effective notch stress concept. *International Journal of Fatigue* **45**, 31–38.
- SCHLEISS, A. J. (1988). Design criteria applied for the lower pressure tunnel of the North Fork Stanislaus River hydroelectric project in California. *Rock Mechanics and Rock Engineering* **21**(3), 161–181.
- SCHLEISS, A. J. (2012). Triebwassersysteme bei Wasserkraftanlagen – Herausforderungen und Tendenzen für die Linienführung und Auskleidung / Waterway systems for hydropower plants – Challenges and tendencies for alignment and lining. In: *Swiss Tunnel Congress*. Luzern, Switzerland.
- SCHLEISS, A. J. (2013). Competitive pumped-storage projects with vertical pressure shafts without steel linings / Konkurrenzfähige Pumpspeicherwerkprojekte dank ungepanzelter, vertikaler Druckschächte. *Geomechanics and Tunneling* **6**(5), 456–463.
- SCHLEISS, A. J. & MANSO, P. A. (2012). Design of pressure relief valves for protection of steel-lined pressure shafts and tunnels against buckling during emptying. *Rock Mechanics and Rock Engineering* **45**(1), 11–20.
- SCHWALBE, K.-H. (1998). The engineering flaw assessment method (EFAM). *Fatigue & Fracture of Engineering Materials & Structures* **21**(10), 1203–1213.
- SCHWALBE, K.-H., KIM, Y.-J., HAO, S., CORNEC, A. & KOÇAK, M. (1997). EFAM ETM-MM 96–the ETM Method for assessing the significance of crack-like defects in joints with mechanical heterogeneity (strength mismatch). GKSS Report GKSS 97/ E/9, GKSS Research Center, Geesthacht, Germany.
- SCHWALBE, K.-H., LANDES, J. D. & HEERENS, J. (2003). 7.02 - Classical fracture mechanics methods. In: *Comprehensive Structural Integrity*, vol. 7. Pergamon, pp. 3–42.
- SCHWALBE, K.-H. & ZERBST, U. (2003). 7.04 - Crack driving force estimation methods. In: *Comprehensive Structural Integrity*, vol. 7. Pergamon, pp. 133–176.
- SCHWALBE, K.-H., ZERBST, U., KIM, Y.-J., BROCKS, W., CORNEC, A., HEERENS, J. & AMSTUTZ, H. (1998). EFAM ETM 97–the ETM Method for assessing crack-like defects in engineering structures. GKSS Report GKSS 98/ E/6, GKSS Research Center, Geesthacht, Germany.
- SCHWARZ, M. & ZEMAN, J. L. (1997). Discussion: "Bending stresses at longitudinal weld joints of pressurized cylindrical shells due to angular distortion" (Ong, L. S., and Hoon, K. H., 1996, ASME J. Pressure Vessel Technol., 118, pp. 369–373). *Journal of Pressure Vessel Technology* **119**(2), 245–246.
- SEEBER, G. (1985). Power conduits for high-head plants; part two. *Water Power & Dam Construction* **37**, 95–98.

- SENN, J. (2014). Design of steel-lined pressure shafts and tunnels considering the initial gap between the steel liner and surrounding materials. Master thesis, Ecole Polytechnique Fédérale de Lausanne, Switzerland.
- SHAMLOO, H. & HAGHIGHI, A. (2009). Leak detection in pipelines by inverse backward transient analysis. *Journal of Hydraulic Research* **47**(3), 311–318.
- SHARMA, S. C., SHARMA, M. K. V. & ROUTELA, T. S. (1997). Design of steel liners in pressure shafts for Theri Power Plant (HPP). In: *Tunnelling Asia '97*. New Delhi, India.
- SHARPLES, J. K., AINSWORTH, R. A., BUDDEN, P. J. & DOWLING, A. R. (2003). Developments in UK defect assessment procedures R6 Revision 4 and BS7910. In: *Proceedings of the 3rd International Conference on Strength, Durability and Stability of Materials and Structures, SDSMS'03*. Klaipeda, Lithuania.
- SHEN, G. & GLINKA, G. (1991). Weight functions for a surface semi-elliptical crack in a finite thickness plate. *Theoretical and Applied Fracture Mechanics* **15**(3), 247–255.
- SHEN, G., PLUMTREE, A. & GLINKA, G. (1991). Weight function for the surface point of semi-elliptical surface crack in a finite thickness plate. *Engineering Fracture Mechanics* **40**(1), 167–176.
- SHIH, C. F., MORAN, B. & NAKAMURA, T. (1986). Energy release rate along a three-dimensional crack front in a thermally stressed body. *International Journal of Fracture* **30**(2), 79–102.
- SINGH, B. (1973). Continuum characterization of jointed rock masses: Part I—The constitutive equations. *International Journal of Rock Mechanics and Mining Sciences & Geomechanics Abstracts* **10**(4), 311–335.
- SINTAP (1999). Structural integrity assessment procedure. EU-project BE 95-1462, Brite Euram Programme, Brussels.
- SONSINO, C. M. (2004). Principles of variable amplitude fatigue design and testing. *Journal of ASTM International* **1**(10), 1–21.
- SONSINO, C. M. (2007). Fatigue testing under variable amplitude loading. *International Journal of Fatigue* **29**(6), 1080–1089.
- SONSINO, C. M. (2009a). A consideration of allowable equivalent stresses for fatigue design of welded joints according to the notch stress concept with the reference radii $r_{\text{ref}} = 1.00$ and 0.05 mm. *Welding in the World* **53**(3/4), R64–R73.
- SONSINO, C. M. (2009b). Effect of residual stresses on the fatigue behaviour of welded joints depending on loading conditions and weld geometry. *International Journal of Fatigue* **31**(1), 88–101.

Bibliography

- SONSINO, C. M. (2011). Reliability aspects in fatigue design of welded structures using selected local approaches: the example of K-nodes for offshore constructions. In: *Fracture and fatigue of welded joints and structures* (MACDONALD, K. A., ed.). Woodhead Publishing Limited, Cambridge.
- SONSINO, C. M., BRUDER, T. & BAUMGARTNER, J. (2010). S-N lines for welded thin joints - suggested slopes and FAT values for applying the notch stress concept with various reference radii. *Welding in the World* **54**(11/12), R375–R392.
- SONSINO, C. M., FRICKE, W., DE BRUYNE, F., HOPPE, A., AHMADI, A. & ZHANG, G. (2012). Notch stress concepts for the fatigue assessment of welded joints – Background and applications. *International Journal of Fatigue* **34**(1), 2–16.
- STENBERG, T., BARSOUM, Z. & BALAWI, S. O. M. (2015). Comparison of local stress based concepts–Effects of low-and high cycle fatigue and weld quality. *Engineering Failure Analysis* **57**(November), 323–333.
- STEPHENS, M. L., SIMPSON, A. R. & LAMBERT, M. F. (2008). Internal wall condition assessment for water pipelines using inverse transient analysis. In: *Proceedings of the 10th Annual Water Distribution Systems Analysis Conference WDSA 2008*. Kruger National Park, South Africa.
- SVENSSON, T., JOHANNESSON, P. & DE MARÉ, J. (2005). Fatigue life prediction based on variable amplitude tests–specific applications. *International Journal of Fatigue* **27**(8), 966–973.
- TADA, H., PARIS, P. C. & IRWIN, G. R. (1985). *The Stress Analysis of Cracks Handbook*. Paris Productions Incorporated.
- TENG, T.-L., FUNG, C.-P. & CHANG, P.-H. (2002). Effect of weld geometry and residual stresses on fatigue in butt-welded joints. *International Journal of Pressure Vessels and Piping* **79**(7), 467–482.
- TERÁN, G., ALBITER, A. & CUAMATZI-MELÉNDEZ, R. (2013). Parametric evaluation of the stress concentration factors in T-butt welded connections. *Engineering Structures* **56**(November), 1484–1495.
- TIJSSELING, A. S. (1996). Fluid-structure interaction in liquid-filled pipe systems: A review. *Journal of Fluids and Structures* **10**(2), 109–146.
- TIJSSELING, A. S. (2003). Exact solution of linear hyperbolic four-equation system in axial liquid-pipe vibration. *Journal of Fluids and Structures* **18**(2), 179–196.
- TIJSSELING, A. S. (2007). Water hammer with fluid-structure interaction in thick-walled pipes. *Computers and Structures* **85**(11-14), 844–851.
- TIMOSHENKO, S. P. & GOODIER, J. N. (1970). *Theory of elastic stability*. MacGraw-Hill International, 3rd ed.

- TONON, F. & AMADEI, B. (2003). Stresses in anisotropic rock masses: an engineering perspective building on geological knowledge. *International Journal of Rock Mechanics and Mining Sciences* **40**(7-8), 1099–1120.
- TRAN MANH, H., SULEM, J. & SUBRIN, D. (2014). A closed-form solution for tunnels with arbitrary cross section excavated in elastic anisotropic ground. *Rock Mechanics and Rock Engineering* .
- TSAI, C.-H. & WU, W.-F. (1994). On the application of probabilistic fracture mechanics to the reliability and inspection of pressure vessels. *International Journal of Pressure Vessels and Piping* **59**(1-3), 323–333.
- USACE (1997). *Tunnels and shafts in rock (EM 1110-2-2901)*. U.S. Army Corps of Engineers.
- VALDEOLIVAS, J. L. G. & MOSQUERA, J. C. (2013). A full 3D finite element model for buckling analysis of stiffened steel liners in hydroelectric pressure tunnels. *Journal of Pressure Vessel Technology* **135**(6), 061205.
- VALDEOLIVAS, J. L. G. & MOSQUERA, J. C. (2015a). Consideration of geometric imperfections in three-dimensional finite element model analysis of stiffened steel liners subjected to external pressure. *Journal of Pressure Vessel Technology* **137**(4), 041202.
- VALDEOLIVAS, J. L. G. & MOSQUERA, J. C. (2015b). Three-dimensional FEM parametric analysis of stiffened steel liners in hydroelectric pressure tunnels. *Journal of Pipeline Systems Engineering and Practice* , 04015019.
- VGB (2014). *VGB Standard: Assessment of fatigue loaded components in hydropower plants*. VGB PowerTech e.V. (VGB-S-034-00-2014-10-EN).
- VIGL, A. (2013). Conventional design of HPP pressure shafts according to G. Seeber, considering the surrounding rock mass. In: *Proceedings of the Conference on High Strength Steels for Hydropower Plants*. Graz, Austria: Graz University of Technology.
- WALBRIDGE, S. (2005). *A probabilistic study of fatigue in post-weld treated tubular bridge structures*. Ph.D. thesis, Ecole Polytechnique Fédérale de Lausanne, Switzerland.
- WALTERS, M. C., PAULINO, G. H. & DODDS JR., R. H. (2005). Interaction integral procedures for 3-D curved cracks including surface tractions. *Engineering Fracture Mechanics* **72**(11), 1635–1663.
- WANG, F. & CUI, W. (2009). Approximate method to determine the model parameters in a new crack growth rate model. *Marine Structures* **22**(4), 744–757.
- WANG, T., YANG, J. G., LIU, X. S., DONG, Z. B. & FANG, H. Y. (2012a). Solution of stress intensity factor for mode I center crack in undermatched butt joint with certain reinforcement. *Science and Technology of Welding and Joining* **17**(3), 191–195.

Bibliography

- WANG, T., YANG, J. G., LIU, X. S., DONG, Z. B. & FANG, H. Y. (2012b). Stress intensity factor expression for butt joint with single-edge crack considering the effect of joint shape. *Materials and Design* **36**, 748–756.
- WANG, X. & LAMBERT, S. B. (1995a). Local weight functions for semi-elliptical surface cracks in finite thickness plates. *Theoretical and Applied Fracture Mechanics* **23**(3), 199–208.
- WANG, X. & LAMBERT, S. B. (1995b). Stress intensity factors for low aspect ratio semi-elliptical surface cracks in finite-thickness plates subjected to nonuniform stresses. *Engineering Fracture Mechanics* **51**(4), 517–532.
- WANG, X. & LAMBERT, S. B. (1996). Stress intensity factors and weight functions for longitudinal semi-elliptical surface cracks in thin pipes. *International Journal of Pressure Vessels and Piping* **65**(1), 75–87.
- WANG, X. & LAMBERT, S. B. (1997). Stress intensity factors and weight functions for high aspect ratio semi-elliptical surface cracks in finite-thickness plates. *Engineering Fracture Mechanics* **57**(1), 13–24.
- WANG, X. & LAMBERT, S. B. (1998). Weight functions and stress intensity factors for semi-elliptical cracks in T-plate welded joints. *Fatigue and Fracture of Engineering Materials and Structures* **21**(1), 99–117.
- WEBSTER, S. & BANNISTER, A. (2000). Structural integrity assessment procedure for Europe – of the SINTAP programme overview. *Engineering Fracture Mechanics* **67**(6), 481–514.
- WELLEIN, R. (1987). Applications of PFM in the nuclear industry to reactor pressure vessel, main coolant piping and steel containment. In: *Probabilistic Fracture Mechanics and Reliability* (PROVAN, J. W., ed.). Martinus Nijhoff Publishers, Dordrecht, The Netherlands.
- WHEELER, O. E. (1972). Spectrum loading and crack growth. *Journal of Basic Engineering* **94**(1), 181–186.
- WIESNER, C. S., MADDOX, S. J., XU, W., WEBSTER, G. A., BURDEKIN, F. M., ANDREWS, R. M. & HARRISON, J. D. (2000). Engineering critical analyses to BS 7910 – the UK guide on methods for assessing the acceptability of flaws in metallic structures. *International Journal of Pressure Vessels and Piping* **77**(14-15), 883–893.
- WILLENBORG, J., ENGLE, R. M. & WOOD, R. A. (1971). A crack growth retardation model using an effective stress concept. Technical Memorandum AFFDL-TM-71-1-FBR, Air Force Flight Dynamics Laboratory.
- WITTKE, W. (1990). *Rock Mechanics: Theory and Applications with Case Histories*. Springer-Verlag Berlin Heidelberg New York.
- WYLIE, E., SUO, L. & STREETER, V. (1993). *Fluid Transients in Systems*. Prentice Hall, Fascimile Edition.

- YAMADA, K. & NAGATSU, S. (1989). Evaluation of scatter in fatigue life of welded details using fracture mechanics. *Structural Engineering / Earthquake Engineering* **6**(1), 13s–21s.
- YANG, J. N., HSI, W. H., MANNING, S. D. & RUDD, J. L. (1987). Stochastic crack growth models for applications to aircraft structures. In: *Probabilistic Fracture Mechanics and Reliability* (PROVAN, J. W., ed.). Martinus Nijhoff Publishers, Dordrecht, The Netherlands.
- YUNG, J. Y. & LAWRENCE, F. V. (1985). Analytical and graphical aids for the fatigue design of weldments. SAE Technical Paper 850803, College of Engineering, University of Illinois, Urbana-Champaign.
- ZAHOOR, A. (1989). Ductile fracture handbook. Research Project 1757-69, vol. 1, Novotech Corporation and EPRI, Palo Alto, CA.
- ZAHOOR, A. (1990). Ductile fracture handbook. Research Project 1757-69, vol. 2, Novotech Corporation and EPRI, Palo Alto, CA.
- ZAHOOR, A. (1991). Ductile fracture handbook. Research Project 1757-69, vol. 3, Novotech Corporation and EPRI, Palo Alto, CA.
- ZEMAN, J. L. (1944). On the problem of angular misalignment at longitudinal weld joints of cylindrical shells. *International Journal of Pressure Vessels and Piping* **58**(2), 179–184.
- ZERBST, U., AINSWORTH, R. A., BEIER, H. T., PISARSKI, H., ZHANG, Z. L., NIKBIN, K., NITSCHKE-PAGEL, T., MÜNSTERMANN, S., KUCHARCZYK, P. & KLINGBEIL, D. (2014). Review on fracture and crack propagation in weldments – A fracture mechanics perspective. *Engineering Fracture Mechanics* **132**(0), 200–276.
- ZERBST, U., SCHÖDEL, M., WEBSTER, S. & AINSWORTH, R. A. (2007). *Fitness-for-Service Fracture Assessment of Structures Containing Cracks*. Elsevier, London.
- ZERBST, U., SCHWALBE, K.-H. & AINSWORTH, R. A. (2003). 7.01 - An overview of failure assessment methods in codes and standards. In: *Comprehensive Structural Integrity*, vol. 7. Pergamon, pp. 1–48.
- ZERJESKI, B. (2007). Pressurized waterway structures. Lecture Notes, Master of Advanced Studies (MAS) in Water Resources Management and Engineering, Ecole Polytechnique Fédérale de Lausanne, Switzerland.
- ZHANG, L. (1999). FSI analysis of liquid-filled pipes. *Journal of Sound and Vibration* **224**(1), 69–99.
- ZHANG, Y.-H. & MADDUX, S. J. (2009). Investigation of fatigue damage to welded joints under variable amplitude loading spectra. *International Journal of Fatigue* **31**(1), 138–152.
- ZIENKIEWICZ, O. C., TAYLOR, R. L. & ZHU, J. Z. (2005). *The Finite Element Method: Its Basis and Fundamentals*. Elsevier, Butterworth-Heinemann.



Acknowledgments

The present research work was performed at the Laboratory of Hydraulic Constructions (LCH) at the Ecole Polytechnique Fédérale de Lausanne. It was funded by the Swiss Competence Center Energy and Mobility (CCEM) within the consortium *HydroNet 2: Modern methodologies for design, manufacturing and operation of hydropower plants*. The author also wishes to acknowledge the contribution of the Swiss Competence Center for Energy Research–Supply of Electricity (SCCER-SoE) and the support of the Swiss Committee On Dams (SwissCOD).

My first expression of gratitude goes to my thesis director Prof. Anton J. Schleiss, who gave me the opportunity to conduct this Ph.D. research project. I owe him my deepest thanks for trusting in my abilities, and for his invaluable guidance, at the same time pragmatic, benevolent and propitious to letting me the freedom to develop my ideas. It was an honor to work under his supervision, and to receive such a scientific, technical and intellectual heritage that I will carry during my entire career.

Secondly, I wish to address my deepest gratitude to my thesis co-director Dr Pedro A. Manso. In addition of sharing his remarkable scientific and technical knowledge, Dr Manso has been an unfailing personal support during my research, and a colleague and friend with inexhaustible passions to share with.

I also would like to thank Dr Giovanni De Cesare and Dr Michael Pfister, with who I had the chance to collaborate in applied research projects and teaching. I am indebted to both of them for their remarkable knowledge, and the amazing moments we shared.

I wish to deeply thank Prof. Alain Nussbaumer, Prof. Georgios Anagnostou and Dr Olivier Chène for being part of the jury of this work, as well as Prof. Katrin Beyer for being the president of the jury. A special mention goes to Prof. Nussbaumer, for his availability and the great values of the technical discussions we had.

I would like to address my acknowledgments to Dr Olivier Chène (ALPIQ) and to Mr Peter Zsak (Pöyry), for their availability and the very helpful technical discussions we could have. I also send them my gratitude for giving me the privilege to visit the construction site of Nant de Drance.

Acknowledgments

The contribution of Dr Fadi Hachem (Stucky SA, a Gruner company) is also acknowledged, for providing the data from his measurements on prototype do develop the loading spectrum.

A very special thank goes to the three Master students that performed astonishing works within the scope of this research, Mrs Jade Senn, Mr Eugenio Mazzocchi, and Mrs Gabrielle Muller. It has been a great pleasure to collaborate with them. I wish to acknowledge their contributions and their great achievements. I also deeply thank Dr Thomas Menouillard (Stucky SA, a Gruner company), for his involvement within the work of Mrs Senn and his invaluable support in computational mechanics, Dr Mohamed Farhat (LMH, EPFL) and Dr Fadi Hachem (Stucky SA, a Gruner company), for their great guidance and scientific expertise within the work of Mr Mazzocchi. I also wish to acknowledge again the contribution of Prof. Nussbaumer within the work of Mrs Muller.

Furthermore, I would like to thank my great colleagues and friends at LCH. During four years, I shared amazing moments with this incredible team. Working in such an intellectual, multi-cultural, creative and humorous ambiance was an invaluable chance. I have learned a lot from each member of the team, scientifically as much as on a personal level. My very special mention goes to Fränz, with who I shared an amazing period of nine years, rich of music, crazy laughs, and great support during our studies in civil engineering. Special reference also goes to Dr Jose Pedro Matos, for his brilliant help in numerical methods and algorithms, and to Nicolas, what have we laughed, *une fois*. I finally specially acknowledge the contributions of Sara and Sev, for the *Sommario* and the *Zusammenfassung*, respectively.

My journey through my university studies was also greatly influenced by many amazing friends, with who my soul and body were fed with arts, travels, sport and many wonderful moments. For the reasons they may know, Witek, Amaia, Nicolas, Raf, Marvin, Camille, Pascal, Floriane, Victor, Mathieu, Maud and Julien, thank you. Many others cannot be named but, I am sure, know the acknowledgments they deserve.

Finally, my love and gratitude goes to my family, and particularly to my parents Diane and Christophe, and my brothers Romain and Mathieu. I had the invaluable chance to receive an education and an unfailing support which allowed me to make the decisions I believed in. Thank you for these loving, true, humble and intense relations.

Finalmente, but not least, few words implying great love and feelings are dedicated to *ma Puce*.

Lausanne, October 2016

ALEXANDRE J. PACHOUD

Curriculum Vitae

ALEXANDRE JEAN PACHOUD

Nationality: French
Date of birth: May 7, 1988
Contact: alexandre.pachoud@alumni.epfl.ch



EDUCATION

2012–2016	Ph.D. in Civil Engineering Laboratory of Hydraulic Constructions (LCH) Ecole Polytechnique Fédérale de Lausanne (EPFL), Switzerland
2010–2012	Master of Science (M.Sc.) in Civil Engineering Specialization in Hydraulics and Energy, focus on Computational Mechanics Ecole Polytechnique Fédérale de Lausanne (EPFL), Switzerland
2007–2010	Bachelor of Science (B.Sc.) in Civil Engineering Ecole Polytechnique Fédérale de Lausanne (EPFL), Switzerland
2006–2007	Classe préparatoire aux Grandes Ecoles (CPGE) Physics, Chemistry and Engineering Sciences (PCSI) Lycée du Parc, Lyon (69), France
2006	French Scientific Baccalaureate With honors Lycée Pasquet, Arles (13), France

Curriculum Vitae

AWARDS

- 2012 **IM Prize (Bureau d'ingénieurs Maggia)**
Reward the Master thesis performed at the Laboratory of Hydraulic
Constructions (LCH) at the Ecole Polytechnique Fédérale de Lausanne
(EPFL), Switzerland, on the influence of anisotropic rock behavior on
the design of steel-lined pressure tunnels and shafts

PROFESSIONAL EXPERIENCE

- 2012–2016 **Ph.D. student and scientific assistant on applied research projects** at
the Laboratory of Hydraulic Constructions (LCH) at the Ecole Polytech-
nique Fédérale de Lausanne (EPFL), Switzerland
Main applied research project: *Pumpspeicherwerk Grimsel III: Hy-
draulische Modellversuche des Ein- und Auslaufbauwerks im Räterichs-
bodensee*, Experimental hydraulic study on the formation of vortices
at an inlet/outlet of a pumped-storage hydropower plant and velocity
measurements by means of Ultrasonic Velocity Profiler to assess flow
separation at the Y-junction
- 2011 **Internship at STUCKY SA** (5 weeks, Renens, Switzerland)
Numerical dynamics of an existing dam in Switzerland (Zsoil), visit of
the studied dam
- 2010 **Internship at KÄLIN & CUEREL SA** (8 weeks, Lausanne, Switzer-
land)
Design of concrete and steel structures (Cubus), visits of construction
sites

COMPUTER SKILLS

- | | |
|---------------------------|--|
| Numerical
Computation | ANSYS (Mechanical APDL), Zsoil, Cubus, SIMSEN |
| Programming | MATLAB, basics of C++ |
| Computed-
aided design | AutoCAD |
| Office | MS Office (Word, Excel, PowerPoint), L ^A T _E X, OpenOffice |

TEACHING

2012–2016 **Doctoral assistant** at the Laboratory of Hydraulic Constructions (LCH) at the Ecole Polytechnique Fédérale de Lausanne (EPFL), Switzerland

- Supervision of 6 Master theses (design and monitoring of steel-lined pressure tunnels and shafts, design of floating ports, design of small-hydropower plants)
- Supervision of several semester projects in civil engineering (design of arch dams, design of small-hydropower plants, design of floating ports)
- Doctoral assistant for several Bachelor and Master courses in civil engineering (General Physics, Hydraulic Networks, Linear Algebra, Hydraulic Structures)

2010–2012 **Teaching assistant** at the Ecole Polytechnique Fédérale de Lausanne (EPFL), Switzerland

- Teaching assistant for several Bachelor courses in civil engineering (General Physics, Statics)

PEER-REVIEWED SCIENTIFIC PUBLICATIONS

Pachoud, A. J. & Schleiss, A. J. (2016) Stresses and displacements in steel-lined pressure tunnels and shafts in anisotropic rock under quasi-static internal water pressure. *Rock Mechanics and Rock Engineering* 49(4):1263-87

Mazzocchi, E., **Pachoud, A. J.**, Farhat, M., Hachem, F. E., De Cesare, G. & Schleiss, A. J. (2016) Signal analysis of an actively generated cavitation bubble in pressurized pipes for detection of wall stiffness drops. *Journal of Fluids and Structures* 65(August):60-75

Pachoud, A. J., Manso, P. A. & Schleiss, A. J. (2017) New parametric equations to estimate notch stress concentration factors at butt welded joints modeling the weld profile with splines. *Engineering Failure Analysis* 72(February):11-24

Curriculum Vitae

PROCEEDINGS OF CONFERENCES

Pachoud, A. J. & Schleiss, A. J. (2015) Parametric study of steel-lined pressure shafts in anisotropic rock. In *Proceedings of the ITA World Tunnel Congress and 41st General Assembly*, Dubrovnik, Croatia

Pachoud, A. J. & Schleiss, A. J. (2014) Steel-lined pressure tunnels and shafts in anisotropic rock. In *Proceedings of the 3rd IAHR Europe Congress: Water-Engineering and Research*. Porto, Portugal

Pachoud, A. J. & De Cesare, G. (2014) Flow field UVP measurements of a Y-shape outlet structure. In *Proceedings of the 9th International Symposium on Ultrasonic Doppler Methods for Fluid Mechanics and Fluid Engineering*, Strasbourg, France

PRESENTATIONS IN CONFERENCES

Pachoud, A. J., Manso, P. A. & Schleiss, A. J. (2016) Parametric study of stress concentration factors for longitudinal butt welded joints of steel penstocks and liners. Presentation given at the *Seventh International Conference on Engineering Failure Analysis ICEFA VII*, Leipzig, Germany

Pachoud, A. J. & Schleiss, A. J. (2015) Parametric study of steel-lined pressure shafts in anisotropic rock. Presentation given at the *ITA World Tunnel Congress and 41st General Assembly*, Dubrovnik, Croatia

Pachoud, A. J. & Schleiss, A. J. (2014) Steel-lined pressure tunnels and shafts in anisotropic rock. Presentation given at the *3rd IAHR Europe Congress: Water-Engineering and Research*. Porto, Portugal

LINGUISTIC PROFICIENCY

French	Mother tongue
English	Fluent, TOEFL iBT 108/120 (2012)
Spanish	Intermediate, B1
German	Beginner, A0/A1

